

# Theoretical and Numerical Study of Shallow Water Models. Applications to Nearshore Hydrodynamics

Fabien Marche

*Current address:* Mathématiques Appliquées de Bordeaux, Université de Bordeaux, 351 cours de la Libération, 33405 Talence, France.

*E-mail address:* `Fabien.Marche@math.u-bordeaux1.fr`

ABSTRACT. In this study we focus on theoretical and numerical questions around the shallow water equations. The first part is devoted to the formal derivation of a new viscous shallow water model with friction and surface tension extra terms. We perform then a mathematical analysis of the obtained model in order to obtain existence results for global weak solutions.

In the second part we develop a new numerical well-balanced model which appears to be particularly well-suited for problems involving a moving shoreline and strong topography variations, in a two dimensional framework.

The third part is devoted to the applications of our numerical model to several problems concerning nearshore hydrodynamics. More precisely, the propagation in coastal domains of long waves regarded as tsunamis are first investigated. Then we perform a study of nonlinear wave/currents interactions in the Inner Surf Zone.

---

# Remerciements

Je tiens tout d'abord à manifester ma plus profonde et sincère reconnaissance envers mes co-directeurs de thèse Pierre Fabrie, Professeur au laboratoire de Mathématiques Appliquées de Bordeaux (MAB) et Philippe Bonneton du Département Géologie et Océanographie (DGO), Chargé de recherches au CNRS, pour m'avoir offert la possibilité de réaliser ce travail.

Pierre a toujours fait preuve d'une totale confiance, d'un soutien et d'une gentillesse permanente à mon égard et malgré ses lourdes fonctions administratives en tant que directeur de l'école d'Ingénieur MATMECA, a toujours su trouver du temps à m'accorder.

Les nombreux échanges scientifiques avec Philippe m'ont permis de découvrir et apprécier un champ d'investigation nouveau pour moi. Sa rigueur scientifique, ses conseils avisés, ses encouragements, sa disponibilité et sa gentillesse m'ont énormément aidé et motivé dans la réalisation de cette thèse, et plus particulièrement dans les moments difficiles, où le doute m'effleurait.

Tout deux ont su m'orienter et m'apporter l'optimisme et la confiance en soi nécessaire à la réalisation d'un tel projet. Pour tout cela, merci...

J'exprime mes plus vifs remerciements aux Professeurs Eric Barthélémy et Thierry Gallouët pour avoir accepté d'être rapporteurs de cette thèse. Leurs remarques pertinentes et conseils avisés m'ont permis d'améliorer de manière significative la qualité de ce travail. Thierry Gallouët n'a pas pu figurer parmi ce jury mais je le remercie tout particulièrement pour sa disponibilité, au travers de nos quelques échanges électroniques.

Je suis sensible à l'honneur que me fait le Professeur Thierry Colin en ayant accepté de présider ce jury.

Je remercie tous les membres du jury de s'être intéressé à cette étude en acceptant de lui apporter leurs compétences et leur attention. Merci en particulier à Michel Benoit pour avoir accepté de participer à mon jury et pour l'intérêt qu'il porte à mon travail.

Un grand merci supplémentaire à David Lannes, qui a su trouver le temps de m'orienter, m'aider et m'encourager au quotidien pour la partie théorique de ce travail, ainsi qu'à Franck Boyer pour son aide ponctuelle.

Merci également à Emmanuel Audusse, à Benoît Desjardins, au Professeur Alain-Yves Leroux et à Nicolas Seguin pour nos échanges autour des équations de Saint-Venant. Vos conseils et travaux m'ont largement inspirés...

Ces trois années auraient été bien morôses sans leur présence au laboratoire : un grand merci à Vincent, Nancy et Thomas pour m'avoir supporté et aidé au quotidien.

Une pensée pour mon ami Bruno, exilé en Australie depuis un an, qui a su me soutenir et m'aider pendant cette thèse, même d'aussi loin. J'espère que nous aurons l'occasion de collaborer dans un futur proche.

Une pensée également pour Carl, instructeur de Shaolin Quanfa. La pratique de cet art martial, tout comme celle du travail de recherche, implique une réalisation de longue haleine au travers un travail rigoureux et quotidien. Carl, ce que j'apprends grâce à tes enseignements transparaît dans de nombreux autres domaines de mon existence. Ta passion est communicative et je souhaite une longue vie à ton école.

La présence d'amis de longue date est toujours bénéfique, quelque soient nos objectifs. Un grand merci à Alex et Antoine, Julien et Delphine, Thomas, James, Ben, FX, Djé, Gwendal, Muriel, Audrey et tant d'autres... Merci à vous tous pour votre présence durant ces trois années. J'espère vous garder longtemps près de moi.

Je profite également de cette page pour remercier une personne à qui je dois beaucoup. Jean-Pierre, tu lira j'espère ces lignes un jour. Saches que tu as su m'aider et changer beaucoup de chose en moi, il y a maintenant presque dix ans. Je n'ai jamais eu l'occasion de te remercier de vive voix, j'espère pouvoir le faire un jour.

Enfin je remercie de tout mon coeur ma famille, et tout particulièrement mes parents et ma soeur. Sans votre soutien et votre amour sans faille, tout ceci n'aurait jamais pu aboutir et je vous serai éternellement reconnaissant d'avoir su me donner les moyens d'arriver jusqu'ici. Aucun mot ne saurait décrire ma pensée, aussi c'est à vous que je dédis ce travail, tout simplement...

Pour finir, merci à ma douce Dorothée, pour sa patience et son soutien durant ces six derniers mois, et plus généralement pour tout l'amour que je reçois au quotidien. Puisse cette thèse être le début de la réalisation de nos rêves...



---

# Contents

Remerciements	iii
Introduction générale	1
<b>Part 1. Theoretical study</b>	
Introduction	13
Chapter 1. Derivation of a new two-dimensional viscous shallow water model	19
1.1. The Navier-Stokes-Coriolis system and boundary conditions	19
1.2. The non-dimensionalized system	24
1.3. The vertically averaged non-dimensionalized system	28
1.4. The Shallow Water system	30
Chapitre 2. Existence de solutions faibles globales	35
2.1. Principaux résultats	36
2.2. Résolution de l'équation de conservation de la hauteur d'eau	39
2.3. Problème approché	48
2.4. Existence d'une solution faible en dimension 1	69
2.5. Existence d'une solution faible en dimension 2	86
Conclusion	95
<b>Part 2. Numerical resolution</b>	
Introduction and numerical strategy	99
Chapter 3. Numerical resolution of the hyperbolic system with bed-slope term	111
3.1. Governing equations and Finite Volume framework	111
3.2. Well-balanced methods	117

3.3. Numerical considerations	131
3.4. Numerical assessments	135
Chapter 4. Improvement of the accuracy at the shoreline	141
4.1. The hydrostatic reconstruction method	141
4.2. The homogeneous “positivity preserving” VFRoe-ncv solver	142
4.3. Discretization of the source term	145
4.4. Second order accuracy: an adapted MUSCL reconstruction	147
4.5. Boundary conditions	157
4.6. Numerical assessments for moving shoreline problems	164
Chapter 5. Numerical method for the resolution of the source terms	185
5.1. Centered discretization of the viscous terms	186
5.2. Centered discretization of the capillary/surface tension terms	191
5.3. Discretization of the parabolic equation	194
5.4. Second order accuracy in time	197
5.5. Numerical assessments	198
Conclusion	203
<b>Part 3. Applications to nearshore hydrodynamics</b>	
Introduction	207
Chapter 6. Simulation of run-up process	209
6.1. Tsunamis and run-up models	209
6.2. One-dimensional run-up and reflexion of a solitary wave over a sloping beach	214
6.3. A two-dimensional test for the run-up of large tsunami waves	215
6.4. Two-dimensional run-up on a conical island	227
Chapter 7. Simulation of breaking waves in the Inner Surf Zone	241
7.1. Introduction	241
7.2. A one dimensional test for breaking wave propagation in the Inner Surf Zone	250
7.3. Wave propagation over a periodical ridge and runnel system	252
Conclusion	263
Conclusion et perspectives	265
Publications	269
Bibliography	271

---

# Introduction générale

La circulation de masses d'eau en milieu littoral est contrôlée principalement par les transformations non-linéaires de la houle et de la marée, liées à la forte diminution de la profondeur d'eau à l'approche du rivage. La compréhension et la modélisation de ces processus hydrodynamiques représentent un enjeu scientifique important, en particulier si l'on veut être capable de prévoir l'évolution morphodynamique du littoral (zones d'embouchures estuariennes et lagunaires, plages sableuses et formation de barres, etc...) et l'impact d'éventuels aménagements.

L'objectif de cette thèse concerne la dérivation de modèles théoriques et le développement d'outils de simulation numérique permettant d'appréhender les écoulements littoraux et l'hydrodynamique associée à la transformation de la houle en milieux peu profonds en présence ou non de marée. Le domaine d'étude est de l'ordre de quelques kilomètres carrés à quelques centaines de kilomètres carrés. Cofinancée par le CNRS et le Conseil Régional d'Aquitaine, cette thèse repose sur une collaboration transverse associant deux UMR Bordeaux 1/CNRS : le Laboratoire de Mathématiques Appliquées (MAB) et le Département de Géologie et Océanographie DGO (UMR EPOC). Plus généralement, les travaux effectués au cours de cette thèse s'intègrent d'une part dans le cadre des activités du Réseau littoral Aquitain et d'autre part dans le cadre du programme national "Atmosphère et Océan à Multi-échelles" (PATOM) de l'INSU.

S'il est possible de calculer la propagation et la transformation des vagues à partir de la résolution des équations de Navier-Stokes diphasiques (NSD) pour des cas idéalisés à petite échelle, il est nécessaire d'adopter une démarche différente lorsque l'on s'intéresse à la modélisation hydrodynamique en milieu naturel aux échelles qui nous intéressent. En l'état actuel, les modèles décrivant la génération des courants par la houle et leurs interactions ne sont pas entièrement satisfaisants tant d'un point de vue théorique que numérique, en particulier en milieu peu profond.

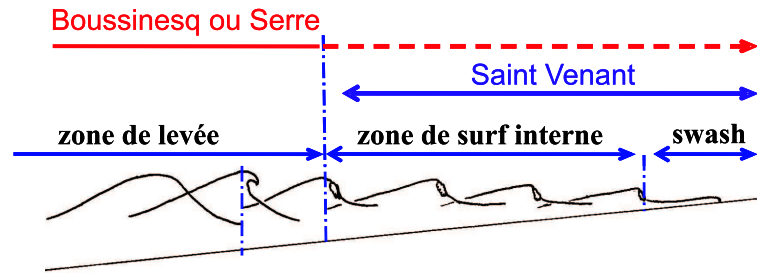


**Figure 0.0.1.** Représentation schématisée de la zone de surf et du domaine de validité des modèles BSV (Bonneton [18]).

Dans la zone littorale, l'échelle horizontale caractéristique de l'écoulement moyen est grande devant la profondeur d'eau. En particulier, l'approximation des "ondes longues", c'est à dire des ondes pour lesquelles la profondeur d'eau est petite devant la longueur d'onde, semble bien adaptée à la description de phénomènes tels que marées, propagation de houle dans la zone de surf interne et zone de swash, ou encore propagation d'ondes de type tsunamis. Il apparaît donc naturel d'essayer de réduire la complexité du problème en travaillant non plus sur les équations tri-dimensionnelles du mouvement, mais sur un système d'équations bi-dimensionnelles obtenu par intégration suivant la verticale des équations de Navier-Stokes. Dans cette optique, deux approches peuvent être envisagées. La première se situe dans un contexte de modélisation statistique 2DH de l'évolution morphodynamique des plages sableuses pour des échelles de temps qui vont de quelques cycles de marée à quelques mois. L'idée est de traiter de façon déterministe les processus lents et de façon statistique les processus rapides. Pour cela, une séparation d'échelles temporelles est effectuée et les équations intégrées selon la verticale sont filtrées. La seconde approche concerne la modélisation de la propagation des ondes de surface en milieu peu profond par les équations bi-dimensionnelles de type Boussinesq d'une part et Saint-Venant d'autre part (Boussinesq et/ou Saint-Venant noté BSV dans la suite). Ici, le calcul de l'évolution temporelle à haute fréquence de l'hydrodynamique est effectué, donnant accès à des valeurs instantanées de certaines quantités caractéristiques (vitesse, vorticité, etc...) et cette approche peut être utilisée également pour déterminer avec précision les variables hydrodynamiques moyennées sur une période de vague.

Nous nous focalisons dans cette étude sur cette dernière approche et en particulier sur le système de Saint-Venant. Ce système permet en effet de décrire de façon naturelle la propagation de vagues dans la zone de surf. Bien sûr, la variabilité verticale de l'écoulement, ainsi que la turbulence ne sont pas explicitement calculées. Toutefois de nombreuses études ont montré que ce modèle décrit de façon très satisfaisante la transformation de la houle à l'approche du rivage et particulièrement dans la zone de surf interne. La classification des différentes zones, ainsi que le domaine de validité des modèles Boussinesq et Saint-Venant sont illustrés Figure 0.0.1.

Le système de Saint-Venant initialement introduit dans sa version mono-dimensionnelle dans un *Compte Rendu* à l'Académie des Sciences en 1871 par A.J.C. Barré de Saint-Venant est un système hyperbolique décrivant l'écoulement d'eau dans un canal rectiligne à fond plat en terme de hauteur d'eau  $h(t, x)$  et de vitesse moyennée selon la direction verticale  $u(t, x)$  :

$$\begin{aligned}\partial_t h + \partial_x(hu) &= 0, \\ \partial_t(hu) + \partial_x\left(hu^2 + \frac{1}{2}gh^2\right) &= 0.\end{aligned}$$

où  $g$  désigne la gravité. La seconde variable conservative  $m(t, x) = h(t, x)u(t, x)$  considérée dans ce modèle désigne le débit. Dans sa version bi-dimensionnelle, ce modèle permet de modéliser bon nombre de phénomènes impliquant des fluides géophysiques à surface libre en écoulement "peu profond". Ce système peut inclure de nombreux termes sources adaptés aux besoins spécifiques des phénomènes modélisés, comme des termes tenant compte des variations de topographie, des termes dissipatifs de diffusion ou de friction ou encore des termes générateurs de mouvements tenant compte par exemple de l'influence du vent en surface. Son champ de validité et d'application s'avère donc être très étendu.

Le travail présenté dans cette thèse s'articule autour de trois parties. La première partie concerne une étude théorique d'un modèle de Saint-Venant bi-dimensionnel comprenant sa dérivation rigoureuse à partir des équations de Navier-Stokes puis la démonstration d'un résultat d'existence de solutions globales pour ce système, dans un sens faible. La deuxième partie s'attachera à la mise en place et à la validation d'une méthode de résolution numérique adaptée à nos besoins et permettant de lever partiellement quelques difficultés récurrentes dans la modélisation des phénomènes de propagation d'ondes longues dans les domaines littoraux. Enfin la troisième et dernière partie sera l'occasion de valider le modèle numérique obtenu à l'aide de cas concrets et plus réalistes du point de vue physique. Les études numériques réalisées dans cette partie concernent notamment le run-up d'ondes de type "tsunamis", ainsi que la transformation et la propagation de la houle sur des topographies réalistes. Plus précisément, le détail des différents chapitres sera le suivant :

## Première partie - Etude théorique

Le premier Chapitre est consacré à la dérivation par analyse asymptotique d'un modèle de Saint-Venant bi-dimensionnel incluant des termes de diffusion, de friction, de tension de surface, de Coriolis, ainsi qu'un terme tenant compte des variations de topographie. Cette dérivation est une généralisation au cas bi-dimensionnel du travail effectué par Gerbeau et Perthame [62] dans le cas uni-dimensionnel.

La dérivation des équations de Saint-Venant en tant que système hyperbolique homogène du premier ordre est classique. Cependant, très peu de travaux concernent la dérivation rigoureuse de modèles visqueux, et beaucoup moins encore de modèles bi-dimensionnel visqueux. Les termes visqueux sont donc souvent ajoutés aux modèles

*a posteriori* sans justifications satisfaisantes. Par ailleurs, l'inclusion d'autres termes sources particuliers comme les termes de friction quadratiques de type Manning, Chezy ou Strickler, les termes de tension de surface ou encore de forçage en surface reposant sur des approximations empiriques, paramétrisations des petites échelles, est également non justifiée d'un point de vue mathématique.

Nous proposons donc ici la dérivation d'un modèle de Saint-Venant bi-dimensionnel visqueux à partir des équations de Navier-Stokes homogènes et incompressibles, dans un domaine borné et régulier de  $\mathbb{R}^3$ , en milieu tournant. Cette dérivation résulte de l'approximation de "couche mince" (ou d'"onde longue") permettant une analyse asymptotique en fonction du rapport  $\varepsilon$  des échelles caractéristiques des mouvements verticaux et horizontaux. Les conditions aux limites appliquées sont de type surface libre avec continuité des contraintes à l'interface air-fluide et tension de surface (phénomènes de capillarité). Le fond est considéré variable et nous introduisons des conditions aux limites de friction (lois de paroi laminaire et quadratique au fond). Les principaux apports de ce travail concernent d'une part l'extension bi-dimensionnelle d'une méthode introduite initialement dans le cas uni-dimensionnel [62], ainsi qu'une justification asymptotique de la présence de termes de diffusion, friction et tension de surface, puisqu'ils sont ici obtenus directement à partir de l'analyse asymptotique. Le caractère bi-dimensionnel de la dérivation fera en particulier apparaître une formulation nouvelle du terme de diffusion. Le modèle dérivé et étudié tout au long de cette thèse est le suivant :

$$\left\{ \begin{array}{l} \partial_t h + \operatorname{div}(h\mathbf{u}) = 0, \\ \partial_t(h\mathbf{u}) + \operatorname{div}(h\mathbf{u} \otimes \mathbf{u}) + g h \nabla h = \\ -\alpha_0(h) \mathbf{u} - \alpha_1(h) h |\mathbf{u}| \mathbf{u} + \mu \operatorname{div} \left( h D(\mathbf{u}) + (2h \operatorname{div} \mathbf{u}) \mathcal{I} \right) \\ + \beta h \nabla \Delta h - f(h\mathbf{u})^\perp - g h \nabla d + \beta h \nabla \Delta d. \end{array} \right.$$

où

$$\alpha_0(h) = \frac{k_l}{1 + \frac{k_l h}{3\mu}}, \quad \alpha_1(h) = \frac{k_t}{\left(1 + \frac{k_l h}{3\mu}\right)^2},$$

et

$$D(\mathbf{u}) = \frac{1}{2} \left( \nabla \mathbf{u} + {}^t \nabla \mathbf{u} \right).$$

Dans ce modèle,  $h(t, x, y)$  et  $\mathbf{u}(t, x, y)$  désignent respectivement la hauteur de la colonne d'eau et la vitesse intégrée selon la direction verticale.  $g$ ,  $f$ ,  $\mu$ ,  $k_l$ ,  $k_t$  et  $\beta$  désignent respectivement l'accélération de pesanteur, le paramètre de Coriolis et les coefficients de viscosité, de friction laminaire et quadratique et de tension de surface.

Le Chapitre 2 est consacré à la démonstration de résultats d'existence de solutions faibles globales pour le modèle précédent. La démonstration proposée ici repose sur des méthodes classiques d'analyse non-linéaire, à savoir l'obtention d'une formulation variationnelle approchée du problème et l'utilisation d'un théorème de point fixe, ici le théorème de point fixe de Schauder. Dans un second temps, l'obtention d'inégalités d'énergie, d'estimation *a priori* sur les solutions approchées permet le passage à la limite dans la formulation approchée. Les critères de compacités nécessaires au passage à la limite s'inspire d'une part des travaux effectués par Bresh et Desjardins [51] dans le cas d'un modèle de Saint-Venant bi-dimensionnel avec terme visqueux classique et coefficients de friction constants, et d'autre part des travaux de Simon [158] et Boyer et Fabrie [22] dans le cadre des équations de Navier-Stokes non-homogènes. Dans le cas uni-dimensionnel, un théorème d'existence de solutions faibles globales pour le modèle complet est obtenu. L'apport de ce résultat vis à vis de celui introduit par Bresh et Desjardins concerne la prise en compte d'une part du terme de viscosité particulier et d'autre part des coefficients de friction  $\alpha_0(h)$  et  $\alpha_1(h)$ . Cependant ce résultat n'a pu être obtenu pour l'instant que sur le modèle uni-dimensionnel.

En effet, dans le cas bi-dimensionnel, des difficultés supplémentaires apparaissent, imputables en particulier à la forme non classique du terme de diffusion qui interdit la simple généralisation de la démonstration effectuée dans le cas uni-dimensionnel, et aux coefficients de friction laminaire et quadratique  $\alpha_0(h)$  et  $\alpha_1(h)$  dont la dépendance en  $h$  conduit à des estimations plus faibles sur la vitesse  $\mathbf{u}$  que celles obtenues en dimension un. Pour lever ces difficultés, un modèle simplifié a donc été étudié et une hypothèse sur la positivité de la solution approchée  $h(t, x, y)$  a été faite.

## Deuxième partie - Etude numérique

La deuxième partie de ce travail concerne l'implémentation d'une méthode numérique permettant de discrétiser le modèle précédent. Le système de Saint-Venant peut être considéré selon deux approches radicalement différentes. D'une part sa dérivation et bon nombre de ses applications physiques mettent en évidence ses relations avec les équations de Navier-Stokes et les méthodes de type éléments finis développées depuis plusieurs dizaines d'années pour la résolution des équations de Navier-Stokes incompressibles peuvent être en partie adaptées. D'autre part, les propriétés mathématiques du système homogène soulignent son caractère hyperbolique et les analogies avec les équations de la dynamique des gaz. L'étude des systèmes hyperboliques du premier ordre, apparaissant dans la modélisation de nombreux phénomènes physiques comme la dynamique des gaz en variables eulériennes ou encore l'électromagnétique, est actuellement un des grands champs d'investigation de l'étude des équations aux dérivés partielles. Ainsi, considérer le caractère hyperbolique du système de Saint-Venant peut nous permettre de bénéficier de l'expérience acquise dans ces autres domaines. C'est dans cette seconde optique que se situe notre approche numérique.

Pour le choix d'une méthode numérique adaptée, nous nous sommes attachés à analyser avec soin les processus physiques impliqués dans le type d'applications recherchées. Les principales caractéristiques considérées, ainsi que les réponses proposées du point de vue numérique sont les suivantes :

- (1) Tout d'abord, les processus de déferlement des vagues dans la zone de surf conduisent à des phénomènes de distorsion des vagues, menant à la formation de fronts d'onde particulièrement raides et à une forme de vagues caractéristique, dite en "dent de scie". De plus, il est classique dans le Génie Côtier d'estimer la dissipation dans les vagues ayant déferlé en faisant une analogie entre ces fronts d'onde et le ressaut hydraulique propagatif, utilisant la théorie hyperbolique des ondes de choc. Ces constatations ont conduit peu à peu à l'adaptation des méthodes de type Volume Finis utilisant un solveur de Riemann afin de permettre la capture et la propagation de discontinuités isolées et d'obtenir une bonne estimation de la dissipation d'énergie sans ajouter de termes correctifs. Nous nous sommes donc orientés vers le choix de méthodes Volumes Finis sur maillage structuré régulier ou non, avec solveurs de Riemann exacts ou approchés. En outre, le caractère souvent fortement diffusif des schémas d'ordre un nous amène à considérer une extension vers un schéma quasi d'ordre deux par une méthode de reconstruction de variables et de limitation de pentes (MUSCL). Dans une optique similaire, Bonneton et Vincent ont déjà développé un code Volumes Finis uni-dimensionnel, *SURF\_SV*, basé sur un schéma du second ordre de type MacCormack. Ce modèle donne de bons résultats concernant les processus évoqués plus haut mais souffre de quelques limitations, notamment concernant la manière de prendre en compte les variations de topographies et l'évolution de la ligne d'eau. D'autres méthodes doivent donc être envisagées.
- (2) Le phénomène de déferlement des vagues qui se produit pour de faibles profondeurs, le déferlement bathymétrique, joue un rôle dominant dans la dynamique littorale. Ce phénomène est très fortement conditionné par les variations topographiques. Dans une autre optique, certaines ondes longues peuvent atteindre le rivage sans avoir déferlé. Comprendre les interactions de telles ondes avec les structures, naturelles ou non, présentes près des côtes est également un sujet important. Ces observations nous amènent à considérer avec soin la manière dont le terme source décrivant les variations de la topographie est intégré au modèle numérique. Nous nous sommes donc orientés vers le choix de schémas de type "schéma équilibre". Ces schémas ont la particularité d'une part de mieux appréhender les fortes variations de topographie et leur influence sur les caractéristiques de l'écoulement considéré, et d'autre part autorisent la préservation au niveau discret des états d'équilibre de type subcritique ou au repos, la convergence vers ces états d'équilibre ainsi que le calcul de faibles oscillations autour de tels états.
- (3) La simulation d'écoulements dans la zone de surf implique également d'être capable de simuler les phénomènes complexes générés dans la zone de swash, qui est alternativement couverte et découverte sous l'effet des ondes incidentes. Ces phénomènes, nommés "run-up" et "run-down" dans la littérature, sont complexes d'un point de vue numérique puisqu'ils impliquent d'être capable de gérer l'apparition ou le recouvrement de zones sèches, sur des topographies souvent irrégulières. La ligne d'eau, définissant la frontière entre

la zone inondée et la zone sèche, est en perpétuel mouvement, générant une variation temporelle du domaine occupé par le fluide. Ce problème de gestion de ligne d'eau est donc souvent assimilé dans la littérature à un problème de condition aux limites, menant à des algorithmes de gestion du domaine de calcul compliqués et difficilement généralisables aux domaines bi-dimensionnels. L'utilisation de méthodes de type Volume Finis apparaît alors comme une alternative intéressante. En effet l'utilisation d'un solveur de Riemann local, combiné avec une gestion souvent simple des cellules de discrétisation "mouillées" ou "sèches" permet de "capturer" les transitions entre ces deux types de cellules et conduit à des résultats encourageants et aisément transposables au cas bi-dimensionnel. Toutefois, l'extension d'une telle méthode de gestion de la ligne d'eau dans le cas de propagation d'ondes sur une topographie variable conjointement à l'utilisation d'un schéma équilibre n'est pas triviale. En effet, une nouvelle difficulté, liée à la préservation de la positivité de la hauteur d'eau, apparaît. A notre connaissance, aucun schéma équilibre n'a encore été appliqué à la gestion de problème de ligne d'eau et de run-up sur des topographies variables.

- (4) Enfin, le choix d'une méthode de type Volume Finis pour discrétiser la partie hyperbolique nous amène inévitablement à considérer un algorithme à pas fractionnaires permettant de prendre en compte les termes sources restant, à savoir les termes de dissipation, de Coriolis et de tension de surface. Cette méthode à pas fractionnaires doit en outre nous permettre de conserver les bénéfices issus du schéma équilibre utilisé pour le système hyperbolique ainsi que la positivité de la hauteur d'eau.

Ainsi, après une étude bibliographique concernant les divers aspects que nous venons d'évoquer, nous rappelons au Chapitre 3 la méthode classique de Volumes Finis de type Godunov, dans un contexte bi-dimensionnel sur maillage cartésien. Les principes généraux sous-jacents aux schémas de type équilibre sont ensuite exposés brièvement avant de rappeler plus en détail le formalisme de deux solveurs "well-balanced" récents basés sur la résolution directe d'un problème de Riemann sur une topographie constante par maille : le schéma équilibre original issu des travaux de Greenberg et Leroux [72], et une version équilibre du solveur VFRoe-ncv introduit par Gallouët et al. [59]. Des validations de type hydraulique sont d'abord présentées pour ces deux solveurs. Puis nous nous intéressons à un problème classique de run-up sur plage en pente afin de mettre en évidence les limitations de ces deux schémas pour ce type de problèmes particuliers.

Dans le Chapitre 4, nous exposons brièvement une méthode récente introduite dans [3], permettant d'obtenir un schéma équilibre qui préserve la positivité de la hauteur d'eau. Cette méthode est ici utilisée conjointement au solveur VFRoe-ncv pour systèmes homogènes, qui, sans assurer la positivité de la hauteur d'eau dans un sens aussi précis que pour les schémas de Godunov ou cinétiques [58], permet toutefois de bien gérer en pratique l'apparition ou le recouvrement de zones sèches. Une extension vers

un schéma équilibre quasi d'ordre deux est ensuite décrite et la question des conditions aux limites génératrices/absorbantes est abordée. Tout ceci nous conduit à un nouveau modèle, nommé *SURF\_SVWB*, permettant de lever en partie les limitations du code *SURF\_SV*. Enfin, des validations numériques s'appuyant sur des cas tests uni-dimensionnels et bi-dimensionnels impliquant des problèmes de ligne d'eau non-triviaux sont effectuées.

Le Chapitre 5 nous permet d'introduire la méthode à pas fractionnaires implémentée pour le traitement des termes sources de diffusion, Coriolis, tension de surface et friction. Nous avons cherché à préserver les propriétés intéressantes induites par le schéma équilibre utilisé dans le pas "hyperbolique", comme la capacité de la méthode à préserver les états d'équilibre au repos ou encore la convergence vers de tels états. Quelques exemples numériques attestent enfin de la bonne gestion de la ligne d'eau pour le modèle numérique complet.

## Troisième partie - Application à l'hydrodynamique littorale

La troisième partie est l'occasion de mettre en oeuvre le modèle numérique développé dans des situations décrivant la propagation de vagues en zone littorale.

Le Chapitre 6 est consacré à l'étude de la propagation et du run-up d'ondes longues non déferlantes de type tsunami sur des topographies non régulières. La propagation littorale de tsunamis et la modélisation du run-up généré par de telles ondes sur des topographies complexes reste un problème ouvert. La plupart des modèles constituant l'état de l'art en la matière et utilisés pour la prévention de tel phénomènes sont toujours basés sur des méthodes à pas fractionnaires. En particulier, la convergence vers les états stationnaires au repos est donc impossible et les simulations sur des topographies complexes conduisent souvent à des phénomènes d'oscillations résonnantes persistantes, en partie dues aux interactions non-linéaires de la topographie avec l'onde mais également aux erreurs numériques dues à la méthode à pas fractionnaires. Le traitement de la ligne d'eau repose aussi souvent sur des algorithmes complexes. Dans cette optique, l'apport d'un schéma équilibre et du traitement précis de la ligne d'eau associé peut apporter des solutions. Plusieurs tests numériques sont donc réalisés, nous permettant d'observer, du moins d'un point de vue qualitatif, les bénéfices apportés par notre modèle. Nous nous intéresserons principalement à deux cas bi-dimensionnels, simulant d'une part le run-up d'une onde solitaire sur une plage avec variations de topographie dans la direction longshore, permettant d'étudier les phénomènes de résonances, et d'autre part le run-up d'un tsunami sur une île cônica idéalisée, mettant en avant les phénomènes de réfraction autour de l'île.

Enfin le Chapitre 7 est centré sur l'étude numérique de la propagation des vagues dans la zone de surf interne. Le phénomène de déferlement bathymétrique qui se produit pour des faibles profondeurs joue un rôle dominant dans la dynamique littorale. La compréhension des processus non-linéaires associés au déferlement bathymétrique reste également un problème scientifique ouvert. Une meilleure compréhension de ces

phénomènes est importante aussi bien du point de vue fondamental que dans l'objectif d'améliorer leur modélisation en vue de simulations méso-échelles ( $10\text{ km} \times 10\text{ km}$ ) et hydro-sédimentaires. Des efforts doivent être consacrés à l'étude de ces processus complexes en particulier en présence de bathymétries fortement irrégulières (barres littorales). En particulier, l'étude de la génération de courants moyens induits par la houle est un domaine complexe et l'approche numérique classique, souvent dans un contexte de modélisation morphodynamique pour de grande échelles de temps [39], repose principalement sur l'utilisation de modèles intégrés selon la verticale et moyennés sur une période de vague. Cette approche, qui apporte par ailleurs des réponses satisfaisantes dans les domaines morphodynamiques, impose certaines limitations importantes. En particulier, l'accès à certaines quantités instantanées, comme les oscillations de la vitesse ou le champ de vorticité, quantités importantes pour l'étude du transport sédimentaire, est impossible. De plus un traitement précis de la ligne d'eau est également difficile. Dans cette optique, l'utilisation de modèles de type BSV peut se révéler avantageuse, permettant en particulier le calcul, à la résolution temporelle désirée, d'un grand nombre de variables instantanées caractéristiques de l'écoulement et éventuellement également de quantités intégrées. Des études bi-dimensionnelles concernant la zone de surf interne ont été menées récemment utilisant des modèles de type Boussinesq. Mais à notre connaissance, aucune étude n'a été réalisée en s'appuyant sur un modèle de type Saint-Venant, profitant ainsi de la description naturelle de la propagation des vagues et de la dissipation d'énergie associée dans la zone de surf interne.

Ainsi, après une validation de la capacité du modèle à appréhender la propagation et la distorsion des vagues dans la zone de surf interne reposant sur un jeu de données expérimentales, nous nous intéressons plus particulièrement à la mise en évidence numérique de la formation de courants sagittaux au dessus d'un système de barre/baïne idéalisé. Notons que la terminologie "courant sagittal" désigne un courant moyen, calculé sur une période de vague. Une mise en évidence de la réfraction des vagues se propageant au dessus du système, ainsi qu'une brève étude du champ de vorticité instantané généré sont également présentées.



---

*Part 1*

# Theoretical study



---

# Introduction

## Derivation of a new two dimensional viscous shallow water model

Modelization of free surface flows is an extensive domain of research which plays an important role in many engineering applications such as ocean circulation, coastal exploitation, man-made structures in rivers or lakes or study of the atmosphere for instance. It is usual to describe this kind of flow in a classical fluid mechanics framework using the three dimensional Navier-Stokes equations, assuming the fluid to be Newtonian, viscous and incompressible. Computationally, the complete resolution of the Navier-Stokes equations for a free surface flow is known to be dramatically onerous and the three dimensional framework often entails numerical complexity in the meshing procedure and the implementation of the discretization method. For these reason, and when the fluid domain can be regarded as a thin layer of fluid (when the ratio between the vertical and the horizontal scales is small enough), it is usual to consider the nonlinear shallow water equations.

More generally, non-linear shallow water equations (NSW) model the dynamics of a shallow, rotating layer of homogeneous incompressible and inviscid fluid and are typically used to describe vertically averaged flows in three dimensional domains, in terms of horizontal velocity and depth variation. This set of equations is particularly well-suited for the study and numerical simulations of a large class of geophysical phenomena, such as river flows, coastal domains, ocean circulation, or even run-off or avalanches when modified with adapted source terms. These models are also extensively used in the field of hydraulic applications. The usual conservative form of NSW equations introduced in [160], without viscosity and capillary effects, is written as a first order hyperbolic system with various source terms as bed slope or bottom friction terms.

The derivation of the NSW system is classical when the viscosity and capillary or wind effects on the free surface are neglected ([53], [182], [161]). In the literature, we often find various NSW models which may include wind effects on the free surface, bottom

topography and friction effects on the bottom, often defined using the Manning-Chezy empirical formula, or viscosity (see [1] and [9] for instance). However, these models are often linked to a particular field of investigation and their derivation is often unclear, relying on some unjustified heuristic and empirical approximations. Moreover, the viscosity is often neglected in the derivation and added *a posteriori* to the NSW model, using turbulent models and leading to empirical and anisotropic eddy viscosity [41], [110]. For numerical purpose, even if empirical NSW models are widely used since over twenty years and often provide suitable results when applied to their domain of validity, it may be an improvement to understand precisely the derivation including viscous terms.

In [62], Gerbeau and Perthame have introduced some ideas leading to the derivation of a viscous one dimensional shallow water model, with a particular laminar friction term at the bottom. Starting from the free surface two dimensional Navier-Stokes equations on a flat bottom with a Navier condition at the bottom which takes into account the friction effects, they derive their one-dimensional model in two steps, relying on an asymptotic analysis with respect to the ratio between the vertical and the horizontal scales (namely the aspect ratio). No stresses on the free surface and no turbulence model for the stress tensor were considered. In the first step, a first order hyperbolic model is derived relying on hydrostatic and shallow water approximation. This first model includes a classical laminar friction term and approximates the free surface Navier-Stokes equations at the first order with respect to the aspect ratio. In a second step, the vertical distribution of the velocity is recovered through a parabolic reconstruction, leading to a second model including viscosity. This model approximates the free surface Navier-Stokes equations at the second order with respect to the aspect ratio. It is worth mentioning that the laminar friction term is modified in this second model, since the viscous effects are recovered in its formulation. Note that this derivation has been generalized by Audusse in [5], where the derivation of a one dimensional multilayer Saint-Venant model which aims at describing more precisely the vertical variability of the relevant quantities.

In the first chapter, we aim at improving the two dimensional derivation of NSW models by introducing a new two dimensional NSW model, including viscosity, laminar and turbulent friction terms, bed slope source term, Coriolis effects and capillary effects on the free surface. This new model is obtained following [62] from an asymptotic analysis of the non-dimensional and incompressible three dimensional Navier-Stokes-Coriolis equations with a large-scale assumption and hydrostatic approximation in a rotating sub-domain of  $\mathbb{R}^3$ . The method for the one-dimensional is extended to the two-dimensional case. The free moving surface boundary condition for the Navier-Stokes-Coriolis equations is completed with normal stress continuity and capillary effects at the air-fluid interface. The bottom is considered as uneven with no assumptions about these variations. Furthermore, we introduce here different kinds of friction terms in the bottom boundary conditions, namely linear and quadratic laws. We do not propose any turbulent model or wind-stresses on the free surface, although it does

not modify the main ideas of the derivation. In our study it is worth noting the originality of introducing surface tensions through the capillary effects at the free surface. This term can be regarded as a small dispersive term. As emphasized in [51], the introduction of the third-order surface-tension term induced by capillary effects and of the quadratic bottom friction term is of a relevant utility in the proof of existence of weak-solutions for this particular model. This problem is addressed in Chapter 2. Furthermore, the quadratic formulation of the bottom friction allows us to extend the validity of this set of NSW equations to coastal hydrodynamic simulations by the use of Manning-Chezy or Strickler numerical formulation (see [133]). The two-dimensional framework also highlights the existence of a particular viscous term, which was only identified as a modified coefficient in the one-dimensional case.

The derivation is realized in two steps. First we derive a shallow water model with Coriolis effects and uneven bottom with a small laminar friction term, resulting from a first order analysis, thanks to the large-scale assumption and the hydrostatic approximation. In a second part, we perform a parabolic correction of the horizontal velocity in order to take into account the vertical variability of the phenomenon. A more accurate asymptotic analysis provides a new model with a particular viscous term, capillary effects and linear and quadratic drag terms with water depth and viscosity dependent coefficients :

$$\left\{ \begin{array}{l} \partial_t h + \operatorname{div}(h\mathbf{u}) = 0, \\ \partial_t(h\mathbf{u}) + \operatorname{div}(h\mathbf{u} \otimes \mathbf{u}) + g h \nabla h = \\ -\alpha_0(h) \mathbf{u} - \alpha_1(h) h |\mathbf{u}| \mathbf{u} + \mu \operatorname{div} \left( h(\nabla \mathbf{u} + {}^t \nabla \mathbf{u}) + (2h \operatorname{div} \mathbf{u}) \mathcal{I} \right) \\ + \beta h \nabla \Delta h - f(h\mathbf{u})^\perp - g h \nabla d + \beta h \nabla \Delta d. \end{array} \right. \quad (0.1)$$

where we have :

$$\alpha_0(h) = \frac{k_l}{1 + \frac{k_l h}{3\mu}} \quad \text{and} \quad \alpha_1(h) = \frac{k_t}{\left(1 + \frac{k_l h}{3\mu}\right)^2}.$$

where  $h$  stands for the water depth,  $\mathbf{u}$  the depth averaged horizontal velocity and  $d$  the variations of topography. Note that we have recently been aware of a recent paper [149] in which Ferrari and Saleri also uses the main ideas of [138] to derive a two-dimensional NSW model, including atmospheric pressure effects and wind effects in the free surface boundary condition. This model does not consider quadratic friction law and does not take into account the variations of topography, since all the terms connected to the bottom topography are canceled through the asymptotic analysis. They suggest in a second step to symmetrize their model using a change of variable. Note that these new non-conservative variables are also used in our numerical study in order to recover suitable numerical properties [58]. Then, they add a viscous perturbation, which transforms the derived hyperbolic system into a parabolic one and

consider numerical solutions of this new parabolic system. The convergence of this new model solution towards the one of the undisturbed problem as the perturbation vanishes is discussed. However the authors added *a posteriori* a standard viscous term to the model after deriving it, and the term does not match the viscous term of [62] in the degenerated one dimensional case. We emphasize that in the derivation proposed here, the new viscous term is asymptotically derived from the Navier-Stokes-Coriolis equations and degenerates into the same term as in [62].

## Existence of weak solutions

We consider in Chapter 2 the shallow water model previously derived, in a bounded two dimensional domain with periodic boundary conditions.

If mathematical theories for the study of the three dimensional Navier Stokes equations for incompressible homogeneous fluids are well-established now, this is not the case for the two dimensional viscous shallow water model.

Bui [34] proved local existence and uniqueness of classical solutions to the Dirichlet problem for the viscous shallow water equations using Lagrangian coordinates and Hölder space estimates. Kloeden [94] proved global existence and uniqueness of classical solutions to the Dirichlet problem using Sobolev space estimates. He further assumes that the solutions are spatially periodic and satisfy Dirichlet Boundary conditions. In other works, Gustafsson and Sundstrom [75] studied mixed hyperbolic-parabolic systems, including the viscous shallow water equations. They assumed existence of sufficiently smooth solutions and derived necessary boundary conditions for well-posedness. Kanayama and Ushijima [89] establish an existence and uniqueness results for weak solutions of the linearized viscous shallow water equations using the Hille-Yosida Theorem. Miglio and Saleri [126] proposed an existence and uniqueness result for the 3D shallow water equations using the convergence of a numerical method. Xin and Zhang [192] studied the uniqueness and large time behavior of the weak solutions to a particular one-dimensional model including third order derivative. Existence of smooth solutions for small enough time or data close to equilibrium was proven by Sundbye [163] with a viscous term of the form  $\operatorname{div}(h\nabla\mathbf{u})$ . Finally, Bresch and Desjardins proved existence of global weak solutions first to a simplified model [24] using a method developed for a Kdv model, and later for a model slightly different to model (0.1), the main differences being constant friction coefficients and a simpler viscous term [51].

Other ways of modelling viscous effects have been studied from a mathematical view point. We can refer for instance to Lions [114] or Bernardi and Pironneau [13], who have shown existence of solutions for various forms of the viscous term and have proved convergence results for certain numerical schemes. Viscous terms of the form  $h\Delta h$  were investigated by Orenca [130], in which existence of weak solutions with small enough data was obtained. But unlike the system studied here, the corresponding model allows to divide by  $h$  the momentum equation. The underlying assumption is of course that  $h$  stay away from vanishing. It is worth mentioning that in the low Reynolds number,

it is possible to assume potential flow, as in [111]. This is not possible with the viscous term of model (0.1), since an equation on the velocity potential cannot be written.

We also refer to [37] where Chatelon and Orenge have studied a non-homogeneous shallow water model or even to [19] where Bosseur and Orenge proposed existence results for shallow water models with boundary conditions using optimal control. In [110], local well-posedness of a particular model relying on semi-empirical anisotropic eddy viscous model is investigated by Levermore and Sammartino.

The result introduced in Chapter 2 is inspired from the demonstration proposed by Bresch and Desjardins in [51]. It relies on an approximated formulation for which the existence and uniqueness of solution is proved by a fixed point method, following ideas of Simon [157] and Boyer and Fabrie [22]. Afterwards, an energy inequality is obtained and *a priori* estimates in Sobolev spaces are obtained. Compactness criteria introduced by Simon [158] and Hanouzet [76] enable us to pass to the limit in non-linear terms and thus to obtain the existence of weak solutions.

We have made the distinction between the one and two-dimensional cases. In the one-dimensional case, we obtain a result for the complete model, without any particular assumption, whereas in the two-dimensional case, we have studied a simplified model with classical viscous term and made a strong assumption on the water depth positivity.



# Derivation of a new two-dimensional viscous shallow water model

This chapter is devoted to the derivation of a new two dimensional shallow water model including viscosity, varying topography, friction and capillary effects, following the ideas proposed by Gerbeau and Perthame [62] in the one dimensional case.

## 1.1. The Navier-Stokes-Coriolis system and boundary conditions

We briefly introduce the classical set of three dimensional Navier-Stokes-Coriolis equations which is considered as the basis of the following analysis. Well-suited boundary conditions are proposed for the free surface and the bottom boundaries.

**1.1.1. The system.** We start from the rotating three dimensional Navier-Stokes equations for incompressible homogeneous fluids, namely the Navier-Stokes-Coriolis system, evolving in a subdomain of  $\mathbb{R}^3$ . These equations are studied in a frame which rotates with the planetary angular velocity  $\Omega$ , considered as constant. For homogeneous and incompressible fluids motions, the condition of mass conservation reduces to the incompressibility condition  $\operatorname{div} \mathbf{U} = 0$ . Expressing the motions in terms of quantities which are observed in the rotating frame, we obtain the following system :

$$\begin{cases} \operatorname{div} \mathbf{U} = 0, \\ \partial_t \mathbf{U} + \operatorname{div} (\mathbf{U} \otimes \mathbf{U}) + 2\Omega \wedge \mathbf{U} + \Omega \wedge (\Omega \wedge \mathbf{r}) = \operatorname{div} \sigma(\mathbf{U}) + F_{ext}, \end{cases} \quad (1.1)$$

where

- $\mathbf{U} = (u, v, w)$  is the velocity seen in the rotating frame.

•  $F_{ext}$  represents the body forces which are applied, mostly the gravitational attraction of the earth, oriented along the radial direction, from the position of the fluid element to the center of the earth. We have the classical expression :

$$F_{ext} = -\frac{GM}{r^2} \mathbf{k}$$

where  $G$  is the gravitational constant,  $M$  the mass of the earth,  $r$  the radius and  $\mathbf{k}$  the unit vector oriented along the radial direction. (see figure 1.1.1).

•  $2\boldsymbol{\Omega} \wedge \mathbf{U}$  and  $\boldsymbol{\Omega} \wedge (\boldsymbol{\Omega} \wedge \mathbf{r})$  are respectively the Coriolis acceleration and the centripetal acceleration, considered in a solid-body rotation, where  $\boldsymbol{\Omega}$  represents the planetary angular velocity vector, of magnitude  $\omega$  and  $\mathbf{r}$  the position vector of the element of fluid in the local frame. We denote by  $r$  its magnitude. If we consider that this magnitude is a constant and that the earth rotation is approximately of  $2\pi$  radian in a sidereal day time length, we have :

$$\omega = \frac{2\pi}{86164} = 0.727 \cdot 10^{-4} \text{ radian/s.}$$

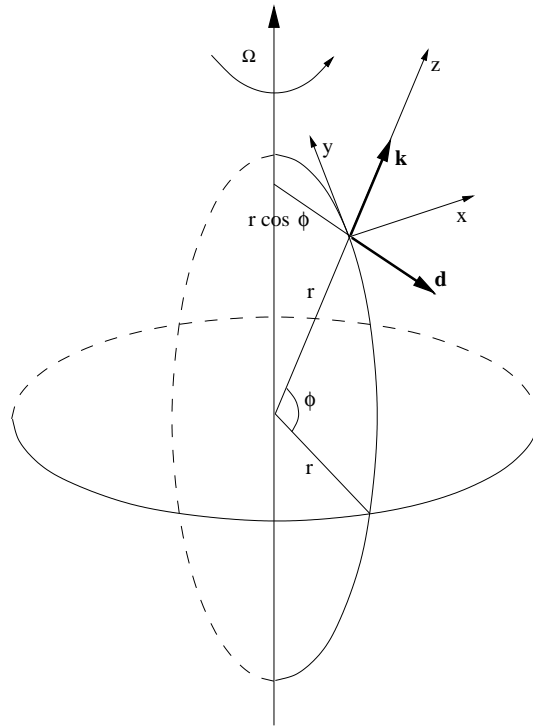


**Figure 1.1.1.** Spherical coordinates and local frame

•  $\text{div } \sigma(\mathbf{U})$  are the viscosity forces and  $\sigma$  the total stress tensor. An explicit form for this tensor is :

$$\sigma(\mathbf{U}) = -p\mathcal{I} + 2\mu D(\mathbf{U}); \quad (1.2)$$

$p(t, x, y, z)$  represents the local pression in the fluid,  $\mu$  is the dynamical viscosity and  $D(\mathbf{U})$  the viscosity tensor :

$$D_{ij}(\mathbf{U}) = \frac{1}{2}(\partial_j u_i + \partial_i u_j) \text{ for } 1 \leq i, j \leq 3, \quad (1.3)$$

where  $(u_1, u_2, u_3) = (u, v, w)$  and  $\partial_1 = \partial_x, \partial_2 = \partial_y, \partial_3 = \partial_z$ .

In a solid body rotation, if we don't take into account the earth center movements, the centripetal acceleration  $\gamma_E = \Omega \wedge (\Omega \wedge \mathbf{r})$  can be rewritten as follows :

$$\gamma_E = -\omega^2 r \cos \phi \mathbf{d}.$$

where  $\mathbf{d}$  is the perpendicular normalized vector, oriented from the rotation axis to the position of the fluid element.  $r \cos \phi$  is the projection of  $\mathbf{r}$  on the axis defined by  $\mathbf{d}$  and can be seen as the perpendicular distance from the rotation axis to the position of the fluid element (Figure 1.1.1).

It is usual to combine the centrifugal acceleration and the earth's gravitational attraction [133] to obtain the effective gravitational acceleration  $g$  :

$$\mathbf{g} = -\frac{GM}{r^2} \mathbf{k} + \omega^2 r \cos \phi \mathbf{d} \quad (1.4)$$

Considering expression (1.4), the gravitational acceleration depends on the latitude  $\phi$ . The centrifugal acceleration is of maximal magnitude at the equator, where it is about  $0.034 m.s^{-1}$ . Thus this term is often neglected in practice and we assume the gravitational acceleration to be of constant magnitude  $g = 9.81 m.s^{-2}$  and directed from the observation point to the earth's center, along the radial direction. The component form becomes  $F_{ext} = (0, 0, -g)$ .

For the sake of simplicity, the equations are written in the local frame  $(x, y, z)$  where  $(x, y)$  defines a tangential surface to the fluid domain. At the latitude  $\Phi$ , the component of  $\Omega$  in this frame are (see figure 1.1.2) :  $(0, \omega \cos \Phi, \omega \sin \Phi)$ .

The Coriolis acceleration term has *a priori* 3 significant components :

$$\gamma_C = \begin{pmatrix} 2\omega \cos \Phi w - 2\omega \sin \Phi v \\ 2\omega \sin \Phi u \\ 2\omega \cos \Phi u \end{pmatrix}.$$

By focusing our attention on large-scale motions only, that is, by characterizing the motion by single scales for velocity and length, the nearly horizontal character of the fluid trajectories makes the vertical velocity  $w$  so small compared to the horizontal ones that we can in first approximation neglect the  $2\omega \cos \Phi w$  component. This approximation will be developed in the next section. Furthermore, the radial projection of  $\gamma_C$  is very small compared to the effective gravitational acceleration ( $\frac{2\omega \cos \Phi u}{|F_{ext}|} = 10^{-5}$ ) and will also be neglected.

So if we collect the consequences of these approximations we obtain, in component

form, the Coriolis acceleration term  $(-fv, fu, 0)$  where  $f = 2\Omega \sin\Phi$  is the local component of the planetary vorticity normal to the earth surface which is usually called the Coriolis parameter. In Europe,  $\Phi$  is nearly equal to  $45^\circ$  and a usual approximation is to consider  $f$  as a constant of magnitude  $10^{-4} s^{-1}$ .

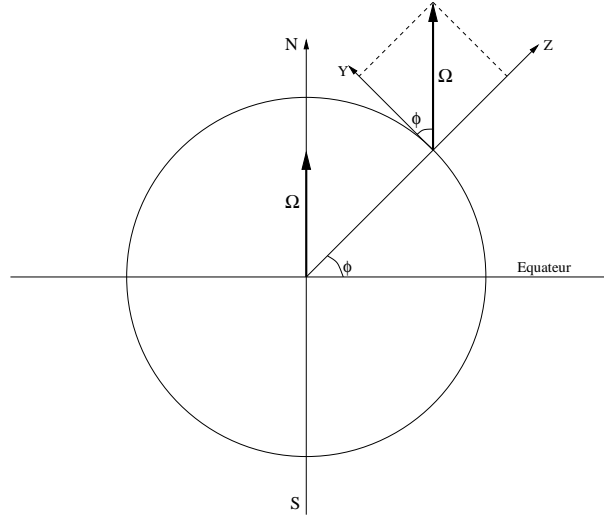


Figure 1.1.2. Projection of  $\Omega$  on the tangential surface.

The system (1.1) thus becomes :

$$\begin{cases} \operatorname{div} \mathbf{U} = 0, \\ \partial_t \mathbf{U} + \operatorname{div} (\mathbf{U} \otimes \mathbf{U}) = \operatorname{div} \sigma(\mathbf{U}) + F, \end{cases} \quad (1.5)$$

where  $F = (fv, -fu, -g)$  represents Coriolis and effective gravitational accelerations.

In the sequel, we will focus our attention on this system for

$$t > 0, \quad (x, y) \in \mathbb{R}^2 \quad \text{and} \quad d(x, y) \leq z \leq \xi(t, x, y),$$

where  $z = \xi(t, x, y)$  represents the local water elevation from the surface  $z = 0$  to the air/fluid interface and  $z = d(x, y)$  represents the description of the topography variations.

We also introduce at once  $h(t, x, y)$  which describes the total height of the water column located at the  $(x, y)$  coordinate with :

$$h(t, x, y) = \xi(t, x, y) - d(x, y) \quad (1.6)$$

**1.1.2. Boundary conditions.** Well-suited boundary conditions are respectively introduced for the bottom and the air-fluid interface boundaries.

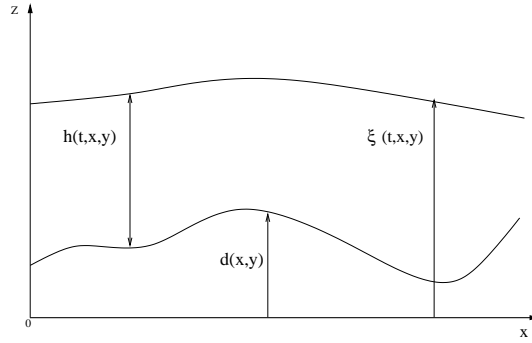


**Figure 1.1.3.** Sketch of the relevant variables.

*Normal stress continuity and surface tension.* On the free surface, we assume a normal-stress continuity condition with surface tension at the air/fluid interface, considering the air viscosity as negligible :

$$\sigma(\mathbf{U}) \cdot n_s - \beta \kappa(t, x, y) n_s = -p_o n_s \quad \text{at } z = \xi(t, x, y), \quad (1.7)$$

where  $n_s$  is the outward normal to the free surface, defined with  $n_s = \frac{\nabla S}{|\nabla S|}$  and  $S = z - \xi(t, x, y)$ ,  $\beta$  is a capillary coefficient,  $\kappa$  the mean curvature of the surface at point  $(x, y)$  and  $p_o(x, y)$  the atmospheric pressure at the surface. We obtain the following expression :

$$n_s = \frac{1}{\sqrt{1 + |\nabla \xi|^2}} \begin{pmatrix} -\partial_x \xi \\ -\partial_y \xi \\ 1 \end{pmatrix},$$

where  $||$  stands for the Euclidian norm.

**Remark 1.1.1.** *It is possible to include the tension due to the wind effect in this free surface boundary condition as in [149]. Giving the wind stresses on the free surface with :*

$$\mathbf{s}_{surf|_{xy}} = C|W|W$$

where  $W$  is an evaluation of the wind velocity at the free surface and  $C$  a suitable coefficient, and introducing

$$\mathbf{s}_{surf|_z} = p_o$$

it raises the following boundary condition :

$$\sigma(\mathbf{U}) \cdot n_s - \beta \kappa(t, x, y) n_s = \mathbf{s}_{surf} \quad \text{at } z = \xi(t, x, y).$$

*Boundary conditions at the bottom.* At the bottom, we assume a wall-law with linear and quadratic terms [133], which respectively refer to laminary and turbulent friction phenomena :

$$(\sigma(\mathbf{U}) \cdot n_b) \cdot \tau_{b_i} = k_l(\mathbf{U} \cdot \tau_{b_i}) + k_t(h|\mathbf{U}|\mathbf{U} \cdot \tau_{b_i}) \quad \text{at } z = d(x, y), \quad (1.8)$$

where  $k_l$  et  $k_t$  are the laminary and the turbulent friction coefficients. The outward normal is defined with :

$$n_b = \frac{1}{\sqrt{1 + |\nabla d|^2}} \begin{pmatrix} -\partial_x d \\ -\partial_y d \\ 1 \end{pmatrix},$$

and  $(\tau_{b_i})_{i=1,2}$  is a basis of the tangential surface :

$$\tau_{b_1} = \frac{1}{|\nabla d|} \begin{pmatrix} -\partial_y d \\ \partial_x d \\ 0 \end{pmatrix} \quad \text{and} \quad \tau_{b_2} = \frac{1}{\sqrt{|\nabla d|^2 + |\nabla d|^4}} \begin{pmatrix} -\partial_x d \\ -\partial_y d \\ -|\nabla d|^2 \end{pmatrix}. \quad (1.9)$$

We complete this condition with a no-penetration condition at the bottom :

$$\mathbf{U} \cdot n_b = 0 \quad \text{at} \quad z = d(x, y). \quad (1.10)$$

**1.1.3. Indicator function.** Following the idea developed in [138], let  $\phi$  denote an indicator function which allows us to define precisely the fluid region at time  $t$  :

$$\phi(t, x, y, z) = \begin{cases} 1 & \text{for } d(x, y) \leq z \leq \xi(t, x, y) \\ 0 & \text{otherwise.} \end{cases} \quad (1.11)$$

The mass conservation equation becomes, using the incompressibility relation :

$$\partial_t \phi + \partial_x(\phi u) + \partial_y(\phi v) + \partial_z(\phi w) = 0 \quad (1.12)$$

## 1.2. The non-dimensionalized system

In this section, we briefly consider some characteristic scales which applied for the shallow water model. Then, a non-dimensionalized set of equations is obtained and the usual hydrostatic approximation is assumed.

**1.2.1. Vertical scales in oceanic circulation.** As previously emphasized, the NSW equations with viscosity, friction terms and varying topography are extensively used in the fields of oceanography and particularly for the numerical simulation of oceanic or coastal circulation. Although the depth of the fluid varies in space and time, we assume that characteristic scale for the depth can be chosen. This average thickness  $H$  of the oceans is nearly 4 km whereas their horizontal characteristic value is about 4000 km. So the ratio of the vertical scale to the horizontal one, the so-called aspect ratio, is about  $\frac{1}{1000}$ . The situation is analogous in coastal domain where the characteristic scale for vertical variations is reduced to 100 m and the horizontal one is about 100 km. In this context, we shall assume that the vertical movements and variations are very small compared to the horizontal ones. The continuity equation allows us in the same way to estimate the ratio of the vertical and horizontal velocity scales, respectively  $W$  and  $V$  :

$$\frac{W}{U} \approx \frac{H}{L} \approx \frac{1}{1000}.$$

**1.2.2. Dimensionless quantities.** According to the previous section, we use in the sequel the thin-layer assumption and introduce a “small” parameter :

$$\varepsilon = \frac{H}{L} = \frac{W}{V} \quad (1.13)$$

where  $H$ ,  $L$ ,  $W$ ,  $V$  are respectively the characteristic scales for the vertical and the horizontal dimension of the fluid domain of interest and for the vertical and the horizontal velocity. We then introduce some characteristic dimensions :  $T = \frac{L}{V}$  et  $P = V^2$  for the time and the pressure.

The dimensionless quantities are temporarily noted with a  $\tilde{\cdot}$  and are defined as follows :  $\tilde{u} = \frac{u}{V}$ ,  $\tilde{v} = \frac{v}{V}$ ,  $\tilde{w} = \frac{w}{W}$ ,  $\tilde{x} = \frac{x}{L}$ ,  $\tilde{y} = \frac{y}{L}$ ,  $\tilde{z} = \frac{z}{H}$ ,  $\tilde{t} = \frac{t}{T}$  and  $\tilde{p} = \frac{p}{P}$ .

Some dimensionless numbers are also introduced : the Reynolds number  $R_e = \frac{VL}{\nu}$ , the Froude number  $F_r = \frac{V}{\sqrt{gH}}$  and the Rossby number  $R_o = \frac{V}{fL}$ . Finally, let us define the modified laminar and quadratic friction coefficient  $k'_l = \frac{k_l}{V}$  and  $k'_t = k_t L$ .

In what follows, we mostly focus on the horizontal velocity. We thus distinguish the horizontal components  $(u, v)$  and the vertical one  $w$ . The tensor  $\sigma(U)$  defined in (1.2) will be denoted by  $\sigma$  for the sake of clarity and we introduce  $U = (u, v)$ . It is also convenient to introduce the tensor  $D_h(U)$  with :

$$(D_h(U))_{ij} = \frac{1}{2}(\partial_j u_i + \partial_i u_j) \text{ for } 1 \leq i, j \leq 2. \quad (1.14)$$

where  $u_1 = u$ ,  $u_2 = v$ ,  $\partial_1 = \partial_x$  and  $\partial_2 = \partial_y$ . Finally we denote by  $U^\perp$  the following quantity :  $U^\perp = (-v, u)$ . The differential operators  $\nabla_{xy}$ ,  $\text{div}_{xy}$  et  $\Delta_{xy}$  refer to horizontal derivations.

Dropping the  $\tilde{\cdot}$ , the non-dimensionalized Navier-Stokes system becomes :

$$\left\{ \begin{array}{l} \text{div}_x U + \partial_z w = 0, \\ \partial_t U + \text{div}_x (U \otimes U) + \partial_z (w U) + \nabla_{xy} p + \frac{U^\perp}{R_o} \\ \quad = \frac{1}{R_e} \left( 2 \text{div}_x (D_h(U)) + \frac{1}{\varepsilon^2} \partial_z^2 U + \nabla_{xy} (\partial_z w) \right), \quad (1.15) \\ \varepsilon^2 \left( \partial_t w + \text{div}_x (w U) + \partial_z (w^2) \right) + \partial_z p \\ \quad = -\frac{1}{F_r^2} + \frac{1}{R_e} \left( \partial_z (2 \text{div}_x U) + \varepsilon^2 \Delta_{xy} w + 2 \partial_z^2 w \right). \end{array} \right.$$

Boundary conditions are also written in a dimensionless form :

$$\left\{ \begin{array}{l} (p - p_o + \beta\kappa) \nabla_{xy} \xi + \frac{1}{Re} \left( \frac{1}{\varepsilon^2} \partial_z U + \nabla_{xy} w - 2D_h(U) \cdot \nabla_{xy} \xi \right) = 0 \\ \text{at } z = \xi(t, x, y), \\ p - p_o + \beta\kappa + \frac{1}{Re} \left( \nabla_{xy} \xi \cdot (\partial_z U + \varepsilon^2 \nabla_{xy} w) - 2 \partial_z w \right) = 0 \text{ at } z = \xi(t, x, y), \end{array} \right. \quad (1.16)$$

and :

$$\left\{ \begin{array}{l} 1/(\varepsilon^2 V^2) (\sigma \cdot n_b) \cdot \tau_{b_1} = -\frac{1}{\varepsilon} (k'_l + \varepsilon k'_t h |U|) (U^\perp \cdot \nabla_{xy} d) \text{ at } z = d(x, y), \\ 1/(\varepsilon^2 V^2) (\sigma \cdot n_b) \cdot \tau_{b_2} = -\frac{1}{\varepsilon} (k'_l + \varepsilon k'_t h |U|) (U \cdot \nabla_{xy} d + \varepsilon^2 w |\nabla_{xy} d|^2) \\ \text{at } z = d(x, y), \\ U \cdot \nabla_{xy} d - w = 0 \text{ at } z = d(x, y). \end{array} \right. \quad (1.17)$$

The hydrostatic approximation, which consists in dropping terms of second order of magnitude in  $\varepsilon$  (1.13) in the relations (see [138], [74] and [133]), enables us to go ahead in the derivation. Actually, the nearly horizontal nature of the fluid evolution induces so small vertical accelerations that the Archimedian principle for a static fluid is applicable. The system (1.15)-(1.17) becomes :

$$\left\{ \begin{array}{l} \text{div}_x U + \partial_z w = 0, \\ \partial_t U + \text{div}_x (U \otimes U) + \partial_z (w U) + \nabla_{xy} p + \frac{U^\perp}{Ro} = \\ \frac{1}{Re} \left( 2 \text{div}_x (D(U)) + \frac{1}{\varepsilon^2} \partial_z^2 U + \nabla_{xy} (\partial_z w) \right), \\ \partial_z p = -\frac{1}{Fr^2} + \frac{1}{Re} \left( \partial_z (\text{div}_x U) + 2 \partial_z^2 w \right), \end{array} \right. \quad (1.18)$$

at the free surface boundary :

$$\left\{ \begin{array}{l} \left( p - p_o + \beta\kappa \right) \nabla_{xy} \xi + \frac{1}{R_e} \left( \frac{1}{\varepsilon^2} \partial_z U + \nabla_{xy} w - 2D(U) \cdot \nabla_{xy} \xi \right) = 0 \\ \text{at } z = \xi(t, x, y), \\ \\ p - p_o + \beta\kappa + \frac{1}{R_e} \left( \nabla_{xy} \xi \cdot \partial_z U - 2\partial_z w \right) = 0 \text{ at } z = \xi(t, x, y), \end{array} \right. \quad (1.19)$$

and at the bottom :

$$\left\{ \begin{array}{l} 1/(\varepsilon^2 V^2) (\sigma \cdot n_b) \cdot \tau_{b_1} = -\frac{1}{\varepsilon} (k'_l + \varepsilon k'_t h |U|) \left( U^\perp \cdot \nabla_{xy} d \right) \text{ at } z = d(x, y) \quad (i) \\ \\ 1/(\varepsilon^2 V^2) (\sigma \cdot n_b) \cdot \tau_{b_2} = \frac{1}{\varepsilon} (k'_l + \varepsilon k'_t h |U|) \left( U \cdot \nabla_{xy} d \right) \text{ at } z = d(x, y) \quad (ii) \\ \\ U \cdot \nabla_{xy} d - w = 0 \text{ at } z = d(x, y) \quad (iii) \end{array} \right. \quad (1.20)$$

The solution of this system always depends on  $\varepsilon$ , owing to the horizontal momentum conservation relation in (1.18). Keeping in mind that we are looking for a solution of order  $O(1)$ , we emphasize that (1.19) gives :

$$\frac{1}{R_e} \partial_z U|_{z=\xi} = -\varepsilon^2 \left( (p - p_o + \beta\kappa) \nabla_{xy} \xi - 2D(U) \cdot \nabla_{xy} \xi + \nabla_{xy} w \right) |_{z=\xi}. \quad (1.21)$$

This term cannot be neglected, since we have the term  $\frac{1}{\varepsilon^2} \partial_z^2 U$  in the horizontal momentum relation.

Moreover, we have, always from relation (1.19) :

$$\left( p - p_o - \frac{2}{R_e} \partial_z w + \beta\kappa \right) |_{z=\xi} = -\frac{1}{R_e} \left( \nabla_{xy} \xi \cdot \partial_z U \right) |_{z=\xi}, \quad (1.22)$$

We notice that the left hand part of (1.22) appears as a  $O(1)$  term when the relations (1.18) are integrated along the vertical direction. Using (1.21) and recalling that we have  $\frac{1}{R_e} \partial_z U|_{z=\xi} = O(\varepsilon^2)$ , we obtain :

$$\left( p - p_o - \frac{2}{R_e} \partial_z w + \beta\kappa \right) |_{z=\xi} = O(\varepsilon^2). \quad (1.23)$$

Integrating the relation (1.18) for the pressure and using (1.23) gives :

$$p(t, x, y, z) - p_o + \beta \kappa(t, x, y) = \frac{1}{F_r^2}(\xi - z) + \frac{1}{R_e} \left( \int_{\xi}^z \partial_x(\partial_z u(t, x, y, \eta)) d\eta + \int_{\xi}^z \partial_y(\partial_z v(t, x, y, \eta)) d\eta + 2 \partial_z w(t, x, y, z) \right) + O(\varepsilon^2).$$

Finally, thanks to the incompressibility relation, we get :

$$p(t, x, y, z) - p_o + \beta \kappa(t, x, y) = \frac{1}{F_r^2}(\xi - z) - \frac{1}{R_e} \left( \partial_x u(t, x, y, z) + \partial_x u(t, x, y, \xi) + \partial_y v(t, x, y, z) + \partial_y v(t, x, y, \xi) \right) + O(\varepsilon^2). \quad (1.24)$$

### 1.3. The vertically averaged non-dimensionalized system

**1.3.1. Free surface condition.** If (1.12) is integrated between  $z = d(x, y)$  and  $z = +\infty$ , we get by Leibniz formula :

$$\partial_t \int_d^{\infty} \phi dz + \partial_x \left( \int_d^{\infty} \phi u dz \right) + \partial_y \left( \int_d^{\infty} \phi v dz \right) + [\phi w]_d^{\infty} + \left( u \partial_x d + v \partial_y d \right)_{|z=d} = 0$$

Using the no-penetration condition (1.10) and keeping in mind the definition of the indicator function  $\phi$  (1.11), we obtain :

$$\partial_t h(t, x, y) + \partial_x \left( \int_d^{\xi} u(t, x, y, z) dz \right) + \partial_y \left( \int_d^{\xi} v(t, x, y, z) dz \right) = 0. \quad (1.25)$$

where  $h(t, x, y)$  is defined by (1.6).

If (1.12) is integrated in a different way, namely between  $z = d(x, y)$  and  $z = \xi(t, x, y)$ , we obtain :

$$\begin{aligned} \partial_t h + \partial_x \left( \int_d^{\xi} u dz \right) + \partial_y \left( \int_d^{\xi} v dz \right) - \left( \partial_t \xi + u \partial_x \xi + v \partial_y \xi - w \right)_{|z=\xi} \\ + \left( u \partial_x d + v \partial_y d - w \right)_{|z=d} = 0. \end{aligned}$$

Finally, gathering these results and using again condition (1.10), we get :

$$\left( \partial_t \xi + U \cdot \nabla_{xy} \xi - w \right)_{|z=\xi} = 0. \quad (1.26)$$

**1.3.2. Momentum equation.** Integrating the horizontal momentum relation (1.18) for  $d(x, y) \leq z \leq \xi(t, x, y)$  gives :

$$\begin{aligned} \partial_t \left( \int_d^{\xi} U dz \right) + \text{div}_x \left( \int_d^{\xi} (U \otimes U) dz \right) + \nabla_{xy} \left( \int_d^{\xi} p dz \right) + \frac{1}{R_o} \int_d^{\xi} U^\perp dz \\ - U \left( \partial_t \xi + U \cdot \nabla_{xy} \xi - w \right)_{|z=\xi} + U \left( U \cdot \nabla_{xy} d - w \right)_{|z=d} \\ = \text{div}_x \left( \int_d^{\xi} \frac{2}{R_e} D_h(U) dz \right) + \frac{1}{R_e} \left( \left( \frac{1}{\varepsilon^2} \partial_z U + \nabla_{xy} w \right)_{|z=\xi} - \left( \frac{1}{\varepsilon^2} \partial_z U + \nabla_{xy} w \right)_{|z=d} \right) \end{aligned}$$

$$+\left(p\nabla_{xy}\xi - \frac{2}{R_e}D_h(U) \cdot \nabla_{xy}\xi\right)_{|z=\xi} - \left(p\nabla_{xy}d - \frac{2}{R_e}D_h(U) \cdot \nabla_{xy}d\right)_{|z=d}.$$

Using (1.26) together with the boundary conditions at the bottom (1.10) and at the free surface (1.19) we obtain :

$$\begin{aligned} \partial_t \left( \int_d^\xi U dz \right) + \operatorname{div}_x \left( \int_d^\xi (U \otimes U) dz \right) + \nabla_{xy} \left( \int_d^\xi p dz \right) + \frac{1}{R_o} \int_d^\xi U^\perp dz \\ = \operatorname{div}_x \left( \int_d^\xi \frac{2}{R_e} D_h(U) dz \right) + (p_o - \beta\kappa) \nabla_{xy} \xi \\ - \left( p\nabla_{xy}d - \frac{2}{R_e} D_h(U) \cdot \nabla_{xy}d + \frac{1}{R_e} \left( \frac{1}{\varepsilon^2} \partial_z U + \nabla_{xy} w \right) \right)_{|z=d}. \end{aligned} \quad (1.27)$$

It remains to use the friction boundary conditions at the bottom (1.20) to conclude this first step in the derivation. Developing these relations, the following linear combination  $(\partial_y d \times (1.20(i)) + \partial_x d \times (1.20(ii)))$  gives :

$$\begin{aligned} \left( (-p + (D_h)_{xx}) \partial_x d + (D_h)_{xy} \partial_y d - \frac{1}{R_e} \left( \frac{1}{\varepsilon^2} \partial_z u + \partial_x w \right) \right)_{|z=d} \\ = -\frac{k'_l}{\varepsilon} u|_{z=d} - k'_t h|U| u|_{z=d} - \partial_x d \left( p - \frac{2}{R_e} \partial_z w \right)_{|z=d} + \frac{1}{R_e} \partial_x d \left( \nabla_{xy} d \cdot \partial_z U \right)_{|z=d}. \end{aligned}$$

in the same way, with the combination  $(\partial_y d \times (1.20(ii)) - \partial_x d \times (1.20(i)))$ , we obtain the second relation :

$$\begin{aligned} \left( (-p + (D_h)_{yy}) \partial_y d + (D_h)_{xy} \partial_x d - \frac{1}{R_e} \left( \frac{1}{\varepsilon^2} \partial_z v + \partial_y w \right) \right)_{|z=d} \\ = -\frac{k'_l}{\varepsilon} v|_{z=d} - k'_t h|U| v|_{z=d} - \partial_y d \left( p - \frac{2}{R_e} \partial_z w \right)_{|z=d} + \frac{1}{R_e} \partial_y d \left( \nabla_{xy} d \cdot \partial_z U \right)_{|z=d}. \end{aligned}$$

Gathering these two scalar relations, we obtain the vectorial one :

$$\begin{aligned} \left( -p\nabla_{xy}d + \frac{2}{R_e} D_h(U) \cdot \nabla_{xy}d - \frac{1}{R_e} \left( \frac{1}{\varepsilon^2} \partial_z U + \nabla_{xy} w \right) \right)_{|z=d} \\ = -\frac{k'_l}{\varepsilon} U|_{z=d} - k'_t h|U| U|_{z=d} - \nabla_{xy} d \left( p - \frac{2}{R_e} \partial_z w \right)_{|z=d} + \frac{1}{R_e} \nabla_{xy} d \left( \nabla_{xy} d \cdot \partial_z U \right)_{|z=d}. \end{aligned} \quad (1.28)$$

This relation (1.28) can be directly used in equation (1.27) and we finally obtain :

$$\partial_t \left( \int_d^\xi U dz \right) + \operatorname{div}_x \left( \int_d^\xi (U \otimes U) dz \right) + \nabla_{xy} \left( \int_d^\xi p dz \right) + \frac{1}{R_o} \int_d^\xi U^\perp dz$$

$$\begin{aligned}
&= -\frac{k'_t}{\varepsilon} U|_{z=d} - k'_t h|U| U|_{z=d} + \operatorname{div}_x \left( \int_d^\xi \frac{2}{R_e} D_h(U) dz \right) + (p_o - \beta\kappa) \nabla_{xy} \xi \\
&\quad - \nabla_{xy} d \left( p - \frac{2}{R_e} \partial_z w \right) |_{z=d} + \frac{1}{R_e} \nabla_{xy} d \left( \nabla_{xy} d \cdot \partial_z U \right) |_{z=d} . \tag{1.29}
\end{aligned}$$

## 1.4. The Shallow Water system

In this section, the derivation of the NSW model by asymptotic analysis of the non-dimensionalized integrated Navier-Stokes system with hydrostatic approximation is performed.

We introduce the following averaged quantity for a generic function  $f$  depending on  $(t, x, y, z)$  :

$$\bar{f}(t, x, y) = \frac{1}{h(t, x, y)} \int_d^\xi f(t, x, y, \eta) d\eta .$$

where we recall that we have :

$$h(t, x, y) = \xi(t, x, y) - d(x, y) .$$

From this, relation (1.25) can be directly expressed in the following form :

$$\partial_t h + \operatorname{div}_x (h \bar{U}) = 0 .$$

In the sequel, we assume the following asymptotic regime (see [138]) :

$$\frac{1}{R_e} = \varepsilon \nu_o \quad , \quad k'_t = \varepsilon r_0 \quad \text{and} \quad k'_t = \varepsilon r_1 . \tag{1.30}$$

**1.4.1. First order approximation.** An asymptotic analysis of relations (1.18), (1.16) and (1.17) (see [138]) gives :

$$\partial_z^2 U = O(\varepsilon) \quad , \quad \partial_z U|_{z=\xi} = O(\varepsilon) \quad \text{and} \quad \partial_z U|_{z=d} = O(\varepsilon) \tag{1.31}$$

This implies that :

$$U(t, x, y, z) = U(t, x, y, -d) + O(\varepsilon) ,$$

and so

$$U(t, x, y, z) = \bar{U}(t, x, y) + O(\varepsilon) . \tag{1.32}$$

Furthermore, at first order, we immediately obtain the following equality :

$$\overline{U \otimes U}(t, x, y) = \bar{U} \otimes \bar{U}(t, x, y) + O(\varepsilon) . \tag{1.33}$$

The relations (1.30) enable us to write (1.24) under the form :

$$p(t, x, y, z) = p_o - \beta \kappa(t, x, y) + \frac{1}{F_r^2} (\xi - z) + O(\varepsilon) . \tag{1.34}$$

The mean curvature of the free surface, denoted by  $\kappa(t, x, y)$ , is usually expressed in term of the local surface elevation  $\xi(t, x, y)$ , in its nondimensional form :

$$\kappa(\xi) = \frac{\varepsilon \xi_{xx} (1 + \varepsilon^2 \xi_y^2) - 2 \varepsilon^3 \xi_x \xi_y \xi_{xy} + \varepsilon \xi_{yy} (1 + \varepsilon^2 \xi_x^2)}{(1 + \varepsilon^2 \xi_x^2 + \varepsilon^2 \xi_y^2)^{\frac{3}{2}}} , \tag{1.35}$$

and then we have :

$$\kappa = \varepsilon \Delta \xi + O(\varepsilon^3). \quad (1.36)$$

Thus, the pressure (1.34) reduces to :

$$p(t, x, y, z) = p_o + \frac{1}{F_r^2}(\xi - z) + O(\varepsilon). \quad (1.37)$$

Using again the relations (1.30), and keeping in mind that  $\partial_z \bar{U} = O(\varepsilon)$ , the relation (1.29) becomes at first order :

$$\begin{aligned} \partial_t(h\bar{U}) + \operatorname{div}_x(h\bar{U} \otimes \bar{U}) + \nabla_{xy} \left( \int_d^\xi p \, dz \right) + \frac{h\bar{U}^\perp}{R_o} \\ = -r_0 \bar{U}|_{z=d} - p|_{z=d} \nabla_{xy} d + p_o \nabla_{xy} \xi + O(\varepsilon). \end{aligned}$$

Plugging (1.34) into this expression yields therefore :

$$\nabla_{xy} \left( \int_d^\xi p \, dz \right) = \frac{1}{2F_r^2} \nabla_{xy}(h^2) + p_o \nabla_{xy} h + O(\varepsilon),$$

and

$$p|_{z=d} \nabla_{xy} d = \frac{1}{F_r^2} h \nabla_{xy} d + p_o \nabla_{xy} d + O(\varepsilon).$$

Finally, dropping the  $O(\varepsilon)$  terms, we obtain the following NSW model, which results of an approximation in  $O(\varepsilon)$  of the system (1.15)-(1.17), where we have set  $\operatorname{div} = \operatorname{div}_x$  and  $\nabla = \nabla_{xy}$ :

$$\left\{ \begin{array}{l} \partial_t h + \operatorname{div}(h\bar{U}) = 0 \quad (i) \\ \partial_t(h\bar{U}) + \operatorname{div}(h\bar{U} \otimes \bar{U}) + \frac{1}{F_r^2} h \nabla h + \frac{(h\bar{U})^\perp}{R_o} = -r_0 \bar{U} - \frac{1}{F_r^2} h \nabla d \quad (ii) \end{array} \right. \quad (1.38)$$

Multiplying by  $\frac{HV^2}{L}$  and setting  $\mathbf{u} = \bar{U}$ , we recover the system in dimensionalized variables :

$$\left\{ \begin{array}{l} \partial_t h + \operatorname{div}(h\mathbf{u}) = 0 \quad (i) \\ \partial_t(h\mathbf{u}) + \operatorname{div}(h\mathbf{u} \otimes \mathbf{u}) + g h \nabla h + f(h\mathbf{u})^\perp = -k_l \mathbf{u} - g h \nabla d \quad (ii) \end{array} \right. \quad (1.39)$$

**1.4.2. Second order approximation and parabolic correction.** We perform here a parabolic correction in  $z$  for the horizontal velocity in order to take the vertical variability of the quantities into account and by this way improve the precision of the NSW model (1.32).

Coming back to the relation (1.18), we have for the horizontal velocity  $U = (u, v)$  :

$$\frac{\partial}{\partial z} \left( \frac{\nu_o}{\varepsilon} \frac{\partial U}{\partial z} \right) = \partial_t U + \operatorname{div} (U \otimes U) + \nabla p + \frac{U^\perp}{R_o} + O(\varepsilon).$$

Considering the incompressibility relation, we have :

$$\frac{\partial}{\partial z} \left( \frac{\nu_o}{\varepsilon} \frac{\partial U}{\partial z} \right) = \partial_t U + U \cdot \nabla U + \nabla p + \frac{U^\perp}{R_o} + O(\varepsilon), \quad (1.40)$$

and using the relations (1.32) and (1.34), (1.40) becomes :

$$\frac{\partial}{\partial z} \left( \frac{\nu_o}{\varepsilon} \frac{\partial U}{\partial z} \right) = \partial_t \bar{U} + \bar{U} \cdot \nabla \bar{U} + \frac{1}{F_r^2} \nabla \xi + \frac{\bar{U}^\perp}{R_o} + O(\varepsilon),$$

so, keeping in mind that  $\xi(t, x, y) = h(t, x, y) + d(x, y)$  and using the equation (1.38 (ii)) we obtain :

$$\frac{\partial}{\partial z} \left( \frac{\nu_o}{\varepsilon} \frac{\partial U}{\partial z} \right) = -\frac{r_0}{h} U|_{z=d} + O(\varepsilon).$$

Integrating from  $d$  to  $z$  we deduce :

$$\frac{\nu_o}{\varepsilon} \frac{\partial U}{\partial z} - \frac{\nu_o}{\varepsilon} \frac{\partial U}{\partial z} \Big|_{z=d} = -\frac{r_0(z+d)}{h} U|_{z=d} + O(\varepsilon).$$

Dropping the  $O(\varepsilon)$  terms, the boundary condition at the bottom (1.28) reads :

$$-\frac{\nu_o}{\varepsilon} \frac{\partial U}{\partial z} \Big|_{z=d} = -r_0 U|_{z=d} + O(\varepsilon). \quad (1.41)$$

and we obtain :

$$\frac{\nu_o}{\varepsilon} \frac{\partial U}{\partial z} = r_0 \left( 1 - \frac{z+d}{h} \right) U|_{z=d} + O(\varepsilon). \quad (1.42)$$

Then, integrating another time we deduce the expansion at second order in  $z$  of the horizontal velocity  $U$  :

$$U(t, x, y, z) = \left( 1 + \frac{r_0 \varepsilon (z+d)}{\nu_o} \left( 1 - \frac{z+d}{2h} \right) \right) U|_{z=d} + O(\varepsilon^2). \quad (1.43)$$

The expression of  $\bar{U} = (\bar{u}, \bar{v})$  is then obtained, integrating (1.43) between  $z = d$  and  $z = \xi$  :

$$\bar{U} = \left( 1 + \frac{r_0 \varepsilon h}{3\nu_o} \right) U|_{z=d} + O(\varepsilon^2). \quad (1.44)$$

Furthermore, we have for the scalar horizontal component  $u$  :

$$u^2(t, x, y, z) = \left(1 + \frac{2\alpha_o \varepsilon (z + d)}{\nu_o} \left(1 - \frac{z + d}{2h}\right)\right) u_{|z=-d}^2 + O(\varepsilon^2),$$

and

$$\overline{u^2} = \frac{1}{h} \int_{-d}^{\xi} u^2 = \left(1 + \frac{2\alpha_o \varepsilon h}{3\nu_o}\right) u_{|z=-d}^2 + O(\varepsilon^2) = \bar{u}^2 + O(\varepsilon^2).$$

It results that :

$$\overline{u^2} = \bar{u}^2 + O(\varepsilon^2).$$

And in the same way we have the following tensorial equality :

$$\overline{U \otimes U} = \bar{U} \otimes \bar{U} + O(\varepsilon^2). \quad (1.45)$$

Using (1.32), (1.36) and (1.30), the pressure (1.24) becomes :

$$p(t, x, y, z) = p_o + \frac{1}{F_r^2} (\xi - z) - \frac{2}{R_e} \partial_x \bar{u}(t, x, y) - \frac{2}{R_e} \partial_y \bar{v}(t, x, y) - \varepsilon \beta \Delta \xi + O(\varepsilon^2). \quad (1.46)$$

The boundary condition at the bottom (1.28) is also simplified, recalling (1.30) and using (1.41) :

$$\frac{1}{R_e} (\partial_z U)_{|z=d} = O(\varepsilon^2).$$

Then, dropping the  $O(\varepsilon^2)$  terms we obtain :

$$\begin{aligned} & \left( -p \nabla_{xy} d + \frac{2}{R_e} D_h(U) \cdot \nabla_{xy} d - \frac{1}{R_e} \left( \frac{1}{\varepsilon^2} \partial_z U + \nabla_{xy} w \right) \right)_{|z=d} \\ &= -r_0 U_{|z=d} - \varepsilon r_1 h |U| U_{|z=d} - \nabla_{xy} d \left( p - \frac{2}{R_e} \partial_z w \right)_{|z=d} + O(\varepsilon^2), \end{aligned}$$

and so

$$\begin{aligned} & \left( -p \nabla_{xy} d + \frac{2}{R_e} D_h(U) \cdot \nabla_{xy} d - \frac{1}{R_e} \left( \frac{1}{\varepsilon^2} \partial_z U + \nabla_{xy} w \right) \right)_{|z=d} \\ &= -r_0 U_{|z=-d} - \varepsilon r_1 h |U| U_{|z=d} - \nabla_{xy} d \left( p + \frac{2}{R_e} \operatorname{div}_x U \right)_{|z=d} + O(\varepsilon^2), \end{aligned} \quad (1.47)$$

thanks to the incompressibility relation.

Gathering (1.44), (1.46) and (1.47) and introducing :

$$\alpha_0(h) = \frac{r_0}{1 + \frac{\varepsilon r_0 h}{3\nu_o}}, \quad \alpha_1(h) = \frac{\varepsilon r_1}{\left(1 + \frac{\varepsilon r_0 h}{3\nu_o}\right)^2} \quad \text{and} \quad \beta' = \varepsilon \beta$$

where  $\alpha_0(h)$  and  $\alpha_1(h)$  are modified friction coefficients, we obtain the following NSW system, which results from an approximation in  $O(\varepsilon^2)$  in the asymptotic analysis of the system (1.15)-(1.17) :

$$\left\{ \begin{array}{l} \partial_t h + \operatorname{div}(h\bar{U}) = 0, \\ \partial_t(h\bar{U}) + \operatorname{div}(h\bar{U} \otimes \bar{U}) + \frac{1}{F_r^2} h \nabla h = \\ -\alpha_0(h) \bar{U} - \alpha_1(h) h |\bar{U}| \bar{U} + \frac{1}{R_e} \operatorname{div} \left( h(\nabla \bar{U} + {}^t \nabla \bar{U}) + (2h \operatorname{div} \bar{U}) \mathcal{I} \right) \\ + \beta' h \nabla \Delta h - \frac{(h\bar{U})^\perp}{R_o} - \frac{1}{F_r^2} h \nabla d + \beta' h \nabla \Delta d. \end{array} \right. \quad (1.48)$$

Multiplying by  $\frac{H V^2}{L}$  and setting  $\mathbf{u} = \bar{U}$ , we recover the system in dimensionalized variables :

$$\left\{ \begin{array}{l} \partial_t h + \operatorname{div}(h\mathbf{u}) = 0, \\ \partial_t(h\mathbf{u}) + \operatorname{div}(h\mathbf{u} \otimes \mathbf{u}) + g h \nabla h = \\ -\alpha_0(h) \mathbf{u} - \alpha_1(h) h |\mathbf{u}| \mathbf{u} + \mu \operatorname{div} \left( h(\nabla \mathbf{u} + {}^t \nabla \mathbf{u}) + (2h \operatorname{div} \mathbf{u}) \mathcal{I} \right) \\ + \beta h \nabla \Delta h - f(h\mathbf{u})^\perp - g h \nabla d + \beta h \nabla \Delta d. \end{array} \right. \quad (1.49)$$

where we have :

$$\alpha_0(h) = \frac{k_l}{1 + \frac{k_l h}{3\mu}} \quad \text{and} \quad \alpha_1(h) = \frac{k_t}{\left(1 + \frac{k_l h}{3\mu}\right)^2}.$$

# Existence de solutions faibles globales

Le but de ce chapitre est l'étude théorique du modèle de Saint-Venant dérivé au chapitre précédent. Notre objectif est d'établir un résultat d'existence de solution faibles globales par des méthodes d'estimations d'énergie et passage à la limite dans une formulation approchée. Ce travail s'inspire des travaux de Simon [157], Boyer et Fabrie [22] et Bresch et Desjardins [51], [24].

Nous allons commencer par étudier l'équation de conservation de la hauteur d'eau pour des données régulières. Nous introduirons ensuite un problème approché complet dans lequel la donnée initiale approchée sera minorée par une constante positive. La résolution de ce problème utilise le théorème du point fixe de Schauder. Nous dériverons alors des estimations d'énergie qui permettront de conclure à l'existence d'au moins une solution vérifiant l'équation dans un sens faible. Il sera nécessaire à ce stade de la démonstration de différencier les cas de la dimension un et de la dimension deux, puisque les estimations obtenues nous permettront de passer à la limite dans le modèle complet en dimension un alors que des hypothèses supplémentaires concernant la positivité de la hauteur d'eau et la forme du terme de diffusion devront être effectuées en dimension deux.

Nous nous intéressons ici au modèle en variable adimensionnées, avec les notations suivantes :

$$\left\{ \begin{array}{l} \partial_t h + \operatorname{div}(h\mathbf{u}) = 0, \\ \partial_t(h\mathbf{u}) + \operatorname{div}(h\mathbf{u} \otimes \mathbf{u}) + \frac{1}{F_r^2} h \nabla h = h f \\ -\alpha_0(h) \mathbf{u} - \alpha_1(h) h |\mathbf{u}| \mathbf{u} + \nu \operatorname{div} \left( h(D(\mathbf{u}) + (2h \operatorname{div} \mathbf{u})\mathcal{I}) \right) \\ + \beta h \nabla \Delta h - \frac{(h\mathbf{u})^\perp}{R_o} - \frac{1}{F_r^2} h \nabla d + \beta h \nabla \Delta d, \end{array} \right. \quad (2.1)$$

avec

$$\alpha_0(h) = \frac{r_0}{1 + \frac{\varepsilon r_0 h}{3\nu_o}}, \quad \alpha_1(h) = \frac{r_1}{\left(1 + \frac{\varepsilon r_0 h}{3\nu_o}\right)^2},$$

et

$$D(\mathbf{u}) = \frac{1}{2} \left( \nabla \mathbf{u} + {}^t \nabla \mathbf{u} \right)$$

où  $\nu = 1/R_e$ ,  $R_o$  et  $F_r$  désignent respectivement l'inverse du nombre de Reynolds, le nombre de Rossby et le nombre de Froude.  $\beta$  désigne le coefficient de tension de surface et  $r_0$  et  $r_1$  représentent respectivement les coefficients de friction laminaire et quadratique.  $f$  désigne ici une fonction représentant un terme source ne faisant pas intervenir les inconnues du problème. Ce terme supplémentaire peut être obtenu directement dans la dérivation précédente.

## 2.1. Principaux résultats

**Notations.** Soit  $I = ]0, L[$ , ouvert borné de  $\mathbb{R}$ . On introduit  $C_{per}^\infty(I)$  l'ensemble des fonctions de régularité  $C^\infty$  et vérifiant des conditions aux limites périodiques sur  $I$ .

**Définition 2.1.1.** On note  $W_{per}^{s,p}(I)$  l'adhérence de  $C_{per}^\infty(I)$  pour la norme de  $W^{s,p}(I)$ .

On définit alors respectivement les espaces  $L_{per}^p(I) = W_{per}^{0,p}(I)$  et  $H_{per}^s(I) = W_{per}^{s,2}(I)$  et on note  $(W_{per}^{s,p}(I))'$  le dual de  $W_{per}^{s,p}(I)$ .

De même soit  $\Omega = ]0, 1[ \times ]0, L[$  et  $C_{per}^\infty(\Omega)$  l'ensemble des fonctions de régularité  $C^\infty$  et vérifiant des conditions aux limites périodiques sur  $\Omega$ .

**Définition 2.1.2.** On note  $W_{per}^{s,p}(\Omega)$  l'adhérence de  $C_{per}^\infty(\Omega)$  pour la norme de  $W^{s,p}(\Omega)$ .

On définit alors respectivement les espaces  $L_{per}^p(\Omega) = W_{per}^{0,p}(\Omega)$  et  $H_{per}^s(\Omega) = W_{per}^{s,2}(\Omega)$  et on note  $(W_{per}^{s,p}(\Omega))'$  le dual de  $W_{per}^{s,p}(\Omega)$ .

### Cas de la dimension 1.

**Théorème 2.1.1** (Existence d'une solution faible en dimension 1). .

Soit  $d \in L_{per}^\infty(I)$  et  $f \in L^2(\mathbb{R}^+; L_{per}^\infty(I))$ . Alors il existe au moins une solution  $(h, u)$  satisfaisant dans  $(\mathcal{D}(\mathbb{R}^+; H_{per}^2(I)))'$

$$\left\{ \begin{array}{l} \partial_t h + \partial_x(hu) = 0, \\ \partial_t(hu) + \partial_x(hu^2) + \frac{1}{F_r^2} h \partial_x h - \beta h \partial_x^3 h + \alpha_0(h)u + \alpha_1(h)h|u|u = \\ hf + 3\nu \partial_x(h \partial_x u) - \frac{1}{F_r^2} h \partial_x d + \beta h \partial_x^3 d, \\ h(0) = h_0, \\ (hu)(0) = h_0 u_0, \end{array} \right. \quad (2.2)$$

avec

$$\alpha_0(h) = \frac{r_0}{1 + \frac{\varepsilon r_0 h}{3\nu_o}}, \quad \alpha_1(h) = \frac{r_1}{\left(1 + \frac{\varepsilon r_0 h}{3\nu_o}\right)^2},$$

et  $r_0 > 0$ ,  $r_1 > 0$ ,  $\beta > 0$ . De plus  $(h, u)$  vérifie les propriétés de régularité suivantes :

- $\forall T > 0$ ,  $h \in L^\infty(0, T; L^\infty_{per}(I)) \cap L^\infty(0, T; H^1_{per}(I)) \cap L^2(0, T; H^2_{per}(I))$ ,
- $\forall T > 0$ ,  $u \in L^2(0, T; L^2_{per}(I))$ ,
- $\forall T > 0$ ,  $hu \in L^3(0, T; L^3_{per}(I)) \cap L^2(0, T; W^{1,1}_{per}(I))$ .

Les conditions initiales  $h_0$  et  $u_0$  sont choisies telles que :

$$\begin{aligned} \sqrt{h_0} &\in H^1_{per}(I), \quad h_0 \geq 0, \\ h_0 u_0^2 &\in L^1_{per}(I) \quad , \quad \log(r_0^{-1} h_0 \alpha_0(h_0)) \in L^1(I), \end{aligned}$$

et satisfaites au sens suivant :

$$\begin{aligned} h(0) &= h_0, \\ \forall \psi \in L^2_{per}(I), \quad \left( \int_I (hu)\psi \right) (0) &= \int_I (h_0 u_0)\psi. \end{aligned}$$

**Remarque 2.1.1.** Remarquons l'hypothèse de positivité stricte faite sur les coefficients  $r_0$ ,  $r_1$  et  $\beta$ . Cette hypothèse s'avère nécessaire dans la démonstration adoptée ici afin d'obtenir des estimations suffisamment régulières sur  $h$ ,  $u$  et  $hu$ . Plus précisément, le terme de tension de surface permet d'obtenir des bornes  $H^1$  et  $H^2$  sur  $h$ , les injections de Sobolev en dimension un fournissant une borne  $L^\infty$ . Les termes de friction laminaire et quadratique permettent respectivement d'obtenir une régularité suffisante sur  $u$  et  $hu$ . Dans [51], il apparaît que le résultat d'existence obtenu en dimension deux par Bresch et Desjardins peut être obtenu en dimension un avec des conditions moins restrictives sur  $\beta$  et  $r_1$ , qui peuvent être choisis positifs au sens large. En effet, dans [51], la compacité n'est pas obtenue sur  $(h_k u_k)$  mais sur  $(\sqrt{h_k} u_k)_k$ , en négligeant les

hautes fréquences uniformément en  $k$ . Ceci permet directement le passage à la limite pour le terme non linéaire  $(h_k u_k^2)_k$ , sans avoir la régularité  $L^2$  sur  $(u_k)_k$ . L'existence de solutions faibles globales peut donc être obtenue pour le modèle unidimensionnel dérivé dans [62].

### Cas de la dimension 2.

**Théorème 2.1.2** (Existence d'une solution faible en dimension 2). .

Soit  $f \in L^2(\mathbb{R}^+; L_{per}^\infty(\Omega))$  et  $d \in L_{per}^\infty(\Omega)$ . On suppose qu'il existe  $\gamma > 0$  tel que l'on ait

$$h(t, \mathbf{x}) > \gamma \quad \forall (t, \mathbf{x}) \in \mathbb{R}^+ \times \Omega.$$

Alors il existe au moins une solution  $(h, \mathbf{u})$  satisfaisant dans  $(\mathcal{D}(\mathbb{R}^+; H_{per}^2(\Omega)))'$

$$\left\{ \begin{array}{l} \partial_t h + \operatorname{div}(h\mathbf{u}) = 0, \\ \partial_t(h\mathbf{u}) + \operatorname{div}(h\mathbf{u} \otimes \mathbf{u}) + \frac{1}{F_r^2} h \nabla h = h f - \alpha_0(h) \mathbf{u} - \alpha_1(h) h |\mathbf{u}| \mathbf{u} \\ + \nu \operatorname{div}(hD(\mathbf{u})) + \beta h \nabla \Delta h - \frac{(h\mathbf{u})^\perp}{R_o} - \frac{1}{F_r^2} h \nabla d + \beta h \nabla \Delta d, \end{array} \right. \quad (2.3)$$

avec  $r_0 > 0$ ,  $r_1 > 0$ ,  $\beta > 0$ . De plus  $(h, \mathbf{u})$  vérifie les propriétés de régularité suivantes :

- $\forall T > 0$ ,  $h \in L^\infty(0, T; H_{per}^1(\Omega)) \cap L^2(0, T; H_{per}^2(\Omega))$ ,
- $\forall T > 0$ ,  $\mathbf{u} \in L^2(0, T; H_{per}^1(\Omega))$ ,
- $\forall T > 0$ ,  $h\mathbf{u} \in L^\infty(0, T; L_{per}^{\frac{2p}{p+2}}(\Omega)) \cap L^2(0, T; W_{per}^{1, \frac{2p}{p+2}}(\Omega)) \quad \forall p < \infty$ .

Les conditions initiales  $h_0$  et  $\mathbf{u}_0$  sont choisies telles que :

$$\begin{aligned} \sqrt{h_0} &\in H_{per}^1(\Omega), \quad h_0 \geq 0, \\ h_0 |\mathbf{u}_0|^2 &\in L_{per}^1(\Omega) \quad , \quad \log(r_0^{-1} h_0 \alpha_0(h_0)) \in L^1(\Omega), \end{aligned}$$

et satisfaites au sens suivant :

$$\begin{aligned} h(0) &= h_0, \\ \forall \psi &\in H_{per}^1(\Omega), \quad \left( \int_{\Omega} (h\mathbf{u}) \psi \right) (0) = \int_{\Omega} (h_0 \mathbf{u}_0) \psi. \end{aligned}$$

**Remarque 2.1.2.** Il semble possible d'obtenir un résultat similaire sans supposer l'existence d'une borne inférieure sur la hauteur d'eau  $h$ . La conséquence est une régularité moins bonne sur la vitesse qui est alors seulement  $L^2(0, T; L_{per}^{\frac{3}{2}}(\Omega))$ . Ce résultat est actuellement à l'étude.

## 2.2. Résolution de l'équation de conservation de la hauteur d'eau

Les résultats présentés ici le sont dans le cas bidimensionnel. Des résultats similaires sont immédiatement déduits pour le cas unidimensionnel en remplaçant  $\Omega$  par  $I$ .

**2.2.1. Equation linéarisée.** On rappelle que  $\Omega = ]0, 1[ \times ]0, L[$  et  $\mathbf{u}(t, x)$  une fonction de classe  $\mathcal{C}^\infty$  de  $\mathbb{R}_t \times \overline{\Omega}$  vérifiant des conditions aux limites périodiques sur les bords de  $\Omega$ . On s'intéresse à la résolution de l'équation :

$$\begin{cases} \partial_t h(t, x) + \operatorname{div} (\mathbf{u}(t, x)h(t, x)) = 0, \\ h(0, x) = h_0(x). \end{cases} \quad (2.4)$$

où  $h(t, x)$  vérifie également des conditions aux limites périodiques.

On pose  $k(t, x) = \ln h(t, x)$  et on obtient l'équation suivante :

$$\begin{cases} \partial_t k(t, x) + \mathbf{u}(t, x) \cdot \nabla k(t, x) = \operatorname{div} \mathbf{u}(t, x), \\ k(0, x) = k_0(x). \end{cases} \quad (2.5)$$

On résout (2.5) par la méthode des caractéristiques en introduisant la fonction  $Z$  solution de :

$$\begin{cases} \frac{d}{ds} Z(s, t, x) = \mathbf{u}(s, Z(s, t, x)), \\ Z(t, t, x) = x. \end{cases} \quad (2.6)$$

La fonction  $Z$  représente la position à l'instant  $s$  d'une particule fluide située au point  $x$  à l'instant  $t$ .

### 2.2.2. Existence et unicité.

**Proposition 2.2.1.** *Soit  $\mathbf{u}$  une fonction de classe  $\mathcal{C}^\infty$  de  $\mathbb{R} \times \Omega$  dans  $\mathbb{R}^2$  vérifiant des conditions aux limites périodiques sur le bord de  $\Omega$ . On suppose que  $h_0$  est une fonction de classe  $\mathcal{C}^2$  de  $\Omega$  dans  $\mathbb{R}$ , vérifiant également des conditions aux limites périodiques. Alors il existe une solution de classe  $\mathcal{C}^2$  du problème linéaire (2.4) donnée par*

$$h(t, x) = h_0(Z(0, t, x)) e^{\int_0^t (\operatorname{div} \mathbf{u})(\tau, Z(\tau, t, x)) d\tau}. \quad (2.7)$$

En particulier, on a les estimations suivantes :

$$\|h(t)\|_{L^2(\Omega)} \leq \|h_0\|_{L^2(\Omega)} e^{\int_0^t \|\mathbf{u}(\tau)\|_{W^{1,\infty}(\Omega)} d\tau} \quad (2.8)$$

$$\|h(t)\|_{L^\infty(\Omega)} \leq \|h_0\|_{L^\infty(\Omega)} e^{\int_0^t \|\mathbf{u}(\tau)\|_{W^{1,\infty}(\Omega)} d\tau}$$

On a de plus les estimations dans  $H^1(\Omega)$  :

$$\|\nabla h(t)\|_{L^2(\Omega)} \leq \left( \|\nabla h_0\|_{L^2(\Omega)} + \|h_0\|_{L^2(\Omega)} \int_0^T \|\mathbf{u}(\tau)\|_{W^{2,\infty}(\Omega)} d\tau \right) e^{\int_0^T 2\|\mathbf{u}(\tau)\|_{W^{1,\infty}(\Omega)} d\tau} \quad (2.9)$$

et dans  $H^2(\Omega)$  :

$$\begin{aligned} \|\nabla^2 h(t, \cdot)\|_{L^2(\Omega)} &\leq \left( \|\nabla^2 h_0\|_{L^2(\Omega)} + 2\|\nabla h_0\|_{L^2(\Omega)} \int_0^T \|\mathbf{u}(\tau)\|_{W^{2,\infty}(\Omega)} d\tau \right. \\ &\quad \left. + \|h_0\|_{L^2(\Omega)} \int_0^T \|\mathbf{u}(\tau)\|_{W^{3,\infty}(\Omega)} d\tau \right. \\ &\quad \left. + \|h_0\|_{L^2(\Omega)} \left( \int_0^T \|\mathbf{u}(\tau)\|_{W^{2,\infty}(\Omega)} d\tau \right)^2 \right) e^{\int_0^T 3\|\mathbf{u}(\tau)\|_{W^{1,\infty}(\Omega)} d\tau} \\ &+ \left( \|\nabla h_0\|_{L^2(\Omega)} \int_0^T \|\mathbf{u}(\tau)\|_{W^{2,\infty}(\Omega)} d\tau \right. \\ &\quad \left. + \|h_0\|_{L^2(\Omega)} \left( \int_0^T \|\mathbf{u}(\tau)\|_{W^{2,\infty}(\Omega)} d\tau \right)^2 \right) e^{\int_0^T 4\|\mathbf{u}(\tau)\|_{W^{1,\infty}(\Omega)} d\tau}. \end{aligned} \quad (2.10)$$

Enfin  $h(t, \cdot)$  vérifie des conditions aux limites périodiques sur le bord de  $\Omega$ .

**Preuve.**

(1) Unicité :

Supposons qu'il existe deux solutions régulières  $\mathbf{u}_1$  et  $\mathbf{u}_2$  de (2.4), alors la différence  $\mathbf{u} = \mathbf{u}_1 - \mathbf{u}_2$  vérifie

$$\begin{aligned} \partial_t h + \operatorname{div}(h \mathbf{u}) &= 0, \\ h(0) &= 0. \end{aligned}$$

En multipliant l'équation précédente par  $h$  et en intégrant sur  $\Omega$  on obtient :

$$\frac{1}{2} \frac{d}{dt} \|h(t)\|_{L^2(\Omega)}^2 - \int_{\Omega} h \mathbf{u} \cdot \nabla h = 0.$$

Comme  $h \nabla h = \frac{1}{2} \nabla(h^2)$ , on obtient en intégrant par parties :

$$\frac{d}{dt} \|h(t)\|_{L^2(\Omega)}^2 + \int_{\Omega} h^2 \operatorname{div} \mathbf{u} = 0.$$

soit :

$$\frac{d}{dt} \|h(t)\|_{L^2(\Omega)}^2 \leq \|\operatorname{div} \mathbf{u}(t)\|_{L^\infty(\Omega)} \|h(t)\|_{L^2(\Omega)}^2.$$

On conclut en utilisant le lemme de Gronwall :

$$\|h(t)\|_{L^2(\Omega)}^2 \leq \|h(0)\|_{L^2(\Omega)}^2 e^{\int_0^t \|\operatorname{div} \mathbf{u}(s)\|_{L^\infty(\Omega)} ds},$$

soit  $\|h(t)\|_{L^2(\Omega)}^2 = 0$  et donc  $h(t, x) = 0$ . ■

(2) Existence :

Posons  $\operatorname{div} \mathbf{u}(t, x) = f(t, x)$ . On s'intéresse à la résolution du système suivant :

$$\begin{cases} \partial_t k(t, x) + \mathbf{u}(t, x) \cdot \nabla k(t, x) = f(t, x), \\ k(0, x) = k_0(x). \end{cases} \quad (2.11)$$

On cherche une solution sous la forme  $k(t, x) = g(t, Z(0, t, x))$ . On note dans cette partie  $f_x$  la dérivation par rapport à  $x$  et  $f_t$  celle par rapport à  $t$  d'une fonction  $f$ . On évalue

$$\begin{aligned} \partial_t k(t, x) + \mathbf{u}(t, x) \nabla k(t, x) - f(t, x) &= g_t(t, Z(0, t, x)) + g_x(t, Z(0, t, x)) Z_t(0, t, x) \\ &\quad + \mathbf{u}(t, x) g_x(t, Z(0, t, x)) Z_x(0, t, x) \\ &\quad - f(t, Z(t, t, x)) = 0. \end{aligned}$$

Posons  $\gamma(s, t, x) = Z_t(s, t, x) + Z_x(s, t, x) \mathbf{u}(t, x)$ . On a alors :

$$g_t(t, Z(0, t, x)) + \gamma(0, t, x) g_x(t, Z(0, t, x)) = 0$$

On va montrer que  $\gamma(t, t, x) = 0$  et que  $\gamma$  vérifie une équation linéaire.

Par construction on a  $Z(t, t, x) = x$  pour tout  $x$  et tout  $t$ , et ainsi en dérivant par rapport à  $t$  il vient

$$Z_t(t, t, x) + Z_s(t, t, x) = 0,$$

et par ailleurs

$$Z_s(t, t, x) = \mathbf{u}(s, Z(s, t, x))|_{s=t} = \mathbf{u}(t, x).$$

Enfin, en dérivant (2.6) par rapport à la donnée  $x$ , il vient

$$Z_x(t, t, x) = Id.$$

Au final,

$$\gamma(t, t, x) = Z_t(t, t, x) + Z_x(t, t, x) \mathbf{u}(t, x) = -\mathbf{u}(t, x) + \mathbf{u}(t, x) = 0.$$

Par ailleurs en appliquant les résultats de dérivation par rapport aux données et à un paramètre, on a

$$\begin{aligned} \frac{d}{ds} \gamma(s, t, x) &= \frac{d}{ds} (Z_t(s, t, x) + Z_x(s, t, x) \mathbf{u}(t, x)), \\ &= \frac{d}{dt} Z_s(s, t, x) + \left( \frac{d}{dx} Z_s(s, t, x) \right) \cdot \mathbf{u}(t, x), \\ &= \mathbf{u}_x(s, Z(s, t, x)) \cdot Z_t(s, t, x) + \mathbf{u}_x(s, Z(s, t, x)) Z_x(s, t, x) \cdot \mathbf{u}(t, x) \\ &= \mathbf{u}_x(s, Z(s, t, x)) \gamma(s, t, x). \end{aligned}$$

Ainsi,  $s \mapsto \gamma(s, t, x)$  est solution d'une EDO linéaire et vérifie  $\gamma(t, t, x) = 0$ , ce qui prouve que  $\forall s, \gamma(s, t, x) = 0$  et donc en particulier  $\gamma(0, t, x) = 0$ .

On obtient alors l'équation suivante :

$$g_t(t, Z(0, t, x)) = f(t, Z(t, t, x)),$$

que l'on intègre pour obtenir :

$$g(t, Z(0, t, x)) = g_0(Z(0, t, x)) + \int_0^t f(\tau, Z(\tau, t, x)) d\tau,$$

soit :

$$k(t, x) = k_0(Z(0, t, x)) + \int_0^t (\operatorname{div} \mathbf{u})(\tau, Z(\tau, t, x)) d\tau,$$

ou encore :

$$h(t, x) = h_0(Z(0, t, x)) e^{\int_0^t (\operatorname{div} \mathbf{u})(\tau, Z(\tau, t, x)) d\tau}.$$

On vérifie sur cette expression que  $h(t, x)$  vérifie des conditions aux limites périodiques. On obtient immédiatement les estimations voulues :

$$\|h(t)\|_{L^2(\Omega)} \leq \|h_0\|_{L^2(\Omega)} e^{\int_0^t \|\nabla \mathbf{u}(\tau)\|_{L^\infty(\Omega)} d\tau}$$

et

$$\|h(t)\|_{L^\infty(\Omega)} \leq \|h_0\|_{L^\infty(\Omega)} e^{\int_0^t \|\nabla \mathbf{u}(\tau)\|_{L^\infty(\Omega)} d\tau}.$$

(3) Estimation  $H^1$  :

En dérivant l'expression (2.7), par rapport à  $x$ , on obtient :

$$\begin{aligned} \partial_{x_i} h(t, x) &= \partial_{x_i} \left( h_0(Z(0, t, x)) \right) e^{\int_0^t (\operatorname{div} \mathbf{u})(\tau, Z(\tau, t, x)) d\tau} \\ &\quad + h_0(Z(0, t, x)) \partial_{x_i} \left( e^{\int_0^t (\operatorname{div} \mathbf{u})(\tau, Z(\tau, t, x)) d\tau} \right) \end{aligned}$$

avec :

$$\partial_{x_i} h_0(Z(0, t, x)) = \sum_j \partial_{x_i} h_0(Z(0, t, x)) \partial_{x_i} Z_j(0, t, x),$$

soit encore :

$$\begin{aligned} \nabla h(t, x) = & \nabla \left( h_0(Z(0, t, x)) \right) e^{\int_0^t (\operatorname{div} \mathbf{u})(\tau, Z(\tau, t, x)) d\tau} \\ & + h_0(Z(0, t, x)) \nabla \left( e^{\int_0^t (\operatorname{div} \mathbf{u})(\tau, Z(\tau, t, x)) d\tau} \right) \end{aligned} \quad (2.12)$$

avec :

$$\nabla \left( h_0(Z(0, t, x)) \right) = (\nabla Z(0, t, x))^t \nabla h_0(Z(0, t, x)). \quad (2.13)$$

Si on dérive l'équation (2.6), par rapport à  $x$ , on obtient l'équation matricielle suivante :

$$\begin{cases} \partial_s (\nabla Z)(s, t, x) = (\nabla \mathbf{u})(s, Z(s, t, x)) \cdot (\nabla Z)(s, t, x), \\ \nabla Z(t, t, x) = I. \end{cases} \quad (2.14)$$

Un lemme classique sur les équations différentielles linéaires montre que l'on a :

$$\partial_s \det(\nabla Z) = \operatorname{Tr}(\nabla \mathbf{u}) \det(\nabla Z),$$

et un calcul immédiat montre que :

$$\operatorname{Tr}(\nabla \mathbf{u}) = \operatorname{div}(\mathbf{u})$$

Comme  $\det(\nabla Z(t, t, x)) = 1$ , on obtient l'équation différentielle ordinaire suivante :

$$\begin{cases} \partial_s \det(\nabla Z)(s, t, x) = \operatorname{div} \mathbf{u}(s, Z(s, t, x)) \det(\nabla Z)(s, t, x), \\ \det(\nabla Z(t, t, x)) = 1. \end{cases} \quad (2.15)$$

On remarque que  $\det(\nabla Z)(s, t, x) = 0 \quad \forall s$  est solution de l'équation :

$$\partial_s \det(\nabla Z)(s, t, x) = \operatorname{div} \mathbf{u}(s, Z(s, t, x)) \det(\nabla Z)(s, t, x).$$

Un résultat classique sur les équations différentielles linéaires du type  $x'(t) = a(t)x(t)$  nous assure alors que toute solution différente de la solution identiquement nulle ne s'annule jamais.

Autrement dit, comme  $\det(\nabla Z(t, t, x)) = 1$  alors l'unique solution de l'équation (2.15) vérifie à  $t$  et  $x$  fixé :

$$\det(\nabla Z)(s, t, x) \neq 0 \quad \forall s,$$

et donc à  $t$  et  $s$  fixés,  $x \mapsto Z(t, s, x)$  est un  $C^1$  difféomorphisme de  $\Omega$  dans lui-même qui conserve le volume. En effet la bijectivité résulte de l'identité  $Z(t, s, Z(s, t, x)) = x$ , et la régularité du théorème d'inversion locale.

Ainsi, grâce au théorème de changement de variable, on a pour toute fonction  $f \in L^1(\Omega)$

$$\int_{\Omega} f(x) dx = \int_{\Omega} f(Z(s, t, x)) dx.$$

Si on revient à (2.12), on obtient, sous l'hypothèse que  $\nabla h_0$  est dans  $L^2(\Omega)$  :

$$\begin{aligned} \|\nabla h(t)\|_{L^2(\Omega)} &\leq \|\nabla h_0\|_{L^2(\Omega)} \|\nabla Z(0, t, \cdot)\|_{L^\infty(\Omega)} e^{\int_0^t \|\nabla \mathbf{u}(\tau)\|_{L^\infty(\Omega)} d\tau} \\ &\quad + \|h_0\|_{L^2(\Omega)} \|\nabla \left( e^{\int_0^t (\operatorname{div} \mathbf{u})(\tau, \cdot) d\tau} \right)\|_{L^\infty(\Omega)} \end{aligned}$$

Par ailleurs l'équation sur  $\nabla Z$  s'écrit :

$$\nabla Z(s, t, x) = I + \int_t^s (\nabla \mathbf{u})(\tau, Z(\tau, t, x)) \cdot (\nabla Z)(\tau, t, x) d\tau,$$

ce qui donne :

$$\|\nabla Z(s, t, \cdot)\|_{L^\infty(\Omega)} \leq 1 + \left| \int_t^s \|\nabla \mathbf{u}(\tau, \cdot)\|_{L^\infty(\Omega)} \|\nabla Z(\tau, t, \cdot)\|_{L^\infty(\Omega)} d\tau \right|,$$

et donc par le lemme de Gronwall :

$$\|\nabla Z(s, t, \cdot)\|_{L^\infty(\Omega)} \leq e^{\left| \int_s^t \|\nabla \mathbf{u}(\tau)\|_{L^\infty(\Omega)} d\tau \right|},$$

soit :

$$\|\nabla Z(s, t, \cdot)\|_{L^\infty(\Omega)} \leq e^{\int_0^T \|\nabla \mathbf{u}(\tau)\|_{L^\infty(\Omega)} d\tau} \quad \forall s, t > 0. \quad (2.16)$$

Il reste à évaluer le second terme :

$$\begin{aligned} \nabla \left( e^{\int_0^t (\operatorname{div} \mathbf{u})(\tau, Z(\tau, t, x)) d\tau} \right) &= \\ \nabla \left( \int_0^t (\operatorname{div} \mathbf{u})(\tau, Z(\tau, t, x)) d\tau \right) e^{\int_0^t (\operatorname{div} \mathbf{u})(\tau, Z(\tau, t, x)) d\tau} & \end{aligned}$$

avec :

$$\nabla \left( (\operatorname{div} \mathbf{u})(s, Z(s, t, x)) \right) = (\nabla Z(s, t, x))^t (\nabla \operatorname{div} \mathbf{u})(s, Z(s, t, x)).$$

Il vient :

$$\begin{aligned} \|\nabla \left( e^{\int_0^t (\operatorname{div} \mathbf{u})(\tau, \cdot) d\tau} \right)\|_{L^\infty(\Omega)} \leq \\ \left( \int_0^t \|\nabla Z(\tau, t, \cdot)\|_{L^\infty(\Omega)} \|u(\tau)\|_{W^{2,\infty}(\Omega)} d\tau \right) e^{\int_0^t \|\nabla \mathbf{u}(\tau)\|_{L^\infty(\Omega)} d\tau} \end{aligned}$$

soit :

$$\begin{aligned} \|\nabla \left( e^{\int_0^t (\operatorname{div} \mathbf{u})(\tau, \cdot) d\tau} \right)\|_{L^\infty(\Omega)} \leq \\ \left( \int_0^T \|\mathbf{u}(\tau)\|_{W^{2,\infty}(\Omega)} d\tau \right) e^{\int_0^T 2\|\nabla \mathbf{u}(\tau)\|_{L^\infty(\Omega)} d\tau} \end{aligned}$$

d'où l'estimation  $H^1$  :

$$\begin{aligned} \|\nabla h(t)\|_{L^2(\Omega)} \leq & \left( \|\nabla h_0\|_{L^2(\Omega)} \right. \\ & \left. + \|h_0\|_{L^2(\Omega)} \int_0^T \|\mathbf{u}(\tau)\|_{W^{2,\infty}(\Omega)} d\tau \right) e^{\int_0^T 2\|\mathbf{u}(\tau)\|_{(W^{1,\infty}\Omega)} d\tau}. \end{aligned} \quad (2.17)$$

(4) Estimation  $H^2$  :

On a :

$$\begin{aligned} \nabla^2 h(t, x) = & \nabla \left( (\nabla Z(0, t, x))^t \nabla h_0(Z(0, t, x)) e^{\int_0^t (\operatorname{div} \mathbf{u})(\tau, Z(\tau, t, x)) d\tau} \right) + \\ & \nabla \left( h_0(Z(0, t, x)) e^{\int_0^t (\operatorname{div} \mathbf{u})(\tau, Z(\tau, t, x)) d\tau} \right. \\ & \left. \times \int_0^t (\nabla Z(\tau, t, x))^t (\nabla \operatorname{div} \mathbf{u})(\tau, Z(\tau, t, x)) d\tau \right), \end{aligned}$$

avec :

$$\begin{aligned}
& \nabla \left( (\nabla Z(0, t, x))^t \nabla h_0(Z(0, t, x)) e^{\int_0^t (\operatorname{div} \mathbf{u})(\tau, Z(\tau, t, x)) d\tau} \right) \\
&= \nabla^2 h_0(Z(0, t, x)) \left( \nabla Z(0, t, x) \right)^2 e^{\int_0^t (\operatorname{div} \mathbf{u})(\tau, Z(\tau, t, x)) d\tau} \\
&+ \nabla h_0(Z(0, t, x)) \nabla^2 Z(0, t, x) e^{\int_0^t (\operatorname{div} \mathbf{u})(\tau, Z(\tau, t, x)) d\tau} \\
&+ \nabla Z(0, t, x))^t \nabla h_0(Z(0, t, x)) e^{\int_0^t (\operatorname{div} \mathbf{u})(\tau, Z(\tau, t, x)) d\tau} \\
&\quad \times \int_0^t (\nabla Z(\tau, t, x))^t (\nabla \operatorname{div} \mathbf{u}) d\tau,
\end{aligned}$$

et

$$\begin{aligned}
& \nabla \left( h_0(Z(0, t, x)) e^{\int_0^t (\operatorname{div} \mathbf{u}) d\tau} \int_0^t (\nabla Z(\tau, t, x))^t (\nabla \operatorname{div} \mathbf{u})(\tau, Z(\tau, t, x)) d\tau \right) \\
&= \nabla Z(0, t, x))^t \nabla h_0(Z(0, t, x)) e^{\int_0^t (\operatorname{div} \mathbf{u}) d\tau} \\
&\quad \times \int_0^t (\nabla Z(\tau, t, x))^t (\nabla \operatorname{div} \mathbf{u})(\tau, Z(\tau, t, x)) d\tau \\
&+ h_0(Z(0, t, x)) \left( \int_0^t \nabla^2 Z(\tau, t, x) \nabla \operatorname{div} \mathbf{u}(\tau, Z) \right. \\
&\quad \left. + (\nabla Z(\tau, t, x))^2 \nabla^2 \operatorname{div} \mathbf{u}(\tau, Z) d\tau \right) e^{\int_0^t (\operatorname{div} \mathbf{u}) d\tau} \\
&+ h_0(Z(0, t, x)) \left( \int_0^t (\nabla Z(\tau, t, x))^t (\nabla \operatorname{div} \mathbf{u})(\tau, Z(\tau, t, x)) d\tau \right)^2 e^{\int_0^t (\operatorname{div} \mathbf{u}) d\tau}.
\end{aligned}$$

Par ailleurs, en dérivant une nouvelle fois l'équation (2.14) on obtient :

$$\begin{cases} \partial_s (\nabla^2 Z)(s, t, x) = (\nabla^2 \mathbf{u})(s, Z) \cdot (\nabla Z)^2(s, t, x) + (\nabla \mathbf{u})(s, Z) \cdot (\nabla^2 Z)(s, t, x), \\ \nabla^2 Z(t, t, x) = 0. \end{cases} \quad (2.18)$$

Ainsi

$$\begin{aligned}
(\nabla^2 Z)(s, t, x) &= \int_t^s (\nabla^2 \mathbf{u})(\tau, Z(\tau, t, x)) \cdot (\nabla Z)^2(\tau, t, x) d\tau \\
&\quad + \int_t^s (\nabla \mathbf{u})(\tau, Z(\tau, t, x)) \cdot (\nabla^2 Z)(\tau, t, x) d\tau,
\end{aligned}$$

d'où :

$$\begin{aligned}
\|(\nabla^2 Z)(s, t, \cdot)\|_{L^\infty(\Omega)} &\leq \left| \int_t^s \|\mathbf{u}(\tau)\|_{W^{2,\infty}(\Omega)} \|\nabla Z(\tau, t, \cdot)\|_{L^\infty(\Omega)}^2 d\tau \right| \\
&\quad + \left| \int_t^s \|\mathbf{u}(\tau)\|_{W^{1,\infty}(\Omega)} \|\nabla^2 Z(\tau, t, \cdot)\|_{L^\infty(\Omega)} d\tau \right|.
\end{aligned}$$

En utilisant (2.16) on obtient :

$$\begin{aligned}
\|(\nabla^2 Z)(s, t, \cdot)\|_{L^\infty(\Omega)} &\leq \left( \int_0^T \|\mathbf{u}(\tau)\|_{W^{2,\infty}(\Omega)} d\tau \right) e^{\int_0^T 2\|\mathbf{u}\|_{W^{1,\infty}(\Omega)} d\tau} \\
&\quad + \left| \int_t^s \|\mathbf{u}(\tau)\|_{W^{2,\infty}(\Omega)} \|\nabla^2 Z(\tau, t, \cdot)\|_{L^\infty(\Omega)} d\tau \right|,
\end{aligned} \tag{2.19}$$

d'où par le lemme de Gronwall :

$$\|(\nabla^2 Z)(s, t, \cdot)\|_{L^\infty(\Omega)} \leq \left( \int_0^T \|\mathbf{u}(\tau)\|_{W^{2,\infty}(\Omega)} d\tau \right) e^{\int_0^T 3\|\mathbf{u}(\tau)\|_{W^{1,\infty}(\Omega)} d\tau}$$

et finalement l'estimation  $H^2(\Omega)$  :

$$\begin{aligned}
\|\nabla^2 h(t, \cdot)\|_{L^2(\Omega)} &\leq \left( \|h_0\|_{H^2(\Omega)} + 2\|h_0\|_{H^1(\Omega)} \int_0^T \|\mathbf{u}(\tau)\|_{W^{2,\infty}(\Omega)} d\tau \right. \\
&\quad + \|h_0\|_{L^2(\Omega)} \int_0^T \|\mathbf{u}(\tau)\|_{W^{3,\infty}(\Omega)} d\tau \\
&\quad \left. + \|h_0\|_{L^2(\Omega)} \left( \int_0^T \|\mathbf{u}(\tau)\|_{W^{2,\infty}(\Omega)} d\tau \right)^2 \right) e^{\int_0^T 3\|\mathbf{u}\|_{W^{1,\infty}(\Omega)} d\tau} \\
&\quad + \left( \|\nabla h_0\|_{L^2(\Omega)} \int_0^T \|\mathbf{u}(\tau)\|_{(W^{2,\infty}\Omega)} d\tau \right. \\
&\quad \left. + \|h_0\|_{L^2(\Omega)} \left( \int_0^T \|\mathbf{u}(\tau)\|_{W^{2,\infty}(\Omega)} d\tau \right)^2 \right) e^{\int_0^T 4\|\mathbf{u}\|_{(W^{1,\infty}\Omega)} d\tau}.
\end{aligned}$$

■

### 2.3. Problème approché

Soit  $h_0 \in H_{per}^1(\Omega)$ ,  $h_0 \geq 0$  et  $\mathbf{u}_0$  tel que  $h_0 |\mathbf{u}_0|^2 \in L_{per}^1(\Omega)$ , par exemple  $\mathbf{u}_0 \in L_{per}^3(\Omega)$ . On prolonge  $h_0$  par 0 en dehors de  $\Omega$ , puis on introduit  $h_0^k = (\eta_{\frac{1}{k}} \star h_0) + \frac{1}{k}$ , où  $(\eta_{\frac{1}{k}})_k$  est une suite régularisante périodique, de sorte que  $h_0^k$  est une fonction périodique de classe  $\mathcal{C}^1(\mathbb{R}^3)$ , minorée par  $\frac{1}{k}$  et qui converge vers  $h_0$  dans  $H_{per}^1(\Omega)$  faible. On pose enfin  $\mathbf{u}_0^k = P_k(\mathbf{u}_0)$  où  $P_k$  est la projection orthogonale dans  $L_{per}^3(\Omega)$  sur  $V_k$ , espace de dimension finie engendré par les  $k$  premières fonctions propres du Laplacien de domaine  $H_{per}^2(\Omega)$ . Le problème approché est alors le suivant :

On cherche un couple  $(h_k, \mathbf{u}_k) \in \mathcal{C}^1([0, T[, \mathcal{C}_{per}^1(\Omega)) \times \mathcal{C}^1([0, T[, V_k)$  solution de :

$$\left\{ \begin{array}{l} \frac{\partial h_k}{\partial t} + \operatorname{div}(h_k \mathbf{u}_k) = 0, \\ h_k(0) = h_0^k, \\ \forall \psi_k \in V_k, \int_{\Omega} \left( \left( \frac{\partial(h_k \mathbf{u}_k)}{\partial t} + \frac{(h_k \mathbf{u}_k)^\perp}{R_0} + \alpha_0(h_k) \mathbf{u}_k + \alpha_1(h_k) h_k |\mathbf{u}_k| \mathbf{u}_k + \frac{h_k \nabla h_k}{F_r^2} \right. \right. \\ \left. \left. - \beta h_k \nabla \Delta h_k \right) \cdot \psi_k \right) dx \\ + \int_{\Omega} \left( (h_k \mathbf{u}_k \otimes \mathbf{u}_k + \nu h_k D(\mathbf{u}_k) + 2\nu (h_k \operatorname{div} \mathbf{u}_k) \mathcal{I}) \cdot \nabla \psi_k \right) dx \\ = \int_{\Omega} \left( h_k \left( f - \frac{\nabla d}{F_r^2} + \beta \nabla \Delta d \right) \cdot \psi_k \right) dx, \\ \mathbf{u}_k(0) = \mathbf{u}_0^k \end{array} \right.$$

**2.3.1. Existence et unicité de la solution du problème approché.** Afin d'alléger les notations on omettra dans ce paragraphe l'indice  $k$ , ainsi que la mesure  $dx$ . On pose de plus :

$$\tilde{f} = f - \frac{\nabla d}{F_r^2} + \beta \nabla \Delta d.$$

Ainsi le problème approché devient :

On cherche un couple  $(h, \mathbf{u}) \in \mathcal{C}^1([0, T[, \mathcal{C}_{per}^1(\Omega)) \times \mathcal{C}^1([0, T[, V_k)$  solution de :

$$\left\{ \begin{array}{l} \frac{\partial h_k}{\partial t} + \operatorname{div}(h_k \mathbf{u}_k) = 0, \\ h_k(0) = h_0^k, \\ \forall \psi_k \in V_k, \int_{\Omega} \left( \frac{\partial(h_k \mathbf{u}_k)}{\partial t} + \frac{(h_k \mathbf{u}_k)^\perp}{R_0} + \alpha_0(h_k) \mathbf{u}_k + \alpha_1(h_k) h_k |\mathbf{u}_k| \mathbf{u}_k \right. \\ \left. + \frac{h_k \nabla h_k}{F_r^2} - \beta h_k \nabla \Delta h_k \right) \cdot \psi_k \\ + \int_{\Omega} \left( h_k \mathbf{u}_k \otimes \mathbf{u}_k + \nu h_k D(\mathbf{u}_k) + 2\nu (h_k \operatorname{div} \mathbf{u}_k) \mathcal{I} \right) \cdot \nabla \psi_k = \int_{\Omega} h_k \tilde{f} \cdot \psi_k, \\ \mathbf{u}_k(0) = \mathbf{u}_0^k \end{array} \right. \quad (2.20)$$

**Proposition 2.3.1.** *Soit  $h_0^k \in C_{per}^1(\overline{\Omega})$  et  $\mathbf{u}_0^k$  donnée dans  $V_k$ . Alors pour tout  $T > 0$  le problème (2.20) possède une unique solution  $(h, \mathbf{u})$  dans*

$$\mathcal{C}^1([0, T]; \mathcal{C}^1(\overline{\Omega})) \times \mathcal{C}^1([0, T], V_k).$$

**Preuve.**

On procède par une technique de point fixe et de linéarisation. On remarque que l'on a :

$$\frac{\partial(h \mathbf{u})}{\partial t} + \operatorname{div}(h \mathbf{u} \otimes v) = \mathbf{u} \left( \frac{\partial h}{\partial t} + \operatorname{div}(h v) \right) + h \left( \frac{\partial \mathbf{u}}{\partial t} + (v \cdot \nabla) \mathbf{u} \right)$$

Soit  $\mathbf{w}$  donnée dans  $\mathcal{C}^0([0, T], V_k)$ , on définit  $\mathbf{u} = \Theta(\mathbf{w})$  par

$$\begin{aligned} \frac{\partial h}{\partial t} + \operatorname{div}(\mathbf{w} h) &= 0, \\ h(0) &= h_0^k, \end{aligned} \quad (2.21)$$

$$\forall \psi \in V_k,$$

$$\begin{aligned} \int_{\Omega} h \left( \frac{\partial \mathbf{u}(t)}{\partial t} + (\mathbf{w} \cdot \nabla) \mathbf{u} \right) \cdot \psi + \int_{\Omega} (\nu h (D(\mathbf{u}) + 2\nu (h \operatorname{div} \mathbf{u}) \mathcal{I}) \cdot \nabla \psi \\ + \int_{\Omega} \left( \frac{(h \mathbf{u})^\perp}{R_0} + \alpha_0(h) \mathbf{u} + \alpha_1(h) h |\mathbf{u}| \mathbf{u} + \frac{h \nabla h}{F_r^2} - \beta h \nabla \Delta h \right) \cdot \psi = \int_{\Omega} h \tilde{f} \psi(x) \end{aligned} \quad (2.22)$$

$$\mathbf{u}(0) = \mathbf{u}_0^k.$$

Nous pouvons alors résoudre le problème précédent. Il est équivalent de résoudre le problème approché (2.20) et de trouver un point fixe de  $\Theta$ . Le problème approché possède une et une seule solution de classe  $\mathcal{C}^1$  en temps. L'équation (2.21) se résout par la méthode des caractéristiques comme on l'a vu à la section précédente, tandis que l'équation (2.22) apparaît comme une équation différentielle ordinaire dans un espace

de dimension finie.

On remarque que comme  $h_k(t, x) \geq \frac{1}{k} > 0$  la matrice de coefficients  $\int_{\Omega} h(t) w_i \cdot w_j dx$  est uniformément définie positive ce qui permet d'écrire le système précédent sous la forme  $\frac{d}{dt}\alpha(t) = F(t, \alpha)$ , où  $\alpha$  est un système de coordonnées de  $\mathbf{u}$  dans la base  $(u_i)$ .

Par ailleurs, l'application  $F$  ainsi définie est linéaire en  $\alpha$ , et continue en temps à condition que  $f(t, x)$  soit continue en temps. On peut remplacer  $f$  par  $f_k = f * \eta_{\frac{1}{k}}$  dans la définition du problème approché, ce qui ne change rien à la suite.

On va donc montrer que  $\Theta$  admet un unique point fixe dans  $\mathcal{C}^0([0, T], V_k)$ .

### (1) Estimation sur $\mathbf{u}$

**Lemme 2.3.1.** *Quelle que soit la fonction  $\mathbf{w} \in \mathcal{C}^0([0, T], V_k)$ , on a*

$$\forall T > 0, \exists K_1(T, k), \sup_{t \leq T} \|\mathbf{u}(t)\|_{L^2(\Omega)} \leq K_1(T, k).$$

#### Preuve du lemme 2.3.1.

On procède par estimation de l'énergie, en posant  $\psi = 2\mathbf{u}$  dans (2.22). Comme  $(\nabla \mathbf{u} + {}^t \nabla \mathbf{u}) \cdot (\nabla \mathbf{u} - {}^t \nabla \mathbf{u}) = 0$ , on a l'identité suivante :

$$(\nabla \mathbf{u} + {}^t \nabla \mathbf{u}) \cdot \nabla \mathbf{u} = \frac{1}{2} |\nabla \mathbf{u} + {}^t \nabla \mathbf{u}|^2.$$

On a également :

$$(\operatorname{div} \mathbf{u}) \mathcal{I} \cdot \nabla \mathbf{u} = (\operatorname{div} \mathbf{u})^2.$$

On obtient :

$$\begin{aligned} & \int_{\Omega} h(t) \left( \frac{\partial |\mathbf{u}(t)|^2}{\partial t} + (\mathbf{w}(t) \cdot \nabla) |\mathbf{u}(t)|^2 + \frac{\nu}{2} |\nabla \mathbf{u}(t) + {}^t \nabla \mathbf{u}(t)|^2 \right. \\ & \quad \left. + 4\nu |\operatorname{div} \mathbf{u}(t)|^2 + 2\alpha_1(h) |\mathbf{u}(t)|^3 \right) \\ & + 2 \int_{\Omega} \alpha_0(h) |\mathbf{u}(t)|^2 + \frac{2}{F_r^2} \int_{\Omega} h(t) \nabla h(t) \cdot \mathbf{u}(t) - 2\beta \int_{\Omega} h(t) \nabla \Delta h(t) \cdot \mathbf{u}(t) \\ & = 2 \int_{\Omega} h(t) \tilde{f}(t) \mathbf{u}(t). \end{aligned} \tag{2.23}$$

En multipliant scalairement l'équation (2.21) par  $|\mathbf{u}|^2$  puis en intégrant par parties, il vient, en utilisant les conditions aux limites périodiques :

$$\int_{\Omega} |\mathbf{u}(t)|^2 \frac{\partial h}{\partial t} dx - \int_{\Omega} h(t) (\mathbf{w}(t) \cdot \nabla) |\mathbf{u}(t)|^2 dx = 0. \tag{2.24}$$

En additionnant (2.23) et (2.24) on obtient :

$$\begin{aligned}
& \frac{d}{dt} \|\sqrt{h(t)} \mathbf{u}(t)\|_{L^2(\Omega)}^2 + \frac{\nu}{2} \|\sqrt{h(t)} (\nabla \mathbf{u}(t) + {}^t \nabla \mathbf{u}(t))\|_{L^2(\Omega)}^2 \\
& + 4\nu \|\sqrt{h(t)} \operatorname{div} \mathbf{u}(t)\|_{L^2(\Omega)}^2 + 2 \|\alpha_0(h)^{\frac{1}{2}} \mathbf{u}(t)\|_{L^2(\Omega)}^2 + 2 \|\alpha_1(h)^{\frac{1}{3}} h^{\frac{1}{3}} \mathbf{u}(t)\|_{L^3(\Omega)}^3 \\
& + \frac{2}{F_r^2} \int_{\Omega} h(t) \nabla h(t) \cdot \mathbf{u}(t) \, dx - 2\beta \int_{\Omega} h(t) \nabla \Delta h(t) \cdot \mathbf{u}(t) \, dx \\
& = 2 \int_{\Omega} h(t) \tilde{f}(t) \mathbf{u}(t) \, dx.
\end{aligned} \tag{2.25}$$

On a en intégrant par partie et en utilisant (2.21), tenant compte des conditions aux limites périodiques :

$$\int_{\Omega} h \nabla h \cdot \mathbf{u} = - \int_{\Omega} h \operatorname{div} (h \mathbf{u}) = \int_{\Omega} h \frac{\partial h}{\partial t} = \frac{d}{dt} \|h(t)\|_{L^2(\Omega)}^2$$

et

$$\begin{aligned}
\int_{\Omega} h \nabla \Delta h \cdot \mathbf{u} &= - \int_{\Omega} \Delta h \operatorname{div} (h \mathbf{u}) = \int_{\Omega} \Delta h \frac{\partial h}{\partial t} \\
&= - \int_{\Omega} \nabla h \cdot \frac{\partial}{\partial t} (\nabla h) \\
&= - \frac{1}{2} \frac{d}{dt} \|\nabla h(t)\|_{L^2(\Omega)}^2
\end{aligned}$$

Ainsi on obtient l'inégalité :

$$\begin{aligned}
& \frac{d}{dt} \left( \|\sqrt{h(t)} \mathbf{u}(t)\|_{L^2(\Omega)}^2 + \frac{2}{F_r^2} \|h(t)\|_{L^2(\Omega)}^2 + 2\beta \|\nabla h(t)\|_{L^2(\Omega)}^2 \right) \\
& \leq 2 \|\sqrt{h(t)}\|_{L^\infty(\Omega)} \|\tilde{f}(t)\|_{L^2(\Omega)} \|\sqrt{h(t)} \mathbf{u}(t)\|_{L^2(\Omega)},
\end{aligned}$$

En intégrant entre 0 et  $t$  on obtient alors :

$$\begin{aligned}
& \|\sqrt{h(t)} \mathbf{u}(t)\|_{L^2(\Omega)}^2 + \frac{2}{F_r^2} \|h(t)\|_{L^2(\Omega)}^2 + 2\beta \|\nabla h(t)\|_{L^2(\Omega)}^2 \\
& \leq a_0 + \int_0^t \|\sqrt{h(s)}\|_{L^\infty(\Omega)} \|\sqrt{h(s)} \mathbf{u}(s)\|_{L^2(\Omega)} \|\tilde{f}(s)\|_{L^2(\Omega)} \, ds,
\end{aligned} \tag{2.26}$$

où

$$a_0 = \|\sqrt{h_0} \mathbf{u}_0\|_{L^2(\Omega)}^2 + \frac{1}{F_r^2} \|h_0\|_{L^2(\Omega)}^2 + \beta \|\nabla h_0\|_{L^2(\Omega)}^2.$$

On conclut en utilisant le lemme suivant :

**Lemme 2.3.2** (Gronwall-carré). *Soient  $y$  et  $g$  deux fonctions continues et positives et  $C \geq 0$ . On suppose que*

$$\forall t \geq 0, y^2(t) \leq C + \int_0^t g(s)y(s) ds.$$

Alors, on a

$$\forall t \geq 0, y(t) \leq \sqrt{C} + \frac{1}{2} \int_0^t g(s) ds.$$

**Preuve.**

On pose

$$h(t) = C + \int_0^t g(s)y(s) ds,$$

qui est une fonction de classe  $\mathcal{C}^1$  vérifiant

$$h'(t) = g(t)y(t) \leq g(t)\sqrt{h(t)},$$

car  $y$  et  $g$  sont positives. Si on suppose  $C > 0$ , alors pour tout  $t \geq 0$ ,  $h(t) > 0$ , on peut donc écrire

$$\frac{h'(t)}{2\sqrt{h(t)}} \leq \frac{1}{2}g(t),$$

ce qui donne en intégrant

$$\sqrt{h(t)} \leq \sqrt{h(0)} + \frac{1}{2} \int_0^t g(s) ds.$$

Or  $y(t) \leq \sqrt{h(t)}$  par hypothèse et  $h(0) = C$ , ce qui fournit le résultat

$$y(t) \leq \sqrt{C} + \frac{1}{2} \int_0^t g(s) ds. \quad (2.27)$$

Dans le cas où  $C = 0$ , l'hypothèse est alors vérifiée en particulier pour toute constante  $C > 0$ , ainsi (2.27) est vraie pour tout  $C > 0$ . Le résultat pour  $C = 0$  en découle par passage à la limite. ■

Ainsi, par application du lemme, on obtient l'inégalité suivante :

$$\|\sqrt{h(t)}\mathbf{u}(t)\|_{L^2(\Omega)} \leq \sqrt{a_0} + \frac{1}{2} \int_0^t \|\sqrt{h(s)}\|_{L^\infty(\Omega)} \|\tilde{f}(s)\|_{L^2(\Omega)} ds$$

Comme la fonction  $h$  est minorée par  $\frac{1}{k}$  et majorée d'après (2.8), on a :

$$\begin{aligned} \|h\|_{L^\infty(0,T;L^\infty(\Omega))} &\leq \|h_0\|_{L^\infty(\Omega)} e^{\int_0^T \|\nabla \mathbf{u}(\tau)\|_{L^\infty(\Omega)} d\tau} \\ &\leq C(\|h_0\|_{L^\infty(\Omega)}, T). \end{aligned}$$

On déduit de l'inégalité précédente que

$$\|\mathbf{u}(t)\|_{L^2(\Omega)} \leq \sqrt{\alpha_0} + \frac{C}{2} \int_0^T \|\tilde{f}(s)\|_{L^2(\Omega)} ds$$

et donc qu'il existe une constante  $K_1(T, k)$  indépendante de  $\|\mathbf{w}\|$  telle que :

$$\sup_{t \leq T} \|\mathbf{u}(t)\|_{L^2(\Omega)} \leq K_1(T, k).$$

Ainsi, si  $\mathbf{u}$  est un point fixe de  $\Theta$ , alors en prenant  $\mathbf{w} = \mathbf{u}$ , le lemme montre que

$$\|\mathbf{u}\|_{L^\infty(]0, T[, V_k)} \leq K_1(T, k).$$

■

Nous pouvons donc nous restreindre à la recherche de points fixes de  $\Theta$  dans l'ensemble des fonctions continues en temps à valeurs dans la boule fermée de  $V_k$  de centre 0 et de rayon  $K_1(T, k)$  (en munissant  $V_k$ , par exemple, de la norme  $L^2(\Omega)$  puisque étant de dimension finie, toutes les normes sont équivalentes).

## (2) Equicontinuité de $\mathbf{u}$

On utilise ici principalement l'équivalence des normes dans  $V_k$ .

**Lemme 2.3.3.** *Si  $\mathbf{w} \in C^1([0, T], V_k)$  est telle que*

$$\|\mathbf{w}\|_{L^\infty(0, T; L^2(\Omega))} \leq K_1(T, k),$$

alors

$$\forall T > 0, \exists K_2(T, k), \sup_{t \leq T - \eta} \|\mathbf{u}(t + \eta) - \mathbf{u}(t)\|_{L^2(\Omega)} \leq \sqrt{\eta} K_2(T, k).$$

### Preuve du Lemme 2.3.3.

On reprend la formulation variationnelle du problème approché (2.22) en effectuant une intégration par parties sur le terme de capillarité :

$$\begin{aligned} - \int_{\Omega} h \nabla \Delta h \cdot \psi &= \int_{\Omega} \Delta h \operatorname{div} (h \psi) \\ &= \int_{\Omega} \Delta h \nabla h \cdot \psi + \int_{\Omega} h \Delta h \operatorname{div} (\psi). \end{aligned}$$

On prend  $\psi = \frac{\partial \mathbf{u}}{\partial t}$ . On remarque que, comme  $(\nabla \mathbf{u} + {}^t \nabla \mathbf{u}) \cdot \frac{\partial}{\partial t} (\nabla \mathbf{u} - {}^t \nabla \mathbf{u}) = 0$ , on a l'identité suivante :

$$(\nabla \mathbf{u} + {}^t \nabla \mathbf{u}) \cdot \nabla \left( \frac{\partial \mathbf{u}}{\partial t} \right) = \frac{1}{2} \frac{\partial}{\partial t} |\nabla \mathbf{u} + {}^t \nabla \mathbf{u}|^2,$$

ainsi que :

$$(\operatorname{div} \mathbf{u}) \mathcal{I} \cdot \nabla \left( \frac{\partial \mathbf{u}}{\partial t} \right) = \frac{1}{2} \frac{\partial}{\partial t} |\operatorname{div} \mathbf{u}|^2.$$

Il vient

$$\begin{aligned}
& \int_{\Omega} h \left| \frac{\partial \mathbf{u}(t)}{\partial t} \right|^2 + \frac{\nu}{4} \int_{\Omega} h \frac{\partial}{\partial t} |\nabla \mathbf{u}(t) + {}^t \nabla \mathbf{u}(t)|^2 + \nu \int_{\Omega} h \frac{\partial}{\partial t} |\operatorname{div} \mathbf{u}(t)|^2 \\
& \quad + \int_{\Omega} \left( \alpha_0(h) \mathbf{u} + \alpha_1(h) h |\mathbf{u}| \mathbf{u} \right) \cdot \frac{\partial \mathbf{u}(t)}{\partial t} \\
& = - \int_{\Omega} h \left( (\mathbf{w} \cdot \nabla) \mathbf{u} + \frac{1}{R_0} \mathbf{u}^\perp + \frac{1}{F_r^2} h \nabla h - \tilde{f} \right) \cdot \frac{\partial \mathbf{u}(t)}{\partial t} \\
& \quad - \beta \int_{\Omega} \Delta h \nabla h \cdot \frac{\partial \mathbf{u}(t)}{\partial t} dx - \beta \int_{\Omega} h \Delta h \operatorname{div} \left( \frac{\partial \mathbf{u}(t)}{\partial t} \right)
\end{aligned} \tag{2.28}$$

ou encore

$$\begin{aligned}
& \int_{\Omega} h \left| \frac{\partial \mathbf{u}(t)}{\partial t} \right|^2 + \frac{\nu}{4} \frac{d}{dt} \int_{\Omega} h |\nabla \mathbf{u}(t) + {}^t \nabla \mathbf{u}(t)|^2 + \nu \frac{d}{dt} \int_{\Omega} h |\operatorname{div} \mathbf{u}(t)|^2 \\
& \quad + \frac{1}{2} \frac{d}{dt} \int_{\Omega} \alpha_0(h) |\mathbf{u}(t)|^2 = \frac{\nu}{4} \int_{\Omega} \frac{\partial h}{\partial t} |\nabla \mathbf{u}(t) + {}^t \nabla \mathbf{u}(t)|^2 + \nu \int_{\Omega} \frac{\partial h}{\partial t} |\operatorname{div} \mathbf{u}(t)|^2 \\
& \quad + \frac{1}{2} \int_{\Omega} \frac{\partial \alpha_0(h)}{\partial t} |\mathbf{u}(t)|^2 - \beta \int_{\Omega} \Delta h \nabla h \cdot \frac{\partial \mathbf{u}(t)}{\partial t} dx - \beta \int_{\Omega} h \Delta h \operatorname{div} \left( \frac{\partial \mathbf{u}(t)}{\partial t} \right) \\
& \quad - \int_{\Omega} h \left( (\mathbf{w} \cdot \nabla) \mathbf{u} + \frac{1}{R_0} \mathbf{u}^\perp + \frac{1}{F_r^2} h \nabla h + \alpha_1(h) |\mathbf{u}| \mathbf{u} - \tilde{f} \right) \cdot \frac{\partial \mathbf{u}(t)}{\partial t}.
\end{aligned} \tag{2.29}$$

Nous reprenons les estimations (2.8) sur  $h$  que nous écrivons sous la forme :

$$\begin{aligned}
\|h\|_{L^\infty(0,T;L^2(\Omega))} & \leq \|h_0\|_{L^2(\Omega)} e^{C_k T \|\mathbf{u}\|_{L^\infty(0,T;L^2(\Omega))}} \\
& \leq \|h_0\|_{L^2(\Omega)} e^{C_k T K_1(T,k)},
\end{aligned} \tag{2.30}$$

et

$$\begin{aligned}
\|h\|_{L^\infty(0,T;L^\infty(\Omega))} & \leq \|h_0\|_{L^\infty(\Omega)} e^{C_k T \|\mathbf{u}\|_{L^\infty(0,T;L^2(\Omega))}} \\
& \leq \|h_0\|_{L^\infty(\Omega)} e^{C_k T K_1(T,k)}.
\end{aligned} \tag{2.31}$$

Ainsi il existe une constante  $A_k$  telle que nous ayons  $\|h\|_{L^\infty(0,T;L^\infty(\Omega))} \leq A_k$ . Ceci implique également :

$$\alpha_0(h) = \frac{r_0}{1 + \frac{\varepsilon r_0 h}{3\nu_o}} \geq \alpha_{0k} = \frac{r_0}{1 + \frac{\varepsilon r_0 A_k}{3\nu_o}} \tag{2.32}$$

et

$$\alpha_1(h) = \frac{r_1}{\left(1 + \frac{\varepsilon r_0 h}{3\nu_o}\right)^2} \geq \alpha_{1k} = \frac{r_1}{\left(1 + \frac{\varepsilon r_0 A_k}{3\nu_o}\right)^2}. \tag{2.33}$$

De plus en écrivant que

$$\frac{\partial h}{\partial t} = -\nabla h \cdot \mathbf{u} - h \operatorname{div} \mathbf{u},$$

on obtient une borne  $L^\infty(0, T; L^\infty(\Omega))$  pour  $\frac{\partial h}{\partial t}$ . En effet, on montre que  $\nabla h$  est borné dans  $L^\infty(0, T; L^\infty(\Omega))$  en remplaçant toutes les bornes  $L^2(\Omega)$  par des bornes  $L^\infty(\Omega)$  dans l'expression (2.17). On a donc également  $\left\| \frac{\partial h}{\partial t} \right\|_{L^\infty(0, T; L^\infty(\Omega))} \leq B_k$

On a donc :

$$\begin{aligned} & \int_{\Omega} h \left| \frac{\partial \mathbf{u}(t)}{\partial t} \right|^2 + \frac{\nu}{4} \frac{d}{dt} \int_{\Omega} h |\nabla \mathbf{u}(t) + {}^t \nabla \mathbf{u}(t)|^2 + \nu \frac{d}{dt} \int_{\Omega} h |\operatorname{div} \mathbf{u}(t)|^2 \\ & + \frac{1}{2} \frac{d}{dt} \int_{\Omega} \alpha_0(h) |\mathbf{u}(t)|^2 \leq \left\| \frac{\partial h}{\partial t} \right\|_{L^\infty(\Omega)} \left( \frac{\nu}{2} \|\nabla \mathbf{u}(t)\|_{L^2(\Omega)}^2 \right. \\ & \quad \left. + \nu \|\operatorname{div} \mathbf{u}(t)\|_{L^2(\Omega)}^2 + \frac{1}{2} c_0 r_0 \|\mathbf{u}(t)\|_{L^2(\Omega)}^2 \right) \\ & + \|h\|_{L^\infty(\Omega)} \left( \|\mathbf{w}\|_{L^\infty(\Omega)} \|\nabla \mathbf{u}\|_{L^2(\Omega)} + \frac{1}{R_0} \|\mathbf{u}\|_{L^2(\Omega)} + \frac{1}{F_r^2} \|\nabla h\|_{L^2(\Omega)} \right. \\ & \quad \left. + r_1 \|\mathbf{u}\|_{L^\infty(\Omega)} \|\mathbf{u}\|_{L^2(\Omega)} + \|\tilde{f}\|_{L^2(\Omega)} \right) \left\| \frac{\partial \mathbf{u}}{\partial t} \right\|_{L^2(\Omega)} \\ & + \beta \|\Delta h\|_{L^2(\Omega)} \|\nabla h\|_{L^2(\Omega)} \left\| \frac{\partial \mathbf{u}}{\partial t} \right\|_{L^\infty(\Omega)} \\ & + \beta \|h\|_{L^\infty(\Omega)} \|\Delta h\|_{L^2(\Omega)} \left\| \operatorname{div} \frac{\partial \mathbf{u}}{\partial t} \right\|_{L^2(\Omega)}, \end{aligned} \quad (2.34)$$

Comme  $h$  est minorée par  $\frac{1}{k}$  et puisque toutes les normes sont équivalentes sur  $V_k$ , on obtient en intégrant sur  $[0, t]$  et en utilisant l'inégalité de Young :

$$\begin{aligned}
& \int_0^t \left\| \frac{\partial \mathbf{u}}{\partial t}(\tau) \right\|_{L^2(\Omega)}^2 d\tau + \frac{\nu}{4} \|\nabla \mathbf{u} + {}^t \nabla \mathbf{u}\|_{L^2(\Omega)}^2 + \nu \|\operatorname{div} \mathbf{u}\|_{L^2(\Omega)}^2 + \frac{\alpha_0 k}{2} \|\mathbf{u}\|_{L^2(\Omega)}^2 \\
& \leq \frac{\nu}{4} \|\nabla \mathbf{u}_0 + {}^t \nabla \mathbf{u}_0\|_{L^2(\Omega)}^2 + \nu \|\operatorname{div} \mathbf{u}_0\|_{L^2(\Omega)}^2 + \frac{r_0}{2} \|\mathbf{u}_0\|_{L^2(\Omega)}^2 \\
& + k C_k \int_0^t \left\| \frac{\partial h}{\partial t} \right\|_{L^\infty(\Omega)} \left( \frac{\nu}{2} \|\mathbf{u}(t)\|_{L^2(\Omega)}^2 \right. \\
& \quad \left. + \nu \|\mathbf{u}(t)\|_{L^2(\Omega)}^2 + \frac{1}{2} c_0 r_0 \|\mathbf{u}(t)\|_{L^2(\Omega)}^2 \right) \\
& + k C_k \int_0^t \|h\|_{L^\infty(\Omega)}^2 \left( \|\mathbf{w}\|_{L^2(\Omega)}^2 \|\mathbf{u}\|_{L^2(\Omega)}^2 + \|\mathbf{u}\|_{L^2(\Omega)}^2 \right. \\
& \quad \left. + \|\nabla h\|_{L^2(\Omega)}^2 + r_1 \|\mathbf{u}\|_{L^2(\Omega)}^4 + \|\tilde{f}\|_{L^2(\Omega)}^2 \right) d\tau \\
& + k C_k \int_0^t \left( \|\Delta h\|_{L^2(\Omega)}^2 \|\nabla h\|_{L^2(\Omega)}^2 + \|h\|_{L^\infty(\Omega)}^2 \|\Delta h\|_{L^2(\Omega)}^2 \right) d\tau.
\end{aligned} \tag{2.35}$$

En supposant  $\|\mathbf{w}\|_{L^\infty(0,T;L^2(\Omega))} \leq K_1(T,k)$  alors, d'après le lemme 2.3.1, nous avons

$$\|\mathbf{u}\|_{L^\infty(0,T;L^2(\Omega))} \leq K_1(T,k).$$

En utilisant (2.30) et (2.31), l'estimation (2.9) devient

$$\begin{aligned}
& \|\nabla h\|_{L^\infty(0,T;L^2(\Omega))} \leq \\
& \left( \|\nabla h_0\|_{L^2(\Omega)} + C_k T \|h_0\|_{L^2(\Omega)} \|\mathbf{u}\|_{L^\infty(0,T;L^2(\Omega))} \right) e^{2C_k T} \|\mathbf{u}\|_{L^\infty(0,T;L^2(\Omega))}
\end{aligned}$$

soit

$$\begin{aligned}
\|\nabla h\|_{L^\infty(0,T;L^2(\Omega))} & \leq \left( \|\nabla h_0\|_{L^2(\Omega)} + C_k T \|h_0\|_{L^2(\Omega)} K_1(T,k) \right) e^{2C_k T} K_1(T,k) \\
& \leq K_{\nabla h}(T,k)
\end{aligned} \tag{2.36}$$

De même en reprenant (2.10), on montre qu'il existe une constante  $K_{\Delta h} > 0$  telle que l'on ait :

$$\|\Delta h\|_{L^\infty(0,T;L^2(\Omega))} \leq K_{\Delta h}(T,k). \tag{2.37}$$

puisque  $\|\Delta h(t)\|_{L^2(\Omega)} \leq \|\nabla^2 h(t)\|_{L^2(\Omega)}$ .

On a alors :

$$\begin{aligned}
\int_0^t \left\| \frac{\partial \mathbf{u}}{\partial t}(\tau) \right\|_{L^2(\Omega)}^2 d\tau &\leq \frac{\nu}{4} \|\nabla \mathbf{u}_0 + {}^t \nabla \mathbf{u}_0\|_{L^2(\Omega)}^2 + \nu \|\nabla \mathbf{u}_0\|_{L^2(\Omega)}^2 + \frac{r_0}{2} \|\mathbf{u}_0\|_{L^2(\Omega)}^2 \\
&+ k B_k C_k T \left( \frac{\nu}{2} K_1(T, k)^2 + \nu K_1(T, k)^2 + \frac{r_0 c_0}{2} K_1(T, k)^2 \right) \\
&+ k C_k T \|h_0\|_{L^\infty(\Omega)}^2 e^{2C_k T} K_1(T, k) \left( K_1(T, k)^4 + K_1(T, k)^2 \right. \\
&\quad \left. + K_{\nabla h}^2 + r_1 K_1(T, k)^4 + \|\tilde{f}\|_{L^1(0, T; L^2(\Omega))} \right) \\
&+ k C_k T \left( K_{\nabla h}^2 K_{\Delta h}^2 + K_{\Delta h}^2 \|h_0\|_{L^\infty(\Omega)}^2 e^{2C_k T} K_1(T, k) \right)
\end{aligned}$$

et donc, il existe une constante  $K_2(T, k)$  tel que :

$$\int_0^t \left\| \frac{\partial \mathbf{u}}{\partial t}(\tau) \right\|_{L^2(\Omega)}^2 d\tau \leq K_2(T, k)^2.$$

Ainsi, pour  $t \leq T - \eta$ , on a

$$\begin{aligned}
\|\mathbf{u}(t + \eta) - \mathbf{u}(t)\|_{L^2(\Omega)} &\leq \int_t^{t+\eta} \left\| \frac{\partial \mathbf{u}}{\partial t}(\tau) \right\|_{L^2(\Omega)} d\tau \\
&\leq \sqrt{\eta} \left\| \frac{\partial \mathbf{u}}{\partial t}(\tau) \right\|_{L^2(0, T; L^2(\Omega))} \\
&\leq \sqrt{\eta} K_2(T, k).
\end{aligned} \tag{2.38}$$

■

Ce lemme permet de montrer que si  $\mathbf{u}$  est un point fixe de  $\Theta$ , alors on a

$$\|\mathbf{u}(t + \eta) - \mathbf{u}(t)\|_{L^\infty(0, T - \eta; V_k)} \leq K_2(T, k) \sqrt{\eta}.$$

Ainsi, tout point fixe éventuel de  $\Theta$  dans  $\mathcal{C}^0([0, T], V_k)$  se trouve nécessairement dans l'ensemble

$$\begin{aligned}
\mathcal{K} &= \{\mathbf{u} \in \mathcal{C}^0([0, T], \bar{B}_{V_k}(0, K_1(T, k)))\}, \\
&\text{tel que } \|\mathbf{u}(t + \eta) - \mathbf{u}(t)\|_{L^2(\Omega)} \leq \sqrt{\eta} K_2(T, k).
\end{aligned} \tag{2.39}$$

### (3) Continuité de l'application $\Theta$

Les lemmes 2.3.1 et 2.3.3, montrent que  $\Theta$  laisse invariant l'ensemble  $\mathcal{K}$  défini par (2.39). On a alors le résultat suivant :

**Lemme 2.3.4.** *L'application  $\Theta$  est Lipschitzienne sur l'ensemble  $\mathcal{K}$ . Plus précisément, il existe une constante  $K_4(T, k)$  telle que pour tous  $\mathbf{w}_1, \mathbf{w}_2 \in \mathcal{K}$  on ait*

$$\forall t \in [0, T], \|\Theta(\mathbf{w}_1) - \Theta(\mathbf{w}_2)\|_{L^\infty(0, t; V_k)} \leq t K_4(T, k) \|\mathbf{w}_1 - \mathbf{w}_2\|_{L^\infty(0, t; V_k)}.$$

**Preuve.**

Soient  $(h_1, \mathbf{u}_1)$  et  $(h_2, \mathbf{u}_2)$  les solutions du problème linéarisé associées à deux fonctions  $\mathbf{w}_1, \mathbf{w}_2 \in \mathcal{K}$ . On pose  $h = h_1 - h_2$ ,  $\mathbf{u} = \mathbf{u}_1 - \mathbf{u}_2$  et  $\mathbf{w} = \mathbf{w}_1 - \mathbf{w}_2$ , et on a :

$$\begin{aligned} & \frac{\partial h}{\partial t} + \operatorname{div} (h_1 \mathbf{w}) + \operatorname{div} (h \mathbf{w}_2) = 0, \\ \forall \psi \in V_k, & \int_{\Omega} \left( h(t) \left( \frac{\partial \mathbf{u}_1}{\partial t} + (\mathbf{w}_1 \cdot \nabla) v_1 \right) + h_2 \left( \frac{\partial \mathbf{u}}{\partial t} + (\mathbf{w} \cdot \nabla \mathbf{u}_1) + (\mathbf{w}_2 \cdot \nabla) \mathbf{u} \right) \right) \cdot \psi \\ & + \int_{\Omega} \frac{\nu}{2} \left( h(\nabla \mathbf{u}_1 + {}^t \nabla \mathbf{u}_1) + h_2(\nabla \mathbf{u} + {}^t \nabla \mathbf{u}) + 4h \operatorname{div} (\mathbf{u}_1) \mathcal{I} + 4h_2 \operatorname{div} (\mathbf{u}) \mathcal{I} \right) \cdot \nabla \psi \\ & + \int_{\Omega} \left( \frac{1}{R_o} (h \mathbf{u}_1)^\perp + \frac{1}{R_o} (h_2 \mathbf{u})^\perp + \alpha_0(h_1) \mathbf{u} + (\alpha_0(h_1) - \alpha_0(h_2)) \mathbf{u}_2 \right) \cdot \psi \, dx \\ & + \int_{\Omega} \left( \alpha_1(h_1) h_1 |\mathbf{u}_1| \mathbf{u} + \alpha_1(h_1) h |\mathbf{u}_1| \mathbf{u}_2 + \alpha_1(h_1) (|\mathbf{u}_1| - |\mathbf{u}_2|) h_2 \mathbf{u}_2 \right. \\ & \qquad \qquad \qquad \left. + (\alpha_1(h_1) - \alpha_1(h_2)) |\mathbf{u}_2| h_2 \mathbf{u}_2 \right) \cdot \psi \\ & + \int_{\Omega} \left( \frac{1}{F_r^2} h \nabla h_1 + \frac{1}{F_r^2} h_2 \nabla h - \beta h \nabla \Delta h_1 - \beta h_2 \nabla \Delta h \right) \cdot \psi = \int_{\Omega} h \tilde{f} \cdot \psi \end{aligned} \tag{2.40}$$

ainsi que les conditions initiales  $h(0) = 0$  et  $\mathbf{u}(0) = 0$ .

On prend  $\psi = \mathbf{u}$  dans (2.40). Il vient :

$$\begin{aligned} & \int_{\Omega} h \mathbf{u} \cdot \left( \frac{\partial \mathbf{u}_1}{\partial t} + (\mathbf{w}_1 \cdot \nabla) \mathbf{u}_1 \right) + \frac{1}{2} \int_{\Omega} h_2 \left( \frac{\partial |\mathbf{u}|^2}{\partial t} + \mathbf{w}_2 \cdot \nabla |\mathbf{u}|^2 \right) + \int_{\Omega} h_2 \mathbf{u} \cdot (\mathbf{w} \cdot \nabla) \mathbf{u}_1 \\ & + \int_{\Omega} \frac{\nu}{2} \left( \left( h(\nabla \mathbf{u}_1 + {}^t \nabla \mathbf{u}_1) + 4h \operatorname{div} (\mathbf{u}_1) \mathcal{I} \right) \cdot \nabla \mathbf{u} \right. \\ & \qquad \qquad \left. + \frac{h_2}{2} |\nabla \mathbf{u} + {}^t \nabla \mathbf{u}|^2 + 4h_2 |\operatorname{div} \mathbf{u}|^2 \right) \\ & + \int_{\Omega} h \mathbf{u} \cdot \left( \frac{1}{R_o} \mathbf{u}_1^\perp + \frac{1}{F_r^2} h \nabla h_1 + \alpha_1(h_1) |\mathbf{u}_1| \mathbf{u}_2 - \tilde{f} \right) \\ & + \int_{\Omega} \alpha_0(h_1) |\mathbf{u}|^2 + \int_{\Omega} \alpha_1(h_1) h_1 |\mathbf{u}_1| |\mathbf{u}|^2 \\ & + \int_{\Omega} \left( (\alpha_1(h_1) - \alpha_1(h_2)) |\mathbf{u}_2| h_2 \mathbf{u}_2 + (\alpha_0(h_1) - \alpha_0(h_2)) \mathbf{u}_2 \right. \\ & \qquad \qquad \left. + \alpha_1(h_1) (|\mathbf{u}_1| - |\mathbf{u}_2|) h_2 \mathbf{u}_2 + \frac{1}{F_r^2} h_2 \nabla h - \beta h \nabla \Delta h_1 - \beta h_2 \nabla \Delta h \right) \cdot \mathbf{u} \\ & = 0. \end{aligned} \tag{2.41}$$

On effectue une intégration par parties sur le terme en  $\mathbf{w}_2 \cdot \nabla |\mathbf{u}|^2$  et on utilise l'équation de conservation de la hauteur d'eau vérifiée par  $h_2$  pour obtenir :

$$\int_{\Omega} h_2 \mathbf{w}_2 \cdot \nabla |\mathbf{u}|^2 = - \int_{\Omega} |\mathbf{u}|^2 \operatorname{div} (h_2 \mathbf{w}_2) = \int_{\Omega} |\mathbf{u}|^2 \frac{\partial h_2}{\partial t}.$$

L'équation (2.41) devient :

$$\begin{aligned} & \frac{1}{2} \frac{d}{dt} \int_{\Omega} h_2 |\mathbf{u}|^2 + \frac{\nu}{4} \int_{\Omega} h_2 \left( |\nabla \mathbf{u} + {}^t \nabla \mathbf{u}|^2 + 8 |\operatorname{div} \mathbf{u}|^2 \right) + \int_{\Omega} \alpha_0(h_1) |\mathbf{u}|^2 \\ & + \int_{\Omega} \alpha_1(h_1) h_1 |\mathbf{u}_1| |\mathbf{u}|^2 = \int_{\Omega} h \mathbf{u} \cdot g - \int_{\Omega} h_2 \mathbf{u} \cdot \ell \\ & - \frac{\nu}{2} \int_{\Omega} \left( h (\nabla \mathbf{u}_1 + {}^t \nabla \mathbf{u}_1) + 4 h \operatorname{div} (\mathbf{u}_1) \mathcal{I} \right) \cdot \nabla \mathbf{u} \\ & - \int_{\Omega} \left( \alpha_0(h_1) - \alpha_0(h_2) \right) \mathbf{u}_2 \cdot \mathbf{u} - \beta \int_{\Omega} \Delta h_1 \operatorname{div} (h \mathbf{u}) - \beta \int_{\Omega} \Delta h \operatorname{div} (h_2 \mathbf{u}) \end{aligned}$$

avec

$$g = \tilde{f} - \frac{1}{F_r^2} \nabla h_1 - \frac{1}{Ro} \mathbf{u}_1^\perp - \frac{\partial \mathbf{u}_1}{\partial t} - (\mathbf{w}_1 \cdot \nabla) \mathbf{u}_1 - \alpha_1(h_1) |\mathbf{u}_1| \mathbf{u}_2,$$

et

$$\ell = (\mathbf{w} \cdot \nabla) \mathbf{u}_1 + \frac{1}{F_r^2} \nabla h + \left( \alpha_1(h_1) - \alpha_1(h_2) \right) |\mathbf{u}_2| \mathbf{u}_2 + \alpha_1(h_1) \left( |\mathbf{u}_1| - |\mathbf{u}_2| \right) \mathbf{u}_2.$$

On a alors les estimations suivantes :

$$\begin{aligned} \|g(t)\|_{L^2(\Omega)} & \leq \|\tilde{f}(t)\|_{L^2(\Omega)} + \frac{1}{F_r^2} \|\nabla h_1(t)\|_{L^2(\Omega)} + \left\| \frac{\partial v_1}{\partial t} \right\|_{L^2(\Omega)} \\ & + \frac{1}{Ro} \|\mathbf{u}_1(t)\|_{L^2(\Omega)} + \|\mathbf{w}_1\|_{L^\infty(\Omega)} \|\nabla \mathbf{u}_1\|_{L^2(\Omega)} + r_1 \|\mathbf{u}_1\|_{L^\infty(\Omega)} \|\mathbf{u}_2\|_{L^2(\Omega)}, \end{aligned}$$

et

$$\begin{aligned} \|\ell(t)\|_{L^2(\Omega)} & \leq \|\mathbf{w}\|_{L^\infty(\Omega)} \|\nabla \mathbf{u}_1\|_{L^2(\Omega)} + \frac{1}{F_r^2} \left( \|\nabla h_1(t)\|_{L^2(\Omega)} + \|\nabla h_2(t)\|_{L^2(\Omega)} \right) \\ & + 2r_1 \|\mathbf{u}_2\|_{L^\infty(\Omega)} \|\mathbf{u}_2\|_{L^2(\Omega)} + r_1 \|\mathbf{u}\|_{L^\infty(\Omega)} \|\mathbf{u}_2\|_{L^2(\Omega)}. \end{aligned}$$

Comme les normes  $L^\infty$ ,  $L^2$  et  $H^1$  sont équivalentes sur  $V_k$ , il existe une constante  $C_k > 0$  telle que

$$\begin{aligned} \|g(t)\|_{L^2(\Omega)} & \leq \|\tilde{f}(t)\|_{L^2(\Omega)} + \frac{1}{F_r^2} \|\nabla h_1(t)\|_{L^2(\Omega)} + \left\| \frac{\partial v_1}{\partial t} \right\|_{L^2(\Omega)} \\ & + \frac{1}{Ro} \|\mathbf{u}_1(t)\|_{L^2(\Omega)} + C_k \|\mathbf{w}_1\|_{L^2(\Omega)} \|\mathbf{u}_1\|_{L^2(\Omega)} + r_1 C_k \|\mathbf{u}_1\|_{L^2(\Omega)} \|\mathbf{u}_2\|_{L^2(\Omega)}, \end{aligned}$$

et

$$\begin{aligned} \|\ell(t)\|_{L^2(\Omega)} & \leq C_k \|\mathbf{w}\|_{L^2(\Omega)} \|\mathbf{u}_1\|_{L^2(\Omega)} + \frac{1}{F_r^2} \left( \|\nabla h_1(t)\|_{L^2(\Omega)} + \|\nabla h_2(t)\|_{L^2(\Omega)} \right) \\ & + 2r_1 C_k \|\mathbf{u}_2\|_{L^2(\Omega)}^2 + r_1 C_k \|\mathbf{u}\|_{L^2(\Omega)} \|\mathbf{u}_2\|_{L^2(\Omega)}. \end{aligned}$$

Si on choisit  $\mathbf{w}_1$  et  $\mathbf{w}_2$  telles que

$$\|\mathbf{w}_1\|_{L^\infty(0,T;L^2(\Omega))} \leq K_1(T, k)$$

et

$$\|\mathbf{w}_2\|_{L^\infty(0,T;L^2(\Omega))} \leq K_1(T, k),$$

alors d'après les lemmes (2.3.1), (2.3.3) et l'estimation (2.9), on obtient :

$$\begin{aligned} \|g\|_{L^1(0,T;L^2(\Omega))} &\leq \|\tilde{f}\|_{L^1(0,T;L^2(\Omega))} + \frac{T}{F_r^2} K_{\nabla h_1} \\ &+ \sqrt{T} K_2(T, k) + \frac{K_1(T, k) T}{Ro} \\ &+ C_k T K_1(T, k)^2 + r_1 C_k T K_1(T, k)^2 \end{aligned} \quad (2.42)$$

et

$$\begin{aligned} \|\ell\|_{L^1(0,T;L^2(\Omega))} &\leq C_k T K_1(T, k)^2 + \frac{T}{F_r^2} \left( K_{\nabla h_1} \right. \\ &\left. + K_{\nabla h_2} \right) + 4r_1 T C_k K_1(T, k)^2. \end{aligned} \quad (2.43)$$

Enfin, en multipliant par  $h$  l'équation de conservation vérifiée par  $h$  et en intégrant par parties, il vient

$$\frac{1}{2} \frac{d}{dt} \|h\|_{L^2(\Omega)}^2 + \int_{\Omega} h \operatorname{div} (h_1 \mathbf{w}) dx + \frac{1}{2} \int_{\Omega} \operatorname{div} \mathbf{w}_2 |h|^2 dx = 0,$$

ce qui donne en sommant cette estimation à celle obtenue sur  $\int_{\Omega} h_2 |\mathbf{u}|^2$  :

$$\begin{aligned} &\frac{1}{2} \frac{d}{dt} \left( \|h\|_{L^2(\Omega)}^2 + \|\sqrt{h_2} \mathbf{u}\|_{L^2(\Omega)}^2 \right) + \frac{\nu}{4} \int_{\Omega} h_2 \left( |\nabla \mathbf{u} + {}^t \nabla \mathbf{u}|^2 + 8 |\operatorname{div} \mathbf{u}|^2 \right) \\ &+ \int_{\Omega} \alpha_0(h_1) |\mathbf{u}|^2 + \int_{\Omega} \alpha_1(h_1) h_1 |\mathbf{u}_1| |\mathbf{u}|^2 = \int_{\Omega} h \mathbf{u} \cdot g - \int_{\Omega} h_2 \mathbf{u} \cdot \ell \\ &- \frac{\nu}{2} \int_{\Omega} \left( h (\nabla \mathbf{u}_1 + {}^t \nabla \mathbf{u}_1) + 4 h \operatorname{div} (\mathbf{u}_1) \mathcal{I} \right) \cdot \nabla \mathbf{u} \\ &- \int_{\Omega} \left( \alpha_0(h_1) - \alpha_0(h_2) \right) \mathbf{u}_2 \cdot \mathbf{u} - \beta \int_{\Omega} \Delta h_1 \operatorname{div} (h \mathbf{u}) \\ &- \beta \int_{\Omega} \Delta h \operatorname{div} (h_2 \mathbf{u}) - \int_{\Omega} h \operatorname{div} (h_1 \mathbf{w}) - \frac{1}{2} \int_{\Omega} \operatorname{div} \mathbf{w}_2 |h|^2 \end{aligned}$$

et donc :

$$\begin{aligned}
& \frac{1}{2} \frac{d}{dt} \left( \|h\|_{L^2(\Omega)}^2 + \|\sqrt{h_2} \mathbf{u}\|_{L^2(\Omega)}^2 \right) + \frac{\nu}{4} \int_{\Omega} h_2 \left( |\nabla \mathbf{u} + {}^t \nabla \mathbf{u}|^2 + 8 |\operatorname{div} \mathbf{u}|^2 \right) \\
& + \int_{\Omega} \alpha_0(h_1) |\mathbf{u}|^2 + \int_{\Omega} \alpha_1(h_1) h_1 |\mathbf{u}_1| |\mathbf{u}|^2 \leq \|h\|_{L^2(\Omega)} \|\mathbf{u}\|_{L^\infty(\Omega)} \|g\|_{L^2(\Omega)} \\
& + \|h_2\|_{L^2(\Omega)} \|\mathbf{u}\|_{L^\infty(\Omega)} \|\ell\|_{L^2(\Omega)} + 2r_0 \|\mathbf{u}\|_{L^2(\Omega)} \|\mathbf{u}_2\|_{L^2(\Omega)} \\
& + \frac{\nu}{2} \|h\|_{L^\infty(\Omega)} \|\nabla \mathbf{u}_1 + {}^t \nabla \mathbf{u}_1 + 4 \operatorname{div}(\mathbf{u}_1) \mathcal{I}\|_{L^2(\Omega)} \|\nabla \mathbf{u}\|_{L^2(\Omega)} \\
& + \beta \left( \|\Delta h_1\|_{L^2(\Omega)} \left( \|h\|_{L^2(\Omega)} \|\operatorname{div} \mathbf{u}\|_{L^\infty(\Omega)} + \|\nabla h\|_{L^2(\Omega)} \|\mathbf{u}\|_{L^\infty(\Omega)} \right) \right. \\
& \quad \left. + \|\Delta h\|_{L^2(\Omega)} \left( \|h_2\|_{L^2(\Omega)} \|\operatorname{div} \mathbf{u}\|_{L^\infty(\Omega)} + \|\nabla h_2\|_{L^2(\Omega)} \|\mathbf{u}\|_{L^\infty(\Omega)} \right) \right) \\
& + \|h\|_{L^2(\Omega)} \left( \|\mathbf{w}\|_{L^\infty(\Omega)} \|\nabla h_1\|_{L^2(\Omega)} + \|\operatorname{div} \mathbf{w}\|_{L^\infty(\Omega)} \|h_1\|_{L^2(\Omega)} \right) \\
& + \|\operatorname{div} \mathbf{w}_2\|_{L^\infty(\Omega)} \|h\|_{L^2(\Omega)}^2
\end{aligned}$$

En utilisant à nouveau l'équivalence des normes dans  $V_k$  et l'inégalité de Young et comme  $\alpha_0(h_1) > 0$  et  $\alpha_1(h_1) > 0$  nous obtenons :

$$\begin{aligned}
& \frac{1}{2} \frac{d}{dt} \left( \|h\|_{L^2(\Omega)}^2 + \|\sqrt{h_2} \mathbf{u}\|_{L^2(\Omega)}^2 \right) \\
& \leq C_k \|h\|_{L^2(\Omega)} \|\mathbf{u}\|_{L^2(\Omega)} \|g\|_{L^2(\Omega)} + C_k \|h_2\|_{L^2(\Omega)} \|\mathbf{u}\|_{L^2(\Omega)} \|\ell\|_{L^2(\Omega)} \\
& + C_k \nu \|h\|_{L^\infty(\Omega)} \|\mathbf{u}_1\|_{L^2(\Omega)} \|\mathbf{u}\|_{L^2(\Omega)} + 2r_0 \|\mathbf{u}\|_{L^2(\Omega)} \|\mathbf{u}_2\|_{L^2(\Omega)} \\
& + \beta \left( \|\Delta h_1\|_{L^2(\Omega)} \left( C_k \|h\|_{L^2(\Omega)} \|\mathbf{u}\|_{L^2(\Omega)} + C_k \|\nabla h\|_{L^2(\Omega)} \|\mathbf{u}\|_{L^2(\Omega)} \right) \right. \\
& \quad \left. + \|\Delta h\|_{L^2(\Omega)} \left( C_k \|h_2\|_{L^2(\Omega)} \|\mathbf{u}\|_{L^2(\Omega)} + C_k \|\nabla h_2\|_{L^2(\Omega)} \|\mathbf{u}\|_{L^2(\Omega)} \right) \right) \\
& + \|\mathbf{w}\|_{L^2(\Omega)}^2 + C_k \|h\|_{L^2(\Omega)}^2 \left( \|\nabla h_1\|_{L^2(\Omega)}^2 + \|h_1\|_{L^2(\Omega)}^2 \right) \\
& + C_k \|\mathbf{w}_2\|_{L^2(\Omega)} \|h\|_{L^2(\Omega)}^2
\end{aligned}$$

On majore  $\|h_{1,2}\|_{L^2(\Omega)}$  par  $\|h_0\|_{L^2(\Omega)} e^{C_k T \|\mathbf{w}_{1,2}\|_{L^\infty(0,T;L^2(\Omega))}}$ , grâce aux estimations (2.8) et en utilisant l'équivalence des normes dans  $V_k$ . On utilise une nouvelle fois l'inégalité de Young pour obtenir, puisque  $h_2$  est minoré :

$$\frac{d}{dt} \left( \|h\|_{L^2(\Omega)}^2 + \|\sqrt{h_2} \mathbf{u}\|_{L^2(\Omega)}^2 \right) \leq \|\mathbf{w}\|_{L^2(\Omega)} + k(t) \left( \|h\|_{L^2(\Omega)}^2 + \|\sqrt{h_2} \mathbf{u}\|_{L^2(\Omega)}^2 \right),$$

où

$$\begin{aligned}
k(t) = C_k & \left( \|g\|_{L^2(\Omega)} + \|\ell\|_{L^2(\Omega)}^2 \|h_0\|_{L^2(\Omega)}^2 e^{2C_k T} \|\mathbf{w}_2\|_{L^\infty(0,T;L^2(\Omega))} \right. \\
& + C_k \nu \|\mathbf{u}_1\|_{L^2(\Omega)} + 2r_0 \|\mathbf{u}_2\|_{L^2(\Omega)}^2 + \beta \|\Delta h_1\|_{L^2(\Omega)} \\
& + \beta \|\Delta h_1\|_{L^2(\Omega)}^2 \|\nabla h\|_{L^2(\Omega)}^2 \\
& + \beta \|\Delta h\|_{L^2(\Omega)}^2 \left( \|h_0\|_{L^2(\Omega)}^2 e^{2C_k T} \|\mathbf{w}_2\|_{L^\infty(0,T;L^2(\Omega))} + \|\nabla h_2\|_{L^2(\Omega)}^2 \right) \\
& \left. + \|\nabla h_1\|_{L^2(\Omega)}^2 + \|h_0\|_{L^2(\Omega)}^2 e^{2C_k T} \|\mathbf{w}_1\|_{L^\infty(0,T;L^2(\Omega))} + \|\mathbf{w}_2\|_{L^2(\Omega)} \right).
\end{aligned}$$

Le lemme de Gronwall permet d'obtenir, sachant que  $\mathbf{u}(0) = 0$ ,  $h(0) = 0$  et  $h_2$  minoré :

$$\begin{aligned}
\|h(t)\|_{L^2(\Omega)}^2 + \|\mathbf{u}(t)\|_{L^2(\Omega)}^2 & \leq C \int_0^t e^{\int_s^t k(\tau) d\tau} \|\mathbf{w}(s)\|_{L^2(\Omega)}^2 ds, \\
& \leq Ct \sup_{s \leq t} \|\mathbf{w}(s)\|_{L^2(\Omega)}^2 e^{TK_3(T,k)}.
\end{aligned}$$

En utilisant le lemme 2.3.1, en remarquant que l'on a  $\|\nabla h\|_{L^2(\Omega)} \leq \|\nabla h_1\|_{L^2(\Omega)} + \|\nabla h_2\|_{L^2(\Omega)}$  ainsi que  $\|\Delta h\|_{L^2(\Omega)} \leq \|\Delta h_1\|_{L^2(\Omega)} + \|\Delta h_2\|_{L^2(\Omega)}$  et en majorant respectivement  $\|\nabla h_i\|_{L^2(\Omega)}$  et  $\|\Delta h_i\|_{L^2(\Omega)}$  par  $K_{\nabla h_i}$  et  $K_{\Delta h_i}$  pour  $i = 1, 2$ , grâce aux estimations (2.9) et (2.10), nous obtenons l'expression de la constante :

$$\begin{aligned}
K_3(T, k) = C_k & \left( \|g\|_{L^1(0,T;L^2(\Omega))} + \|\ell\|_{L^1(0,T;L^2(\Omega))}^2 \|h_0\|_{L^2(\Omega)}^2 e^{2C_k T} K_1(T, k) \right. \\
& + C_k \nu K_1(T, k) + 2r_0 K_1(T, k)^2 + \beta K_{\Delta h_1} + \beta K_{\Delta h_1}^2 \left( K_{\nabla h_1} + K_{\nabla h_2} \right)^2 \\
& + \beta \left( K_{\Delta h_1} + K_{\Delta h_2} \right)^2 \left( \|h_0\|_{L^2(\Omega)}^2 e^{2C_k T} K_1(T, k) + K_{\nabla h_2}^2 \right) \\
& \left. + K_{\nabla h_1}^2 + \|h_0\|_{L^2(\Omega)}^2 e^{2C_k T} K_1(T, k) + K_1(T, k) \right).
\end{aligned}$$

On obtient donc :

$$\|\mathbf{u}_1(t) - \mathbf{u}_2(t)\|_{L^2(\Omega)}^2 \leq C e^{TK_3(T,k)} t \sup_{s \leq t} \|\mathbf{w}_1(s) - \mathbf{w}_2(s)\|_{L^2(\Omega)}^2.$$

Il existe donc une constante  $K_4(T, k)$  telle que pour tous  $\mathbf{w}_1, \mathbf{w}_2 \in \mathcal{K}$  on ait

$$\forall t \in [0, T], \|\Theta(\mathbf{w}_1) - \Theta(\mathbf{w}_2)\|_{L^\infty(0,t;V_k)} \leq tK_4(T, k) \|\mathbf{w}_1 - \mathbf{w}_2\|_{L^\infty(0,t;V_k)}.$$

#### (4) Fin de la démonstration de la proposition 2.3.1

D'après le lemme 2.3.3 l'ensemble  $\mathcal{K}$  est équicontinu. De plus l'ensemble  $K(t)$  défini par  $K(t) = \{\mathbf{u}(t), \mathbf{u} \in \mathcal{K}\}$  est d'adhérence compacte dans  $\bar{B}_{V_k}(0, K_1(T, k))$  car  $V_k$  étant de dimension finie,  $\bar{B}_{V_k}(0, K_1(T, k))$  est compacte. Ainsi, d'après le théorème d'Ascoli, l'ensemble  $\mathcal{K}$  défini par (2.39) est un ensemble convexe

compact dans  $\mathcal{C}^0([0, T], V_k)$ . De plus, l'application  $\Theta$  est continue (car lipshitzienne) de  $\mathcal{K}$  dans lui-même et laisse invariant ce compact d'après les lemmes 2.3.1 et 2.3.3. On utilise le théorème suivant :

**Théorème 2.3.1** (Point fixe de Schauder). *Soit  $X$  un espace de Banach et  $C$  une partie compacte convexe de  $X$ . Si  $T$  est une application continue de  $C$  dans  $C$ , elle admet un point fixe dans  $C$ .*

**Preuve.**

Voir [91] ■

Ainsi, d'après le théorème de Schauder,  $\Theta$  possède au moins un point fixe dans  $\mathcal{K}$ .

On a donc montré l'existence d'une solution pour le problème approché (2.20). ■

### 2.3.2. Unicité et globalité de la solution du problème approché.

**Proposition 2.3.2.** *Le problème approché (2.20) possède une unique solution sur  $[0, T]$  pour tout  $T > 0$ . En conséquence, cette solution est définie sur  $\mathbb{R}^+$  tout entier.*

**Preuve.**

L'unicité est une conséquence immédiate du lemme 2.3.4. En effet, si  $\mathbf{u}_1$  et  $\mathbf{u}_2$  sont deux points fixes de  $\Theta$ , on a déjà vu que nécessairement  $\mathbf{u}_1$  et  $\mathbf{u}_2$  sont dans  $\mathcal{K}$ , et on a donc

$$\forall t \geq 0, \|\mathbf{u}_1 - \mathbf{u}_2\|_{L^\infty(0,t; V_k)} \leq tK_4(T, k)\|\mathbf{u}_1 - \mathbf{u}_2\|_{L^\infty(0,t; V_k)}.$$

Ainsi, pour  $t_0 > 0$  assez petit ( $t_0 < \frac{1}{K_4(T, k)}$ ) on a

$$\|\mathbf{u}_1 - \mathbf{u}_2\|_{L^\infty(0,t; V_k)} = 0.$$

Ceci montre l'unicité locale au voisinage de  $t = 0$ . En fait, cela montre que si  $\mathbf{u}_1$  et  $\mathbf{u}_2$  coïncident en  $t_1$  alors elles coïncident sur un intervalle  $[t_1, t_1 + \varepsilon]$ , ce qui permet de conclure à l'unicité de la solution sur  $[0, T]$ .

Pour montrer le caractère global de la solution, on recolle les solutions construites sur des intervalles  $[0, n]$ . Ce recollement peut avoir lieu sans problème grâce à l'unicité obtenue ci-dessus qui assure que les solutions se recouvrent de façon adéquate. ■

**2.3.3. Estimations *a priori*.** Il s'agit maintenant d'obtenir des estimations sur la solution du problème approché indépendantes de  $k$ . C'est la raison pour laquelle on reprend la notation initiale  $(h_k, \mathbf{u}_k)$  pour la solution du problème approché.

**Proposition 2.3.3.** *La solution du problème approché (2.20) vérifie l'inégalité d'énergie suivante :*

$$\begin{aligned} & \int_{\Omega} \left( \frac{h_k^2}{2F_r^2} + h_k \frac{|\mathbf{u}_k|^2}{2} + \beta \frac{|\nabla h_k|^2}{2} \right) + \int_0^t \int_{\Omega} \alpha_0(h_k) |\mathbf{u}_k|^2 + \int_0^t \int_{\Omega} \alpha_1(h_k) h_k |\mathbf{u}_k|^3 \\ & + \frac{\nu}{4} \int_0^t \int_{\Omega} h_k |\nabla \mathbf{u}_k + {}^t \nabla \mathbf{u}_k|^2 + 2\nu \int_0^t \int_{\Omega} h_k |\operatorname{div} \mathbf{u}_k|^2 \\ & \leq \int_{\Omega} \left( \frac{h_0^2}{2F_r^2} + h_0 \frac{|\mathbf{u}_0|^2}{2} + \beta \frac{|\nabla h_0|^2}{2} \right) + \int_0^t \int_{\Omega} h_k \tilde{f} \cdot \mathbf{u}_k \end{aligned} \quad (2.44)$$

**Preuve.**

Remarquons tout d'abord que l'on a l'identité suivante :

$$\frac{\partial(h_k \mathbf{u}_k)}{\partial t} + \operatorname{div} (h_k \mathbf{u}_k \otimes \mathbf{u}_k) = h_k \left( \frac{\partial \mathbf{u}_k}{\partial t} + \operatorname{div} (\mathbf{u}_k \otimes \mathbf{u}_k) \right) + \left( \frac{\partial h_k}{\partial t} + \operatorname{div} (\mathbf{u}_k h_k) \right) \mathbf{u}_k.$$

Le dernier terme étant nul grâce à l'équation vérifiée par  $h_k$ , nous obtenons :

$$\frac{\partial(h_k \mathbf{u}_k)}{\partial t} + \operatorname{div} (h_k \mathbf{u}_k \otimes \mathbf{u}_k) = h_k \left( \frac{\partial \mathbf{u}_k}{\partial t} + \operatorname{div} (\mathbf{u}_k \otimes \mathbf{u}_k) \right), \quad (2.45)$$

et en multipliant (2.45) par  $\mathbf{u}_k$  :

$$\frac{\partial(h_k \mathbf{u}_k)}{\partial t} \mathbf{u}_k + \operatorname{div} (h_k \mathbf{u}_k \otimes \mathbf{u}_k) \mathbf{u}_k = h_k \mathbf{u}_k \left( \frac{\partial \mathbf{u}_k}{\partial t} + \operatorname{div} (\mathbf{u}_k \otimes \mathbf{u}_k) \right).$$

Chacun de ces deux termes est donc égal à leur demi-somme, ce qui donne :

$$\begin{aligned} \frac{\partial(h_k \mathbf{u}_k)}{\partial t} \mathbf{u}_k + \operatorname{div} (h_k \mathbf{u}_k \otimes \mathbf{u}_k) \mathbf{u}_k &= \frac{1}{2} \left( \frac{\partial(h_k \mathbf{u}_k)}{\partial t} \mathbf{u}_k + \operatorname{div} (h_k \mathbf{u}_k \otimes \mathbf{u}_k) \mathbf{u}_k \right. \\ & \quad \left. + h_k \mathbf{u}_k \left( \frac{\partial \mathbf{u}_k}{\partial t} + \operatorname{div} (\mathbf{u}_k \otimes \mathbf{u}_k) \right) \right) \\ &= \frac{1}{2} \frac{\partial h_k |\mathbf{u}_k|^2}{\partial t} + \frac{1}{2} \operatorname{div} (h_k \mathbf{u}_k \otimes \mathbf{u}_k) \mathbf{u}_k \\ & \quad + \frac{1}{2} h_k \mathbf{u}_k \operatorname{div} (\mathbf{u}_k \otimes \mathbf{u}_k) \\ &= \frac{1}{2} \frac{\partial h_k |\mathbf{u}_k|^2}{\partial t} + \frac{1}{2} \operatorname{div} (h_k |\mathbf{u}_k|^2 \mathbf{u}_k). \end{aligned}$$

Ainsi pour  $\psi_k = \mathbf{u}_k$  dans (2.20) et comme  $\mathbf{u}_k \cdot \mathbf{u}_k^\perp = 0$  on obtient :

$$\begin{aligned}
& \frac{1}{2} \frac{d}{dt} \int_{\Omega} h_k |\mathbf{u}_k|^2 dx + \frac{1}{2} \int_{\Omega} \operatorname{div} (h_k \mathbf{u}_k |\mathbf{u}_k|^2) dx + \int_{\Omega} \alpha_0(h_k) |\mathbf{u}_k|^2 + \int_{\Omega} \alpha_1(h_k) h_k |\mathbf{u}_k|^3 \\
& + \frac{1}{F_r^2} \int_{\Omega} h_k \nabla h_k \cdot \mathbf{u}_k + \frac{\nu}{2} \int_{\Omega} h_k \left( \nabla \mathbf{u}_k + {}^t \nabla \mathbf{u}_k \right) \cdot \nabla \mathbf{u}_k + 2\nu \int_{\Omega} (h_k \operatorname{div} \mathbf{u}_k) \mathcal{I} \cdot \nabla \mathbf{u}_k \\
& - \beta \int_{\Omega} h_k \nabla \Delta h_k \cdot \mathbf{u}_k = \int_{\Omega} h_k \tilde{f} \cdot \mathbf{u}_k.
\end{aligned} \tag{2.46}$$

Le second terme de (2.46) est nul, en utilisant la formule de la divergence, car les conditions aux limites sont de type périodiques. On a en intégrant par partie et en utilisant (2.20), tenant compte des conditions aux limites périodiques :

$$\begin{aligned}
\frac{1}{F_r^2} \int_{\Omega} h_k \nabla h_k \cdot \mathbf{u}_k &= -\frac{1}{F_r^2} \int_{\Omega} h_k \operatorname{div} (h_k \mathbf{u}_k) \\
&= \frac{1}{F_r^2} \int_{\Omega} h_k \frac{\partial h_k}{\partial t} \\
&= \frac{1}{2F_r^2} \frac{d}{dt} \|h_k\|_{L^2(\Omega)}^2,
\end{aligned} \tag{2.47}$$

et

$$\begin{aligned}
\beta \int_{\Omega} h_k \nabla \Delta h_k \cdot \mathbf{u}_k &= -\beta \int_{\Omega} \Delta h_k \operatorname{div} (h_k \mathbf{u}_k) \\
&= \beta \int_{\Omega} \Delta h_k \frac{\partial h_k}{\partial t} \\
&= -\beta \int_{\Omega} \nabla h_k \cdot \frac{\partial}{\partial t} (\nabla h_k) \\
&= -\frac{\beta}{2} \frac{d}{dt} \|\nabla h_k\|_{L^2(\Omega)}^2.
\end{aligned}$$

On obtient donc l'égalité suivante :

$$\begin{aligned}
\frac{1}{2} \frac{d}{dt} \int_{\Omega} \left( h_k |\mathbf{u}_k|^2 + \frac{h_k^2}{F_r^2} + \beta |\nabla h_k|^2 \right) + \int_{\Omega} \alpha_0(h_k) |\mathbf{u}_k|^2 + \int_{\Omega} \alpha_1(h_k) h_k |\mathbf{u}_k|^3 \\
+ \frac{\nu}{4} \int_{\Omega} h_k |\nabla \mathbf{u}_k + {}^t \nabla \mathbf{u}_k|^2 + 2\nu \int_{\Omega} h_k |\operatorname{div} \mathbf{u}_k|^2 = \int_{\Omega} h_k \tilde{f} \cdot \mathbf{u}_k
\end{aligned} \tag{2.48}$$

que l'on intègre entre 0 et  $t$  :

$$\begin{aligned}
& \frac{1}{2} \int_{\Omega} \left( h_k |\mathbf{u}_k|^2 + \frac{h_k^2}{F_r^2} + \beta |\nabla h_k|^2 \right) + \int_0^t \int_{\Omega} \alpha_0(h_k) |\mathbf{u}_k|^2 + \int_0^t \int_{\Omega} \alpha_1(h_k) h_k |\mathbf{u}_k|^3 \\
& \quad + \frac{\nu}{4} \int_0^t \int_{\Omega} h_k |\nabla \mathbf{u}_k + {}^t \nabla \mathbf{u}_k|^2 + 2\nu \int_0^t \int_{\Omega} h_k |\operatorname{div} \mathbf{u}_k|^2 \\
& = \frac{1}{2} \int_{\Omega} \left( \frac{(h_0^k)^2}{F_r^2} + h_0^k |\mathbf{u}_0^k|^2 + \beta |\nabla h_0^k|^2 \right) + \int_0^t \int_{\Omega} h_k \tilde{f} \cdot \mathbf{u}_k
\end{aligned} \tag{2.49}$$

pour obtenir finalement l'inégalité d'énergie suivante :

$$\begin{aligned}
& \frac{1}{2} \int_{\Omega} \left( h_k |\mathbf{u}_k|^2 + \frac{h_k^2}{F_r^2} + \beta |\nabla h_k|^2 \right) + \int_0^t \int_{\Omega} \alpha_0(h_k) |\mathbf{u}_k|^2 + \int_0^t \int_{\Omega} \alpha_1(h_k) h_k |\mathbf{u}_k|^3 \\
& \quad + \frac{\nu}{4} \int_0^t \int_{\Omega} h_k |\nabla \mathbf{u}_k + {}^t \nabla \mathbf{u}_k|^2 + 2\nu \int_0^t \int_{\Omega} h_k |\operatorname{div} \mathbf{u}_k|^2 \\
& \leq \frac{1}{2} \int_{\Omega} \left( \frac{(h_0)^2}{F_r^2} + h_0 |\mathbf{u}_0|^2 + \beta |\nabla h_0|^2 \right) + \int_0^t \int_{\Omega} h_k \tilde{f} \cdot \mathbf{u}_k.
\end{aligned} \tag{2.50}$$

**Proposition 2.3.4.** *Nous avons les estimations a priori suivantes :*

- (1)  $(h_k)_k$  bornée dans  $L^\infty(0, T; H_{per}^1(\Omega))$ ,
- (2)  $(\sqrt{h_k} \mathbf{u}_k)_k$  bornée dans  $L^\infty(0, T; (L_{per}^2(\Omega))^2)$ ,
- (3)  $(\alpha_0(h_k)^{\frac{1}{2}} \mathbf{u}_k)_k$  bornée dans  $L^2(0, T; (L_{per}^2(\Omega))^2)$ ,
- (4)  $(\alpha_1(h_k)^{\frac{1}{3}} h_k^{\frac{1}{3}} \mathbf{u}_k)_k$  bornée dans  $L^3(0, T; (L_{per}^3(\Omega))^2)$ ,
- (5)  $\left( \sqrt{h_k} (\nabla \mathbf{u}_k + {}^t \nabla \mathbf{u}_k) \right)_k$  bornée dans  $L^2(0, T; (L_{per}^2(\Omega))^4)$ ,
- (6)  $(\sqrt{h_k} \operatorname{div} \mathbf{u}_k)_k$  bornée dans  $L^2(0, T; L_{per}^2(\Omega))$ ,
- (7)  $\left( \frac{\partial h_k}{\partial t} \right)_k$  bornée dans  $L^\infty(0, T; H_{per}^{-3}(\Omega))$ , car  $(h_k \mathbf{u}_k)$  est bornée dans  $L^\infty(0, T; (L_{per}^{\frac{4}{3}}(\Omega))^2)$ .

**Preuve.**

L'égalité (2.48) peut être mise sous la forme :

$$\begin{aligned}
& \frac{1}{2} \frac{d}{dt} \left( \|\sqrt{h_k} \mathbf{u}_k\|_{L^2(\Omega)}^2 + \frac{1}{F_r^2} \|h_k\|_{L^2(\Omega)}^2 + \beta \|\nabla h_k\|_{L^2(\Omega)}^2 \right) + \|\alpha_0(h_k)^{\frac{1}{2}} \mathbf{u}_k\|_{L^2(\Omega)}^2 \\
& + \|\alpha_1(h_k)^{\frac{1}{3}} h_k^{\frac{1}{3}} \mathbf{u}_k\|_{L^3(\Omega)}^3 + \frac{\nu}{4} \|\sqrt{h_k}(\nabla \mathbf{u}_k + {}^t \nabla \mathbf{u}_k)\|_{L^2(\Omega)}^2 + 2\nu \|\sqrt{h_k} \operatorname{div} \mathbf{u}_k\|_{L^2(\Omega)}^2 \\
& = \int_{\Omega} h_k \tilde{f} \cdot \mathbf{u}_k,
\end{aligned} \tag{2.51}$$

soit

$$\begin{aligned}
& \frac{1}{2} \frac{d}{dt} \left( \|\sqrt{h_k} \mathbf{u}_k\|_{L^2(\Omega)}^2 + \frac{1}{F_r^2} \|h_k\|_{L^2(\Omega)}^2 + \beta \|\nabla h_k\|_{L^2(\Omega)}^2 \right) \\
& \leq \|\sqrt{h_k}\|_{L^4(\Omega)} \|\sqrt{h_k} \mathbf{u}_k\|_{L^2(\Omega)} \|\tilde{f}\|_{L^4(\Omega)} \\
& \leq \left( \frac{1}{2} \|\sqrt{h_k} \mathbf{u}_k\|_{L^2(\Omega)}^2 + \frac{1}{2} \|\sqrt{h_k}\|_{L^4(\Omega)}^2 \right) \|\tilde{f}\|_{L^4(\Omega)} \\
& \leq \left( \frac{1}{2} \|\sqrt{h_k} \mathbf{u}_k\|_{L^2(\Omega)}^2 + \frac{1}{2} \|\sqrt{h_k}\|_{L^4(\Omega)}^4 + C \right) \|\tilde{f}\|_{L^4(\Omega)},
\end{aligned} \tag{2.52}$$

et comme  $\|\sqrt{h_k}\|_{L^4(\Omega)}^4 = \|h_k\|_{L^2(\Omega)}^2$  il vient

$$\begin{aligned}
& \frac{1}{2} \frac{d}{dt} \left( \|\sqrt{h_k} \mathbf{u}_k\|_{L^2(\Omega)}^2 + \frac{1}{F_r^2} \|h_k\|_{L^2(\Omega)}^2 + \beta \|\nabla h_k\|_{L^2(\Omega)}^2 \right) \\
& \leq C \left( \|\sqrt{h_k} \mathbf{u}_k\|_{L^2(\Omega)}^2 + \frac{1}{F_r^2} \|h_k\|_{L^2(\Omega)}^2 + C' \right) \|\tilde{f}\|_{L^4(\Omega)}.
\end{aligned} \tag{2.53}$$

En intégrant entre 0 et  $t$  on obtient alors :

$$\begin{aligned}
& \|\sqrt{h_k(t)} \mathbf{u}_k(t)\|_{L^2(\Omega)}^2 + \frac{1}{F_r^2} \|h_k(t)\|_{L^2(\Omega)}^2 + \beta \|\nabla h_k(t)\|_{L^2(\Omega)}^2 \\
& \leq \|\sqrt{h_0} \mathbf{u}_0\|_{L^2(\Omega)}^2 + \frac{1}{F_r^2} \|h_0\|_{L^2(\Omega)}^2 + \beta \|\nabla h_0\|_{L^2(\Omega)}^2 \\
& + C \int_0^t \left( \|\sqrt{h_k} \mathbf{u}_k\|_{L^2(\Omega)}^2 + \|h_k\|_{L^2(\Omega)}^2 \right) \|\tilde{f}\|_{L^4(\Omega)} + C' \int_0^t \|\tilde{f}\|_{L^4(\Omega)}
\end{aligned} \tag{2.54}$$

ou encore

$$\begin{aligned}
& \|\sqrt{h_k(t)} \mathbf{u}_k(t)\|_{L^2(\Omega)}^2 + \frac{1}{F_r^2} \|h_k(t)\|_{L^2(\Omega)}^2 + \beta \|\nabla h_k(t)\|_{L^2(\Omega)}^2 \\
& \leq C_0 + C \int_0^t \left( \|\sqrt{h_k} \mathbf{u}_k\|_{L^2(\Omega)}^2 + \frac{1}{F_r^2} \|h_k\|_{L^2(\Omega)}^2 \right) \|\tilde{f}\|_{L^4(\Omega)}.
\end{aligned} \tag{2.55}$$

On conclut pour les termes  $\|\sqrt{h_k(t)}\mathbf{u}_k(t)\|_{L^2(\Omega)}^2 + \frac{1}{F_r^2}\|h_k(t)\|_{L^2(\Omega)}^2$  en utilisant le lemme de Gronwall pour obtenir l'inégalité suivante :

$$\|\sqrt{h_k}\mathbf{u}_k(t)\|_{L^2(\Omega)} + \frac{1}{F_r^2}\|h_k(t)\|_{L^2(\Omega)}^2 \leq C_0 e^{C \int_0^t \|\tilde{f}(\tau)\|_{L^4(\Omega)} d\tau}, \quad (2.56)$$

où

$$C_0 = \|\sqrt{h_0}\mathbf{u}_0\|_{L^2(\Omega)}^2 + \frac{1}{F_r^2}\|h_0\|_{L^2(\Omega)}^2 + \beta\|\nabla h_0\|_{L^2(\Omega)}^2 + C' \int_0^t \|\tilde{f}\|_{L^4(\Omega)}.$$

On a alors en utilisant les bornes  $L^\infty(0, T; L_{per}^2(\Omega))$  que l'on vient d'obtenir sur  $(\sqrt{h_k}\mathbf{u}_k)_k$  et  $(h_k)_k$  :

$$\beta\|\nabla h_k(t)\|_{L^2(\Omega)}^2 \leq C_0 + C \int_0^t \|\tilde{f}(s)\|_{L^4(\Omega)}, \quad (2.57)$$

soit

$$\beta\|\nabla h_k(t)\|_{L^2(\Omega)}^2 \leq C \left( C_0, \|\sqrt{h_k}\mathbf{u}_k\|_{L^\infty(0, T; L^2(\Omega))}, \|h_k\|_{L^\infty(0, T; L^2(\Omega))}, \|\tilde{f}\|_{L^1(0, T; L^4(\Omega))} \right). \quad (2.58)$$

On revient à l'équation (2.51) que l'on intègre entre 0 et  $t$  pour obtenir :

$$\begin{aligned} & \int_0^t \|\alpha_0(h_k)^{\frac{1}{2}}\mathbf{u}_k(t)\|_{L^2(\Omega)}^2 + \int_0^t \|\alpha_1(h_k)^{\frac{1}{3}}h_k^{\frac{1}{3}}\mathbf{u}_k(t)\|_{L^3(\Omega)}^3 + 2\nu \int_0^t \|\sqrt{h_k(t)}\operatorname{div} \mathbf{u}_k(t)\|_{L^2(\Omega)}^2 \\ & + \frac{\nu}{4} \int_0^t \|\sqrt{h_k(t)}(\nabla \mathbf{u}_k(t) + {}^t\nabla \mathbf{u}_k(t))\|_{L^2(\Omega)}^2 \leq C \int_0^t \|\tilde{f}\|_{L^4(\Omega)}. \end{aligned} \quad (2.59)$$

Enfin on remarque que comme  $(\sqrt{h_k}\mathbf{u}_k)_k$  et  $(h_k)_k$  sont bornées dans  $L^\infty(0, T; L_{per}^2(\Omega))$  alors  $(h_k \mathbf{u}_k)_k$  est bornée dans  $L^\infty(0, T; L_{per}^{\frac{4}{3}}(\Omega))$  et en particulier  $(\operatorname{div} (h_k \mathbf{u}_k))_k$  dans  $L^\infty(0, T; W_{per}^{-1,1}(\Omega))$ . Comme on a l'injection  $W_{per}^{-1,1}(\Omega) \subset H_{per}^{-3}(\Omega)$  on obtient  $\left(\frac{\partial h_k}{\partial t}\right)_k$  bornée dans  $L^\infty(]0, T[, H_{per}^{-3}(\Omega))$ .

Ceci termine la démonstration de la proposition 2.3.3. ■

A partir de maintenant nous allons différencier le cas de la dimension un du cas de la dimension deux. En fait, nous sommes en mesure de passer à la limite en utilisant ces estimations, ainsi que des estimations supplémentaires, et d'obtenir un résultat d'existence pour le modèle complet en dimension un d'espace. Dans le cas de la dimension

deux, les estimations sont moins fortes et nous sommes obligés d'avoir recours à une hypothèse supplémentaire sur la positivité de  $h_k$ , inspiré de [24], afin d'obtenir un résultat d'existence pour un modèle avec terme de diffusion simplifié.

## 2.4. Existence d'une solution faible en dimension 1

**2.4.1. Modèle unidimensionnel.** Nous nous intéressons ici au cas de la dimension un. Dans le cas unidimensionnel, nous sommes capables de passer à la limite sur le modèle complet sans aucune hypothèse supplémentaire. On considère le système 2.1, défini sur un ouvert  $I = ]0, 1[$ , avec des conditions aux limites périodiques. Le système devient :

$$\left\{ \begin{array}{l} \partial_t h + \partial_x(hu) = 0, \\ \partial_t(hu) + \partial_x(hu^2) + \frac{1}{F_r^2} h \partial_x h - \beta h \partial_x^3 h + \alpha_0(h) u + \alpha_1(h) h |u| u = \\ hf + 3\nu \partial_x(h \partial_x u) - \frac{1}{F_r^2} h \partial_x d + \beta h \partial_x^3 d. \\ h(0) = h_0, \\ (hu)(0) = (hu)_0. \end{array} \right. \quad (2.60)$$

L'inégalité d'énergie (2.44) devient en dimension un :

$$\begin{aligned} \int_I \left( \frac{h_k^2}{2F_r^2} + \frac{h_k}{2} u_k^2 + \beta \frac{(\partial_x h_k)^2}{2} \right) + \int_0^t \int_I \alpha_0(h_k) u_k^2 + \int_0^t \int_I \alpha_1(h_k) h_k |u_k|^3 \\ + 3\nu \int_0^t \int_I h_k (\partial_x u_k)^2 \leq \int_I \left( \frac{h_0^2}{2F_r^2} + h_0 \frac{(u_0)^2}{2} + \beta \frac{(\partial_x h_0)^2}{2} \right) + \int_0^t \int_I h_k \tilde{f} u_k \end{aligned} \quad (2.61)$$

**2.4.2. Nouvelles estimations.** A partir des estimations (2.3.4) obtenues en dimension deux, on obtient la proposition suivante, valable en dimension un :

**Proposition 2.4.1.** *Nous avons les estimations a priori suivantes :*

- (1)  $(h_k)_k$  bornée dans  $L^\infty(0, T; L_{per}^\infty(I)) \cap L^\infty(0, T; H_{per}^1(I))$ ,
- (2)  $(\sqrt{h_k} u_k)_k$  bornée dans  $L^\infty(0, T; L_{per}^2(I))$ ,
- (3)  $(u_k)_k$  bornée dans  $L^2(0, T; L_{per}^2(I))$ ,
- (4)  $(h_k^{\frac{1}{3}} u_k)_k$  bornée dans  $L^3(0, T; L_{per}^3(I))$ ,
- (5)  $(\sqrt{h_k} \partial_x u_k)_k$  bornée dans  $L^2(0, T; L_{per}^2(I))$ ,
- (6)  $\left( \frac{\partial h_k}{\partial t} \right)_k$  bornée dans  $L^\infty(0, T; H_{per}^{-1}(I))$ .

**Preuve.**

La borne  $L^\infty(0, T; L_{per}^\infty(I))$  pour  $(h_k)_k$  vient du fait qu'en dimension un nous avons l'injection continue  $H_{per}^1(I) \subset L_{per}^\infty(I)$ . L'estimation sur  $(u_k)_k$  provient alors de l'identité suivante :

$$u_k = \frac{\alpha_0(h_k)^{\frac{1}{2}} uk}{\alpha_0(h_k)^{\frac{1}{2}}} = r_0^{-\frac{1}{2}} \alpha_0(h_k)^{\frac{1}{2}} uk (1 + c_0 h_k)^{\frac{1}{2}} \quad (2.62)$$

où  $c_0 = \frac{\varepsilon r_0}{3\nu_0}$ . Nous avons  $(\alpha_0(h_k)^{\frac{1}{2}} u_k)_k$  qui est bornée dans  $L^2(0, T; L^2(I))$  d'après (2.3.4) et  $(1 + c_0 h_k)_k$  bornée dans  $L^\infty(0, T; L^\infty(I))$  d'après ce qui précède. On a donc bien  $(\alpha_0(h_k)^{\frac{1}{2}} uk (1 + c_0 h_k)^{\frac{1}{2}})_k$  bornée dans  $L^2(0, T; L^2(I))$ . De même nous avons :

$$h_k^{\frac{1}{3}} u_k = \frac{\alpha_1(h)^{\frac{1}{3}} h_k^{\frac{1}{3}} uk}{\alpha_1(h)^{\frac{1}{3}}} = r_1^{-\frac{1}{3}} \alpha_1(h)^{\frac{1}{3}} h_k^{\frac{1}{3}} uk (1 + c_0 h_k)^{\frac{2}{3}} \quad (2.63)$$

d'où, puisque nous avons  $((1 + c_0 h_k)^{\frac{2}{3}})_k$  bornée dans  $L^\infty(0, T; L_{per}^\infty(I))$ ,  $(h_k^{\frac{1}{3}} u_k)_k$  est bornée dans  $L^3(0, T; L_{per}^3(I))$ .

Enfin nous avons, d'après ce qui précède,  $(h_k u_k)_k$  bornée dans  $L^\infty(0, T; L_{per}^2(I))$  puisque  $(\sqrt{h_k} u_k)_k$  est bornée dans  $L^\infty(0, T; L_{per}^2(I))$ . Donc  $\left(\frac{\partial h_k}{\partial t}\right)_k$  bornée dans  $L^\infty(0, T; W_{per}^{-1,2}(I))$ .

Pour le passage à la limite nous avons besoin d'estimations supplémentaires, notamment concernant la dérivée seconde de  $h$ . Les différents lemmes techniques démontrés ici pour obtenir les estimations *a priori* qui suivent sont inspirés du travail présenté par Bresch et Desjardins dans [51] pour le cas bidimensionnel, et adaptés au problème qui nous intéresse. Des difficultés d'ordre technique supplémentaires apparaissent et sont en particulier dues à la présence des coefficients  $\alpha_0(h)$  et  $\alpha_1(h)$ .

**Proposition 2.4.2.** *Nous avons les estimations a priori supplémentaires suivantes, fondamentales pour le passage à la limite dans le problème approché :*

- (1)  $(h_k u_k)_k$  bornée dans  $L^3(0, T; L_{per}^3(I)) \cap L^\infty(0, T; L_{per}^2(I)) \cap L^2(0, T; W_{per}^{1,1}(I))$ ,
- (2)  $(\alpha_0(h_k))_k$  bornée dans  $L^\infty(0, T; H_{per}^1(I)) \cap L^\infty(0, T; L_{per}^\infty(I))$ ,
- (3)  $(\alpha_1(h_k))_k$  bornée dans  $L^\infty(0, T; H_{per}^1(I)) \cap L^\infty(0, T; L_{per}^\infty(I))$ ,
- (4)  $(\partial_x \sqrt{h_k})_k$  bornée dans  $L^\infty(0, T; L_{per}^2(I))$ ,
- (5)  $(h_k)_k$  bornée dans  $L^2(0, T; H_{per}^2(I))$ .

**Preuve.**

La première estimation se démontre en écrivant que l'on a  $\partial_x(h_k u_k) = \partial_x h_k u_k + \sqrt{h_k} \sqrt{h_k} \partial_x u_k$ . Les estimations précédentes permettent alors de conclure immédiatement que  $(h_k u_k)_k$  est bornée dans  $L^2(0, T; W_{per}^{1,1}(I))$ . Les bornes dans  $L^3(0, T; L_{per}^3(I))$  et  $L^\infty(0, T; L_{per}^2(I))$  sont évidentes aux vues des estimations (2.4.1).

Les estimations sur  $(\alpha_0(h_k))_k$  et  $(\alpha_1(h_k))_k$  s'obtiennent d'une part en remarquant que l'on a  $0 < \alpha_0(h_k) < r_0$  et  $0 < \alpha_1(h_k) < r_1$ , pour tout indice  $k$ , puisque  $h_k > 0$ . D'autre part on a  $\partial_x \alpha_0(h_k) = \alpha'_0(h_k) \partial_x h_k$  et  $\partial_x \alpha_1(h_k) = \alpha'_1(h_k) \partial_x h_k$ . Comme  $(\alpha'_0(h_k))_k$  et  $(\alpha'_1(h_k))_k$  sont également uniformément bornées et que l'on a une borne dans  $L^\infty(0, T; L^2_{per}(I))$  pour  $(\partial_x h_k)_k$ , on obtient bien les bornes voulues.

Les deux dernières estimations nécessitent plus de travail et sont démontrées en adaptant des idées introduites dans [51] et [24]. Nous montrons tout d'abord deux lemmes techniques.

**Lemme 2.4.1.** *Nous avons les deux identités suivantes :*

$$\frac{1}{2} \frac{d}{dt} \int_I h_k |\partial_x \log h_k|^2 + \int_I h_k \partial_x^2 u_k \partial_x \log h_k + \int_I h_k \partial_x u_k (\partial_x \log h_k)^2 = 0 \quad (2.64)$$

$$\begin{aligned} \frac{3}{2} \nu^2 \frac{d}{dt} \int_I h_k (\partial_x \log h_k)^2 + \nu \int_I \alpha_0(h_k) u_k \partial_x \log h_k + \nu \int_I \alpha_1(h_k) |u_k| u_k \partial_x h_k \\ + \nu \beta \int_I (\partial_x^2 h_k)^2 + \nu \int_I \frac{(\partial_x h_k)^2}{F_r^2} = -\nu \frac{d}{dt} \int_I u_k \partial_x h_k \\ + \nu \int_I h_k (\partial_x u_k)^2 + \nu \int_I \tilde{f} \partial_x h_k \end{aligned} \quad (2.65)$$

**Preuve du lemme 2.4.1.**

La première identité s'obtient en divisant l'équation de conservation de la masse par  $h_k$  (n'oublions pas que l'on a par définition  $h_k > \frac{1}{k}$ ). On obtient :

$$\partial_t (\log h_k) + u_k \partial_x (\log h_k) + \partial_x u_k = 0 \quad (2.66)$$

En dérivant cette équation par rapport à  $x$ , en la multipliant par  $h_k \partial_x \log h_k$  et en intégrant sur  $I$  on obtient :

$$\begin{aligned} \frac{1}{2} \int_I h_k \partial_t (\partial_x \log h_k)^2 + \int_I h_k \partial_x u_k (\partial_x \log h_k)^2 \\ + \frac{1}{2} \int_I h_k u_k \partial_x (\partial_x \log h_k)^2 + \int_I h_k \partial_x^2 u_k \partial_x \log h_k = 0 \end{aligned}$$

Enfin, comme :

$$\frac{d}{dt} \int_I h_k (\partial_x \log h_k)^2 = \int_I \partial_t (h_k (\partial_x \log h_k)^2) + \int_I \partial_x (h_k u_k (\partial_x \log h_k)^2)$$

et en utilisant le fait que, grâce à l'équation de conservation de la hauteur d'eau, nous avons :

$$\int_I \partial_t h_k (\partial_x \log h_k)^2 + \int_I \partial_x (h_k u_k) (\partial_x \log h_k)^2 = 0,$$

nous obtenons :

$$\frac{1}{2} \frac{d}{dt} \int_I h_k |\partial_x \log h_k|^2 + \int_I h_k \partial_x u_k (\partial_x \log h_k)^2 + \int_I h_k \partial_x^2 u_k \partial_x \log h_k = 0$$

.

■

Pour la deuxième identité, on remarque tout d'abord que l'on a :

$$\partial_t (h_k u_k) + \partial_x (h_k u_k^2) = h_k (\partial_t u_k + u_k \partial_x u_k + u_k (\partial_t h_k + \partial_x (h_k u_k))).$$

L'équation sur  $h_k$  permet d'éliminer le terme en facteur de  $u_k$ . On multiplie ensuite l'équation de conservation de la quantité de mouvement par  $\nu \partial_x \log h_k$  pour obtenir :

$$\begin{aligned} \nu \int_I (\partial_t u_k + u_k \partial_x u_k) \partial_x h_k + 3\nu^2 \int_I h_k \partial_x u_k \partial_x \left( \frac{\partial_x h_k}{h_k} \right) + \nu \beta \int_I (\partial_x^2 h_k)^2 \\ + \nu \int_I \alpha_0(h_k) u_k \partial_x \log h_k + \nu \int_I \alpha_1(h_k) |u_k| u_k \partial_x h_k + \nu \int_I \frac{(\partial_x h_k)^2}{F_r^2} = \nu \int_I \tilde{f} \partial_x h_k, \end{aligned} \quad (2.67)$$

ou encore, en développant le terme en  $\nu^2$  :

$$\begin{aligned} \nu \int_I (\partial_t u_k + u_k \partial_x u_k) \partial_x h_k + 3\nu^2 \int_I \partial_x u_k \partial_x^2 h_k - 3\nu^2 \int_I \partial_x u_k \frac{(\partial_x h_k)^2}{h_k} \\ + \nu \beta \int_I (\partial_x^2 h_k)^2 + \nu \int_I \alpha_0(h_k) u_k \partial_x \log h_k + \nu \int_I \alpha_1(h_k) |u_k| u_k \partial_x h_k \\ + \nu \int_I \frac{(\partial_x h_k)^2}{F_r^2} = \nu \int_I \tilde{f} \partial_x h_k. \end{aligned} \quad (2.68)$$

Multipliant l'identité (2.64) par  $3\nu^2$  et l'ajoutant à (2.68), et en remarquant que l'on a, en intégrant par parties

$$3\nu^2 \int_I \partial_x u_k \partial_x^2 h_k + 3\nu^2 \int_I \partial_x^2 u_k h_k \partial_x \log h_k = 0$$

on obtient :

$$\begin{aligned} \frac{3}{2} \nu^2 \frac{d}{dt} \int_I h_k (\partial_x \log h_k)^2 + \nu \int_I \frac{(\partial_x h_k)^2}{F_r^2} + \nu \beta \int_I (\partial_x^2 h_k)^2 + \nu \int_I \alpha_0(h_k) u_k \partial_x \log h_k \\ + \nu \int_I \alpha_1(h_k) |u_k| u_k \partial_x h_k = \mathcal{I}_k \end{aligned} \quad (2.69)$$

avec

$$\mathcal{I}_k = -\nu \int_I \partial_t u_k \partial_x h_k - \nu \int_I u_k \partial_x u_k \partial_x h_k + \nu \int_I \tilde{f} \partial_x h_k.$$

Réécrivons  $\mathcal{I}_k$  en tenant compte de l'équation de conservation de la masse et en intégrant par parties :

$$\begin{aligned} \mathcal{I}_k &= -\nu \frac{d}{dt} \int_I u_k \partial_x h_k + \nu \int_I u_k \partial_x \partial_t h_k - \nu \int_I u_k \partial_x u_k \partial_x h_k + \nu \int_I \tilde{f} \partial_x h_k \\ &= -\nu \frac{d}{dt} \int_I u_k \partial_x h_k - \nu \int_I u_k \partial_x^2 (h_k u_k) - \nu \int_I u_k \partial_x u_k \partial_x h_k + \nu \int_I \tilde{f} \partial_x h_k \\ &= -\nu \frac{d}{dt} \int_I u_k \partial_x h_k + \nu \int_I (\partial_x u_k)^2 h_k + \nu \int_I \tilde{f} \partial_x h_k. \end{aligned}$$

Ceci termine la démonstration de la deuxième identité. ■

**Lemme 2.4.2.** *Nous avons l'inégalité suivante :*

$$\begin{aligned} &\frac{3}{2} \frac{d}{dt} \int_I \left( h_k \left( \frac{1}{3} u_k + \nu \partial_x \log h_k \right)^2 + \frac{h_k^2}{9 F_r^2} + \beta \frac{(\partial_x h_k)^2}{9} \right) - \nu r_0 \frac{d}{dt} \int_I \log (r_0^{-1} h_k \alpha_0(h_k)) \\ &\quad + \nu \int_I \alpha'_0(h_k) \partial_x h_k u_k + \nu \int_I \alpha_1(h_k) |u_k| u_k \partial_x h_k + \nu \beta \int_I (\partial_x^2 h_k)^2 \\ &\quad + \nu \int_I \frac{(\partial_x h_k)^2}{F_r^2} + \frac{1}{3} \int_I \alpha_0(h_k) u_k^2 + \frac{1}{3} \int_I \alpha_1(h_k) h_k |u_k|^3 \\ &\leq \nu \int_I h_k (\partial_x u_k)^2 + \frac{1}{3} \int_I \tilde{f} (h_k u_k + 3 \nu \partial_x h_k) \end{aligned} \tag{2.70}$$

**Preuve du lemme 2.4.2.**

L'égalité (2.65) se réécrit sous la forme suivante :

$$\begin{aligned} &\frac{3}{2} \frac{d}{dt} \int_I h_k \left( \frac{1}{3} u_k + \nu \partial_x \log h_k \right)^2 + \nu \int_I \frac{(\partial_x h_k)^2}{F_r^2} + \nu \beta \int_I (\partial_x^2 h_k)^2 \\ &\quad + \nu \int_I \alpha_0(h_k) u_k \partial_x \log h_k + \nu \int_I \alpha_1(h_k) |u_k| u_k \partial_x h_k \\ &= \frac{1}{6} \frac{d}{dt} \int_I h_k u_k^2 + \nu \int_I (\partial_x u_k)^2 h_k + \nu \int_I \tilde{f} \partial_x h_k \end{aligned} \tag{2.71}$$

En multipliant l'inégalité d'énergie (2.61) par  $\frac{1}{3}$  on obtient :

$$\begin{aligned} &\frac{1}{6} \frac{d}{dt} \int_I \left( h_k u_k^2 + \frac{h_k^2}{F_r^2} + \beta (\partial_x h_k)^2 \right) + \frac{1}{3} \int_I \alpha_0(h_k) u_k^2 + \frac{1}{3} \int_I \alpha_1(h_k) h_k |u_k|^3 \\ &\quad + \nu \int_I h_k (\partial_x u_k)^2 = \frac{1}{3} \int_I h_k \tilde{f} u_k \end{aligned} \tag{2.72}$$

En ajoutant (2.72) à (2.71,) on obtient :

$$\begin{aligned}
& \frac{3}{2} \frac{d}{dt} \int_I \left( h_k \left( \frac{1}{3} u_k + \nu \partial_x \log h_k \right)^2 + \frac{h_k^2}{9 F_r^2} + \beta \frac{(\partial_x h_k)^2}{9} \right) + \nu \int_I \alpha_0(h_k) u_k \partial_x \log h_k \\
& + \nu \int_I \alpha_1(h_k) |u_k| u_k \partial_x h_k + \nu \beta \int_I (\partial_x^2 h_k)^2 + \nu \int_I \frac{(\partial_x h_k)^2}{F_r^2} + \frac{1}{3} \int_I \alpha_0(h_k) u_k^2 \\
& + \frac{1}{3} \int_I \alpha_1(h_k) h_k |u_k|^3 \leq \nu \int_I h_k (\partial_x u_k)^2 + \frac{1}{3} \int_I \tilde{f}(h_k u_k + 3 \nu \partial_x h_k).
\end{aligned} \tag{2.73}$$

Remarquons enfin que le terme  $\int_I \alpha_0(h_k) u_k \partial_x \log h_k$  peut s'écrire, en utilisant l'équation de conservation de la masse et en intégrant par partie :

$$\begin{aligned}
\int_I \alpha_0(h_k) u_k \partial_x \log h_k &= - \int_I \frac{\alpha_0(h_k)}{h_k} \partial_t h_k - \int_I \alpha_0(h_k) \partial_x u_k \\
&= - \int_I \partial_t (F_0(h_k)) + \int_I \alpha'_0(h_k) \partial_x h_k u_k
\end{aligned} \tag{2.74}$$

où  $F_0(h_k)$  est telle que  $F'_0(h_k) = \frac{\alpha_0(h_k)}{h_k}$ . On obtient donc :

$$\int_I \alpha_0(h_k) u_k \partial_x \log h_k = -r_0 \frac{d}{dt} \int_I \log (r_0^{-1} h_k \alpha_0(h_k)) + \int_I \alpha'_0(h_k) \partial_x h_k u_k \tag{2.75}$$

En injectant cette égalité dans (2.73), nous obtenons bien (2.70). Ceci termine la démonstration du lemme 2.4.2. ■

A partir de (2.70), nous pouvons obtenir les deux dernières estimations supplémentaires. En effet, intégrant (2.70) entre 0 et  $t$ , nous obtenons :

$$\begin{aligned}
& \frac{3}{2} \int_I \left( h_k \left( \frac{1}{3} u_k + \nu \partial_x \log h_k \right)^2 + \frac{h_k^2}{9 F_r^2} + \beta \frac{(\partial_x h_k)^2}{9} \right) - \nu r_0 \int_I \log (r_0^{-1} h_k \alpha_0(h_k)) \\
& + \nu \int_0^t \int_I \alpha'_0(h_k) \partial_x h_k u_k + \nu \int_0^t \int_I \alpha_1(h_k) |u_k| u_k \partial_x h_k + \nu \beta \int_0^t \int_I (\partial_x^2 h_k)^2 \\
& + \nu \int_0^t \int_I \frac{(\partial_x h_k)^2}{F_r^2} + \frac{1}{3} \int_0^t \int_I \alpha_0(h_k) u_k^2 + \frac{1}{3} \int_0^t \int_I \alpha_1(h_k) h_k |u_k|^3 \\
& \leq A_0 - \nu r_0 \int_I \log (r_0^{-1} h_{k0} \alpha_0(h_{k0})) + \frac{1}{3} \int_0^t \int_I \tilde{f}(h_k u_k + 3 \nu \partial_x h_k),
\end{aligned} \tag{2.76}$$

avec  $A_0$  constante liée aux données initiales, indépendante de  $k$ . Tenant compte des termes positifs présents dans le membre de gauche de cette inégalité, nous obtenons :

$$\begin{aligned}
& \frac{3}{2} \int_I h_k \left( \frac{1}{3} u_k + \nu \partial_x \log h_k \right)^2 - \nu r_0 \int_I \log (r_0^{-1} h_k \alpha_0(h_k)) + \nu \int_0^t \int_I \alpha'_0(h_k) \partial_x h_k u_k \\
& \quad + \nu \int_0^t \int_I \alpha_1(h_k) |u_k| u_k \partial_x h_k + \nu \beta \int_0^t \int_I (\partial_x^2 h_k)^2 \\
& \leq A_0 - \nu r_0 \int_I \log (r_0^{-1} h_{k0} \alpha_0(h_{k0})) + \frac{1}{3} \int_0^t \int_I \tilde{f}(h_k u_k + 3 \nu \partial_x h_k).
\end{aligned} \tag{2.77}$$

Contrôlons les termes non positifs apparaissant dans le membre de gauche. On a tout d'abord :

$$\begin{aligned}
\left| \nu \int_0^t \int_I \alpha'_0(h_k) \partial_x h_k u_k \right| & \leq \nu \int_0^t \int_I |\alpha'_0(h_k) \partial_x h_k u_k| \\
& \leq \nu r_0 c_0 \|h_k\|_{L^2(0,T; H^1(I))} \|u_k\|_{L^2(0,T; L^2(I))}.
\end{aligned} \tag{2.78}$$

En effet, nous avons  $|\alpha'_0(h_k)| = \frac{r_0 c_0}{(1 + c_0 h_k)^2} \leq r_0 c_0$ . On a également :

$$\begin{aligned}
\left| \nu \int_0^t \int_I \alpha_1(h_k) |u_k| u_k \partial_x h_k \right| & \leq \left| \nu \int_0^t \int_I \partial_x(\alpha_1(h_k)) |u_k| u_k h_k \right| \\
& \quad + \left| \nu \int_0^t \int_I \alpha_1(h_k) \partial_x(|u_k|) u_k h_k \right| + \left| \nu \int_0^t \int_I \alpha_1(h_k) |u_k| \partial_x(u_k) h_k \right|
\end{aligned} \tag{2.79}$$

On a d'après la première estimation démontrée de la proposition 2.4.2, une borne dans  $L^2(0, T; L^1_{per}(I))$  pour  $((\partial_x(h_k u_k))_k)$ , c'est à dire que l'on a  $(h_k u_k)_k$  bornée dans  $L^2(0, T; W^{1,1}_{per}(I))$ . On a en dimension un l'injection  $W^{1,1}_{per}(I) \subset L^\infty_{per}(I)$  et donc  $(h_k u_k)_k$  bornée dans  $L^2(0, T; L^\infty_{per}(I))$ .

Ainsi, puisque  $\partial_x(\alpha_1(h_k)) = \alpha'_1(h_k) \partial_x h_k$  et que l'on a  $|\alpha'_1(h_k)| = \frac{2 r_1 c_0}{(1 + c_0 h_k)^3} \leq 2 r_1 c_0$ , on a pour le premier terme du membre de droite de (2.96) :

$$\begin{aligned}
\left| \nu \int_0^t \int_I \partial_x(\alpha_1(h_k)) |u_k| u_k h_k \right| & \leq \\
& C \|\partial_x h_k\|_{L^\infty(0,T; L^2(I))} \|u_k\|_{L^2(0,T; L^2(I))} \|h_k u_k\|_{L^2(0,T; L^\infty(I))}.
\end{aligned} \tag{2.80}$$

Nous obtenons donc, puisque  $0 \leq \alpha_1(h_k) \leq r_1$  :

$$\begin{aligned}
\left| \nu \int_0^t \int_I \alpha_1(h_k) |u_k| u_k \partial_x h_k \right| &\leq \\
C \|\partial_x h_k\|_{L^\infty(0,T; L^2(I))} \|u_k\|_{L^2(0,T; L^2(I))} \|h_k u_k\|_{L^2(0,T; L^\infty(I))} & \\
+ C \|\sqrt{h_k} \partial_x u_k\|_{L^2(0,T; L^2(I))} \|\sqrt{h_k} u_k\|_{L^\infty(0,T; L^2(I))}. &
\end{aligned} \tag{2.81}$$

Il reste à contrôler les termes  $\nu r_0 \int_I \log(r_0^{-1} h_k \alpha_0(h_k))$  et  $\nu r_0 \int_I \log(r_0^{-1} h_{k0} \alpha_0(h_{k0}))$ . Remarquons que le premier terme se développe de la manière suivante :

$$-\nu r_0 \int_I \log(r_0^{-1} h_k \alpha_0(h_k)) = -\nu r_0 \int_I \log h_k + \nu r_0 \int_I \log(1 + c_0 h_k).$$

Le terme  $\nu r_0 \int_I \log(1 + c_0 h_k)$  est toujours positif et ne pose donc pas de problème particulier. De même, lorsque l'on a  $h_k \leq 1$ , le terme  $-\nu r_0 \int_I \log h_k$  est positif.

Il reste donc à contrôler le terme  $|\nu r_0 \int_I \log_+ h_k|$  où  $\log_+ g$  est définie par  $\log_+ g = \log \max(g, 1)$ , ce qui est immédiat puisque l'on a  $\log_+ x < x$  et donc, comme  $(h_k)_k$  est bornée dans  $L^2(0, T; L^2_{per}(I))$ , on a bien  $(\log_+ h_k)_k$  bornée dans  $L^2(0, T; L^1(I))$ .

Enfin, en choisissant la donnée initiale telle que  $\log(r_0^{-1} h_{k0} \alpha_0(h_{k0}))$  soit uniformément bornée dans  $L^1(I)$ , on contrôle le terme  $-\nu r_0 \int_I \log(r_0^{-1} h_{k0} \alpha_0(h_{k0}))$ .

On obtient donc l'inégalité suivante :

$$\begin{aligned}
\frac{3}{2} \int_I h_k \left( \frac{1}{3} u_k + \nu \partial_x \log h_k \right)^2 + \nu \beta \int_0^t \int_I (\partial_x^2 h_k)^2 &\leq C_1 \\
+ C_2 \|\tilde{f}\|_{L^2(0,T; L^2(I))} \left( \|h_k u_k\|_{L^2(0,T; L^\infty(I))} + \|\partial_x h_k\|_{L^2(0,T; L^2(I))} \right) &
\end{aligned} \tag{2.82}$$

où  $C_1$  et  $C_2$  sont des constantes indépendantes de  $k$ .

L'estimation  $L^2$  pour  $(\partial_x^2 h_k)_k$  est immédiate. En remarquant que  $|\partial_x \sqrt{h_k}|^2 = \frac{|\partial_x h_k|^2}{4 h_k} = \frac{1}{4} h_k |\partial_x \log h_k|^2$ , on obtient bien l'estimation supplémentaire sur  $(\sqrt{h_k})_k$ .

Ceci termine la démonstration de la proposition (2.4.2). ■

**2.4.3. Estimation supplémentaire sur  $h_k u_k$ .** Une estimation supplémentaire est nécessaire afin d'obtenir de la compacité sur  $h_k u_k$ . Cette propriété va en effet s'avérer nécessaire au passage à la limite dans les termes non-linéaires du problème approché. Nous cherchons ici à obtenir de la compacité sur  $(h_k u_k)_k$ . Notons que dans [51], la compacité est obtenue sur  $(\sqrt{h_k} u_k)_k$ . On introduit l'opérateur de translation  $\tau_\eta$ ,  $\eta \geq 0$ , défini par  $\tau_\eta(u)(t, x) = u(t + \eta, x)$  et on va chercher à estimer  $(\tau_\eta(h_k u_k) - h_k u_k)$  i.e.

chercher une propriété d'équicontinuité en temps dans un espace *ad hoc*. on a la proposition suivante :

**Proposition 2.4.3.** *Il existe une constante  $C > 0$  indépendante des données telle que*

$$\left\| \tau_\eta(h_k u_k) - h_k u_k \right\|_{L^\infty(0, T-\eta; (W_{per}^{1,\infty}(I))')} \leq C\eta^{\frac{1}{3}} \quad (2.83)$$

**Preuve.**

Soit  $\psi \in V_k$  indépendant du temps. L'équation (2.60) permet d'écrire :

$$\begin{aligned} & \int_I \left( \tau_\eta(h_k u_k)(t) - h_k u_k(t) \right) \psi = \int_I \int_t^{t+\eta} \partial_t(h_k u_k) \\ & = \int_t^{t+\eta} \int_I \left( -\alpha_0(h_k) u_k - \alpha_1(h_k) h_k |u_k| u_k - \frac{1}{F_r^2} h_k \partial_x h_k + \beta h_k \partial_x^3 h_k + h_k \tilde{f} \right) \psi \\ & + \int_t^{t+\eta} \int_I \left( -h_k u_k^2 - 3\nu h_k \partial_x u_k \right) \partial_x \psi \end{aligned} \quad (2.84)$$

Evaluons chaque terme :

$$\begin{aligned} \bullet \left| \int_I (h_k u_k^2) \partial_x \psi \right| & \leq \|h_k u_k^2\|_{L^{\frac{3}{2}}(I)} \|\partial_x \psi\|_{L^3(I)} \\ & \leq g_1(t) \|\partial_x \psi\|_{L^3(I)} \end{aligned}$$

où  $g_1(t) = \|h_k(t) u_k(t)^2\|_{L^{\frac{3}{2}}(I)}$ . En effet, on a les estimations suivantes :

$$\begin{aligned} (h_k^{\frac{1}{3}}) & \text{ borné dans } L^\infty(0, T; L_{per}^\infty(I)), \\ (h_k^{\frac{1}{3}} u_k) & \text{ borné dans } L^3(0, T; L_{per}^3(I)), \\ (h_k^{\frac{2}{3}} u_k^2) & \text{ borné dans } L^{\frac{3}{2}}(0, T; L_{per}^{\frac{3}{2}}(I)). \end{aligned}$$

La fonction  $g_1$  est donc bornée indépendamment de  $k$  dans  $L^{\frac{3}{2}}(0, T)$ .

$$\begin{aligned} \bullet \left| \nu \int_I h_k \partial_x u_k \partial_x \psi \right| & \leq \|h_k^{\frac{1}{2}}\|_{L^\infty(I)} \|h_k^{\frac{1}{2}} \partial_x u_k\|_{L^2(I)} \|\partial_x \psi\|_{L^2(I)} \\ & \leq g_2(t) \|\nabla \psi\|_{L^2(I)} \end{aligned}$$

où  $g_2(t) = \|h_k(t)^{\frac{1}{2}}\|_{L^\infty(I)} \|h_k(t)^{\frac{1}{2}} \partial_x u_k(t)\|_{L^2(I)}$ . Comme  $(\|h_k(t)^{\frac{1}{2}}\|_{L^\infty(I)})_k$  et  $(\|h_k(t)^{\frac{1}{2}} \partial_x u_k(t)\|_{L^2(I)})_k$  sont bornées respectivement dans  $L^\infty(0, T)$  et  $L^2(0, T)$ ,  $g_2$  est donc bornée indépendamment de  $k$  dans  $L^2(0, T)$ .

$$\begin{aligned} \bullet \left| \int_I \alpha_0(h_k) u_k \psi \right| & \leq r_0^{\frac{1}{2}} \|\alpha_0(h_k)^{\frac{1}{2}} u_k\|_{L^2(I)} \|\psi\|_{L^2(I)} \\ & \leq C \|\alpha_0(h_k)^{\frac{1}{2}} u_k\|_{L^2(I)} \|\partial_x \psi\|_{L^2(I)} \\ & \leq g_3(t) \|\partial_x \psi\|_{L^2(I)} \end{aligned}$$

où  $g_3(t) = C\|\alpha_0(h_k)^{\frac{1}{2}} u_k(t)\|_{L^2(I)}$  est bornée indépendamment de  $k$  dans  $L^2(0, T)$ .

$$\begin{aligned} \bullet \left| \frac{1}{F_r^2} \int_I h_k \partial_x h_k \psi \right| &\leq \|h_k \partial_x h_k\|_{L^2(I)} \|\psi\|_{L^2(I)} \\ &\leq C \|h_k \partial_x h_k\|_{L^2(I)} \|\partial_x \psi\|_{L^2(I)} \\ &\leq g_4(t) \|\partial_x \psi\|_{L^2(I)} \end{aligned}$$

où  $g_4(t) = C\|h_k(t) \partial_x h_k(t)\|_{L^2(I)}$  est  $L^\infty(0, T)$ .

$$\begin{aligned} \bullet \left| \int_I \alpha_1(h_k) h_k |u_k| u_k \psi \right| &\leq C \|\alpha_1(h_k)^{\frac{2}{3}} h_k^{\frac{2}{3}} |u_k| u_k\|_{L^{\frac{3}{2}}(I)} \|\psi\|_{L^3(I)} \\ &\leq g_5(t) \|\partial_x \psi\|_{L^3(I)} \end{aligned}$$

où  $g_5(t) = C\|\alpha_1(h_k)^{\frac{2}{3}} h_k(t)^{\frac{2}{3}} |u_k(t)| u_k(t)\|_{L^{\frac{3}{2}}(I)}$  est  $L^{\frac{3}{2}}(0, T)$ .

Pour le dernier terme, on a en intégrant par partie :

$$\begin{aligned} -\beta \int_I h_k \partial_x^3 h_k \psi &= \beta \int_I \partial_x^2 h_k \partial_x (h_k \psi) \\ &= \beta \int_I h_k \partial_x^2 h_k \partial_x \psi + \beta \int_I \partial_x^2 h_k \partial_x h_k \psi, \end{aligned}$$

et donc :

$$\left| \varepsilon \beta \int_I h_k \partial_x^3 h_k \psi \right| \leq \|h_k \partial_x^2 h_k\|_{L^2(I)} \|\partial_x \psi\|_{L^2(I)} + \|\partial_x h_k \partial_x^2 h_k\|_{L^1(I)} \|\psi\|_{L^\infty(I)}$$

$$\leq C \|h_k \partial_x^2 h_k\|_{L^2(I)} \|\partial_x \psi\|_{L^2(I)} + C \|\partial_x h_k \partial_x^2 h_k\|_{L^1(I)} \|\partial_x \psi\|_{L^\infty(I)},$$

et

$$\left| \varepsilon \beta \int_I h_k \partial_x^3 h_k \psi \right| \leq g_6(t) \|\partial_x \psi\|_{L^\infty(I)},$$

où  $g_6(t) = C\|h_k(t) \partial_x^2 h_k(t)\|_{L^2(I)} + C\|\partial_x h_k(t) \partial_x^2 h_k(t)\|_{L^1(I)}$ . On a les estimations suivantes :

$$\begin{aligned} (h_k \partial_x^2 h_k)_k &\text{ borné dans } L^2(0, T; L_{per}^2(I)), \\ (\partial_x h_k \partial_x^2 h_k)_k &\text{ borné dans } L^2(0, T; L_{per}^1(I)), \end{aligned}$$

et  $g_6$  est donc bornée indépendamment de  $k$  dans  $L^2(0, T)$ .

Finalement on obtient :

$$\left| \int_I \left( \tau_\eta(h_k u_k)(t) - h_k u_k(t) \right) \psi \right| \leq \left( \int_t^{t+\eta} g(s) ds \right) \|\partial_x \psi\|_{L^\infty(I)},$$

ou encore

$$\left| \int_I \left( \tau_\eta(h_k u_k)(t) - h_k u_k(t) \right) \psi \right| \leq \left( \int_t^{t+\eta} g(s) ds \right) \|\psi\|_{W^{1,\infty}(I)},$$

où  $g$  est bornée dans  $L^{\frac{3}{2}}(0, T)$  indépendamment de  $k$ . Comme on a de plus :

$$\int_t^{t+\eta} g(s) ds \leq \left( \int_t^{t+\eta} |g|^{\frac{3}{2}} \right)^{\frac{2}{3}} \eta^{\frac{1}{3}}$$

il vient :

$$\|\tau_\eta(h_k u_k)(t) - h_k u_k(t)\|_{(W_{per}^{1,\infty}(\Omega))'} \leq \eta^{\frac{1}{3}} \|g\|_{L^{\frac{3}{2}}(0, T)}$$

soit

$$\|\tau_\eta(h_k u_k) - h_k u_k\|_{L^\infty(0, T-\eta; (W_{per}^{1,\infty}(I))')} \leq C \eta^{\frac{1}{3}}.$$

Ceci termine la démonstration de la proposition 2.4.3. ■

**Corollaire 2.4.1.** *Soit  $E$  un espace de Banach. Pour  $1 \leq q \leq +\infty$  et  $0 < \sigma < 1$ , on définit les espaces de Nikolskii  $N_q^\sigma(0, T; E)$  par :*

$$N_q^\sigma(0, T; E) = \{f \in L^q(0, T; E), \exists C > 0, \|\tau_\eta(f) - f\|_{L^q(0, T-\eta; E)} \leq C \eta^\sigma\}.$$

On a alors l'estimation suivante :

$$(h_k u_k)_k \text{ est bornée dans } N_\infty^{\frac{1}{3}}(0, T; (W_{per}^{1,\infty}(\Omega))').$$

**2.4.4. Convergence et compacité.** Nous disposons à présent de tous les outils nécessaires pour pouvoir passer à la limite dans le problème approché (2.20). Etudions les convergences et les propriétés de compacité qui découlent des estimations obtenues précédemment.

On utilise dans cette partie les théorèmes suivant d'Aubin-Lions et de J.Simon [157] pour obtenir des convergences fortes :

**Théorème 2.4.4** (Aubin-Lions). *Soient  $B_0 \subset B_1 \subset B_2$  trois espaces de Banach. On suppose que l'injection de  $B_1$  dans  $B_2$  est continue et que l'injection de  $B_0$  dans  $B_1$  est compacte. Soient  $p, r$  deux réels tels que  $1 < p, r < +\infty$ . Pour  $T > 0$ , on note*

$$W = \left\{ v \in L^p(0, T; B_0), \frac{\partial v}{\partial t} \in L^r(0, T; B_2) \right\}.$$

Alors l'injection de  $W$  dans  $L^p(0, T; B_1)$  est compacte.

**Preuve.**

Voir [22] ■

**Théorème 2.4.5** (J. Simon). *Soient  $B_0, B_1, B_2$  trois espaces de Banach avec  $B_0 \subset B_1 \subset B_2$ . On suppose que l'injection de  $B_0$  dans  $B_1$  est compacte. Alors les injections suivantes sont compactes :*

- i) Pour  $1 \leq q \leq +\infty$ ,  $L^q(0, T; B_0) \cap \left\{ \psi, \frac{d}{dt}\psi \in L^1(0, T; B_2) \right\} \rightarrow L^q(0, T; B_1)$
- ii) Pour  $1 < r \leq +\infty$ ,  $L^\infty(0, T; B_0) \cap \left\{ \psi, \frac{d}{dt}\psi \in L^r(0, T; B_2) \right\} \rightarrow \mathcal{C}^0([0, T], B_1)$
- iii) Pour  $1 \leq q \leq +\infty$ ,  $L^q(0, T; B_0) \cap N_q^\sigma(0, T; B_2) \rightarrow L^q(0, T; B_1)$

**Preuve.**

Voir [157] ■

On utilise également le théorème de continuité des produits dans les espaces de Besov :

**Théorème 2.4.6** (B. Hanouzet). *Soit  $\Omega$  un ouvert de  $\mathbb{R}^d$ . Soient  $p_1, p_2, p, m$  dans  $[1, \infty]$  tels que*

$$\max\left(1, \frac{p_1 p_2}{p_1 + p_2}\right) \leq p \leq \min(p_1, p_2) \quad \text{et} \quad \frac{1}{m} = \frac{1}{p_1} + \frac{1}{p_2} - \frac{1}{p}.$$

*Pour  $s$  et  $t$  réels on pose  $\sigma = \min\left(s, t, s + t - \frac{n}{m} - \varepsilon\right), \varepsilon > 0$ . Alors, sous l'une des conditions suivantes :*

- i)  $s + t > \max\left(0, d\left(\frac{1}{p_1} + \frac{1}{p_2} - 1\right)\right)$
- ii)  $s + t = \max\left(0, d\left(\frac{1}{p_1} + \frac{1}{p_2} - 1\right)\right)$  et  $\frac{1}{q_1} + \frac{1}{q_2} \geq 1$

*le produit est continu de  $B_{p_1, q_1}^s(\Omega) \times B_{p_2, q_2}^t(\Omega)$  dans  $B_{p, q}^\sigma(\Omega)$ ,  $q = \max(q_1, q_2)$ .*

**Preuve.**

Voir [76] ■

Nous pouvons maintenant obtenir des propriétés de compacité. Comme  $(h_k)_k$  est bornée dans  $L^\infty(0, T; H_{per}^1(I))$  et  $\left(\frac{\partial h_k}{\partial t}\right)_k$  est bornée dans  $L^\infty(0, T; H_{per}^{-1}(I))$  et que l'on a les injections  $H_{per}^1(I) \subset L_{per}^2(I) \subset H_{per}^{-1}(I)$  avec injection compacte de  $H_{per}^1(I)$  dans  $L_{per}^2(I)$ , la suite  $(h_k)_k$  est compacte dans  $\mathcal{C}^0([0, T], L_{per}^2(I))$  d'après le Théorème (2.4.5). Donc, à une sous suite extraite près,

$$\begin{aligned} h_k &\rightharpoonup h \text{ dans } L^\infty(0, T; H_{per}^1(I)) \text{ faible}\star, \\ \frac{\partial h_k}{\partial t} &\rightharpoonup \frac{\partial h}{\partial t} \text{ dans } L^\infty(0, T; H_{per}^{-1}(I)) \text{ faible}, \\ h_k &\rightarrow h \text{ dans } \mathcal{C}^0([0, T], L_{per}^2(I)) \text{ fort.} \end{aligned}$$

On a d'après les estimations des propositions 2.4.1 et 2.4.2 une borne  $L^2(0, T; L^2_{per}(I))$  pour  $(u_k)_k$  et pour  $(\alpha_0(h_k) u_k)_k$ , ainsi qu'une borne  $L^\infty(0, T; L^\infty_{per}(I))$  pour  $(\alpha_0(h_k))_k$  et  $(\alpha_1(h_k))_k$ . On a donc les convergences suivantes :

$$\begin{aligned} u_k &\rightharpoonup u \text{ dans } L^2(0, T; L^2_{per}(I)) \text{ faible,} \\ \alpha_0(h_k) u_k &\rightharpoonup g \text{ dans } L^2(0, T; L^2_{per}(I)) \text{ faible,} \\ \alpha_0(h_k) &\rightharpoonup \ell_0 \text{ dans } L^\infty(0, T; L^\infty_{per}(I)) \text{ faible } \star, \\ \alpha_1(h_k) &\rightharpoonup \ell_1 \text{ dans } L^\infty(0, T; L^\infty_{per}(I)) \text{ faible } \star. \end{aligned}$$

D'autre part, d'après le théorème des accroissements finis, nous avons :

$$\|\alpha_0(h_k) - \alpha_0(h)\|_{L^2(I)} \leq \sup(\alpha'_0(h)) \|h - h_k\|_{L^\infty(0, T; L^2(I))}, \quad \forall t.$$

et donc

$$\|\alpha_0(h_k) - \alpha_0(h)\|_{L^\infty(0, T; L^2(I))} \leq c \|h - h_k\|_{L^\infty(0, T; L^2(I))},$$

puisque  $\alpha'_0(h)$  est uniformément bornée. On récupère donc de la compacité sur  $(\alpha_0(h_k))_k$  grâce à la compacité obtenue sur  $(h_k)_k$  et la limite est bien celle attendue. Un raisonnement identique permet également d'obtenir de la compacité dans  $\mathcal{C}^0([0, T], L^2_{per}(I))$  pour  $(\alpha_1(h_k))_k$ , avec la limite voulue. On a donc les convergences suivantes :

$$\begin{aligned} u_k &\rightharpoonup u \text{ dans } L^2(0, T; L^2_{per}(I)) \text{ faible,} \\ \alpha_0(h_k) &\rightarrow \alpha_0(h) \text{ dans } \mathcal{C}^0([0, T], L^2_{per}(I)) \text{ fort,} \\ \alpha_1(h_k) &\rightarrow \alpha_1(h) \text{ dans } \mathcal{C}^0([0, T], L^2_{per}(I)) \text{ fort.} \end{aligned}$$

Ainsi par produit de convergence fort-faible on a, à une sous suite extraite près :

$$\begin{aligned} \alpha_0(h_k) u_k &\rightarrow \alpha_0(h) u \text{ dans } L^1(0, T; L^1_{per}(I)) \text{ fort,} \\ \alpha_1(h_k) u_k &\rightarrow \alpha_1(h) u \text{ dans } L^1(0, T; L^1_{per}(I)) \text{ fort,} \\ h_k u_k &\rightarrow hu \text{ dans } L^1(0, T; L^1_{per}(I)) \text{ fort.} \end{aligned}$$

et par unicité de la limite , on a donc :

$$\begin{aligned} \alpha_0(h_k) u_k &\rightharpoonup \alpha_0(h) u \text{ dans } L^2(0, T; L^2_{per}(I)) \text{ faible,} \\ \alpha_1(h_k) |u_k| &\rightharpoonup \alpha_1(h) |u| \text{ dans } L^2(0, T; L^2_{per}(I)) \text{ faible,} \\ h_k u_k &\rightharpoonup hu \text{ dans } L^2(0, T; L^2_{per}(I)) \text{ faible.} \end{aligned}$$

De plus, d'après la proposition 2.4.1 et le corollaire 2.4.1 on a l'estimation suivante :

$$(h_k u_k)_k \text{ bornée dans } L^2(0, T; W^{1,1}_{per}(I)) \cap N^{\frac{1}{3}}_2(0, T; (W^{1,\infty}_{per}(I))'),$$

avec les injections suivantes :

$$W_{per}^{1,1}(I) \subset L_{per}^2(I) \subset (W_{per}^{1,\infty}(I))',$$

l'injection  $W_{per}^{1,1}(I) \subset L_{per}^2(I)$  étant compacte en dimension un. Ainsi, d'après le Théorème 2.4.5, la suite  $(h_k u_k)$  est compacte dans  $L^2(0, T; (L_{per}^2(I))^2)$ . Comme par ailleurs elle est convergente vers  $hu$  dans  $L^1(0, T; L_{per}^1(I))$  on a :

$$\begin{aligned} h_k u_k &\rightharpoonup hu \text{ dans } L^2(0, T; W_{per}^{1,1}(I)) \text{ faible,} \\ h_k u_k &\rightarrow hu \text{ dans } L^2(0, T; L_{per}^2(I)) \text{ fort.} \end{aligned}$$

Par produit de convergence fort-faible, il vient :

$$\begin{aligned} h_k u_k^2 &\rightarrow hu^2 \text{ dans } L^1(0, T; L_{per}^1(I)) \text{ fort,} \\ \alpha_1(h_k) h_k |u_k| u_k &\rightarrow \alpha_1(h) h |u| u \text{ dans } L^1(0, T; L_{per}^1(I)) \text{ fort.} \end{aligned}$$

Par ailleurs, on a une borne pour  $(h_k u_k^2)$  dans  $L^{\frac{3}{2}}(0, T; L_{per}^{\frac{3}{2}}(I))$  et donc, à extraction d'une sous suite près, converge faiblement vers un certain  $g$  dans cet espace. Mais, à nouveau par unicité de la limite dans  $L^1(0, T; L_{per}^1(I))$ , la limite  $g$  n'est autre que  $hu^2$ . De même, comme  $(h_k u_k)_k$  est bornée dans  $L^3(0, T; L_{per}^3(I))$  et  $(u_k)_k$  bornée dans  $L^2(0, T; L_{per}^2(I))$ , on obtient une borne dans  $L^{\frac{6}{5}}(0, T; L_{per}^{\frac{6}{5}}(I))$  pour  $(\alpha_1(h_k) h_k |u_k| u_k)_k$ . On a donc montré :

$$\begin{aligned} h_k u_k^2 &\rightharpoonup hu^2 \text{ dans } L^{\frac{3}{2}}(0, T; L_{per}^{\frac{3}{2}}(I)) \text{ faible,} \\ \alpha_1(h_k) h_k |u_k| u_k &\rightharpoonup \alpha_1(h) h |u| u \text{ dans } L^{\frac{6}{5}}(0, T; L_{per}^{\frac{6}{5}}(I)) \text{ faible.} \end{aligned}$$

On utilise le théorème de continuité des produits 2.4.6 pour obtenir le corollaire suivant :

**Corollaire 2.4.2.** *Soit  $I$  un ouvert de  $\mathbb{R}$ . Le produit  $(u, v) \mapsto uv$  est continu de*

$$H^1(I) \times H^{-1}(I) \text{ dans } H^{-1}(I).$$

■

Comme  $(u_k)_k$  est bornée dans  $L^2(0, T; L_{per}^2(I))$ ,  $(\partial_x u_k)_k$  est bornée dans  $L^2(0, T; W_{per}^{-1,2}(I))$ . Le produit  $(h_k, \partial_x u_k) \mapsto h_k \partial_x u_k$  est donc continu de  $L^\infty(0, T; H_{per}^1(I)) \times L^2(0, T; W_{per}^{-1,2}(I))$  dans  $L^2(0, T; W_{per}^{-1,2}(I))$ . Donc, quitte à extraire une sous suite, il vient :

$$h_k \partial_x u_k \rightharpoonup h \partial_x u \text{ dans } L^2(0, T; H_{per}^{-1}(I)) \text{ faible.}$$

De plus, comme  $(h_k^{\frac{1}{2}} \partial_x u_k)_k$  est borné dans  $L^2(0, T; L_{per}^2(I))$  et  $(\sqrt{h_k})_k$  dans  $L^\infty(0, T; L_{per}^\infty(I))$  on a une borne dans  $L^2(0, T; L_{per}^2(I))$  pour  $(h_k \partial_x u_k)_k$  et donc, par unicité de la limite, converge faiblement vers  $h \partial_x u$  dans cet espace. On a donc montré :

$$h_k \partial_x u_k \rightharpoonup h \partial_x u \text{ dans } L^2(0, T; L^2_{per}(\Omega)) \text{ faible.}$$

On a également le corollaire suivant en dimension un :

**Corollaire 2.4.3.** *Soit  $I$  un ouvert de  $\mathbb{R}$ . Le produit  $(u, v) \mapsto uv$  est continu de  $H^1(I) \times L^2(I)$  dans  $L^2(I)$ .*

■

Ainsi le produit  $(h_k, \partial_x h_k) \mapsto h_k \partial_x h_k$  est continu de  $L^\infty(0, T; H^1_{per}(I)) \times L^\infty(0, T; L^2_{per}(I))$  dans  $L^\infty(0, T; L^2_{per}(I))$ . On obtient donc une convergence vers  $h \partial_x h$  dans  $L^\infty(0, T; L^2_{per}(I))$  faible  $\star$  :

$$h_k \partial_x h_k \rightharpoonup h \partial_x h \text{ dans } L^\infty(0, T; L^2_{per}(I)) \text{ faible } \star,$$

Nous allons enfin nous intéresser aux termes  $(h_k \partial_x^2 h_k)_k$  et  $(\partial_x h_k \partial_x^2 h_k)_k$  qui permettront le passage à la limite pour le terme de capillarité  $(h_k \partial_x^3 h_k)_k$ . Le premier terme  $(h_k \partial_x^2 h_k)_k$  est borné dans  $L^2(0, T; L^2_{per}(I))$ . On a par ailleurs les convergences suivantes :

$$\begin{aligned} \partial_x^2 h_k &\rightharpoonup \partial_x^2 h \text{ dans } L^2(0, T; L^2_{per}(I)) \text{ faible,} \\ h_k &\rightarrow h \text{ dans } C^0([0, T], L^2_{per}(I)) \text{ fort,} \end{aligned}$$

qui permettent d'obtenir par produit de convergences fort-faible :

$$h_k \partial_x^2 h_k \rightarrow h \partial_x^2 h \text{ dans } L^1(0, T; L^1_{per}(I)) \text{ fort,}$$

d'où par unicité de la limite

$$h_k \partial_x^2 h_k \rightharpoonup h \partial_x^2 h \text{ dans } L^2(0, T; L^2_{per}(I)) \text{ faible.}$$

Le passage à la limite faible dans le deuxième terme  $(\partial_x h_k \partial_x^2 h_k)_k$  nécessite d'obtenir de la compacité sur  $(\partial_x h_k)_k$ . Nous l'obtenons grâce au Théorème 2.4.4, puisque l'on a  $(\partial_x h_k)_k$  bornée dans  $L^2(0, T; H^1_{per}(I))$  et  $\left(\partial_t (\partial_x h_k)\right)_k$  bornée dans  $L^\infty(0, T; H^{-2}_{per}(I))$  puisque  $\left(\partial_t h_k\right)_k$  bornée dans  $L^\infty(0, T; H^{-1}_{per}(I))$ . Comme l'injection de  $H^1_{per}(I)$  dans  $L^2_{per}(I)$  est compacte en dimension un, cela nous donne bien de la compacité sur  $(\partial_x h_k)_k$  dans  $L^2(0, T; L^2_{per}(I))$ . On a donc par compacité et produit de convergence fort-faible :

$$\begin{aligned} \partial_x h_k &\rightarrow \partial_x h \text{ dans } L^2(0, T; L^2_{per}(I)) \text{ fort,} \\ \partial_x h_k \partial_x^2 h_k &\rightarrow \partial_x h \partial_x^2 h \text{ dans } L^1(0, T; L^1_{per}(I)) \text{ fort.} \end{aligned}$$

Le passage à la limite dans le problème approché 2.20 est donc possible.

**2.4.5. Passage à la limite.** Nous allons maintenant vérifier que les fonctions limites obtenues  $h$  et  $u$  sont bien solutions au sens des distributions du modèle obtenu en dimension un.

– Equation de conservation de la hauteur d'eau :

Donnons-nous une fonction test  $\phi \in \mathcal{D}(]0, T[; H_{per}^2(I))$  et intégrons la contre l'équation (2.20) vérifiée par la solution approchée  $(h_k, u_k)$ , on obtient après intégration par parties :

$$- \int_{]0, T[ \times I} h_k \partial_t \phi \, dt \, dx - \int_{]0, T[ \times I} h_k u_k \partial_x \phi(t, x) \, dt \, dx = 0.$$

Les convergences obtenues précédemment permettent de passer à la limite car on a en particulier :

$$\frac{\partial \phi}{\partial t} \in L^2(0, T; L_{per}^2(I)), \text{ et } \partial_x \phi \in L^2(0, T; L_{per}^2(I)).$$

Il vient alors :

$$\int_{]0, T[ \times I} \partial_t h \phi(t, x) \, dt \, dx - \int_{]0, T[ \times I} h u \partial_x \phi(t, x) \, dt \, dx = 0.$$

– Equation de conservation de la quantité de mouvement :

Soient  $k \geq n$ ,  $\theta \in \mathcal{C}^1([0, T])$   $\theta(T) = 0$  et  $\psi_n$  fixée dans  $V_n$ . La solution approchée construite précédemment vérifie en intégrant par parties :

$$\begin{aligned} & - \int_0^T \int_I (h_k u_k) \psi_n \partial_t \theta \, dx \, d\tau - \int_0^T \int_I h_k u_k^2 \partial_x \psi_n \theta \, dx \, d\tau \\ & + \int_0^T \int_I \alpha_0(h_k) u_k \psi_n \theta \, dx \, d\tau + \int_0^T \int_I \alpha_1(h_k) h_k |u_k| u_k \psi_n \theta \, dx \, d\tau \\ & + \frac{1}{F_r^2} \int_0^T \int_I h_k \partial_x h_k \psi_n \theta \, dx \, d\tau + \beta \int_0^T \int_I \partial_x^2 h_k \partial_x (h_k \psi_n) \theta \, dx \, d\tau \\ & + 3\nu \int_0^T \int_I h_k \partial_x u_k \partial_x \psi_n \theta \, dx \, d\tau \\ & = \int_0^T \int_I h_k \tilde{f} \psi_n \theta \, dx \, d\tau + \theta(0) \int_I h_0^k u_0^k \psi_n \, dx. \end{aligned}$$

On développe le terme de capillarité :

$$\begin{aligned} \int_0^T \int_I \partial_x^2 h_k \partial_x (h_k \psi_n) \theta \, dx \, d\tau & = \int_0^T \int_I \partial_x^2 h_k \partial_x h_k \psi_n \theta \, dx \, d\tau \\ & + \int_0^T \int_I h_k \partial_x^2 h_k \partial_x \psi_n \theta \, dx \, d\tau, \end{aligned}$$

et l'on passe à la limite en  $k$  dans chacun des 2 termes.

La fonction test  $\psi_n$  étant fixée, les convergences précédentes permettent de passer à la limite en  $k$  pour obtenir :

$$\begin{aligned}
& - \int_0^T \int_I (hu) \psi_n \partial_t \theta \, dx \, d\tau - \int_0^T \int_I hu^2 \partial_x \psi_n \theta \, dx \, d\tau + \int_0^T \int_I \alpha_0(h) u \psi_n \theta \, dx \, d\tau \\
& \quad + \int_0^T \int_I \alpha_1(h) h |u| u \psi_n \theta \, dx \, d\tau + \frac{1}{F_r^2} \int_0^T \int_I h \partial_x h \psi_n \theta \, dx \, d\tau \\
& \quad + \beta \int_0^T \int_I \partial_x^2 h \partial_x (h \psi_n) \theta \, dx \, d\tau + 3\nu \int_0^T \int_I h \partial_x u \partial_x \psi_n \theta \, dx \, d\tau \\
& = \int_0^T \int_I h \tilde{f} \psi_n \theta \, dx \, d\tau + \theta(0) \int_I h_0 u_0 \psi_n \, dx.
\end{aligned}$$

Par combinaisons linéaires de fonctions tests de la forme  $\theta(t)\psi_n(x)$ , on obtient que pour tout  $n \geq 1$  et pour toute fonction test  $\phi \in \mathcal{C}^1([0, T], V_n)$  telle que  $\phi(T) = 0$ , on a :

$$\begin{aligned}
& - \int_0^T \int_I (hu) \partial_t \phi \, dx \, d\tau - \int_0^T \int_I hu^2 \partial_x \phi(\tau, x) \, dx \, d\tau + \int_0^T \int_I \alpha_0(h) u \phi(t, x) \, dx \, d\tau \\
& \quad + \int_0^T \int_I \alpha_1(h) h |u| u \phi(\tau, x) \, dx \, d\tau + \frac{1}{F_r^2} \int_0^T \int_I h \partial_x h \phi(\tau, x) \, dx \, d\tau \\
& \quad + \beta \int_0^T \int_I \partial_x^2 h \partial_x (h \phi) \, dx \, d\tau + 3\nu \int_0^T \int_I h \partial_x u \partial_x \phi(t, x) \, dx \, d\tau \\
& = \int_0^T \int_I h \tilde{f} \phi(\tau, x) \, dx \, d\tau + \int_I h_0 u_0 \phi(0) \, dx.
\end{aligned}$$

La régularité obtenue sur  $h$  et  $u$  permet ensuite de prolonger par densité l'identité ci-dessus aux fonctions tests de  $\mathcal{C}^1([0, T], H_{per}^2(I))$  telles que  $\phi(T) = 0$ . En se restreignant aux fonctions tests  $\mathcal{C}^\infty$  à support compact en temps dans  $]0, T[$ , on obtient bien l'équation au sens des distributions. ■

Ceci termine la démonstration du Théorème 2.1.1 ■

## 2.5. Existence d'une solution faible en dimension 2

Le cas de la dimension deux introduit de nouvelles difficultés. Tout d'abord la forme particulière du terme de diffusion

$$\nu \operatorname{div} \left( h D(\mathbf{u}) + (2h \operatorname{div} \mathbf{u}) \mathcal{I} \right)$$

où

$$D(\mathbf{u}) = \frac{1}{2}(\nabla \mathbf{u} + {}^t \nabla \mathbf{u})$$

rend délicate l'obtention des bornes supplémentaires introduites à la proposition 2.4.2. Plus précisément les identités du lemme 2.4.1 et l'inégalité du lemme 2.4.2 obtenues dans le cas de la dimension un ne sont plus valables, la présence du terme  $(2h \operatorname{div} \mathbf{u}) \mathcal{I}$  ne permettant plus de suivre le même raisonnement que dans le cas de la dimension un. C'est pour cette raison que le modèle étudié ici est un modèle simplifié dans lequel ce terme a été négligé. La justification de cette simplification est purement d'ordre technique, afin de nous permettre d'obtenir les estimations supplémentaires nécessaires au passage à la limite. De plus la présence des coefficients  $\alpha_0(h_k)$  et  $\alpha_1(h_k)$  ajoute des difficultés supplémentaires en dimension deux par rapport au modèle étudié dans [51]. En effet en dimension un, l'injection de  $H^1(\Omega)$  dans  $L^\infty(\Omega)$  permettait d'obtenir une borne uniforme en temps en espace sur  $(h_k)_k$  et permettait de récupérer la régularité sur  $(\mathbf{u}_k)_k$  nécessaire au passage à la limite. En dimension deux, on a seulement l'injection  $H^1(\Omega) \subset L^p(\Omega)$ ,  $\forall p < \infty$ . Ainsi, la régularité obtenue sur  $(\mathbf{u}_k)_k$  via les termes de friction est beaucoup moins forte et ne permet pas de passer à la limite de façon simple dans les termes non linéaires. Une hypothèse supplémentaire est donc faite sur la suite approximante  $(h_k)_k$ , afin de récupérer plus de régularité sur  $(\mathbf{u}_k)_k$ .

**Proposition 2.5.1.** *On suppose qu'il existe  $\gamma > 0$  tel que l'on ai pour tout  $k$  :*

$$h_k(t, \mathbf{x}) \geq \gamma \quad \text{pour } (t, \mathbf{x}) \in \mathbb{R}^+ \times \Omega.$$

Alors nous avons les estimations supplémentaires suivantes :

- (1)  $(\mathbf{u}_k)_k$  bornée dans  $L^2(0, T; (H_{per}^1(\Omega))^2)$ ,
- (2)  $(\nabla \sqrt{h_k})_k$  bornée dans  $L^\infty(0, T; (L_{per}^2(\Omega))^2)$ ,
- (3)  $(h_k)_k$  bornée dans  $L^2(0, T; H_{per}^2(\Omega))$ .

**Preuve.**

Comme dans le cas de la dimension un, ces estimations sont obtenues grâce à une deuxième inégalité d'énergie, démontrée à l'aide des deux lemmes techniques suivants :

**Lemme 2.5.1.** *Nous avons les deux identités suivantes :*

$$\frac{1}{2} \frac{d}{dt} \int_{\Omega} h_k |\nabla \log h_k|^2 + \int_{\Omega} h_k \nabla \operatorname{div} \mathbf{u}_k \cdot \nabla \log h_k + \int_{\Omega} h_k \nabla \mathbf{u}_k : \nabla \log h_k \otimes \nabla \log h_k = 0 \quad (2.85)$$

$$\begin{aligned}
& \frac{1}{2} \nu^2 \frac{d}{dt} \int_{\Omega} h_k |\nabla \log h_k|^2 + \nu \int_{\Omega} \alpha_0(h_k) \mathbf{u}_k \cdot \nabla \log h_k + \nu \int_{\Omega} \alpha_1(h_k) |\mathbf{u}_k| \mathbf{u}_k \cdot \nabla h_k \\
& + \nu \beta \int_{\Omega} |\nabla^2 h_k|^2 + \nu \int_{\Omega} \frac{|\nabla h_k|^2}{F_r^2} + \nu \int_{\Omega} \frac{\mathbf{u}_k^\perp \cdot \nabla h_k}{R_o} = -\nu \frac{d}{dt} \int_{\Omega} \mathbf{u}_k \cdot \nabla h_k \quad (2.86) \\
& + \nu \int_{\Omega} h_k \nabla \mathbf{u}_k : {}^t \nabla \mathbf{u}_k + \nu \int_{\Omega} \tilde{f} \nabla h_k
\end{aligned}$$

### Preuve du lemme 2.5.1.

La première identité s'obtient en adaptant directement la démonstration effectuée dans le cas de la dimension un. Elle est effectuée dans [51].

Pour la deuxième identité, on multiplie ensuite l'équation de conservation de la quantité de mouvement par  $\nu \nabla \log h_k$  pour obtenir :

$$\begin{aligned}
& \nu \int_{\Omega} \left( \partial_t \mathbf{u}_k + (\mathbf{u}_k \cdot \nabla) \mathbf{u}_k \right) \cdot \nabla h_k + \nu^2 \int_{\Omega} h_k D(\mathbf{u}_k) : \nabla \left( \frac{\nabla h_k}{h_k} \right) + \nu \beta \int_{\Omega} |\nabla^2 h_k|^2 \\
& + \nu \int_{\Omega} \alpha_0(h_k) \mathbf{u}_k \cdot \nabla \log h_k + \nu \int_{\Omega} \alpha_1(h_k) |\mathbf{u}_k| \mathbf{u}_k \cdot \nabla h_k + \nu \int_{\Omega} \frac{|\nabla h_k|^2}{F_r^2} \quad (2.87) \\
& + \nu \int_{\Omega} \frac{\mathbf{u}_k^\perp \cdot \nabla h_k}{R_o} = \nu \int_{\Omega} \tilde{f} \cdot \nabla h_k,
\end{aligned}$$

ou encore, en développant le terme en  $\nu^2$  :

$$\begin{aligned}
& \nu \int_{\Omega} \left( \partial_t \mathbf{u}_k + (\mathbf{u}_k \cdot \nabla) \mathbf{u}_k \right) \cdot \nabla h_k + \nu^2 \int_{\Omega} h_k D(\mathbf{u}_k) : \left( \nabla \nabla h_k - \frac{\nabla h_k \otimes \nabla h_k}{h_k} \right) \\
& + \nu \beta \int_{\Omega} |\nabla^2 h_k|^2 + \nu \int_{\Omega} \alpha_0(h_k) \mathbf{u}_k \cdot \nabla \log h_k + \nu \int_{\Omega} \alpha_1(h_k) |\mathbf{u}_k| \mathbf{u}_k \cdot \nabla h_k \quad (2.88) \\
& + \nu \int_{\Omega} \frac{|\nabla h_k|^2}{F_r^2} + \nu \int_{\Omega} \frac{\mathbf{u}_k^\perp \cdot \nabla h_k}{R_o} = \nu \int_{\Omega} \tilde{f} \cdot \nabla h_k,
\end{aligned}$$

Multipliant l'identité (2.85) par  $\nu^2$  et l'ajoutant à (2.88), et en remarquant que l'on a d'une part

$$\int_{\Omega} h_k \nabla \mathbf{u}_k : \nabla \log h_k \otimes \nabla \log h_k = \int_{\Omega} h_k D(\mathbf{u}_k) : \frac{\nabla h_k \otimes \nabla h_k}{h_k}$$

et d'autre part en intégrant par parties :

$$\nu^2 \int_{\Omega} D(\mathbf{u}_k) : \nabla \nabla h_k + \nu^2 \int_{\Omega} \nabla \operatorname{div} \mathbf{u}_k \cdot \nabla h_k = 0$$

on obtient :

$$\begin{aligned}
& \frac{1}{2}\nu^2 \frac{d}{dt} \int_{\Omega} h_k |\nabla \log h_k|^2 + \nu \int_{\Omega} \frac{|\nabla h_k|^2}{F_r^2} + \nu \beta \int_{\Omega} |\nabla^2 h_k|^2 + \nu \int_{\Omega} \alpha_0(h_k) \mathbf{u}_k \cdot \nabla \log h_k \\
& + \nu \int_{\Omega} \alpha_1(h_k) |\mathbf{u}_k| \mathbf{u}_k \cdot \nabla h_k + \nu \int_{\Omega} \frac{\mathbf{u}_k^\perp \cdot \nabla h_k}{R_o} = \mathcal{I}_k
\end{aligned} \tag{2.89}$$

avec

$$\mathcal{I}_k = -\nu \int_{\Omega} \partial_t \mathbf{u}_k \cdot \nabla h_k - \nu \int_{\Omega} \left( (\mathbf{u}_k \cdot \nabla) \mathbf{u}_k \right) \cdot \nabla h_k + \nu \int_{\Omega} \tilde{f} \cdot \nabla h_k.$$

Réécrivons  $\mathcal{I}_k$  en tenant compte de l'équation de conservation de la masse et en intégrant par partie :

$$\begin{aligned}
\mathcal{I}_k &= -\nu \frac{d}{dt} \int_{\Omega} \mathbf{u}_k \cdot \nabla h_k + \nu \int_{\Omega} \mathbf{u}_k \cdot \nabla \partial_t h_k - \nu \int_{\Omega} \left( (\mathbf{u}_k \cdot \nabla) \mathbf{u}_k \right) \cdot \nabla h_k + \nu \int_{\Omega} \tilde{f} \cdot \nabla h_k, \\
&= -\nu \frac{d}{dt} \int_{\Omega} \mathbf{u}_k \cdot \nabla h_k - \nu \int_{\Omega} \mathbf{u}_k \cdot \nabla \operatorname{div} (h_k \mathbf{u}_k) - \nu \int_{\Omega} \left( (\mathbf{u}_k \cdot \nabla) \mathbf{u}_k \right) \nabla h_k + \nu \int_{\Omega} \tilde{f} \cdot \nabla h_k, \\
&= -\nu \frac{d}{dt} \int_{\Omega} \mathbf{u}_k \cdot \nabla h_k + \nu \int_{\Omega} \nabla \mathbf{u}_k : {}^t \nabla \mathbf{u}_k + \nu \int_{\Omega} \tilde{f} \cdot \nabla h_k.
\end{aligned}$$

Ceci termine la démonstration de la deuxième identité. ■

**Lemme 2.5.2.** *Nous avons l'inégalité suivante :*

$$\begin{aligned}
& \frac{1}{2} \frac{d}{dt} \int_{\Omega} \left( h_k |\mathbf{u}_k + \nu \nabla \log h_k|^2 + \frac{h_k^2}{F_r^2} + \beta |\nabla h_k|^2 \right) - \nu r_0 \frac{d}{dt} \int_{\Omega} \log (r_0^{-1} h_k \alpha_0(h_k)) \\
& + \nu \int_{\Omega} \alpha'_0(h_k) \nabla h_k \cdot \mathbf{u}_k + \nu \int_{\Omega} \alpha_1(h_k) |\mathbf{u}_k| \mathbf{u}_k \cdot \nabla h_k + \nu \beta \int_{\Omega} |\nabla^2 h_k|^2 \\
& + \nu \int_{\Omega} \frac{|\nabla h_k|^2}{F_r^2} + \int_{\Omega} \alpha_0(h_k) |\mathbf{u}_k|^2 + \int_{\Omega} \alpha_1(h_k) h_k |\mathbf{u}_k|^3 \\
& \leq \nu \int_{\Omega} h_k |\nabla \mathbf{u}_k|^2 + \int_{\Omega} \tilde{f} (h_k \mathbf{u}_k + \nu \nabla h_k)
\end{aligned} \tag{2.90}$$

**Preuve du lemme 2.5.2.**

L'égalité (2.86) se réécrit sous la forme suivante :

$$\begin{aligned}
& \frac{1}{2} \frac{d}{dt} \int_{\Omega} h_k |\mathbf{u}_k + \nu \nabla \log h_k|^2 + \nu \int_{\Omega} \frac{|\nabla h_k|^2}{F_r^2} + \nu \beta \int_{\Omega} |\nabla^2 h_k|^2 \\
& + \nu \int_{\Omega} \alpha_0(h_k) \mathbf{u}_k \cdot \nabla \log h_k + \nu \int_{\Omega} \alpha_1(h_k) |\mathbf{u}_k| \mathbf{u}_k \cdot \nabla h_k \\
& = \frac{1}{2} \frac{d}{dt} \int_{\Omega} h_k |\mathbf{u}_k|^2 + \nu \int_{\Omega} h_k \nabla \mathbf{u}_k : {}^t \nabla \mathbf{u}_k + \nu \int_{\Omega} \tilde{f} \cdot \nabla h_k
\end{aligned} \tag{2.91}$$

En ajoutant l'inégalité d'énergie (2.3.3) à (2.91) on obtient :

$$\begin{aligned}
& \frac{1}{2} \frac{d}{dt} \int_{\Omega} \left( h_k |\mathbf{u}_k + \nu \nabla \log h_k|^2 + \frac{h_k^2}{F_r^2} + \beta |\nabla h_k|^2 \right) + \nu \int_{\Omega} \alpha_0(h_k) \mathbf{u}_k \cdot \nabla \log h_k \\
& + \nu \int_{\Omega} \alpha_1(h_k) |\mathbf{u}_k| \mathbf{u}_k \cdot \nabla h_k + \nu \beta \int_{\Omega} |\nabla^2 h_k|^2 + \nu \int_{\Omega} \frac{|\nabla h_k|^2}{F_r^2} + \int_{\Omega} \alpha_0(h_k) |\mathbf{u}_k|^2 \\
& + \int_{\Omega} \alpha_1(h_k) h_k |\mathbf{u}_k|^3 \leq \nu \int_{\Omega} h_k |\nabla \mathbf{u}_k|^2 + \int_{\Omega} \tilde{f} \cdot (h_k \mathbf{u}_k + \nu \nabla h_k).
\end{aligned} \tag{2.92}$$

Comme dans le cas de la dimension un on a :

$$\int_{\Omega} \alpha_0(h_k) \mathbf{u}_k \cdot \nabla \log h_k = -r_0 \frac{d}{dt} \int_{\Omega} \log(r_0^{-1} h_k \alpha_0(h_k)) + \int_{\Omega} \alpha'_0(h_k) \nabla h_k \cdot \mathbf{u}_k \tag{2.93}$$

En injectant cette égalité dans (2.92), nous obtenons bien (2.90). Ceci termine la démonstration du lemme 2.5.2.  $\blacksquare$

A partir de (2.90), nous pouvons obtenir les deux dernières estimations supplémentaires. En effet, intégrant (2.90) entre 0 et  $t$ , nous obtenons :

$$\begin{aligned}
& \frac{1}{2} \int_{\Omega} h_k |\mathbf{u}_k + \nu \nabla \log h_k|^2 - \nu r_0 \int_{\Omega} \log(r_0^{-1} h_k \alpha_0(h_k)) + \nu \int_0^t \int_{\Omega} \alpha'_0(h_k) \nabla h_k \cdot \mathbf{u}_k \\
& + \nu \int_0^t \int_{\Omega} \alpha_1(h_k) |\mathbf{u}_k| \mathbf{u}_k \cdot \nabla h_k + \nu \beta \int_0^t \int_{\Omega} |\nabla^2 h_k|^2 \\
& \leq A_0 - \nu r_0 \int_{\Omega} \log(r_0^{-1} h_{k0} \alpha_0(h_{k0})) + \int_0^t \int_{\Omega} \tilde{f} \cdot (h_k \mathbf{u}_k + \nu \nabla h_k).
\end{aligned} \tag{2.94}$$

avec  $A_0$  constante liée aux données initiales, indépendante de  $k$ . On a tout d'abord :

$$\left| \nu \int_0^t \int_{\Omega} \alpha'_0(h_k) \nabla h_k \cdot \mathbf{u}_k \right| \leq \nu r_0 c_0 \|h_k\|_{L^2(0,T; H^1(\Omega))} \|\mathbf{u}_k\|_{L^2(0,T; L^2(\Omega))}. \tag{2.95}$$

On a également :

$$\begin{aligned}
\left| \nu \int_0^t \int_{\Omega} \alpha_1(h_k) |\mathbf{u}_k| \mathbf{u}_k \cdot \nabla h_k \right| & \leq \left| \nu \int_0^t \int_{\Omega} \nabla(\alpha_1(h_k)) \cdot \mathbf{u}_k |\mathbf{u}_k| h_k \right| \\
& + \left| \nu \int_0^t \int_{\Omega} \alpha_1(h_k) \nabla |\mathbf{u}_k| \cdot \mathbf{u}_k h_k \right| + \left| \nu \int_0^t \int_{\Omega} \alpha_1(h_k) \operatorname{div} \mathbf{u}_k |\mathbf{u}_k| h_k \right|
\end{aligned} \tag{2.96}$$

Nous obtenons donc :

$$\begin{aligned}
\left| \nu \int_0^t \int_{\Omega} \alpha_1(h_k) |\mathbf{u}_k| \mathbf{u}_k \cdot \nabla h_k \right| &\leq \\
C \|\nabla h_k\|_{L^\infty(0,T;L^2(\Omega))} \|\mathbf{u}_k\|_{L^2(0,T;L^6(\Omega))}^2 \|h_k\|_{L^\infty(0,T;L^6(\Omega))} &\quad (2.97) \\
+ C \|\sqrt{h_k} \nabla \mathbf{u}_k\|_{L^2(0,T;L^2(\Omega))} \|\sqrt{h_k} \mathbf{u}_k\|_{L^\infty(0,T;L^2(\Omega))}. &
\end{aligned}$$

puisque  $(h_k)_k$  est bornée dans  $L^\infty(0, T; H_{per}^1(\Omega))$  et  $(\mathbf{u}_k)_k$  est bornée dans  $L^2(0, T; H_{per}^1(\Omega))$  et qu'en dimension deux nous avons l'injection  $H_{per}^1(\Omega) \subset L_{per}^p(\Omega)$ ,  $\forall p < \infty$ .

Enfin, les termes  $\nu r_0 \int_{\Omega} \log(r_0^{-1} h_k \alpha_0(h_k))$  et  $\nu r_0 \int_{\Omega} \log(r_0^{-1} h_{k0} \alpha_0(h_{k0}))$  se contrôlent comme en dimension un.

On obtient donc l'inégalité suivante :

$$\begin{aligned}
\frac{1}{2} \int_{\Omega} h_k |\mathbf{u}_k + \nu \nabla \log h_k|^2 + \nu \beta \int_0^t \int_{\Omega} |\nabla^2 h_k|^2 &\leq C_1 \\
+ C_2 \|\tilde{f}\|_{L^2(0,T;L^2(\Omega))} \left( \|h_k \mathbf{u}_k\|_{L^2(0,T;L^2(\Omega))} + \|\nabla h_k\|_{L^2(0,T;L^2(\Omega))} \right) &\quad (2.98)
\end{aligned}$$

où  $C_1$  et  $C_2$  sont des constantes indépendantes de  $k$ . On obtient bien les estimations supplémentaires sur  $(\nabla^2 h_k)_k$  et  $(\nabla \sqrt{h_k})_k$ .

Ceci termine la démonstration de la proposition (2.5.1). ■

Comme dans le cas de la dimension un, une estimation supplémentaire est nécessaire afin d'obtenir de la compacité sur  $(h_k \mathbf{u}_k)_k$  et de pouvoir passer à la limite dans le problème approché. Le résultat est similaire à celui obtenu en dimension un :

**Proposition 2.5.2.** *Il existe une constante  $C > 0$  indépendante des données telle que*

$$\|\tau_\eta(h_k \mathbf{u}_k) - h_k \mathbf{u}_k\|_{L^\infty(0,T-\eta; (W_{per}^{1,\infty}(\Omega))')} \leq C \eta^{\frac{1}{3}} \quad (2.99)$$

**Preuve.**

La démonstration est identique à celle proposée en dimension un, en adaptant les majorations aux nouvelles estimations *a priori* obtenue avec l'hypothèse de positivité effectuée sur  $(h_k)_k$ . ■

**Corollaire 2.5.1.** *On a l'estimation suivante :*

$$(h_k \mathbf{u}_k)_k \text{ est bornée dans } N_\infty^{\frac{1}{3}}(0, T; (W_{per}^{1,\infty}(\Omega))')$$

**2.5.1. Convergence et compacité.** Comme  $(h_k)_k$  est bornée dans  $L^\infty(0, T; H_{per}^1(\Omega))$

et  $\left(\frac{\partial h_k}{\partial t}\right)_k$  est bornée dans

$L^\infty(0, T; H_{per}^{-3}(\Omega))$ , la suite  $(h_k)_k$  est compacte dans  $\mathcal{C}^0([0, T], L_{per}^2(\Omega))$  d'après le Théorème 2.4.4. Donc, à une sous suite extraite près,

$$h_k \rightarrow h \text{ dans } \mathcal{C}^0([0, T], L_{per}^2(\Omega)) \text{ fort.}$$

On a d'après les estimations de la proposition 2.5.1 une borne  $L^2(0, T; (L_{per}^p(\Omega))^2) \forall p < \infty$  pour  $(\mathbf{u}_k)_k$  et une borne  $L^2(0, T; (L_{per}^2(\Omega))^2)$  pour  $(\alpha_0(h_k)^{\frac{1}{2}} \mathbf{u}_k)_k$ . De plus, on obtient de la compacité sur  $(\alpha_0(h_k))_k$  et  $(\alpha_1(h_k))_k$  à partir de celle obtenue sur  $(h_k)_k$ , comme en dimension un. On a donc les convergences suivantes :

$$\begin{aligned} \mathbf{u}_k &\rightharpoonup \mathbf{u} \text{ dans } L^2(0, T; (L_{per}^p(\Omega))^2) \forall p < \infty \text{ faible,} \\ \alpha_0(h_k) &\rightarrow \alpha_0(h) \text{ dans } \mathcal{C}^0([0, T], L_{per}^2(\Omega)) \text{ fort,} \\ \alpha_1(h_k) &\rightarrow \alpha_1(h) \text{ dans } \mathcal{C}^0([0, T], L_{per}^2(\Omega)) \text{ fort.} \end{aligned}$$

Ainsi par produit de convergence fort-faible et unicité de la limite, on a, à une sous suite extraite près :

$$\begin{aligned} \alpha_0(h_k) \mathbf{u}_k &\rightarrow \alpha_0(h) \mathbf{u} \text{ dans } L^1(0, T; (L_{per}^1(\Omega))^2) \text{ fort,} \\ \alpha_1(h_k) \mathbf{u}_k &\rightarrow \alpha_1(h) \mathbf{u} \text{ dans } L^1(0, T; (L_{per}^1(\Omega))^2) \text{ fort,} \\ \alpha_0(h_k) \mathbf{u}_k &\rightharpoonup \alpha_0(h) \mathbf{u} \text{ dans } L^2(0, T; (L_{per}^2(\Omega))^2) \text{ faible,} \\ \alpha_1(h_k) \mathbf{u}_k &\rightharpoonup \alpha_1(h) \mathbf{u} \text{ dans } L^2(0, T; (L_{per}^2(\Omega))^2) \text{ faible,} \\ h_k \mathbf{u}_k &\rightarrow h \mathbf{u} \text{ dans } L^1(0, T; (L_{per}^1(\Omega))^2) \text{ fort,} \end{aligned}$$

De plus, d'après la proposition 2.5.1 on a l'estimation suivante :

$$(h_k \mathbf{u}_k)_k \text{ borné dans } L^2(0, T; (W_{per}^{1, \frac{2p}{p+2}}(\Omega))^2) \cap L^\infty(0, T; (L_{per}^{\frac{2p}{p+2}}(\Omega))^2),$$

en effet on a  $\nabla(h_k \mathbf{u}_k) = \nabla h_k \mathbf{u}_k + \sqrt{h_k} \sqrt{h_k} \nabla \mathbf{u}_k$ . Comme  $(h_k)_k$  et  $(\sqrt{h_k})_k$  sont bornées dans  $L^\infty(0, T; L_{per}^p(\Omega)) \forall p < \infty$ ,  $(\mathbf{u}_k)_k$  bornée dans  $L^2(0, T; (L_{per}^p(\Omega))^2) \forall p < \infty$  et  $(\sqrt{h_k} \nabla \mathbf{u}_k)_k$  bornée dans  $L^2(0, T; (L_{per}^2(\Omega))^2)$ , nous obtenons bien les bornes voulues.

En particulier, pour  $p = 4$  et d'après le corollaire 2.5.1 nous obtenons alors l'estimation suivante :

$$(h_k \mathbf{u}_k)_k \text{ est bornée dans } L^2(0, T; (W_{per}^{1, \frac{4}{3}}(\Omega))^2) \cap N_2^{\frac{1}{3}}(0, T; (W_{per}^{1, \infty}(\Omega))'),$$

avec les injections suivantes en dimension 2 :

$$W_{per}^{1, \frac{4}{3}}(\Omega) \subset L_{per}^2(\Omega) \subset (W_{per}^{1, \infty}(\Omega))'.$$

Ainsi, d'après le Théorème 2.4.5, comme l'injection de  $W_{per}^{1, \frac{4}{3}}(\Omega)$  dans  $L_{per}^2(\Omega)$  est compacte, nous avons :

$$h_k \mathbf{u}_k \rightharpoonup h \mathbf{u} \text{ dans } L^2(0, T; (W_{per}^{1, \frac{4}{3}}(\Omega))^2) \text{ faible,}$$

$$h_k \mathbf{u}_k \rightharpoonup h \mathbf{u} \text{ dans } L^\infty(0, T; (L_{per}^{\frac{3}{2}}(\Omega))^2) \text{ faible,}$$

$$h_k \mathbf{u}_k \rightarrow h \mathbf{u} \text{ dans } L^2(0, T; (L_{per}^2(\Omega))^2) \text{ fort,}$$

et par produit de convergence fort-faible, il vient

$$h_k \mathbf{u}_k \otimes \mathbf{u}_k \rightarrow h \mathbf{u} \otimes \mathbf{u} \text{ dans } L^1(0, T; (L_{per}^1(\Omega))^4),$$

$$\alpha_1(h_k) h_k |\mathbf{u}_k| \mathbf{u}_k \rightarrow \alpha_1(h) h |\mathbf{u}| \mathbf{u} \text{ dans } L^1(0, T; (L_{per}^1(\Omega))^2).$$

Par ailleurs, comme  $(h_k \mathbf{u}_k)_k$  est borné dans  $L^\infty(0, T; (L_{per}^{\frac{3}{2}}(\Omega))^2)$  et  $(\mathbf{u}_k)_k$  dans  $L^2(0, T; (L_{per}^6(\Omega))^2)$  on a une borne pour  $(h_k \mathbf{u}_k \otimes \mathbf{u}_k)$  et  $(\alpha_1(h_k) h_k |\mathbf{u}_k| \mathbf{u}_k)_k$  dans  $L^2(0, T; L_{per}^{\frac{6}{5}}(\Omega))$ . Par unicité de la limite dans  $L^1(0, T; L_{per}^1(\Omega))$  on a :

$$(h_k \mathbf{u}_k) \otimes \mathbf{u}_k \rightharpoonup h \mathbf{u} \otimes \mathbf{u} \text{ dans } L^2(0, T; (L_{per}^{\frac{6}{5}}(\Omega))^4) \text{ faible,}$$

$$\alpha_1(h_k) h_k |\mathbf{u}_k| \mathbf{u}_k \rightharpoonup \alpha_1(h) h |\mathbf{u}| \mathbf{u} \text{ dans } L^2(0, T; (L_{per}^{\frac{6}{5}}(\Omega))^2).$$

On utilise le Théorème 2.4.6 pour obtenir le corollaire suivant :

**Corollaire 2.5.2.** *Soit  $\Omega$  un ouvert de  $\mathbb{R}^2$ . Le produit  $(\mathbf{u}, \mathbf{v}) \mapsto \mathbf{u}\mathbf{v}$  est continu de*

$$H^1(\Omega) \times H^{-1}(\Omega) \text{ dans } H^{-1-\varepsilon}, \forall \varepsilon > 0.$$

■

Comme  $(\mathbf{u}_k)_k$  est bornée dans  $L^2(0, T; (L_{per}^2(\Omega))^2)$ ,  $(D(\mathbf{u}_k))_k$  est bornée dans  $L^2(0, T; (H_{per}^{-1}(\Omega))^4)$ . Le produit  $(h, D(\mathbf{u})) \mapsto hD(\mathbf{u})$  est donc continu de  $L^\infty(0, T; H_{per}^1(\Omega)) \times L^2(0, T; (H_{per}^{-1}(\Omega))^4)$  dans  $L^2(0, T; (H_{per}^{-1-\varepsilon}(\Omega))^4)$ . Donc, quitte à extraire une sous suite, il vient :

$$h_k D(\mathbf{u}_k) \rightharpoonup h D(\mathbf{u}) \text{ dans } L^2(0, T; (H_{per}^{-1-\varepsilon}(\Omega))^4) \text{ faible.}$$

On a donc par unicité de la limite :

$$h_k D(\mathbf{u}_k) \rightharpoonup h D(\mathbf{u}) \text{ dans } L^2(0, T; (L_{per}^{\frac{4}{3}}(\Omega))^4) \text{ faible.}$$

On a le corollaire suivant, valable en dimension deux :

**Corollaire 2.5.3.** Soit  $\Omega$  un ouvert de  $\mathbb{R}^2$ . Le produit  $(\mathbf{u}, \mathbf{v}) \mapsto \mathbf{uv}$  est continu de

$$H^1(\Omega) \times L^2(\Omega) \text{ dans } H^{-\varepsilon}(\Omega), \forall \varepsilon > 0.$$

■

Ainsi le produit  $(h_k, \nabla h_k) \mapsto h_k \nabla h_k$  est continu de  $L^\infty(0, T; H_{per}^1(\Omega)) \times L^\infty(0, T; (L_{per}^2(\Omega))^2)$  dans  $L^\infty(0, T; (H_{per}^{-\varepsilon}(\Omega))^2)$ ,  $\forall \varepsilon > 0$ . On obtient donc une convergence vers  $h \nabla h$  dans  $L^\infty(0, T; (H_{per}^{-\varepsilon}(\Omega))^2)$   $\forall \varepsilon > 0$  faible  $\star$ . Par ailleurs on a :

$$\begin{aligned} (h_k)_k &\text{ borné dans } L^\infty(0, T; L_{per}^p(\Omega)) \quad \forall p < \infty, \\ (\nabla h_k)_k &\text{ borné dans } L^2(0, T; (L_{per}^p(\Omega))^2) \quad \forall p < \infty, \end{aligned}$$

et donc, en particulier pour  $p = 3$ ,  $(h_k \nabla h_k)$  bornée dans  $L^2(0, T; (L_{per}^{\frac{3}{2}}(\Omega))^2)_k$ . On a donc les convergences suivantes :

$$\begin{aligned} h_k \nabla h_k &\rightharpoonup h \nabla h \text{ dans } L^\infty(0, T; (H_{per}^{-\varepsilon}(\Omega))^2) \text{ faible } \star, \\ h_k \nabla h_k &\rightharpoonup h \nabla h \text{ dans } L^2(0, T; (L_{per}^{\frac{3}{2}}(\Omega))^2) \text{ faible.} \end{aligned}$$

Enfin les termes  $(h_k \Delta h_k)_k$  et  $(\nabla h_k \Delta h_k)_k$  se traitent comme en dimension un :

$$\begin{aligned} (h_k)_k &\text{ borné dans } L^\infty(0, T; L_{per}^p(\Omega)) \quad \forall p < \infty, \\ (\Delta h_k)_k &\text{ borné dans } L^2(0, T; L_{per}^2(\Omega)), \end{aligned}$$

d'où, pour  $p = 3$  par exemple, une borne dans  $L^2(0, T; L_{per}^{\frac{6}{5}}(\Omega))$  pour  $(h_k \Delta h_k)_k$ . Par ailleurs les convergences suivantes :

$$\begin{aligned} \Delta h_k &\rightharpoonup \Delta h \text{ dans } L^2(0, T; L_{per}^2(\Omega)) \text{ faible,} \\ h_k &\rightarrow h \text{ dans } \mathcal{C}^0([0, T], L_{per}^2(\Omega)) \text{ fort,} \end{aligned}$$

permettent d'obtenir par produit de convergences fort-faible et unicité de la limite :

$$\begin{aligned} h_k \Delta h_k &\rightarrow h \Delta h \text{ dans } L^1(0, T; L_{per}^1(\Omega)) \text{ fort,} \\ h_k \Delta h_k &\rightharpoonup h \Delta h \text{ dans } L^2(0, T; L_{per}^{\frac{6}{5}}(\Omega)) \text{ faible.} \end{aligned}$$

Le passage à la limite faible dans le deuxième terme  $(\nabla h_k \Delta h_k)_k$  nécessite d'obtenir de la compacité sur  $(\nabla h_k)_k$ . Nous l'obtenons grâce au Théorème 2.4.4 en utilisant les estimations suivantes, l'injection de  $H^1(\Omega)$  dans  $L^2(\Omega)$  étant compacte :

$$\begin{aligned} (\nabla h_k)_k &\text{ borné dans } L^2(0, T; (H_{per}^1(\Omega))^2), \\ \left( \frac{\partial \nabla h_k}{\partial t} \right)_k &\text{ borné dans } L^\infty(0, T; (H_{per}^{-4}(\Omega))^2) \text{ puisque } \left( \frac{\partial h_k}{\partial t} \right)_k \text{ borné dans} \\ &L^\infty(0, T; H_{per}^{-3}(\Omega)). \end{aligned}$$

On a donc par compacité et produit de convergence fort-faible :

$$\begin{aligned}\nabla h_k &\rightarrow \nabla h \text{ dans } L^2(0, T; (L^2_{per}(\Omega))^2) \text{ fort,} \\ \nabla h_k \Delta h_k &\rightarrow \nabla h \Delta h \text{ dans } L^1(0, T; (L^1_{per}(\Omega))^2) \text{ fort.}\end{aligned}$$

A partir de ces convergences le passage à la limite est possible, comme dans le cas de la dimension un. ■

---

# Conclusion

This first part is devoted to the derivation of a viscous two-dimensional NSW model, and to the demonstration of an existence result for global weak solutions.

In the first Chapter, the derivation of a new two-dimensional NSW model, including a particular viscous term, laminar and turbulent friction terms, bed slope source term, Coriolis effects and capillary effects on the free surface is stressed out. This new model is obtained following [62] from an asymptotic analysis of the non-dimensional and incompressible three dimensional Navier-Stokes-Coriolis equations with a large-scale assumption and hydrostatic approximation in a rotating sub-domain of  $\mathbb{R}^3$ . The improvements brought-up by this study concern first the extension to the two-dimensional framework, since very few study proposed in the literature are devoted to such two-dimensional derivations of viscous NSW models. This new two-dimensional model is consistent with the one-dimensional system previously introduced in [62] since equations (1.49) degenerate into the system obtained in [62]. The addition of a quadratic drag term with water depth dependent friction coefficients is consistent with the usual friction formulation used in oceanographical simulations, namely the Manning-Chezy formulation.

In the recent article [149] Ferrari and Saleri also uses the main ideas of [62] to derive a two-dimensional NSW model. However the authors added in [149] a standard viscous term after deriving the model, and the term does not match the viscous term of [62] in the degenerated one dimensional case. We emphasize that in the derivation proposed here, the new viscous term is asymptotically derived from the Navier-Stokes-Coriolis equations and degenerates into the same term as in [62].

In addition, this derivation can be regarded as a way of justifying from a mathematical point of view the addition of various source terms, like quadratic friction terms, wind effects on the free surface, eddy viscosity or even surface tension effects. It is worth mentioning that these terms are usually added to the NSW models with semi-empirical approximation.

In Chapter 2, we have established an existence result concerning global weak solutions for the previously derived model. We have used classical methods in nonlinear analysis, namely the achievement of *a priori* estimates in Sobolev spaces and compactness results which allow us to pass to the limit in an approximated problem. The demonstration proposed here shares ideas between the recent paper of Bresch and Desjardins [51] and classical studies concerning the non-homogeneous Navier-Stokes equations [22]. We have made a distinction between the one and two-dimensional cases. In the one-dimensional case we have obtained a result for the complete model with strictly positive coefficients. In the two-dimensional case, the particular viscous term is a source of trouble and we have studied a simplified model with the same viscous term as Bresch and Desjardins. Hence, the only differences with their model that remain are the friction coefficients which depend on the water depth. These coefficients lead to poor estimates on the velocity and in this work we have made an assumption concerning the positivity of the water depth. This enables us to obtain a better estimate on  $\mathbf{u}$  and therefore to cope with the previous difficulty. However, it seems possible to obtain the same result without such an assumption on  $h$ . This is actually under study.

---

*Part 2*

## **Numerical resolution**



---

# Introduction and numerical strategy

## Shallow water equations and finite volume method

Numerical solutions of hydrodynamic problems offer the possibility of predicting the behavior of the relevant variables in practical situations. Computational models of the shallow water equations are well-established tools in many research fields involving free surface flows, like for instance hydraulic, ocean circulation or coastal engineering. Many finite difference methods have been first developed to solve these equations in the one and two dimensional framework. The time integration schemes of these methods ranges from fully explicit to fully implicit. Concerning fully explicit schemes, we can refer for instance to the works of Peraire et al. [134]. Currently, implicit or semi-implicit schemes are more popular than explicit schemes due to their computational efficiency, since the severe limitation imposed by explicit schemes stability criteria requires a much smaller time step in the numerical integration than the time step permitted by accuracy considerations. We can refer for instance to the early model of Blumberg and Mellor [14] which has been used successfully in numerous application problems, like general circulation in estuaries for example. This model is based on an explicit finite difference scheme with the exception that the vertical eddy viscosity terms are discretized implicitly. Several existing numerical models are based on an Alternating Direction Implicit (ADI) method or even on semi-implicit methods (see Backhaus [6] and Casulli [40] for the one-dimensional case, Casulli and Cheng [41] for two-dimensional simulations). Another popular method is the Leendertse-type method [104]. A number of difference schemes have been also applied to solve the depth-averaged equations in tidal current flows using staggered grids, for which the velocity and the water depth are calculated at different points of the mesh (see for instance Ponce and Yabusaki [139] or Benque et al. [9]). Finite element methods were also proposed to solve NSW system, following the methods previously introduced for the Navier-Stokes equations. We can refer for example to the work of Hervouet [79]

and its implementation in **TELEMAC**, to Bermudez et al. [12] or more recently to [90].

Nevertheless, all these finite difference or finite element methods were suitable for slowly varying flows but much less powerful for rapidly varying flow problems. In addition, they provide poor results when they are applied to flow problems which exhibit discontinuities. Theoretically, they are only able to model subcritical flows, whereas observations show that in hydraulic or surf zone modeling, supercritical flows and hydraulic jumps often occur, particularly in the case of high flood flows. In order to cope with this limitation, authors using finite difference schemes try to construct empirical formulae which are used in the part of the computational domain where supercritical flows appear. Another method is to include a large amount of artificial viscosity to damp the numerical oscillations entailed by the finite-difference method itself. From these investigations, it appears that the use of empirical formulae is highly “problem-dependent” and requires an accurate parameterization. Furthermore, it is obvious that if the addition of non-physical viscosity enables to preserve the stability of the model with the regularization process, it significantly reduces the accuracy of the computed solution when high water depth or velocity gradients are involved. It is worth mentioning that in some particular cases, even the introduction of very high artificial viscosity cannot stabilize the model.

However, when viscosity and friction are neglected, the NSW equations on a flat bottom become a nonlinear system of first-order hyperbolic equations. The numerical solutions of this kind of system are extensively studied, since they appear in some important research domain, as aeronautical and aerospace engineering for instance. Actually, in the 1970s, computational fluid dynamics (CFD) has made dramatic progress, especially for shock wave capturing capabilities. Lax and Wendroff highlight the suitability of models based on conservation laws and it leads to the introduction and generalization of central difference schemes, like the Lax-Wendroff scheme or the MacCormack scheme. The importance of the monotonicity property, first discussed by Godunov [67], becomes well-established and Harten [77] introduces the more general notion of Total Variation Diminishing (TVD) schemes in the one dimensional framework. Van Leer in a series of paper [176] suggested various second-order accuracy Godunov-like schemes and in addition many approximate Riemann solvers like for example the solvers of Roe and Osher, which are more computationally efficient than the initial Riemann solver of Godunov, are developed.

Following these breakthroughs several new methods are gradually proposed in hydraulic fields. These methods are in most cases adaptations of previous schemes developed in CFD. These new schemes are able to simultaneously handle calculations of slowly varying flows as well as rapidly varying flows involving shocks or discontinuities such as those commonly observed in man-made hydraulic structures. Rajar [142] suggested to extend the Lax-Wendroff scheme to shallow water equations in order to compute dam-break problems, which become classical benchmarks for supercritical flows and bore-capturing capabilities. García and Kahawita [61] use the MacCormack

time splitting scheme to compute two-dimensional solutions of various problems from hydraulic classical benchmarks to idealized “real-world” problems. Glaister [64] derived a Roe-type approximate Riemann solver for the one-dimensional shallow water equations, Toro [172] proposed a modified HLL approximate Riemann solver for the two-dimensional case and Yang and Hsu [185] successfully used the flux vector splitting method to solve the dam-break problem.

As an evaluation of numerical fluxes at cells interfaces is needed for the application of Godunov-type methods, a finite volume formalism seems to be particularly suitable for the practical implementation, since it uses the conservative form of the equations. Thus, finite volume methods with shock capturing abilities have come to the fore because of their suitability for modeling a large range of types of flows; steady or unsteady, subcritical or supercritical, continuous or discontinuous and its ability to cope with complex topography. For instance, first and second order accuracy Osher schemes are used by Erduran and Kutija [54] for flows in channel, the second order accuracy HLL scheme is used by Mingham and Causon [127] and Hu et al. [82], the first order HLLC scheme is used by Zoppou et al. [191], the second order Roe scheme is applied by Alcrudo and García-Navarro in [2] and Hubbard and Dodd in [84]. In addition several reviews and comparisons can be found in the literature as for example Zhao et al. in [187] who perform a comparison of accuracy and stability for three first order approximate Riemann solvers, or Erduran et al. in [55] who compare five Riemann solvers (Osher, HLL, HLLC, Roe and FVS) in their second order accuracy version, with classical two dimensional benchmarks.

Concerning the problems of interests, these schemes enable the computation of a large range of type of flows from the slowly varying tidal flows in coastal engineering to the rapidly evolving flows of hydraulic fields. For instance, Zhao et al. [187] suggested simulations of dam-break problems, Hu et al. [83] investigate the computation of oblique shock wave and transcritical flows, hydraulic jumps are studied by Chippada [44] and tidal wave propagation by Bermudez [10]. We can also find simulations of flows in initially dry areas [191].

## Discretization of the source terms

In the previous section, we have emphasized the fact that when the viscosity and the friction terms are neglected, the NSW equations on flat bottom become a nonlinear system of first-order hyperbolic equations. Thus, a large set of methods developed in CFD can be adapted to the NSW system, and leads to robust solvers and accurate solutions. Nevertheless, source terms can become of importance in the NSW equations. For example, the presence of the bed-slope source term is often crucial, since it enables the model to take into account the variability of the bottom and to handle complex geometry of basins. The friction terms are also significant, especially when the layer of water becomes relatively thin. When the NSW equations are adapted to model avalanche problems, this friction term becomes fundamental, since it enables the introduction of some non-trivial equilibrium states. The importance of viscous terms is much debated. Several authors assume that the numerical resolution of NSW first order hyperbolic models generates enough artificial viscosity to handle properly

the physical process of dissipation. However, as it has been highlighted in the first chapter, these viscous terms are formally derived from the three dimensional Navier-Stokes equations with free surface and are issued from a second order approximation in the asymptotic expansion. Since these terms naturally arise from the averaging of Navier-Stokes equations, we consider their introduction in the numerical models as fully justified. More precisely, it appears from a literature review that these viscous terms may be required for the computation of several problems whereas they can be neglected for others. For instance, in coastal engineering numerous models which aim at modeling macro-tidal circulation naturally include the viscous terms, which are associated with the Reynolds formulation of turbulence, leading to approximated eddy viscous terms. Accurate discretizations of these viscous terms with parameterizations of the eddy viscosity coefficients are often proposed, while the system's anisotropy with respect to the vertical and longitudinal scales is taken into account through a distinction between horizontal and vertical eddy viscosity is introduced (see Levermore et al.[110] for example). On the contrary, viscosity is neglected in most of the model used in the computation of hydraulic problems.

Nevertheless, we want to preserve the improvements obtained with the shock-capturing finite volume methods even in the presence of various source terms. It leads to the mathematical framework of conservation laws with source terms (see Godlewski and Raviart [66]). Numerous methods have been suggested to cope with these source terms, and especially with the bed-slope and friction source terms, but there is essentially two main approaches. The first one is the fractional step method (FSM) or splitting method. The idea is to split the whole system with flux gradients and source terms into a pure "advection problem" and a "source problem", for each time step. The advection problem is exactly the homogeneous hyperbolic system of conservation laws, whereas the source problem often resumes to the resolution of a set of ordinary differential equations. At first sight, this approach may appear unreasonable but it can be shown that this method is exact in the case of a linear model equation with source term [170]. The reader is referred to [108], [184] or [112] for a complete description of this method. Many authors such as Hu et al. [82], Brocchini et al. [27] and more generally most of the authors introduced in the brief review above, have applied it to take into account the source terms in their model. The main advantage of this method is its simplicity since the global discretization is divided into two steps, one for the convection terms and one for the source terms. It allows to use an accurate method for each different step. The homogeneous system is solved using an accurate solver designed for hyperbolic conservation laws and all the benefits of the shock capturing methods are conserved, while the treatment of the source term is reduced to the implementation of an ODE solver, which can be of the needed accuracy. In addition, this approach is one of the very few existing methods which enable to take into accounts viscous terms, while resolving the homogeneous system with a shock-capturing finite volume method. For instance, Toro and Brown proposed in [173] a model which relies on the weight averaged flux (WAF) method and splitting procedure for viscous shocked flows.

However, it is well-known today that this class of methods gives poor results when the solution or even a small part of the solution is close to a steady state, especially for the shallow water equations with bed-slope source terms. Actually, fractional step methods are not designed to preserve numerical steady states and so, are unable to accurately compute the convergence towards steady states or at least the evolution of small perturbations around such states. Furthermore, such methods often induce numerical instabilities and non-physical oscillations when they have to deal with strong bed slope variations. From these considerations it appears that the use of a coherent treatment of the whole system is needed, in order to preserve the balance between flux gradients and source terms. In what follows, we only focus on the balance with the bed-slope source term since this term is the most relevant term which can lead to non-trivial steady states in the study of various type of flows. For the study of avalanches for example, similar considerations are suitable for the friction terms, since in this particular context, friction and bed-slope source terms can lead together to non-trivial equilibrium [20].

The ability of a numerical scheme to achieve the exact preservation with respect to time of discrete steady states and to accurately compute the convergence towards steady states is directly linked to the way this balance property is preserved at the discrete level. A method which preserves this balance property and fits all these requirements is called a well-balanced method.

To cope with this difficulty, numerical computation of source terms in hyperbolic systems of conservation laws has been recently improved and the discretization of the bed slope source term has been studied by a large number of authors, like for instance Priestley in [141], Roe in [146] who shows that for linear systems source terms may be upwinded in the same way as the flux gradient terms or Leveque and Yee in [109] who solve a model advection equation with a parameter dependent source term. One popular approach is to upwind the source term in a way that mimics the discretization of the flux gradients, as suggested by Roe in [146] and in the extension of the Q-schemes introduced by Bermudez and Vasquez-Cendon in [11], [178] and generalized for two-dimensional problems in [10]. Other methods are the quasi-steady wave propagation algorithm of Leveque [107] or the surface gradient method of Zhou et al. introduced in [190] which is an improvement for the computation of steady states of the model introduced in [82].

A powerful and elegant approach is to directly solve Riemann problems with piecewise constant topography. This approach, introduced by Greenberg and Leroux in [72], [73] and extended later by Gallouet et al. in [57] for linearized Riemann problems is the more general well-balanced method, since it can preserve all the steady states. These two methods are detailed in the next chapter. An other recent and extremely interesting method is the hydrostatic reconstruction method introduced in [3]. This method, initially proposed with a homogeneous kinetic Riemann solver is very flexible in practice, since it may be used in conjunction with any homogeneous Riemann solver. Furthermore, this method can easily preserve the water depths positivity if used in conjunction with a positivity preserving homogeneous solver. As it will be emphasized later, this positivity preserving property may be crucial when the numerical model has to deal with the occurrence or the flooding of dry areas. This positivity preserving

property is theoretically provided by the original Godunov method for homogeneous system but seems to be difficult to obtain in a well-balanced framework. This hydrostatic reconstruction, although being able to preserve only steady states “at rest”, will appear to be a very powerful tool.

## The moving shoreline problem

As already exposed, the NSW equations are particularly well-suited for the study and simulation of a large class of geophysical phenomena. These models are extensively used in the field of coastal engineering and especially for the study of nearshore flows, in the surf and swash zones. A large part of our numerical investigations will lie in these research fields. Our goal is to model some important wave properties which are observable in the surf zone, like the formation and reorganization of periodical bore-like waves, or even phenomena which are generated in the swash zone like flooding of initially dry area, run-up and run-down processes over sloping beaches and sometimes overtopping phenomena on arbitrary sloping beaches or coastal structures. To properly model the run-up process, an efficient treatment of the shoreline, which is defined as the dividing line between inundated and dry area, is needed. Actually, wave run-up on a sloping beach is a very complex phenomenon which has been studied extensively since a few decades. It involves wave shoaling and breaking, reflection, refraction and nonlinear interactions with the bottom profile. Moreover, flow properties change rapidly near the shoreline, as the water depth vanishes. The position of the shoreline is always evolving and we can consider that this position is part of the computed solution.

Computational models based on the NSW equations have been developed since a few decades to model wave run-up. Various methods have been suggested in order to cope with these difficulties but there is essentially two approaches.

The first one relies on coordinate transformations, which generate a map between the time-varying physical domain and a time invariant computational domain. This class of method often leads to complex algorithms. The second approach is based on the use of conservative schemes on a fixed grid and the direct computation of flow properties is used to compute the shoreline position, without special tracking algorithm. In particular, the use of a local Riemann solver enables to track the wet/dry interfaces in the same ways it tracks local discontinuities. Numerical treatments of the wetting and drying procedure, like a numerical definition of a dry cell, has to be introduced and the shoreline can then be accurately computed with high resolution bore-capturing schemes.

Following these ideas, Brocchini et al.[26], [27] have recently use the Weight Averaged Flux (WAF) method introduced by Toro in [171] in a Godunov-like scheme and Hu et al. have implemented a HLL approximate Riemann solver for the study of overtopping. For the fully two-dimensional simulation, Hubbard and Dodd [84] have developed a model using adaptive mesh refinement algorithm and based on the classical approximate Riemann solver of Roe. All these methods, although relying on a fractional step method, provide accurate results. A more detailed study of run-up

processes and a moving shoreline tracking methods review are performed in Chapter 6.

## Numerical strategy

**Numerical requirements.** We recall that we aim at developing a numerical method to study the solutions of the following shallow water system :

$$\left\{ \begin{array}{l} \partial_t h + \operatorname{div}(h\mathbf{u}) = 0, \\ \partial_t(h\mathbf{u}) + \operatorname{div}(h\mathbf{u} \otimes \mathbf{u}) + g h \nabla h = \\ -\alpha_0(h)\mathbf{u} - \alpha_1(h)h|\mathbf{u}|\mathbf{u} + \mu \operatorname{div}\left(h(\nabla\mathbf{u} + {}^t\nabla\mathbf{u}) + (2h \operatorname{div}\mathbf{u})\mathcal{I}\right) \\ + \beta h \nabla \Delta h - f(h\mathbf{u})^\perp - g h \nabla d + \beta h \nabla \Delta d. \end{array} \right. \quad (2.100)$$

where we have :

$$\alpha_0(h) = \frac{k_l}{1 + \frac{k_l h}{3\mu}} \quad \text{and} \quad \alpha_1(h) = \frac{k_t}{\left(1 + \frac{k_l h}{3\mu}\right)^2}.$$

From the previous considerations, we can infer a numerical strategy in order to solve this system. We must keep in mind that we are looking for a numerical model which can deal with a large range of applications and in particular with wave propagations in the surf zone, a process involving waves breaking and generation of bore waves. Hence, our model should provide shock capturing abilities. As it has been exposed, shock-capturing finite volume methods relying on one-dimensional Riemann solver, which can be exact or approximate, appears as an efficient and elegant class of method, well-suited for many types of flows. Thus, we will investigate the use of such finite volume method. In addition, as we aim at modeling nearshore flows and especially the propagation of waves and wave-induced current in the surf and swash zone, and considering that the topography profile is of dramatic interest in the evolution of these flows, we must pay attention to the discretization of the bed-slope source term. Therefore we should use a well-balanced method which enables us to accurately model the convergence or even the small evolutions around steady or quasi-steady states. On top of that, it appears that the framework of well-balanced shock-capturing methods may be well-suited for the simulation of moving shoreline situations. As most of the reviewed methods used for this kind of problem rely on FSM, the choice of an adequate well-balanced method can considerably improve the results found in the literature. Consequently we will investigate the use of various finite volume well-balanced methods which appear as suitable for our purpose. Moreover, the consequence of the numerical preservation of the water depths positivity on the accuracy of moving shoreline prediction will be highlighted with numerical assessments. Finally, concerning the numerical treatment of the remaining source terms, namely the friction, the viscous and the Coriolis source terms for two dimensional problems, we may develop

a fractional step method, which can also leads to high order accuracy when used in combination with a high order time discretization.

The end of this chapter is devoted to a brief introduction of the classical fractional step method for hyperbolic systems with source terms. Then we introduce the new splitting algorithm which is applied for the numerical resolution of system (2.100).

**Fractional step method.** The fractional step method usually consists in splitting, for a time  $\Delta t$ , the “advection problem” and the “source problem”. The main convenience of FSM is the fact that one can deploy the optimal existing methods for each subproblems. The reader is referred to [108], [184] or [112] for a complete description of the theoretical background.

We first introduce the formalism on a simple nonlinear hyperbolic model :

$$\begin{cases} w_t + f(w)_x = s(w) , & 0 < x < L , \\ w(t^n, x) = w^n . \end{cases} \quad (2.101)$$

where  $w(x, t) \in \mathbb{R}$  is the conserved quantity and  $s(w)$  stands for the source terms. We aim at computing the unknown values  $w^{n+1}$  at time  $t = t^{n+1}$  obtained after an evolution of  $\Delta t$ , knowing the values  $w^n$  at time  $t = t^n$ . assuming that the computational domain  $[0, L]$  is discretized into  $N$  cells , in a cell-centered finite volume approach.  $\{w^n\}$  stands for the discrete values  $w_i^n$  at time  $t^n$ . Introducing an intermediate state  $(t^*, w^*)$ , the fractional step method is defined as follows ;

$$\begin{cases} w_t + f(w)_x = 0 , \\ w(t^n, x) = w^n , \end{cases} \rightarrow w^* \quad (2.102)$$

and then

$$\begin{cases} \frac{dw}{dt} = s(w) , \\ w(t^*, x) = w^* , \end{cases} \rightarrow w^{n+1} \quad (2.103)$$

The initial condition for the whole problem (2.101) is used as initial condition of the homogeneous hyperbolic problem (2.102). We introduce  $w^*$  which is the solution of this homogeneous problem after a time  $\Delta t$ .  $w^*$  is then used as the initial condition for the second initial value problem (2.103). This second problem accounts for the presence of the source term  $s(w)$  and is also solved for a complete time step  $\Delta t$ . The final solution is then regarded as an approximation of the solution  $w^{n+1}$  of the full problem (2.101) at time  $t^{n+1} = t^n + \Delta t$ .

This method can be expressed in the following form, using operators :

$$w^{n+1} = S_{\Delta t} C_{\Delta t}(w^n) \quad (2.104)$$

where  $C_{\Delta t}$  can be interpreted as the solution operator for the convection problem applied over a time  $\Delta t$  and  $S_{\Delta t}$  as the solution operator for the ordinary differential equation defined by (2.103).

Each numerical sub-problem (2.102), (2.103) is resolved separately, for a time step  $\Delta t$ .

One requires a numerical method to solve the homogeneous conservation law (2.108) and another numerical method to solve the ordinary differential equation (2.103). This procedure is first order accurate in time if operator  $C_{\Delta t}$  and  $S_{\Delta t}$  are both first order. Numerical extension to second order accuracy will be developed later.

**Remark 2.5.1.** *The time step  $\Delta t$  is imposed by classical restriction both for the advection step and the source step. Actually, the time evolution of the ODE is often dictated by the stability time step restriction inherited from the finite volume explicit solver used for the advection problem. From a practical point of view, the restricted time step  $\Delta t_c$  used for the resolution of the advection step is computed using the usual adapted stability criteria. Then a stability analysis of the chosen explicit ODE method for the source step is performed, leading to a second stable time step  $\Delta t_s$ . Then the final time step is obviously  $\Delta t = \min(\Delta t_c, \Delta t_s)$ . If the ODE method is an implicit method, there is no stability restriction and the whole problem can be advanced with  $\Delta t = \Delta t_c$ .*

The extension to nonlinear systems is straightforward and can be expressed as follows, considering an initial value problem involving  $n$  nonlinear equations where  $\mathbf{W}(t, X)$  is the vector of conserved quantities with  $\mathbf{W}(t, X) \in \mathbb{R}^n$  and  $X \in \mathbb{R}^p$  :

$$\begin{cases} \mathbf{W}_t + \operatorname{div}(F(\mathbf{W})) = S(\mathbf{W}), \\ \mathbf{W}(t^n, X) = \mathbf{W}^n, \end{cases} \quad (2.105)$$

where  $S(\mathbf{W})$  stands for the source terms.

We want to obtain the set of values  $\{\mathbf{W}^{n+1}\}$  at time  $t = t^{n+1}$ , knowing the discrete values  $\{\mathbf{W}^n\}$  at time  $t^n$ . Introducing the intermediate state  $(t^*, \mathbf{W}^*)$  the fractional step method is written as follows :

$$\begin{cases} \mathbf{W}_t + \operatorname{div}(F(\mathbf{W})) = 0, \\ \mathbf{W}(t^n, X) = \mathbf{W}^n, \end{cases} \rightarrow \mathbf{W}^* \quad (2.106)$$

and then :

$$\begin{cases} \frac{d\mathbf{W}}{dt} = S(\mathbf{W}), \\ \mathbf{W}(t^*, x) = \mathbf{W}^*, \end{cases} \rightarrow \mathbf{W}^{n+1} \quad (2.107)$$

This method can be expressed in term of solution operators, with the same notations as in the scalar case :

$$\mathbf{W}^{n+1} = S_{\Delta t} C_{\Delta t}(\mathbf{W}^n) \quad (2.108)$$

**Application to the viscous shallow water model.** Keeping in mind the notation introduced in the previous subsection, we consider here the application of the FSM to the shallow water system with source terms (2.100). We consider the following initial value problem in dimensionalized variables :

$$\left\{ \begin{array}{l} \partial_t h + \operatorname{div}(h\mathbf{u}) = 0, \\ \partial_t(h\mathbf{u}) + \operatorname{div}(h\mathbf{u} \otimes \mathbf{u}) + g h \nabla h = \\ -\alpha_0(h) \mathbf{u} - \alpha_1(h) h |\mathbf{u}| \mathbf{u} + \mu \operatorname{div} \left( h(\nabla \mathbf{u} + {}^t \nabla \mathbf{u}) + (2h \operatorname{div} \mathbf{u}) \mathcal{I} \right) \\ + \beta h \nabla \Delta h - f(h\mathbf{u})^\perp - g h \nabla d + \beta h \nabla \Delta d, \\ h(0) = h_0, \\ (h\mathbf{u})(0) = (h\mathbf{u})_0. \end{array} \right.$$

where we have :

$$D(\mathbf{u}) = \frac{1}{2}(\nabla \mathbf{u} + {}^t \nabla \mathbf{u}),$$

and

$$\alpha_0(h) = \frac{k_l}{1 + \frac{k_l h}{3\mu}} \quad \text{and} \quad \alpha_1(h) = \frac{k_t}{\left(1 + \frac{k_l h}{3\mu}\right)^2}.$$

with  $k_l > 0$  et  $k_t > 0$ . Using the values  $(h^n, (h\mathbf{u})^n)$  at time  $t = t^n$ , and an intermediate state  $(h^*, (h\mathbf{u})^*)$ , we want to compute the new values  $(h^{n+1}, (h\mathbf{u})^{n+1})$  at time  $t = t^{n+1}$ .

We introduce here a new splitting procedure which not follows the classical decomposition into ‘‘advection part’’ and ‘‘source part’’ but is more suitable for our purpose. As we aim at deriving a well-balanced method which enables the preservation of the largest class of steady states, we choose to include the bed slope source term in the first ‘‘advection step’’, which will be named ‘‘hyperbolic step’’ in the following, suggesting that we are more interested in resolving an hyperbolic problem with bed slope source term than a pure advection problem. We will introduce in the next chapter some well-balanced methods which are suitable for the global discretization of this system and the preservation at the discrete levels of some relevant equilibrium states. Thus, providing the solution at time  $t^n$  as the initial condition, we are looking for the resolution of the following initial value problem :

$$\left. \begin{array}{l} h_t + \operatorname{div}(h\mathbf{u}) = 0, \\ (h\mathbf{u})_t + \operatorname{div}(h\mathbf{u} \otimes \mathbf{u}) + gh \nabla h = -g h \nabla d, \\ h(t^n) = h^n, \\ (h\mathbf{u})(t^n) = (h\mathbf{u})^n. \end{array} \right\} \rightarrow (h^*, (h\mathbf{u})^*) \quad (2.109)$$

This first step yields to an intermediate numerical state, denoted by  $(h^*, (h\mathbf{u})^*)$ .

In a second step, we perform the computation of the solution of the ordinary differential equation system including the remaining source terms, namely the friction terms, the Coriolis term and the viscous terms. This source step is solved using a semi-implicit accurate EDO solver which will be detailed in chapter 5. Injecting the intermediate state  $(h^*, (h\mathbf{u})^*)$  as the initial condition :

$$\left. \begin{aligned} h_t &= 0, \\ (h\mathbf{u})_t + f(h\mathbf{u})^\perp + \alpha_0(h)\mathbf{u} + \alpha_1(h)h|\mathbf{u}|\mathbf{u} &= \\ \beta h\nabla\Delta h + \mu \operatorname{div} \left( h D(\mathbf{u}) + (2h \operatorname{div} \mathbf{u})\mathcal{I} \right) + \beta h\nabla\Delta d, & \\ h(t^*) &= h^*, \\ (h\mathbf{u})(t^*) &= (h\mathbf{u})^*, \end{aligned} \right\} \rightarrow (h^{n+1}, (h\mathbf{u})^{n+1}) \quad (2.110)$$

We obtain from this source step the solution  $(h^{n+1} = h^*, (h\mathbf{u})^{n+1})$  of the initial value problem (2.5.1) at time  $t^{n+1} = t + \Delta t$ .

In the next chapter, we recall two elegant and robust well-balanced methods for the resolution of the hyperbolic step. These methods, based on the direct resolution of an augmented Riemann problem with a piecewise constant topography, have been proved to be very powerful and accurate in the computation of a large class of subcritical steady states and the occurrence of dry area. Nonetheless, numerical investigations highlight their limitations when one try to deal with moving shoreline problems. To improve these results, an other up-to-date well-balanced method which is only able to deal with steady states “at rest” but allows the preservation of the positivity of the water depth is introduced in chapter 4. Numerical assessments of this method against one and two dimensional benchmarks involving moving shorelines are proposed. In chapter 5 we finally introduce the semi-implicit EDO solver used for the remaining source terms, which can preserve the well-suited properties inherited from the well-balanced method.



# Numerical resolution of the hyperbolic system with bed-slope term

## 3.1. Governing equations and Finite Volume framework

**3.1.1. The Saint-Venant system with bed slope source term.** In this section we introduce the NSW equations with bed slope source term. The two-dimensional NSW equations with bed slope source term may be written as follows :

$$\mathbf{U}_{,t} + F(\mathbf{U})_{,x} + G(\mathbf{U})_{,y} = S(\mathbf{U}), \quad (3.1)$$

with

$$\mathbf{U} = \begin{pmatrix} h \\ hu \\ hv \end{pmatrix}, \quad F(\mathbf{U}) = \begin{pmatrix} hu \\ hu^2 + \frac{g}{2}h^2 \\ huv \end{pmatrix}, \quad G(\mathbf{U}) = \begin{pmatrix} hv \\ huv \\ hv^2 + \frac{g}{2}h^2 \end{pmatrix},$$

and

$$S(\mathbf{U}) = \begin{pmatrix} 0 \\ -g h d_x \\ -g h d_y \end{pmatrix}$$

where  $(\cdot)_{,x}$  (resp.  $(\cdot)_{,y}$ ) stands for the derivative along the  $x$  direction (resp. the  $y$  direction),  $\mathbf{u} = {}^t(u, v)$  is the depth-averaged velocity with  $u$  and  $v$  the scalar components in the horizontal  $x, y$  directions and  $h$  is the local water depth (see Figure 3.1.1).  $\mathbf{U}$  is the vector for the conservative variables,  $F(\mathbf{U})$  and  $G(\mathbf{U})$  stand for the flux functions respectively along the  $x$  and  $y$  directions and  $S(\mathbf{U})$  represents the bed slope source

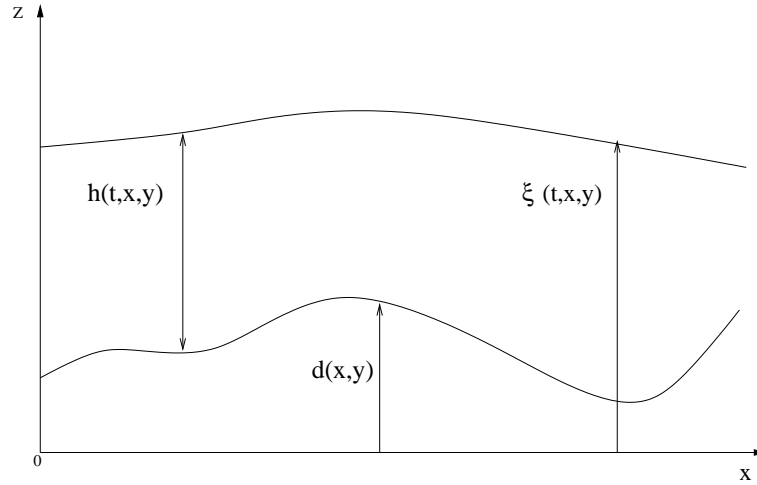


**Figure 3.1.1.** Surface elevation, water depth and topography

term with the bed slope  $\nabla d = {}^t(d_{,x}, d_{,y})$ .

When neglecting the bed-slope source term or when the topography is constituted of a flat bottom, we obtain the classical homogeneous shallow water system, also known as the Saint-Venant equations :

$$\mathbf{U}_{,t} + F(\mathbf{U})_{,x} + G(\mathbf{U})_{,y} = 0, \quad (3.2)$$

with the same notations. In the next subsection, we introduce the general finite volume formalism.

**3.1.2. Finite volume framework and Riemann solver.** The finite volume method is a class of discretization method which is well-suited for the numerical simulation of conservation laws and especially for hyperbolic conservation laws. This method has been extensively applied in many domains of engineering, such as fluid mechanics or heat and mass transfers. Even if we choose to use Cartesian meshes in our studies, FVM may be applied on unstructured meshes, for arbitrary geometries. Finite volume schemes are known to be robust in practice and well-suited for any problem involving a modelization based on fluxes, since local conservativity of numerical fluxes is achieved. The finite volume method is locally conservative because it is built on a local conservation relation on each discretization cell, obtained from the integral formulation of the conservation law. Using the divergence formula, an integral formulation of the fluxes through the boundaries of the control volume may be obtained. Then, an adapted discretization of these fluxes need to be found. The reader is referred to [56] for a detailed introduction of finite volume methods for both hyperbolic and elliptic systems.

A two-dimensional semi-discrete finite volume formulation of system (3.1) is given by :

$$\frac{d}{dt} \mathbf{U}_{ij}(t) + \frac{1}{\Delta x} (\mathbf{F}_{i+\frac{1}{2},j}^* - \mathbf{F}_{i-\frac{1}{2},j}^*) + \frac{1}{\Delta y} (\mathbf{G}_{i,j+\frac{1}{2}}^* - \mathbf{G}_{i,j-\frac{1}{2}}^*) = \mathbf{S}_{ij} \quad (3.3)$$

where the cell-centered vector of conservative discrete variables is

$$\mathbf{U}_{ij} = {}^t(h_{i,j}, h_{i,j}u_{i,j}, h_{i,j}v_{i,j}),$$

and  $\mathbf{F}_{i\pm\frac{1}{2},j}^*$ ,  $\mathbf{G}_{i,j\pm\frac{1}{2}}^*$  stands respectively for the numerical flux functions through the  $\Gamma_{i\pm\frac{1}{2},j}$  and  $\Gamma_{i,j\pm\frac{1}{2}}$  interfaces (see Figure 3.1.2) and  $\mathbf{S}_{ij}$  represents a discretization of the source term. To define the finite volume method, we must choose a discretization method in order to compute the numerical fluxes  $\mathbf{F}_{i\pm\frac{1}{2},j}^*$ ,  $\mathbf{G}_{i,j\pm\frac{1}{2}}^*$  and the source terms  $\mathbf{S}_{ij}$ .

When the bed slope source term is neglected, the semi-discrete finite volume formulation (3.3) is simplified to obtain the following conservative formulation :

$$\frac{d}{dt}\mathbf{U}_{ij}(t) + \frac{1}{\Delta x}(\mathbf{F}_{i+\frac{1}{2},j}^* - \mathbf{F}_{i-\frac{1}{2},j}^*) + \frac{1}{\Delta y}(\mathbf{G}_{i,j+\frac{1}{2}}^* - \mathbf{G}_{i,j-\frac{1}{2}}^*) = 0. \quad (3.4)$$

and in the one dimensional framework we have :

$$\frac{d}{dt}\mathbf{U}_i(t) + \frac{1}{\Delta x}(\mathbf{F}_{i+\frac{1}{2}}^* - \mathbf{F}_{i-\frac{1}{2}}^*) = 0. \quad (3.5)$$

In what follows, we will first focus on this homogeneous conservative formulation, in the one dimensional framework and briefly recall the formalism of two fundamentals Riemann solvers which lead to the computation of the numerical fluxes  $\mathbf{F}_{i\pm\frac{1}{2},j}^*$  and  $\mathbf{G}_{i,j\pm\frac{1}{2}}^*$ . A third and more recent Riemann solver is also introduced, namely the VFRoe solver, which relies on common ideas and gathers the advantages of the two previous solvers.

**3.1.3. The Godunov scheme.** This scheme was first introduced by Godunov [67] in 1959. It is based on the exact resolution of each local Riemann problem at each interface between two discretization cells.

Precisely, we consider the hyperbolic homogeneous system (3.2) in the one dimensional framework and we assume that  $\mathbf{U}_j^n \forall j \in \mathbb{Z}$  is known. The Godunov scheme constructs the approximation of the numerical solution at time  $t^{n+1} = t^n + \Delta t$  in two steps. First we compute the exact similarity solution  $\mathbf{U}^*(\frac{x}{t}, \mathbf{U}_L, \mathbf{U}_R)$  of the following Riemann problem at each interface of the mesh :

$$\begin{cases} \mathbf{U}_t + F(\mathbf{U})_x = 0, \\ \mathbf{U}(x, 0) = \begin{cases} \mathbf{U}_L = (h_L, (hu)_L) & \text{if } x < 0 \\ \mathbf{U}_R = (h_R, (hu)_R) & \text{if } x > 0. \end{cases} \end{cases} \quad (3.6)$$

In the case of the interface  $i + \frac{1}{2}$  between the cells  $C_i$  and  $C_{i+1}$ , we have  $L = i$ ,  $R = i + 1$  and the solution of problem (3.6) become  $\mathbf{U}^*(\frac{x}{t}, \mathbf{U}_i^n, \mathbf{U}_{i+1}^n)$ .

Then we define the numerical solution by  $L^2$ -projection of the exact solution on the space of constant cell functions :

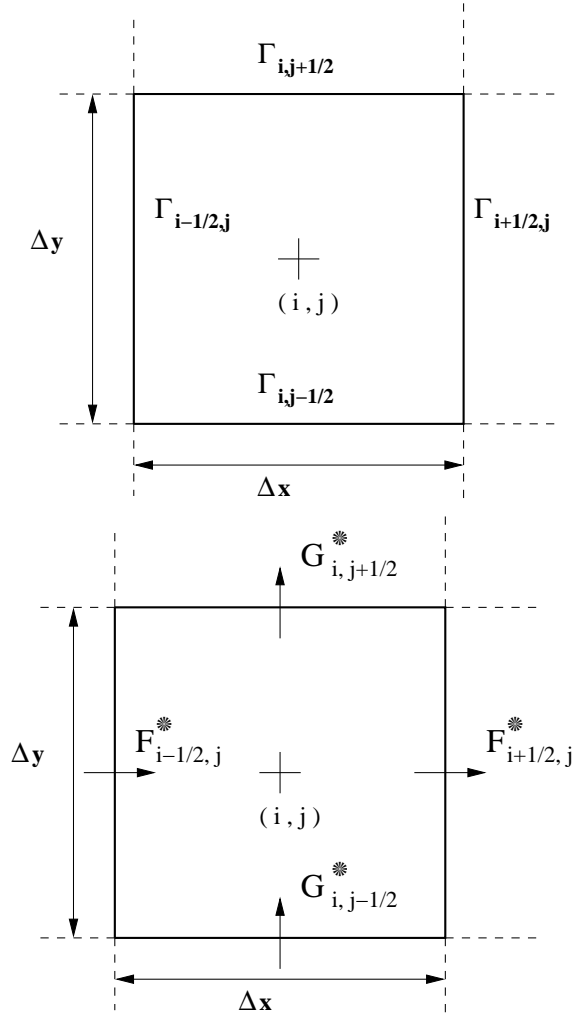


**Figure 3.1.2.** Discretization cell, interfaces (on the left) and numerical fluxes (on the right).

$$\mathbf{U}_i^{n+1} = \frac{1}{\Delta x} \int_{x_{i-\frac{1}{2}}}^{x_i} \mathbf{U}^* \left( \frac{x - x_{i-\frac{1}{2}}}{\Delta t}, \mathbf{U}_{i-1}^n, \mathbf{U}_i^n \right) dx + \frac{1}{\Delta x} \int_{x_i}^{x_{i+\frac{1}{2}}} \mathbf{U}^* \left( \frac{x - x_{i+\frac{1}{2}}}{\Delta t}, \mathbf{U}_i^n, \mathbf{U}_{i+1}^n \right) dx \quad (3.7)$$

Following the previous finite volume formalism, the conservative form of the scheme may be obtained with the integration of the exact solution on every volume  $M_i \times [t^n, t^{n+1}]$ . Since the function  $\xi \rightarrow F(\mathbf{U}^*(\xi, \mathbf{U}, V))$  is continuous in  $\xi = 0$ , it leads to :

$$\mathbf{U}_i^{n+1} = \mathbf{U}_i^n - \frac{\Delta t}{\Delta x} (F(\mathbf{U}^*(0, \mathbf{U}_i^n, \mathbf{U}_{i+1}^n)) - F(\mathbf{U}^*(0, \mathbf{U}_{i-1}^n, \mathbf{U}_i^n))) \quad (3.8)$$

The numerical flux  $\mathbf{F}_{i+\frac{1}{2}}^*$  at the interface  $i + \frac{1}{2}$  is thus defined with :

$$\mathbf{F}_{i+\frac{1}{2}}^{God} = F(\mathbf{U}^*(0, \mathbf{U}_i^n, \mathbf{U}_{i+1}^n)), \quad (3.9)$$

The main drawback of the Godunov scheme is its computational cost due to the calculation with iterations (Newton-Raphson iteration method) of the exact solutions of each local Riemann problem. This computational cost may soon become a trouble for complex applications on large computational domains with a fine resolution or in a two dimensional framework.

**3.1.4. The Roe scheme.** This scheme was first proposed by Roe in [145]. It's a Godunov-like scheme also based on the resolution of local Riemann problems (3.6) at each interface of the mesh but the Riemann problem is linearized around an averaged state and the Roe scheme is based on the computation of exact solutions of such linearized Riemann problem. The linearized Riemann problem is defined with the introduction of a matrix  $\tilde{A}(\mathbf{U}_L, \mathbf{U}_R)$  as follows :

$$\left\{ \begin{array}{l} \partial_t \mathbf{U} + \tilde{A}(\mathbf{U}_L, \mathbf{U}_R) \partial_x \mathbf{U} = 0, \\ \mathbf{U}(x, 0) = \begin{cases} \mathbf{U}_L = (h_L, (hu)_L) & \text{if } x < 0 \\ \mathbf{U}_R = (h_R, (hu)_R) & \text{if } x > 0. \end{cases} \end{array} \right. \quad (3.10)$$

The matrix  $\tilde{A}(\mathbf{U}_L, \mathbf{U}_R)$  must satisfy the following Roe's properties :

- (1)  $\tilde{A}(\mathbf{U}_L, \mathbf{U}_R)$  is diagonalizable with real eigenvalues,
- (2)  $F(\mathbf{U}_R) - F(\mathbf{U}_L) = \tilde{A}(\mathbf{U}_L, \mathbf{U}_R)(\mathbf{U}_L - \mathbf{U}_R)$ ,
- (3)  $\tilde{A}(\mathbf{U}, \mathbf{U}) = \partial_{\mathbf{U}} F(\mathbf{U})$ .

These properties ensure the conservativity of the scheme and provide the shock capturing ability of the method since they enable the scheme to recognize isolated discontinuities. The associated numerical flux is defined as follows :

$$\mathbf{F}^{Roe}(\mathbf{U}_L, \mathbf{U}_R) = \frac{1}{2}(F(\mathbf{U}_L) + F(\mathbf{U}_R) - |\tilde{A}(\mathbf{U}_L, \mathbf{U}_R)| \cdot (\mathbf{U}_R - \mathbf{U}_L)) \quad (3.11)$$

and the conservative form of the scheme is given by :

$$\mathbf{U}_i^{n+1} = \mathbf{U}_i^n - \frac{\Delta t}{\Delta x} (\mathbf{F}_{i+\frac{1}{2}}^{Roe}(\mathbf{U}_i^n, \mathbf{U}_{i+1}^n) - \mathbf{F}_{i-\frac{1}{2}}^{Roe}(\mathbf{U}_{i-1}^n, \mathbf{U}_i^n)) \quad (3.12)$$

The Roe scheme may be seen as the generalization of the classical upwind scheme to nonlinear hyperbolic system, since the linearization may be regarded as a field by field decomposition.

The main drawback of this scheme is the fact that one must construct explicitly the linearization matrix  $\tilde{A}(\mathbf{U}_L, \mathbf{U}_R)$  which satisfies the three previous Roe's properties. In practice, recovering the second property which ensures the consistency is the more

laborious task. To this end, Roe proposed to use the vector parameter method [145] to determine this linearization matrix. But in a general way, it is a painful job and in the literature we find many authors who suggest the construction of an approximate linearization matrix which achieves Roe's condition with a certain order of accuracy.

**Remark 3.1.1.** *An relevant weakness of this scheme is the occurrence of entropy violation problems. More precisely, the scheme may converge toward non-physical weak solutions when the Riemann problem has a sonic rarefaction wave which crosses the considered interface. Several simple methods which enable to fix this problem have been pointed out (see [108] for instance).*

**Remark 3.1.2.** *Another serious problem is the possible occurrence of negative density values in the case of gas dynamics problems, or negative water depth values in the case of hydrodynamic problems. A simple and usual numerical trick is to artificially set to zero all negative values which may arise during the computation (a "clipping treatment"). This usually prevents the occurrence of numerical instabilities but the loss of accuracy can be pronounced.*

**3.1.5. The VFRoe scheme.** As exposed before, the determination of a Roe's matrix which satisfies Roe's conditions may sometime be a challenging problem. Nonetheless, the idea of introducing linearized Riemann problems is a real improvement. To preserve the benefits inherited from Roe's idea a new solver has been introduced in [125], [31], [59]. This scheme, called VFRoe scheme, is inspired by Godunov and Roe schemes and does not require any analytical computations or construction of linearized matrix fulfilling Roe's condition. Following Roe's idea, this scheme relies on the solution of linearized Riemann problems and as in Godunov scheme, the numerical flux is defined as the physical flux function computed at the interface solution of the approximate Riemann problem :

$$\mathbf{F}^{VFRoe}(\mathbf{U}_L, \mathbf{U}_R) = F(\mathbf{U}_{VFRoe}(0, \mathbf{U}_L, \mathbf{U}_R)) \quad (3.13)$$

where  $\mathbf{U}_{VFRoe}(0, \mathbf{U}_L, \mathbf{U}_R)$  is the solution of the linearized Riemann problem (3.10) with

$$\tilde{A}(\mathbf{U}_L, \mathbf{U}_R) = \partial_{\mathbf{U}} F(\tilde{\mathbf{U}}) \text{ with } \tilde{\mathbf{U}} = \tilde{\mathbf{U}}(\mathbf{U}_L, \mathbf{U}_R). \quad (3.14)$$

This leads to a conservative scheme for any linearization matrix  $\tilde{A}(\mathbf{U}_L, \mathbf{U}_R)$ . It is worth mentioning that this matrix does not necessary verify the second Roe's relation. Actually, the flux is obviously consistent for any value of  $\tilde{\mathbf{U}}$ , as for the Godunov scheme, since we have :

$$\mathbf{U}_{VFRoe}(0, \mathbf{U}, \mathbf{U}) = \mathbf{U} \Rightarrow \mathbf{F}^{VFRoe}(\mathbf{U}, \mathbf{U}) = F(\mathbf{U}).$$

We compute the eigenvalues and the left and right eigenvectors of  $\tilde{A}(\mathbf{U}_L, \mathbf{U}_R)$ , since the Jacobian of the physical flux function  $F(\mathbf{U})$  is diagonalizable. Let us denote by  $(\tilde{\lambda}_k)_{k=1\dots p}$  the eigenvalues of this averaged linearized matrix and by  $(\tilde{\mathbf{l}}_k)_{k=1\dots p}$  and  $(\tilde{\mathbf{r}}_k)_{k=1\dots p}$  the associated left and right eigenvectors. The exact solution of the Riemann problem (3.37) is defined as follows :

$$\begin{aligned}
\mathbf{U}_{VFRoe}\left(\frac{x}{t}, \mathbf{U}_L, \mathbf{U}_R\right) &= \mathbf{U}_L + \sum_{\frac{x}{t} > \tilde{\lambda}_k} ({}^t\tilde{\mathbf{I}}_k \cdot [\mathbf{U}]_L^R) \tilde{\mathbf{r}}_k, \\
&= \mathbf{U}_R - \sum_{\frac{x}{t} < \tilde{\lambda}_k} ({}^t\tilde{\mathbf{I}}_k \cdot [\mathbf{U}]_L^R) \tilde{\mathbf{r}}_k,
\end{aligned} \tag{3.15}$$

where  $[\mathbf{U}]_L^R = \mathbf{U}_R - \mathbf{U}_L$ . The numerical flux is then defined as previously exposed, using the physical flux function :

$$\mathbf{F}^{VFRoe}(\mathbf{U}_L, \mathbf{U}_R) = F(\mathbf{U}_{VFRoe}(0, \mathbf{U}_L, \mathbf{U}_R)). \tag{3.16}$$

Thus, considering the Riemann problem at the interface  $i + \frac{1}{2}$  we obtain

$$\mathbf{F}_{i+\frac{1}{2}}^{VFRoe}(\mathbf{U}_i, \mathbf{U}_{i+1}) = F(\mathbf{U}_{VFRoe}(0, \mathbf{U}_i, \mathbf{U}_{i+1}))$$

and it yields the following conservative scheme :

$$\mathbf{U}_i^{n+1} = \mathbf{U}_i^n - \frac{\Delta t}{\Delta x} (F(\mathbf{U}_{VFRoe}(0, \mathbf{U}_i^n, \mathbf{U}_{i+1}^n)) - F(\mathbf{U}_{VFRoe}(0, \mathbf{U}_{i-1}^n, \mathbf{U}_i^n))) \tag{3.17}$$

The stability of the VFRoe scheme in the scalar case is studied in [125].

**Remark 3.1.3.** *As for the Roe scheme, this scheme may suffer in particular case of entropy violation problems. Sonic entropy corrections can be introduced (see Masella et al. [125]) to cope with this limitation. This entropy fix is detailed in the next section, with the study of the well-balanced VFRoe-ncv scheme.*

**Remark 3.1.4.** *Occurrence of negative water depth values can be observed, as for the Roe scheme. In this special case, the numerical flux cannot be computed. We will see in the next chapter a method based on a symmetrizing change of variables introduced in [57] for the shallow water system which leads to the “preservation” of water depth positivity, without any numerical tricks.*

## 3.2. Well-balanced methods

**3.2.1. Main ideas.** We give here a brief description of the main ideas concerning the well-balanced numerical treatment of the bed slope source term. Then, we present with more details, in the one-dimensional case, two well-balanced methods proposed in the literature, namely the Exact Well-Balanced Riemann solver of Greenberg and Leroux [72], [73] and the well-balanced VFRoe-ncv solver introduced by Gallouët et al. in [57].

Keeping in mind the semi-discrete finite volume formulation 3.3, we develop how it is possible to obtain a numerical approximation of the whole system with bed slope source term which provides the preservation of discrete steady states. Moreover our scheme must be able to compute accurately convergence towards steady states. A relevant instance is the run-up and reflection of a solitary wave on a sloping beach, which is studied in the third part of this study. After the complete reflection, the mean water level settles back to its initial value and the model must be able to accurately

compute this convergence.

in the more general case, and in the one dimensional framework, the steady states which must be preserved are exactly the functions  $h(x)$  and  $u(x)$  satisfying :

$$\begin{cases} hu = Cst, \\ \frac{u^2}{2} + g(h + d) = Cst. \end{cases} \quad (3.18)$$

Among these steady states, the steady states at rest play an important part in the study of nearshore flows over sloping beach, since small variations around such states often occur. Preserving such states would already be an important improvement when compared to FSM. Those states are defined by :

$$\begin{cases} u = 0, \\ h + d = Cst. \end{cases} \quad (3.19)$$

The reason for the generation of errors caused by the use of FSM in the computation of such steady states is well-established today. It is due to the imbalance between flux gradients and the bed slope source term and FSM may introduce discretization errors which are greater than the signal itself. The competition between the convection term and the bed-slope source term can be highlighted when we consider that steady states are a particular kind of solutions of system (3.1) which are independent of time. In the one-dimensional case, system (3.1) reduces to the following balance equation :

$$F(\mathbf{U})_{,x} = S(\mathbf{U}). \quad (3.20)$$

The solutions of system (3.20) are important since they are often obtained as limits when time tends to infinity of the solutions of system (3.1). Thus, the ability of a numerical scheme to accurately compute the convergence towards a steady state is directly linked to the way this balance property is preserved at the discrete level. Therefore, we focus on the necessity to treat the flux gradient and the source term as a whole to achieve the exact preservation with respect to time of discrete steady states, the ability to compute small evolutions around such steady states and the convergence towards them.

To numerically preserve this balance, several alternative methods have been introduced in the literature. One popular approach, first suggested by Roe [146] is to upwind the source term in the same way as the fluxes, as in the extension of the Q-schemes introduced by Bermudez and Vasquez-Cendon in [11], [178] and generalized for two-dimensional problems in [10]. But this method has only been introduced for Roe's scheme or Van Leer Q-scheme and is not easy to generalize to other Riemann solver. Other ways are the early quasi-steady wave propagation algorithm of Leveque [107] or the surface gradient method of Zhou et al. introduced in [190] or the method proposed by Jin [88] but these methods are highly "problem-dependent" and quite heavy in practice. Approaches based on central schemes are proposed by Kurganov and Levy [100] and Russo [147]. An efficient and elegant approach is to directly solve Riemann problems with piecewise constant topography, adding a third equation for

the variable describing the topography. This approach, introduced by Greenberg and Leroux in [72] and extended later by Gosse [68] with the well-balanced flux vector splitting scheme and Gallouët et al.[57] for linearized Riemann problems is the more general well-balanced method, since it is able to preserve the largest class of steady states. This method is briefly detailed in the next subsection.

**Remark 3.2.1.** *Note that in the two-dimensional framework, the definition of the subcritical steady states is more complicated. However, our numerical approach will rely on one-dimensional Riemann solver, even in the two-dimensional framework.*

**3.2.2. The Exact Well-Balanced Riemann solver.** We want to emphasize here the early idea of Greenberg and Leroux [72] with their Exact Well-Balanced Riemann solver and briefly detail the formalism of the method in the one-dimensional case. Greenberg and Leroux proposed to approximate the topography with a piecewise constant function. Then, considering the topography as a variable, they added an equation describing the evolution of  $d$  in order to obtain a Riemann problem with a piecewise constant topography. We obtain the following augmented Riemann problem :

$$\begin{cases} \mathbf{U}_t + F(\mathbf{U})_x = S_x(\mathbf{U}), \\ \mathbf{U}(x, 0) = \begin{cases} (d_L, h_L, (hu)_L) & \text{if } x < 0 \\ (d_R, h_R, (hu)_R) & \text{if } x > 0 \end{cases} \end{cases} \quad (3.21)$$

where

$$\mathbf{U} = \begin{pmatrix} d \\ h \\ hu \end{pmatrix}, \quad F(\mathbf{U}) = \begin{pmatrix} 0 \\ hu \\ hu^2 + \frac{g}{2}h^2 \end{pmatrix}, \quad S_x(\mathbf{U}) = \begin{pmatrix} 0 \\ 0 \\ -ghd_x \end{pmatrix}.$$

Note that this Riemann problem is not the one-dimensional Riemann problem associated with system (3.1) since we have replaced the smooth topography by a piecewise constant topography. The source term  $-ghd_x$  is reduced to a sum of Dirac masses occurring on each interface. This problem has three eigenvalues :  $u - c$ ,  $0$ ,  $u + c$  where  $c = \sqrt{gh}$ . The fields induced by the  $u - c$  and  $u + c$  waves are Genuinely NonLinear fields whereas the field induced by the  $0$  eigenvalue is linearly degenerated.

The computation of the solution relies on the generalization of the results obtain for the one dimensional Riemann problem on a flat bottom.

*Analysis of the homogeneous Riemann problem.* This subsection is devoted to the recalling of fundamental relations concerning the classical Riemann problem on a flat bottom and the characterization of the shock waves and rarefaction waves that may arise, using the Rankine-Hugoniot relation and the conservation of Riemann invariant.

We first analyze the occurrence of rarefaction wave, following the introduction proposed in [106]. Assuming that the solution is regular in the case of the occurrence of a rarefaction wave,  $h$  and  $u$  can locally be considered as monotonic function with respect to  $x$ . We can therefore eliminate the  $x$  coordinate between these two functions and obtain a relationship of the form  $u = u(h)$ . Of source this approximation is only

locally relevant but it is enough for our purpose. From this, the one dimensional NSW equations without bed slope source term can be expressed in the following matricial form :

$$\begin{pmatrix} 1 & hu' + u \\ hu' + u & u^2 + 2huu' + gh \end{pmatrix} \cdot \begin{pmatrix} h_{,t} \\ u_{,t} \end{pmatrix} = \begin{pmatrix} 0 \\ 0 \end{pmatrix} \quad (3.22)$$

We obtain a linear system and as non-uniform and unsteady solutions may naturally arise, the matrix can not be singular. It leads to the following relation :

$$hu'^2 - g = 0. \quad (3.23)$$

The solutions of this ordinary differential equation are :

$$u \pm 2\sqrt{gh} = C^{st} \quad (3.24)$$

We have obtain two quantities  $\beta^- = u - 2c$  and  $\beta^+ = u + 2c$  which remains constant along the rarefaction wave. These two quantities are exactly the Riemann invariants and we verify that we have :

$$\begin{cases} \beta_{,t}^- + (u - c)\beta_{,x}^- = 0, \\ \beta_{,t}^+ + (u + c)\beta_{,x}^+ = 0. \end{cases} \quad (3.25)$$

Thus, the classical result concerning the conservation of the Riemann invariants across a rarefaction wave has been recovered.

For the characterization of shock wave, we use the Rankine-Hugoniot relation which is expressed by the following jump relations across the discontinuity  $x = x(t)$  :

$$\Delta(hu) = \dot{x}\Delta(h) \quad \text{and} \quad \Delta(hu^2 + g\frac{h^2}{2}) = \dot{x}\Delta(hu) \quad (3.26)$$

where  $\dot{x}$  is the derivative of  $x$  with respect to time and thus represents the speed of the discontinuity and  $\Delta\Phi = \Phi_+ - \Phi_-$  for an arbitrary variable  $\Phi$  with  $\Phi_+$  and  $\Phi_-$  the respective states at each side of the discontinuity. Algebraic manipulations of these two jump relations in order to eliminate  $\Delta(hu)$  yield the following jump relation between  $\Delta u$  and  $\Delta h$  :

$$\Delta u = \pm \sqrt{\frac{g(h_+ + h_-)}{2h_+h_-}} \Delta h \quad (3.27)$$

From this, the entropy condition enables us to predict the apparition of a shock wave or a rarefaction wave. A rapid investigation of the convexity or the concavity of the associated flux function yields to the characterization of the two genuinely nonlinear waves.

Hence, to connect a state  $\mathbf{U} = (h, u)$  to a state  $\mathbf{U}_l = (h_l, u_l)$  through the  $u - c$  wave, we have the following relations :

$$u = \begin{cases} u_l - 2(\sqrt{gh} - \sqrt{gh_l}) & \text{if } h < h_l, \\ u_l - (h - h_l)\sqrt{g\frac{h + h_l}{2hh_l}} & \text{if } h > h_l. \end{cases} \quad (3.28)$$

A rarefaction wave occurs when  $h < h_l$  and a shock wave occurs when  $h > h_l$ . Similarly, to connect a state  $\mathbf{U} = (h, u)$  to a state  $\mathbf{U}_r = (h_r, u_r)$  through the  $u + c$  wave we have the following relation :

$$u = \begin{cases} u_r + 2(\sqrt{gh} - \sqrt{gh_r}) & \text{if } h < h_r, \\ u_r + (h - h_r)\sqrt{g\frac{h+h_r}{2hh_r}} & \text{if } h > h_r. \end{cases} \quad (3.29)$$

A rarefaction wave occurs when  $h < h_r$  and a shock wave occurs when  $h > h_r$ . To resume, for the  $u - c$  wave, decreasing values of  $h$  with respect to the  $x$  coordinate lead to a rarefaction wave, whereas increasing values of  $h$  generate a shock wave. For the  $u + c$  wave decreasing values of  $h$  lead to a shock wave whereas increasing values generate a rarefaction wave.

*The Riemann problem with a piecewise constant topography.* We are interested here in the computation of the exact solution of the Riemann problem (3.21) with a bottom step. The idea introduced by Greenberg and Leroux is to solve first the regularized Riemann problem obtained when substituting the step by a ramp. The solution for the ramp is obtained by considering all the interactions between shock waves and rarefactions arising from the left and the right side of the considered interface. Then, considering the limit in which the ramp angle increases to  $90^\circ$ , the solution for the step is obtained.

Thus, we consider the case of the following bottom profile :

$$d_\varepsilon = \begin{cases} d_g & \text{for } x \leq 0, \\ d_g - \frac{x}{\varepsilon}(d_g - d_d) & \text{for } 0 \leq x < \varepsilon, \\ d_d & \text{for } x \geq \varepsilon. \end{cases} \quad (3.30)$$

where the states  $(d_g, h_g, u_g)$  and  $(d_d, h_d, u_d)$  are known and  $\varepsilon$  is a positive parameter. The solution is constructed for each value of  $\varepsilon$  and afterwards, we study the limit of vanishing  $\varepsilon$ . This topography is shown on Figure 3.2.1.

We can observe that two Genuinely NonLinear fields also compose the solution of this new Riemann problem, which are the same as in the homogeneous case. Consequently, relation (3.28) and (3.29) are still meaningful and can be used to link the states  $U_L$  and  $U^-$  through the  $u - c$  wave and the states  $U_R$  and  $U^+$  through the  $u + c$  wave. Hence, to connect a state  $\mathbf{U}_l$  to a state  $\mathbf{U}$  through the  $u - c$  wave, we have the following relations :

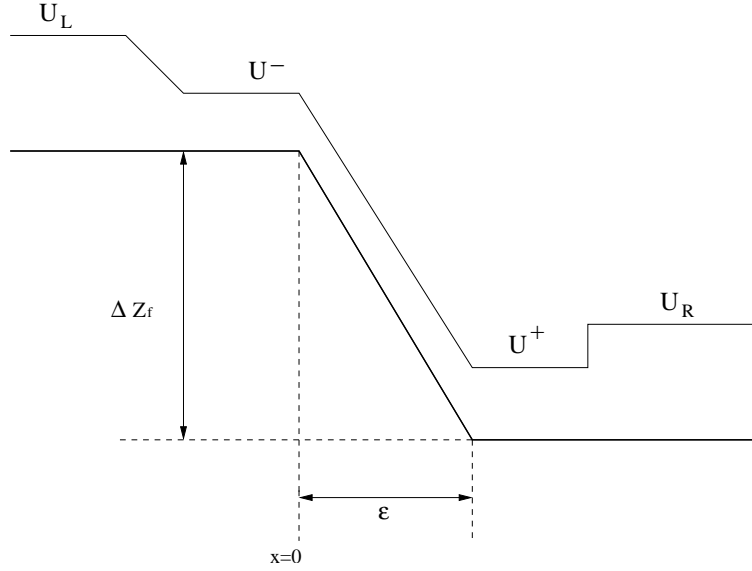


**Figure 3.2.1.** Regularized bed slope for the construction of the Riemann problem solution in the Exact Well-Balanced Riemann solver.

$$\begin{cases} d = d_l, \\ u = \begin{cases} u_l - 2(\sqrt{gh} - \sqrt{gh_l}) & \text{if } h < h_l, \\ u_l - (h - h_l)\sqrt{g\frac{h+h_l}{2hh_l}} & \text{if } h > h_l. \end{cases} \end{cases} \quad (3.31)$$

and to connect a state  $\mathbf{U}$  to a state  $\mathbf{U}_r$  through the  $u + c$  wave we have the following relation :

$$\begin{cases} d = d_r, \\ u = \begin{cases} u_r + 2(\sqrt{gh} - \sqrt{gh_r}) & \text{if } h < h_r, \\ u_r + (h - h_r)\sqrt{g\frac{h+h_r}{2hh_r}} & \text{if } h > h_r. \end{cases} \end{cases} \quad (3.32)$$

Therefore, it only remains to derive relations between the two states  $\mathbf{U}^-$  and  $\mathbf{U}^+$  which are separated by the ramp.

Assuming that the solution is regular, we consider equations (3.22), adding the bed slope source term :

$$\begin{pmatrix} 1 & hu' + u \\ hu' + u & u^2 + 2huu' + gh \end{pmatrix} \cdot \begin{pmatrix} h_{,t} \\ u_{,t} \end{pmatrix} = \begin{pmatrix} 0 \\ -gh(d_r - d_l)/\varepsilon \end{pmatrix} \quad (3.33)$$

Details are not provided here but it can be shown that the associated solution wave is necessary a stationary wave. Thus, when the ramp becomes vertical, it generates

a stationary contact discontinuity. A few additional relations are derived through the stationary wave. First, introducing the quantity  $\psi = \frac{u^2}{2} + g(h + d)$  which is defined at each side of the ramp, it can be proved that through the stationary wave we have conservation of the discharge and of the previously introduced quantity  $\psi$ . Thus, two states  $\mathbf{U}^-$  and  $\mathbf{U}^+$  verify through the stationary wave :

$$\begin{cases} (hu)^- = (hu)^+ \\ \psi^- = \psi^+ \end{cases} \quad (3.34)$$

Finally, it appears that except when a stationary shock wave occurs, the two states at each side of the ramp must be either both subcritical or both supercritical. Therefore, this last relation enables the determination of only one possible solution satisfying all the above requirements. This solution is still reliable when the ramp increases towards a step.

**Remark 3.2.2.** *It is worth mentioning that the quantity  $\psi$  has already been introduced in the characterization of the steady states (3.18). In [57], Gallouët et al. proposed, in the framework of their VFRoe-ncv class of methods, a change of variable involving  $\psi$  which leads to the preservation of the largest class of steady states.*

Gathering these results, the construction of the solver is performed using dichotomy and Newton iterative methods in a complex algorithm which must also take into account all the specific situations that may arise, like for instance the occurrence of stationary shock or sonic rarefaction, the resonance phenomenon when a genuinely nonlinear field is superposed with the stationary contact discontinuity or even the occurrence of dry area which implies the resolution of the Riemann problem (3.21) with a dry state. This complete algorithm is not exposed here but can be found for instance in [151] and [43].

To update the values of  $\mathbf{U}^n$ , instead of computing the interface value needed to evaluate the numerical fluxes across the interface, we may compute the values at each side of the stationary contact discontinuities, denoted by  $\mathbf{U}_{i+\frac{1}{2}}(0-, \mathbf{U}_i, \mathbf{U}_{i+1})$  and  $\mathbf{U}_{i-\frac{1}{2}}(0+, \mathbf{U}_{i-1}, \mathbf{U}_i)$  where  $\mathbf{U}_{i+\frac{1}{2}}(\frac{x}{t}, \mathbf{U}_i, \mathbf{U}_{i+1})$  is the exact solution of the Riemann problem (3.21) provided by the Exact Well-Balanced Riemann solver. The semi-discrete formulation becomes in this context :

$$\frac{d}{dt}\mathbf{U}_i(t) + \frac{1}{\Delta x}(F(\mathbf{U}_{i+\frac{1}{2}}(0-, \mathbf{U}_i, \mathbf{U}_{i+1})) - F(\mathbf{U}_{i-\frac{1}{2}}(0+, \mathbf{U}_{i-1}, \mathbf{U}_i))) = 0 \quad (3.35)$$

Note that the source term only contributes to the computation of the exact solution  $\mathbf{U}_{i+\frac{1}{2}}(\frac{x}{t}, \mathbf{U}_i, \mathbf{U}_{i+1})$  and does not appear explicitly in the expression of the semi-discrete scheme (3.35).

The solver based on this method is extremely robust and accurate. It enables the preservation of all steady states. Numerical benchmarks involving hydraulic jumps

with a supercritical/subcritical smooth transition over a parabolic obstacle and generation or even flooding of dry zones over varying bottom [43] have proved the ability of the solver to deal with dry zones. This solver has been implemented in industrial and hydraulic models.

**3.2.3. The well-balanced VFRoe-ncv scheme.** The resolution of exact Riemann problems at each interface of the mesh can rapidly become a drawback. Furthermore, the Exact Well-Balanced Riemann solver is far more expensive than a usual Godunov method since the computation of the exact solution of the Riemann problem (3.21) is not straightforward and various cases must be analyzed. Actually, when the grid becomes finer, especially for two-dimensional problems, the computational cost becomes a dilemma. To improve this limitation, Gallouët et al. proposed in [57] a class of VFRoe scheme also relying on the Riemann problem with a piecewise constant topography (3.21). As in the homogeneous case, they compute exact solutions  $\mathbf{U}_{i+\frac{1}{2}}^*\left(\frac{x}{t}, \mathbf{U}_i, \mathbf{U}_{i+1}\right)$  of a linearized Riemann problem, instead of directly solving problem (3.21).

Their second idea is to use symmetrizing non-conservative variables. This change of variable entails the preservation of the water depth positivity in the flat case [58] without any clipping treatment (no *a posteriori* numerical treatment needs to be implemented to deal with negative water depth, as in the Roe's original method for example). The VFRoe solver with non-conservative variable is called VFRoe-ncv solver. To emphasize the whole treatment of flux gradient and source term, we will refer to this solver in the sequel as the "well-balanced VFRoe-ncv solver". An homogeneous VFRoe-ncv solver will also be introduced in the next chapter.

*Formalism.* Following [57], we introduce briefly the formalism of the VFRoe-ncv solver for the one-dimensional NSW system which can be divided into three steps :

- First, we write the initial system under a non-conservative form, with the change of variable  $\mathbf{W}(\mathbf{U}) = (d, 2c, u)$  where  $c = \sqrt{gh}$ . The inverse change of variable is denoted  $\mathbf{U}(\mathbf{W})$ . It raises the following new Riemann problem :

$$\left\{ \begin{array}{l} \mathbf{W}_{,t} + C_x(\mathbf{W})\mathbf{W}_{,x} = 0, \\ \mathbf{W}(x,0) = \begin{cases} \mathbf{W}_L = \mathbf{W}(\mathbf{U}_L) & \text{if } x < 0, \\ \mathbf{W}_R = \mathbf{W}(\mathbf{U}_R) & \text{if } x > 0, \end{cases} \end{array} \right. \quad (3.36)$$

where  $C_x(\mathbf{W})$  is called the convection matrix.

- Then, the Riemann problem (3.36) is linearized, averaging the convection matrix. It reads :

$$\left\{ \begin{array}{l} \mathbf{W}_{,t} + C_x(\tilde{\mathbf{W}})\mathbf{W}_{,x} = 0, \\ \mathbf{W}(x, 0) = \begin{cases} \mathbf{W}_L = \mathbf{W}(\mathbf{U}_L) & \text{if } x < 0, \\ \mathbf{W}_R = \mathbf{W}(\mathbf{U}_R) & \text{if } x > 0, \end{cases} \end{array} \right. \quad (3.37)$$

where the averaged convection matrix is defined with  $\tilde{\mathbf{W}} = \frac{\mathbf{W}_L + \mathbf{W}_R}{2}$ .

- Third, we introduce eigenvalues  $(\tilde{\lambda}_k)_{k=1\dots p}$  of the averaged convection matrix  $C_x(\tilde{\mathbf{W}})$  and associated left and right eigenvectors, respectively noted  $(\tilde{\mathbf{l}}_k)_{k=1\dots p}$  and  $(\tilde{\mathbf{r}}_k)_{k=1\dots p}$ . The exact solution of the Riemann problem (3.37) is defined as follows :

$$\begin{aligned} \mathbf{W}^*\left(\left(\frac{x}{t}\right)^-, \mathbf{W}_L, \mathbf{W}_R\right) &= \mathbf{W}_L + \sum_{\frac{x}{t} > \tilde{\lambda}_k} (\tilde{\mathbf{l}}_k \cdot [\mathbf{W}]_L^R) \tilde{\mathbf{r}}_k, \\ \mathbf{W}^*\left(\left(\frac{x}{t}\right)^+, \mathbf{W}_L, \mathbf{W}_R\right) &= \mathbf{W}_R - \sum_{\frac{x}{t} < \tilde{\lambda}_k} (\tilde{\mathbf{l}}_k \cdot [\mathbf{W}]_L^R) \tilde{\mathbf{r}}_k, \end{aligned} \quad (3.38)$$

where  $[\mathbf{W}]_L^R = \mathbf{W}_R - \mathbf{W}_L$ . The exact solution  $\mathbf{W}^*_{i+\frac{1}{2}}\left(\frac{x}{t}, \mathbf{W}_i, \mathbf{W}_{i+1}\right)$  of the linearized Riemann problem (3.37) with  $L = i$  and  $R = i+1$  can be computed using (3.38) and we can thus recover the solution in terms of conservative variable, using the inverse change of variable :

$$\mathbf{U}^*_{i+\frac{1}{2}}\left(\frac{x}{t}, \mathbf{U}_i, \mathbf{U}_{i+1}\right) = \mathbf{U}\left(\mathbf{W}^*_{i+\frac{1}{2}}\left(\frac{x}{t}, \mathbf{W}_i, \mathbf{W}_{i+1}\right)\right). \quad (3.39)$$

Finally, the numerical fluxes are computed using  $\mathbf{F}^*_{i+\frac{1}{2}} = F(\mathbf{U}^*_{i+\frac{1}{2}})$ . The two values  $\mathbf{W}^*\left(\left(\frac{x}{t}\right)^-, \mathbf{W}_L, \mathbf{W}_R\right)$  and  $\mathbf{W}^*\left(\left(\frac{x}{t}\right)^+, \mathbf{W}_L, \mathbf{W}_R\right)$  are equal when  $x/t \neq \tilde{\lambda}_k$ . The cases  $x/t = 0$  which is needed for the computation of the numerical flux corresponds to a discontinuity and as for the exact Riemann solver, we have to compute the values of the solution at each side of the interface, since the solution provides a stationary contact discontinuity located at the interface. These values are then injected into the finite volume formulation (3.35).

Note that this scheme differs from Roe's flux-difference splitting method since Roe's scheme do not take  $\mathbf{F}^*_{i+\frac{1}{2}} = F(\mathbf{U}^*_{i+\frac{1}{2}})$  but relies on a direct approximation of the flux function  $\mathbf{F}^*_{i+\frac{1}{2}}$ , using the averaged values of Roe and the projection on eigenvectors of the averaged Jacobian matrix.

This scheme is easier to implement than the Exact Well-Balanced Riemann solver and provides accuracy for a large number of tests. It has been validated, in its one-dimensional and "second order" accuracy in space and time version, against benchmarks involving a dam-break over dry bed [32], the exact preservation of a flow at rest over a parabolic obstacle, subcritical and transcritical flows over a bump or even the occurrence of dry zone by a double rarefaction wave over a step [57]. This scheme has high bore-capturing abilities [125], is less diffusive than the FSM for problems

involving varying topography [57], and is able to preserve a large class of steady state, depending on the chosen change of variable. Furthermore, the computational cost is far less expensive than for the exact solver (between 10 and 100 times lower).

*Application to the shallow water system with bed slope source term.* Let us introduce the application of this formalism to the special case of the two dimensional NSW equations with bed slope source term, for a practical implementation. We perform the following change of variable  $(h, hu, hv) \rightarrow (2c, u, v)$ . As emphasized in [58], this change of variable leads to a symmetrical convection matrix and enables to handle properly the occurrence of dry areas in the flat bottom case. As shown in [57], the well-balanced VFRoe-ncv scheme also benefits from this good behavior in several cases.

Following the previous idea of Greenberg and Leroux, the topography is described by a piecewise constant function and we add the partial differential equation concerning  $d$ , leading to the Riemann problem with piecewise constant topography (3.21). We obtain :

$$\begin{cases} \partial_t d = 0, \\ \partial_t h + \operatorname{div}(h\mathbf{u}) = 0, \\ \partial_t(h\mathbf{u}) + \operatorname{div}(h\mathbf{u} \otimes \mathbf{u}) + g h \nabla h + g h \nabla d = 0, \\ (d, h, h\mathbf{u})(x, 0) = \begin{cases} (d_L, h_L, (h\mathbf{u})_L) & \text{if } x < 0 \\ (d_R, h_R, (h\mathbf{u})_R) & \text{if } x > 0 \end{cases} \end{cases} \quad (3.40)$$

The change of variables  $\mathbf{W}(\mathbf{U}) = {}^t(d, 2c, u, v)$  leads to :

$$\begin{cases} \partial_t d = 0, \\ \partial_t(2c) + \mathbf{u} \cdot \nabla(2c) + c \operatorname{div}(\mathbf{u}) = 0, \\ \partial_t \mathbf{u} + c \nabla(2c) + (\mathbf{u} \cdot \nabla) \mathbf{u} + g \nabla d = 0, \\ (d, 2c, \mathbf{u})(x, 0) = \begin{cases} (d_L, (2c)_L, \mathbf{u}_L) & \text{if } x < 0 \\ (d_R, (2c)_R, \mathbf{u}_R) & \text{if } x > 0 \end{cases} \end{cases} \quad (3.41)$$

The convection matrix  $B_x(\mathbf{W})$  and  $B_y(\mathbf{W})$  respectively associated with the  $x$  and  $y$  directions are given by :

$$B_x(\mathbf{W}) = \begin{pmatrix} 0 & 0 & 0 & 0 \\ 0 & u & c & 0 \\ g & c & u & 0 \\ 0 & 0 & 0 & u \end{pmatrix} \quad \text{et} \quad B_y(\mathbf{W}) = \begin{pmatrix} 0 & 0 & 0 & 0 \\ 0 & v & 0 & c \\ 0 & 0 & v & 0 \\ g & c & 0 & v \end{pmatrix} \quad (3.42)$$

The eigenvalues respectively associated with  $B_1(\mathbf{W})$  and  $B_2(\mathbf{W})$  are :

$$\lambda_1^x = 0, \quad \lambda_2^x = u - c, \quad \lambda_3^x = u, \quad \lambda_4^x = u + c$$

and

$$\lambda_1^y = 0, \quad \lambda_2^y = v - c, \quad \lambda_3^y = v, \quad \lambda_4^y = v + c$$

Note the occurrence of a zero eigenvalue, which is linked to a stationary contact discontinuity located at the interface  $\frac{x}{t} = 0$ , as in the previous solver where the exact solution is computed. This eigenvalue is linked to the presence of the topography discontinuity and introduces a jump of the numerical flux across it.

Let us introduce  $\Omega_x^R$  and  $\Omega_y^R$ , which stand for the right eigenvectors matrix respectively in the  $x$  and  $y$  directions :

$$\Omega_x^R(\mathbf{W}) = \begin{pmatrix} u^2 - c^2 & 0 & 0 & 0 \\ gc & 1 & 0 & 1 \\ -gu & -1 & 0 & 1 \\ 0 & 0 & 1 & 0 \end{pmatrix} \quad \text{and} \quad \Omega_y^R(\mathbf{W}) = \begin{pmatrix} v^2 - c^2 & 0 & 0 & 0 \\ cg & 1 & 0 & 1 \\ 0 & 0 & 1 & 0 \\ -gv & -1 & 0 & 1 \end{pmatrix}$$

The left eigenvectors matrix  $\Omega_x^L$  and  $\Omega_y^L$  are thus given by :

$$\Omega_x^L(\mathbf{W}) = \frac{1}{2} \begin{pmatrix} \frac{2}{u^2 - c^2} & \frac{g}{(c - u)} & 0 & \frac{g}{(c + u)} \\ 0 & 1 & 0 & 1 \\ 0 & -1 & 0 & 1 \\ 0 & 0 & 2 & 0 \end{pmatrix}$$

and

$$\Omega_y^L(\mathbf{W}) = \frac{1}{2} \begin{pmatrix} \frac{2}{v^2 - c^2} & \frac{g}{(c - v)} & 0 & \frac{g}{(c + v)} \\ 0 & 1 & 0 & 1 \\ 0 & 0 & 2 & 0 \\ 0 & -1 & 0 & 1 \end{pmatrix}$$

Using these eigen-elements and using relations (3.38) we can develop the expressions which link the various possible states through the three possible types of wave associated with the three eigenvalues. We begin with the numerical fluxes in the horizontal  $x$  direction. The solution of the linearized Riemann problem, composed of the two states  $\mathbf{W}^*(0^+, \mathbf{W}_L, \mathbf{W}_R)$  and  $\mathbf{W}^*(0^-, \mathbf{W}_L, \mathbf{W}_R)$  at each side of the stationary contact discontinuity verify :

$$\mathbf{W}(0^+, \mathbf{W}_L, \mathbf{W}_R) = \mathbf{W}(0^-, \mathbf{W}_L, \mathbf{W}_R) + \left( \frac{[d]_L^R}{2(\tilde{u}^2 - \tilde{c}^2)} \right) \begin{pmatrix} \tilde{u}^2 - \tilde{c}^2 \\ \tilde{c}g \\ -g\tilde{u} \\ 0 \end{pmatrix} \quad (3.43)$$

A state  $\mathbf{W}$  is linked to a state  $\mathbf{W}_a$  through the  $u - c$  wave by the relation :

$$\mathbf{W} = \mathbf{W}_a + \left( \frac{g}{2(\tilde{c} - \tilde{u})} [d]_L^R + [c]_L^R - \frac{[u]_L^R}{2} \right) \begin{pmatrix} 0 \\ 1 \\ -1 \\ 0 \end{pmatrix} \quad (3.44)$$

Two states  $\mathbf{W}$  and  $\mathbf{W}_b$  verify through the  $u + c$  wave :

$$\mathbf{W} = \mathbf{W}_b + \left( \frac{g}{2(\tilde{c} + \tilde{u})} [d]_L^R + [c]_L^R + \frac{[u]_L^R}{2} \right) \begin{pmatrix} 0 \\ 1 \\ 1 \\ 0 \end{pmatrix} \quad (3.45)$$

and we have the relation which links two states  $\mathbf{W}$  and  $\mathbf{W}_c$  through the contact discontinuity associated with the  $u$  wave :

$$\mathbf{W} = \mathbf{W}_c + [v]_L^R \begin{pmatrix} 0 \\ 0 \\ 0 \\ 1 \end{pmatrix} \quad (3.46)$$

Similar relationships are deduced for the horizontal fluxes in the  $y$  direction, at the interface defined with  $\frac{y}{t} = 0$ . It yields :

$$\mathbf{W}(0^+, \mathbf{W}_L, \mathbf{W}_R) = \mathbf{W}(0^-, \mathbf{W}_L, \mathbf{W}_R) + \left( \frac{[d]_L^R}{2(\tilde{v}^2 - \tilde{c}^2)} \right) \begin{pmatrix} \tilde{v}^2 - \tilde{c}^2 \\ \tilde{c}g \\ 0 \\ -g\tilde{v} \end{pmatrix} \quad (3.47)$$

through the stationary wave,

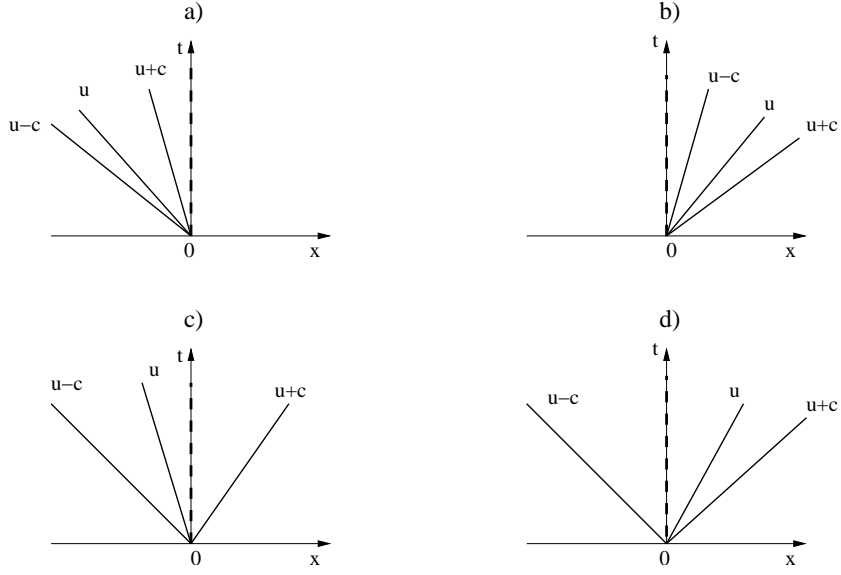


**Figure 3.2.2.** Four possible wave patterns in the solution of the linearized Riemann problem.

$$\mathbf{W} = \mathbf{W}_a + \left( \frac{g}{2(\tilde{c} - \tilde{v})} [d]_L^R + [c]_L^R - \frac{[v]_L^R}{2} \right) \begin{pmatrix} 0 \\ 1 \\ 0 \\ -1 \end{pmatrix} \quad (3.48)$$

through the  $v - c$  wave,

$$\mathbf{W} = \mathbf{W}_b + \left( \frac{g}{2(\tilde{c} + \tilde{v})} [d]_L^R + [c]_L^R + \frac{[v]_L^R}{2} \right) \begin{pmatrix} 0 \\ 1 \\ 0 \\ 1 \end{pmatrix} \quad (3.49)$$

through the  $v + c$  wave and

$$\mathbf{W} = \mathbf{W}_c + [u]_L^R \begin{pmatrix} 0 \\ 0 \\ 1 \\ 0 \end{pmatrix} \quad (3.50)$$

through the contact discontinuity associated to the  $v$  wave.

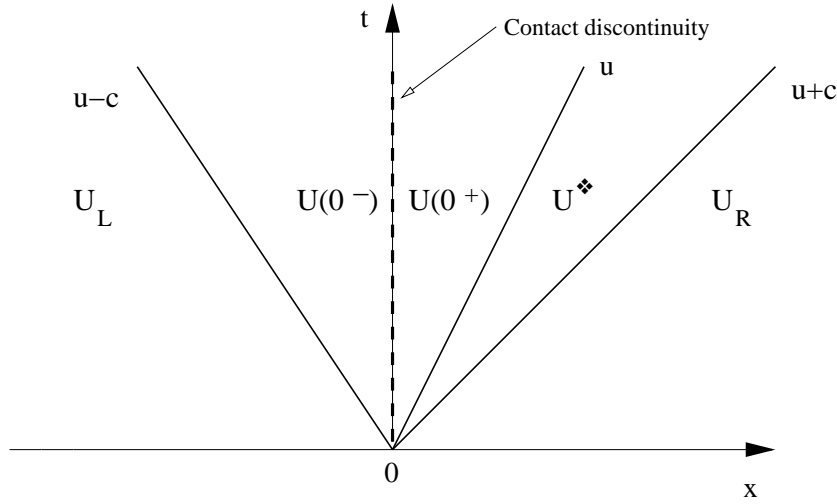


**Figure 3.2.3.** Solution of the linearized Riemann problem in the  $(x, t)$  plan, in the case of a subcritical flow. The stationary contact discontinuity is plotted with a dashed line. The waves associated to the eigenvalues  $u - c$ ,  $u$ ,  $u + c$  are plotted in large solid line.

Using these expressions, we are able to compute the solution of the linearized Riemann problem, for all the possible patterns shown in Figure 3.2.2. For instance, for the case of a subcritical flow in the  $x$  direction, as illustrated on Figure 3.2.3, we aim at finding the values of  $\mathbf{U}(0^-)$  and  $\mathbf{U}(0^+)$  in order to compute the associated numerical fluxes, knowing the values of  $\mathbf{U}_L$  and  $\mathbf{U}_R$ . Therefore, the state  $\mathbf{U}_L$  is linked to  $\mathbf{U}(0^-)$  by relation (3.44) whereas  $\mathbf{U}^*$  is calculated from the state  $\mathbf{U}_R$  using (3.45). It remains to compute the state  $\mathbf{U}(0^+)$  which is linked to  $\mathbf{U}^*$  through the contact discontinuity by relation (3.46).

**Remark 3.2.3.** *It is worth mentioning that if some suitable properties concerning the preservation of the water depth positivity are exposed in [58] for the VFRoe-ncv homogeneous solver with the change of variable  $\mathbf{W}(\mathbf{U}) = (2c, u, v)$  (see the next chapter for details), this is no more the case for the well-balanced VFRoe-ncv scheme, when the topography is varying. However, in practice, the change of variable  $\mathbf{W}(\mathbf{U}) = (d, 2c, u, v)$  for the well-balanced scheme seems to inherit these properties in several cases and can lead to an efficient treatment for the occurrence of dry areas over varying topography, as shown in the “Vacuum occurrence by a double rarefaction wave over a step” test shown in [57]. We will see in the following numerical assessments that it is not always the case.*

**Remark 3.2.4.** *The change of variable  $\mathbf{W}(\mathbf{U}) = (d, 2c, u, v)$  leads to a scheme which is able to maintain steady states at rest (3.19). Another change of variable  $\mathbf{W}(\mathbf{U}) = (d, hu, \psi)$ , where  $\psi = \frac{u^2}{2} + g(h+d)$ , proposed in [57] in the one dimensional framework enables the preservation of all subcritical steady states (3.18) but this change of variable is not invertible.*

**Remark 3.2.5.** Analyzing relation (3.43), it appears that the discharge computed through the stationary contact discontinuities is discontinuous. Hence, the scheme is no more conservative and following [57], a new finite volume approximation is introduced for the computation of the flow in the water depth's conservation equation, which enables to recover the conservativity. For the sake of simplicity, this new approximation is introduced in the one-dimensional case, the generalization to the two dimensional case being straightforward :

$$h_i^{n+1} = h_i^n - \frac{\Delta t}{\Delta x} \left( \frac{((hu)_{i+\frac{1}{2}}^+ + (hu)_{i+\frac{1}{2}}^-)}{2} - \frac{((hu)_{i-\frac{1}{2}}^+ + (hu)_{i-\frac{1}{2}}^-)}{2} \right) \quad (3.51)$$

**Remark 3.2.6.** As for the VFRoe scheme, the VFRoe-ncv solver can produce non-physical weak solutions in the special case of the occurrence of a sonic rarefaction wave which crosses the interface. Therefore a sonic entropy correction must be added in order to converge towards the relevant physical solution, that is the solution which verifies the entropy condition. These special cases occur when either

$$u_L - c_L < 0 \quad \text{and} \quad u_R - c_R > 0 \quad (3.52)$$

for a  $u - c$  sonic rarefaction or when

$$u_L + c_L < 0 \quad \text{and} \quad u_R + c_R > 0 \quad (3.53)$$

for a  $u + c$  sonic rarefaction. In order to fix this problem, we have introduced an intermediate state  $\mathbf{W}_m$  which ensures that the scheme is still consistency, following the correction proposed in [125] and adapting this idea to the VFRoe-ncv scheme with topography. Then, the states at each side of the discontinuities are set equal to  $\mathbf{W}_m$  if one of the condition (3.52) and (3.53) is verified. In practice this entropy fix gives good results.

**Remark 3.2.7.** When the topography is not flat, we can observe from expression (3.43) that in the case of vanishing  $u - c$  or  $u + c$  eigenvalues, the numerical flux can take infinite values. In practice this situation is not usual but when these eigenvalues take very small values, this appears as an obvious limitation of the method. In the next section, for the numerical assessments for moving shoreline problems, we exhibit a test for which this limitation can generate large instabilities.

### 3.3. Numerical considerations

**3.3.1. Boundary conditions.** For the first validations of these first order accuracy schemes we have implemented three different boundary conditions, which are first order accurate. Classically, fictitious cells are introduced around the computational domain in order to define values at the boundaries (see Figure 3.3.1). The interface fluxes through the external boundaries of the computational domain are thus computed using the states imposed in the fictitious cells, defining a well-posed boundary Riemann problems.

It leads to the following boundary conditions :

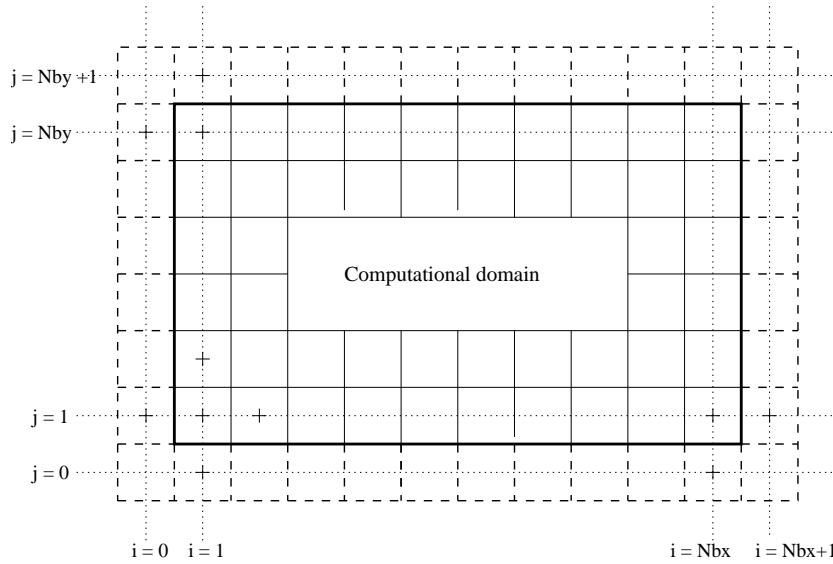


**Figure 3.3.1.** Sketch of the computational domain with the surrounding fictitious cells

*Non-slip reflective solid boundary condition.* The non-slip boundary condition aims at modeling the presence of a solid wall. The fixed non-slip and reflective boundary condition is given by :

$$h_{N+1} = h_N, \quad u'_{N+1} = -u'_N, \quad v'_{N+1} = -v'_N \quad (3.54)$$

where  $N$  denotes the last cell inside the computational domain,  $N + 1$  the fictitious cell outside of the computational domain and  $u'$  and  $v'$  are the component of velocity  $\mathbf{u}$  respectively normal and tangential to the boundary.

*Transmissive boundary condition.* This boundary condition corresponds to the Neumann boundary condition in the framework of finite difference methods. The fictitious cells are overwritten with the solution values in the cells of the computational domain along the boundary. It provides a simple absorbing boundary condition, efficient for outflows configurations. Therefore, transmissive boundary conditions also called “transparent boundaries” are specified with :

$$h_{N+1} = h_N, \quad u'_{N+1} = u'_N, \quad v'_{N+1} = v'_N \quad (3.55)$$

with the same notations.

*Inlet generating boundary condition.* For the study of some hydraulic phenomena we need for instance to force the value of the water depth at a specific boundary, where incoming flows are observed. In other problems, we need to specify the discharge at the outflow boundary. More generally, the kind of boundary conditions that must be applied at the inflow and outflow boundaries when we want to obtain a well-posed problem are well-known and mainly depend on the nature of the flows, subcritical or supercritical. For supercritical flows, we must specify both wave profile and currents at the inflow boundary whereas no information is needed at the outflow boundary. For subcritical flows, only one information is required at inflow and outflow boundaries.

The second information may be computed using characteristic theory and the conservation of the Riemann invariants. In the special case of transcritical flows, which appears in some hydraulic problems, the boundary condition may be adaptive and must produce the corresponding number of information. This kind of boundary conditions can be derived from relations (3.28) and (3.29), considering the special case of Riemann problems with a dry state and depending on the occurrence of a rarefaction or a shock wave. The effective implementation requires the use of Newton-Raphson procedures in order to solve analytically these Riemann problems with a dry state. The eventually time-dependent nature of the flow (subcritical or supercritical) can be tested with the evaluation of the Froude number at the considered boundary and this leads to an adaptive boundary condition which is able to cope with the various configurations. Since our goal is not to reproduce here the whole set of hydraulic benchmarks which has been extensively used in order to validate the previously introduced well-balanced methods (see [43], [57]), we won't focus here on the description of such specific boundary conditions, even if in practice we have effectively implemented them in order to allow a complete assessment of our numerical implementations. We refer the reader to [103] or [151] for a more detailed description of these boundary conditions.

We only focus here on the description of a simple generating boundary condition for subcritical flows, which allows us to force the value of the water surface profile at the inflow boundary and generates the motion. The corresponding value of the velocity at the inflow boundary is computed using the characteristic theory and the conservation of the Riemann invariants. This choice is mainly motivated by the fact that such a condition is needed in most of the cases that will be studied in the third part of this study. In this third part, nearshore hydrodynamic will be investigated and for this purpose, we need to generate water waves at the seaward boundary, the other boundaries being often transparent or periodic.

Assuming that the flow is subcritical at the boundary and that values of the solution are known at time  $t^n$ , we impose the value of water depth  $h^{n+1}$  at time  $t^{n+1}$  at the fictitious boundary cell, where  $h^{n+1} = h_0 + \eta_i^{n+1}$  with  $h_0$  the still water depth and  $\eta_i$  the amplitude of the forced incident wave. Our goal is then to compute the corresponding value of the velocity  $u'^{n+1}$ , where  $u'$  is the component of velocity normal to the boundary. The outgoing Riemann invariant  $\beta^- = u' - 2c$  is constant along the line  $C^-$  defined with  $\frac{dx}{dt} = u' - c$  and  $c = \sqrt{gh}$ . Therefore, the unknown velocity  $u'$  can be calculated (see Figure 3.3.2). The initial location of point  $R$ , which stands for the location of the outgoing characteristic at time  $t^n$ , is not known a priori. This location is obtained by integrating the following characteristic trajectory :

$$\frac{d\beta^-}{dt} = S \quad \text{along} \quad \frac{dx}{dt} = u - c. \quad (3.56)$$

where  $S$  accounts for the bed-slope. It leads the following equation for  $d_R$  :

$$d_R = (u'^n - c^n) \Delta t + S \Delta t \quad (3.57)$$

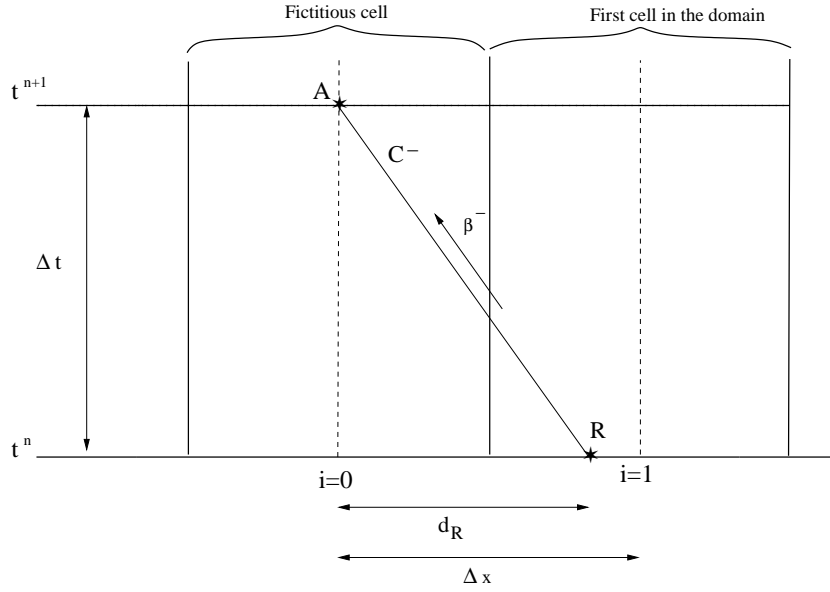


**Figure 3.3.2.** Sketch of the derivation of the inlet generating boundary condition

where  $u'^n$  and  $c^n$  are interpolated between the fictitious boundary cell and the first interior cell of the last time step. This yields an implicit equation which can be solved easily with Newton-Raphson method. Once the location of point  $R$  is found, the velocity  $u'^{n+1}$  can be obtained by :

$$u'^{n+1} = \beta^- + 2c^{n+1} + S\Delta t \quad (3.58)$$

where  $c^{n+1} = \sqrt{gh^{n+1}}$ .

**Remark 3.3.1.** *This approach can be also applied when the discharge is imposed at the inflow boundary. In such situation, the water surface profile at the boundary becomes the unknown. The extension to outflow boundaries, using the Riemann invariant  $\beta^+$  is straightforward.*

**Remark 3.3.2.** *In this approach we have neglected the possible reflected waves which may be generated if the bed-slope is steep or if the non-slip reflective solid boundary condition is applied at the outflow boundary. Therefore, this boundary condition should be applied when a physical set of data, which takes into accounts both incident and reflected waves, is used to force the motion or when we can reasonably assume that no consequent reflected waves are generated. An extension which enables to deal with reflected waves, allowing them to exit the computational domain with very small reflection is introduced in the next chapter.*

**3.3.2. Numerical treatment for the shoreline.** We emphasize here that no special clipping treatment is used (i.e. we don't artificially set to zero non-physical negative values of the water depth). In addition, no special tracking method is used to compute the position of the shoreline and only the direct computation of flow

properties is used.

As specified in the second section for the Exact Well-Balanced Riemann Solver, we introduce a distinction between wet and dry cells. In dry cells, the water depth  $h$  is less than a specified threshold value  $h_{min}$ , which can be a very small number. For such cells, the water depth is forced to be  $h_{min}$ , since  $h_{min}$  may be seen as the numerical definition of the zero water depth, and the velocity is set to zero. Then, we compute the shoreline by solving Riemann problems at the interfaces between wet and dry cells, which generates no further difficulties. During the computation of the new flows properties at the next time step by resolving Riemann problems on flat bottoms, no distinctions are made between wet and dry cells since the VFRoe-ncv solver is robust enough to deal with the three possible configurations (wet/wet, wet/dry and dry/dry). In practice, we have defined  $h_{min} = 10^{-20} m$ . This value has been used for all the test cases presented in the next section. We emphasize that the two schemes, namely the Exact Well-Balanced and the well-balanced VFRoe-ncv solvers, are sensitive to the definition of this value: a change of the value  $h_{min}$  can slightly modify the results in some special situations.

**3.3.3. Numerical stability.** Explicit schemes are far more easy to implement than implicit schemes, which require the resolution of large systems of equations at each time step. But the counterpart is that they need a careful selection of the time step to fulfill stability requirements. Thus, the time step needs to be restricted in such a way that no interaction is possible between waves from different cells during each time step. This restriction can result in expensive computations. Courant, Friedrichs and Lewy [49] defined a stability criterion for fully explicit schemes given by  $CFL < 1$  where  $CFL$  is known as the Courant number. Different authors propose different definitions for this number, leading to different time step restrictions. We choose here to define the time step as follows :

$$\Delta t \leq CFL \frac{\min(\Delta x, \Delta y)}{\max_{i,j}(|\mathbf{u}_{i,j}| + c_{i,j})} \quad (3.59)$$

where  $c = \sqrt{gh}$ . The maximum is evaluated over all the possible values of  $(i, j)$  in the computational domain. For each studied case, a numerical analysis relying on this stability criterion enables us to choose the maximum time step which prevents us from the occurrence of noise in the numerical solution.

## 3.4. Numerical assessments

This section is devoted to the numerical validation against several classical test cases. We have implemented the two previously detailed solvers, namely the Exact Well-Balanced solver and the well-balanced VFRoe-ncv solver in a Godunov-like scheme, in a two dimensional framework and first order accuracy original version. Three tests are performed here : the classical one-dimensional dam-break over a dry bed, the preservation of a steady state at rest and a classical test for moving shoreline problems. These tests are presented to assess the ability of our model to compute propagating fronts, to deal with the occurrence of dry area, to preserve discrete steady states and to

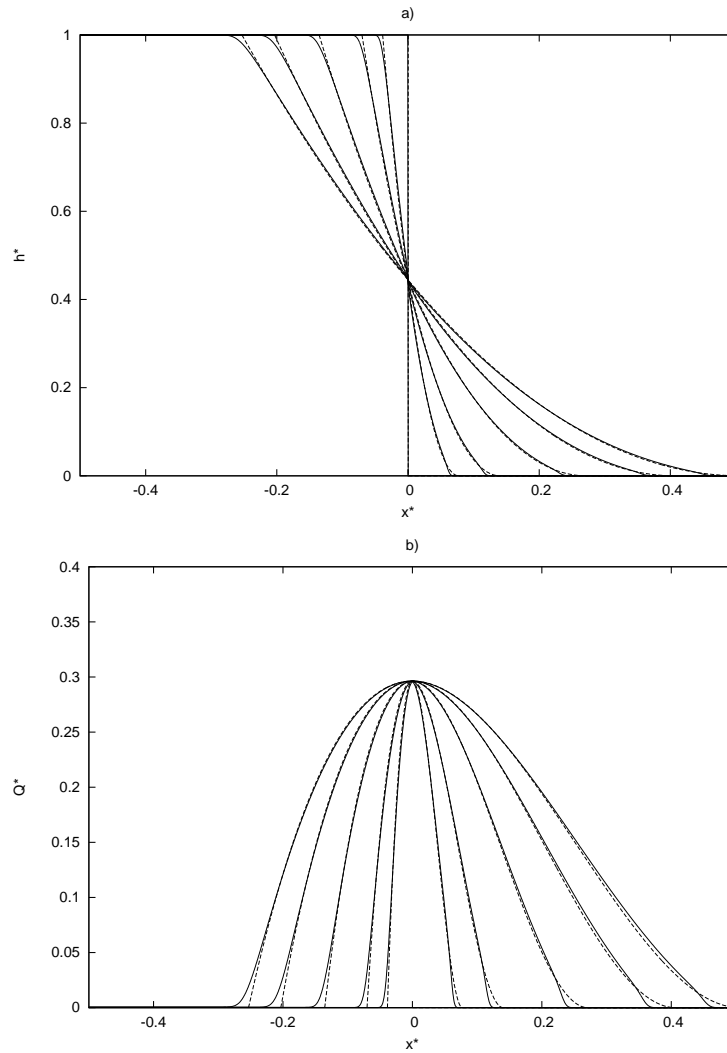


**Figure 3.4.1.** The dam-break problem on a flat bottom for  $h_0^* = 1$ . Comparison between numerical results for both two well-balanced solver (solid lines) and analytical solution (dotted lines) for a) the water height  $h^*$  and b) the discharge  $Q^* = (hu)^*$  at different times  $t^* = 0.0$ ,  $t^* = 0.03$ ,  $t^* = 0.07$ ,  $t^* = 0.14$ ,  $t^* = 0.21$  and  $t^* = 0.26$ .

accurately capture moving shoreline. Besides, a large set of hydraulic benchmarks have been performed to assess our own implementation : subcritical flow, transcritical flow with shock and supercritical flow over a bump, drain on a non-flat bottom, vacuum occurrence by a double rarefaction wave over a step, flow in stairs or even flooding of initially dry area. Most of these tests have already been performed in [59] for the VFRoe-ncv scheme or in [43] for the Exact Well-Balanced scheme. Thus we don't show these results here.

**3.4.1. The one-dimensional dam-break problem.** We study here the evolution of an idealized one-dimensional dam-break problem on a flat bottom. The

VFRoe-ncv scheme has already been validated in its second order accuracy version against this useful test case in [57]. A dam is initially located in the middle of the domain and the initial flow condition is given as a mound of water at rest of height  $h_0$  upstream the dam and a dry zone downstream. The dam is removed instantaneously at  $t = 0$ . It raises a simple super-critical rarefaction wave. We have the classical Ritter's solution [161] which reads in dimensionless form :

$$h^* = \frac{1}{9} \left[ 2 - \frac{x^*}{t^*} \right]^2, \quad u^* = \frac{2}{3} \left[ \frac{x^*}{t^*} + 1 \right]. \quad (3.60)$$

We use the scales  $h_0$ ,  $c_0 = \sqrt{gh_0}$  and  $t_0 = c_0/g$  in order to obtain respectively non-dimensionalized length, velocity and time. Values of  $\Delta x^* = 0.01$  and  $CFL = 0.9$  have been used for this test.

It is worth noting that the results provided by the two well-balanced solvers are similar, with a double computational time for the Exact Well-Balanced solver. We can observe on Figure 3.4.1 a quite good agreement between the analytical solution and numerical results provided by the two solvers. The front is accurately captured with a little discrepancy. The two schemes seem to be much diffusive, owing to the first order accuracy. As it has been emphasized in [57], the speed of convergence of the VFRoe-ncv scheme is the same as the one provided by Godunov's scheme with a less expensive computational cost. These results can be considerably improved with a second order extension, using a MUSCL reconstruction. This method is detailed in chapter 4.

**3.4.2. Preservation of a steady state at rest.** The initial condition of this test is a flow at rest. The topography is an arbitrary sloping beach, along the whole domain which is constituted of a  $10m$  long channel. We impose  $h + d = \max(d, 0.18)$  and  $\mathbf{u} = 0$  as an initial condition on the whole domain. As expected both VFRoe-ncv and Exact Well-Balanced solver preserve exactly this steady state, even for large values of time. The fractional step method is unable to maintain such steady states and oscillations are generated at the shoreline, since the slope of topography induces small convection.

The velocity remains zero for both well-balanced schemes whereas large oscillations are observable near the shoreline for FSM. It appears with this test that the use of a well-balanced method is fundamental for problems involving initially fixed shoreline which is perturbed after a short time by an incoming wave. This is a commonly observed situation in nearshore hydrodynamics, where waves are propagating from the seaward boundary towards the shoreline. These problems are addressed in the third part of this study.

**3.4.3. A numerical test for moving shoreline problem.** Considering the good behavior of this two solvers, they seem to be well-suited for the study of nearshore flows over varying bottom and we investigate here their application to moving shoreline problems. Hence, they have been tested against an analytical benchmark for run-up simulations, namely the Carrier and Greenspan's periodic solution [35]. A detailed description of this test case is given in the next chapter and we only say here that this solution represents a monochromatic wave which is let run-up and run-down on

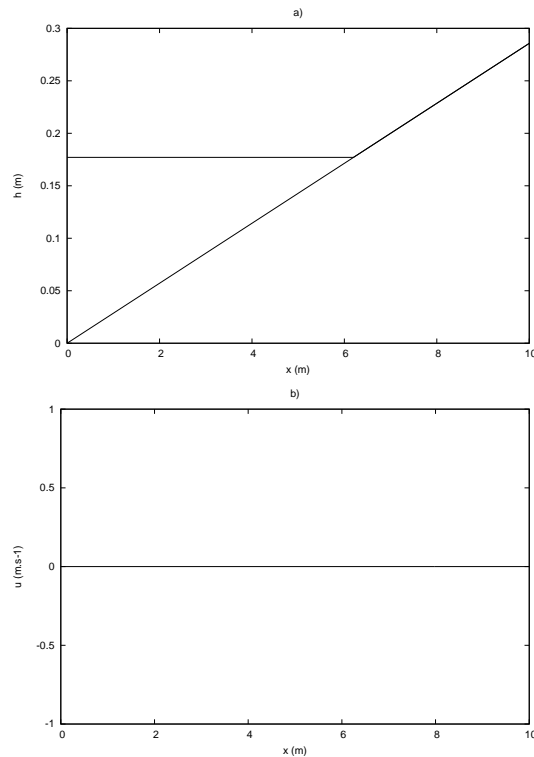


**Figure 3.4.2.** Preservation of a steady state at rest. Numerical results for both Exact Well-Balanced Riemann solver and well-balanced VFRoe-ncv solver: a) the water depth and b) the velocity are plotted versus the  $x$  coordinate for  $t = 500$  s.

a plane beach. It is a classical benchmark used to assess for the ability of numerical model to deal with moving shoreline.

In Figure 3.4.4 we can observe the comparison between the numerical results provided by the Exact Well-Balanced Riemann solver and the analytical solution for different time values during the first half period of the evolution. An inaccuracy in the computation of the shoreline becomes obvious after a short time. The use of a finer grid does not enable us to improve this. Actually, it appears from numerical investigations that if tests involving steep beach slopes may be successfully computed, the use of slowly varying bottom can lead to non-physical solutions. Nonetheless, we must emphasize the extreme robustness of this solver, since we have been able to compute this solution for a large number of period without any amplification of these small perturbations. We must also notice that this Exact Well-Balanced Riemann solver has appeared to be extremely sensitive to the threshold value  $h_{min}$ , since large instabilities can be generated if this value is greater than  $10^{-6}$  m.

Concerning the well-balanced VFRoe-ncv solver we can see on Figure 3.4.5 little spurious oscillations which propagate from the initial position of the shoreline. With the use of a refined grid near the shoreline, we are able to compute an accurate solution during one complete period. For larger values of time, distortions become too important. These non-physical oscillations may be justified by the fact that this scheme is

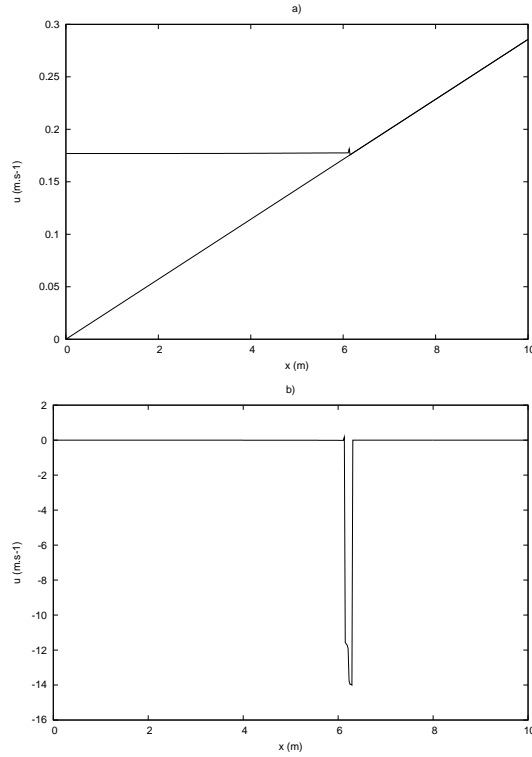


**Figure 3.4.3.** Preservation of a steady state at rest. Numerical results for the fractional step method: a) the water depth and b) the velocity are plotted versus the  $x$  coordinate for  $t = 500$  s.

not defined in the particular case of vanishing eigenvalues  $\tilde{\lambda}_k$  [57], as exposed in the previous section. In this particular context, the associated Froude number is equal to unity and we can verify with the help of the analytical solution that this situation can effectively occur two times during a period. Another possible explanation may be the fact that if the VFRoe-ncv solver on flat bottom with the symmetrizing change of variable is “positivity preserving”, this property is not rigorously extended to the well-balanced version with topography, even if several numerical cases involving wetting and drying processes over varying bottom have been accurately computed in [57].

It appears from these numerical investigations that even if these two well-balanced schemes have been proved to be accurate and robust in several cases involving wetting and drying processes over varying topography, they fail to provide accurate results for moving shoreline problems. The use of adaptive refinement methods or even numerical filters [152] may help to improve them and to smooth the non-physical oscillations. However, these two solvers definitively fail when we try to validate them against two-dimensional benchmarks on Cartesian meshes. That’s why we present in the next section a new model which combines the “positivity preserving” property of the VFRoe-ncv solver on flat bottom and the well-balanced properties provided by the recent reconstruction method introduced in [3].

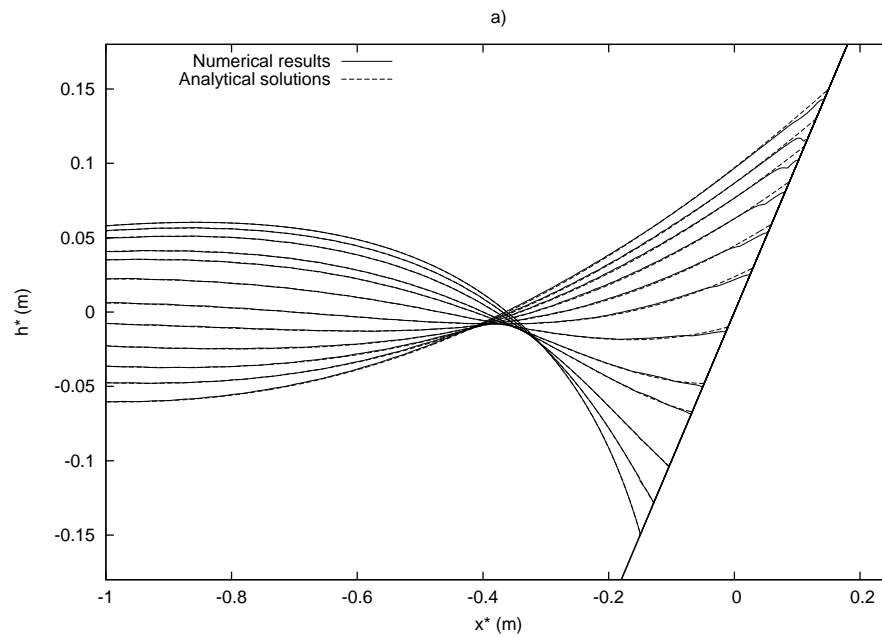


**Figure 3.4.4.** The Carrier and Greenspan's periodic wave solution. Comparison between numerical (solid lines) and analytical (dashed lines) results. Profiles of dimensionless water surface elevation  $h^*$  are plotted versus the onshore dimensionless coordinate  $x^*$  for the Exact Well-Balanced Riemann solver.

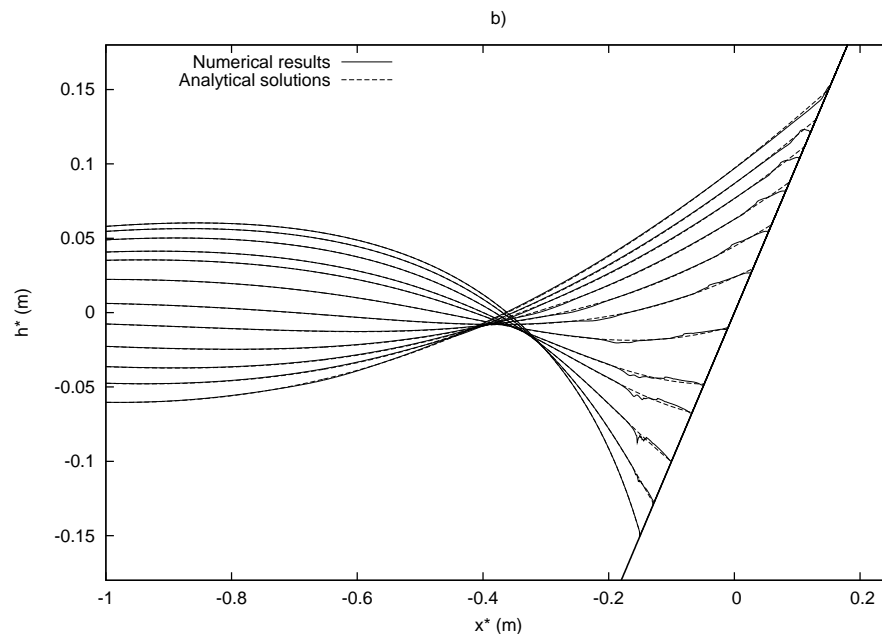


**Figure 3.4.5.** The Carrier and Greenspan's periodic wave solution. Comparison between numerical (solid lines) and analytical (dashed lines) results. Profiles of dimensionless water surface elevation  $h^*$  are plotted versus the onshore dimensionless coordinate  $x^*$  for the VFroe-ncv solver.

# Improvement of the accuracy at the shoreline

## 4.1. The hydrostatic reconstruction method

This chapter is devoted to the introduction of a two-dimensional “second order” bore-capturing and positivity preserving well-balanced model suitable for the computation of moving shoreline problems.

We propose here to use the recent “hydrostatic reconstruction” method introduced by Audusse et al. in [3] in order to achieve well-balanced properties and to improve the inaccuracies observed with the previous methods. This method has been validated in [3] with a classical test case involving bore (a constant discharge transcritical flow with shock over a bump) and with a quasi-stationary case first proposed by Leveque in [107] which consists in computing small perturbations around a steady state at rest on varying topography. Actually, as the NSW equations is initially derived with the hydrostatic approximation, the name “hydrostatic reconstruction” has no really physical meaning and stands for the fact that this reconstruction is performed from the study of nearly static flows (i.e. flows with very small Froude number). Note that this method has been recently generalized for two-dimensional simulations on unstructured meshes in [4]. Whereas the original method was combined with a kinetic homogeneous positivity preserving solver, we choose here to use the VFRoe-ncv solver for homogeneous system. As introduced in the previous section, this solver is able to deal with the occurrence of dry zone [58]. Furthermore, this solver is robust and more easier to implement than the kinetic scheme. The reconstruction method of Audusse et al. and the well-balanced discretization of the source term are also simple and efficient ways to obtain preservation properties for steady states “at rest”. In this

chapter we describe briefly the VFRoe-ncv solver for homogeneous system for the two-dimensional NSW equations and we recall how we can obtain a well-balanced scheme with the reconstruction method proposed in [3]. Then we describe a “second order” MUSCL reconstruction and second order accuracy suitable boundary conditions. This chapter ends with extensive numerical assessments in the one and two dimensional case, especially for moving shoreline problems.

## 4.2. The homogeneous “positivity preserving” VFRoe-ncv solver

We give here a description of the numerical method used for the computation of  $\mathbf{F}_{i\pm\frac{1}{2},j}^*$  and  $\mathbf{G}_{i,j\pm\frac{1}{2}}^*$ . The computation of the  $\mathbf{F}_{i\pm\frac{1}{2},j}^*$  fluxes is developed in details, the extension for the  $\mathbf{G}_{i,j\pm\frac{1}{2}}^*$  fluxes is straightforward. As exposed in [58], the symmetrizing change of variable  $\mathbf{W}(\mathbf{U}) = (2c, u, v)$ , where  $c = \sqrt{gh}$ , enables us to obtain a property concerning the positivity of the water depth. Actually, it can be proved that this choice of variables leads to positive values of  $h$  at each side of the considered interface, for each Riemann problem. This property does not imply *a priori* that the computed averaged cell’s values remain also positive. Yet, in practice, we have never encountered any situations leading to negative values of the water depth and this scheme seems to be far more reliable for such problems than the classical Roe scheme. Therefore, in the following, this property of the  $(2c, u, v)$ -VFRoe-ncv scheme will be regarded as a positivity preserving property, even if it cannot be proved in the same satisfying way as for the Godunov or the kinetic schemes.

The solver described here is actually a simplified form of the well-balanced VFRoe-ncv solver described in the previous chapter, since the topography has not been taken into account. However the formalism is similar. Departing from the following Riemann problem in conservative variables :

$$\left\{ \begin{array}{l} \partial_t h + \operatorname{div}(h\mathbf{u}) = 0, \\ \partial_t(h\mathbf{u}) + \operatorname{div}(h\mathbf{u} \otimes \mathbf{u}) + gh\nabla h = 0, \\ (h, h\mathbf{u})(x, 0) = \begin{cases} (h_L, (h\mathbf{u})_L) & \text{if } x < 0 \\ (h_R, (h\mathbf{u})_R) & \text{if } x > 0 \end{cases} \end{array} \right. \quad (4.1)$$

we obtain the following Riemann problem in non-conservative variables, at each interface :

$$\left\{ \begin{array}{l} \partial_t(2c) + \mathbf{u} \cdot \nabla(2c) + c\operatorname{div}(\mathbf{u}) = 0, \\ \partial_t\mathbf{u} + c\nabla(2c) + (\mathbf{u} \cdot \nabla)\mathbf{u} = 0, \\ (2c, \mathbf{u})(x, 0) = \begin{cases} ((2c)_L, \mathbf{u}_L) & \text{if } x < 0 \\ ((2c)_R, \mathbf{u}_R) & \text{if } x > 0 \end{cases} \end{array} \right. \quad (4.2)$$

This system can be written in the following matrix form :

$$\mathbf{W}_{,t} + C_x(\mathbf{W})\mathbf{W}_{,x} + C_y(\mathbf{W})\mathbf{W}_{,y} = 0, \quad (4.3)$$

$$C_x(\mathbf{W}) = \begin{pmatrix} u & c & 0 \\ c & u & 0 \\ 0 & 0 & u \end{pmatrix} \quad \text{and} \quad C_y(\mathbf{W}) = \begin{pmatrix} v & 0 & c \\ 0 & v & 0 \\ c & 0 & v \end{pmatrix}, \quad (4.4)$$

where  $C_x(\mathbf{W})$  and  $C_y(\mathbf{W})$  are the symmetric convection matrix respectively in the  $x$  and  $y$  direction.

The Riemann problem (3.36) becomes, with this choice of symmetrizing variables :

$$\begin{cases} \mathbf{W}_{,t} + C_x(\mathbf{W})\mathbf{W}_{,x} = 0, \\ \mathbf{W}(x, 0) = \begin{cases} ((2c)_L, u_L, v_L) & \text{if } x < 0 \\ ((2c)_R, u_R, v_R) & \text{if } x > 0. \end{cases} \end{cases} \quad (4.5)$$

This Riemann problem is then linearized around the averaged value  $\tilde{\mathbf{W}} = \frac{\mathbf{W}_L + \mathbf{W}_R}{2}$ .

The eigenvalues of the linearized convection matrix  $C_x(\tilde{\mathbf{W}})$  are

$$\tilde{\lambda}_1 = \tilde{u} - \tilde{c}, \quad \tilde{\lambda}_2 = \tilde{u}, \quad \tilde{\lambda}_3 = \tilde{u} + \tilde{c},$$

where  $c = \sqrt{gh}$ . If we denote by  $\Omega_R$  and  $\Omega_L$  respectively the matrix of right and left eigenvectors associated with these averaged eigenvalues, we may write :

$$\Omega^R = \begin{pmatrix} 1 & 0 & 1 \\ -1 & 0 & 1 \\ 0 & 1 & 0 \end{pmatrix} \quad \text{and} \quad \Omega^L = \begin{pmatrix} \frac{1}{2} & 0 & \frac{1}{2} \\ -\frac{1}{2} & 0 & \frac{1}{2} \\ 0 & 1 & 0 \end{pmatrix}.$$

Then, using Equation(3.38), the relation between a state  $\mathbf{W}$  and a state  $\mathbf{W}_a$  through the  $\tilde{u} - \tilde{c}$  wave may be written :

$$\mathbf{W} = \mathbf{W}_a + \left( [c]_L^R - \frac{[u]_L^R}{2} \right) \begin{pmatrix} 1 \\ -1 \\ 0 \end{pmatrix}, \quad (4.6)$$

the relation to connect a state  $\mathbf{W}$  to a state  $\mathbf{W}_b$  through the  $\tilde{u} + \tilde{c}$  wave is given by :

$$\mathbf{W} = \mathbf{W}_b + \left( [c]_L^R + \frac{[u]_L^R}{2} \right) \begin{pmatrix} 1 \\ 1 \\ 0 \end{pmatrix}, \quad (4.7)$$

and the relation between two states  $\mathbf{W}$  and  $\mathbf{W}_c$  through the contact-discontinuity associated with the  $\tilde{u}$  wave is :

$$\mathbf{W} = \mathbf{W}_c + [v]_L^R \begin{pmatrix} 0 \\ 0 \\ 1 \end{pmatrix}. \quad (4.8)$$

From a practical point of view, using these relations, the exact solution of the linearized Riemann problem (3.37) which is needed for the implementation of the VFRoe-ncv solver is given by the sign of the eigenvalues  $\tilde{\lambda}_k$ . Actually, only two cases are distinguished :

- If  $\tilde{\lambda}_1 > 0$  or  $\tilde{\lambda}_3 < 0$ , then the flow is super-critical and we recover a classical upwinding. The interface value is defined as follows :

$$\mathbf{W}_{i+\frac{1}{2},j}^* = \begin{cases} \mathbf{W}_i & \text{if } \tilde{\lambda}_k > 0 \forall k \\ \mathbf{W}_{i+1} & \text{if } \tilde{\lambda}_k < 0 \forall k. \end{cases} \quad (4.9)$$

- If  $\tilde{\lambda}_1 < 0$  and  $\tilde{\lambda}_3 > 0$  then the flow is subcritical and we use relations (4.6) or (4.7) to obtain the interface values. We obtain :

$$c_{i+\frac{1}{2},j}^* = \tilde{c} - \frac{1}{4}(u_{i+1,j} - u_{i,j}), \quad (4.10)$$

and

$$u_{i+\frac{1}{2},j}^* = \tilde{u} - (c_{i+1,j} - c_{i,j}). \quad (4.11)$$

The value of  $v_{i+\frac{1}{2},j}^*$  is obtained from the sign of  $\tilde{\lambda}_2$ , using the relation (4.8). For  $\tilde{\lambda}_2 > 0$  we take  $v_{i+\frac{1}{2},j}^* = v_i$  whereas for  $\tilde{\lambda}_2 < 0$  we may choose  $v_{i+\frac{1}{2},j}^* = v_{i+1}$ . We can finally recover conservative variables, using the inverse change of variable and then compute the numerical fluxes  $\mathbf{F}_{i+\frac{1}{2},j}^*$ .

Similar expressions result for  $\mathbf{F}_{i-\frac{1}{2},j}^*$  and  $\mathbf{G}_{i,j\pm\frac{1}{2}}^*$ . For the  $\mathbf{G}_{i,j\pm\frac{1}{2}}^*$  fluxes, the eigen-elements  $(\tilde{\lambda}_k)_{k=1,2,3}$ ,  $(\tilde{\mathbf{l}}_k)_{k=1,2,3}$  and  $(\tilde{\mathbf{r}}_k)_{k=1,2,3}$  are related to the averaged convection matrix  $C_y(\tilde{\mathbf{W}})$ . We have obtained a fast solver, easy to implement, with bore-capturing abilities and able to deal with dry zone without any "clipping" treatment.

**Remark 4.2.1.** *Remark that we have also implemented an Exact Riemann solver relying on the resolution of relations (3.28) and (3.29) for the rarefaction and shock waves, with newton-Raphson method. We have observed that the computational time was between five and ten times greater than with the linearized scheme, without any significant improvement of the results.*

### 4.3. Discretization of the source term

In this section we briefly recall how to obtain a well-balanced scheme satisfying the preservation of steady states at rest using the reconstruction method proposed in [3]. This method is compatible with the VFRoe-ncv solver on flat bottom exposed in the previous section and thus, also ensures the positivity of the water depth.

The first step is to build an effective reconstruction of the values on each side of the mesh interfaces, taking into account the variations of the bottom and the balance obtained for flows with very small Froude number, which are considered as “static” flows. We define interface topography values  $d_{i+\frac{1}{2},j}$  as follows :

$$d_{i+\frac{1}{2},j} = \max(d_{i,j}, d_{i+1,j}) \quad (4.12)$$

Then, the reconstruction of the water height on each side of the considered interface, which must be positivity preserving, is defined as follows :

$$h_{i+\frac{1}{2}-,j} = \max(0, h_{i,j} + d_{i,j} - d_{i+\frac{1}{2},j}), \quad h_{i+\frac{1}{2}+,j} = \max(0, h_{i+1,j} + d_{i+1,j} - d_{i+\frac{1}{2},j}) \quad (4.13)$$

and we deduce from it the complete reconstructed values on each side of the interface :

$$\mathbf{U}_{i+\frac{1}{2}-,j} = \begin{pmatrix} h_{i+\frac{1}{2}-,j} \\ h_{i+\frac{1}{2}-,j} u_{i,j} \\ h_{i+\frac{1}{2}-,j} v_{i,j} \end{pmatrix}, \quad \mathbf{U}_{i+\frac{1}{2}+,j} = \begin{pmatrix} h_{i+\frac{1}{2}+,j} \\ h_{i+\frac{1}{2}+,j} u_{i+1,j} \\ h_{i+\frac{1}{2}+,j} v_{i+1,j} \end{pmatrix}. \quad (4.14)$$

Note that only the values of the water height are reconstructed and used in the expressions of the momentum.

These reconstructed values are used instead of  $\mathbf{U}_{i,j}$  and  $\mathbf{U}_{i+1,j}$  to compute the interface solution with the VFRoe-ncv solver on flat bottom. More precisely, the numerical flux function  $\mathbf{F}_{i+\frac{1}{2},j}^*$  is defined as follows :

$$\mathbf{F}_{i+\frac{1}{2},j}^* = F(\mathbf{U}_{i+\frac{1}{2},j}^*(0, \mathbf{U}_{i+\frac{1}{2}-,j}, \mathbf{U}_{i+\frac{1}{2}+,j})). \quad (4.15)$$

where  $\mathbf{U}_{i+\frac{1}{2},j}^*(0, \mathbf{U}_{i+\frac{1}{2}-,j}, \mathbf{U}_{i+\frac{1}{2}+,j})$  is the interface value computed with the VFRoe-ncv solver on flat bottom, using the new reconstructed values  $\mathbf{U}_{i+\frac{1}{2}-,j}$  and  $\mathbf{U}_{i+\frac{1}{2}+,j}$  at each side of the considered interface.

In the mean time, the numerical source term discretization  $\mathbf{S}_{i,j}$  is discretized and distributed to the cell interfaces, using the reconstructed values of the water height. It gives :

$$\mathbf{S}_{i,j}^x = \mathbf{S}_{i+\frac{1}{2}-,j}^x + \mathbf{S}_{i-\frac{1}{2}+,j}^x = \begin{pmatrix} 0 \\ \frac{g}{2} h_{i+\frac{1}{2}-,j}^2 - \frac{g}{2} h_{i,j}^2 \\ 0 \end{pmatrix} + \begin{pmatrix} 0 \\ \frac{g}{2} h_{i,j}^2 - \frac{g}{2} h_{i-\frac{1}{2}+,j}^2 \\ 0 \end{pmatrix}. \quad (4.16)$$

This choice is motivated by a balancing requirement for nearly hydrostatic flows, with vanishing velocity (see [3] and [20]). A similar discretization can be obtained for the  $y$  direction.

Then, the two dimensional semi-discrete finite volume formulation may be written as follows :

$$\frac{d}{dt} \mathbf{U}_{ij}(t) + \frac{1}{\Delta x} (\mathbf{F}_{i+\frac{1}{2},j}^- - \mathbf{F}_{i-\frac{1}{2},j}^+) + \frac{1}{\Delta y} (\mathbf{G}_{i,j+\frac{1}{2}}^- - \mathbf{G}_{i,j-\frac{1}{2}}^+) = 0 \quad (4.17)$$

with left and right numerical fluxes through the  $\Gamma_{i\pm\frac{1}{2},j}$  and  $\Gamma_{i,j\pm\frac{1}{2}}$  interfaces are defined as follows :

$$\begin{aligned} \mathbf{F}_{i+\frac{1}{2},j}^- &= \mathbf{F}_{i+\frac{1}{2},j}^* + \mathbf{S}_{i+\frac{1}{2}-,j}^x \\ &= F(\mathbf{U}_{i+\frac{1}{2},j}^*(0, \mathbf{U}_{i+\frac{1}{2}-,j} \mathbf{U}_{i+\frac{1}{2}+,j})) + \begin{pmatrix} 0 \\ \frac{g}{2} h_{i,j}^2 - \frac{g}{2} h_{i+\frac{1}{2}-,j}^2 \\ 0 \end{pmatrix}, \end{aligned} \quad (4.18)$$

$$\begin{aligned} \mathbf{F}_{i+\frac{1}{2},j}^+ &= \mathbf{F}_{i+\frac{1}{2},j}^* + \mathbf{S}_{i+\frac{1}{2}+,j}^x \\ &= F(\mathbf{U}_{i+\frac{1}{2},j}^*(0, \mathbf{U}_{i+\frac{1}{2}-,j} \mathbf{U}_{i+\frac{1}{2}+,j})) + \begin{pmatrix} 0 \\ \frac{g}{2} h_{i+1,j}^2 - \frac{g}{2} h_{i+\frac{1}{2}+,j}^2 \\ 0 \end{pmatrix}, \end{aligned}$$

$$\begin{aligned} \mathbf{G}_{i,j+\frac{1}{2}}^- &= \mathbf{G}_{i,j+\frac{1}{2}}^* + \mathbf{S}_{i,j+\frac{1}{2}-}^y \\ &= G(\mathbf{U}_{i,j+\frac{1}{2}}^*(0, \mathbf{U}_{i,j+\frac{1}{2}-} \mathbf{U}_{i,j+\frac{1}{2}+})) + \begin{pmatrix} 0 \\ 0 \\ \frac{g}{2} h_{i,j}^2 - \frac{g}{2} h_{i,j+\frac{1}{2}-}^2 \end{pmatrix}, \end{aligned} \quad (4.19)$$

$$\begin{aligned} \mathbf{G}_{i,j+\frac{1}{2}}^+ &= \mathbf{G}_{i,j+\frac{1}{2}}^* + \mathbf{S}_{i,j+\frac{1}{2}+}^y \\ &= G(\mathbf{U}_{i,j+\frac{1}{2}}^*(0, \mathbf{U}_{i,j+\frac{1}{2}-} \mathbf{U}_{i,j+\frac{1}{2}+})) + \begin{pmatrix} 0 \\ 0 \\ \frac{g}{2} h_{i,j+1}^2 - \frac{g}{2} h_{i,j+\frac{1}{2}+}^2 \end{pmatrix}. \end{aligned}$$

We have obtained a very compact formulation of the flux functions, relying on the previous homogeneous VFRoe-ncv solver, taking into account the variations of topography and able to preserve positivity. As shown in the following, this scheme is robust, allows us to deal easily with wetting and drying phenomena and provides solid foundations for an accurate computation of the moving shoreline.

## 4.4. Second order accuracy: an adapted MUSCL reconstruction

The previous well-balanced scheme is derived from a Godunov “first-order” method in space and time and as seen in the previous chapter, the one order accuracy VFRoe scheme is much diffusive. Thus, we aim at constructing a numerical scheme that has the following properties :

- i) a higher order of accuracy in smooth parts of the solution,
- ii) the production of numerical solutions which are free from non-physical oscillations,
- iii) a higher resolution of discontinuities with less diffusion in solutions involving strong variations,
- iv) the preservation of the mass conservation property inherited from the first order finite volume method,
- v) the preservation of the discrete steady states “at rest”,
- vi) the preservation of the positivity of the water depth, as in the first order method.

To obtain more accurate results and to increase the rate of convergence, classically linked to the mesh size, we use the method proposed in [3] and generalized for a two-dimensional reconstruction on unstructured meshes in [4]. This method is based on a linear reconstruction on each cell, providing more accurate values on both sides of each interface, using the method introduced by Van-Leer in [176], namely the MUSCL method (Monotonic Upwind Scheme for Conservation Law). Note that the formalism of this method has been introduced in a homogeneous framework and so the bed slope source term naturally induces modifications in the linear reconstruction. The method used here relies on the classical three steps of the MUSCL method, namely a construction of the gradients in each cell, a linear extrapolation of the variables and a limitation of the slopes in order to preserve the extrema and to ensure the total variation diminishing property. But in the presence of source terms, a linear reconstruction of the topography  $d$  must be added. This reconstruction is not straightforward and must be deduced from the reconstruction of  $h + d$  to preserve the well-balanced properties (ie to preserve the steady states at the discrete level), whereas a cell-centered source term is needed to preserve the consistency. In addition, for two-dimensional reconstruction on unstructured meshes, a correction inspired from [138] is also needed. In the following, we recall some basic and important results concerning Total Variation Diminishing and Monotonicity Preserving schemes. Then we introduce the formalism of

the MUSCL method in a simple scalar one dimensional case, the extension to systems being straightforward. Finally we detail the modification induced by the bed slope source term and introduced the “second order” well-balanced scheme issued from the hydrostatic reconstruction method.

**4.4.1. Total Variation Diminishing schemes.** It is well-known that high-order schemes produce spurious oscillations in the vicinity of large gradients. On the other hand, the class of monotone methods do not produce any spurious oscillations but monotone methods are at most first order accurate. One way of resolving this problem is to use monotonicity preserving schemes. In particular, for the one dimensional case, the use of Total Variation Diminishing methods (TVD) appears as an efficient solution.

**Définition 4.4.1.** *A scheme is said to be Monotonicity Preserving if whenever the data  $\mathbf{U}_i^n$  is monotone the solution set  $\mathbf{U}_i^{n+1}$  is monotone in the same sense: if  $\mathbf{U}_i^n$  is monotone increasing, thus  $\mathbf{U}_i^{n+1}$  is also monotone increasing and if  $\mathbf{U}_i^n$  is monotone decreasing, thus  $\mathbf{U}_i^{n+1}$  is also monotone decreasing.*

Next we introduce the notion of total variation :

**Définition 4.4.2.** *If  $\mathbf{U}_i^n$  is a discrete mesh function, the total variation of  $\mathbf{U}^n$  is defined as :*

$$TV(\mathbf{U}^n) = \sum_i |\mathbf{U}_i^n - \mathbf{U}_{i-1}^n| \quad (4.20)$$

and the Total Variation Diminishing property is introduced as follows :

**Définition 4.4.3.** *A scheme is said to be a Total Variation Diminishing (TVD) scheme if*

$$TV(\mathbf{U}^{n+1}) \leq TV(\mathbf{U}^n), \quad \forall n$$

An important result which links TVD and Monotonicity Preserving schemes for nonlinear conservation laws is given by the following theorem :

**Theorem 4.4.1.** *The set  $S_{tvd}$  of TVD schemes is contained in the set  $S_{mpr}$  of monotonicity preserving schemes :*

$$S_{tvd} \subseteq S_{mpr}.$$

**Proof.**

See [77] for instance. ■

The most useful class is the class of TVD schemes which are far more convenient for the proofs of convergence. Therefore we will focus on constructing a TVD method which achieves the previous required properties. To this end, use is made of the classical MUSCL reconstruction method with slope limiters which is a common and easy way to obtain a formal extension to second order accuracy.

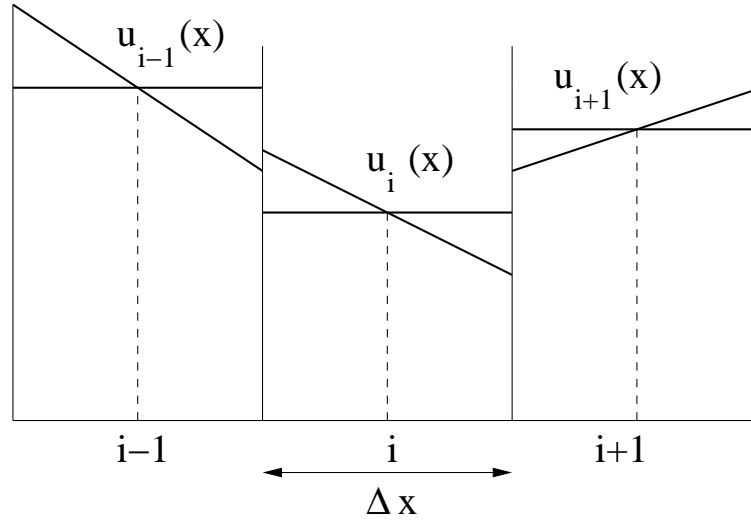


**Figure 4.4.1.** The piecewise linear MUSCL reconstruction for three computing cells.

#### 4.4.2. The “second order” reconstruction for homogeneous system.

Classically, a “second order” extension is obtained by computing the fluxes from limited linear reconstructed values on both sides of each interface rather than cell-centered values (see [107] for instance). These new values are obtained in three steps :

- (i) the computation of the gradients used for the linear reconstruction in each cell,
- (ii) The linear extrapolation of the initial piecewise constant data set,
- (iii) the limitation procedure in order to obtain the TVD property.

For our purpose, we choose to applied the classical minmod reconstruction. In the case of a scalar function  $U \in \mathbb{R}$ , the three steps of the reconstruction applied to the cell  $C_i$  where the piecewise constant function takes the value  $U_i$  are defined as follows :

$$U_{i,l} = U_i - \frac{\Delta x}{2} \nabla U_i, \quad U_{i,r} = U_i + \frac{\Delta x}{2} \nabla U_i, \quad (4.21)$$

where  $U_{i,r}$  and  $U_{i,l}$  stand respectively for the linear reconstructed value at  $i + \frac{1}{2}-$  and  $i - \frac{1}{2}+$  (see Figure 4.4.2) and the slope gradient  $\nabla U_i$  is defined with

$$\nabla U_i = \text{minmod} \left( \frac{U_i - U_{i-1}}{\Delta x}, \frac{U_{i+1} - U_i}{\Delta x} \right) \quad (4.22)$$

and

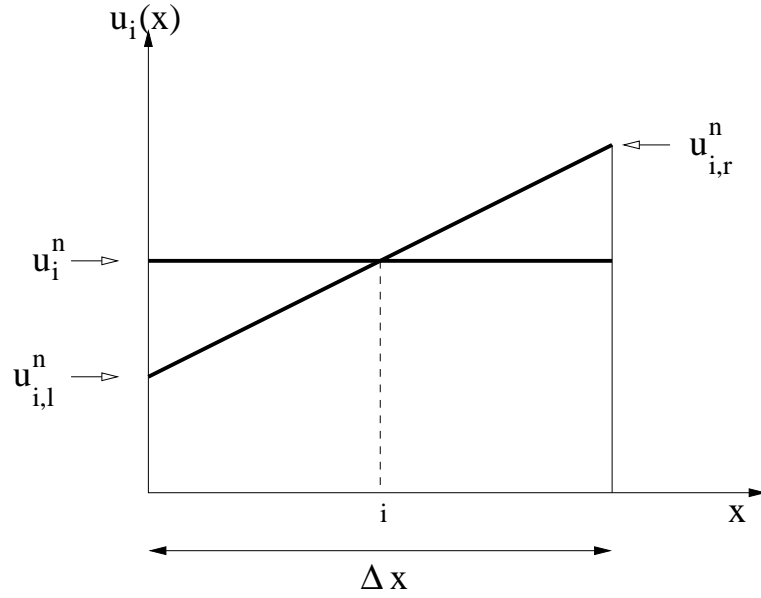


**Figure 4.4.2.** Piecewise linear MUSCL reconstruction. Definition sketch of the boundary extrapolated values  $U_{i,l}$  and  $U_{i,r}$

$$\text{minmod}(x, y) = \begin{cases} \min(x, y) & \text{if } x, y \geq 0 \\ \max(x, y) & \text{if } x, y \leq 0 \\ 0 & \text{otherwise} \end{cases} \quad (4.23)$$

where we have assumed that the space discretization step  $\Delta x$  is constant for the sake of simplicity.

**Remark 4.4.1.** *This reconstruction is conservative, since we have :*

$$\frac{U_{i,l} + U_{i,r}}{2} = U_i \quad (4.24)$$

**Remark 4.4.2.** *It appears that the values  $U_{i-1}$ ,  $U_i$  and  $U_{i+1}$  of the data at cells  $C_{i-1}$ ,  $C_i$  and  $C_{i+1}$  are needed for the computation of the gradient  $\nabla U_i$  used in the reconstruction of the data in the cell  $C_i$ . This remark will be useful when we will discuss the topic of adapted boundary conditions.*

Therefore, to compute the numerical fluxes at an interface  $\Gamma_{i+\frac{1}{2}}$  the initial data at each side of this interface used for the resolution of the local Riemann problem become  $U_{i,r}$  and  $U_{i+1,l}$  instead of  $U_i$  and  $U_{i+1}$ . In other words, if the first order numerical flux  $F(U_L, U_R)$  is given, the associated second order in space scheme is given by :

$$U_i^{n+1} = U_i^n + \frac{\Delta t}{\Delta x} (F_{i+\frac{1}{2}} - F_{i-\frac{1}{2}}) \quad (4.25)$$

with

$$F_{i+\frac{1}{2}} = F(U_{i,l}^n, U_{i+1,l}^n) \quad (4.26)$$

instead of  $F_{i+\frac{1}{2}} = F(U_i^n, U_{i+1}^n)$  in the first order scheme.

**4.4.3. A “second order” well-balanced extension for the hydrostatic reconstruction method.** This previous method is the classical MUSCL limited reconstruction, usually used in the framework of homogeneous systems of conservation laws. In our case, the presence of the bed-slope source term induces some modifications if we want to achieve the preservation of the discrete steady states and of the positivity of the water depth. These modifications, detailed in [3] and [20] for the one dimensional case and in [4] for the two-dimensional case are briefly recalled here in the one-dimensional case. The first difference which is emphasized is that a linear reconstruction of the topography  $d(x, y)$  is needed, although it is a data. This reconstruction must be deduced from the reconstruction of  $h + d$  to preserve the steady states at the discrete level. Considering that among the three quantities  $h$ ,  $h + d$  and  $d$ , only two need to be reconstructed, since the last one is a combination of the other two. In practice, we begin performing the linear reconstruction of  $\mathbf{U}_i$  and obtain the second order accuracy values  $\mathbf{U}_{i,l}$  and  $\mathbf{U}_{i,r}$ . In a second step we perform a similar reconstruction for the quantity  $(h + d)_i$ , leading to  $(h + d)_{i,l}$  and  $(h + d)_{i,r}$ . From this, we can obtain the reconstructed values for the topography with :

$$d_{i,l} = (h + d)_{i,l} - h_{i,l}, \quad \text{and} \quad d_{i,r} = (h + d)_{i,r} - h_{i,r}. \quad (4.27)$$

As emphasized in [3], this choice is the only way to ensure the preservation of the steady states (3.19) and the positivity of the water depth at a wet/dry interface simultaneously. In addition, considering the reconstruction of  $h + d$ , it is obvious that the steady states at rest are preserved in the case of a wet/wet interface.

The second difference that needs to be highlighted is the addition of a cell-centered source term  $S_{ci}$ . This additional source term is needed to ensure the consistency (see [3]). Gathering all these considerations, it yields the following “second order” well-balanced and positivity preserving scheme, which is exposed in the one-dimensional case for the sake of clarity :

$$\frac{d}{dt} \mathbf{U}_i(t) + \frac{1}{\Delta x} (\mathbf{F}_{i+\frac{1}{2}}^- - \mathbf{F}_{i-\frac{1}{2}}^+) = \mathbf{S}_{ci} \quad (4.28)$$

with left and right numerical fluxes through the  $\Gamma_{i\pm\frac{1}{2}}$  interfaces defined as follows :

$$\begin{aligned} \mathbf{F}_{i+\frac{1}{2}}^- &= \mathbf{F}_{i+\frac{1}{2}}^* + \mathbf{S}_{i+\frac{1}{2}}^x \\ &= F(\mathbf{U}_{i+\frac{1}{2}}^*(0, \mathbf{U}_{i+\frac{1}{2}-}, \mathbf{U}_{i+\frac{1}{2}+})) + \begin{pmatrix} 0 \\ \frac{g}{2} h_{i,r}^2 - \frac{g}{2} h_{i+\frac{1}{2}-}^2 \end{pmatrix}, \end{aligned} \quad (4.29)$$

$$\begin{aligned} \mathbf{F}_{i+\frac{1}{2}}^+ &= \mathbf{F}_{i+\frac{1}{2}}^* + \mathbf{S}_{i+\frac{1}{2}}^x \\ &= F(\mathbf{U}_{i+\frac{1}{2}}^*(0, \mathbf{U}_{i+\frac{1}{2}-}, \mathbf{U}_{i+\frac{1}{2}+})) + \begin{pmatrix} 0 \\ \frac{g}{2} h_{i+1,l}^2 - \frac{g}{2} h_{i+\frac{1}{2}+}^2 \end{pmatrix}, \end{aligned}$$

with

$$\mathbf{U}_{i+\frac{1}{2}-} = \begin{pmatrix} h_{i+\frac{1}{2}-} \\ h_{i+\frac{1}{2}-} u_{i,r} \end{pmatrix}, \quad \mathbf{U}_{i+\frac{1}{2}+} = \begin{pmatrix} h_{i+\frac{1}{2}+} \\ h_{i+\frac{1}{2}+} u_{i+1,l} \end{pmatrix} \quad (4.30)$$

The hydrostatic reconstruction is now defined as follows :

$$h_{i+\frac{1}{2}-} = \max(0, h_{i,r} + d_{i,r} - d_{i+\frac{1}{2}}), \quad h_{i+\frac{1}{2}+} = \max(0, h_{i+1,l} + d_{i+1,l} - d_{i+\frac{1}{2}}) \quad (4.31)$$

with

$$d_{i+\frac{1}{2}} = \max(d_{i,r}, d_{i+1,l}) \quad (4.32)$$

The cell-centered source term  $\mathbf{S}_{\text{ci}}$  is finally defined as follows :

$$\mathbf{S}_{\text{ci}} = \begin{pmatrix} 0 \\ g \frac{h_{i,l} + h_{i,r}}{2} (d_{i,l} - d_{i,r}) \end{pmatrix}. \quad (4.33)$$

Besides, it is worth noticing that a correction inspired from [138] is needed for two-dimensional reconstruction on unstructured meshes in order to preserve the mass conservation property, since the classical MUSCL method is only relevant in the one dimensional framework. On Cartesian meshes, we don't need to perform such correction, since the conservativity is recovered for each direction (see Remark 4.4.1).

**Remark 4.4.3.** *The idea of taking into account the topography variations in the MUSCL reconstruction is not new and was already introduced in Gallouët et al. [57] for instance. In order to perform the most complete numerical investigations, we have also implemented second order versions of the well-balanced VFRoe-ncv scheme and of the Exact Well-Balanced Riemann solver introduced in the previous chapter, using the method proposed in [57]. This method also uses the MUSCL formalism but the way the well-balanced properties are preserved relies on a limitation on  $h + d$  in the reconstruction of  $h$ . Precisely, when the topography is not flat, the limited slope for the reconstruction of the water depth  $h$  is computed from a first limitation on the variations of  $h + d$ . In addition, a second limitation is performed. Keeping in mind that the Exact Well-Balanced Riemann solver is able to preserve a larger class of steady states than the steady states at rest, the associated linear limited reconstruction must inherit of this property. The method proposed in [3] becomes inadequate since it only preserves the steady states at rest. We recall that considering the quantity  $\psi$  defined by :*

$$\psi = \frac{Q^2}{2h^2} + g(h + Z_f), \quad (4.34)$$

the largest class of steady states is defined by :

$$\begin{cases} hu = C^{st} \\ \psi = C^{st} \end{cases}$$

The idea introduced in [57] is to build a reconstruction which does not modify these states. To achieve this goal, the conservative variables  $h$  and  $hu$  are linearly reconstructed using the classical minmod limitation described above. Then, a TVD-like

property is imposed on  $\psi$  :

$$\begin{aligned} 0 \leq |\psi_i - \psi_{i,l}| &\leq \frac{|\psi_i - \psi_{i,l}|}{2}, \\ 0 \leq |\psi_{i,r} - \psi_i| &\leq \frac{|\psi_{i,r} - \psi_i|}{2}. \end{aligned} \quad (4.35)$$

where the value of  $\psi_{i,l}$  and  $\psi_{i,r}$  are obtained from the reconstructed values of  $h$  and  $hu$ . If this condition is not fulfilled, the slope  $\nabla h_i$  is set to zero. Note that the reconstruction of  $hu$  is not modified and is performed classically, whereas the reconstruction is performed on the velocity  $u$  in the method introduced in [3].

In practice, this method gives very good results, since all the subcritical steady states preserved by the first order method are not modified. But for our purpose, that is the study of moving shoreline problems, we recover the inaccuracies exhibited for the first order method. These discrepancies may even be amplified by this reconstruction process.

**Remark 4.4.4.** The second order accuracy of these reconstructions is justified in a weak sense (see Proposition 2.26 of [20]). Even if the rate of convergence is  $(\Delta x)^2$  in the weak sense, if we measure the error in strong norm, we observe that it converges to 0 with a slower rate as shown in the next section.

**Remark 4.4.5.** A simple extension towards an ENO second order scheme [20] has been recently implemented. But at this date we have not studied the effective improvement in accuracy.

**4.4.4. Second-order accuracy in time.** The second-order accuracy in time is usually recovered using one of the following approaches, namely the Hancock two stages time integration method [177], the predictor-corrector method proposed by Hirsch [81] or even the Heun scheme, which is a second order Runge-Kutta method. We choose here to use the Heun scheme as proposed in [20] or [57]. If we write the second-order method in space with the one-step classical Euler upwind scheme as follows :

$$\mathbf{U}^{n+1} = \mathbf{U}^n + \Delta t \Phi(\mathbf{U}^n) \quad (4.36)$$

where  $\Phi$  is a nonlinear operator which stands for the fluxes difference in the two directions  $x$  and  $y$ , therefore the second-order scheme in time and space is given by :

$$\begin{aligned} \tilde{\mathbf{U}}^{n+1} &= \mathbf{U}^n + \Delta t \Phi(\mathbf{U}^n), \\ \tilde{\mathbf{U}}^{n+2} &= \tilde{\mathbf{U}}^{n+1} + \Delta t \Phi(\tilde{\mathbf{U}}^{n+1}), \\ \mathbf{U}^{n+1} &= \frac{\mathbf{U}^n + \tilde{\mathbf{U}}^{n+2}}{2} \end{aligned} \quad (4.37)$$

If this method does not theoretically modify the *CFL* restriction [20], we have notice in practice that for a same problem the *CFL* for the second-order accuracy simulation should be smaller than in the first order case.

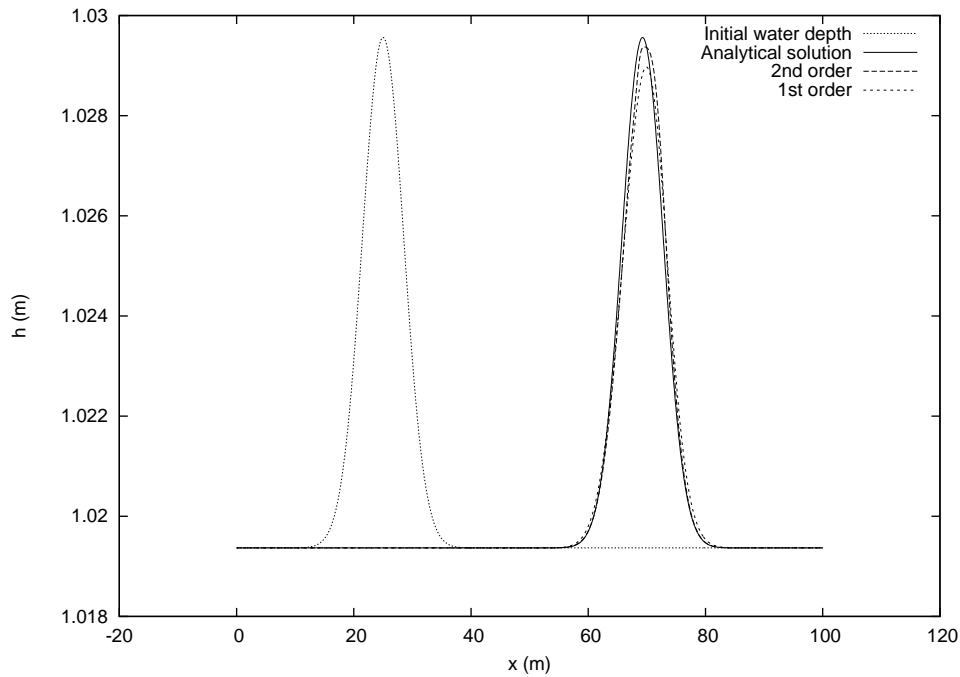


**Figure 4.4.3.** Propagation of a Gaussian wave in a rectangular channel. Comparison between analytical solution and numerical results obtained with first and second order methods at time  $t = 14$  s.

**4.4.5. Assessment of the second order reconstruction.** The *SURF\_SVWB* model has been extensively tested and successfully validated against numerous hydraulic cases involving bores and preservation of steady states “at rest”, as for the first order well-balanced schemes in the previous chapter. For the sake of clarity we don’t show these results in this work but all these cases have been successfully performed and both the well-balanced property and the positivity preserving property inherited from the first order method are preserved. We show in this subsection the improvements obtained by the second order reconstruction for the simple test of the propagation of a Gaussian wave and the previously introduced dam-break over a dry bed problem in one and two dimension.

*Propagation of a Gaussian.* This simple test enables to demonstrate the improvement in accuracy and numerical diffusion obtained with the “second order” reconstruction. In this test a Gaussian wave propagates along a one dimensional channel over a flat bottom. The ratio between the gaussian’s amplitude to the still water depth is chosen to be 0.01 and the test is run for 20 s. We have used 500 cells and the *CFL* is set equal to 0.8.

On Figure 4.4.3, it is obvious that the “second-order” version of the scheme is far less diffusive than the first order version. In addition, we will show in the next section that the rate of convergence of the “second order” scheme is increased compared to the classical first order method.

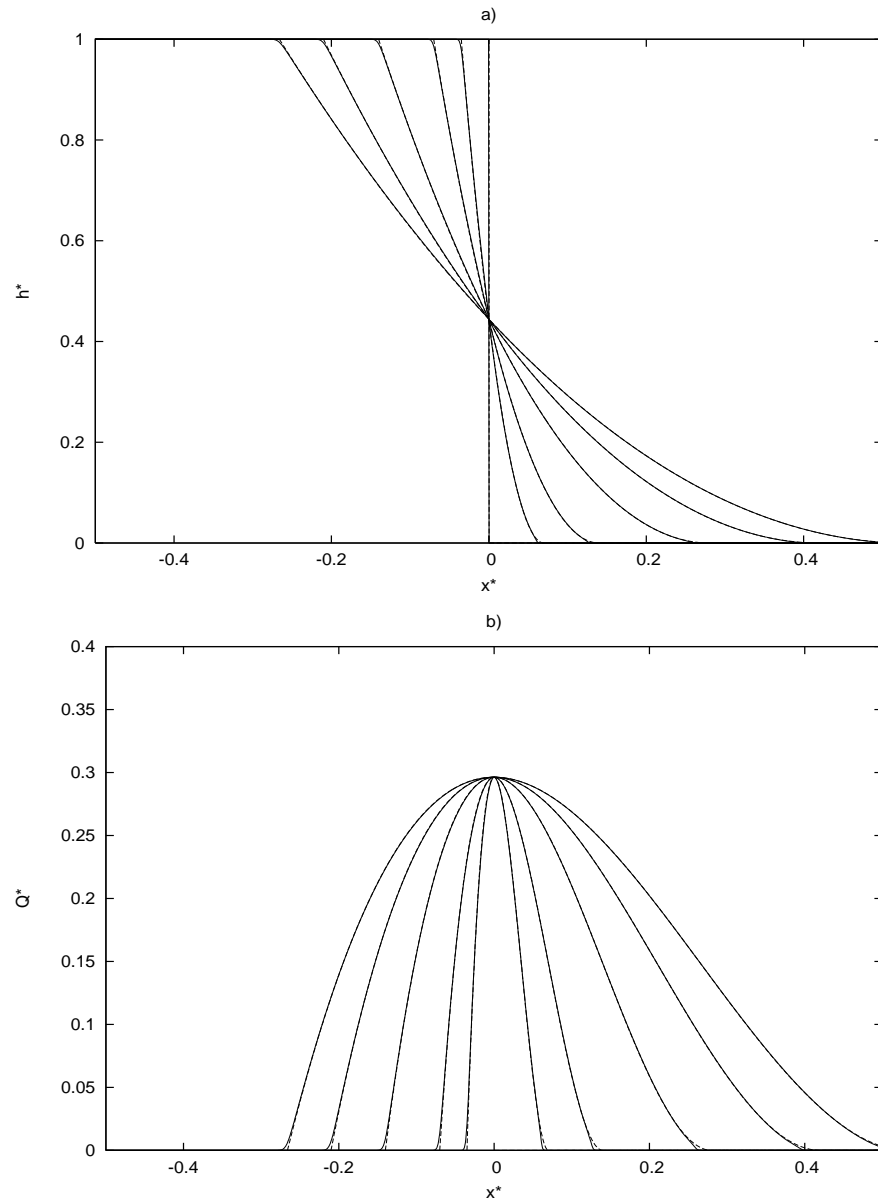


**Figure 4.4.4.** The dam-break problem on a flat bottom for  $h_0^* = 1$ . Comparison between numerical results provided by the *SURF-SVWB* model (solid lines) and analytical solution (dotted lines) for a) the water height  $h^*$  and b) the discharge  $Q^* = (hu)^*$  at different times  $t^* = 0.0$ ,  $t^* = 0.03$ ,  $t^* = 0.07$ ,  $t^* = 0.14$ ,  $t^* = 0.21$  and  $t^* = 0.26$ .

*The one-dimensional dam-break problem.* This test is the same as the one introduced in chapter 2 for the validation of the Exact Well-Balanced solver and the well-balanced VFRoe-ncv solver. We show here the improvement in the shock capturing ability obtained by the second order reconstruction. We use the scales  $h_0$ ,  $c_0 = \sqrt{gh_0}$  and  $t_0 = c_0/g$  in order to obtain respectively non-dimensionalized length, velocity and

time. Values of  $\Delta x^* = 0.01$  and  $CFL = 0.9$  have been used for this test, as in chapter 3.

We can observe on Figure 4.4.4 a very good agreement between the analytical solution and numerical results provided by the *SURF-SVWB* model. The front is accurately captured without any discrepancy. The “second order” scheme is far less diffusive, especially in the upper part of the solution, where the improvement is very significant. A comparison with the results proposed in [27] shows that *SURF-SVWB* may provide a slightly more accurate computation of the propagating front. The computation of the discharge seems to be also more accurate than the results provided by the WAF method.

**Remark 4.4.6.** *This test has also been performed with the Exact Well-Balanced solver using the “second order” reconstruction method proposed in [57]. The results are improved in the same way and are similar to those presented here.*

*The two-dimensional oblique dam-break problem.* We study in this test the evolution of a mound of water which is suddenly released from an initial position such as the front of the water propagates with an inclination of  $45^\circ$  with respect to the boundaries of the computational domain. The base of this domain is a  $[-0.5, 0.5] \times [-0.5, 0.5]$  square. With this test we validate our model in the case of a two-dimensional propagation and study the effect of the Cartesian mesh on the oblique propagation. Flow properties computed on the central cross-section orthogonal to the propagating front (the  $x^* = y^*$  plane) are compared to the one-dimensional analytical solution, assuming that the effects induced by the boundaries can be neglected for this section and for a small time of evolution. This assumption is clearly not true for the sections close to the boundary. A comparison with the analytical solution in the direction of propagation is reported on Figure 4.4.7. A good agreement is observed both for the water height and the discharge. The front of the numerical solution remains close to the analytical one during all the computational time but we can observe small under-predictions near this front for the discharge. As this error has not been observed in the one-dimensional case, these under-predictions may be due to the two-dimensional treatment of the fluxes. Values of  $\Delta x^* = \Delta y^* = 0.008$  and  $CFL = 0.7$  have been used for this test.

**Remark 4.4.7.** *This test has also been performed using the “second order” accuracy version of the Exact Well-Balanced solver. The results are as accurate to those presented here.*

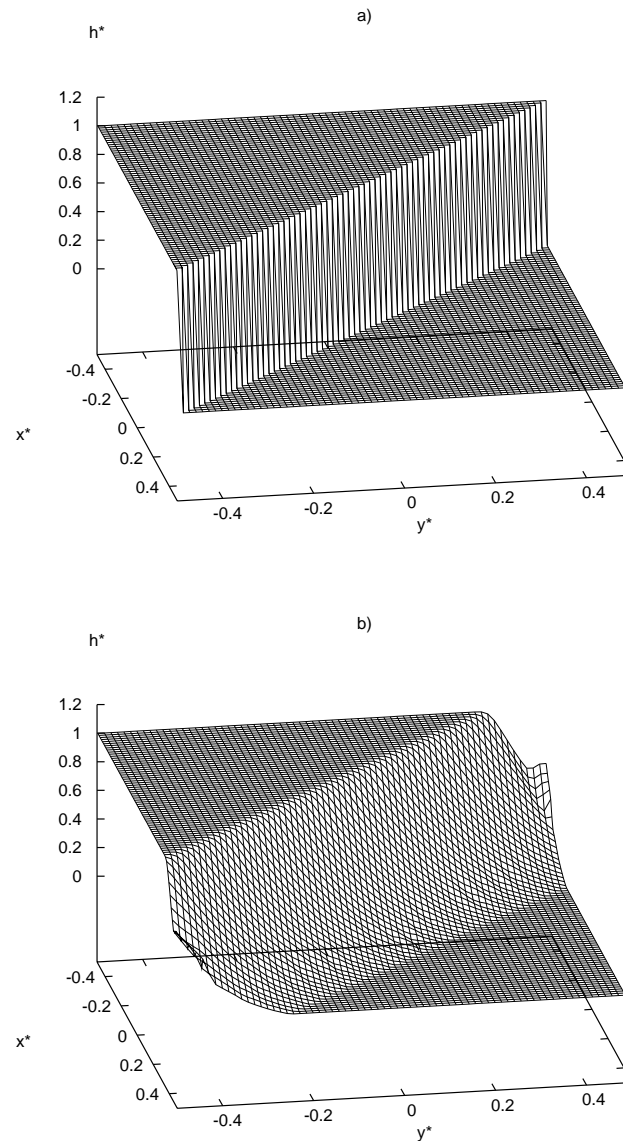


**Figure 4.4.5.** The two-dimensional oblique dam-break problem on a flat bottom for  $h_0^* = 1$ . Numerical results provided by *SURF\_SVWB*. The two-dimensional profile of the water height is plotted versus the dimensionless space coordinates  $x^*$  and  $y^*$  for: a)  $t^* = 0.0$ , b)  $t^* = 0.06$ , c)  $t^* = 0.15$ , d)  $t^* = 0.21$ .

## 4.5. Boundary conditions

**4.5.1. Preservation of the second order accuracy.** The use of the MUSCL reconstruction process induces some modifications in the construction of the boundary conditions. Actually, as seen previously, the reconstruction of the piecewise constant

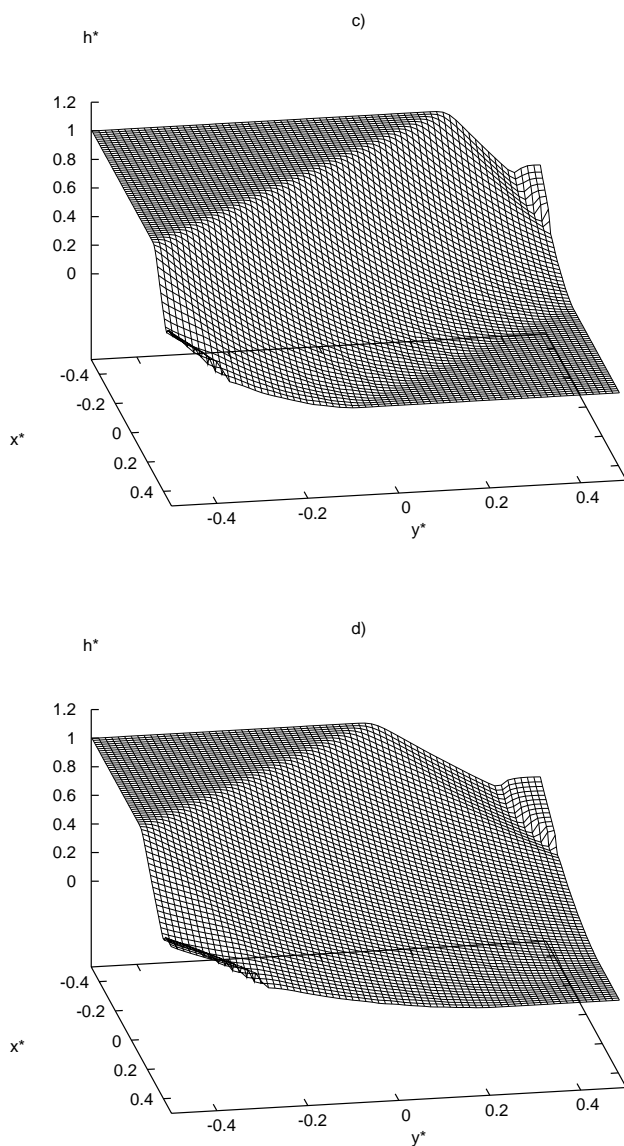


**Figure 4.4.6.** The two-dimensional oblique dam-break problem on a flat bottom for  $h_0^* = 1$ . Numerical results provided by *SURF-SVWB*. The two-dimensional profile of the water height is plotted versus the dimensionless space coordinates  $x^*$  and  $y^*$  for: a)  $t^* = 0.0$ , b)  $t^* = 0.06$ , c)  $t^* = 0.15$ , d)  $t^* = 0.21$ .

data into piecewise linear data makes use of a larger stencil: to construct the piecewise linear data on cell  $i$ , use is made of the values at cells  $i-1$ ,  $i$  and  $i+1$  (see Figure 4.4.1). Consequently, as we want to preserve the second order accuracy at the boundaries, we have implemented the following approach, which consists in adding a second line of fictitious cells around the computational domain previously introduced for the case of

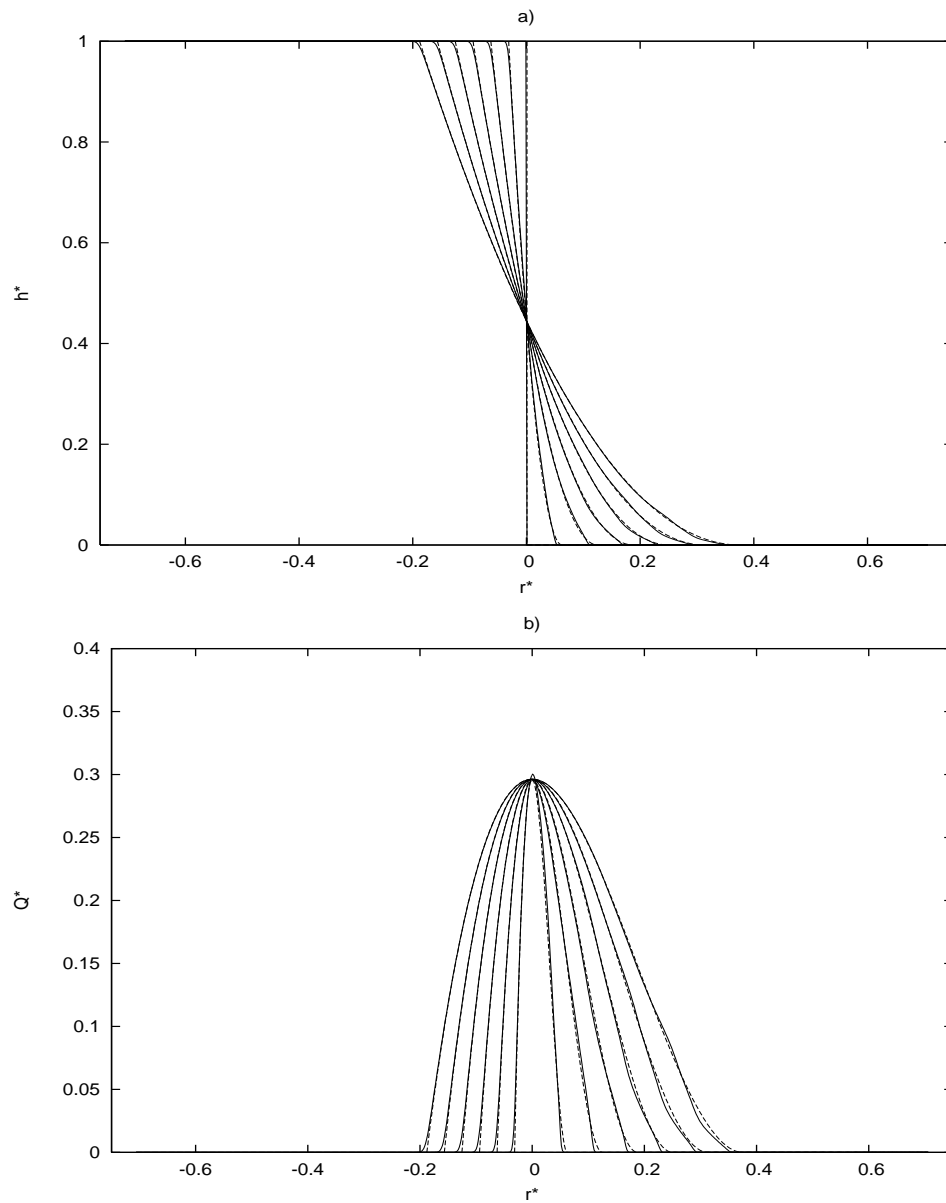


**Figure 4.4.7.** The two-dimensional oblique dam-break problem on a flat bottom for  $h_0^* = 1$ . Comparison between *SURF-SVWB* numerical results (solid lines) and analytical solution (dashed lines) for: a) the profile of the water depth  $h^*$  in the direction of propagation and b) the profile of the discharge  $Q^* = (hu)^*$  in the propagation direction at different times  $t^*$  between  $t^* = 0$  and  $t^* = 0.18$  with a step of 0.03.

first order boundary conditions. Let us consider the simple case of a one dimensional domain where two fictitious cells, namely  $C_0$  and  $C_{-1}$  have been added, as illustrated on Figure 4.5.1.

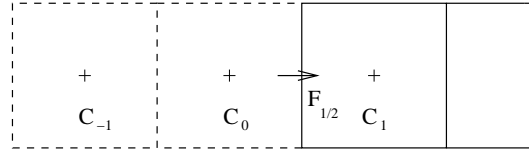


**Figure 4.5.1.** Sketch of the two added fictitious cells for the second order boundary conditions.

The introduction of the new ghost cell  $C_{-1}$  enables us to compute the linearly reconstructed data on cell  $C_0$  relying on the MUSCL algorithm introduced above. This reconstruction makes use of the data at cells  $C_{-1}$ ,  $C_0$  and  $C_1$ . The reconstructed  $C_0$  data is then used in the computation of the fluxes  $F_{\frac{1}{2}}$  through the interface between  $C_0$  and  $C_1$ . It's a simple and efficient way to preserve the second order accuracy at the boundaries.

It leads to the following boundary conditions :

**4.5.2. Non-slip reflective solid boundary condition.** A fixed non-slip and reflective boundary condition is given by :

$$h_{N+1} = h_N \ , \ u'_{N+1} = -u'_N \ , \ v'_{N+1} = -v'_N \quad (4.38)$$

$$h_{N+2} = h_{N-1} \ , \ u'_{N+2} = -u'_{N-1} \ , \ v'_{N+2} = -v'_{N-1} \quad (4.39)$$

where  $N$  and  $N - 1$  denote the last two cells inside the computational domain in the considered direction,  $N + 1$  and  $N + 2$  two fictitious cells outside of the computational domain and  $u'$  and  $v'$  are the components of velocity  $\mathbf{u}$  respectively normal and tangential to the boundary.

**4.5.3. Transmissive boundary condition.** Transmissive second order boundary conditions are specified with :

$$h_{N+1} = h_N \ , \ u'_{N+1} = u'_N \ , \ v'_{N+1} = v'_N \quad (4.40)$$

$$h_{N+2} = h_{N-1} \ , \ u'_{N+2} = u'_{N-1} \ , \ v'_{N+2} = v'_{N-1} \quad (4.41)$$

with the same notations.

**4.5.4. Periodic boundary condition.** Periodic second order boundary conditions are specified with :

$$h_{N+1} = h_1 \ , \ u'_{N+1} = u'_1 \ , \ v'_{N+1} = v'_1 \quad (4.42)$$

$$h_{N+2} = h_2 \ , \ u'_{N+2} = u'_2 \ , \ v'_{N+2} = v'_2 \quad (4.43)$$

**4.5.5. Absorbing/Generating non-reflective inlet boundary condition.**

When analyzing nearshore circulation using numerical models, it is usual necessary to limit the computational domain to a small region of interest. This implies introducing artificial boundaries for the computational region at the opensea boundary, where flows are allowed to enter or leave the computational domain. The particularity of such problems lies in the fact that the seaward boundary condition is expected to provide variables which are upgrading in time, along the cross-shore direction (see the third part). The flow is assumed to be subcritical and as exposed previously, only one

information needs to be specified, the second information, concerning currents for instance if the water surface profile is specified, can be recovered using the characteristic theory and the conservation of Riemann invariants, as exposed in the first order case. In addition, the long waves which are introduced in the computational domain are often partially reflected as they propagate towards the shoreline and these reflected waves may propagate in the cross shore direction toward the seaward boundary, interfering with the incident waves. These reflected waves must be allowed to exit the computational domain without being re-reflected. From this it appears the necessity to develop a boundary condition which is able to generate a specified long wave and simultaneously absorb outgoing waves. Most of the existing literature on the topic deals with absorbing conditions, sometimes called radiating, non reflective or open boundary conditions.

The expected boundary condition needs to satisfy the following criteria :

- i) It must guarantee a unique and well-posed solution to the differential problem,
- ii) The region outside the computational domain can influence the propagation inside only through the incident waves and through the currents along the boundary. Therefore, we assume that those currents and incident waves are known and can be specified,
- iii) Waves propagating out of the computational domain must be allowed to exit freely with minimal reflection.

To achieve these properties, Kobayashi et al. in [95] propose to use the outgoing characteristic, as for the previous first order subcritical boundary condition, but in addition they introduce a linear long-wave relationship between the velocity and the surface elevation to solve the outgoing problem. This provides an expression for the reflected waves amplitude which is included in the computation. Neglecting the bottom slope, once the evaluation of the conserved Riemann outgoing invariant is performed as exposed in the previous chapter, the required velocity  $u'^{n+1}$  can be obtained using

$$u'^{n+1} = \beta^- + 2c^{n+1} \quad (4.44)$$

where  $c^{n+1} = \sqrt{g\tilde{h}}$  and  $\tilde{h} = h_0 + \eta_i + \eta_r$ . In this expression  $\eta_i$  and  $\eta_r$  are the free surface elevation of the incident and reflected waves respectively,  $h_0$  is the mean water depth. The free surface elevation of the reflected waves is obtained using the linear theory which provides the relationships  $u'_i = \sqrt{\frac{g}{h_0}}\eta_i$  and  $u'_r = \sqrt{\frac{g}{h_0}}\eta_r$ . It yields the following expression for  $\eta_r$  :

$$\eta_r = -\frac{1}{2}\frac{h_0}{g}\beta^- - h_0 \quad (4.45)$$

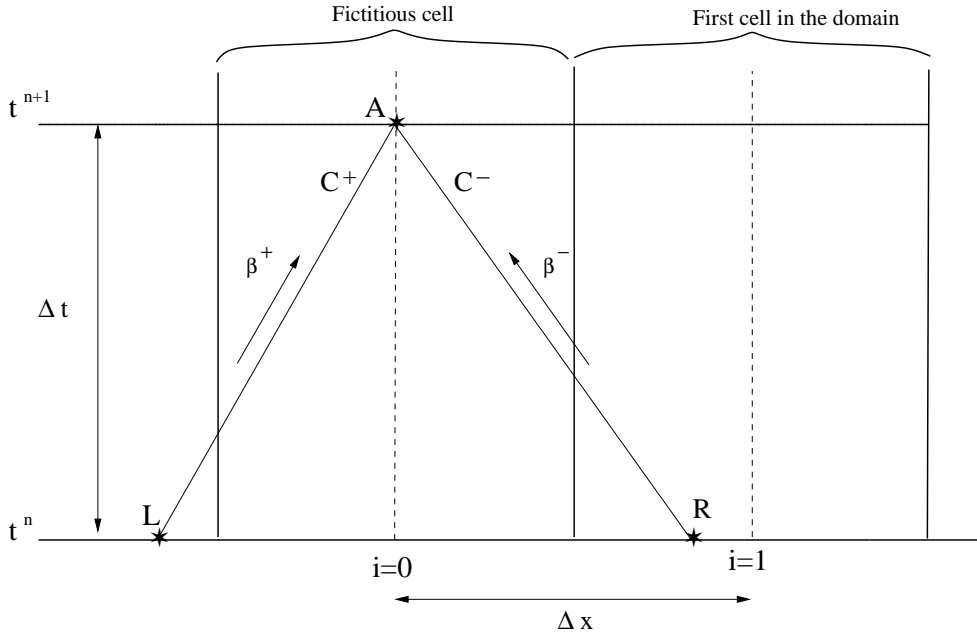


**Figure 4.5.2.** Sketch of the derivation of the absorbing/generating inlet boundary condition.

From this, we impose at the boundary the updated water depth  $\tilde{h}$  which takes into account both incident and reflected waves, and the associated velocity  $u'^{n+1}$  obtained from relation (4.44).

A correction is proposed in [82] in order to achieve second order accuracy. The idea is to add a nonlinear term to the expression of  $\eta_r$  to account for nonlinear interactions between incident and reflected waves. It gives :

$$\eta_r = -\frac{1}{2} \frac{h_0}{g} \beta^- - h_0 + \frac{(\sqrt{\tilde{h}} - \sqrt{h_0})^2}{2}. \quad (4.46)$$

We have obtained an implicit equation, since the value of  $\tilde{h}$  is unknown. This system can be solved with Newton-Raphson algorithm with low computational cost. As emphasized in [82], this approach provides second-order accuracy when used in combination with a piecewise linear reconstruction. However no numerical analysis have been performed in this paper to validate this second order accuracy and we can only validate this boundary condition with numerical investigations.

Another approach inspired from [48], which also makes use of linear approximation and leads to quasi similar results in practice, relies on both the incoming  $\beta^+$  and outgoing  $\beta^-$  Riemann invariants (see Figure 4.5.2) and on the resolution of the system composed by these two invariants in order to obtain the updated values of  $h^{n+1}$  and  $u'^{n+1}$  at the considered boundary. More precisely, the incoming Riemann invariant is defined from point  $L$  using the given amplitude  $\eta_i$  of the incident wave and the

corresponding velocity obtained from linear theory. It raises :

$$\beta^+ = 2\sqrt{g(\eta_i + h_0)} + \sqrt{\frac{g}{h_0}}\eta_i. \quad (4.47)$$

The outgoing Riemann invariant  $\beta^-$  is computed as previously from point  $R$  with linear interpolation and Newton-Raphson method, using the conservation along the  $u' - c$  characteristic. Finally, the system composed by these two invariants is solved. It yields :

$$\begin{aligned} h_A^{n+1} &= \frac{1}{16g}(\beta^+ - \beta^-)^2 \\ u_A'^{n+1} &= \frac{1}{2}(\beta^+ + \beta^-) \end{aligned} \quad (4.48)$$

where  $A$  is the point where the boundary condition is applied. This last approach has been extended in the two dimensional case, for an arbitrary angle of incidence in [175]. The two approaches above, which share common ideas, have been implemented and tested.

This benchmark proposed by Hu et al. in [82] to validate their boundary condition has been performed here in order to compare these two approaches. The geometry for this test is a one dimensional rectangular channel of 500 m with flat bottom. Sinusoidal waves are generated at the left inflow boundary whereas the right boundary is closed with a wall, using the no-slip solid reflective boundary condition. The sinusoidal waves is defined by  $\eta_i = 0.5 H \sin(2\Pi t/T)$  where the wave height  $H$  is given by  $H = 0.04 m$  and the wave period  $T$  is equal to 20.193 s. The corresponding wavelength calculated with linear theory is 200 m. The still water depth at rest is  $h_0 = 10 m$ . The ratio between the wave height and the still water depth is thus equal to 0.004 and nonlinear effects can be neglected. Theoretically this configuration will lead to a standing wave pattern of height 0.8 m. This test is performed with 400 cells and the time step is set to 0.05 s. We highlight that any small non-physical reflection at the inlet boundary may distort the standing wave, since the error will be amplified after several reflections at the two boundaries. Therefore, the non-reflecting property of the boundary conditions is seriously tested.

Numerical results are shown on Figure 4.5.3 where time series of the computed water depth at  $x = 250 m$  are plotted for a large value of time. It can be observed that no spurious distortion are generated even for a long time simulation and that the boundary conditions work reasonably good. However, we have tested both methods : the method of Hu et al [82] with nonlinear correction and the method using the evaluation of the two invariants which also relies on the linear theory but without any nonlinear correction. From our investigations it appears that the improvement linked to the nonlinear correction of Hu et al. is very small, since the results obtained with each of these two methods are very similar.

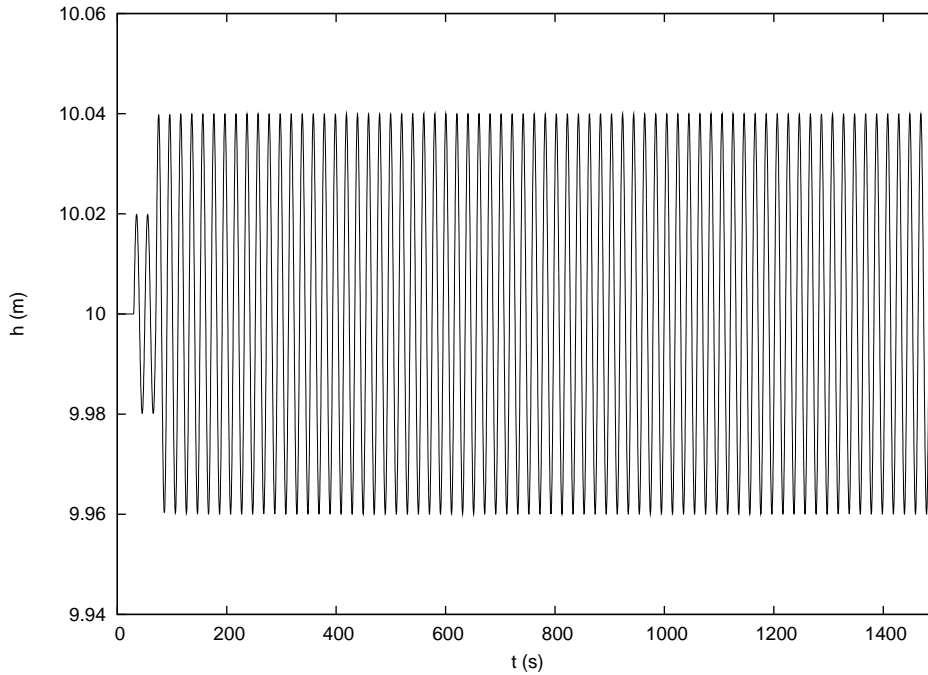


**Figure 4.5.3.** Standing wave reflection at a vertical wall. Computed water depth at  $x = 250\text{ m}$  during 1500 s.

## 4.6. Numerical assessments for moving shoreline problems

In this subsection we only focus on moving shoreline problems in one and two dimensions and highlight the ability of the new well-balanced scheme to accurately compute the wet/dry interface. We perform a comparison with three important one-dimensional analytical solutions for waves propagating at a uniform sloping beach. They model the run-up and run-down of a periodic wave traveling shoreward and being reflected out to sea, leading to a standing wave (the Carrier and Greenspan’s periodic solution), the run-up and the asymptotical convergence toward a steady state due to a depression of the water level at the coastline (the fluid held motionless) which is suddenly released (the Carrier and Greenspan’s transient solution) and the run-up and reflection of a solitary wave (the Synolakis run-up solution). In the two-dimensional case, we validate the model against the two important Thacker’s analytical solutions for periodic oscillating motions with moving boundaries in parabolic basins. The “second order” in space and time scheme is used for all the test cases presented here. For clarity numerical results are plotted with solid lines and the analytical solutions with dots. The grids which are used for the different test cases are uniform, with  $\Delta x = \Delta y$  in the two-dimensional case.

In order to compare numerical results provided by *SURF-SVWB* and analytical solutions use is made of the  $L^2$ -error defined at the  $n^{\text{th}}$  time for  $h$  and  $\mathbf{u}$  as follows ;

$$Err^{L^2}(h) = \left\{ \frac{\sum_{i,j} (h_{ij}^n - h_a)^2}{\sum_{i,j} h_a^2} \right\}^{\frac{1}{2}}, \quad (4.49)$$

$$Err^{L^2}(\mathbf{u}) = \left\{ \frac{\sum_{i,j} [(u_{ij}^n - u_a)^2 + (v_{ij}^n - v_a)^2]}{\sum_{i,j} [u_a^2 + v_a^2]} \right\}^{\frac{1}{2}}, \quad (4.50)$$

where  $U_a = {}^t(h_a, (hu)_a, (hv)_a)$  represents the analytical solution at the appropriate time.

Time series of these  $L^2$  errors are presented in the sequel for two cases. The  $L^2$ -convergence curves for the water height  $h$  and the velocity  $\mathbf{u}$  are also shown for a few cases. The  $L^2$ -error is plotted versus the discretization step  $\Delta x$  in log/log scale at a given time. Classically, these curves enable us to estimate the rate of convergence of the scheme.

#### 4.6.1. One dimensional assessments.

*The Carrier and Greenspan transient solution.* As a first validation of the shoreline description, the initial water surface elevation is assumed to be depressed near the shoreline, the fluid held motionless and then released at  $t = 0$ . This initial condition is the upper curve on Figure 4.6.1. Let  $l$  be the typical length scale of this specific problem and  $\alpha$  the beach slope. Non-dimensional variables are defined as follows :

$$x^* = x/l, \quad \xi^* = \xi/(\alpha l), \quad u^* = u/\sqrt{g\alpha l}, \quad t^* = t/\sqrt{l/\alpha g}, \quad (4.51)$$

and the non-dimensional phase speed is given by :

$$c^* = \sqrt{(\xi^* - x^*)}. \quad (4.52)$$

Carrier and Greenspan [35] used a hodograph transformation to solve the NSW equations and obtain an analytical solution, relying on the introduction of the two dimensionless variables  $\sigma^*$  and  $\lambda^*$  respectively linked to the space and time coordinate. These variables are defined as follows :

$$\sigma^* = 4c^*, \quad \lambda^* = 2(u^* + c^*). \quad (4.53)$$

Starting from the one-parameter family of wave-forms at  $t = 0$  :

$$\left\{ \begin{array}{l} \xi^* = e \left[ 1 - \frac{5}{2} \frac{a^3}{(a^2 + \sigma^{*2})^{\frac{3}{2}}} + \frac{3}{2} \frac{a^5}{(a^2 + \sigma^{*2})^{\frac{5}{2}}} \right], \\ x^* = -\frac{\sigma^{*2}}{16} + e \left[ 1 - \frac{5}{2} \frac{a^3}{(a^2 + \sigma^{*2})^{\frac{3}{2}}} + \frac{3}{2} \frac{a^5}{(a^2 + \sigma^{*2})^{\frac{5}{2}}} \right]. \end{array} \right. \quad (4.54)$$

where  $a = \frac{3}{2}(1 + 0.9e)^{\frac{1}{2}}$  and  $e$  is a small parameter which characterizes the surface elevation profile and using some relations between dimensionless ordinary variables, hodograph coordinates and a potential function depending on this specific problem Carrier and Greenspan ([35]) obtain the following complete analytical solution given by :

$$\left\{ \begin{array}{l} u^* = \frac{8e}{a} \mathcal{I}_m \left[ \frac{1}{[(1-i\lambda)^2 + \sigma^2]^{\frac{3}{2}}} - \frac{3}{4} \frac{1-i\lambda}{[(1-i\lambda)^2 + \sigma^2]^{\frac{5}{2}}} \right] \\ \xi^* = -\frac{u^{*2}}{2} + e \mathcal{R}_e \left[ 1 - 2 \frac{5/4 - i\lambda}{[(1-i\lambda)^2 + \sigma^2]^{\frac{3}{2}}} + \frac{3}{2} \frac{(1-i\lambda)^2}{[(1-i\lambda)^2 + \sigma^2]^{\frac{5}{2}}} \right] \\ t^* = \frac{1}{2} a \lambda - u^* \\ x^* = \xi^* - \frac{a^2 \sigma^2}{16} \end{array} \right. \quad (4.55)$$

where we have set  $\sigma^* = a\sigma'$ ,  $\lambda^* = a\lambda'$  and then dropped the prime notation. This set of equations is solved by iterative processes and we use the values of this analytical solution at the left boundary as the inlet left boundary condition in order to generate the motion.

During the evolution, the maximum penetration distance reached by the wave occurs when the coastline velocity is zero. The shoreline rises above the mean sea level of value  $e$  and then the water surface elevation asymptotically settles back to it. We have performed numerical investigations with the VFRoe-ncv solver on flat bottom and a fractional step method. It shows that FSM are clearly not suitable for this test case, since they generate large instabilities as the surface elevation slowly moves toward the mean level. Thus, this test provides a particularly valuable occasion to test the ability of the model to compute nearly steady state.

In [35], it is emphasized that  $e$  should be less than 0.23 for non-breaking cases and the results are presented here for  $e = 0.1$ . The bottom slope  $\alpha$  is taken to be  $1/50$  and the initial surface profile (4.54) is imposed in the dimensional case with the length scale  $l = 20$  m. Values of  $\Delta x^* = 0.002$  and  $CFL = 0.7$  have been used for this test.

In Figure 4.6.2 the analytical and numerical surface elevation are plotted versus the onshore coordinate for several values of time, in non-dimensional quantities. These surface elevation profiles have been scaled with the parameter  $e$ . The numerical results are plotted in solid lines and the analytical curves in dashed-dot lines. We see that the *SURF-SVWB* model provides excellent agreement with the analytical solution.

We can see on Figure 4.6.3 the time series of the shoreline surface elevation. The motion of the instantaneous shoreline is obtained by setting  $\sigma = 0$  in (4.55). This is explicitly developed in [35]. We can observe that the shoreline position asymptotically settles to  $e$  and that the *SURF-SVWB* model provides stability and a good accuracy in the computation of this slow convergence. We emphasize that the use of FSM for this test may lead to instabilities for large values of time since the errors induced by the discretization may become greater than the variations of the solution. In the

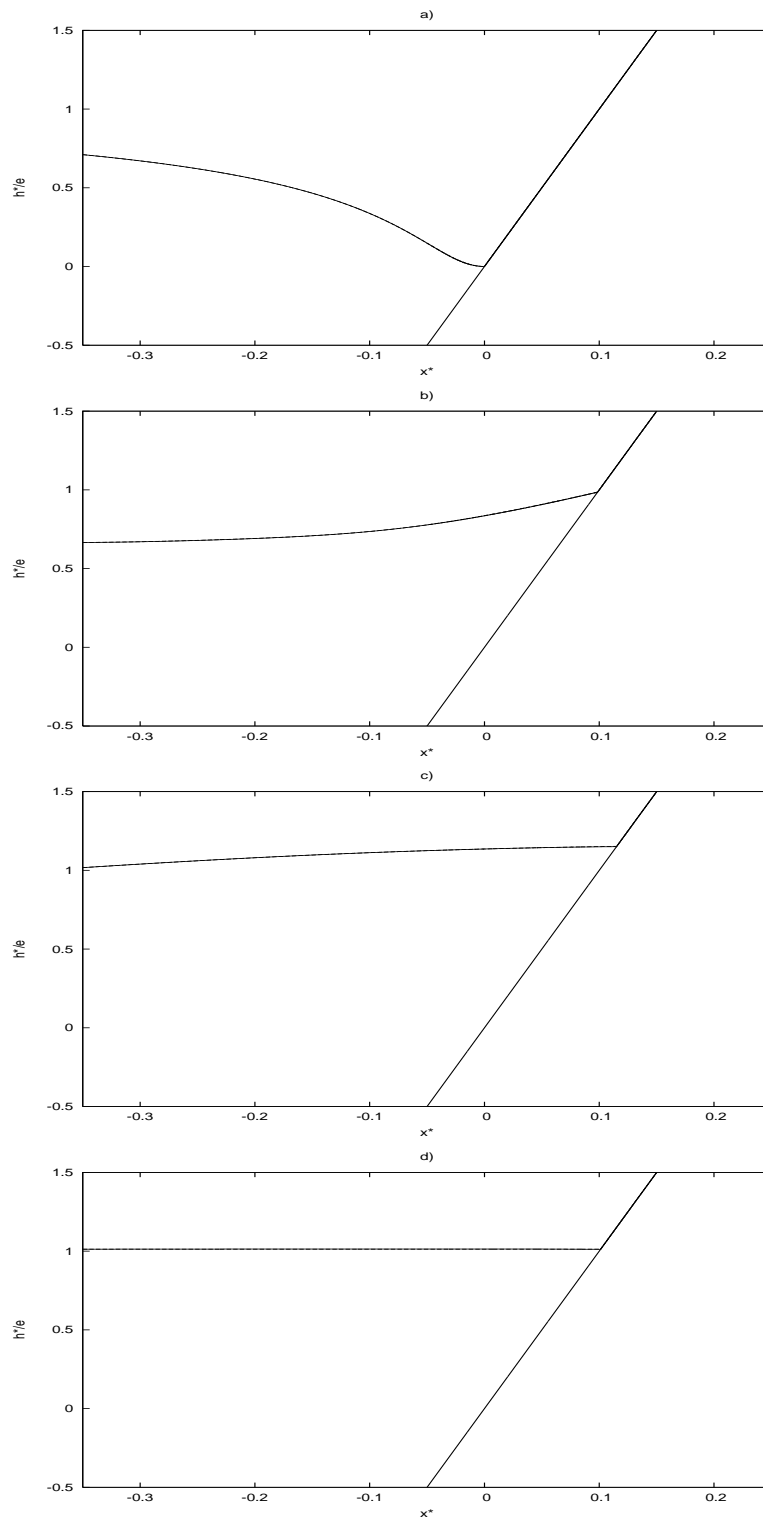


**Figure 4.6.1.** The Carrier and Greenspan's transient solution on a uniform plane beach. Comparison between numerical results (in solid lines) and analytical solutions (in dots) for the surface elevation. Profiles of water depth  $h^*/e$  are plotted versus the onshore coordinate  $x^*$ , for: a)  $t^* = 0s$ , b)  $t^* = 1$ , c)  $t^* = 2$  and d)  $t^* = 10$

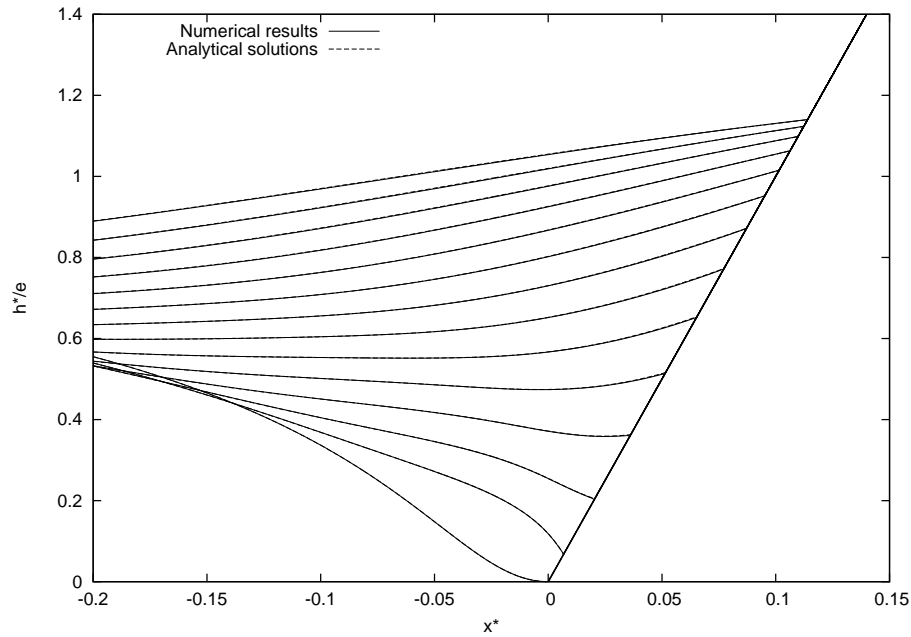


**Figure 4.6.2.** The Carrier and Greenspan's transient solution on a uniform plane beach. Comparison between numerical results (in solid lines) and analytical solutions (in dots) for the surface elevation. Zoomed profiles of water depth  $h^*/e$  are plotted versus the onshore coordinate  $x^*$ , for different values of time  $t^*$  between  $t^* = 0$  and  $t^* = 1.4$ .

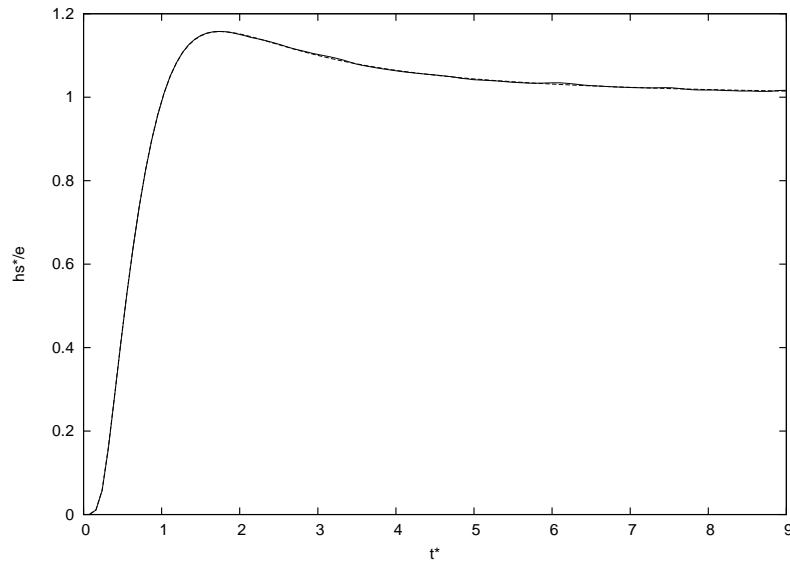


**Figure 4.6.3.** The Carrier and Greenspan's transient solution on a uniform plane beach. Comparison between numerical results (in solid line) and the analytical solution (in dashed-dot line) for the motion of the shoreline. Water surface elevation of the dimensionless shoreline  $h_s^*/e$  is plotted versus the dimensionless time coordinate  $t^*$ .

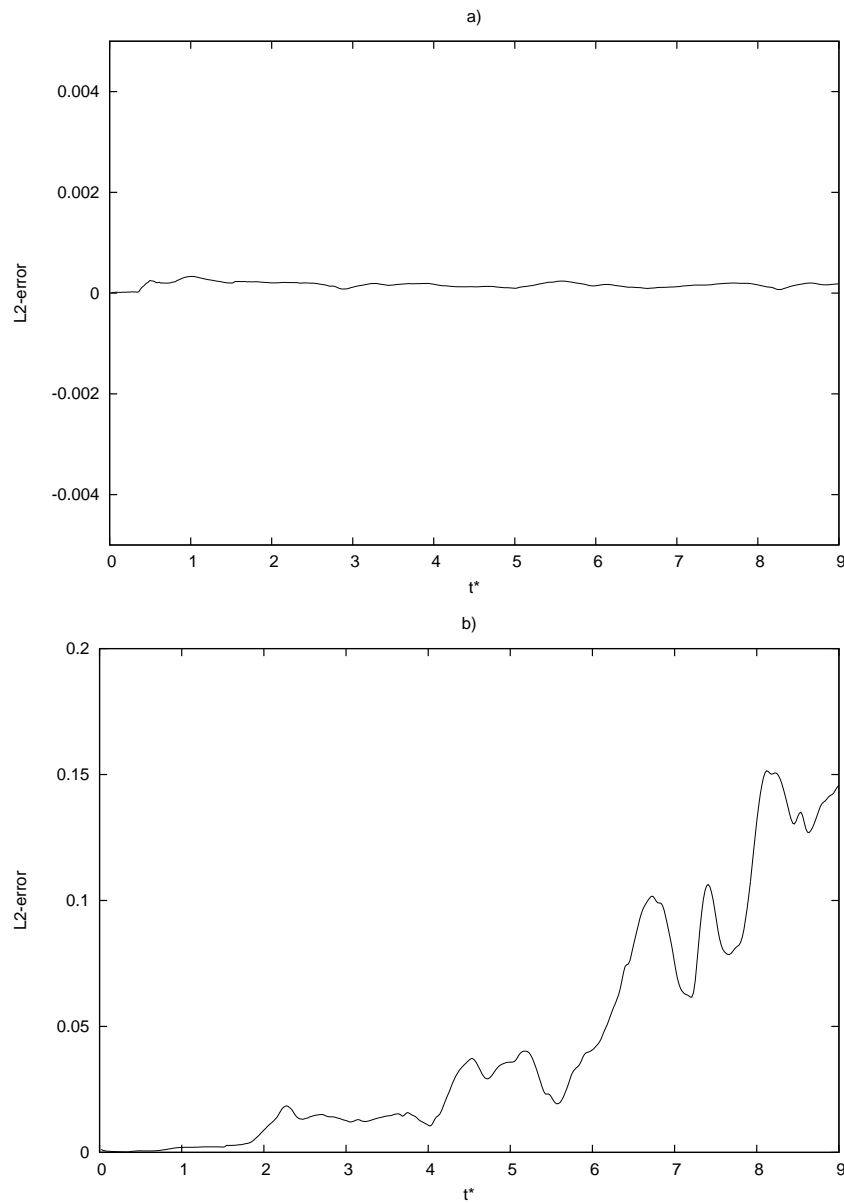


**Figure 4.6.4.** The Carrier and Greenspan's transient solution on a uniform plane beach. Time series of the  $L^2$ -error for : a)  $h^*$  and b)  $u^*$  between numerical results provided by *SURF-SVWB* and the analytical solution. The  $L^2$ -error is plotted versus  $t^*$  for  $\Delta x^* = 0.005$ .

literature, most of the authors use FSM and so, the computation is rarely performed for large values of time.

For this test, we show on Figure 4.6.4 a) and Figure 4.6.4 b) the time series of the  $L^2$  normalized error between the numerical results provided by *SURF-SVWB* and the analytical solution for the water height and the velocity, for the given resolution  $\Delta x^* = 0.002$ . For the water height, this error remains small even after the run-up

when the water level slowly converges toward the mean level. The error on the velocity is much greater than for the water height but remains controlled even for long times. Actually, this is a drawback which appears for both FSM and well-balanced schemes and in the literature the authors rarely show error estimations on the velocity.

**Remark 4.6.1.** *We have also implemented a one dimensional variable mesh generating procedure and applied it to the present case. Numerical investigations show that to obtain accuracy, we only need to have small discretization steps  $\Delta x_i$  near the shoreline, while the use of a coarser grid at the inflow boundary don't modify the quality of the results and enables to divide by three and sometimes more the total number of cells for a similar accuracy. But this approach is more difficult to extend in two dimensions. A possible method is the one suggested in [103].*

*The Carrier and Greenspan periodic wave solution.* In this test, a monochromatic wave is let run-up and run-down on a plane beach. This solution of the NSW equations represents the motion of a periodic wave of dimensionless amplitude  $A^*$  and frequency  $\omega^*$  traveling shoreward and being reflected out to sea generating a standing wave on a plane beach. The previous dimensionless quantities (4.51) and (4.52) are used and the analytical solution is obtained using the dimensionless hodograph coordinates (4.53). We obtain for this specific problem :

$$\left\{ \begin{array}{l} u^* = -\frac{A^* J_1(\sigma^*) \sin(\lambda^*)}{\sigma^*} \\ \xi^* = \frac{A^*}{4} J_0(\sigma^*) \cos(\lambda^*) - \frac{u^{*2}}{4} \\ t^* = \frac{1}{2} \lambda^* - u^* \\ x^* = \xi^* - \frac{\sigma^{*2}}{16} \end{array} \right. \quad (4.56)$$

where  $J_0$  and  $J_1$  stand for the Bessel functions of zero and first order and the dimensionless frequency  $\omega^*$  is equal to one. This analytical solution is frequently used to validate the ability of the model to deal with run-up and run-down phenomenon and to study the dynamics of waves near a continental shelf. This expression is valid for  $0 \leq A^* \leq 1$  and  $A^*/4$  represents the maximum vertical excursion of the shoreline. The value of this solution at  $t = 0$  is supplied as initial condition and as for the previous transient case, the analytical variations of the surface elevation at the left boundary is used as an offshore inlet boundary condition and enable us to generate the motion. We refer the reader to the original study of Carrier and Greenspan [35] for a complete description of the solution.

We compute this numerical solution with a dimensionless amplitude  $A^* = 0.6$ , a length scale  $l = 20 m$  and a bottom slope  $\alpha = 1/30$ . Extensive numerical investigations

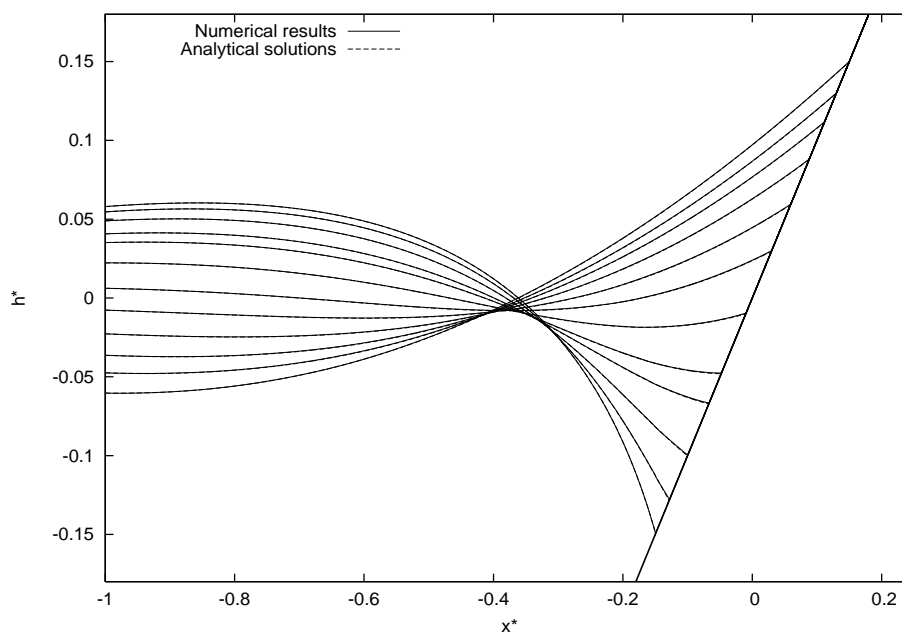


**Figure 4.6.5.** The Carrier and Greenspan's periodic wave solution on a uniform plane beach. Comparison between numerical results (solid lines) and analytical solutions (in dots) for the surface elevation. Profiles of water surface elevation  $h^*$  are plotted versus the onshore coordinate  $x^*$  for different values of time  $t^*$  between  $t^* = 3T^*$  and  $t^* = 3T^* + T^*/2$ .

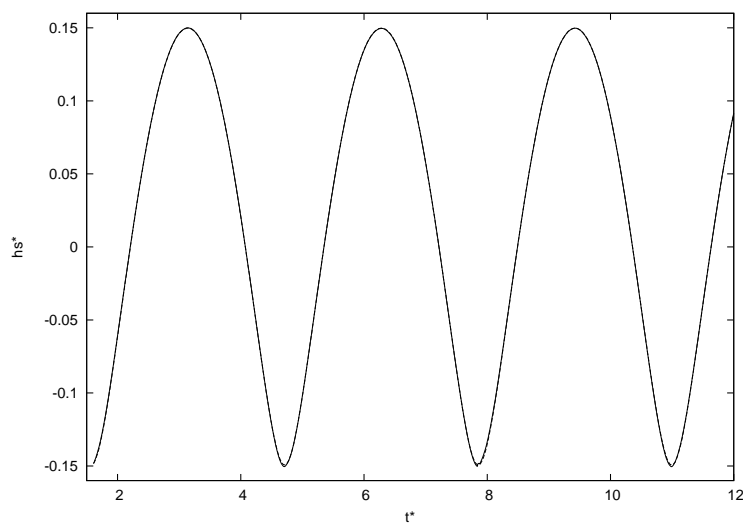


**Figure 4.6.6.** The Carrier and Greenspan periodic wave solution on a uniform plane beach. Comparison between numerical results (in solid lines) and the analytical solution (in dots) for the vertical motion of the shoreline. Water surface elevation of the shoreline  $h_s^*$  is plotted versus the dimensionless time coordinate  $t^*$ , during three periods.

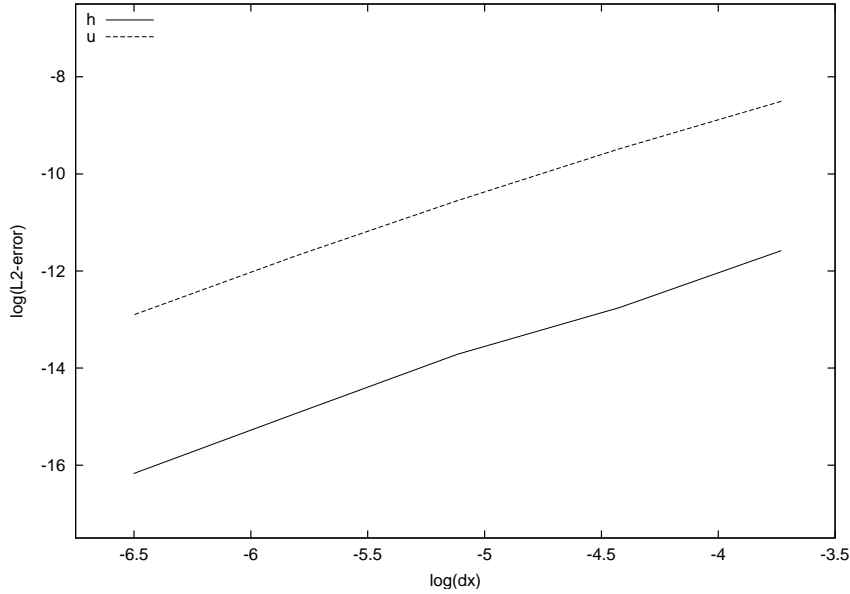


**Figure 4.6.7.** The Carrier and Greenspan’s periodic solution on a uniform plane beach.  $L^2$ -convergence curves for the surface elevation  $h^*$  (in solid line) and the velocity  $u^*$  (in dashed-dots line) at  $t^* = 1.5$ .  $\log(L^2\text{-error})$  is plotted versus  $\log(\Delta x)$  at  $t^* = 1.5$ .

show that *SURF\_SVWB* is robust enough to deal with a large range of bottom slope whereas the Exact Well-Balanced Riemann solver or the well-balanced VFRoe-ncv solver were very sensitive to the bottom slope as it has been emphasized in the third section. The numerical results provided by *SURF\_SVWB* are compared to the analytical solution for a significant range of time, in order to be sure that small instabilities which may eventually be amplified later are not generated.

We show on Figure 4.6.5 the comparison between numerical results and analytical solution for the surface elevation, for different values of time  $t^*$  between  $3T^*$  and  $3T^* + T^*/2$  where  $T^*$  is the dimensionless period of the oscillations. Value of  $\Delta x^* = 0.002$  and  $CFL = 0.7$  have been used. for this test. We can observe that the moving shoreline is accurately computed even after a few periods. We can see on Figure 4.6.6 the time series of the surface elevation at the shoreline, during a few periods. The accuracy of the results and the robustness of the model are clearly highlighted. A comparison with the results presented in the literature (see Brocchini et al. [26] or Prasad and Svendsen [140] for example), shows a more accurate agreement with the analytical solution for the *SURF\_SVWB* model. Even if we don’t show here the  $L^2$ -error curves, we can mention that this error is once again more significant for the velocity and we stress out that this error is periodical and is only important at the times of maximum run-up and run-down, when the theoretical velocity vanishes. However, this error is not amplified and never goes over three per cent during ten complete periods. We can see on Figure 4.6.7 the  $L^2$ -convergence curves for the water height (in solid line) and the velocity (in dot-dashed line). The measured rate of convergence are above 1.66 for the water height and 1.63 for the velocity.

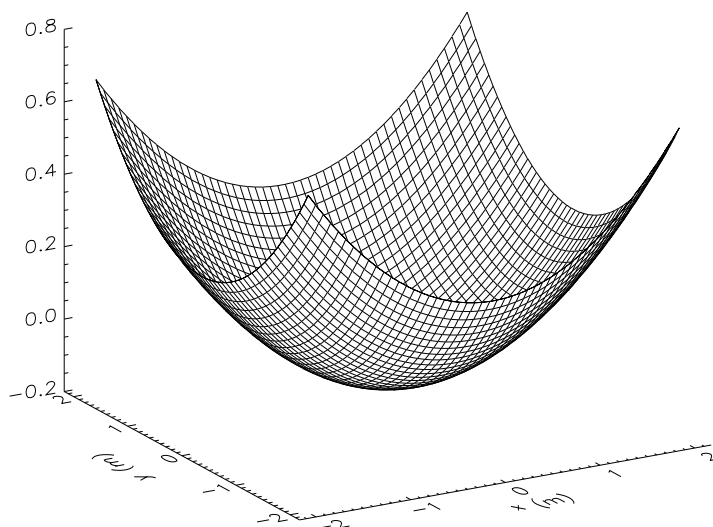


**Figure 4.6.8.** Thacker's solutions. Topography of the paraboloidal basin.

**4.6.2. Two dimensional assessments.** Very few analytical solutions are available for the two-dimensional NSW equations with free moving boundary, involving run-up and run-down phenomena. In his study [168], Thacker provides a set of two different classes of solutions corresponding to time-dependent non-linear oscillations in parabolic basins. The most relevant feature of this set of solutions is that boundary conditions can't be used as inlet boundary condition in order to generate the motion as in Carrier and Greenspan's solutions for example. As in the one-dimensional cases, no bore are generated while the water runs-up the sloping sides of the basins. The motion is oscillatory with a small enough amplitude limit, imposed by the long wave assumption, and since bottom frictions are not included in the model there is no energy dissipation.

In the first test, the solution is a radially symmetrical oscillating paraboloid whereas in the second test the surface remains planar as it oscillates, without any radial symmetry. For these two tests, the flow takes place inside a parabola of revolution defined as :

$$d(r) = -h_0 \left( 1 - \frac{r^2}{a^2} \right) \quad (4.57)$$

on the computational domain  $[-2, 2] \times [-2, 2]$ , where  $h_0$  is the depth of water at the center point for a zero elevation and  $a$  is the distance from the center point to the zero elevation of the shoreline (see Figure 4.6.9).

*Thacker's axisymmetrical solution.* The curved solution provides in [168] is given by :

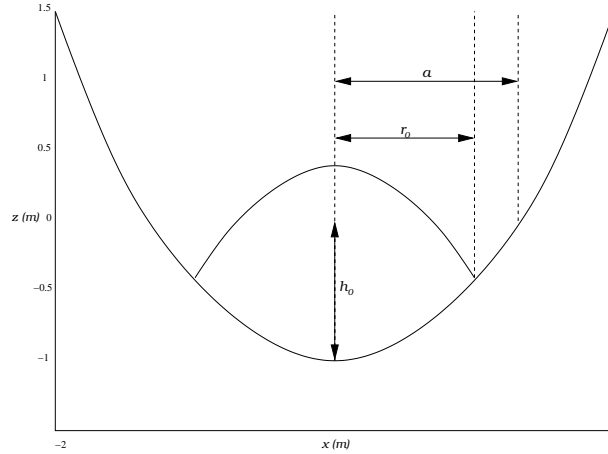


**Figure 4.6.9.** Centerline shape of the parabolic basin and initial free surface for the Thacker's paraboloid solution.

$$\left\{ \begin{array}{l} h(r, t) = h_0 \left[ \frac{(1 - A^2)^{\frac{1}{2}}}{1 - A \cos(\omega t)} - 1 - \frac{r^2}{a^2} \left( \frac{1 - A^2}{(1 - A \cos(\omega t))^2} - 1 \right) \right], \\ u = \frac{1}{1 - A \cos(\omega t)} \left( \frac{1}{2} \omega x A \sin(\omega t) \right), \\ v = \frac{1}{1 - A \cos(\omega t)} \left( \frac{1}{2} \omega y A \sin(\omega t) \right). \end{array} \right. \quad (4.58)$$

where the frequency  $\omega$  is given by

$$\omega = \sqrt{\frac{8g h_0}{a^2}}, \quad (4.59)$$

$r$  is the distance from the center point,  $r_0$  the distance from the center point to the point where the shoreline is initially located (see Figure 4.6.9) and

$$A = \frac{a^2 - r_0^2}{a^2 + r_0^2}. \quad (4.60)$$

The analytical solution at  $t = 0$  is supplied as initial condition. The boundary conditions are transmissive but this choice has no further importance since water flows never reach the boundaries. The depth profile for the basin and the definitions of  $a$ ,  $r_0$  and  $h_0$  are shown on Figure 4.6.9. The values used for this numerical test are  $a = 1$ ,  $r_0 = 0.8 \text{ m}$  and  $h_0 = 0.1 \text{ m}$ . We use  $\Delta x = \Delta y = 0.008 \text{ m}$  and the  $CFL$  is set to 0.4.

The centerline initial condition (for  $y = 0$ ) is shown in Figure 4.6.10 a) together with comparisons between numerical and analytical results at three different values of time. These numerical surface elevations are computed after three complete periods  $T$  and these results are in excellent agreement with the analytical solutions. Furthermore,

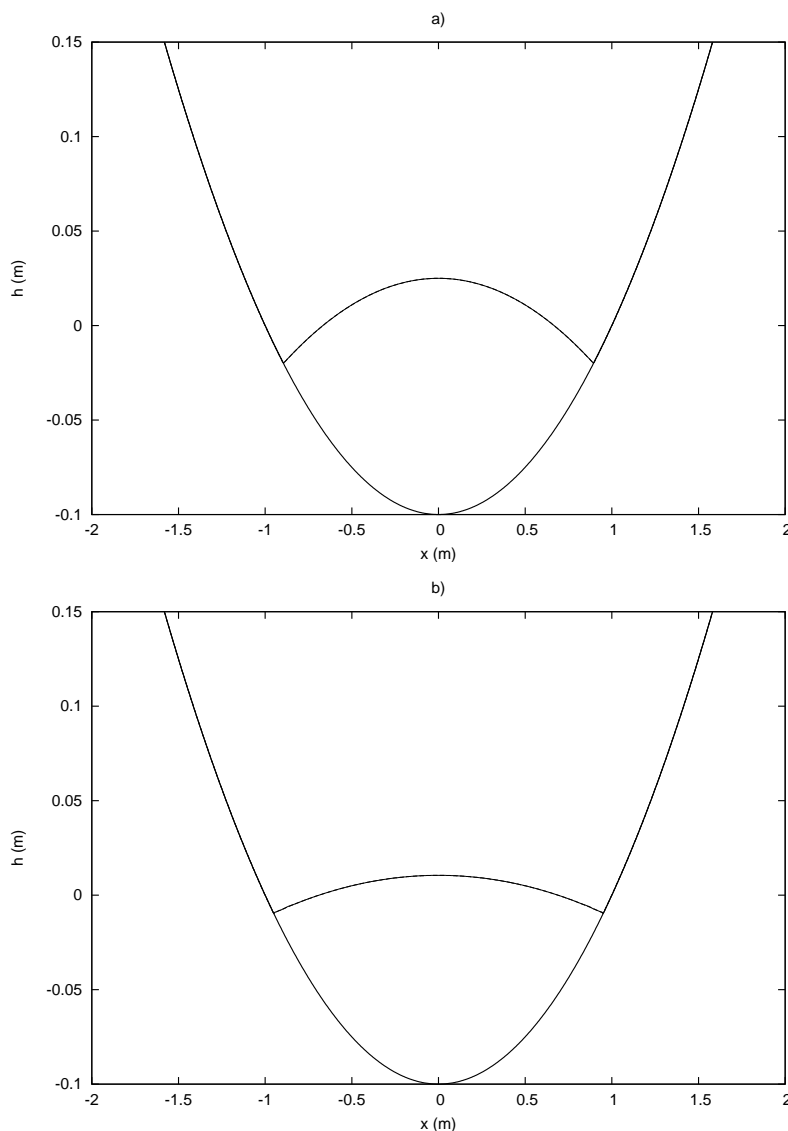


**Figure 4.6.10.** Thacker's 2D paraboloid solution. Comparison between numerical results (in solid lines) and analytical solution (in dashed lines) for the centerline free surface profile. Water surface elevation profiles  $h$  are plotted versus the  $x$  coordinate, for  $y = 0$ , for a)  $t=3T$  and b)  $t=3T+T/6$ , where  $T$  is the oscillations period

it seems that no spurious oscillations are present near the shoreline even after three periods.

In Figure 4.6.12, we focus on the run-up and run-down phenomena during an half period. We can see on this zoom that actually, very small distortions appear in the intermediates states between the minimum and maximum surface elevation. But these distortions are small enough to be smoothed during the next numerical iterations and thus, they don't propagate.

For this first two-dimensional test, we show on Figure 4.6.14 the  $L^2$ -error time series

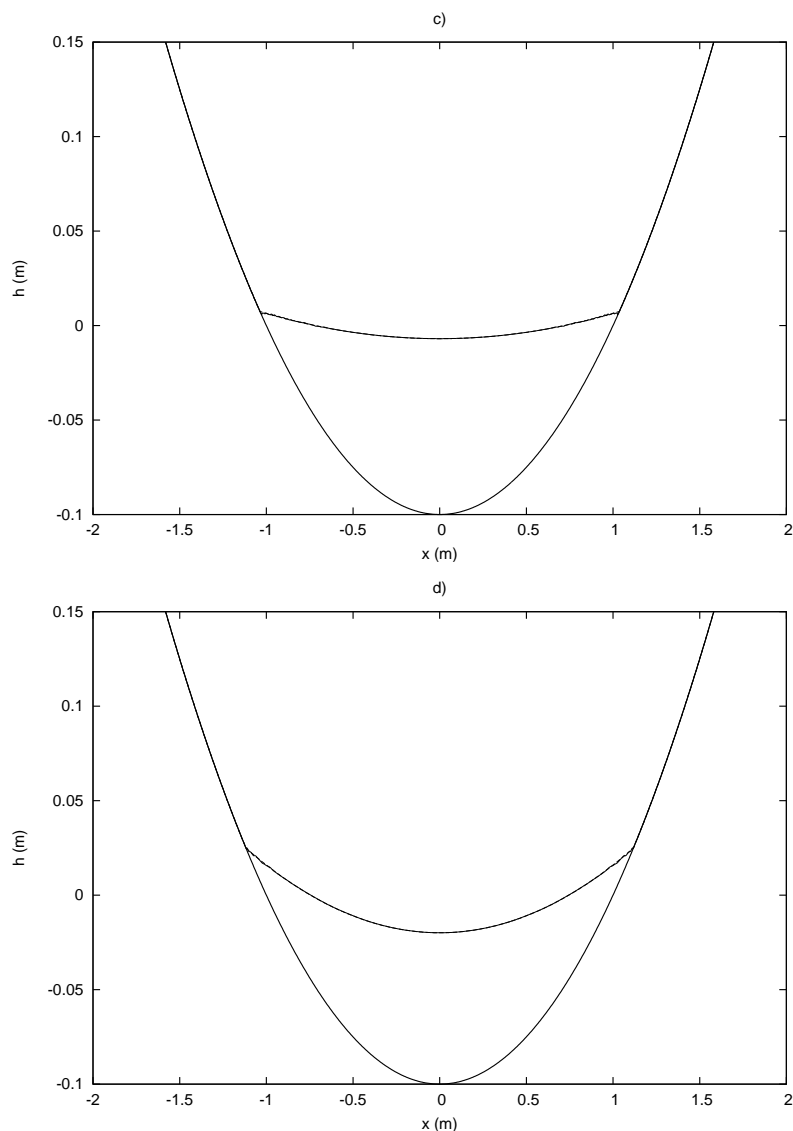


**Figure 4.6.11.** Thacker's 2D paraboloid solution. Comparison between numerical results (in solid lines) and analytical solution (in dashed lines) for the centerline free surface profile. Water surface elevation profiles  $h$  are plotted versus the  $x$  coordinate, for  $y = 0$ , for c)  $t = 3T + T/3$  and d)  $t = 3T + T/2$ , where  $T$  is the oscillations period

for the water height and the velocity. As for the one dimensional test, the error on the water height remains very small during all the computational time. On the velocity curve we can observe periodic points or errors which are much greater than for the water height. They correspond to the times at which the velocity vanishes before the change of sign and may be due to a phase shift between numerical and analytical data. This error is not amplified and smoothed for long time evolutions. Actually after ten periods the error always remains under ten per cents. We can also observe

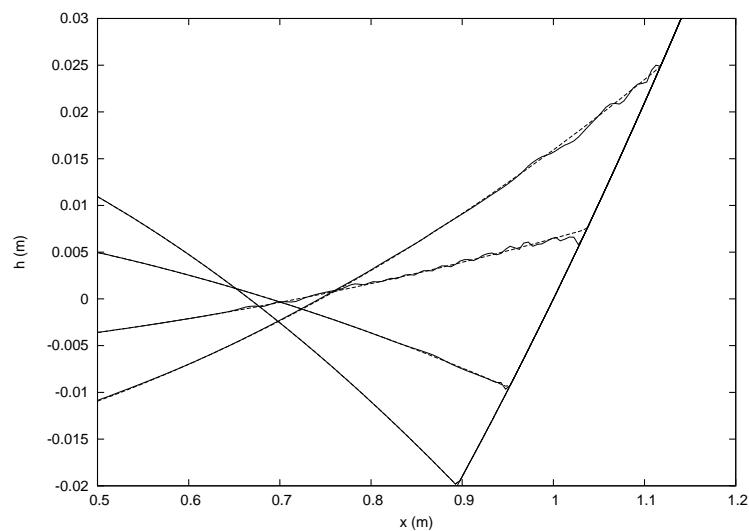


**Figure 4.6.12.** Thacker's paraboloid solution. Zoom of the centerline free surface profile for the water surface elevation near the shoreline. Analytical (in dots) and numerical (solid lines) profiles are plotted versus the  $x$  coordinate, for  $y = 0$  for different  $t=3T$ ,  $t=3T+T/6$ ,  $t=3T+T/3$ ,  $T=3T+T/2$ .

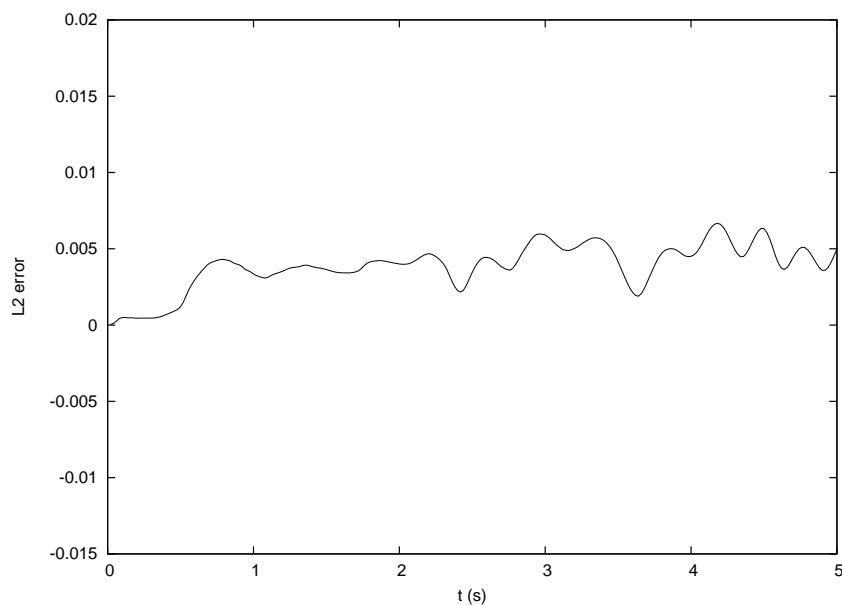


**Figure 4.6.13.** Thacker's paraboloid solution. Time series of the  $L^2$ -error for  $h$  between numerical results provided by *SURF-SVWB* and the analytical solution. The  $L^2$ -error is plotted versus  $t$  for  $\Delta x = \Delta y = 0.008$ .

on Figure 4.6.15 the  $L^2$ -convergence curves for the water height  $h$  and the velocity  $\mathbf{u}$ . The rate of convergence is around 1.4 for the water height and 1.2 for the velocity.

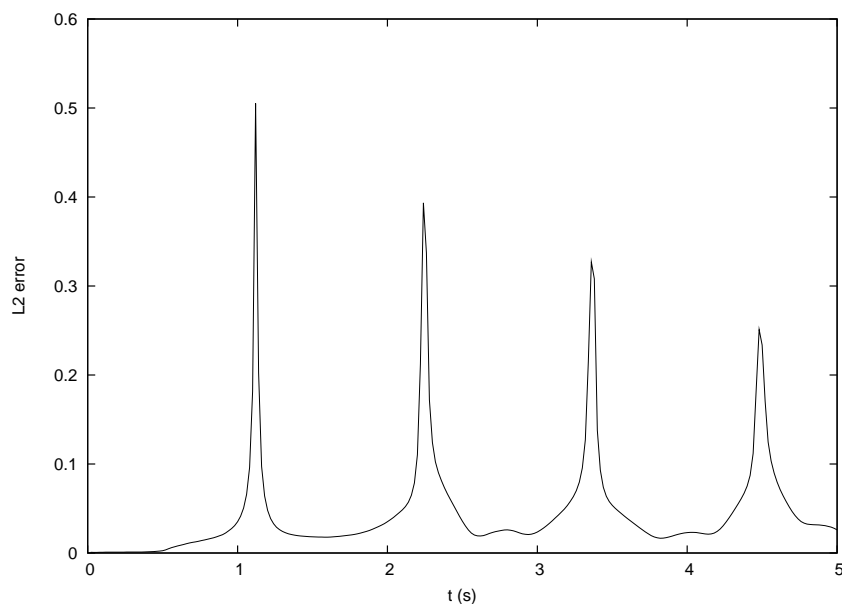


**Figure 4.6.14.** Thacker's paraboloid solution. Time series of the  $L^2$ -error for  $u$  between numerical results provided by *SURF-SVWB* and the analytical solution. The  $L^2$ -error is plotted versus  $t$  for  $\Delta x = \Delta y = 0.008$ .

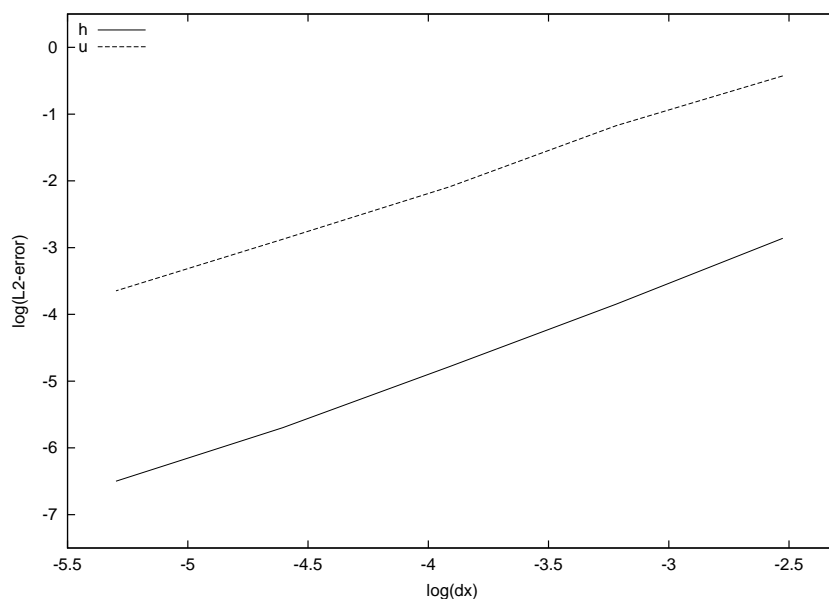


**Figure 4.6.15.** Thacker's paraboloid solution.  $L^2$ -convergence curves for the surface elevation  $h$  (in solid line) and the velocity  $\mathbf{u}$  (in dashed-dots line).  $\log(L^2\text{-error})$  is plotted versus  $\log(\Delta x)$  at  $t = 3$  s.

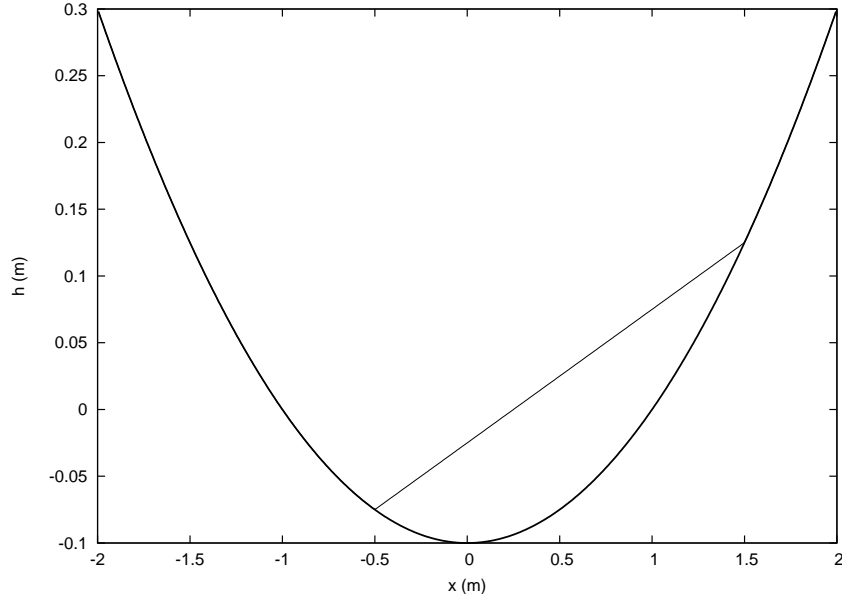


**Figure 4.6.16.** Thacker's planar solution. Centerline initial condition.

*Thacker's planar solution.* This test case is perhaps the most difficult for the numerical model since it involves a wetting and drying procedure on a non radially symmetric initial configuration, unlike the previous test case. The exact periodic solution of the NSW equations provided in [168] is given by :

$$\begin{cases} h(x, y, t) = \frac{\eta h_0}{a^2} (2x \cos(\omega t) + 2y \sin(\omega t) - \eta), \\ u = -\eta \omega \sin(\omega t), \\ v = \eta \omega \cos(\omega t), \end{cases} \quad (4.61)$$

where  $\omega = \sqrt{2gh_0}/a$ . The values used for this numerical test are  $a = 1$ ,  $\eta = 0.5 m$  and  $h_0 = 0.1 m$ .

This exact solution evaluated at  $t = 0$  is used as initial values for the surface elevation and velocity. The moving shoreline is a circle in the  $(x, y)$  plane and the motion is such that the center of the circle orbits the center of the basin, while the surface remains planar with constant gradient at any given instant as the water oscillates. For this test we also use the values  $\Delta x = \Delta y = 0.008 m$  and  $CFL = 0.4$ .

The numerical results obtained are compared to the analytical solution in Figure 4.6.16. We can observe an accurate matching between the two solutions, even after a period. We note a very small distortion near the shoreline, which can be reduced with a finer spatial discretization. The moving shoreline is accurately computed during several periods with no signs of spurious oscillations. In order to give an idea of the two dimensional behavior of the numerical solution, we have plotted on Figure 4.6.18 the

contours of water depth for both exact and approximate solution at four times during a complete period. On Figure 4.6.18 a) we can observe the contours at  $t = 0$  s whereas Figure 4.6.18 e) shows the same contours after a complete revolution around the basin. A very tiny distortion can be observed but the contours remain quasi perfectly circular during the complete period and these results are more accurate than those presented by Hubbard and Dodd [84] with their Riemann solver of Roe and their adaptive refinement procedure. On Figure 4.6.19 a comparison of the contour profiles for the quantity  $h + d$  between  $t = 0$  and  $t = 2T$  is possible. These figures enable us to see how the planar aspect of the water surface is preserved during the computation. These results are considered as very satisfactory.

It is more difficult to model accurately the velocity. As seen in the previous case with Figure 4.6.14 the  $L^2$ -error is always larger for the velocity and we can see on Figure 4.6.20 that the largest discrepancies are located at the periphery, close to the moving wet/dry interface and where the water depth is vanishing. We have observed this behavior for the Carrier and Greenspan's periodic solution and for the previous Thacker's axisymmetrical solution. When compared to the results shown by Hubbard and Dodd [84], the numerical results for  $u$  are considered satisfactory and the results concerning  $v$  seem to be a little more accurate. However these difficulties in modeling the velocity near the shoreline are not amplified for long time simulations and don't seem to disturb the accuracy of the moving shoreline predictions. Therefore, these results concerning the velocity are considered satisfactory for our purpose.

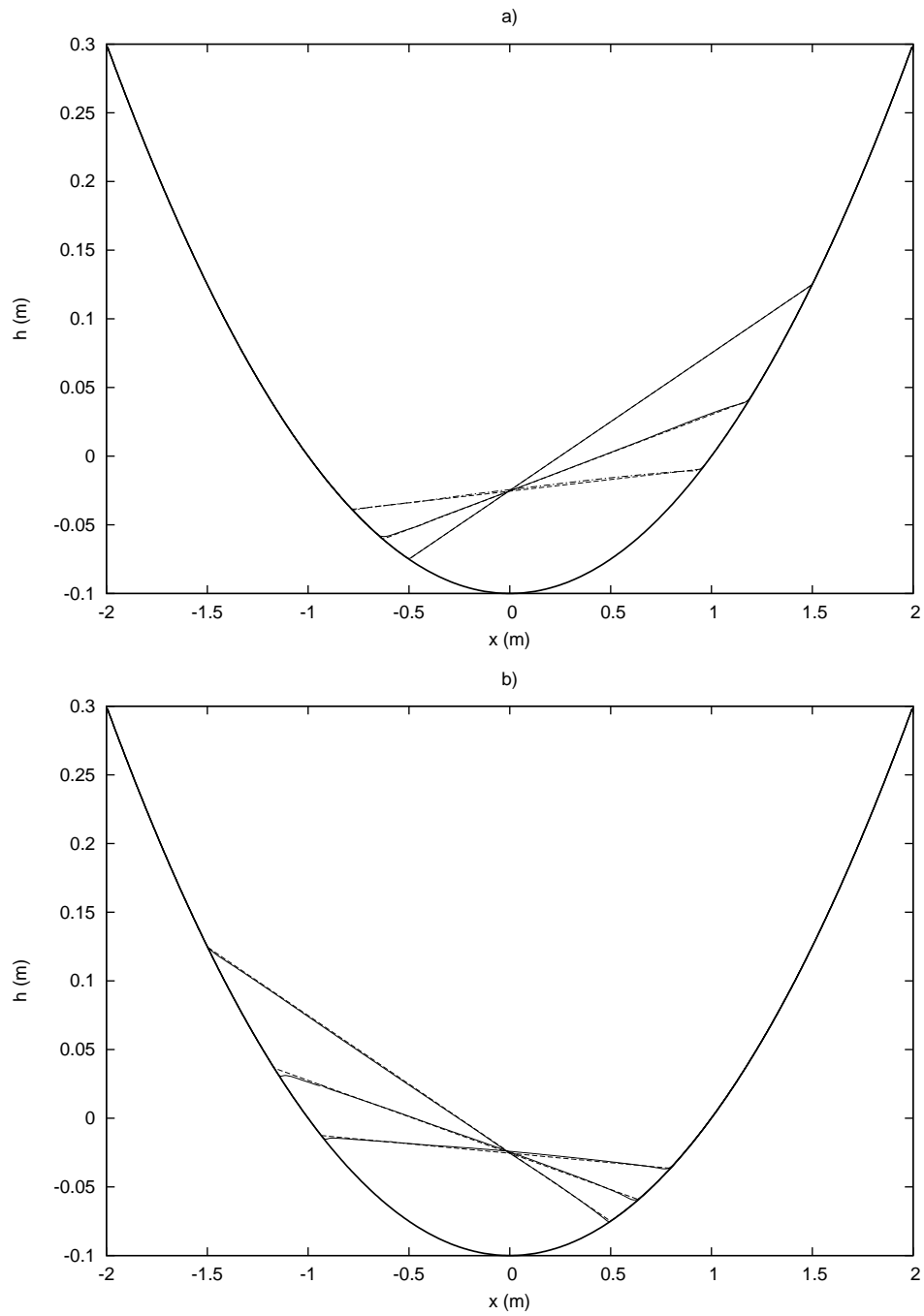


**Figure 4.6.17.** Thacker's planar solution. Comparison between numerical results (in solid lines) and analytical solution (in dots). Centerline free surface profiles for the surface elevation  $h$  are plotted versus the  $x$  coordinate, for  $y = 0$ , at a)  $t = 2T$ ,  $t = 2T + T/6T$ ,  $t = 2T + T/5T$  and b)  $t = 2T + T/4$ ,  $t = 2T + T/3$ ,  $t = 2T + T/2$ .

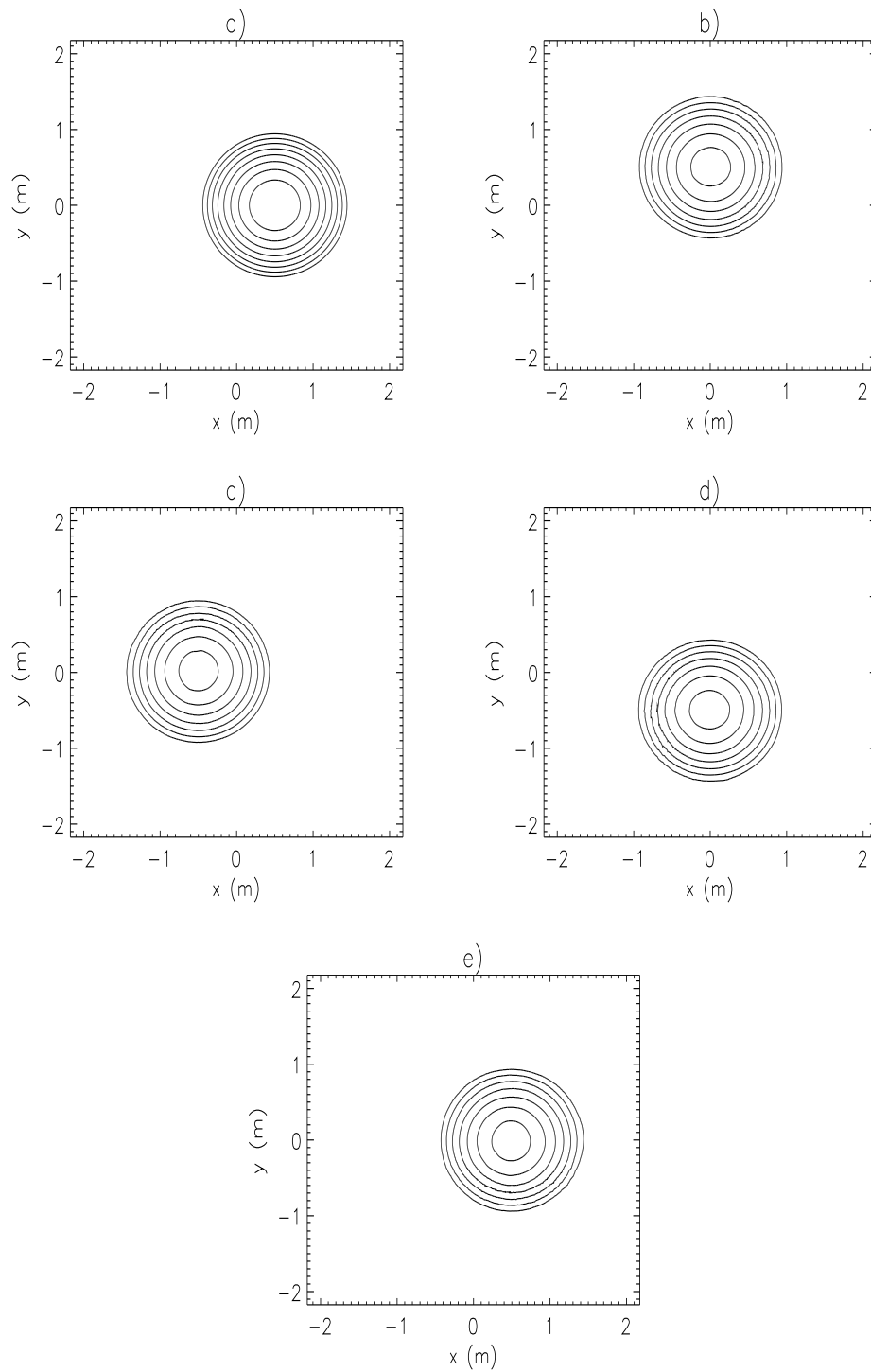


**Figure 4.6.18.** Thacker's planar solution. Comparison between numerical results (in solid lines) and analytical solution (in dotted lines). Contours of water depth for both exact and approximate solutions are shown at a)  $t=0$ , b)  $t=T/4$ , c)  $t=T/2$  and d)  $t=3T/4$  and e)  $t=2T$ .

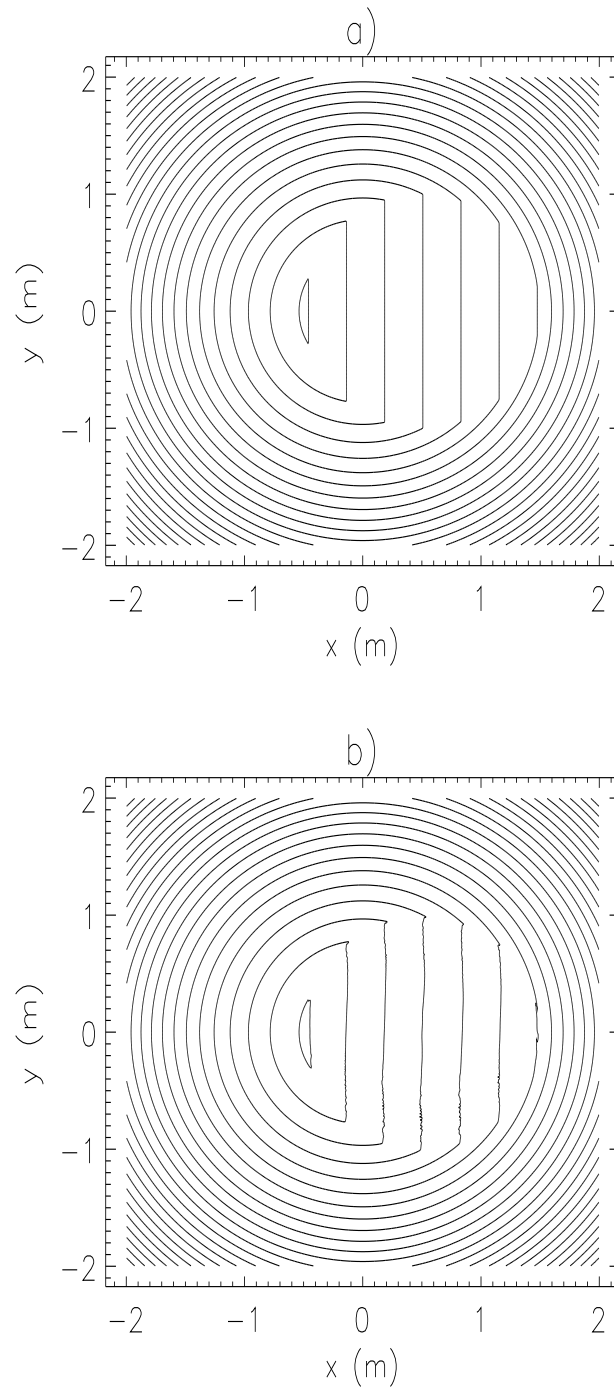


**Figure 4.6.19.** Thacker's planar solution. Comparison between initial contour plots for  $h + d$  (a):  $t=0$ s), and contour plots for  $h + d$  after two periods (b):  $t=2T$ )

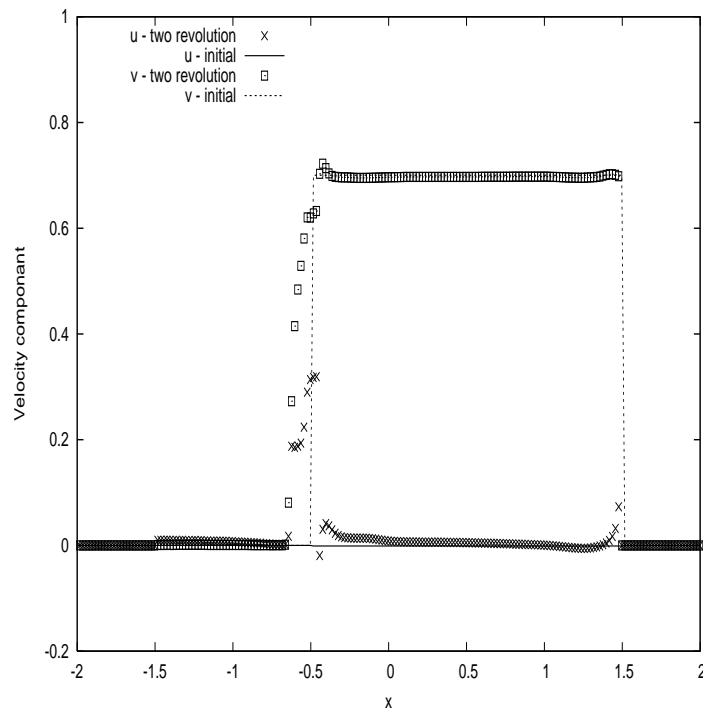


**Figure 4.6.20.** Thacker's planar solution. Comparison between initial centerline profiles for the two components (in solid and dashed lines) of the velocity and the same centerline profile after two complete revolution (in dots).

# Numerical method for the resolution of the source terms

In this chapter we detail the discretization of the parabolic step. The remaining source terms which were not included in the hyperbolic step, namely the friction terms, the Coriolis term, the capillary effects term and the diffusion terms are discretized here.

Since we have developed an efficient model with particular abilities for the “hyperbolic” step, it would be useful if this “source” step could preserve the qualities inherited from the “hyperbolic” step. More precisely :

- i) the “source step” must preserve the positivity of the water depth,
- ii) it must be able to deal easily with the occurrence of dry area,
- iii) it must preserve the steady states “at rest”.

This parabolic step can be viewed as solving a set of ordinary differential equations where the terms at the right hand side can be evaluated using either the intermediate values  $\mathbf{U}^*$  obtained from the previous hyperbolic step, or the updated values  $\mathbf{U}^{n+1}$ . In the first case, the method is fully explicit whereas the second choice lead to a fully implicit scheme. We choose here to use a semi-implicit method which leads to very small restrictions on the time discretization step. The discretization of the involved derivative is performed using centered second order accuracy schemes.

We investigate here the resolution of the following system :

$$\left\{ \begin{array}{l} h_t = 0 , \\ (h\mathbf{u})_t + \alpha_0(h) \mathbf{u} + \alpha_1(h) |\mathbf{u}|\mathbf{u} = \\ -\frac{(h\mathbf{u})^\perp}{R_o} + \beta h \nabla \Delta h + \frac{1}{R_e} \operatorname{div} \left( h D(\mathbf{u}) + (2h \operatorname{div} \mathbf{u}) \mathcal{I} \right) + \beta h \nabla \Delta d . \\ h(t^*) = h^* , \\ (h\mathbf{u})(t^*) = (h\mathbf{u})^* , \end{array} \right. \quad (5.1)$$

We aim at computing the new values  $(h^{n+1}, (h\mathbf{u})^{n+1})$  at time  $t^{n+1}$  from the intermediate states  $(h^*, (h\mathbf{u})^*)$  at time  $t^*$ , obtained from the previous hyperbolic time step. From the equation  $h_t = 0$ , it appears that this second step only contributes to the advancement of the velocity  $\mathbf{u}$ , since we have  $h^{n+1} = h^*$ . Therefore, system (5.1) can be expressed in a pseudo non-conservative form as follows :

$$\left\{ \begin{array}{l} h^{n+1} = h^* , \\ h^* \mathbf{u}_t + \alpha_0(h^*) \mathbf{u} + \alpha_1(h^*) |\mathbf{u}|\mathbf{u} = \\ -\frac{(h^*\mathbf{u})^\perp}{R_o} + \beta h^* \nabla \Delta h^* + \frac{1}{R_e} \operatorname{div} \left( h^* D(\mathbf{u}) + (2h^* \operatorname{div} \mathbf{u}) \mathcal{I} \right) + \beta h^* \nabla \Delta d . \\ u(t^*) = u^* , \end{array} \right. \quad (5.2)$$

Using a classical upwind Euler explicit scheme for the time discretization, the chosen semi-implicit discretization is thus defined as follows :

$$\begin{aligned} h^* \left( \frac{\mathbf{u}^{n+1} - \mathbf{u}^*}{\Delta t} \right) + \alpha_0(h^*) \mathbf{u}^{n+1} + \alpha_1(h^*) |\mathbf{u}^*| \mathbf{u}^{n+1} - h^* \nabla \Delta h^* \\ = \frac{((h\mathbf{u})^*)^\perp}{R_o} + \frac{1}{R_e} \operatorname{div} \left( h^* D(\mathbf{u}^{n+1}) + (2h^* \operatorname{div} \mathbf{u}^{n+1}) \mathcal{I} \right) + h^* \nabla \Delta d . \end{aligned} \quad (5.3)$$

As no derivative are involved in the friction and the Coriolis terms, we only have to develop in details the discretization of the viscous terms  $\frac{1}{R_e} \operatorname{div} \left( h^* D(U^{n+1}) + (2h^* \operatorname{div} U^{n+1}) \mathcal{I} \right)$  and the capillary terms. This is addressed in the next sections.

### 5.1. Centered discretization of the viscous terms

As in the first part, the viscosity tensor  $D(\mathbf{u})$  is defined with :

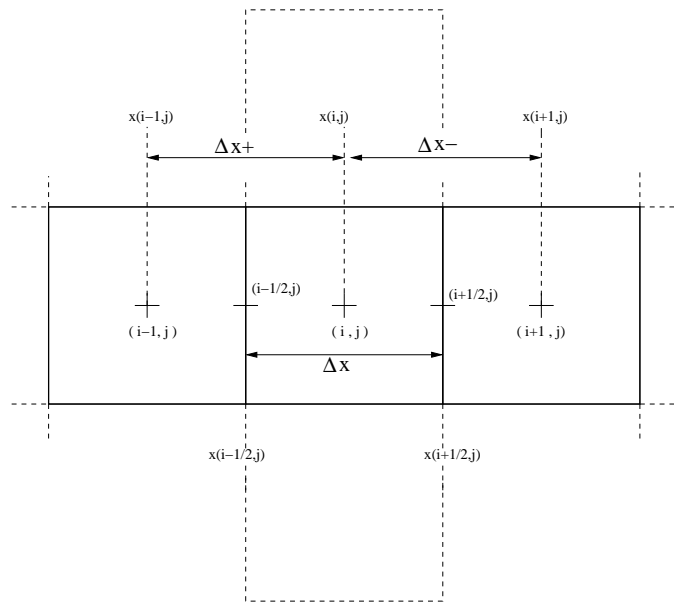


Figure 5.1.1. Discretization sketch in the  $x$  direction.

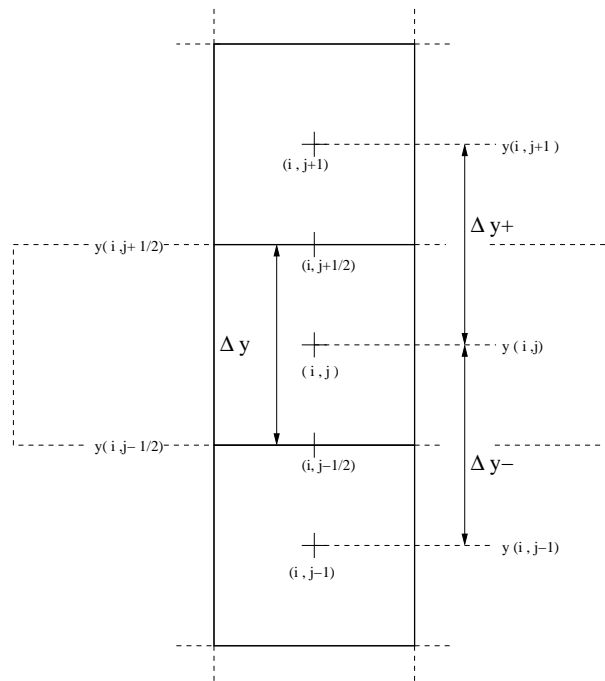


Figure 5.1.2. Discretization sketch in the  $y$  direction.

$$D(\mathbf{u}) = \frac{1}{2}(\nabla \mathbf{u} + {}^t \nabla \mathbf{u}). \quad (5.4)$$

**Remark 5.1.1.** *As exposed in the first chapter a turbulent model can be added in the expression of this stress tensor, leading to eddy anisotropic viscosity. The vertical eddy viscosity coefficient is recovered in the expressions of the friction coefficients  $\alpha_0(h)$  and  $\alpha_1(h)$ , while the horizontal eddy viscosity coefficient is used in the definition of the Reynolds number. However, it does not modify the following discretization.*

In terms of spatial derivation we obtain the following expression :

$$hD(\mathbf{u}) + (2h \operatorname{div} \mathbf{u})\mathcal{I} = \frac{1}{2} \begin{pmatrix} 6h u_x + 4h v_y & h(u_y + v_x) \\ h(u_y + v_x) & 6h v_y + 4h u_x \end{pmatrix} \quad (5.5)$$

Therefore, the whole term  $\frac{1}{R_e} \operatorname{div} (hD(\mathbf{u}) + (2h \operatorname{div} \mathbf{u})\mathcal{I})$  is developed as follows :

$$\frac{1}{R_e} \operatorname{div} (hD(\mathbf{u}) + (2h \operatorname{div} \mathbf{u})\mathcal{I}) = \frac{1}{R_e} \begin{pmatrix} 3(hu_x)_x + 2(hv_y)_x + \frac{1}{2}(hu_y)_y + \frac{1}{2}(hv_x)_y \\ 3(hv_y)_y + 2(hu_x)_y + \frac{1}{2}(hv_x)_x + \frac{1}{2}(hu_y)_x \end{pmatrix} \quad (5.6)$$

We next develop in details the finite difference derivations of each derivate involved in this expression. The second order derivatives are approximate with the usual second order centered discretization. We obtain for an arbitrary quantity  $\alpha$  and a derivation along the  $x$  direction :

$$\left( (h\alpha_x)_x \right)_{i,j} = \frac{1}{(\Delta x)_{ij}} \left( h_{i+\frac{1}{2},j}(\alpha_x)_{i+\frac{1}{2},j} - h_{i-\frac{1}{2},j}(\alpha_x)_{i-\frac{1}{2},j} \right) + O((\Delta x)_{ij}^2)$$

where  $(\Delta x)_{ij} = x(i + \frac{1}{2}, j) - x(i - \frac{1}{2}, j)$ . This expression is valid for variable space discretization but for the sake of clarity, and when no confusion is possible, we set  $\Delta x = (\Delta x)_{ij}$  in the following. The notation  $(\Delta x)_{ij}$  will only be used when necessary.

The first order derivatives at the locations  $(i + \frac{1}{2}, j)$  and  $(i - \frac{1}{2}, j)$  are given by :

$$(\alpha_x)_{i+\frac{1}{2},j} = \frac{\alpha_{i+1,j} - \alpha_{i,j}}{(\Delta x)_{ij}^+} + O(\Delta x_{ij}^+) \quad \text{and} \quad (\alpha_x)_{i-\frac{1}{2},j} = \frac{\alpha_{i,j} - \alpha_{i-1,j}}{(\Delta x)_{ij}^-} + O(\Delta x_{ij}^-)$$

where  $(\Delta x)_{ij}^+ = x(i + 1, j) - x(i, j)$  and  $(\Delta x)_{ij}^- = x(i, j) - x(i - 1, j)$  stand for the distance between the centers of the cells  $(i + 1, j)$  and  $(i, j)$  for  $(\Delta x)_{ij}^+$  and between the cells  $(i, j)$  and  $(i - 1, j)$  for  $(\Delta x)_{ij}^-$ .

As for  $\Delta x$  we set  $\Delta x^+ = (\Delta x)_{ij}^+$  and  $\Delta x^- = (\Delta x)_{ij}^-$  in the following. This is illustrated on Figure 5.1.1 for the considered  $x$  direction and Figure 5.1.2 for the  $y$  direction which

will be considered hereinafter.

We also define  $\delta x = \max_{i,j}((\Delta x)_{ij}, (\Delta x)_{ij}^+, (\Delta x)_{ij}^-)$  and the accuracy of the previous discretization can be expressed in terms of  $\delta x$  which is no more cell dependent.

The complete discretized expression is thus given by :

$$\left(\partial_x(h\partial_x\alpha)\right)_{i,j} \simeq \frac{1}{\Delta x \Delta x_+} \left(h_{i+\frac{1}{2},j}(\alpha_{i+1,j} - \alpha_{i,j})\right) - \frac{1}{\Delta x \Delta x_-} \left(h_{i-\frac{1}{2},j}(\alpha_{i,j} - \alpha_{i-1,j})\right) \quad (5.7)$$

The discretization of the derivation along the  $y$  expression is obtained in the same way. We obtain :

$$\left(\partial_y(h\partial_y\alpha)\right)_{i,j} \simeq \frac{1}{\Delta y \Delta y_+} \left(h_{i,j+\frac{1}{2}}(\alpha_{i,j+1} - \alpha_{i,j})\right) - \frac{1}{\Delta y \Delta y_-} \left(h_{i,j-\frac{1}{2}}(\alpha_{i,j} - \alpha_{i,j-1})\right) \quad (5.8)$$

For the crosses derivatives we have, :

$$\left(\partial_x(h\partial_y\alpha)\right)_{i,j} \simeq \frac{1}{\Delta x \Delta y} \left(h_{i+\frac{1}{2},j}(\alpha_{i+\frac{1}{2},j+\frac{1}{2}} - \alpha_{i+\frac{1}{2},j-\frac{1}{2}}) - h_{i-\frac{1}{2},j}(\alpha_{i-\frac{1}{2},j+\frac{1}{2}} - \alpha_{i-\frac{1}{2},j-\frac{1}{2}})\right) \quad (5.9)$$

and

$$\left(\partial_y(h\partial_x\alpha)\right)_{i,j} \simeq \frac{1}{\Delta x \Delta y} \left(h_{i,j+\frac{1}{2}}(\alpha_{i+\frac{1}{2},j+\frac{1}{2}} - \alpha_{i-\frac{1}{2},j+\frac{1}{2}}) - h_{i,j-\frac{1}{2}}(\alpha_{i+\frac{1}{2},j-\frac{1}{2}} - \alpha_{i-\frac{1}{2},j-\frac{1}{2}})\right). \quad (5.10)$$

Hence, gathering these expressions, we obtain the complete discretization of the diffusion terms at point  $(i, j)$ , for the scalar velocity component  $u$  :

$$\begin{aligned}
& \frac{1}{R_e} (3(hu_x)_x + 2(hv_y)_x + \frac{1}{2}(hu_y)_y + \frac{1}{2}(hv_x)_y) \simeq \\
& \frac{1}{R_e} \left[ \left( \frac{3h_{i+\frac{1}{2},j}}{\Delta x \Delta x^+} + \frac{3h_{i-\frac{1}{2},j}}{\Delta x \Delta x^-} + \frac{h_{i,j+\frac{1}{2}}}{2\Delta y \Delta y^+} + \frac{h_{i,j-\frac{1}{2}}}{2\Delta y \Delta y^-} \right) u_{i,j} \right. \\
& - \left( \frac{3h_{i+\frac{1}{2},j}}{\Delta x \Delta x^+} \right) u_{i+1,j} - \left( \frac{3h_{i-\frac{1}{2},j}}{\Delta x \Delta x^-} \right) u_{i-1,j} - \left( \frac{h_{i,j+\frac{1}{2}}}{2\Delta y \Delta y^+} \right) u_{i,j+1} - \left( \frac{h_{i,j-\frac{1}{2}}}{2\Delta y \Delta y^-} \right) u_{i,j-1} \\
& - \left( \frac{2h_{i+\frac{1}{2},j}}{\Delta x \Delta y} + \frac{h_{i,j+\frac{1}{2}}}{2\Delta x \Delta y} \right) v_{i+\frac{1}{2},j+\frac{1}{2}} - \left( \frac{2h_{i-\frac{1}{2},j}}{\Delta x \Delta y} + \frac{h_{i,j-\frac{1}{2}}}{2\Delta x \Delta y} \right) v_{i-\frac{1}{2},j-\frac{1}{2}} \\
& \left. + \left( \frac{2h_{i+\frac{1}{2},j}}{\Delta x \Delta y} + \frac{h_{i,j-\frac{1}{2}}}{2\Delta x \Delta y} \right) v_{i+\frac{1}{2},j-\frac{1}{2}} + \left( \frac{2h_{i-\frac{1}{2},j}}{\Delta x \Delta y} + \frac{h_{i,j+\frac{1}{2}}}{2\Delta x \Delta y} \right) v_{i-\frac{1}{2},j+\frac{1}{2}} \right]
\end{aligned} \tag{5.11}$$

Remark that values of the advanced component  $v^{n+1}$  are involved in this expression which enables the computation of the component  $u^{n+1}$ .

Similarly, we obtain the following expression for the velocity component  $v$  :

$$\begin{aligned}
& \frac{1}{R_e} (3(hv_y)_y + 2(hu_x)_y + \frac{1}{2}(hv_x)_x + \frac{1}{2}(hu_y)_x) \simeq \\
& \frac{1}{R_e} \left[ \left( \frac{3h_{i,j+\frac{1}{2}}}{\Delta y \Delta y^+} + \frac{3h_{i,j-\frac{1}{2}}}{\Delta y \Delta y^-} + \frac{h_{i+\frac{1}{2},j}}{2\Delta x \Delta x^+} + \frac{h_{i-\frac{1}{2},j}}{2\Delta x \Delta x^-} \right) v_{i,j} \right. \\
& - \left( \frac{3h_{i,j+\frac{1}{2}}}{\Delta y \Delta y^+} \right) v_{i,j+1} - \left( \frac{3h_{i,j-\frac{1}{2}}}{\Delta y \Delta y^-} \right) v_{i,j-1} - \left( \frac{h_{i+\frac{1}{2},j}}{2\Delta x \Delta x^+} \right) v_{i+1,j} - \left( \frac{h_{i-\frac{1}{2},j}}{2\Delta x \Delta x^-} \right) v_{i-1,j} \\
& - \left( \frac{2h_{i,j+\frac{1}{2}}}{\Delta x \Delta y} + \frac{h_{i+\frac{1}{2},j}}{2\Delta x \Delta y} \right) u_{i+\frac{1}{2},j+\frac{1}{2}} - \left( \frac{2h_{i,j-\frac{1}{2}}}{\Delta x \Delta y} + \frac{h_{i-\frac{1}{2},j}}{2\Delta x \Delta y} \right) u_{i-\frac{1}{2},j-\frac{1}{2}} \\
& \left. + \left( \frac{2h_{i,j+\frac{1}{2}}}{\Delta x \Delta y} + \frac{h_{i-\frac{1}{2},j}}{2\Delta x \Delta y} \right) u_{i+\frac{1}{2},j-\frac{1}{2}} + \left( \frac{2h_{i,j-\frac{1}{2}}}{\Delta x \Delta y} + \frac{h_{i+\frac{1}{2},j}}{2\Delta x \Delta y} \right) u_{i-\frac{1}{2},j+\frac{1}{2}} \right]
\end{aligned} \tag{5.12}$$

These expressions are second order accuracy in space. Note that interface values, denoted with fractional indices, appear in these expressions. These values are computed with linear interpolation. For an arbitrary quantity  $\alpha$ , the values  $\alpha_{i\pm\frac{1}{2},j}$  and  $\alpha_{i,j\pm\frac{1}{2}}$  are obtained as follows :

$$\begin{aligned}
\alpha_{i+\frac{1}{2},j} &= \frac{(\Delta x)_{i+1,j} \alpha_{i+1,j} + (\Delta x)_{i,j} \alpha_{i,j}}{(\Delta x)_{i,j} + (\Delta x)_{i+1,j}}, & \alpha_{i-\frac{1}{2},j} &= \frac{(\Delta x)_{i,j} \alpha_{i,j} + (\Delta x)_{i-1,j} \alpha_{i-1,j}}{(\Delta x)_{i-1,j} + (\Delta x)_{i,j}}, \\
\alpha_{i,j+\frac{1}{2}} &= \frac{(\Delta y)_{i,j+1} \alpha_{i,j+1} + (\Delta y)_{i,j} \alpha_{i,j}}{(\Delta y)_{i,j} + (\Delta y)_{i,j+1}}, & \alpha_{i,j-\frac{1}{2}} &= \frac{(\Delta y)_{i,j} \alpha_{i,j} + (\Delta y)_{i,j-1} \alpha_{i,j-1}}{(\Delta y)_{i,j-1} + (\Delta y)_{i,j}}.
\end{aligned} \tag{5.13}$$

For the fully two dimensional case, we have implemented the case of Cartesian meshes with variable discretization step in each direction but without global refinement. This avoid the difficulty of considering interfaces between cells with different sizes. Consequently, the discretization step  $\Delta x$  can only vary in the  $x$  direction, that is to say that we have necessarily  $(\Delta x)_{i,j-1} = (\Delta x)_{i,j} = (\Delta x)_{i,j+1}$ , whereas it is possible to have  $(\Delta x)_{i+1,j} \neq (\Delta x)_{i,j}$  and  $(\Delta x)_{i,j} \neq (\Delta x)_{i-1,j}$ . Therefore the linear interpolations on variable mesh for the  $\alpha_{i\pm\frac{1}{2},j\pm\frac{1}{2}}$  values are given by :

$$\begin{aligned}
\alpha_{i\mp\frac{1}{2},j\pm\frac{1}{2}} &= \frac{(\Delta y)_{i,j}(\Delta x)_{i\mp 1,j} \alpha_{i\mp 1,j} + (\Delta y)_{i,j}(\Delta x)_{i,j} \alpha_{i,j}}{[(\Delta y)_{i,j\pm 1} + (\Delta y)_{i,j}] [(\Delta x)_{i\mp 1,j} + (\Delta x)_{i,j}]} \\
&\quad + \frac{(\Delta y)_{i,j\pm 1}(\Delta x)_{i\mp 1,j} \alpha_{i\mp 1,j\pm 1} + (\Delta y)_{i,j\pm 1}(\Delta x)_{i,j} \alpha_{i,j\pm 1}}{[(\Delta y)_{i,j\pm 1} + (\Delta y)_{i,j}] [(\Delta x)_{i\mp 1,j} + (\Delta x)_{i,j}]}
\end{aligned} \tag{5.14}$$

## 5.2. Centered discretization of the capillary/surface tension terms

We suggest in this section a simple way to discretize the capillary terms given by  $\beta h \nabla \Delta h$ . This discretization is performed in two steps. In a first step, we compute the Laplacian of the water depth  $h$ . It raises :

$$\begin{aligned}
(\Delta h)_{i,j} &= \left( \partial_x^2 h \right)_{i,j} + \left( \partial_y^2 h \right)_{i,j} \\
&\simeq \frac{1}{\Delta x \Delta x_+} \left( h_{i+1,j} - h_{i,j} \right) - \frac{1}{\Delta x \Delta x_-} \left( h_{i,j} - h_{i-1,j} \right) \\
&\quad + \frac{1}{\Delta y \Delta y_+} \left( h_{i,j+1} - h_{i,j} \right) - \frac{1}{\Delta y \Delta y_-} \left( h_{i,j} - h_{i,j-1} \right)
\end{aligned} \tag{5.15}$$

with the notations introduced at the previous section. this centered discretization is second order accuracy in space. In a second step, we perform the following centered discretization of the remaining gradient :

$$\left(\nabla(\Delta h)\right)_{i,j} = \begin{pmatrix} \left(\partial_x(\Delta h)\right)_{i,j} \\ \left(\partial_y(\Delta h)\right)_{i,j} \end{pmatrix} \simeq \begin{pmatrix} \frac{(\Delta h)_{i+1,j} - (\Delta h)_{i-1,j}}{\Delta x^+ + \Delta x^-} \\ \frac{(\Delta h)_{i,j+1} - (\Delta h)_{i,j-1}}{\Delta y^+ + \Delta y^-} \end{pmatrix} \quad (5.16)$$

Finally, the nonlinear capillary term is computed with :

$$\left(h^*\nabla\Delta h^*\right)_{i,j} = h_{i,j}^*\left(\nabla(\Delta h^*)\right)_{i,j}. \quad (5.17)$$

The remaining term  $h\nabla\Delta d$  is computed following the same idea. We emphasized that no stability study has been performed for this discretization. It has been implemented and tested in a few cases to ensure that it does not lead to numerical instabilities. This is the case for small enough values of the capillary coefficient  $\beta$ .

Another idea which has been investigated is to consider that  $\Delta h$  as a new artificial variable, by setting  $\omega = \Delta h$ . Therefore, the capillary term  $\beta h\nabla\Delta h$  is written under the form  $\beta h\nabla\omega$  and the idea is then to upwind this term in the same way as the convection or the bed-slope source term, while the artificial variable  $\omega = \Delta h$  is recovered at each time step by a relaxation method. This second approach is perhaps more promising since the nonlinear product is taken into account through the upwind process, as for the convection terms. Nonetheless, these two approaches don't preserve the steady states at rest and further investigations are required.

In practice, we do not include the capillary effects in our simulations. This choice is motivated by several reasons. The first is the fact that for numerous test cases, especially those for which we have analytical results, the surface tension effects are not taken into account in the NSW model. Thus, to be consistent with the analytical solutions, surface tensions effects have been neglected for these cases. The second reason is that for more realistic cases as those introduced in the third part of this study, we have performed qualitative comparison with results introduced in the literature and these results have been obtained with models based on NSW equations without capillary effects. Another reason is that at this time, we are not aware of realistic cases which enables us to validate the good "physical behavior" of this discretization. In addition, as we mainly aim at modeling nearshore hydrodynamic cases, we can wonder about the effects of surface tension on the considered phenomena. As emphasized by Peregrine in [136], the clearest effect of surface tension is on steep waves less than about 10 *cm* high, leading to an inhibition of both the development of a plunging jet and the entrainment of air.

To conclude, we can remark that this third order surface tension term can be regarded as a small weakly dispersive term. An efficient and accurate discretization of this term can be a first step towards the introduction of realistic dispersive terms into our NSW model, in order to extend its domain of validity seaward of the breaking zone. Achieving such an extension could be a far-reaching alternative to the parametrized Boussinesq-like models which have seen their validity domain extended to the surf and

swash zone. Hence, a more detailed study of this term seems to be needed and is under investigations.

### 5.3. Discretization of the parabolic equation

Gathering the previous discretizations of the viscous and capillary terms, we are able to compute the updated values of the velocity  $\mathbf{u}$  for this parabolic step. It is convenient to introduce the following coefficients :

$$\left\{ \begin{array}{l} (a_0)_{i,j}^u = h_{i,j}^* + \frac{3}{R_e} \cdot \frac{\Delta t}{\Delta x \cdot \Delta x^+} h_{i+\frac{1}{2},j}^* + \frac{3}{R_e} \cdot \frac{\Delta t}{\Delta x \cdot \Delta x^-} h_{i-\frac{1}{2},j}^* \\ \quad + \frac{1}{2R_e} \cdot \frac{\Delta t}{\Delta y \cdot \Delta y^+} h_{i,j+\frac{1}{2}}^* + \frac{1}{2R_e} \cdot \frac{\Delta t}{\Delta y \cdot \Delta y^-} h_{i,j-\frac{1}{2}}^*, \\ (a_1)_{i,j}^u = -\frac{3}{R_e} \cdot \frac{\Delta t}{\Delta x \cdot \Delta x^+} h_{i+\frac{1}{2},j}^*, \\ (a_{-1})_{i,j}^u = -\frac{3}{R_e} \cdot \frac{\Delta t}{\Delta x \cdot \Delta x^-} h_{i-\frac{1}{2},j}^*, \\ (a_2)_{i,j}^u = -\frac{1}{2R_e} \cdot \frac{\Delta t}{\Delta y \cdot \Delta y^+} h_{i,j+\frac{1}{2}}^*, \\ (a_{-2})_{i,j}^u = -\frac{1}{2R_e} \cdot \frac{\Delta t}{\Delta y \cdot \Delta y^-} h_{i,j-\frac{1}{2}}^*, \end{array} \right. \quad (5.18)$$

and

$$\left\{ \begin{array}{l} (a_0)_{i,j}^v = h_{i,j}^* + \frac{3}{R_e} \cdot \frac{\Delta t}{\Delta y \cdot \Delta y^+} h_{i,j+\frac{1}{2}}^* + \frac{3}{R_e} \cdot \frac{\Delta t}{\Delta y \cdot \Delta y^-} h_{i,j-\frac{1}{2}}^* \\ \quad + \frac{1}{2R_e} \cdot \frac{\Delta t}{\Delta x \cdot \Delta x^+} h_{i+\frac{1}{2},j}^* + \frac{1}{2R_e} \cdot \frac{\Delta t}{\Delta x \cdot \Delta x^-} h_{i-\frac{1}{2},j}^*, \\ (a_1)_{i,j}^v = -\frac{3}{R_e} \cdot \frac{\Delta t}{\Delta y \cdot \Delta y^+} h_{i,j+\frac{1}{2}}^*, \\ (a_{-1})_{i,j}^v = -\frac{3}{R_e} \cdot \frac{\Delta t}{\Delta y \cdot \Delta y^-} h_{i,j-\frac{1}{2}}^*, \\ (a_2)_{i,j}^v = -\frac{1}{2R_e} \cdot \frac{\Delta t}{\Delta x \cdot \Delta x^+} h_{i+\frac{1}{2},j}^*, \\ (a_{-2})_{i,j}^v = -\frac{1}{2R_e} \cdot \frac{\Delta t}{\Delta x \cdot \Delta x^-} h_{i-\frac{1}{2},j}^*. \end{array} \right. \quad (5.19)$$

We also introduce the following coefficients which are involved in the cross derivatives :

$$\left\{ \begin{array}{l}
(b_1)_{i,j}^u = \frac{1}{4R_e} \cdot \frac{\Delta t}{\Delta x \cdot \Delta y} \left( -\frac{1}{2} h_{i,j+\frac{1}{2}}^* + \frac{1}{2} h_{i,j-\frac{1}{2}}^* \right), \\
(b_{-1})_{i,j}^u = -(b_1)_{i,j}^u, \\
(b_2)_{i,j}^u = \frac{1}{4R_e} \cdot \frac{\Delta t}{\Delta x \cdot \Delta y} \left( 2h_{i-\frac{1}{2},j}^* + \frac{1}{2} h_{i,j+\frac{1}{2}}^* \right), \\
(b_{-2})_{i,j}^u = \frac{1}{4R_e} \cdot \frac{\Delta t}{\Delta x \cdot \Delta y} \left( 2h_{i+\frac{1}{2},j}^* + \frac{1}{2} h_{i,j-\frac{1}{2}}^* \right), \\
(b_3)_{i,j}^u = \frac{1}{4R_e} \cdot \frac{\Delta t}{\Delta x \cdot \Delta y} \left( -2h_{i+\frac{1}{2},j}^* + 2h_{i-\frac{1}{2},j}^* \right), \\
(b_{-3})_{i,j}^u = -(b_3)_{i,j}^u, \\
(b_4)_{i,j}^u = \frac{1}{4R_e} \cdot \frac{\Delta t}{\Delta x \cdot \Delta y} \left( -2h_{i+\frac{1}{2},j}^* - \frac{1}{2} h_{i,j+\frac{1}{2}}^* \right), \\
(b_{-4})_{i,j}^u = \frac{1}{4R_e} \cdot \frac{\Delta t}{\Delta x \cdot \Delta y} \left( -2h_{i-\frac{1}{2},j}^* - \frac{1}{2} h_{i,j-\frac{1}{2}}^* \right),
\end{array} \right. \quad (5.20)$$

and

$$\left\{ \begin{array}{l}
(b_1)_{i,j}^v = \frac{1}{4R_e} \cdot \frac{\Delta t}{\Delta x \cdot \Delta y} \left( -2h_{i,j+\frac{1}{2}}^* + 2h_{i,j-\frac{1}{2}}^* \right), \\
(b_{-1})_{i,j}^v = -(b_1)_{i,j}^v, \\
(b_2)_{i,j}^v = \frac{1}{4R_e} \cdot \frac{\Delta t}{\Delta x \cdot \Delta y} \left( \frac{1}{2} h_{i-\frac{1}{2},j}^* + 2h_{i,j+\frac{1}{2}}^* \right), \\
(b_{-2})_{i,j}^v = \frac{1}{4R_e} \cdot \frac{\Delta t}{\Delta x \cdot \Delta y} \left( \frac{1}{2} h_{i+\frac{1}{2},j}^* + 2h_{i,j-\frac{1}{2}}^* \right), \\
(b_3)_{i,j}^v = \frac{1}{4R_e} \cdot \frac{\Delta t}{\Delta x \cdot \Delta y} \left( -\frac{1}{2} h_{i+\frac{1}{2},j}^* + \frac{1}{2} h_{i-\frac{1}{2},j}^* \right), \\
(b_{-3})_{i,j}^v = -(b_3)_{i,j}^v, \\
(b_4)_{i,j}^v = \frac{1}{4R_e} \cdot \frac{\Delta t}{\Delta x \cdot \Delta y} \left( -\frac{1}{2} h_{i+\frac{1}{2},j}^* - 2h_{i,j+\frac{1}{2}}^* \right), \\
(b_{-4})_{i,j}^v = \frac{1}{4R_e} \cdot \frac{\Delta t}{\Delta x \cdot \Delta y} \left( -\frac{1}{2} h_{i-\frac{1}{2},j}^* - 2h_{i,j-\frac{1}{2}}^* \right).
\end{array} \right. \quad (5.21)$$

From these values, the discretization of equation (5.3) at point  $(i, j)$  yields the following system, involving the unknown  $u_{i,j}$  et  $v_{i,j}$  :

$$\left\{ \begin{array}{l}
 \left( (\alpha_0^u)_{i,j}^* + \Delta t \alpha_0(h_{i,j}^*) + \Delta t \alpha_1(h_{i,j}^*) |\mathbf{u}_{i,j}^*| \right) u_{i,j}^{n+1} \\
 + (a_1^u)_{i,j}^* u_{i+1,j}^{n+1} + (a_{-1}^u)_{i,j}^* u_{i-1,j}^{n+1} + (a_2^u)_{i,j}^* u_{i,j+1}^{n+1} + (a_{-2}^u)_{i,j}^* u_{i,j-1}^{n+1} \\
 + (b_1^u)_{i,j}^* v_{i+1,j}^{n+1} + (b_{-1}^u)_{i,j}^* v_{i-1,j}^{n+1} + (b_2^u)_{i,j}^* v_{i-1,j+1}^{n+1} + (b_{-2}^u)_{i,j}^* v_{i+1,j-1}^{n+1} \\
 + (b_3^u)_{i,j}^* v_{i,j+1}^{n+1} + (b_{-3}^u)_{i,j}^* v_{i,j-1}^{n+1} + (b_4^u)_{i,j}^* v_{i+1,j+1}^{n+1} + (b_{-4}^u)_{i,j}^* v_{i-1,j-1}^{n+1} \\
 = h_{i,j}^* u_{i,j}^* + \frac{\Delta t}{R_o} (hv)_{i,j}^*, \\
 \\
 \left( (\alpha_0^v)_{i,j}^* + \Delta t \alpha_0(h_{i,j}^*) + \Delta t \alpha_1(h_{i,j}^*) |\mathbf{u}_{i,j}^*| \right) v_{i,j}^{n+1} \\
 + (a_1^v)_{i,j}^* v_{i,j+1}^{n+1} + (a_{-1}^v)_{i,j}^* v_{i,j-1}^{n+1} + (a_2^v)_{i,j}^* v_{i+1,j}^{n+1} + (a_{-2}^v)_{i,j}^* v_{i-1,j}^{n+1} \\
 + (b_1^v)_{i,j}^* u_{i+1,j}^{n+1} + (b_{-1}^v)_{i,j}^* u_{i-1,j}^{n+1} + (b_2^v)_{i,j}^* u_{i-1,j+1}^{n+1} + (b_{-2}^v)_{i,j}^* u_{i+1,j-1}^{n+1} \\
 + (b_3^v)_{i,j}^* u_{i,j+1}^{n+1} + (b_{-3}^v)_{i,j}^* u_{i,j-1}^{n+1} + (b_4^v)_{i,j}^* u_{i+1,j+1}^{n+1} + (b_{-4}^v)_{i,j}^* u_{i-1,j-1}^{n+1} \\
 = h_{i,j}^* v_{i,j}^* - \frac{\Delta t}{R_o} (hu)_{i,j}^*.
 \end{array} \right. \tag{5.22}$$

where we have neglected the capillary terms, considering the previous remarks.

**Remark 5.3.1.** *As emphasized in Chapter 3, the chosen time step  $\Delta t$  for both hyperbolic and parabolic steps is defined with  $\Delta t = \min(\Delta t_c, \Delta t_s)$  where  $\Delta t_c$  and  $\Delta t_s$  are respectively obtained from stability analysis for the “convection” hyperbolic step and the parabolic “source” step. Moreover, it appears from numerical investigations that we may choose  $\Delta t = \Delta t_c$  since the restriction on the time step derived from our semi-implicit method is far less constraining than those provides by the hyperbolic stability requirements.*

Since these two equations are coupled, it raises an unsymmetric sparse matrix with 21 non-zero diagonals. This system, which can become very large for fine meshes, is solved using the *UMFPACK* solver ([174]). This solver is written in ANSI/ISO C and

relies on the Unsymmetric-pattern MultiFrontal method and direct sparse LU factorization. This program includes a basic Fortran interface to some of the C *UMFPACK* routines which have been slightly modified in order to be suitable for our purpose. The matrix is represented in compressed column form, which consists of three arrays :  $A_p$ ,  $A_i$  and  $A_x$ . Considering that our matrix is  $m$ -by- $m$  with  $nz$  entries, the row indices of entries in column  $j$  are stored in  $A_i(A_p(j) \cdots A_p(j+1) - 1)$ . The corresponding numerical values are stored in  $A_x(A_p(j) \cdots A_p(j+1) - 1)$ . This program can use the *Level - 3* Basic Linear Algebra Subprograms (*BLAS*, dense matrix multiply), which enable to considerably improve its performance.

**Remark 5.3.2.** *This discretization of the source step enable us to achieve the previous requirements concerning the preservation of the abilities of the well-balanced method used in the hyperbolic step. More precisely, we highlight the following properties :*

- *i) the source step preserves the positivity of the water depth since values of  $h$  are not modified,*
- *ii) this step is able to cope with the occurrence of dry area, since we have pay attention to avoid any division by  $h$ , which could lead to infinite values when the water depth vanishes.*
- *iii) this step preserves the steady states “at rest” since values of the velocity  $\mathbf{u}$  are not modified by the source step when we have  $\mathbf{u} = 0$ .*

We have implemented the modified *UMFPACK* interface and the previous discretization in our *SURF\_SVWB* model in order to enable the resolution of the whole system (2.5.1). Since analytical solutions of the NSW equations involving friction and diffusion source terms are not available, the numerical discretization of the whole system has been performed using some of the previous test cases. This is addressed in section 5.5.

## 5.4. Second order accuracy in time

All the derivatives involved in this parabolic source step are discretized using centered second order accuracy finite difference schemes. To recover the second order accuracy in time when solving the complete system with both hyperbolic and parabolic steps, the Heun scheme introduced in chapter 4 to obtain second order accuracy in time for the hyperbolic step is extended to the complete system with source terms. We obtain the following sequence :

- (1) First step : hyperbolic problem

$$\tilde{\mathbf{U}}_c^{n+1} = \mathbf{U}^n + \Delta t \Phi(\mathbf{U}^n), \quad (5.23)$$

(2) First step : source problem

$$\tilde{\mathbf{U}}^{n+1} = \mathbf{S}_{\Delta t} \tilde{\mathbf{U}}_c^{n+1}, \quad (5.24)$$

(3) Second step : hyperbolic problem

$$\tilde{\mathbf{U}}_c^{n+2} = \tilde{\mathbf{U}}^{n+1} + \Delta t \Phi(\tilde{\mathbf{U}}^{n+1}), \quad (5.25)$$

(4) Second step : source problem

$$\tilde{\mathbf{U}}^{n+2} = \mathbf{S}_{\Delta t} \tilde{\mathbf{U}}_c^{n+2}, \quad (5.26)$$

(5) Final updated state :

$$\mathbf{U}^{n+1} = \frac{\mathbf{U}^n + \tilde{\mathbf{U}}^{n+2}}{2}. \quad (5.27)$$

**Remark 5.4.1.** *We must keep in mind that our “hyperbolic problem” is not the classical “convection problem”, since this step also takes into account the bed-slope source term with a well-balanced method, as exposed in the previous chapter. Therefore, this complete sequence is able to preserve non-trivial steady states “at rest” involving a balance between flux gradients and the bed slope source term. An extension which aims at including the friction source terms into the “hyperbolic problem” in order to preserve non-trivial equilibrium involving friction phenomena is under study.*

## 5.5. Numerical assessments

It is difficult to validate the numerical method implemented for this source step in the same way as for the hyperbolic step, since we do not have analytical solutions, even in the one dimensional case, for problems involving friction and diffusion. Nonetheless, we can partially assess our method with qualitative analyzes. Therefore, we propose here to perform several previously validated test cases adding some friction and diffusion effects, in order to observe the induced modifications.

Hence, we present here a one dimensional bore-generating dam-break test and a two dimensional test using the Thacker’s axisymmetrical solution. This solution is adapted to our purpose since the motion is not driven by a boundary condition, as in the Carrier and Greenspan solutions. Moreover we have already study the solution without any friction or diffusion terms and a qualitative comparison can be performed.

**5.5.1. A bore solution.** The present test is similar to the previous dam-break problem with the exception of the non-zero initial height  $h_R$  at the right of the dam position.

Thus, departing from the following initial condition :

$$\begin{cases} h = h_L & u = 0 & \text{for } x < 50, \\ h = h_R & u = 0 & \text{for } x > 50, \end{cases} \quad (5.28)$$

the flow evolves with the generation of a right moving bore which advances in still water. The analytical solution is known (see [161] for example).

We have taken for this test  $h_L = 5\text{ m}$  and  $h_R = 3\text{ m}$  and the channel is  $100\text{ m}$  long. To be consistent with the asymptotic regime introduced in Chapter 1, we set  $\varepsilon = \frac{h_L - h_R}{L}$ , leading to  $\varepsilon = 0.02$ , and we defined the viscosity  $\mu = \varepsilon\mu_0$  and the friction coefficient  $k_t = \varepsilon r_1$ . The laminar viscosity is neglected for this test. In the present test, the viscosity coefficient  $\mu_0$  varies in the range  $0, 20, 50, 100$  and the friction coefficient  $r_1$  can take the values  $0, 5, 20, 50$ . We have performed a comparison between the numerical solution without any friction or diffusion (which is very close to the analytical bore solution) and on one hand the numerical solution with friction but without diffusion and on the other hand the numerical results with diffusion but without any friction. This enables us to clearly analyze the growing and distinct effects of each terms. Numerical results are shown on Figure 5.5.1. These results are considered as qualitatively satisfactory.

**5.5.2. Thacker's axisymmetrical solution with friction.** For this test, the viscosity is neglected and we only introduce some dissipation with a large enough friction term. The laminar friction coefficient  $k_l$  is set to zero and the turbulent friction coefficient  $k_t$  is first set to 0.1. Consequently, we only consider here a quadratic friction law. The results are shown on Figure 5.5.2 where we have plotted on each sub-figure the numerical solutions with friction and the corresponding analytical solution without friction at the same time, in order to highlight the decreasing amplitudes. As expected the friction entails a significant loss of energy and the motion is no more periodical. The oscillation's amplitude decreases with respect to time and the free surface profile slowly settles back to the mean water level. The mass of fluid is conserved. It is worth noting that the convergence towards the steady state at rest is not perturbed by the source step, as previously emphasized.

We show on Figure 5.5.4 time series of the free surface oscillations at the center of the basin ( $x = 0, y = 0$ ) for different values of  $k_t$ . We can observe the impact of this coefficient on the motions, since the steady state at rest is achieved very soon, approximatively at  $t = 18\text{ s}$ , for  $k_t = 0.5$ , the motion being quasi completely inhibited. For  $k_t = 0.05$  and  $k_t = 0.1$  the steady state is reached respectively around  $t = 300\text{ s}$  and  $t = 100\text{ s}$ .

**5.5.3. Thacker's axisymmetrical solution with diffusion.** For this test, the friction are neglected and we only introduce some diffusion. Our goal is to compare qualitatively these results to the previous ones with only the friction. In order to consider the same asymptotic regime as in Chapter 1, the viscosity is defined with  $\mu = \varepsilon\mu_0$  where  $\mu$  is set to 100 and  $\varepsilon$  is linked to the considered problem scales. Precisely, as the basin dimension are  $4 \times 4$  meters and the oscillations amplitude is nearly  $0.04\text{ m}$  we set  $\varepsilon = 0.04/4 = 0.01$ .

We show on Figure 5.5.4 time series of the free surface oscillations at the center of the basin ( $x = 0, y = 0$ ). We can observe that a large diffusion term produces enough

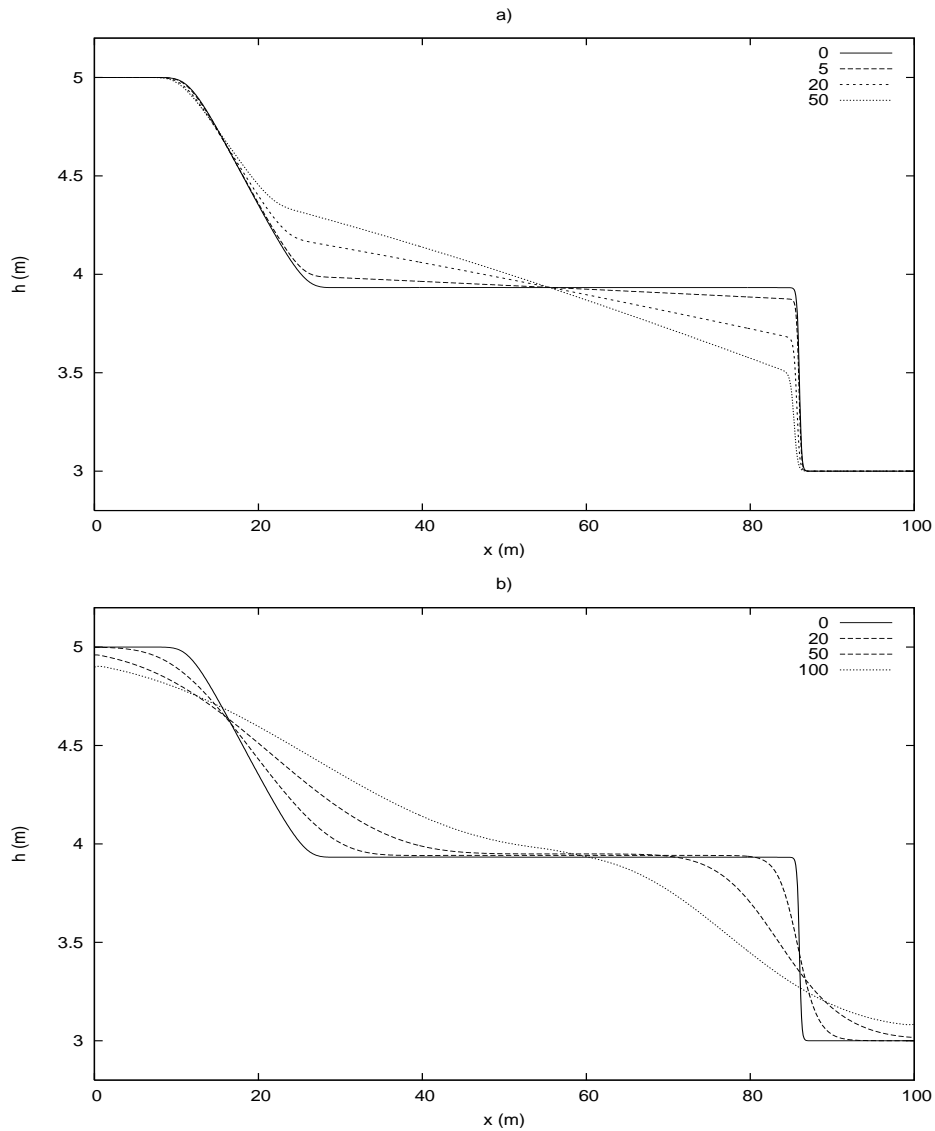


**Figure 5.5.1.** A bore solution. Comparison between numerical results without any friction or diffusion and the numerical results with a) friction and varying  $r_1$  and b) diffusion and varying  $\mu_0$ . The applied values of the relevant coefficients are specified on top right corners of each figure.

dissipation to rapidly inhibit the motion. However, our goal is only to validate the good implementation of the previous method. Further investigations are needed in order to add a relevant anisotropic turbulent model and obtain a significant parameterization of the involved coefficients.

**Remark 5.5.1.** *Note that it would be interesting in further investigations to compute numerical Thacker's solution with only the Coriolis terms, since analytical solutions provided by Thacker initially include the Coriolis effects.*

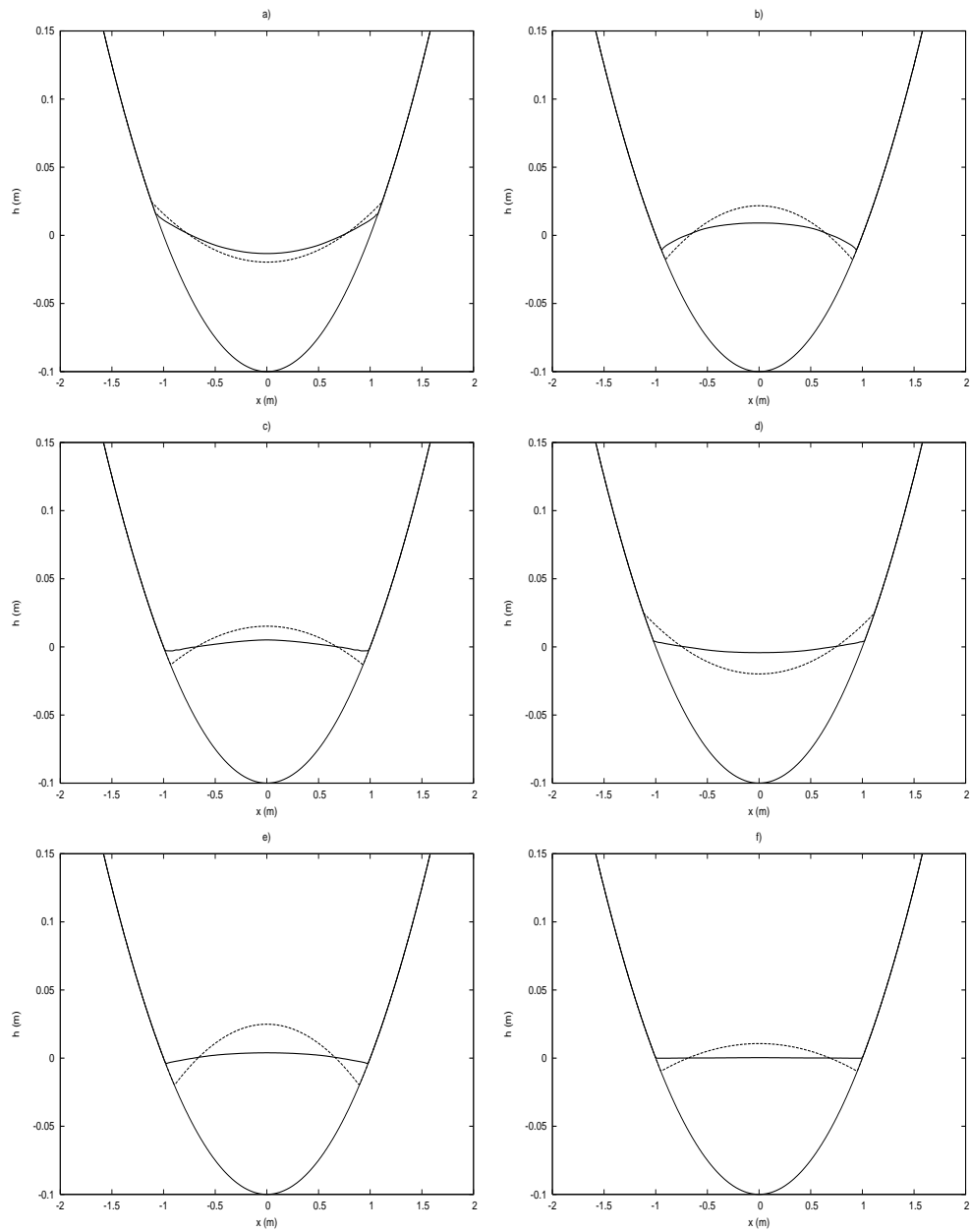


**Figure 5.5.2.** Thacker's 2D paraboloid solution with friction. Comparison between numerical results with a  $k_t = 0.1$  friction coefficient (in solid lines) and analytical solution without friction (in dashed lines) for the centerline free surface profile. Water surface elevation profiles  $h$  are plotted versus the  $x$  coordinate, at  $y = 0$ , for a)  $t = 1.2$  s, b)  $t = 2.4$  s, c)  $t = 4.2$  s, d)  $t = 7.8$  s, e)  $t = 9.0$  s and e)  $t = 40.0$  s

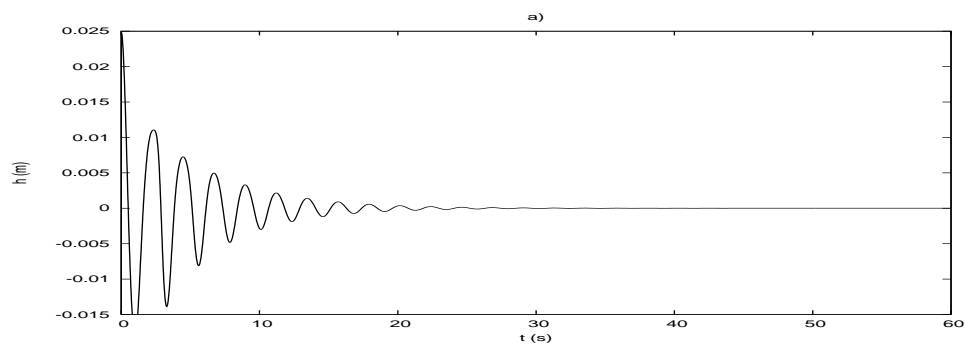


**Figure 5.5.3.** Thacker's 2D paraboloid solution with diffusion. Time series of the free surface profile at the center of the basin for  $\mu = 1$

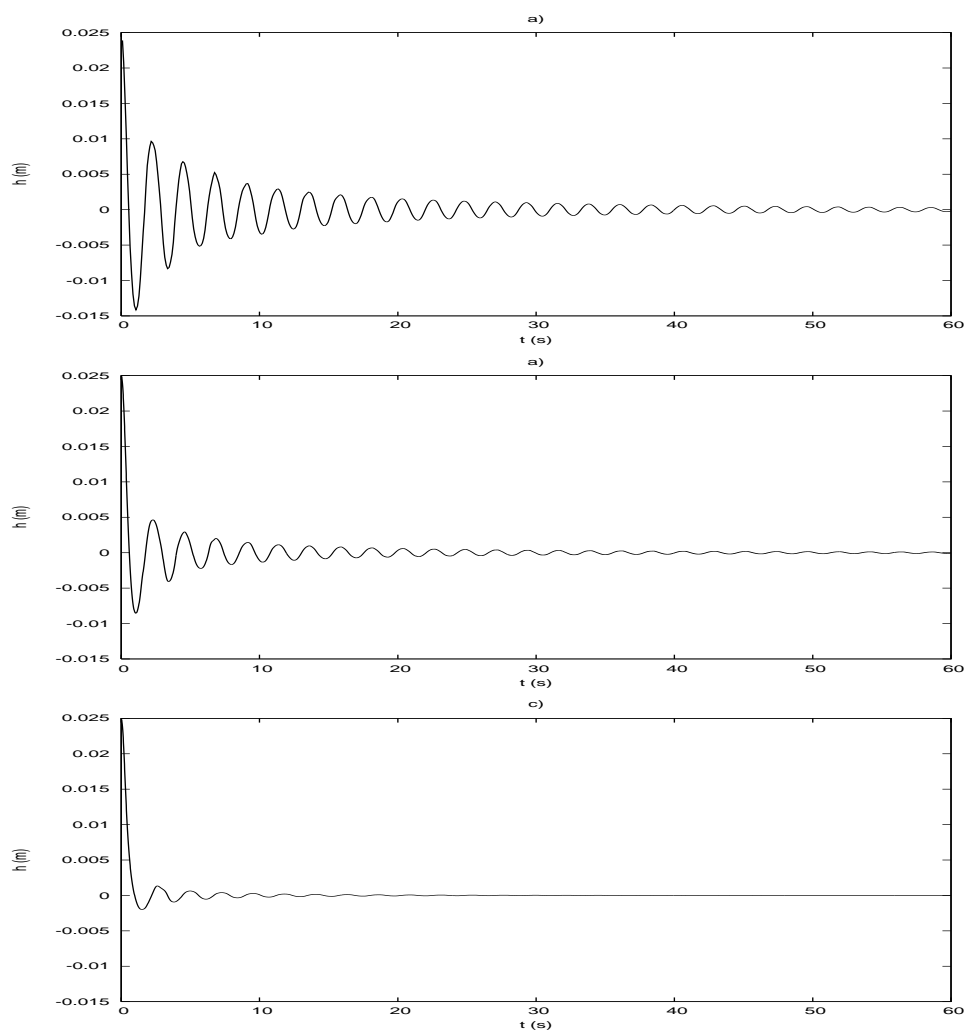


**Figure 5.5.4.** Thacker's 2D paraboloid solution with friction. Time series of the free surface profile at the center of the basin for different values of the friction coefficient  $k_t$ : a)  $k_t = 0.05$ , b)  $k_t = 0.1$ , c)  $k_t = 0.5$ .

---

# Conclusion

In this chapter, we have introduced a numerical method which leads to the resolution of the two dimensional shallow water model derived in Chapter 1. This method rely on a fractional step method which splits the complete system into two distinct systems, namely an hyperbolic system with bed slope source term and a parabolic system which contains the remaining source terms. The hyperbolic problem is solved using a well-balanced and shock capturing finite volume method. We have first investigated the use of the Exact Well-Balanced Riemann solver or Greenberg and Leroux [72] and its simplified linearized version the well-balanced VFRoe-ncv Riemann solver [57]. These two solvers rely on the direct resolution of an augmented Riemann problem with piecewise constant topography. Numerical investigations have highlighted that even if these two solvers have been proved to be powerful and accurate for a large range of hydraulic problems involving occurrence and flooding of dry area, they fail to provide accurate enough results for classical moving shoreline problems. Consequently, we have investigated the use of the recent “hydrostatic” reconstruction method [3] which can be used together with any homogeneous Riemann solver. The VFRoe-ncv Riemann solver has been chosen. This choice is mainly motivated by the fact that suitable properties concerning the non-negativity of the computed water depth have been obtained for this scheme [58]. An exact Riemann solver has also been tested but the computational times were almost five to ten times greater than with the VFRoe-ncv without any significant improvements in the accuracy.

A “second order” accuracy MUSCL reconstruction has also been performed. This reconstruction preserves the qualities inherited from the well-balanced method. It raises a fast, robust and accurate bore-capturing well-balanced model, nicknamed *SURF\_SVWB*, very easy to implement even in the two-dimensional case on unregular Cartesian meshes, and able to preserve steady states at rest. This model has been validated against several analytical solutions in situations involving multiple moving shorelines, strong variations of bed slope and convergence towards steady states. This scheme introduces very little artificial viscosity and numerical results are in very good

agreement with the analytical solutions. Nonetheless, as for most Riemann solver, the velocity seems to be far more difficult to model with precision and further investigations are needed.

Numerical investigations have shown that the application of well-balanced schemes for moving shoreline problems is not trivial, since two others schemes which have been implemented and extensively validated in numerical tests involving occurrence of dry area and strong bottom variations have failed to provide relevant results. From this, the *SURF\_SVWB* model appears as an efficient and robust tool which can be of a great utility for the numerical simulation of run-up and run-down of waves. A comparison with a few models introduced in the literature shows that the results provided by the *SURF\_SVWB* model are at least as accurate as those presented by Brocchini et al. [26] or Prasad and Svendsen [140] with their fixed grid method and perhaps even with their moving grid method. Besides, *SURF\_SVWB* enables us to overcome the problems due to the fractional step method which was used in all these models. It can also be noticed that *SURF\_SVWB* is able to deal with strong variations of topography as well as the robust and accurate Exact Well-Balanced Riemann solver of Greenberg and Leroux and ensures more accurate results for moving shoreline problems.

In a second step, the source problem involving the Coriolis, friction and viscous terms is approximated using a semi-implicit time discretization and a centered second order accuracy finite difference method. It raises an unsymmetrical large sparse matrix which is solved using an efficient and fast solver. This source step is proved to deal without problems with the occurrence of dry areas and to preserve steady states at rest. In the literature, viscous shallow water models with such properties are uncommon. Hence, this model appears as a promising tool for more realistic simulations, as performed in the third part of this work.

Moreover, relevant absorbing/generating second order accuracy inlet boundary conditions have been implemented and tested. This type of boundary condition will be of great utility in the next part where applications to various nearshore hydrodynamic problems are performed.

It is worth noticing that some overtopping simulations inspired from those suggested in [82] and [84] have also been investigated. The *SURF\_SVWB* model appears to be stable enough to deal with such extreme situations, which are at the limit of the domain of validity of the shallow water assumptions. Nonetheless, such problems require a meticulous assessment using experimental data and need further investigations.

---

*Part 3*

**Applications to  
nearshore  
hydrodynamics**



---

# Introduction

In this third part, we investigate the use of the “second order” accuracy well-balanced *SURF\_SVWB* model to study some important processes which occur in the nearshore. We restrict ourselves to the study of breaking or non-breaking solitary or periodic train of longshore uniform waves of normal incidence.

A major distinction between breaking and non-breaking waves needs first to be highlighted. Physically, the transformation due to breaking leads to motions of various

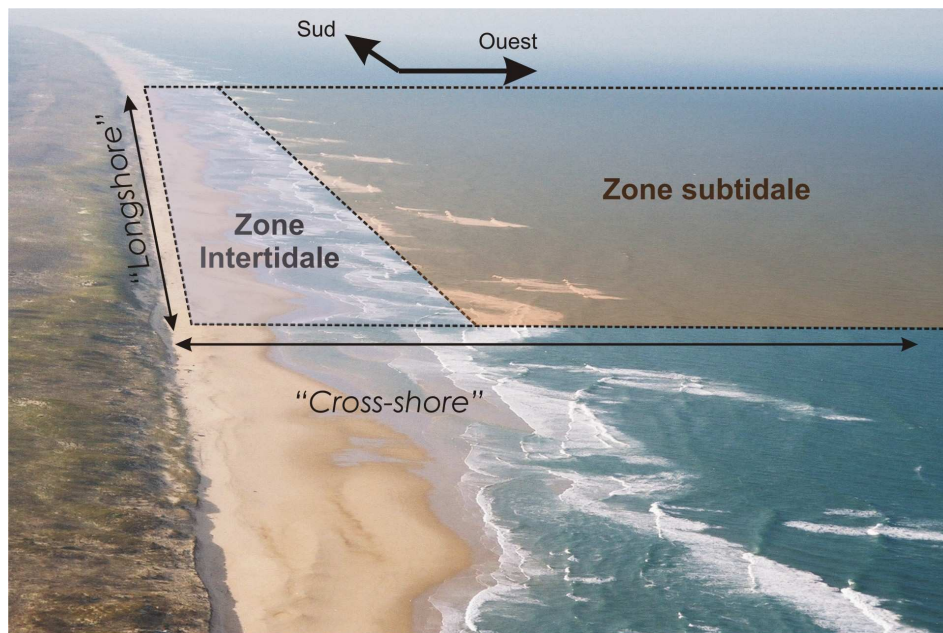


**Figure 5.5.5.** Aerial view of the Truc Vert Aquitanian beach. The cross-shore and longshore direction are sketched and the intertidal and subtidal zones are indicated (Castelle [39]).

kinds and scales, including small-scale turbulence, larger-scale vorticity motions, low frequency waves and steady flows and is mainly concerned with dissipation process. On the other hand, non-breaking long waves often lead to large run-up processes, eventually overtopping phenomena and reflection.

Theoretically, criteria for the onset of breaking of periodic waves have been stressed out, often as limiting conditions for non-breaking solutions. A relevant example is the previously introduced analytical solution of Carrier and Greenspan which is only valid under a non-breaking criteria involving the beach slope, the frequency of the incident periodic wave and the vertical waterline excursion. It provides a local solution near the shoreline for perfect reflection of incident periodic waves for gentle beach slopes. When the critical value is reached, the surface becomes locally vertical. However, this breaking criteria often predict earlier breaking than those observed experimentally and Meyer [115] hypothesized that this criteria may represent an intrinsic failure in the shallow water model rather than physical wave breaking. Hence the definition of a faithful breaking criteria appears to be a highly empirical and complex topic and the reader is referred to the papers of Battjes [8], [7] for a comprehensive study.

We finally introduce here on Figure 5.5.5 the definition of the longshore and the cross-shore directions, and the subtidal and intertidal areas, which are usual terminologies in coastal engineering.

The distinction between breaking and non-breaking waves will lead us in the sequel. In the next chapter, we investigate the use of the *SURF\_SVWB* model for the simulation of the propagation in coastal areas and run-up over various topographies of one and two dimensional non-breaking solitary long waves, regarded as tsunamis. In Chapter 7, the propagation of periodic trains of breaking waves in the surf zone is investigated in the one and two dimensional cases. Wave features and wave-induced horizontal circulation are studied.

# Simulation of run-up process

## 6.1. Tsunamis and run-up models

**6.1.1. Tsunamis.** Tsunamis are serious natural hazards, which can be generated by many different mechanisms including submarine earthquakes, landslides or submarine volcano eruptions. Tsunamis that can travel across an ocean and attack a coastal area far away from the initial generation location are called distant tsunamis, while tsunamis that are confined near the source are called local tsunamis.

In the deep ocean, tsunami wavelengths are about  $100 - 400 \text{ km}$ , whereas the average depth of the Pacific ocean, for instance, is nearly  $4 \text{ km}$ . Consequently, the long wave approximation is fully justified for the study of such phenomena and the shallow water theory leads to the propagation speed  $c = \sqrt{gh}$  where  $h$  is the water depth and  $g$  the acceleration of gravity. Typical propagation speeds are of order of  $700 \text{ km/h}$ . Considering the fact that tsunami amplitudes in deep ocean regions are generally less than  $1 \text{ m}$ , they often pass unnoticed, masked by the wind generated swell, until they reach the coastal domain, where the water depth decreases.

When a tsunami propagates over the continental shelf, its amplitude dramatically increases and its wavelength decreases as the wave shoals. Considering the processes of refraction, reflection, diffraction and shoaling, the wave may be dramatically distorted as reaching the shore. A tsunami which is nearly imperceptible in the deep ocean can see its amplitude becoming large enough to cause serious damages landward.

The nearshore topography and coastline geometry appears as relevant factors with respect to the devastating feature of a tsunami. The tsunami amplitude can be greatly enhanced by specific man-made coastal structures, like harbors. This topic has been investigated by Zelt in [188]. The longshore length of the tsunami may also be an important feature for the impact on coastal structures.

Many areas in the world are susceptible to tsunami attack. The regions which are mainly concerned are the seismically active Japanese coast and the Pacific “Ring of Fire”. But we have seen recently that other regions can also be dramatically devastated, leading to enormous loss of both life and money.

The protection of life and coastal landwards from tsunamis is thus an important topic. It depends on a reliable understanding of the involved physical processes, in order to accurately predict the inundated area at a given location knowing the main features of the incident long waves. As exposed before, the evolution of the tsunami propagating on continental shelf and reaching the shore is determined mainly by the nearshore topography, the shoreline geometry and the wave characteristics. The off-shore topography can also be of significant importance.

Several numerical models have been developed for simulating tsunamis and may be used to predict the inundated region and the construction of civil defense structures. These models are mostly based on the NSW equations with various methods for the discretization and the moving shoreline tracking algorithm. This subject is investigated in the next section. We can mention for example the Cornell model developed by Liu et al. [117], the PMEL/MOST model by Titov and Synolakis [169], and the Japanese model by Imamura et al. [85].

It is worth noticing that in the numerical models, idealized and well-defined solitary waves evolve over constant depth area and then over idealized topography, whereas in the real phenomenon, the initial wave profile is never known and the wave propagates over complex topography. Hence, a realistic tsunami simulation model must be able to predict the complete physical processes of the tsunami including the initial tsunami generation due to landslides or earthquakes, the propagation of the tsunami in the open ocean and coastal region, the shoreward run-up of tsunami, causing a coastal inundation and the convergence towards the steady state at rest after the evacuation of the wave. Several attempts to model these entire processes have been performed, with less or more success. For example Gica and Teng [63] used the Cornell propagation and run-up model with an earthquake model, generating a sea floor quantitative displacement. More recently, Liu et al. [119] used the Large Eddy Simulation (LES) approach and the Volume of Fluid (VOF) method to predict run-up due to three dimensional sliding masses induced long waves. Yet, a faithful validation of such models is not always possible, since comparisons between tsunami field data with numerical prediction is often arduous. For a general survey of tsunami related topics, the reader is referred to the discussion of Carrier [36].

In this chapter we focus on the propagation of non-breaking solitary long waves in coastal areas, which can be regarded as a tsunami propagation model, and we study with attention the induced run-up and run-down processes, using the *SURF\_SVWB* model. This model may allow the computation of the convergence towards the steady states at rest after the run-up and the dissipation of residual ringing effects. Hence, a better estimation of the involved time scales may be provided for more realistic studies. Moreover, we expect the well-balanced nature of the model to improve the computation

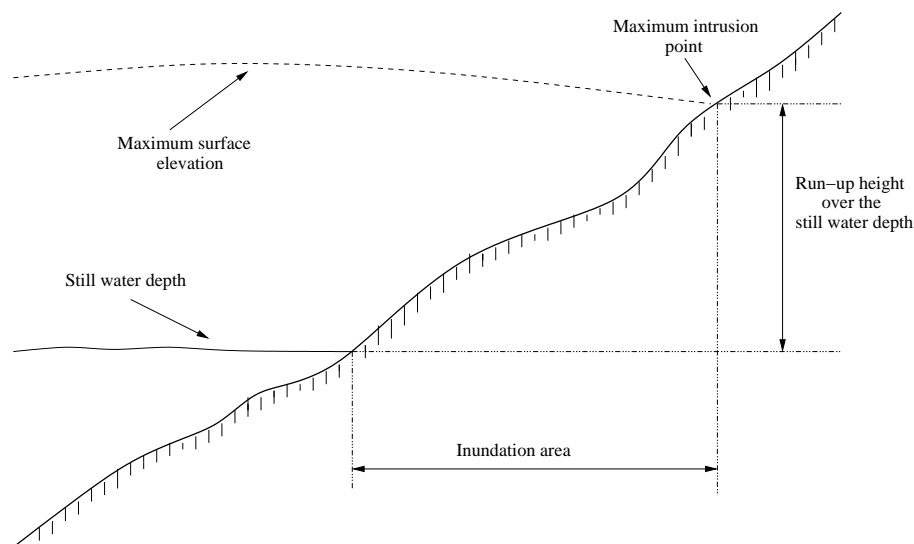


**Figure 6.1.1.** Definition sketch of wave run-up over the still water depth.

of the impact of coastal topography on the incident wave. The computation of the two dimensional effects due to the longshore variations of topography, especially for wave refraction and diffraction, may also be improved.

**6.1.2. The run-up process.** The run-up of waves on a sloping beach is an exceedingly complex phenomenon, involving reflexion, wave shoaling and refraction and still many aspects are not well-understood. Besides, flow motions near the inundated region exhibit strong nonlinearity in comparison to the motions away from the shoreline. Nonetheless, a faithful model for predicting run-up motions is crucial for the study of forces on coastal structures exposed to ocean environments and the impact on the coastal area of tsunami or storm waves. For that reason most of the models which deal with this process are numerical.

Yet, the run-up of breaking and non-breaking waves on sloping boundaries is generally more difficult to introduce into numerical models than the usual boundary condition for vertical boundaries where the normal mass flux is zero. Actually, we may have an intuitive and qualitative idea of the involved processes since for very steep slope the situation can be compared to the reflection of an incident wave on a vertical wall. Furthermore, the process of run-down is often far more difficult to predict accurately since a large part of the information used to compute the shoreline motion comes from the recently inundated area.

The most critical step in the inundation calculation is the shoreline computation, which involves a moving boundary between three different phases : liquid, air and solid. For most numerical problems concerning ocean's hydrodynamic, the fluid occupies a given fixed domain. If this domain is not fixed but varies with time in an unknown manner as the waves swash up and down the beach, the domain of the problem depends of the solution itself. Accordingly, we can't determine the domain of the problem and then the solution and the two have to be found simultaneously. Consequently, one

of the most relevant challenges faced when modeling nearshore hydrodynamics and wave propagation in coastal areas is to derive a reliable description of the shoreward boundary of the domain.

The simplest method is to introduce an imaginary vertical barrier near the boundary which is assumed to be a moving shoreline. The water depth at this barrier is nonzero and the position of the shoreline is then approximated by an inland extrapolation from the wave height at this barrier. For steep bed slope it could be a reliable approximation but for gentle bed slopes and large shoreline motion it gives poor results. Thus more sophisticated methods have been pointed out. There is mainly two approaches, as previously stressed out in Part 2.

The first category of methods for treatment of the moving shoreline is the use of coordinate transformations, with Eulerian techniques, on deforming grids. In this method the real time-varying physical domain is transformed onto a time-invariant computational domain. As the moving shoreline changes the cross-shore length of the domain, most of the coordinate transformation schemes change the grid only in the cross-shore direction. The simplest scheme using this method was suggested by Johns [87] with a linear mapping of the time-varying domain. Shi and Su [153] proposed a transformation method in the generalized curvilinear coordinate. Lynch and Gray [120] proposed a method based on continuously deforming finite elements in which the finite elements track the shoreline since the basis functions are chosen to be functions of time. They use this method to compute the propagation and the run-up of waves on plane beach. Özkan-Haller and Kirby [131] proposed a shoreline transformation technique using a Chebyshev collocation method for the computation of derivatives in the cross shore direction. More recently Brocchini, Prasad and Svendsen [26] have proposed a moving boundary condition method based on coordinate transformation and a fourth order predictor-corrector scheme. Several of these methods have been generalized to fully two-dimensional models but they are not particularly easy to implement.

Lagrangian methods have also been proposed in the framework of coordinate transformation schemes. The fluid is represented as a large number of fluid particles that move with the local fluid velocity and the particles are tracked over the beach slope in the same way they may be tracked in the offshore region. We can cite the works of Heitner [78] which were limited to the treatment of plane waves propagating over linearly sloping beach and have difficulty to model the subsequent run-down problem for large waves. Shuto [154], [155] used the linear non-dispersive Lagrangian long-wave equations to study theoretically the run-up of periodic waves on a sloping beach, while Goto [69] derived a set of nonlinear non-dispersive long wave equations. They both extended later their model to the fully two dimensional case for the study of tsunamis [70]. Zelt and Raichlen [188], [189] proposed a finite element model based on Lagrangian techniques which aims at studying the response of harbors with sloping boundaries to long waves excitation.

The second approach is the use of Eulerian methods with fixed grids. The conservation property of the schemes are used to predict the dry cells or nodes, relying on a specific treatment of the wet/dry interface. Among the many methods which have been introduced we can cite the early works of Keller and Keller [92] who looked at the propagation of time harmonic waves through water of slowly varying depth and derived an expression for the height of a wave at the shoreline involving its offshore wavelength, the offshore depth and the nearshore beach slope. Yeh and Chou [186] developed a nonlinear finite difference surge model with complicated algorithm used to add or remove grid points during run-up or run-down. They obtain a significant improvement of the results obtained with a model with fictitious vertical wall and extrapolation. Hibbert and Peregrine [80] used linear extrapolation to describe the run-up of an uniform bore on a sloping beach. Tanaka et al. [167] introduced a finite element model which aims at simulating run-up and overtopping. The moving shoreline was simulated by adding wet elements into the domain as the shore propagated or by removing dry elements as it receded. The rate of flow into a wet element and the overtopping flow rate were determined from empirical equations. Kobayashi et al [95] introduced the IBREAK model, which is actually an improved version of the model of Hibbert and Peregrine, especially designed for the study of run-up process. Liu et al. [115] proposed a finite difference model with a complex shoreline-tracking algorithm and applied it to the run-up over a conical island. Among others we can mention Titov and Synolakis [169] or Imamura et al. [85] with various treatments of the wet/dry interface. More recently Brocchini et al [27] and Hu et al [82] suggested the use of a Godunov-like second order accuracy bore capturing scheme, which rely on exact or approximated Riemann solver. Most of these models have primarily been developed with the modeling of tsunami run-up in mind. It is worth mentioning that all these methods are based on fractional step methods, with all the entailed drawbacks. Consequently, the method implemented in the *SURF-SVWB* model in the well-balanced framework may lead to the computation of accurate run-up solutions with the possibility of convergence towards equilibrium states at rest.

As already stressed out, exact solutions to nonlinear wave theories are rare, especially when the fluid boundaries are free to deform with the run-up and run-down processes of waves on a sloping beach. For that reason, the analytical run-up solutions of Carrier and Greenspan and Synolakis are well-suited solutions to validate the model's ability to handle the nonlinear aspects of wave run-up, in the one-dimensional framework. The results obtained for the Carrier and Greenspan solutions have already been exposed and in the next section we investigate the Synolakis solution. Relevant two-dimensional benchmarks involving longshore variations of the topography are also uncommon. The two-dimensional test suggested by Zelt [188] has been performed by many authors to validate their model and we investigate it in Section 6.3. Furthermore, good validatory wave basin data are also difficult to find. Thus the test of Liu et al. [115] seems to become a standard. It is investigated qualitatively in Section 6.4.

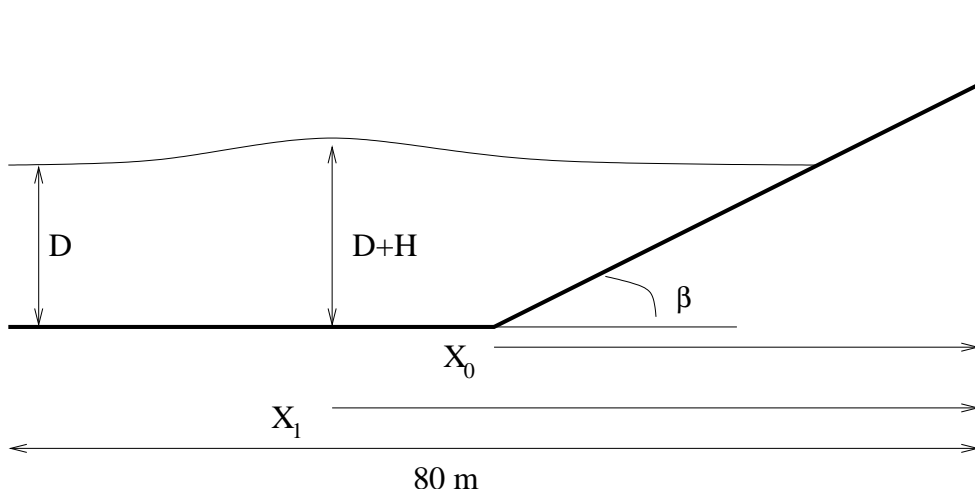


**Figure 6.2.1.** Definition sketch for the initial condition of the Synolakis' solution.

## 6.2. One-dimensional run-up and reflexion of a solitary wave over a sloping beach

Solitary wave run-up phenomena were investigated experimentally and numerically by Synolakis in [166]. Although it is well known that solitary waves are not classical solutions of the NLSW equations, it has been found that for small amplitudes and over limited distances, the Synolakis solution provides a good model of beach inundation by a solitary wave. This set of data has been extensively used in order to validate experimental and numerical models.

In this test, a solitary wave traveling from the shoreward is let run-up and run-down on a plane beach, before being fully reflected and evacuated from the computational domain. The topography for this test of wave run-up and reflection is made of a constant depth area juxtaposed with a plane sloping beach of slope  $\beta$ . The right boundary condition is transmissive. However, this right boundary is kept sufficiently far for the toe of the beach in order to prevent any interaction with the water waves during the run-up process.

The initial condition is a solitary wave, centered at a distance  $x_1$  from the toe of the beach equal to its half wave length :

$$\begin{cases} h(x, t = 0) = \frac{H}{D} \operatorname{sech}^2(\gamma(x - x_1)) \\ u(x, t = 0) = \sqrt{\frac{g}{D}} \cdot h_0(x). \end{cases} \quad (6.1)$$

where

$$\gamma = \sqrt{\frac{3H}{4D}} \quad (6.2)$$

and

$$x_1 = \sqrt{\frac{4D}{3H}} \operatorname{arcosh} \left( \sqrt{\frac{1}{0.05}} \right) \quad (6.3)$$

is the initial position of the center of the solitary wave (see Figure 6.2.1). The initial amplitude is set to be  $H = 0.019 \text{ m}$ , the mean water depth is  $D = 1.0 \text{ m}$  and the beach slope is defined with  $\cot(\beta) = 19.85$ . The analytical solution, obtained by the combination of the Carrier and Greenspan's hodograph transformation and a Fourier transform is provided in the original paper of Synolakis [166]. A simplified form is exposed in [82]. For this test, we have used  $\Delta x = 0.02$  and the CFL is set to 0.8.

The numerical results obtained with the *SURF-SVWB* model are shown in Figure 6.2.3 for different values of time between the initial condition and the complete evacuation of the wave from the computational domain. We can perform a qualitative comparison with the results proposed in [82] and [166] and observe that the moving shoreline is accurately computed. Moreover, the model is extremely stable, since several tests with various beach slopes and wave amplitudes have been performed without any occurrence of non-physical oscillations. It is worth noticing that no perturbations are induced in the water surface profile when the wave propagates over the toe of the beach, as it may occur with a fractional step method.

Time series of the evolution of water height at  $x = 72.5 \text{ m}$  are presented in Figure 6.2.2. We emphasize that after the total reflection of the incident wave, the convergence toward the steady state at rest is accurately computed whereas FSM used in the literature may be simply unable to provide any valuable results related to this convergence since non-physical oscillations are generated. For this reason, authors never show the results for large values of time and only exhibit their results for the run-up process and sometimes for the subsequent run-down which is far more difficult to model.

**Remark 6.2.1.** *Note that the use of the Exact well-Balanced Riemann solver or the well-balanced VFRoe-ncv solver for this test leads to unphysical oscillations during the run-down procedure. These solvers are unable to provide a reliable solution for large values of time.*

### 6.3. A two-dimensional test for the run-up of large tsunami waves

**6.3.1. Motivations.** To further illustrate the abilities of the model in the computation of moving shoreline, a strongly two-dimensional test is performed, which combines several aspects of importance in the processes of run-up and run-down. This test involving run-up phenomena in a two-dimensional framework is the test performed by Zelt in [188] in the course of studying the response of harbors to long wave excitation. It involves the run-up of a large pulse-like wave in a bay with a sloping bottom. The test geometry combines a curved (sinusoidal) still water shoreline with a

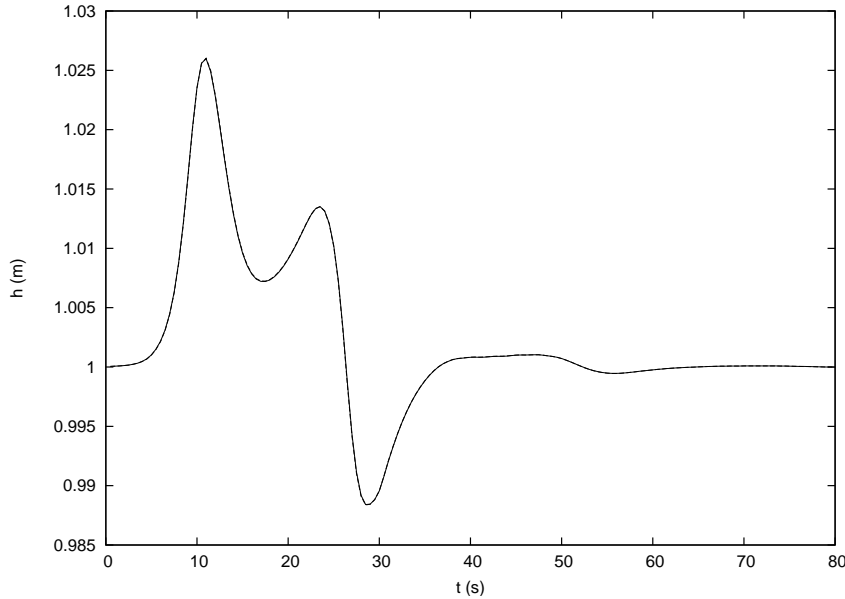


**Figure 6.2.2.** The Synolakis run-up solution. Time series of the water height. The numerical results for the profile of the water height  $h$  are plotted versus the time coordinate  $t$  at  $x=72.5$  m.

sloping nearshore bathymetry that merges with a constant depth region offshore (see Figure 6.3.1).

Such geometry was chosen to demonstrate interaction of different processes that may influence the shoreline movements. The shoreline is, in plan view, one period of a sine wave. In [188], Zelt has performed numerical simulations using a Lagrangian finite element model. There is no analytical solution for this test, but several NSW models have been tested against the Lagrangian model of Zelt (see [131], [140], [84] for instance). Here we only test the present model *SURF-SVWB* in order to obtain qualitative results and compare the shoreline behavior to other NSW equations solvers which can be found in the literature. We define the basin topography as :

$$d(x, y) \begin{cases} h_0 - h_0 \left( \frac{x - 3L/\pi}{\zeta_0(y) - 3L/\pi} \right) & \text{for } x \leq 3L/\pi, \\ h_0 & \text{for } x > 3L/\pi, \end{cases} \quad (6.4)$$

where  $L$  is the half width of the bay,  $h_0$  is the offshore constant water height and

$$\zeta_0(y) = -\frac{L}{\pi} \cos\left(\frac{\pi y}{L}\right).$$

It results in a beach slope of 1:10 at the center of the basin and of 1:5 near the boundaries of the longshore direction.

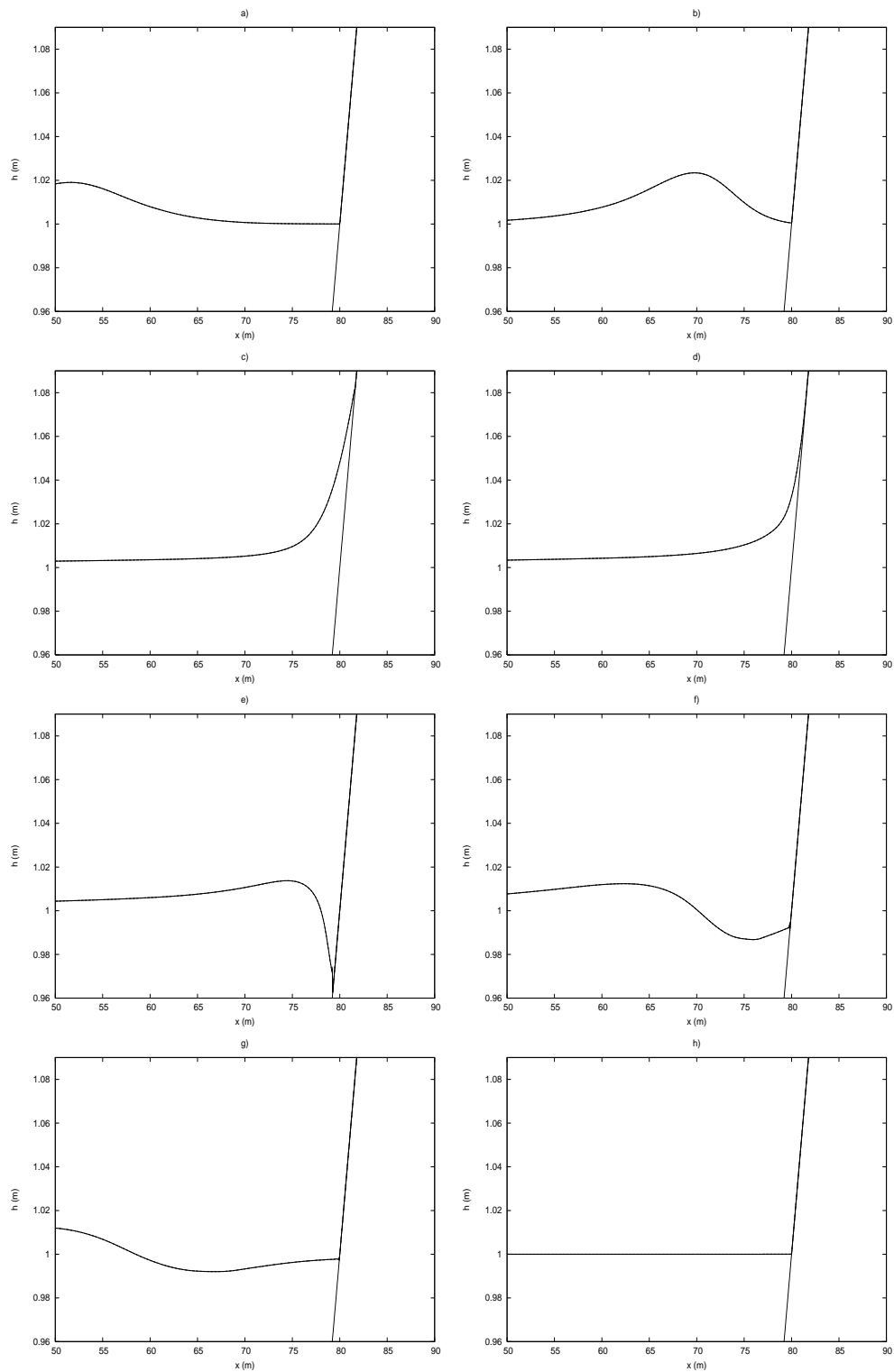


**Figure 6.2.3.** The Synolakis run-up and reflection solution. Numerical results for the profiles of water depth  $h$  are plotted versus the onshore coordinate  $x$  for: a)  $t=3.0s$ , b)  $t=9.0s$ , c)  $t=17.0s$ , d)  $t=19.5s$ , e)  $t=23.0s$ , f)  $t=28.0s$ , g)  $t=32.5s$  and h)  $t=75.0s$

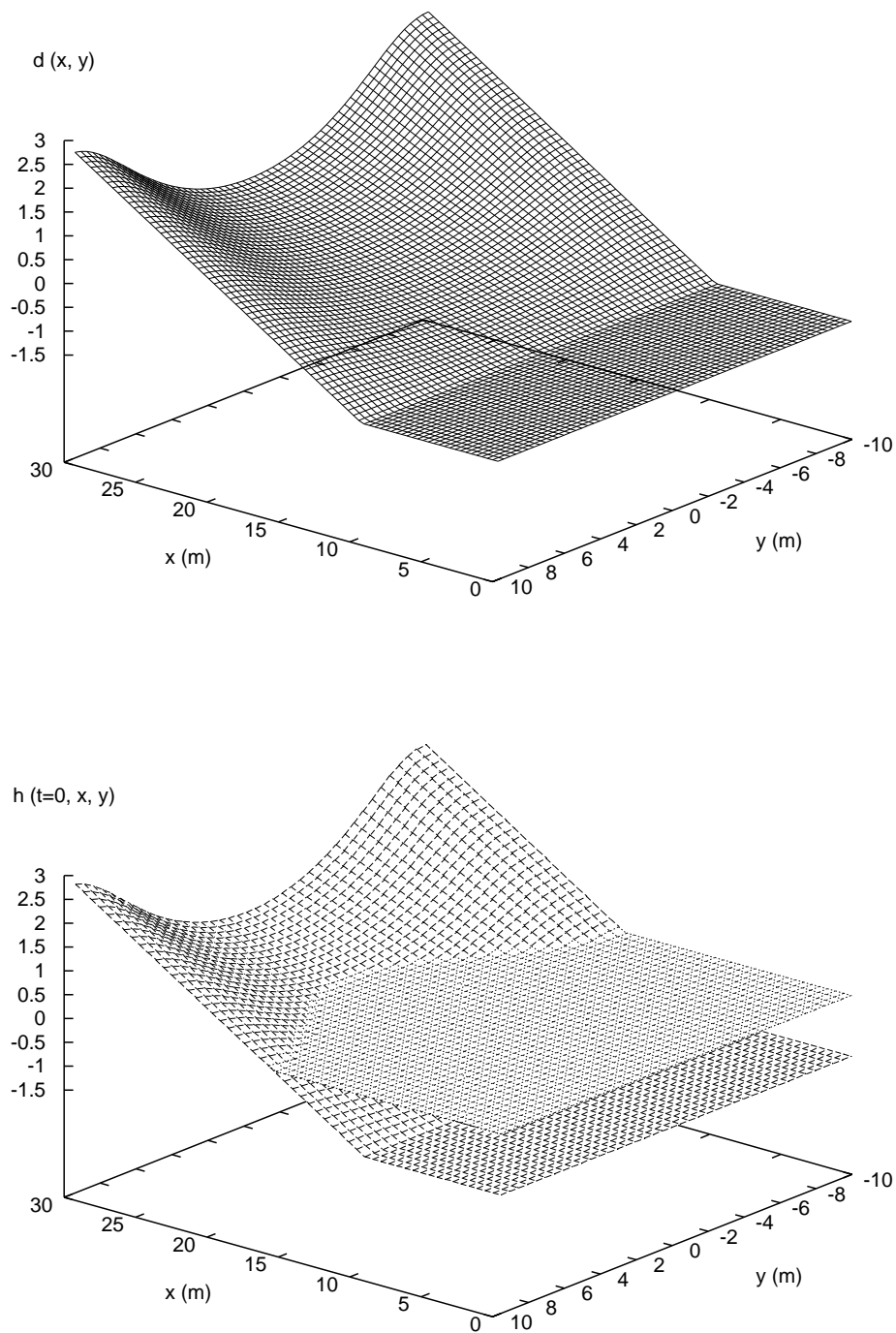


**Figure 6.3.1.** Zelt's test for the run-up of large tsunami wave. a) Bottom topography of the basin. b) Profile of the initial free surface.

the initial condition is the still water depth  $h_0$  (see Figure 6.3.1) and at the offshore boundary, the incoming wave is supplied as a solitary pulse using the absorbing/generating boundary condition, as follows :

$$h_i(t) = h_0 + \alpha h_0 \operatorname{sech}^2 \left\{ \frac{\sqrt{gh_0}}{L} \chi \left( t + \frac{x}{\sqrt{gh_0(1+\alpha)}} \right) \right\} \quad (6.5)$$

where

$$\chi = \sqrt{\frac{3\alpha}{4\beta}} (1 + \alpha). \quad (6.6)$$

The dispersive parameter  $\beta$  is defined by  $(h_0/L)^2$  and is independent of the solitary wave. The nonlinear parameter  $\alpha$  is the wave height to the offshore water height ratio  $H/h_0$ . The shape of the solitary wave depends on the non-linear parameter  $\alpha$  and breaking may occur if  $\alpha > 0.03$  [188]. The values of the velocity at the boundary are specified using the conservation of the outgoing Riemann invariant along the characteristic as exposed in Chapter 3, assuming that the flow is subcritical. In addition, the computation is performed assuming that the lateral boundaries are vertical walls. The geometry of the basin is equivalent to treating a periodic coastline constituted from bays located between steep structures and so a periodic extension is possible.

Let us now analyze the expecting behavior of the solitary wave during the run-up process when the wave amplitude is large enough. The wave may bend towards the lateral boundaries at each edge of the domain because of refraction. Run-up first occurs at these lateral boundaries because of the steep slope. While the wave still propagates shoreward at the center of the bay, where the slope is more gentle, a run-down can be observed from the lateral boundaries and reflection may tend to direct wave energy toward the shoreline at the center of the bay. Furthermore, the sloping topography may help to partially trap energy in the nearshore region. The combination of these various processes may enhance the run-up processes at the center of the bay.

For this simulation we take  $L = 10 \text{ m}$  and  $h_0 = 1.273 \text{ m}$  and the position of the flat section of the topography is at  $x = 9.55 \text{ m}$ . This set of values is taken from the simulation introduced in [84]. In order to highlight the increasing of nonlinear effects with respect to the incident wave amplitude, three cases are run. For the first run, we set  $\alpha = 0.0015$ , which corresponds to a wave height of  $H = 0.0025$ . For the second run, we choose  $\alpha = 0.01$  and it results in a wave height of  $H = 0.0127 \text{ m}$ . For the third and last case we set  $\alpha = 0.02$  and the corresponding wave amplitude is thus  $H = 0.0255 \text{ m}$ . The choice of these three values prevents the incoming wave from breaking while propagating from the offshore region toward the coast. The spatial discretization is defined by  $\Delta x = \Delta y = 0.1$  and the  $CFL$  is set to 0.7. Bed stresses are assumed to be negligible. Although their importance is difficult to estimate, typical laboratory studies and various numerical experiments in the literature have shown

that frictions don't alter the run-up process more than three per cents [188].

The results of the simulations performed by Zelt in [188] were presented as time series of the surface elevation of the shoreline in the cross-shore direction at five different locations along the bay in the longshore direction, respectively  $y/L = 0$ ,  $y/L = 0.25$ ,  $y/L = 0.5$ ,  $y/L = 0.75$ ,  $y/L = 1$ , where  $y = \pm L$  denotes the boundaries in the longshore direction, and as the normalized maximum run-up and run-down in the cross-shore direction as a function of the longshore location. A first normalization by  $H$  gives a good representation of the absolute magnitude of the shoreline motion within the bay. The normalization by  $h_0$  gives a good representation of the relative amplitude of the shoreline motion along the shore of the bay. In order to perform a qualitative comparison, we shows on Figure 6.3.5 time series of the surface elevation of the shoreline in the cross-shore direction at the five different locations and Figure 6.3.4 shows the maximum run-up and run-down in the cross-shore direction as a function of the longshore location.

The numerical results provided by the *SURF\_SVWB* model seem to be qualitatively similar to those presented by Zelt in [188]. We observe a good behavior with respect to the non-linear parameter  $\alpha$ . We describe the results for each run in what follows.

**6.3.2. Case  $\alpha = 0.0015$ .** For the case  $\alpha = 0.0015$  the amplitude of the wave is very small and nonlinear effects seem to be negligible. As we can observe on Figure 6.3.2 the run-up is tiny and is almost uniform across the bay with a magnitude of nearly twice the amplitude of the incident wave. This results is close to the expected result for a small amplitude long wave reflecting on a vertical wall. Actually, for this value of  $\alpha$ , the length scale of the incident wave is very long with respect to the nearshore sloping region and the sloping beach can be seen as a vertical wall when compared to the magnitude of the wave. We can observe a small effect of the two-dimensional geometry of the topography since the run-up is slightly larger at the center of the bay than near the boundaries. This is due to the small reflection of wave energy toward the center of the bay. In comparison to the run-up, the run-down is negligible in the whole domain. As it is emphasized in [188], the topography has a very little impact on the run-up and run-down processes when the length scale of the incident wave is greater than the length scale of the sloping region. As for the one-dimensional case of Synolakis, the convergence toward the steady state at rest is accurately computed. Note that at this scale, we need to use a finer grid in the cross-shore direction near the initial shoreline ( $\Delta x = 0.05 m$ ) if we want to compute accurately the variations of the water surface.

**6.3.3. Case  $\alpha = 0.01$ .** Figure 6.3.3 shows the effect of increasing the amplitude of the incident solitary wave beyond  $\alpha = 0.0015$ . The effects mentioned in the previous case become more pronounced, as the run-up and run-down amplitude increase. However the maximum run-down amplitude does not exceed the maximum run-up. We observe that the run-up and run-down become far much greater at the center of the bay. The maximum run-up amplitude along the shore occurs on the first advance of

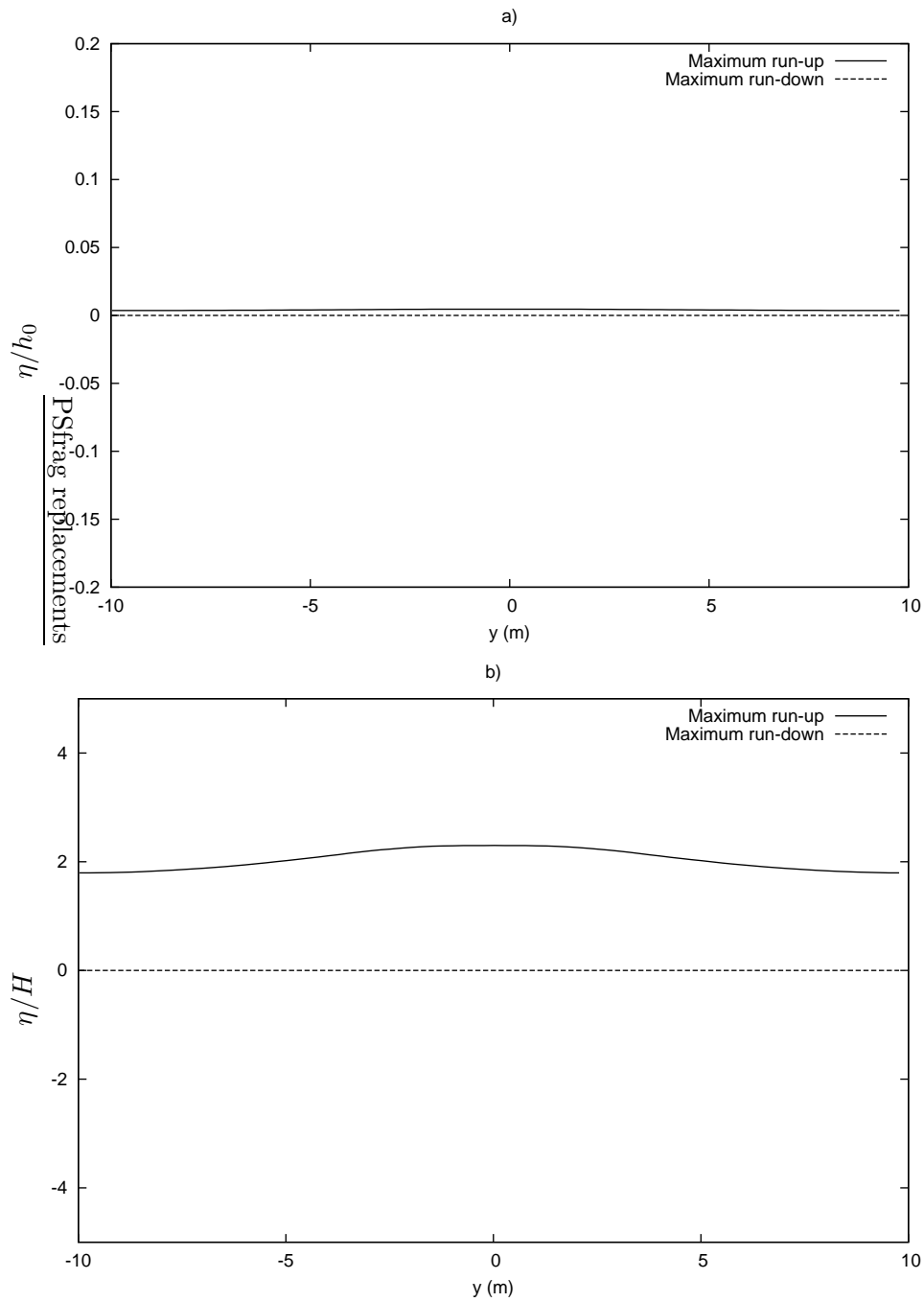


**Figure 6.3.2.** Zelt's test for the run-up of large tsunami wave. The maximum run-up and the minimum run-down as a function of the longshore position, for the case  $\alpha = 0.0015$ . a) the run-up is normalized by the still water depth  $h_0$ , b) the run-up is normalized by the solitary wave amplitude  $H$ .

the shoreline but the maximum run-down amplitude does not necessarily occur on the first retreat of the shoreline, especially near the lateral boundaries. This phenomenon is illustrated in the next case, where it seems to be more important.

**6.3.4. Case  $\alpha = 0.02$ .** This case has been used as a benchmark for several models, as those introduced by Hubbard and Dodd [84], Özkan and Kirby [131] or even Prasad and Svendsen [140].

On Figure 6.3.4 we can observe the results for  $\alpha = 0.02$ . The effects of an increasing incident wave's amplitude are still obvious. Figure 6.3.5 highlights the two-dimensional aspects of the run-up and run-down processes when the nonlinear effects become important. The results have been plotted for values of time between 0 and 60 s to enable the comparison with other results that can be found in the literature. Figure 6.3.5 also provides time scales concerning these processes at each location in the longshore direction. Actually a good evaluation of these time scales are of great importance in coastal engineering for the deployment of warning systems. The amplitudes of the run-up still increase in the entire bay and the run-down is greatly more pronounced, with an amplitude of the same order as for the run-up in the center of the bay. The two-dimensional effects of the topography become important since the run-up amplitude is seriously linked to the location along the longshore direction. Actually run-up and run-down are clearly enhanced at the center of the bay. This is due to reflections from the boundaries at each side of the domain which lead to the focusing of wave energy to the center.

We can also observe persistent oscillations of the surface level even after the forcing from the incident wave has stopped, which may be due to the trapping of wave energy along the coast as the topography and the shoreline geometry have an important impact on the response of the basin to the wave forcing (see [188] and [27]). Actually these oscillations are not exactly the same as those generated by other models in the literature but here, the well-balanced method ensures that these oscillations are not the consequences of the drawbacks of the fractional step method usually used.

Concerning the qualitative comparison with the results of Zelt or Kirby et al., we can observe that our model provides a reasonable simulation of the water surface motion since a similar general behavior in the time series of the run-up and the maximum run-up and run-down is observed. The major difference with the results provided by the Lagrangian model of Zelt is a slight under-prediction of the maximum run-up and run-down in the center of the bay for the case  $\alpha = 0.02$ .

From these qualitative comparisons with the results provided by the finite elements Lagrangian model of Zelt, we can conclude that the *SURF\_SVWB* model may be an efficient tool for the study of two-dimensional tsunami propagation over complex topography and that the two-dimensional complex physical processes involved in these phenomena may be accurately reproduced. the shoreline tracking method proposed here is far more simpler to implement than the Lagrangian tracking algorithms of zelt or Özkan and Kirby, with similar results. Furthermore, even if we have not shown

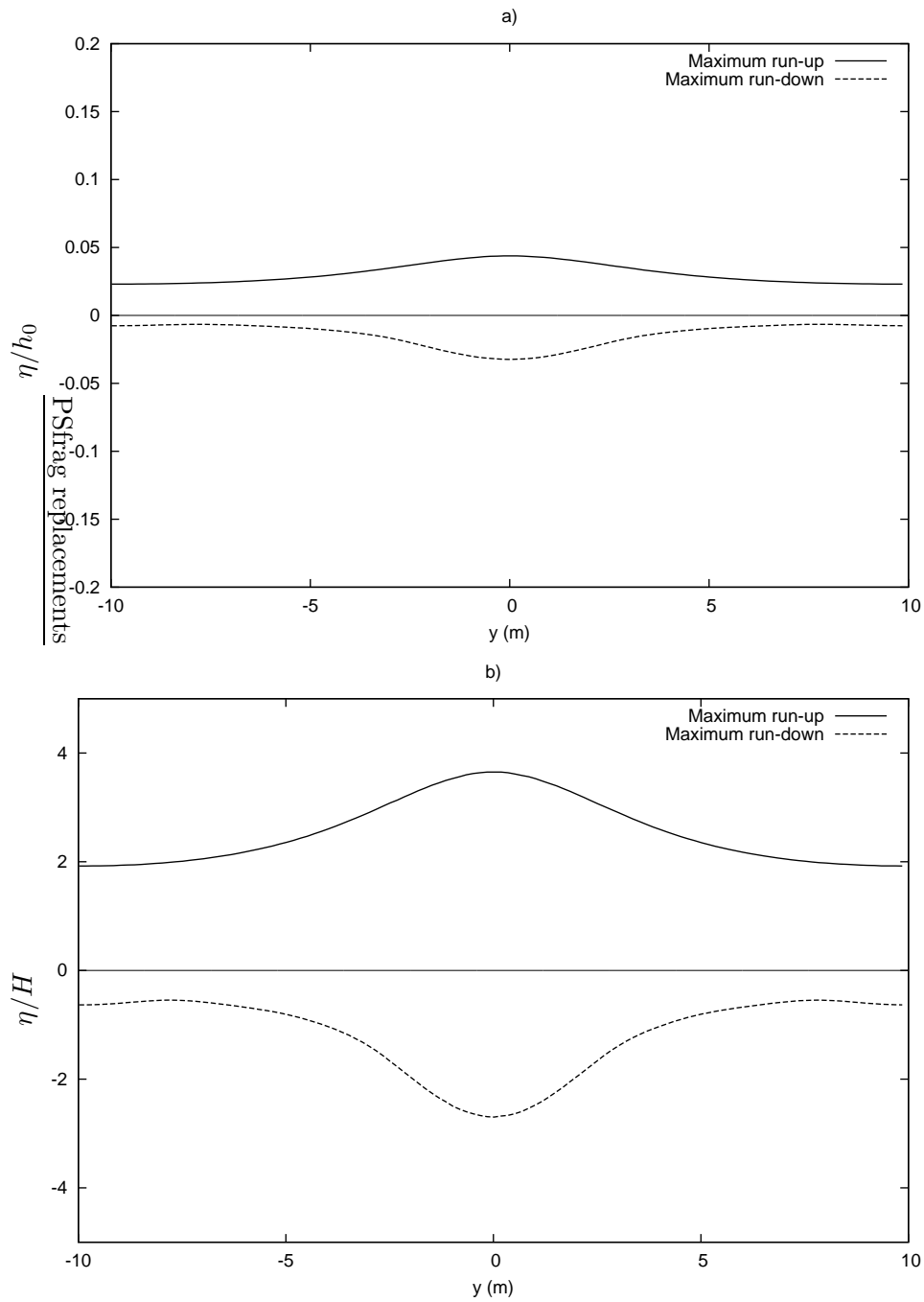


**Figure 6.3.3.** Zelt's test for the run-up of large tsunami wave. The maximum run-up and the minimum run-down as a function of the longshore position, for the case  $\alpha = 0.01$ . a) the run-up is normalized by the still water depth  $h_0$ , b) the run-up is normalized by the solitary wave amplitude  $H$ .

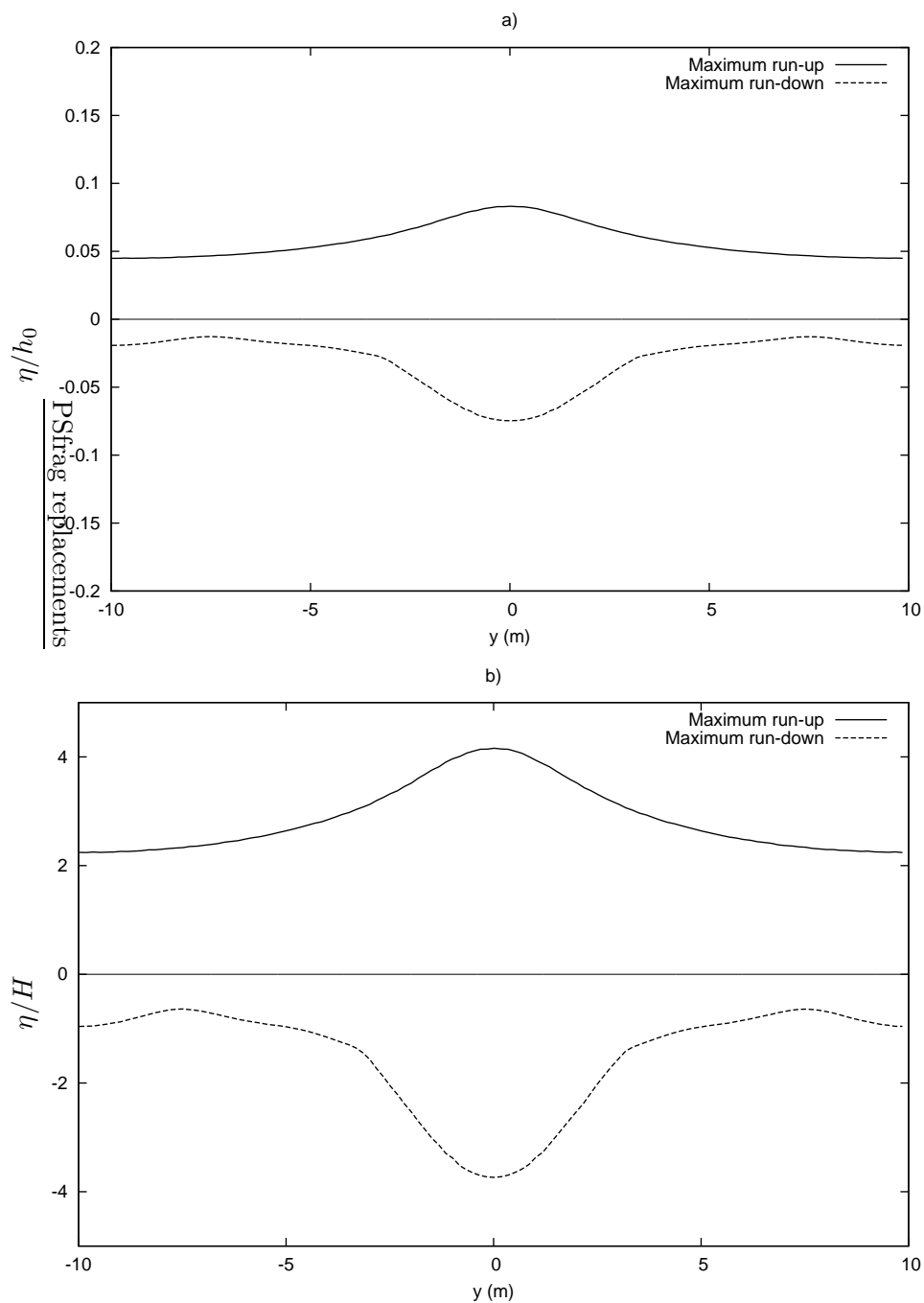


**Figure 6.3.4.** Zelt's test for the run-up of large tsunami wave. The maximum run-up and the minimum run-down as a function of the longshore position, for the case  $\alpha = 0.02$ . a) the run-up is normalized by the still water depth  $h_0$ , b) the run-up is normalized by the solitary wave amplitude  $H$ .

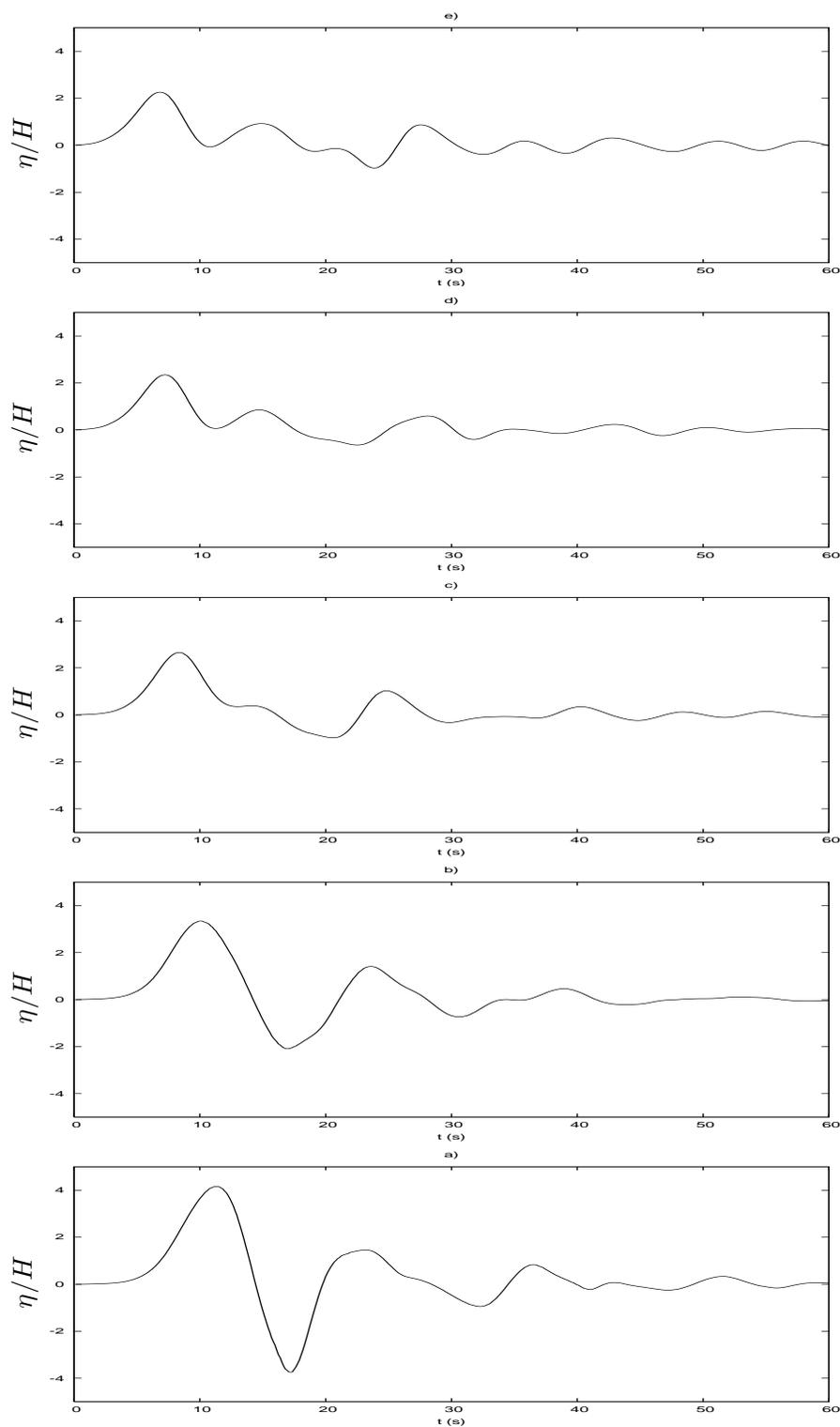


**Figure 6.3.5.** Zelt's test for the run-up of large tsunami wave. Time series of the run-up perpendicular to the shoreline along different longshore locations for the case  $\alpha = 0.02$ . a)  $y/L=0$ , b)  $y/L=0.25$ , c)  $y/L=0.5$ , d)  $y/L=0.75$ , e)  $y/L=1$ .

the time series of the surface elevation for large values of time, we emphasize that the use of the well-balanced method enables to compute the convergence toward the steady state at rest after approximately 150 *s*. This convergence was not possible for the previous models proposed in the literature. However, we need to validate the model with more realistic data to assess the real improvements brought up by the well-balanced method.

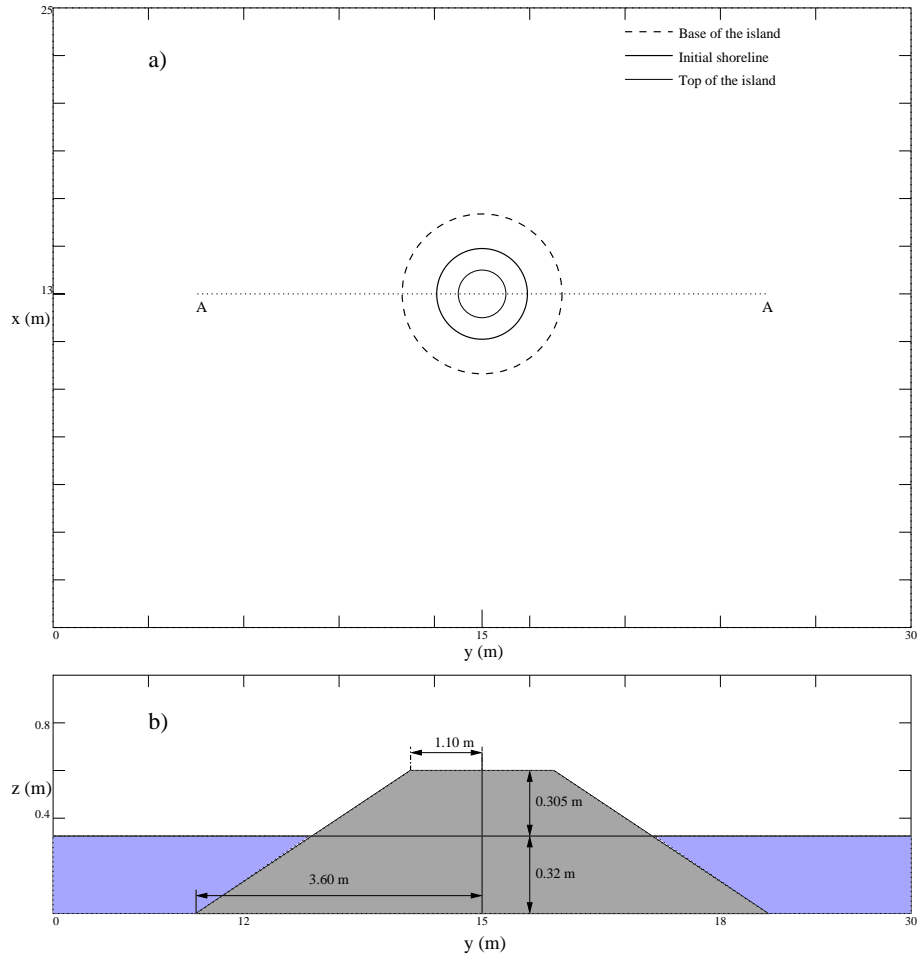


**Figure 6.4.1.** Sketch of the conical island. a) Top view of the basin and the island. b) Vertical view in the central cross-section A-A in the longshore direction. This figure is not to scale.

## 6.4. Two-dimensional run-up on a conical island

**6.4.1. Motivations.** During several events involving large tsunami waves, unexpectedly large run-up heights were observed in the lee side of small islands. A significant instance is the event that happened in 1993 on the Okushiri Island of Japan, a small island of approximately 20 km long and 10 km wide. The tsunami attacked from the northwestern direction and as the maximum run-up height was observed along the coastline which faces the tsunami directly, the second larger run-up height was recorded in the southern region [115].

In order to recover such results with experimental and numerical simulations, Briggs et al. [25] performed a series of laboratory experiments, at the US Army Engineer Waterways Experiment Station, for the study of three dimensional tsunami run-up on an idealized conical island. The experimental basin was 30 m wide by 25 m long and the 7.2 m-diameter conical island was positioned in its center. The island was

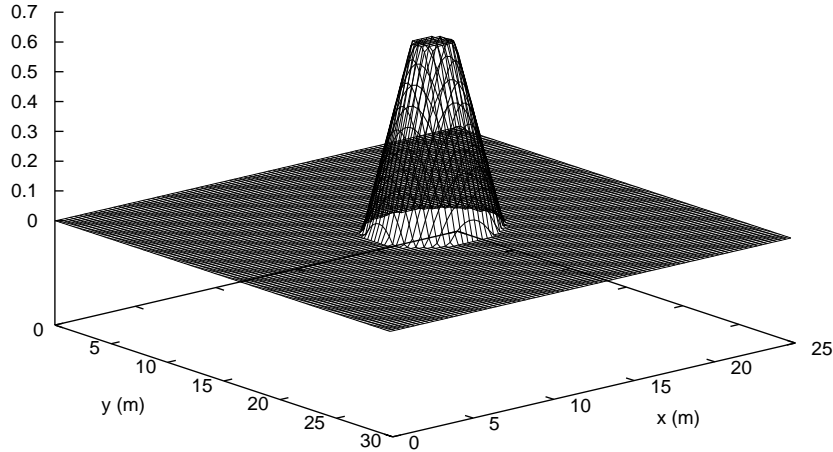


**Figure 6.4.2.** Run-up on a conical island. Wave basin topography in the experiment of Liu et al. [115]

62.5 m tall and the side slope was 1:4. A sketch of the island and basin geometry is shown in Figure 6.4.1 and Figure 6.4.2. A directional spectral wave generator was installed along the x-axis and produced plane solitary waves of specified crest lengths and heights propagating towards the island. Several height-to-depth ratios were tested while two water depths were used in the experiments : 0.32 m and 0.42 m.

Twenty seven wave gages were distributed around the island and maximum vertical run-up measurements were made at 20 locations around the island. A subset of these experiments was used as a benchmark test for a number of numerical models, for the International Workshop on Long Wave Run-up (see Yeh et al. in [118]). In [115], Liu et al. developed a numerical model based on a finite difference method and validated it against their set of data. Here, we perform a qualitative comparison between the numerical results provided by the present model *SURF\_SVWB* and the results which can be found in the literature [115], [84], [121].

Numerical simulation was performed on a computational domain defined with  $0 < x < 25$  and  $0 < y < 30$ . The initial condition is the flow at rest and at the seaward boundary  $x = 0$  we input a solitary wave as in the previous section. The velocity is evaluated by the use of characteristic method within the inlet absorbing/generating boundary condition. We perform a test of 50 s. Therefore, we focus on the initial run-up and run-down processes and on the convergence toward the steady state after the evacuation of the wave from the computational domain.

We have performed numerical simulation for a value of the nonlinear parameter  $\alpha = 0.1$  and the longshore length of the incident wave is  $30\text{ m}$ . Values of  $\Delta x = 0.08$  and  $\Delta y = 0.1$  have been used and the  $CFL$  is set to 0.8. The still water depth is set to  $h_0 = 0.32\text{ m}$  and the ratio  $H/h_0$  where  $H$  is the wave amplitude is set to 0.1.

**6.4.2. Evolution of the water depth.** On Figure 6.4.3 we can observe the time series of the surface elevation at six locations around the island, in order to perform a qualitative comparison with the results presented in the literature. These locations correspond to the position of six wave gages, namely gages number 3, 6, 7, 10, 13 and 16. A comparison with experimental measurements are shown in [115], [84] and [121] for instance. Unfortunately, experimental data were not available for this work and we can only perform a qualitative comparison with these results. Our results have been plotted for values of time less than  $18\text{ s}$  in order to obtain similar scaled curves as those introduced in [84] and perform a qualitative comparison.

As far as it can be judged, our *SURF-SVWB* model provides valuable results since the general behavior of the shoreline motions at the six locations is close to the curves introduced in [84]. The expected run-up at the lee-side of the island can be observed on Figure 6.4.3 e). There is no spurious oscillations and so the predicted results obtained by Liu et al. with the Cornell model [115] seem to be improved. Moreover, as for the previous test, the convergence towards the steady state at rest is rapidly and accurately computed, without numerical oscillations.

Moreover, in most cases, the run-up height is larger at the front side of the island and decreases as the wave moves towards the back of the island. When the length of the incoming wave in the longshore direction is much larger than the base diameter of the island, as in our simulations, a serious run-up occurs at the back of the island because of wave refraction around the island which generates two trapped waves. As emphasized in [115], in the case  $\varepsilon = 0.1$  the maximum run-up experimentally measured at the lee side is actually of the same order of magnitude than at the front side, but focused on a small area. Our numerical results agree with this observation as seen on Figure 6.4.3 and Figure 6.4.9.

**6.4.3. The solitary wave evolution.** A sequence of snapshot-type figures of the free-surface profile around the island are presented in Figure 6.4.4, 6.4.5 and 6.4.6. We observe that the incident solitary wave generates high run-up in the front side of the island. As the maximum run-up magnitude is reached on this front area, the wave runs down the inundated area back to the initial waterline while a portion of the refracted wave propagates around the island towards the lee side, generating two trapped waves at each side of the island. After a short time, we observe a collision of these two waves at the lee side, generating the second high run-up. Then, these waves pass through each other and go further propagating around the island and die gradually. In general, maximum run-up height is larger at the front of the island and decreases as the wave moves toward the lee side. After a short time, the water level settles back to the still

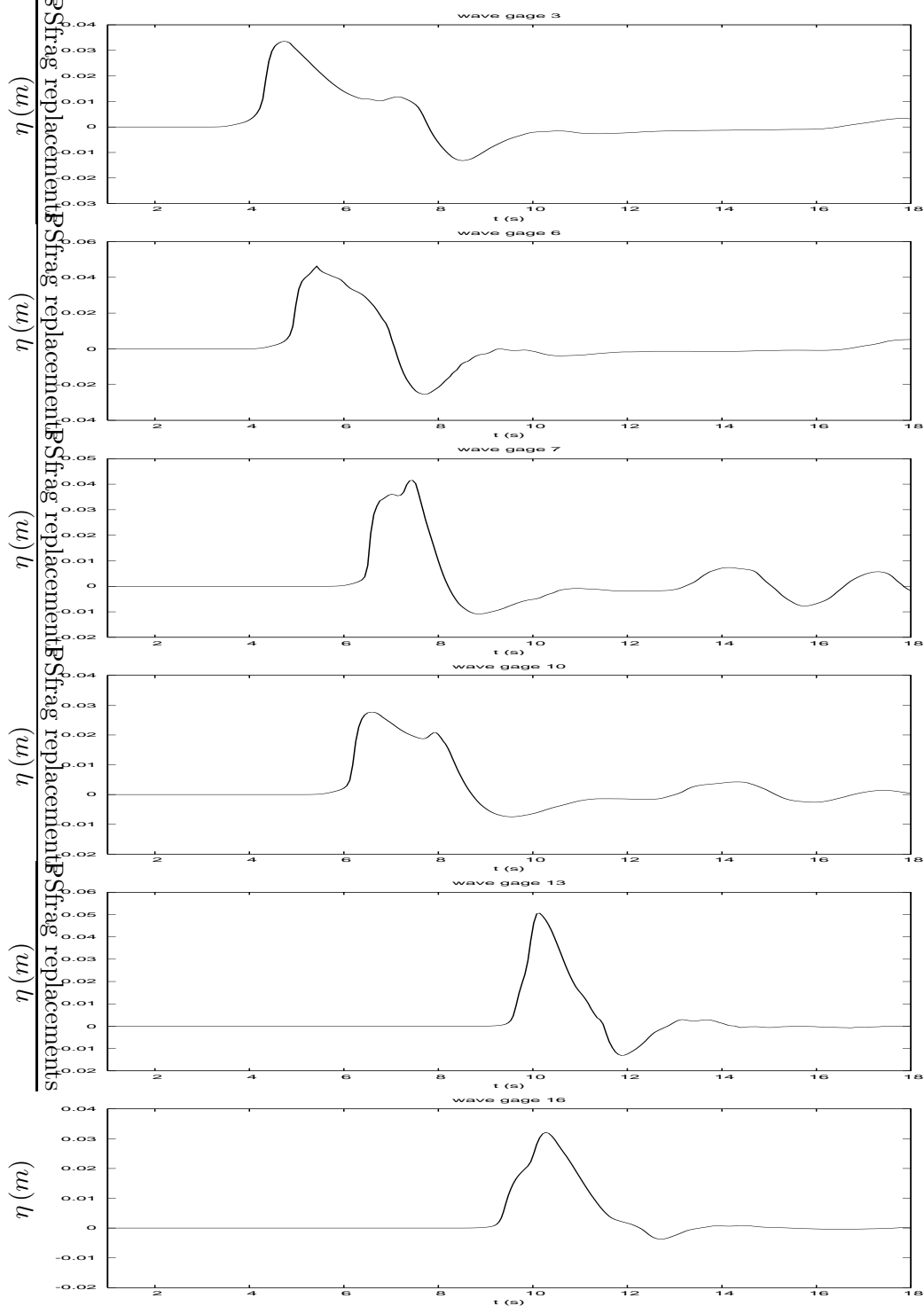


**Figure 6.4.3.** Run-up on a conical island. Time series of the free surface elevation at wave gages 3, 6, 7, 10, 13, 16 of the simulation proposed in [115], for a  $\alpha = 0.1$  incident solitary wave.

water depth.

**6.4.4. Evolution of the velocity field.** Figure 6.4.7 and 6.4.8 show sequences of velocity distributions at the back of the island. We can observe that the depth averaged velocity is greater near the shoreline, whereas the wave celerity is smaller. The velocity is maximum during the collision of the two trapped waves. We can observe that the velocities are first in the longshore direction before the collision between the trapped waves. When the waves collide, the velocities near the shoreline turn into the cross-shore direction very sharply. This entails the inundation of a focused area. During the run-down, the velocities turn in the opposite direction, while the trapped waves still propagate around the island.

**6.4.5. Maximum run-up.** A sequence of shoreline locations respectively in the front side and in the lee side of the island are shown in Figure 6.4.9. We can clearly observe that the inundated area during the run-up is much wider at the front of the island than in the lee but the maximum amplitudes are similar. At maximum run-up, which occurs near  $t = 9$  s, almost the entire front half of the island is affected, whereas the run-up in the lee side is also consequent but floods a smaller area. A possible explanation is given in [115] and this difference between front and lee side may be due to the fact that during the run-up phase in the front side of the island, the velocity field is entirely directed towards the onshore direction and the incident wave attacks directly the sloping shore. In the lee side, the velocity field is directed towards the longshore direction before the collision between the trapped waves and, at the time of collision, alongshore velocities turn suddenly along the onshore direction towards the island, generating the enhanced and focused run-up at the lee side.

**6.4.6. Wave history at the lee-side.** Finally we show on Figure 6.4.10, 6.4.11 and 6.4.12 a sequence of snapshots of the free surface motions at the lee side of the island, which aims at illustrating the dynamic of the enhanced run-up. The two trapped waves propagate around the island and wave crest in the deeper water move faster than those along the shoreline. The two wave crests meet offshore first, generating a surge which propagates towards the shore, as the velocities near the shoreline turn into the onshore direction during the collision. This surge is then enhanced by the collision of the wave crests along the shoreline leading to a consequent run-up. The run-up generated by the surge decreases rapidly and the trapped waves still propagate around the island, with a decreasing amplitude ( $h$ ,  $i$ ).

It appears from this qualitative analysis that our model gives almost as accurate results as those introduced by Hubbard and Dodd [84] with their model with adaptive mesh refinement. We recall that we have used a regular mesh with constant discretization steps in each direction. In addition our moving shoreline treatment is simpler than the algorithm introduced in [115] in a finite difference context. The maximum run-up at the lee-side of the island is clearly recovered and the scheme rapidly converges towards

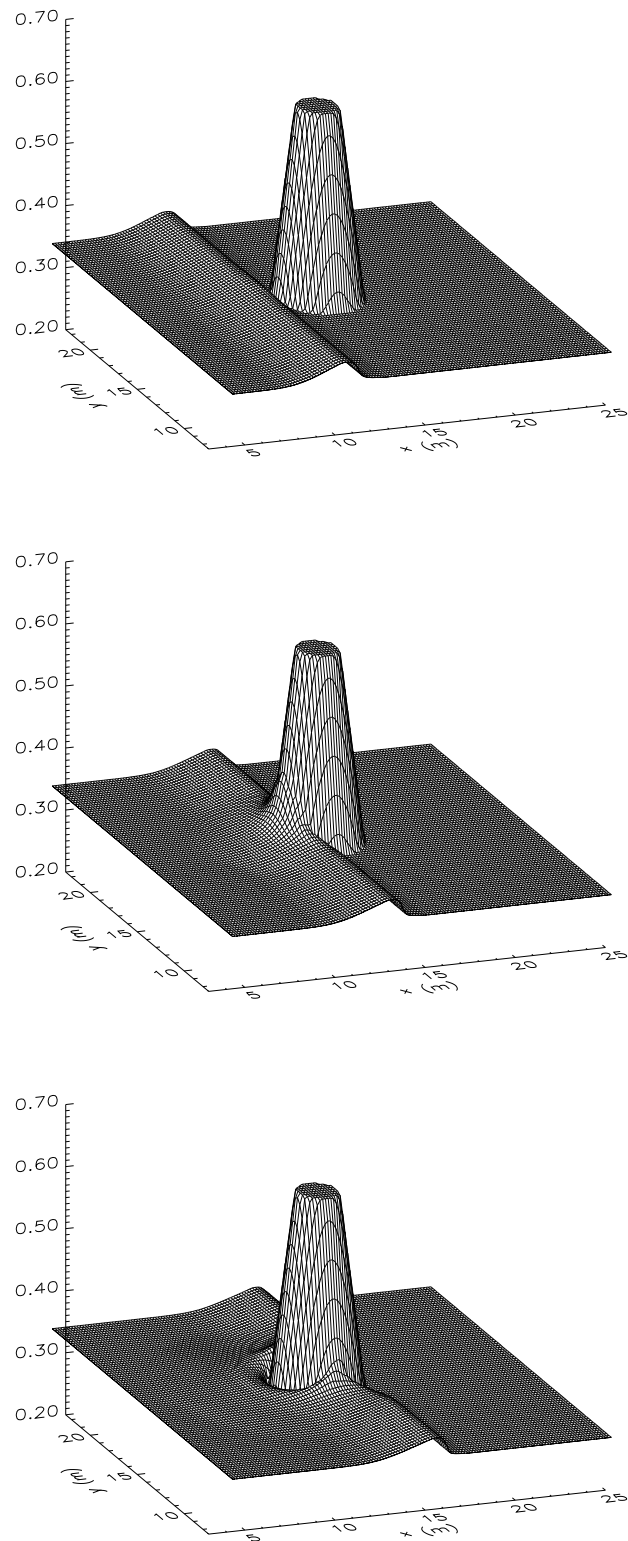


**Figure 6.4.4.** Run-up on a conical island. Snapshots of free surface elevation at different times for a  $\alpha = 0.1$  incident solitary wave: a)  $t=7.5$  s, b)  $t=9$  s, c)  $t=10.5$  s.

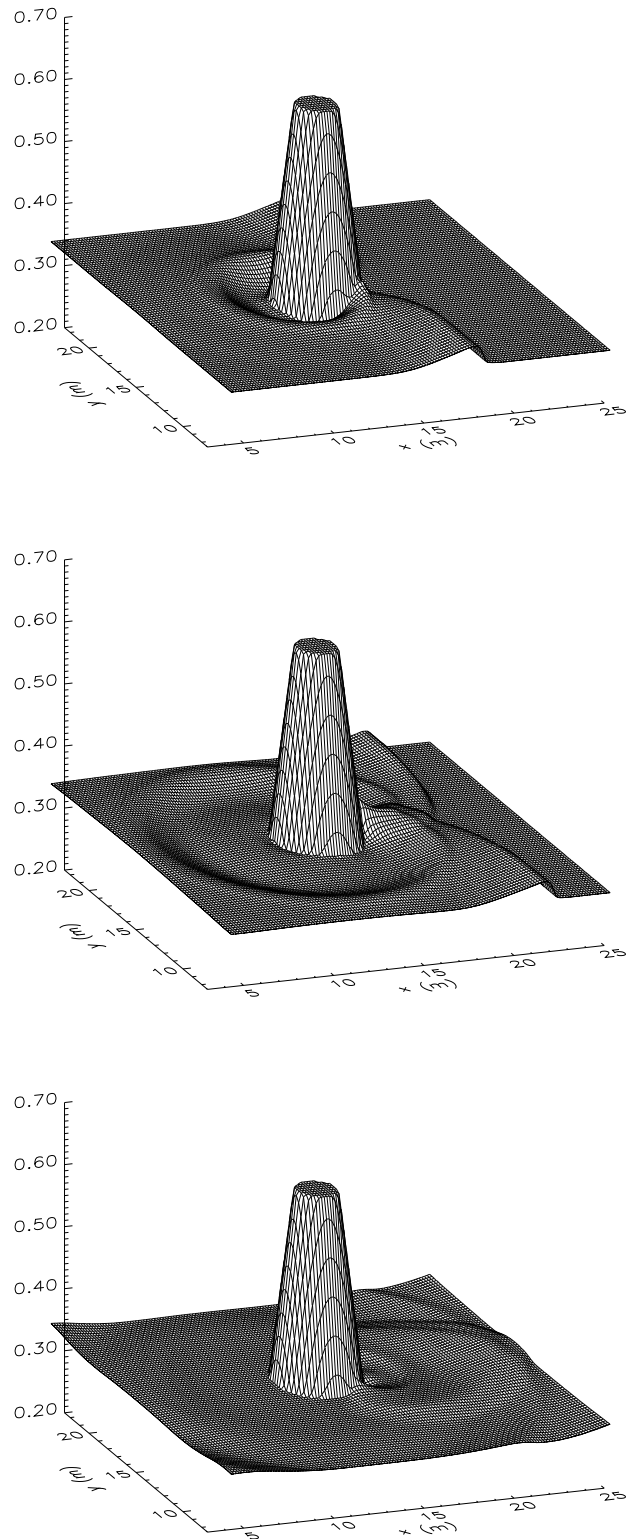


**Figure 6.4.5.** Run-up on a conical island. Snapshots of free surface elevation at different times for a  $\alpha = 0.1$  incident solitary wave: d)  $t=12$  s, e)  $t=15$  s, f)  $t=18$  s.

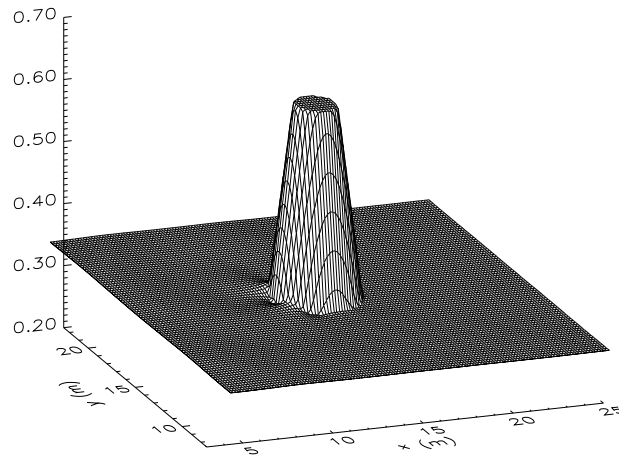


**Figure 6.4.6.** Run-up on a conical island. Snapshots of free surface elevation at different times for a  $\alpha = 0.1$  incident solitary wave: g)  $t = 26$  s.

the steady state at rest after the complete evacuation of both incident and reflected waves from the computational domain.

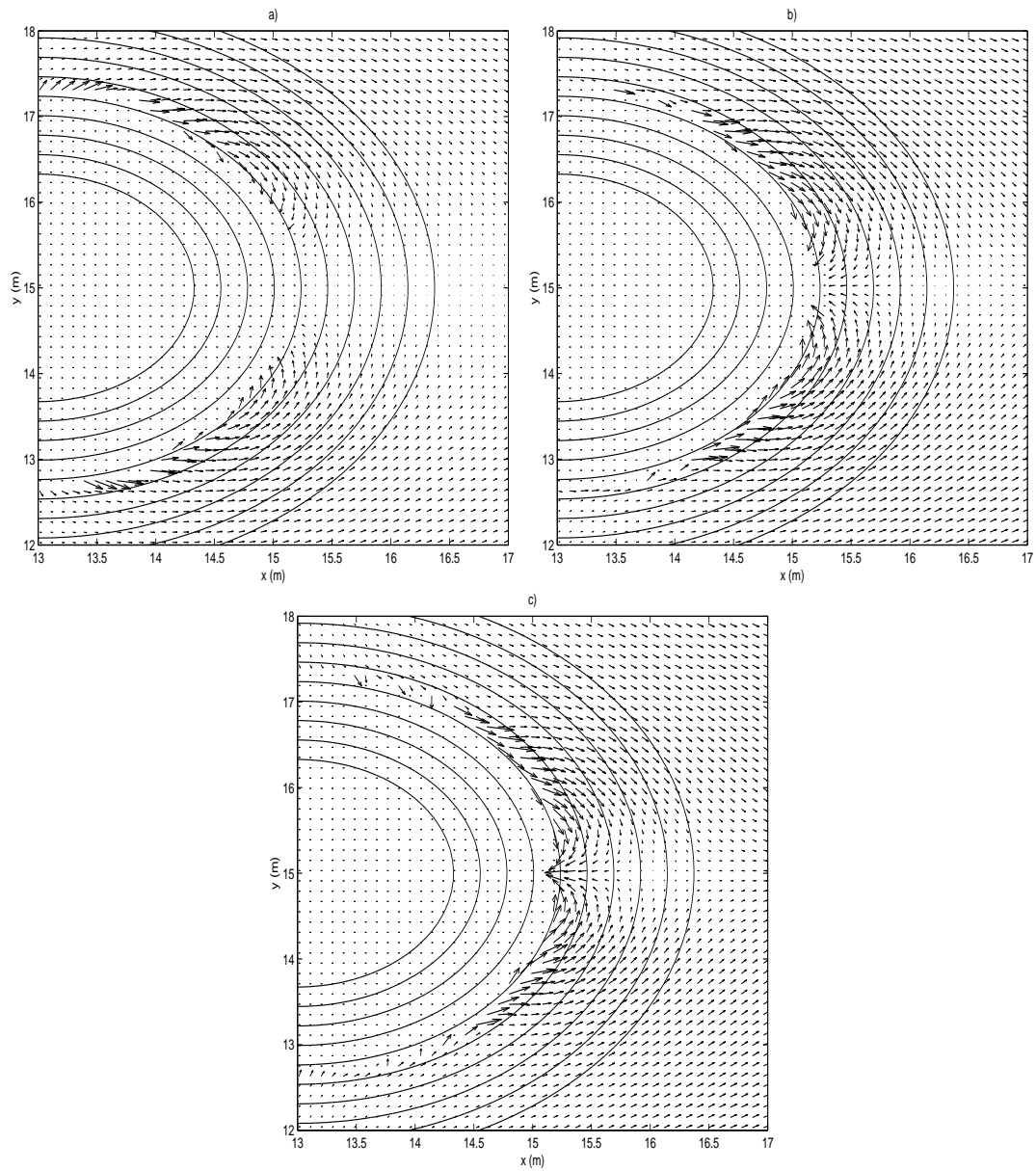


**Figure 6.4.7.** Run-up on a conical island. Snapshots of velocity distribution at the lee side of the island for  $\alpha = 0.1$  and different times : a)  $t = 11.0$  s, b)  $t = 11.5$  s, c)  $t = 12.0$  s.

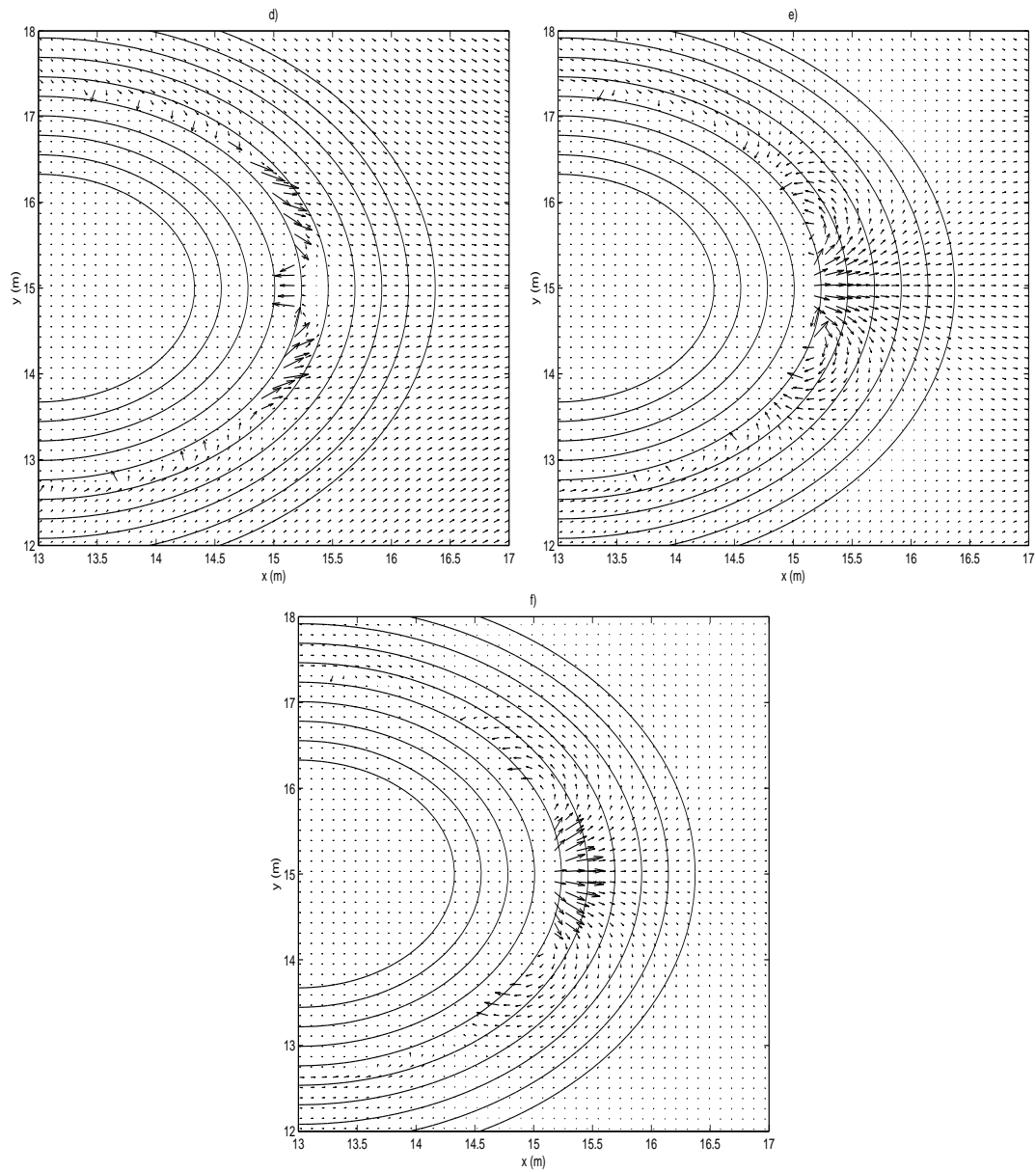


**Figure 6.4.8.** Run-up on a conical island. Snapshots of velocity distribution at the lee side of the island for  $\alpha = 0.1$  and different times : d)  $t = 13.0$  s, b)  $t = 13.5$  s, c)  $t = 14.0$  s.

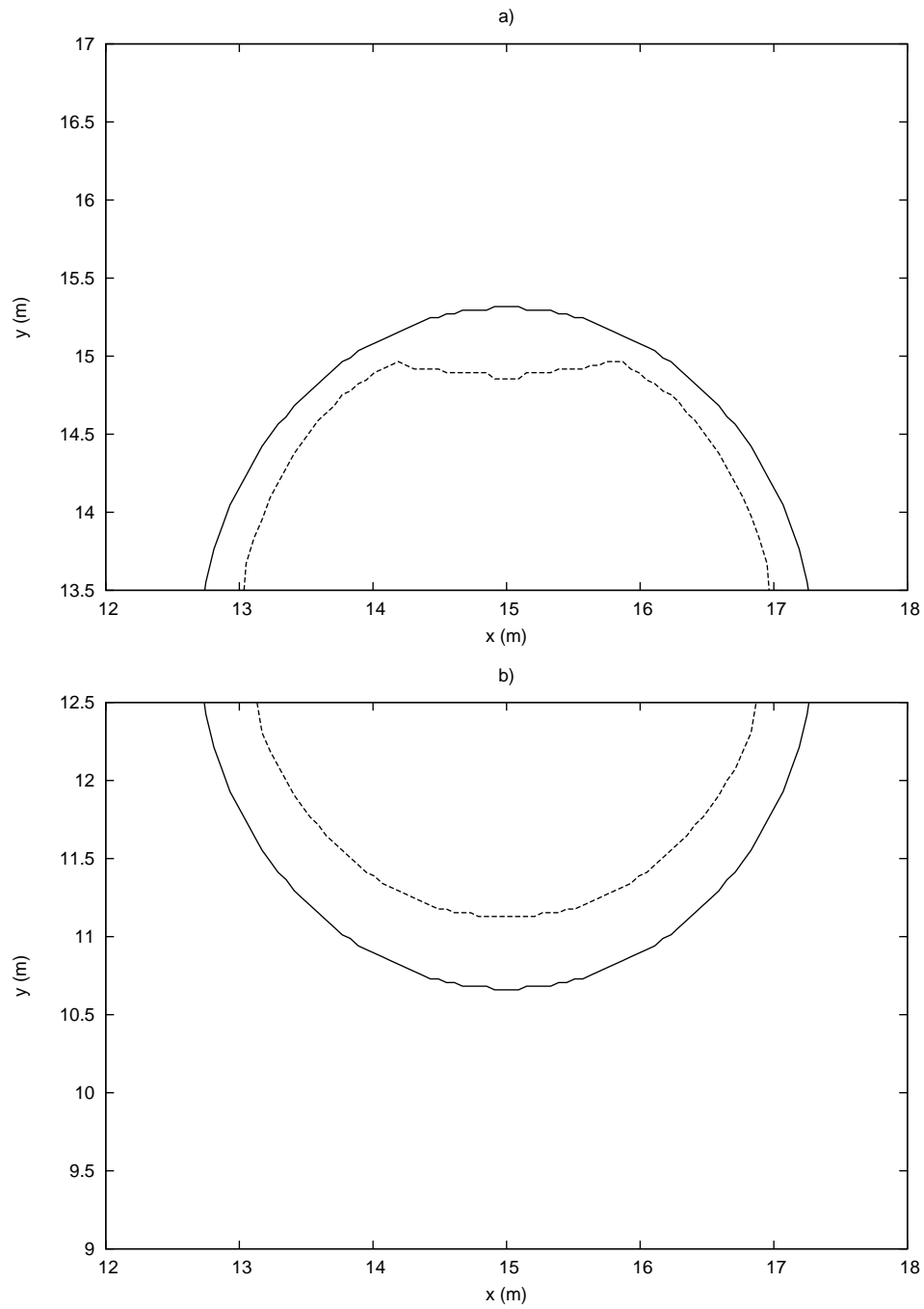


**Figure 6.4.9.** Run-up on a conical island. Maximum run-up during the simulation : a) at the lee side of the island; b) at the front side of the island, for a  $\alpha = 0.1$  incident solitary wave. The initial shoreline is in solid lines. The computed location of the maximum run-up during the simulation is plotted in dotted lines.

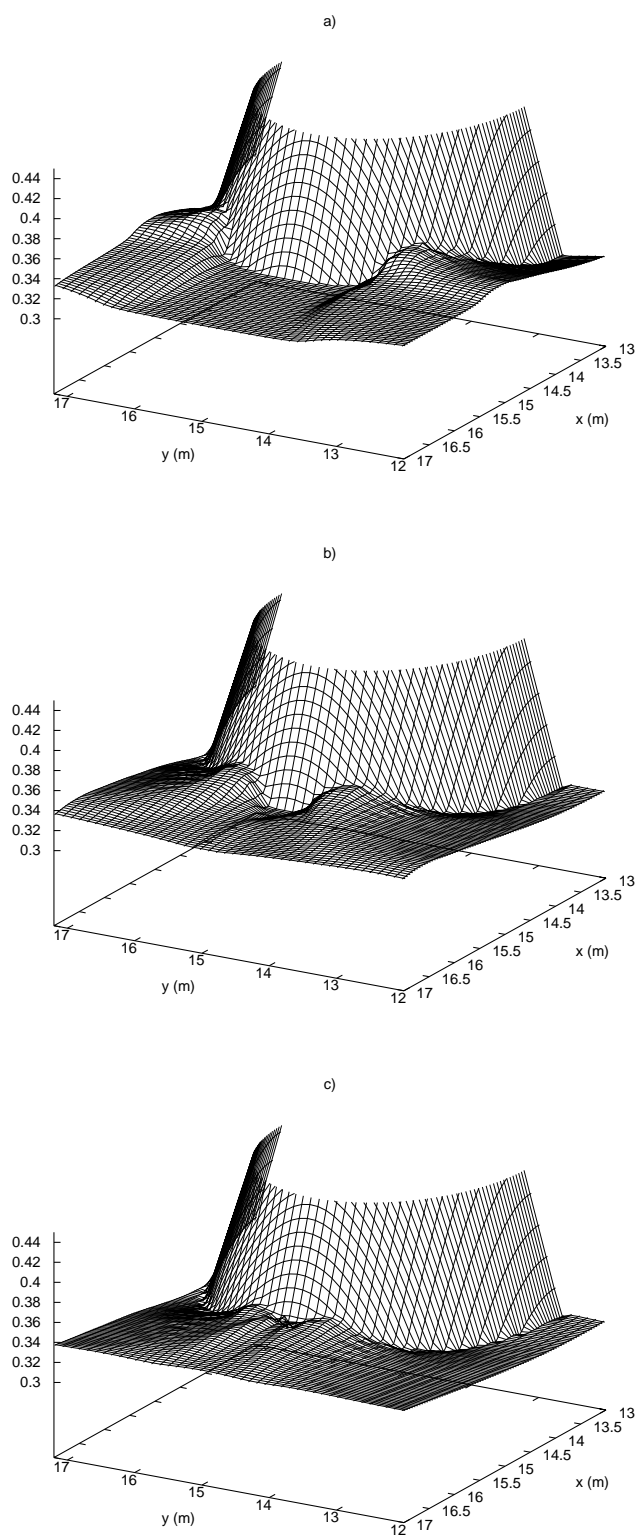


**Figure 6.4.10.** Run-up on a conical island. Snapshots of free surface elevation in the lee side of the island at different times for a  $\alpha = 0.1$  incident solitary wave: a)  $t = 10.0$  s, b)  $t = 11.0$  s, c)  $t = 11.5$  s.

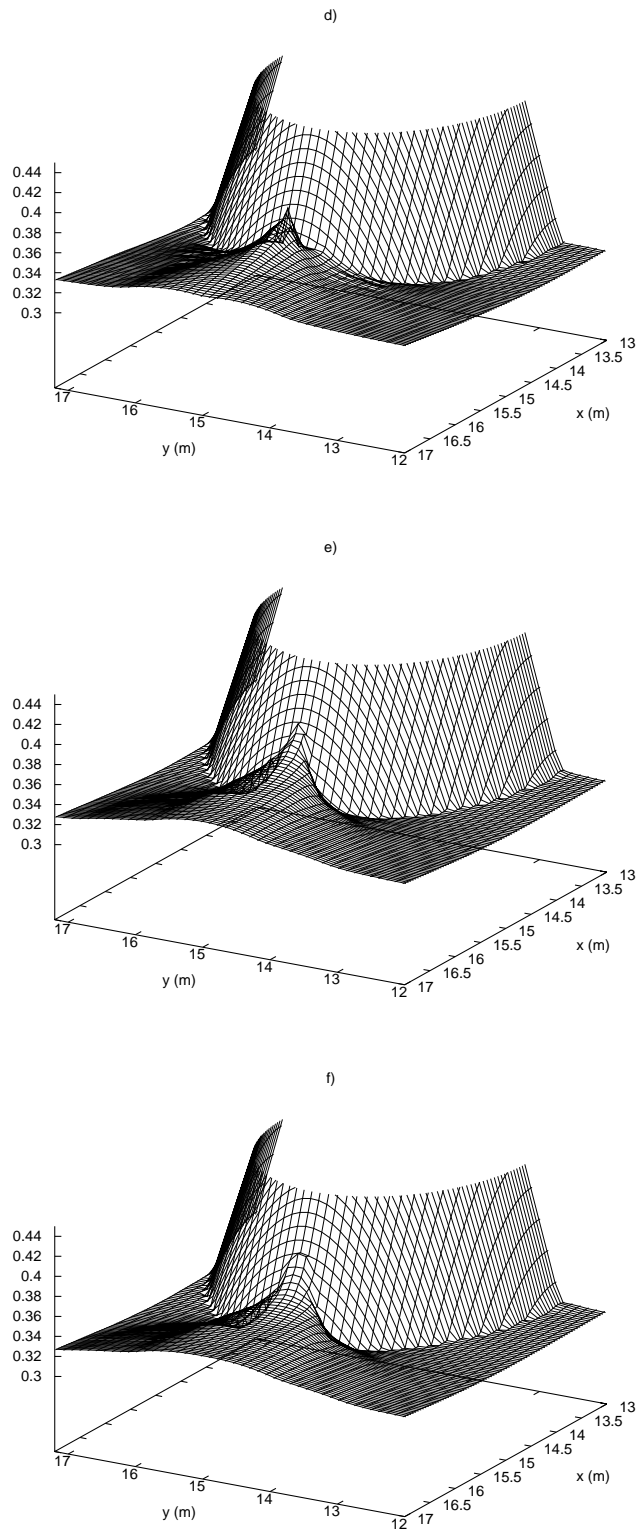


**Figure 6.4.11.** Run-up on a conical island. Snapshots of free surface elevation in the lee side of the island at different times for a  $\alpha = 0.1$  incident solitary wave: d)  $t = 12.0$  s, e)  $t = 12.5$  s, f)  $t = 13.0$  s.

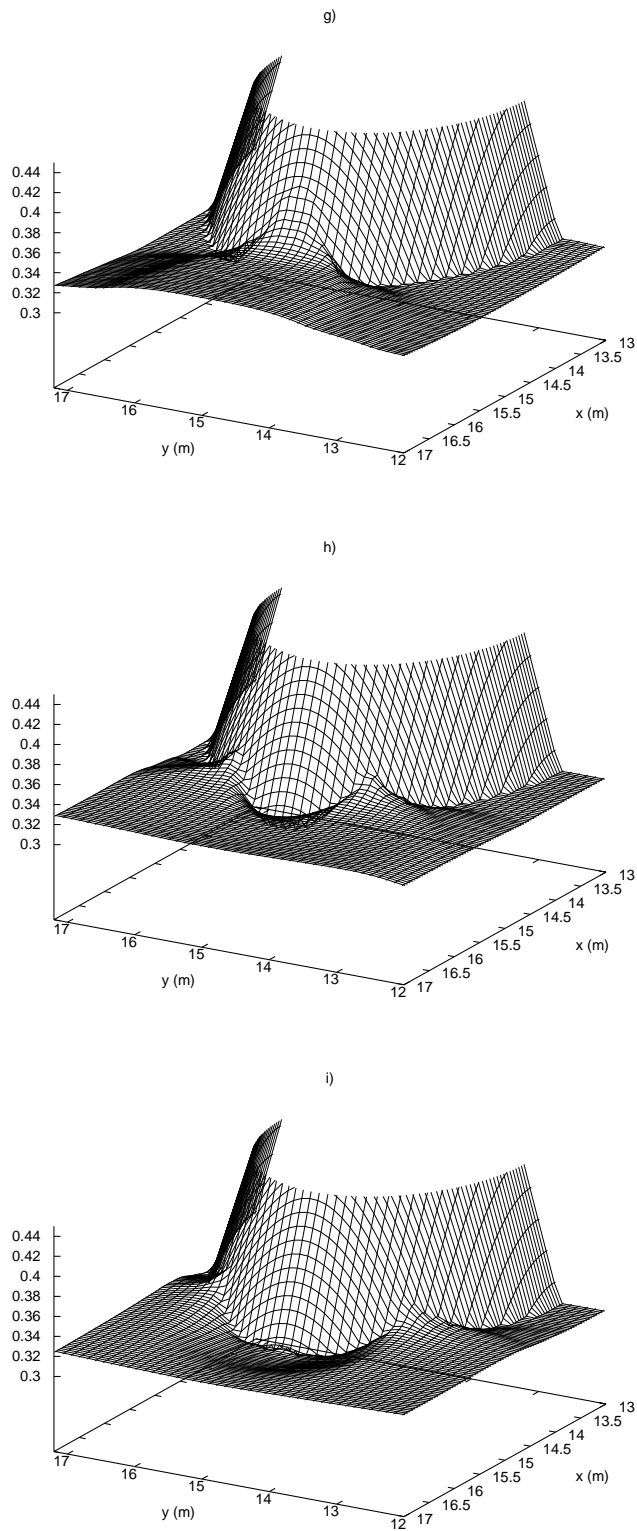


**Figure 6.4.12.** Run-up on a conical island. Snapshots of free surface elevation in the lee side of the island at different times for a  $\alpha = 0.1$  incident solitary wave: g)  $t = 13.5$  s h)  $t = 14$  s, i)  $t = 14.5$  s.

# Simulation of breaking waves in the Inner Surf Zone

## 7.1. Introduction

Wave breaking on beaches is an impressive natural phenomena and surf zone dynamics is a highly complex topic which deals with waves in the region between the breaker line on a beach and the shoreline. From the fluid mechanics theories, the surf zone is characterized by the irreversible transformation, due to breaking, of the motion of the incident wind-generated waves into motions of various kinds and scales, including small-scale turbulence, larger-scale vorticity motions, low frequency waves and steady flows. The spectrum of frequencies involved in these various phenomena is shown in Figure 7.1.1. The dynamics of this transformation and the induced motions and currents are the subjects of this introduction.

It is worth mentioning that even if large progress have been made in the understanding and the modelization of several kind of processes involved in the breaking transformation, their interactions are still poorly understood. For instance, the great importance of low frequency motions for the nearshore dynamics has been highlighted by spectral analysis of observed oscillations and velocity fields and also by the fact that natural sedimentary coasts often exhibits morphological length scales considerably greater than the scales of the wind-generated waves [7]. But the understanding of such low frequency motions are still unsatisfactory. Another relevant example is the observations of strong interactions between sediment transport, morphological evolution and flow fields for long time scales [39].

At this day, there is still no model which enables to deal with the complete spectrum

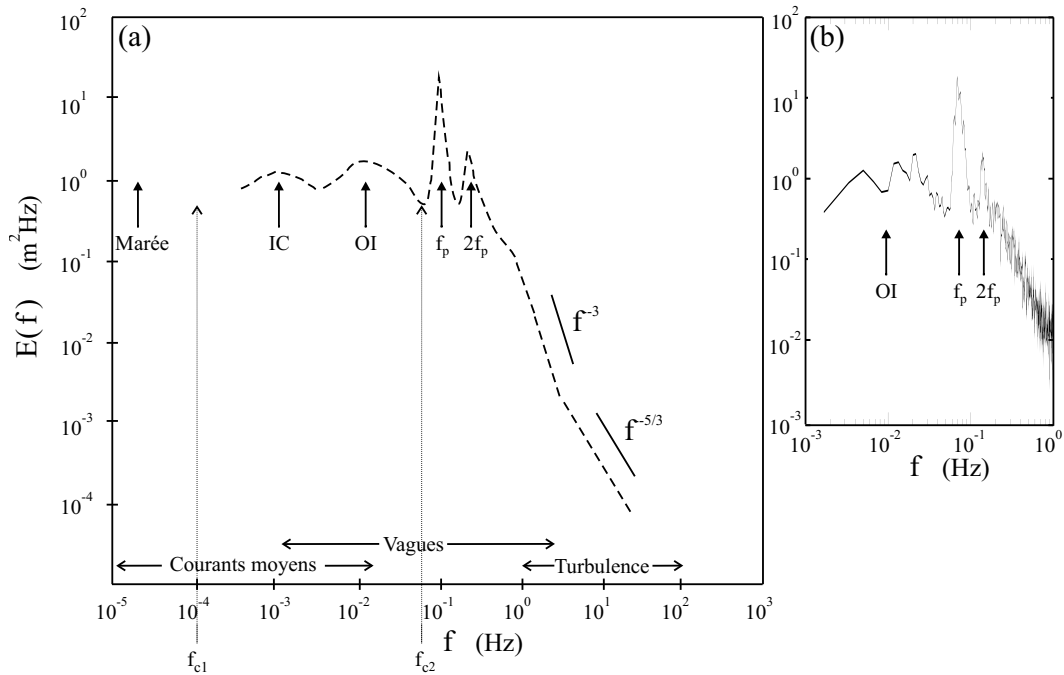


**Figure 7.1.1.** Energy spectrum of cross-shore velocity in the ISZ. a) sketch of a typical spectrum illustrating the main hydrodynamic processes, b) measured spectrum on Truc Vert beach, Aquitanian coast. OI : “Ondes Infragravitaires”, IC : “Instabilités du courant moyen”,  $f_p$  : fréquence pic de la houle (Bonneton [18]).

of flows from the point of breaking to the shoreline.

**Breaking waves.** As waves propagate into shallow water, shoaling process leads the waves heights to increase until the breaking process. As stressed out in [136], the term “wave breaking” is used to describe the transition from a smooth wave to a quasi-steady bore-like state rather than to any particular instant within the transition. This breaking is due to the steepness of the waves which becomes very large as the depth becomes shallower and an instability is generated as the velocity at the crest of the wave becomes larger than the velocity at the base. The breaking process is characterized by a large loss of energy, leading to a decreasing wave height as the waves propagate towards the shore. Hence the surf zone, which extends from the point of breaking to the shoreward, is associated with a large dissipation of the wave energy flux from the offshore into turbulence.

Immediately after the initiation of breaking, a rapid change in the wave shape occurs over a relatively short distance of 8-10 water depths after the breaker point, in a region that has been named Outer Surf Zone or “transition region” (Svendsen et al. [164]). The rapid transition and the specificity of each waves are difficult to describe and modelize. As a consequence, very few theories concerning this zone are available and, most of the time the literature is descriptive, based on qualitative observation, with some attempts to quantify the processes. The reader is referred for instance to the works of Janssen [86], who mapped the variations of the surface level in this region using video recordings of fluorescent tracers, or Okayasu [129] who performed measurements of the velocity using laser Doppler velocimetry.

The way in which the waves break can occur in a continuous gradation of regimes and mainly depends on the wave characteristics (deep-water wave height, wave period) and the bottom slope. A qualitative description of the different types of breakers (with gradual transition) is proposed by Galvin in [60]. There is essentially four different types of breaking waves, usually classified as collapsing, plunging, surging and spilling, as shown in Figure 7.1.2.

In spilling breakers, the forward slope at the top of the wave becomes unstable and an increasing mixing of water and air bubbles slides down the front slope from the crest, traveling with the wave as a surface roller. The spilling breaking process is usually associated with very gentle beach slope and relatively steep incoming waves. For plunging breakers, most of the steepening wave’s front overturns and the crest falls down and plunges down into the water ahead of the wave, as a single mass of water, generating a splash-up of water which is pushed up. This jet of water propagates forward and continues the breaking process. Plunging breakers are usually found over steep beach slopes. For surging breakers, the foot of the steep front becomes unstable and rushes forward, leading to a decreasing water height. No significant disturbance of the smooth wave profile occurs except near the shoreline. This process is often observed over very steep beach slope and, for instance, on many natural beaches, where the foreshore is much steeper than the rest of the beach. In the so-called collapsing breakers, the lower portion of the front face overturns and behaves like a truncated plunging breaker.

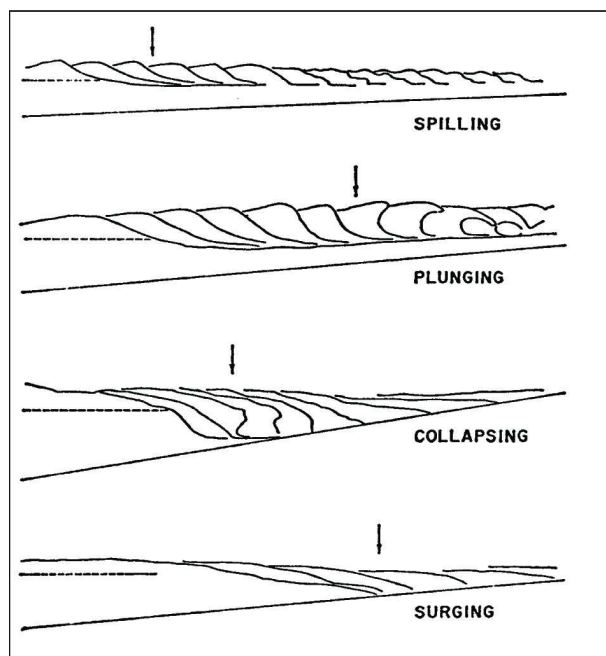


**Figure 7.1.2.** Cross-shore profiles of the four main breaker types [60]. The arrows show the initiation of breaking process.

In special cases where the slope becomes sufficiently steep, the waves stop breaking and full reflection may occur. Breaking or reflection of solitary waves on uniform slopes has been studied intensively. We can cite for instance Synolakis [166] who performed experimental and analytical studies.

Of course, the criteria for onset of breaking are far more complex and one can observe various breaker types on the same beach at different times, depending on the wind condition or specific swell's features. It is worth noticing that in most cases plunging or spilling breakers, or a transition between these two types, occur generally on most sandy beaches, and in particular on Aquitanian beaches.

Shoreward of the transition region, the wave field changes more slowly and broken waves are reorganized into quasi-periodic bore-like waves which propagate toward the shore. This is the so-called Inner Surf Zone (ISZ) or "bore region", since broken waves have many features in common with bores in this region. The Inner Surf Zone, has been the subject of intense studies during the last decades. Until recently, information concerning the ISZ were also mostly descriptive and a few models which aim at understanding and predicting hydrodynamics in this region have appeared. Svendsen et al. [164] have shown that the wave surface profiles develop a relatively steep front with a more gently sloping rear side. The shape of the rear side may change from a concave form towards a nearly linear variation as the waves propagate to the shore, leading to a characteristic sawtooth shape.

Shoreward of the ISZ, we found the "swash zone" which is intermittently covered and uncovered by wave run-up on the shore.

**Energy dissipation in the ISZ.** The energy dissipation due to breaking on a sloping beach in the ISZ is often assumed to be equal to the dissipation in a hydraulic jump or bore height. This method seems to have been first exploited by Le Mehauté [105].

The energy dissipation is thus modeled on the basis of the classical expression for the dissipation in a bore connecting two areas of uniform flow, with depths  $h_1$  and  $h_2$  respectively ( $h_2 > h_1$ ), which implies that energy is dissipated at a rate  $D'$  per unit span given by (see [102]) :

$$D' = \frac{1}{4} \rho g^{\frac{3}{2}} \left( \frac{h_1 + h_2}{2h_1 h_2} \right)^{\frac{1}{2}} (h_2 - h_1)^3. \quad (7.1)$$

Svendsen et al. [164] stressed out that this relation underestimates the dissipation in waves breaking on a beach, mainly because the turbulent fluxes of momentum and energy are neglected. Nonetheless, this relation yields a good order-of-magnitude estimation.

**Vorticity and turbulence generation.** An interesting feature of the ISZ is the evolution of the velocity field during the breaking process. Actually, two basically types of motion can be observed during the wave propagation from the offshore to the shoreline. The first is the essentially irrotational motion during the steepening and eventually overturning period. The second is the gradual development of large vortical and turbulent motions during the bore propagation, after the breaking. As Kelvin's circulation theorem applied to the shallow water equation leads to the conservation of the potential vorticity (vorticity divided by water depth) along streamlines, one may wonder how such transition may occur. This is mainly a consequence of the overturning and the water jet impact or splash-up for plunging breakers and of the formation of the roller in spilling breakers [7]. Peregrine [135] also stresses out that non-uniformities in the bed slope may induce non-uniformity in the dissipation rate through the propagating bores in the ISZ and consequently generate vorticity. This topic is developed in the next subsection. As time elapses, the initially generated large-scale and coherent vortex motions degenerate into small-scale motions with increasing disorder, leading to turbulence. But this source of turbulence is minor when compared to the acute turbulence generated by plunging or spilling breakers.

**Wave breakers induced macro-vorticity.** In the nearshore domain, we can observe important variations of topography which may be natural (like bars generated by rearrangements of transported bottom sand) or man-made (breakwater heads for instance). As already stated the propagation of a steep wave over a submerged structure can lead to the generation of bores of finite length [29]. The variations of topography modify the incident wave fields, generating waves breaking on these structures with different intensity on different locations. In the case of coastline with almost-uniform orientation and uniformly sloping beaches, breakers of finite length are essentially induced by longshore bars. As shown theoretically in [135], the variation

of intensity in the breaking phenomenon along the breakwaters generates vorticity which re-organized in the shape of large-scale horizontal eddies with vertical axis, also named macro-vortices. This phenomenon is extremely complex, since various processes of similar strength are interacting simultaneously.

The mechanism of vorticity generation by breakers of finite length can be highlighted with some simple analytical results first introduced by Peregrine in [135]. We analyze the flow in terms of the vorticity  $\omega = \partial_x v - \partial_y u$  which is the only non-zero component of the vorticity vector, orthogonal to the plane of motion. Within the NSW assumptions, the potential vorticity  $\omega/h$  is conserved when following a particle of fluid in the Lagrangian description (water columns). The conservation equation for the vorticity is :

$$\frac{D\omega}{Dt} = -\omega \nabla \cdot \mathbf{v},$$

where  $\frac{D}{Dt}$  stands for the Lagrangian derivation, or equivalently

$$\frac{D\omega}{Dt} = \frac{\omega}{h} \frac{Dh}{Dt}. \quad (7.2)$$

It raises that an increasing of water depth  $h$  induces intensification of  $\omega$ . This phenomenon is true when flow properties are smooth. The discontinuities of water depth and velocity introduced to model bores are source of energy dissipation and vorticity generation. These mechanisms are not taken into account in Equation 7.2. Actually, the amount of vorticity generated by the bore is directly related to the depth jump across the discontinuity. The jump in potential vorticity between locations '1' and '2' respectively downstream and upstream of a bore moving with front parallel to the coastline is :

$$\left[ \frac{\omega}{h} \right]_1^2 = \sqrt{\frac{2}{gh_1 h_2 (h_1 + h_2)}} \partial_y E_D \quad (7.3)$$

with

$$E_D = \frac{g(h_2 - h_1)}{4 h_1 h_2}. \quad (7.4)$$

In this expression,  $\partial_y E_D$  is the rate of change parallel to the bore front of the energy dissipated by the bore. This rate is of important magnitude when there is a sudden variation in flow properties like, for instance, when uniform fronts of waves propagate over a submerged obstacle and break locally.

**Wave-induced mean currents.** Wave-induced mean currents are generated partly by induced mean pressure gradients and partly by induced dissipative processes. The excess flux of momentum due to waves (the radiation stresses) plays a crucial role in the generation of horizontal circulation, leading to a set-up of the mean water level and the generation of wave-induced currents (longshore current, rip current). The set-up cross-shore gradient in the surf zone appears to be approximatively proportional to

the bottom slope. Therefore, in the case of normally incident waves, strong three dimensional variations of the topography entail variations of the set-up in the longshore direction and may yield non-uniform longshore motions (wave-induced currents) and circulation cells (see Chapter 7 for a study of rip currents). Note that in this case, the current is not directly generated by dissipation-induced shear, like for the large scale vortical motions previously introduced, but it is an indirect consequence since it arises from the set-up longshore variations. In a general way, alongshore non-uniformities in the bed slope and/or incident waves yield longshore non-uniform horizontal circulation. This will be developed in Chapter 7 for the specific case of a rip current over an idealized ridge and runnel system. Note that these mean coastal currents and more generally the nearshore circulation are usually simulated using a statistical approach with time-averaged equations. This is developed in the following.

**Numerical models.** The classical approach for ISZ-wave modeling is based on the depth integrated momentum and energy equations time-averaged over a wave period. Equations of motions are filtered in time with respect to a wave period and this enables the use of a larger time step and thus to perform simulations over long time (from one hour to a few months) with a reasonable computational cost. We can cite for example the models of Wu and Liu [183], Watanabe [180] and more recently Castelle et al. [38] for the study nearshore sandy bars morphodynamics. The reader is referred to Svendsen and Petruvu [165] for a more complete review. In such models, wave height and set-up variations are computed from integral wave properties, such as the energy flux, the radiation stress and the energy dissipation. These model are relatively simple and useful for practical applications except in the swash zone. However in some applications, like for accurate modelization of sediment transport, the prediction of time-varying quantities, such as the ISZ oscillating velocities or swash oscillations, is required. In addition these time-varying quantities can be used to compute wave-averaged values and eventually highlight some processes with more precision.

Several models have been pointed out since the two last decades in order to describe and simulate the variations of the instantaneous water level and velocity and the wave motions in the nearshore domain, from the shoaling zone to the shoreline, where run-up occurs. The most favored approximate model equations for studying nearshore hydrodynamics are both the NSW equations and the many available Boussinesq-type equations. In recent years, most of the research was focussed on the latter. Actually, Boussinesq type equations, in which dispersive effects are modelized, are initially well-fitted for the modelization of shoaling process. They became far more popular when it was proved that they could model fairly well breaking waves, with the use of a roller model and suitable parameterizations to account for dissipation (see Schaffer et al [150]). From this, several works have stressed out that Boussinesq-like models may be applied successfully to the surf zone (Madsen et al [123]), including even the swash zone and the run-up process. We can refer for instance to Kennedy et al. [93]) or to the recent studies of Cienfuegos et al. [46], [47] who introduced a new breaking wave parameterization and developed a fourth order accuracy compact finite volume method

for the Serre equations, including a shoreline boundary condition. However the main disadvantage of all these methods is that effects of waves breaking are incorporated into Boussinesq models by means of semi-empirical methods, which imply the use of many “tunable parameters” and calibration. In addition, the boundary conditions for the shoreline are often artificial methods. We can refer to the slot method of Madsen et al. [123] or the extrapolation method of Lynett et al [121] for which extra filtering procedures are needed to prevent any non-physical oscillations. Hence the stability is often restricted and the extension to the two-dimensional case is arduous.

On the other hand, it is well-known that every propagating solution of the NSW equation will steepen, owing to the lack of dispersive effects. Shallow water steepening can be simply stressed out in the case where a wave is propagating into still water of constant depth. Each part of the wave travels with the long-wave velocity  $u + \sqrt{gh}$  where  $u$  is the velocity and  $h$  the total water depth. Hence, the higher part of the wave travels faster. As a consequence, the breaking is predicted too far offshore and the use of NSW equations is more relevant in the ISZ.

Concerning the swash zone, the NSW equations have been proved to accurately model wave motions. For instance, Hibbert and Peregrine [80] proposed a numerical simulation of the entire process of bore propagation and run-up. Raubenheimer et al. [143] showed a good agreement between numerical results provided by the NSW equations and field data for wave motions in the swash zone over gentle sloping beach. Computation of the run-up process and moving shoreline has also been extensively studied using NSW equations, as exposed in Chapter 6.

However, some important remarks concerning the validity of the shallow water assumptions in the ISZ must be stressed out. We know that NSW equations provide accurate approximation to flow motions when the vertical acceleration is negligibly small and when the length scale of the variations of the water surface level or the mean velocity is large in comparison with the water depth. Hence, any numerical model based on the shallow water theory must satisfy these assumptions at every discretized point, including the regions of strong shear flow. But as any propagating solution of the NSW equations will steepen on its front side, due to the lack of dispersion process, the underlying shallow water assumptions break down since turbulence and vertical variations of the velocity are induced near the bore front. Actually, turbulence and variations in vertical acceleration are strongly localized and it is possible to distinguish two regions in ISZ broken waves : a thin “wave front” where flow properties are rapidly evolving and a “regular wave region” where the horizontal velocity field is nearly vertically uniform and the turbulence intensity is weak [15]. At the top of the wave front, the plume of water and air bubbles carried with the wave is called the “roller” region. Experiments from Nadaoka et al. [128] have shown that turbulence is mainly located in this wave front and the velocity field presents strong vertical variations (Govender et al. [71]). From these observations it appears that the assumptions for the NSW equations may be only satisfied in the regular wave region.

Despite this, numerical models based on finite difference methods and second order Lax-Wendroff schemes have been pointed out in order to describe waves propagation in the ISZ. They first rely on the addition of artificial dissipation which prevents the steepening waves from becoming vertical fronts. The first models were proposed by Hibbert and Peregrine [80] and Packwood and Peregrine [132]. The difficulty with this empirical approach is to estimate the appropriate artificial viscosity which introduces the needed dissipation. Some comparisons with large-scale laboratory measurements and field data have proved the ability of the NSW equations to model the complex dynamics of long waves in the nearshore. For instance, Kobayashi and coauthors (Kobayashi et al. [97], [96], [98], [99]) developed a bore-capturing NSW model, also based on the Lax-Wendroff scheme with artificial viscosity and highlight its accurate results in comparison with laboratory ISZ experiments. More recently, Bonneton and Vincent [179] proposed to use a TVD flux limiter scheme based on a MacCormack second order scheme. This method introduces a rational way for the estimation of artificial dissipation. Concerning comparison with data, Raubenheimer et al. [144] and Bonneton et al. [16], [15] found a good agreement between computed ISZ wave solutions and field observations on gently sloping beaches and the ability of the NSW equations to accurately predict wave distortion and energy dissipation of periodic broken waves in the ISZ is proven. Thus, even though some assumptions of the shallow water theory may be violated in the ISZ, promising results have been obtained. As emphasized by Liu et al. [115], this is puzzling.

From these considerations, we will keep in mind that an accurate modelization of instantaneous and mean wave-induced motions relies on a proper evaluation of the wave's energy dissipation due to breaking. This is possible with the use of "second order" accuracy shock capturing finite volume methods based on a local Riemann solver, which enables the generation and propagation of bores. Thus, these numerical methods enable the modeling of broken waves without having to directly model turbulent dissipation, even if the region of initial breaking and the details of breaking are poorly represented. The energy's dissipation during the bores propagation is thus taking into account as an intrinsic feature of the model, with the jump relation imposed through the bores.

Moreover, as the wave's energy dissipation during the propagation is closely linked to the variations of topography, an accurate modelization of the interactions between flux gradients and bed slopes is crucial. Consequently, the well-balanced method previously introduced seems particularly well-suited for surf zone modelization.

The first test proposed here is a validation of the ability the *SURF\_SVWB* model to compute the distortion and the propagation of a periodic train of breaking waves in the ISZ. It has already been performed by Bonneton [15] with his *SURF\_SV* model. The second test proposed in this chapter brings out some improvements in the state of the art in the modelization of two-dimensional circulation in the ISZ, since to our knowledge there is still no application of the NSW equations to the study of waves-induced mean currents generation in the surf zone.

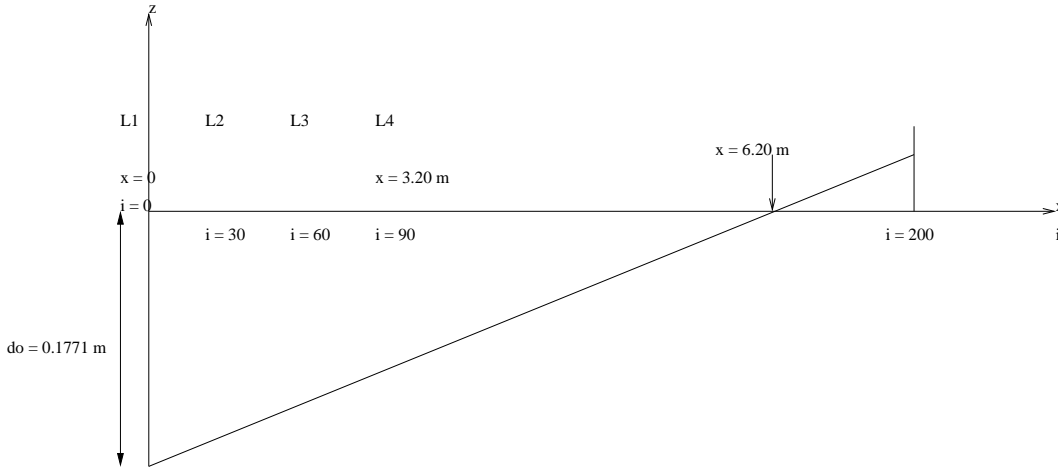


**Figure 7.2.1.** The wave propagation experiment of Cox. Sketch of the topography and the computational domain.

## 7.2. A one dimensional test for breaking wave propagation in the Inner Surf Zone

In this section we will investigate the ability of our model to accurately compute the transformation of regular broken waves in the Inner Surf Zone. We show a comparison, inspired from [15], [17], between numerical results provided by the *SURF-SVWB* model and a set of data based on an experiment performed by Cox [50]. This experiment was carried out in a wave flume of 33 m long, 0.6 m wide and 1.5 m deep. Waves were generated on a horizontal bottom at a depth of 0.40 m, shoaled and broke on a 1 : 35 sloping beach. The wave height at the wave-maker is 0.115 m and the period is  $T = 2.2$  s. Measurements of the surface elevation and velocity were taken at four locations inside the ISZ.

For this numerical simulation, the seaward boundary condition is located in the ISZ and is given by time series of water depth measured at the first location *L1*, using the inlet generating/absorbing boundary condition, since we assume that the flow is subcritical in the ISZ. It is worth mentioning that the wave amplitude provided at the seaward boundary is the *physical* value, issued from the measurements. Hence, the possible reflected waves are already taken into account and the inlet boundary condition only compute the corresponding value of the velocity using the outgoing Riemann invariant, as exposed in Chapter 3.

The computational domain is discretized by 200 nodes using a horizontal step  $\Delta x = 0.04$  m and the simulation was run with a constant time step  $\Delta t = 0.01$  in order to compare the numerical results with the experimental set of data. As emphasized by Peregrine [115], when a uniform train of bores approaches the shore, the solution settles to a quasi steady state shortly after several bores have climbed up the beach. Once this steady state has been reached, it yields relatively small shoreline motions. Hence, the initial condition of steady state at rest leads to a transient period of 200 s

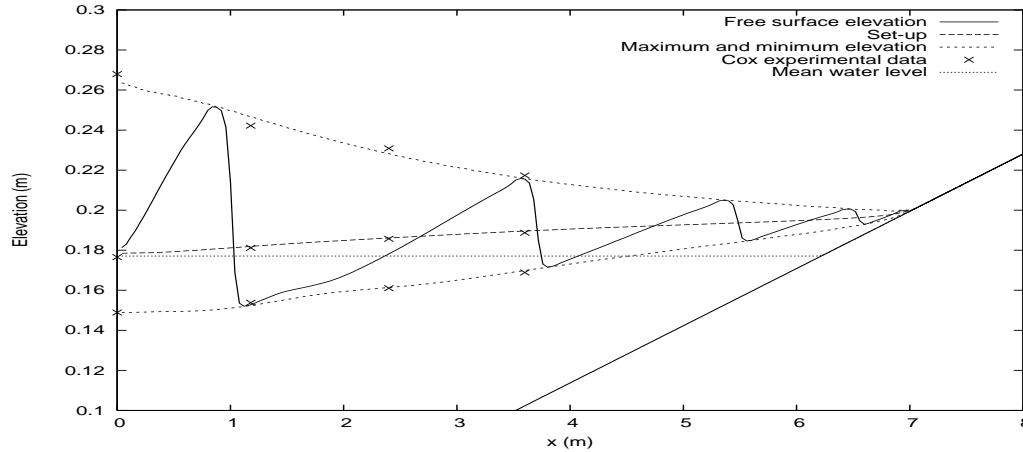


**Figure 7.2.2.** One dimensional propagation of breaking waves. Spatial evolution of the wave train elevation. Comparison between numerical results and the experimental data of Cox for the set-up and the maximum and minimum elevation.

before reaching the steady state, which is not shown in the time series presented in the sequel. Previous numerical studies by Kobayashi et al. [95] and Cox [50] have shown that simulations in the ISZ are not much sensitive to the value of the friction coefficient  $k_t$  when  $0.001 \leq k_t \leq 0.1$  and we choose to use  $k_t = 0.01$  in our simulation.

We can observe on Figure 7.2.3 the comparison between computed and measured time series of the surface elevation at the four locations inside the ISZ. It appears that our model provides accurate results with small discrepancies. The nonlinear wave distortion is computed and the wave height is accurately predicted. A comparison with the numerical results shown in [17] with the MacCormack second order scheme highlights the same small over-prediction for the maximum wave elevation at the location  $x = 1.2\text{ m}$  and quasi-similar slight under-prediction for the maximum wave elevation at  $x = 2.4\text{ m}$  and  $x = 3.6\text{ m}$ . The minimum wave elevations and the periodicity of the waves are accurately computed. As emphasized in [16], previous simulations based on Lax-Wendroff schemes for the NSW equations [95] or on Boussinesq models [123] showed numerical oscillations at the rear of the wave fronts. Our model overcomes this drawback. In addition, the shock velocity is also accurately computed since there is no phase shift between numerical results and measurements.

Moreover, we can observe on Figure 7.2.2 numerical results for the wave elevation profile, the maximum and minimum wave elevation and the set-up. The sharpened wave profile and the dissipation due to the breaking are clearly observable. Experimental measurements are also plotted and as previously stressed the most relevant discrepancies concern the maximum elevation. The set-up is accurately computed.

According to the results presented in [15] and [17], the NSW equations enable a valuable description of wave propagation in the ISZ with a good prediction of broken wave celerity, set-up and an accurate computation of nonlinear wave distortion leading to the sawtooth shape.

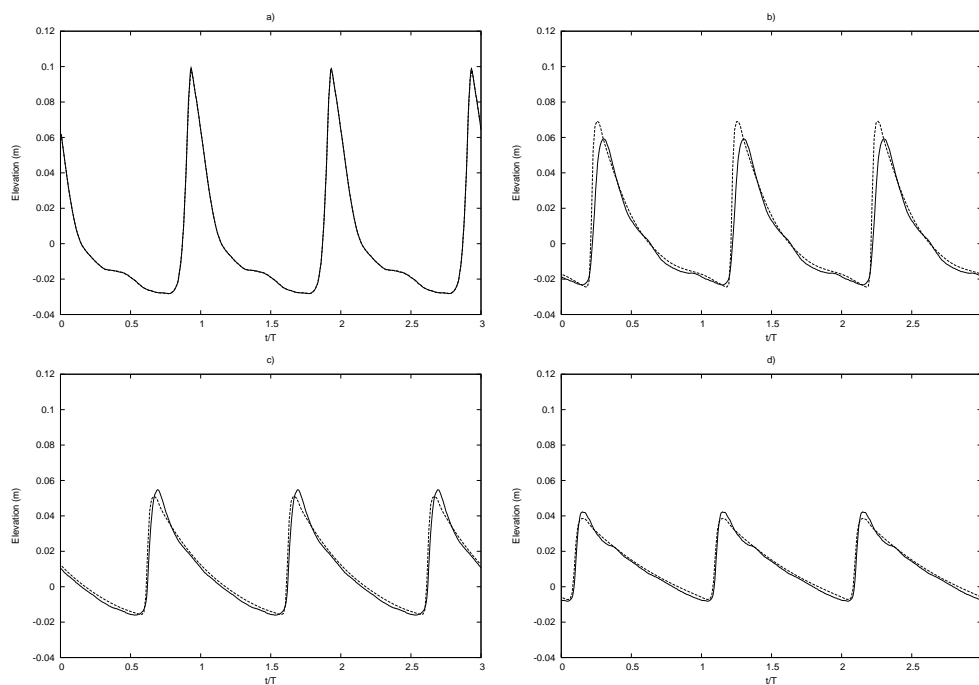


**Figure 7.2.3.** One dimensional propagation of breaking waves. Time series of wave elevation at different locations in the inner surf zone. Comparison between the numerical model (in dashed line) and experiments by Cox (solid line) at a)  $x = 0$  m, b)  $x = 1.2$  m, c)  $x = 2.4$  m, d)  $x = 3.6$  m.

### 7.3. Wave propagation over a periodical ridge and runnel system

On natural beaches, accurate prediction of wave-induced current circulations which control the nearshore sediment transport, and therefore the morphological changes in the nearshore, remains an open issue. Particularly, the modelization of longshore and rip currents behaviour over alongshore non-uniform barred-beaches are important topics.

Cross-shore variability and magnitude of longshore currents have been investigated in several studies [45], [101]. Rip currents are other horizontal flow patterns which can be observed on beaches exhibiting three dimensional topography and exposed to normal or near-normal incident swells. Such currents are actually strong and narrow seaward oriented currents, responsible for significant sediment transport [23], morphological changes in the nearshore [156] and for numerous misadventures or even drowning accidents during the touristic season. In the last decade, field studies have been performed to improve the knowledge of this flow pattern [23], [122].

As exposed in the introduction, the classical approach for modelling ISZ wave-induced circulation is based on time averaged over a wave period equations. For instance,

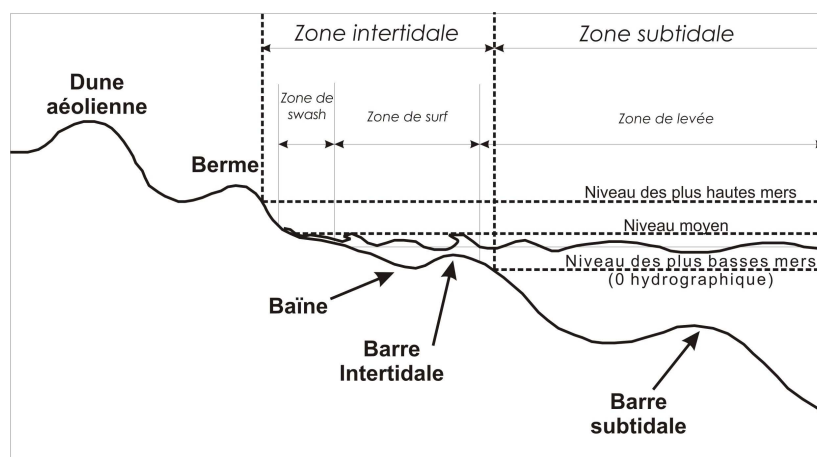


**Figure 7.3.1.** Sketched section view of the typical Aquitanian beach with ridge and runnel system (Castelle [39]).

a study of rip currents on the Aquitanian coast, with extensive comparisons using field measurements, has been recently performed by Castelle et al. in [38] and [39]. They have investigated the simulation of wave induced currents and morphodynamics of nearshore sandy bars on the Aquitanian coast beaches. More precisely, they have highlighted the sensitivity of the horizontal circulation, the generation of rip and longshore currents generated by ridge and runnel systems and crescentic bars and the morphodynamic coupling have shown that self-organization mechanisms are responsible for the formation of ridge and runnel systems in the intertidal domain and crescentic bar systems in the nearshore zone. Comparison with data collected during the PNEC 2001 field measurements have shown that the morphological characteristics of simulated systems are in agreement with observations.

Two-dimensional numerical studies of ISZ mean currents using time-varying BSV models is still an open issue. Very few studies relying on Boussinesq-like models have been introduced recently, as for example Sorensen et al. [159] or Chen et al. [42] who focused on the modelization of rip current. But to our knowledge, the NSW equations have still not been applied to such two-dimensional problems. Such an approach may provide a large amount of information not available with time-averaged models, especially concerning time-varying quantities, like velocity oscillations, instantaneous vorticity fields or motions in the swash zone. These time-varying information may be of great utility in the modelling of sediment transport for instance.

Actually, the Aquitanian coast beaches exhibit longshore non-uniform multiple bars, leading to complex horizontal wave-induced currents which behave differently than those reported in the literature and are poorly understood. The nearshore is characterized by two distinct sand bar patterns: the crescentic bar system in the subtidal zone and the ridge and runnel system in the intertidal zone. In this study, we mainly focus on the ridge and runnel system, in which ridges are regularly interrupted by down-currents oriented runnels, with a mean wave length of about 400 m. Of course,

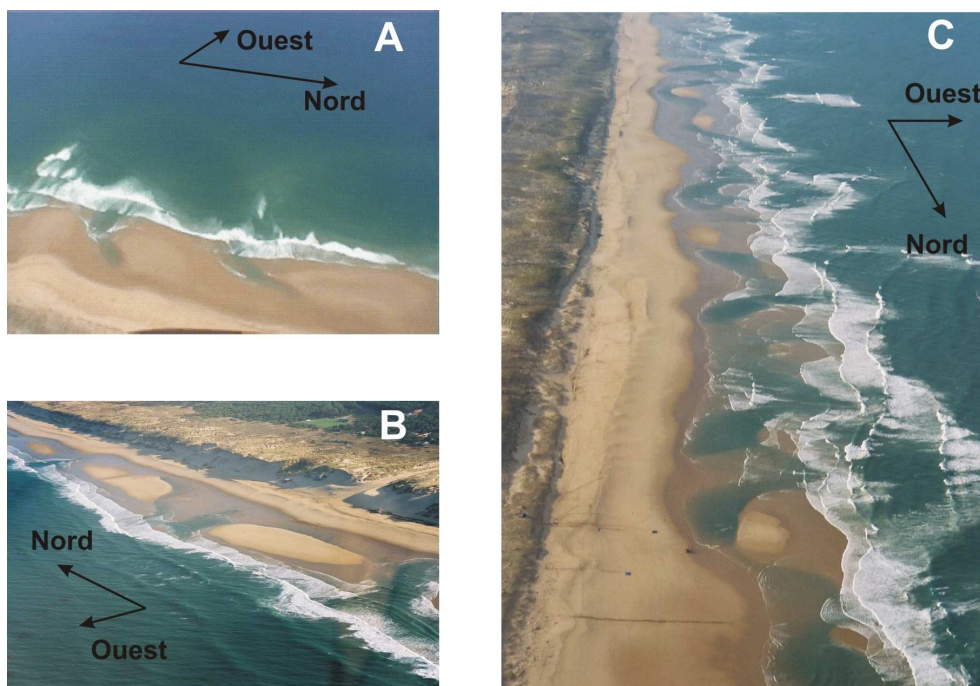


**Figure 7.3.2.** Aerial photograph of ridge and runnel systems in the intertidal domain, Aquitanian coast (Castelle [39]).

this morphological description slowly evolves in time (rip channel migration is about 3 meters per day during summer) and this order of magnitude is a year-averaged value. Figure 7.3.2 shows aerial views of a ridge and runnel system on the Aquitanian coast and Figure 7.3.1 shows a sketched section view of an Aquitanian beach, where the ridge and the runnel are observable.

Rip cell circulations are controlled by topographic feed-back and are supposed to be responsible for strong water and sediment exchanges between the surf zone and the nearshore zone [156]. On the Aquitanian coast, these rip currents occur at each runnel outlet and their intensity depends on the length, the shape of the system, the offshore wave conditions and the tide level [38]. The mechanism leading to the generation of a rip current can be summarized as exposed by Castelle et al. [38]. The main idea is that longshore variations of the topography are associated with similar variations in the pressure, due to mean water level changes and hence, lead to longshore pressure gradients. More precisely, assuming that the incoming wave field is longshore uniform, waves approaching the bar will break before waves approaching the runnel. Since the wave-induced set-up in the surf zone varies more or less in proportion to the local breaker height, the induced set-up in the runnel will then begin further inshore inducing alongshore set-up variations. The longshore pressure gradients associated with this variation inshore the ridge and runnel system induce an intensification of the longshore current in the runnel. On the upper part of the beach, the longshore pressure gradients force the feeder currents. Water convergence inshore the runnel outlet results in the

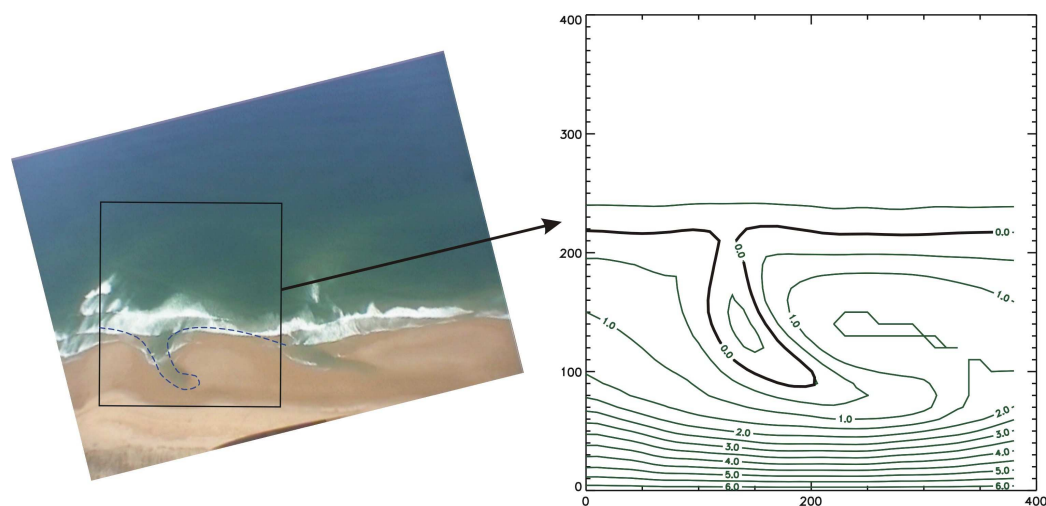


**Figure 7.3.3.** Aerial photograph and corresponding idealized contour plot of the ridge and runnel system used in our simulations (inspired from Castelle [39]).

formation of a seaward oriented current, a rip current, which balances the water mass conservation equation inshore the runnel outlet. Observations show that this seaward flow tends to be narrow and relatively strong but rapidly desintegrates outside the surf zone.

The study proposed here is inspired from the simulations proposed by Castelle [39]. For our analysis, we have neglected first the tidal variations even if the previous studies have shown an intense modulation of physical processes. However we have perform several simulations for various mean water level, in order to highlight the impact of tidal variations on the wave-induced circulation. Our aim is to study the mean wave-induced currents in the ISZ, and especially the rip currents, over an idealized ridge and runnel system, which is characteristic of the Aquitanian coast ridge and runnel systems. Figure 7.3.3 shows the idealized ridge and runnel topography used for our simulations.

It is worth mentioning that at this level of analysis, the study will only be qualitative, since the underlying assumptions of the NSW approximation may be violated in the offshore area. More precisely, we know that NSW equations are unable to predict accurate shoaling and that the lack of dispersive effects leads to an anticipated steepening of the solution, with energy dissipation, too far offshore. However, we have chosen in our study to generate a periodic train of wave offshore of the surf zone, which may propagate towards the shore. When this train of waves reaches the ISZ and the ridge and runnel system, the wave shape has change to the characteristic bore-like shape. Hence, the simulation may be realistic enough in the ISZ. But the computational area corresponding to the shoaling zone may be regarded as an artificial zone which is needed to obtain numerical results which are realistic enough in the ISZ. Therefore, in the following, we only focus on results obtained in an area corresponding to the

ISZ and we neglect the computation in the initiation area. Such qualitative studies in the ISZ have been performed for instance by Brocchini et al. [29] for the study of macro-vortices induced by single breakwaters.

Wave period controls the strength and shape of the rip currents. As emphasized in [38], longer waves lead to stronger and narrower rip currents, whereas for  $T_w > 14 s$  the rip velocity slightly decreases with increasing wave period. Therefore we set the wave period at  $T_w = 12 s$ . The offshore wave amplitude is the main characteristic controlling the rip velocities, as changes in the breaking patterns control the rip current characteristics. Our aim is to obtain a large enough bore-like wave amplitude in the area corresponding to the ISZ, taking into account the energy dissipation which occurs during all the propagation process. For this purpose, we have set  $H_w = 1 m$  offshore. Further investigations seem to be needed to determine optimum offshore amplitude.

For this simulation we use a variable mesh in the cross-shore direction, since the motions scales are different between the seaward boundary and the shoreline. The largest cell size is  $\Delta x = 2 m$  near the offshore boundary, while the finest cell size is  $\Delta x = 0.05 m$  near the shoreline. In the longshore direction, the mesh is regular and the discretization step is  $\Delta y = 1 m$ . It yields a variable Cartesian mesh of 450 cells in the cross-shore direction and a constant mesh of 380 cells in the longshore direction. The time step is constant and fixed at  $\Delta t = 0.05 s$ . The various water depth values used for the several tests are chosen in order to describe the tidal variations between almost mid-tide and high-tide. For all the tests, the ridge and runnel system is completely covered by water. Note that the moving shoreline treatment may theoretically enable us to simulate with accuracy the flooding and drying of the system. Such situations will be studied in further simulations.

**7.3.1. Wave refraction and set-up.** We show on Figure 7.3.5 a contour plot of the free surface profile over the ridge and runnel system, in order to highlight the wave refraction induced on one hand by the longshore variations of topography, and on the other hand by the wave-induced circulation. We can observe that the wave is seriously refracted while propagating over the runnel, induces longshore variations in the mean water level. This refraction can also be observed on Figure 7.3.4 where profiles of the free water surface are plotted at three different locations in the longshore direction. We have also plotted on the same Figure the three corresponding set-up profiles.

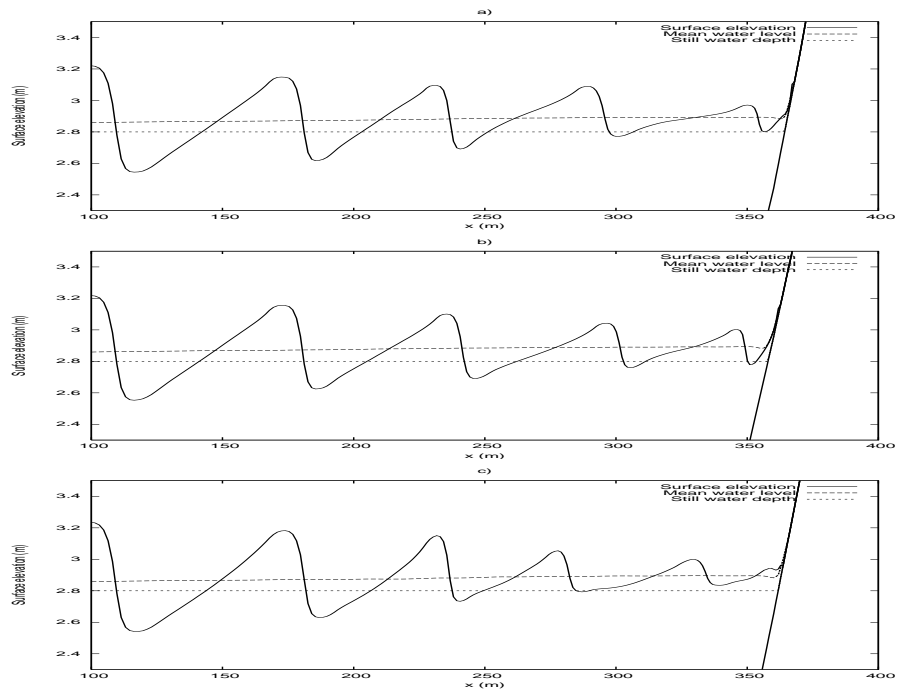


**Figure 7.3.4.** Propagation over a ridge and runnel system. Section views of the free surface elevation and the corresponding computed set-up in the cross-shore direction at three locations : a)  $y = 95.25$  m, b)  $y = 190.5$  m, c)  $y = 285.75$  m.

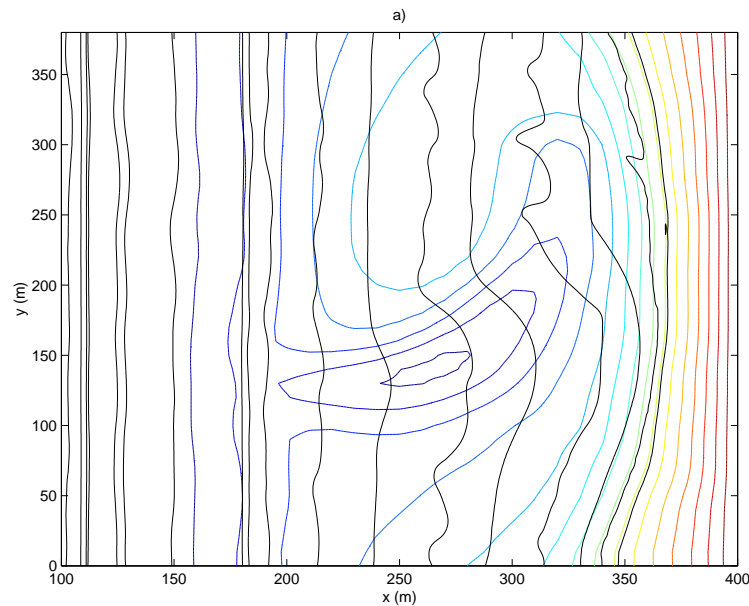


**Figure 7.3.5.** Propagation over a ridge and runnel system. Contour plot of the water surface levels at  $t=800$  s.

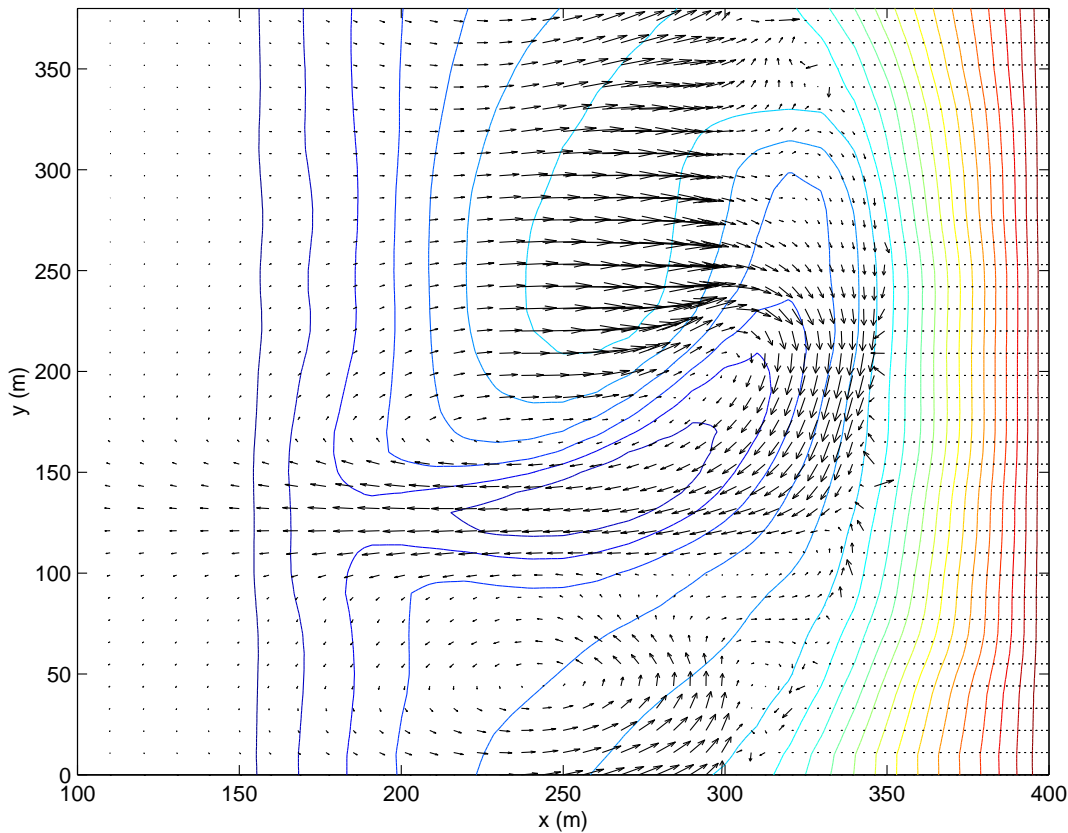


**Figure 7.3.6.** Wave propagation over a ridge and runnel system. Two dimensional view of the computed wave-induced mean currents, for  $h_m = 1.5\text{ m}$  (between low-tide and mid-tide). The maximum mean velocity is about  $0.3\text{ m/s}$ .

**7.3.2. Wave-induced mean currents.** In the sequel  $h_m$  stands for the value of water depth over the zero isobath. Figure 7.3.6, 7.3.7 and 7.3.8 show the two dimensional mean wave-induced current patterns simulated during a normally incident swell, for values of water depth  $h_m = 1.5\text{ m}$ ,  $h_m = 2.0\text{ m}$  and  $h_m = 2.5\text{ m}$ . Note that according to [39] the value  $h_m = 2.0\text{ m}$  corresponds to mid-tide and high-tide occurs around  $h_m = 4.0\text{ m}$ . The steady state is reached after approximately  $800\text{ s}$  and the instantaneous velocity field is averaged over a wave period. A narrow seaward oriented current can be observed at the runnel outlet, associated with a large circulation cell. As suggested by Castelle et al. [38], the maximum of rip velocity occurs at mid tide. The intensity of this maximum rip velocity then decreases with respect to the increasing mean water level. We observe that for  $h_m = 1.5\text{ m}$  the maximum mean velocity occurs on the ridge, due to the thin layer of water (see Figure 7.3.6). The rip velocity is already strong at the runnel outlet with a small space shift when compared to [38]. The circulation cells observed near the lateral boundary seem to be more pronounced. On Figure 7.3.7 we observe the maximum rip velocity at the runnel outlet, according to [38]. Still comparing with [38], the second circulation cell near the lateral boundary is slightly shifted in the cross-shore direction, towards offshore.

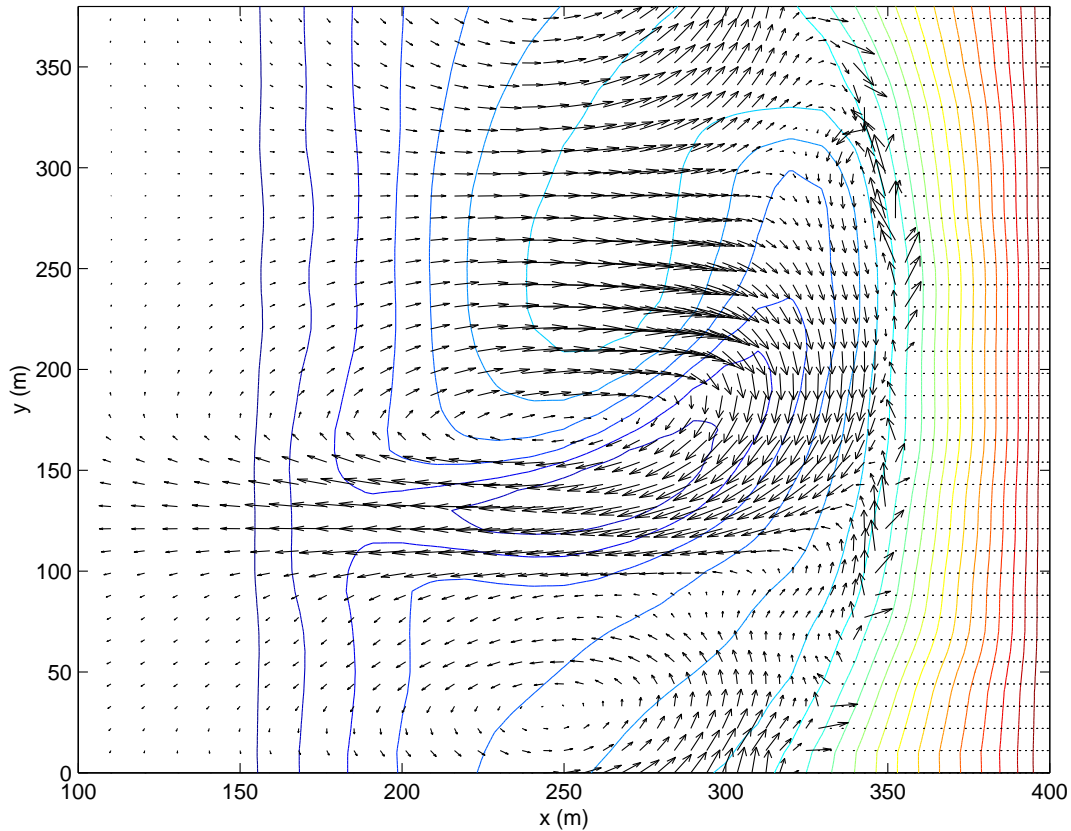


**Figure 7.3.7.** Wave propagation over a ridge and runnel system. Two dimensional view of the computed wave-induced mean currents,  $h_m = 2.0\text{ m}$  (mid-tide). The maximum mean velocity is about  $0.4\text{ m/s}$ .

On Figure 7.3.8 we observe a decreasing velocity field, as the water depth is increasing. The structure of the circulation cells is conserved. We still observe a slight rip velocity at the runnel outlet, while the circulation cell near the lateral boundary seems to be vanishing. All these results are qualitatively similar to those shown in [38] with slight differences. Note that as in all the previous cases, the velocity at the shoreline seems to be over-estimated. Nonetheless, observations show that it does not modify the qualitative behavior of the wave-induced circulation. Note that the maximum value of the velocity indicated for each figure do not take into account the mean velocities near the shoreline.

### 7.3.3. Macro-vorticity generated by longshore topography variations.

In this subsection, we investigate the mechanism of vorticity generation by wave breaking over varying topography. It is worth mentioning that field observations and experimental measurements of breaking wave-generated macro-vortices are rare. The first numerical study relating to vorticity generation by breakwaters has focused on vortex generation on longshore uniform topographies (Buhler and Jacobson [33]). More

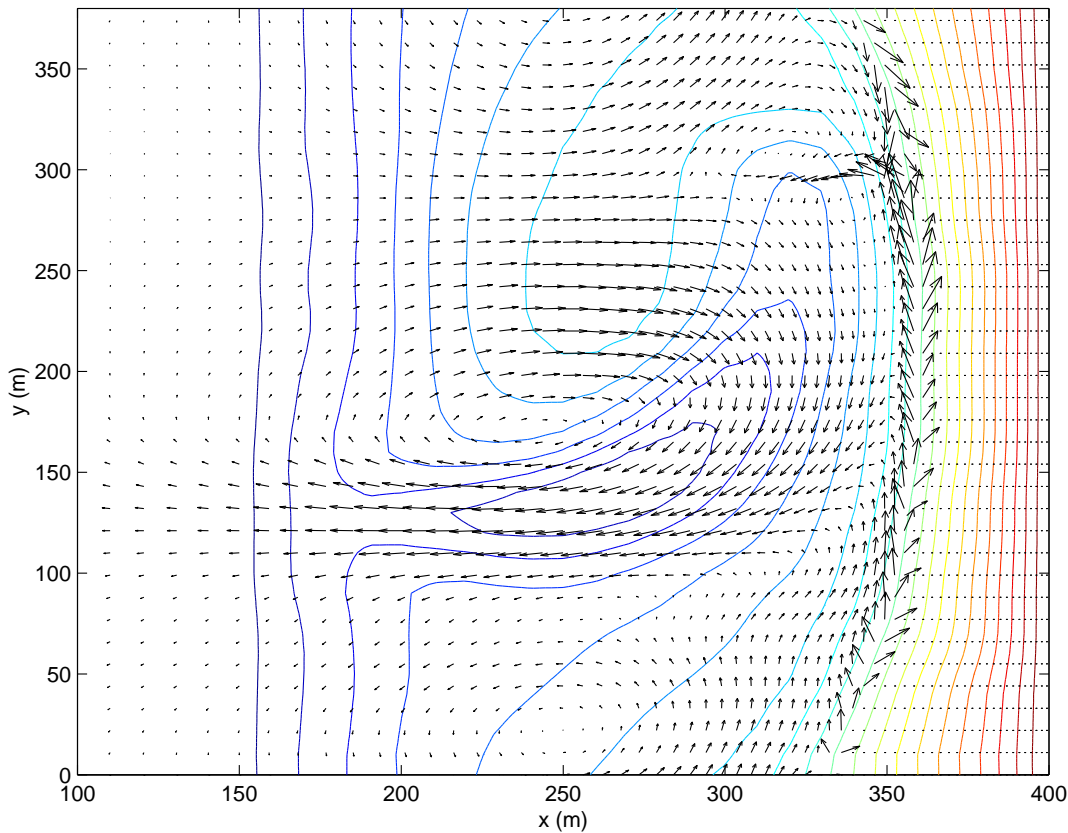


**Figure 7.3.8.** Wave propagation over a ridge and runnel system. Two dimensional view of the computed wave-induced mean currents, for  $h_m = 2.5$  m. (between mid-tide and high-tide). The maximum mean velocity is about 0.2 m/s

recently Peregrine [137] has investigated the use of high resolution ENO and CENO schemes, and numerical studies of topographically-controlled rip-currents based on a Boussinesq model have predicted vortex shedding on bar edges and the vortices were shown to advect towards the offshore region (Chen et al. [42]. Brocchini et al. [29], [30] have performed simulations of wave breaking on single breakwaters using their scheme based on the WAF method. A similar vortex generation has been computed, with vortices advected towards the shore. In [29], the limitations of schemes relying on fractional step methods are highlighting, since spurious vorticity may be generated on top of the bar-like obstacle before the incident waves have reached the submerged structure.

We show on Figure 7.3.9 and Figure 7.3.10 contour plots of the vorticity at two arbitrary times during a period. Even if it is not shown here, we stress out that the periodicity of the motion is recovered in the mechanism of macro-vorticity generation. We observe the formation of large vortices located at the runnel outlet. Some of the vortices are advected toward the shore.

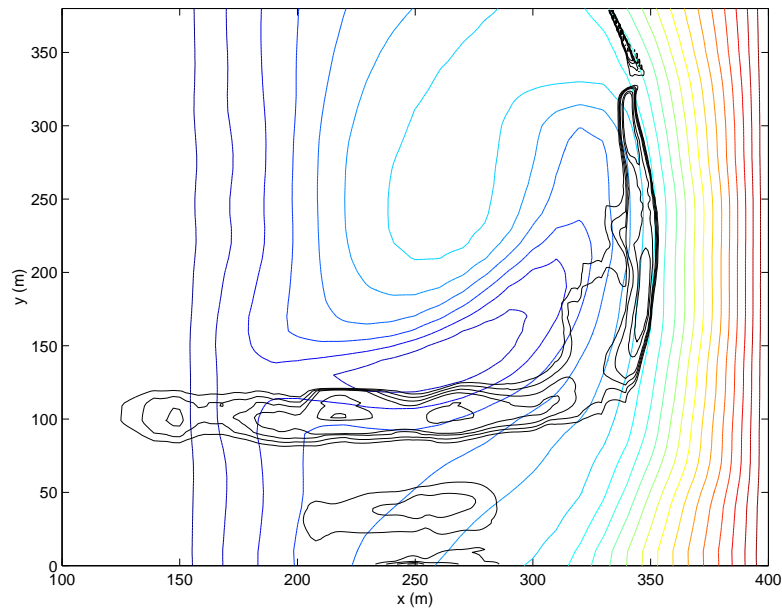


**Figure 7.3.9.** Wave propagation over a ridge and runnel system. Two dimensional contour plot of the vorticity field for  $h_m = 2.0\text{ m}$  (mid-tide) at  $t=800\text{ s}$ .

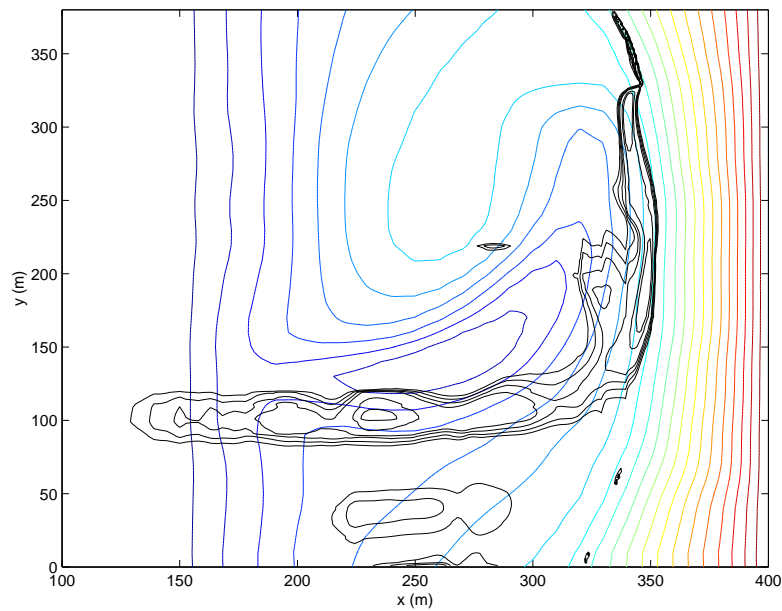


**Figure 7.3.10.** Wave propagation over a ridge and runnel system. Two dimensional contour plot of the vorticity field for  $h_m = 2.0\text{ m}$  (mid-tide) at  $t=804\text{ s}$ .



---

# Conclusion

In this third part we have applied the *SURF-SVWB* model to nearshore hydrodynamics. We have made a distinction between breaking and non-breaking waves and suggested to study in Chapter 6 the run-up of long non-breaking waves over two-dimensional topographies, whereas Chapter 7 is devoted to the study of wave propagation in the Inner Surf Zone.

In Chapter 6, we have performed a short review concerning the propagation of tsunamis in coastal areas and the main feature of such long waves. We have stressed out that most of the tsunamis propagation models available around the world rely on NSW equations. A more complete review of the various run-up models introduced in the literature highlights that all these models rely on fractional step methods. Therefore, the *SURF-SVWB* model seems to be particularly well-suited for such large run-up simulations.

In order to stress out the ability of the model, we have performed in the following a few tests, including complex two-dimensional benchmarks with longshore non-uniform topographies. From qualitative comparisons with other results available in the literature, it appears, as far as it can be judged, that the *SURF-SVWB* provides relevant results, in agreement with the literature. The run-up is accurately computed, even in two-dimensional cases, without any spurious oscillations at the shoreline as it has been reported for several other models. It is worth mentioning that the run-down process is also provided accurately. In the literature, authors often shows the run-up process but rarely the run-down, since it seems to be the most challenging process for the moving shoreline boundary conditions.

The wave refraction due to the variations of topography seems also to be accurately computed. Moreover, the use of the well-balanced method enables to converge towards the steady states at rest after the evacuation from the computational domain of both incident and reflected waves. This feature is not available in other models. To our knowledge, there is no model available in the literature which is able to compute the entire process of tsunami run-up, including the propagation towards the shore,

the run-up, run-down and the evacuation from the computational domain of all the ringing oscillations, as the water level settles back to its initial still level. Hence, the *SURF\_SVWB* clearly improved the state of the art in this class of tsunami propagation models.

In Chapter 7 we have investigated the numerical simulation of breaking waves propagation in the Inner Surf Zone. After a one dimensional validation of the ability of the model to simulate the propagation and distortion of a train of bore in the ISZ, we have focused on the simulation of wave-induced mean currents generated by breaking waves and especially on the generation of a rip current over an idealized ridge and runnel system. This kind of phenomena is usually modeled using depth integrated momentum and energy equations time-averaged over a wave period. The use of time-varying BSV model for such problem is still an open issue and in the literature we only find very few studies relying on Boussinesq-like models. Thus the simulation of this phenomenon using the NSW equations appears as a novelty. The *SURF\_SVWB* model gives a good representation of the waves refraction over the ridge and runnel system, leading to longshore variations in the set-up and hence to a narrow seaward oriented rip current. The *SURF\_SVWB* model has then been used to compute time-averaged values of the velocity and these results have been qualitatively compared with previous studies relying on a time-averaged model and only slight discrepancies are observable, leading to very satisfactory results. A brief study of the generation of macro-vortices has also been performed. This subject is also an open issue and needs further investigations. The improvements which are brought-up by the well-balanced method are significant, since fractional step methods are unable to compute such small wave's features oscillations.

---

# Conclusion et perspectives

## Conclusion

Au cours de cette thèse nous nous sommes attaché à développer des outils du point de vue de la modélisation tant théorique que numérique, nous permettant d'appréhender quelques problèmes d'hydrodynamique littorale. En particulier, des éléments de réponses ont été mis en évidences dans le domaine numérique.

La première partie de cette thèse est consacrée à l'étude théorique d'un modèle de Saint-Venant bi-dimensionnel particulier. Nous avons conduit la modélisation à partir des équations de Navier-Stokes tridimensionnelles à surface libre, en effectuant une analyse asymptotique reposant sur une séparation des échelles spatiales. Nous avons obtenu un modèle visqueux bi-dimensionnel, intégrant des termes de friction laminaire et quadratique, un terme de diffusion particulier, un terme classique de Coriolis et un terme tenant compte des tensions de surface. Un terme de forçage par effet du vent en surface peut également être introduit. Les nouveautés introduites dans ce travail concernent d'une part l'extension bi-dimensionnelle d'une méthode initialement proposée dans le cas unidimensionnel et d'autre part une justification asymptotique de tous les termes sources intégrés au modèle, et plus particulièrement du terme de viscosité. Nous observons, comme dans le cas unidimensionnel, l'influence du coefficient de viscosité dans l'expression des coefficients de friction. A notre connaissance, l'unique travail concernant la dérivation d'un modèle de Saint-Venant bi-dimensionnel par analyse asymptotique a été introduit très récemment dans [149]. Ce travail n'inclut pas la dérivation des termes de viscosité.

Nous nous sommes ensuite intéressé à la démonstration de résultats d'existence de solutions faibles globale pour le modèle précédemment dérivé. Un résultat a été obtenu dans le cas uni-dimensionnel pour le modèle complet. Dans le cas bi-dimensionnel,

nous avons étudié une version simplifiée du modèle, en négligeant une partie du terme de viscosité. Nous avons également fait une hypothèse forte sur la positivité de la hauteur d'eau. Ceci nous a permis d'obtenir un résultat d'existence pour ce modèle bi-dimensionnel simplifié.

Dans la deuxième partie, nous avons décrit l'implémentation d'une méthode de résolution numérique pour ce modèle bi-dimensionnel. Nous avons obtenu un schéma équilibre Volume Finis quasi d'ordre deux permettant la capture des discontinuités isolées. La qualité du traitement de la ligne d'eau a été particulièrement soignée et la question des conditions aux limites à la fois génératrices et absorbantes au large a été abordée. Nous avons ensuite présenté une série de validations numériques de ce modèle en utilisant des solutions analytiques impliquant des phénomènes de run-up, run-down et des mouvement complexes de la ligne d'eau, à la fois dans les cas uni- et bi-dimensionnels. Si de nombreux modèles permettant de simuler efficacement les phénomènes de run-up ont été introduits dans la littérature dans le cas uni-dimensionnel, ils reposent bien souvent sur des algorithmes de suivi d'interface complexes pour gérer la ligne d'eau. En conséquence, leur généralisation à l'ordre deux est souvent délicate et les modèles proposant l'étude de phénomènes de run-up en dimension deux sont plus rares. La comparaison entre les résultats obtenus avec notre modèle et ceux proposés dans la littérature indique une amélioration significative de la précision, surtout dans les cas bi-dimensionnels. De plus, à notre connaissance, aucun schéma équilibre n'avait été appliqué à l'étude de ce type de phénomène et ce travail apporte donc une réponse efficace aux problèmes numériques souvent rencontrés dans l'étude des phénomènes de run-up d'ondes longues sur des topographies irrégulières. En particulier, la convergence vers l'état stationnaire au repos ou encore le calcul précis de faibles oscillations autour de tels équilibres est désormais possible. Une limitation, observable également sur la quasi totalité des méthodes proposées dans la littérature, reste la modélisation de la vitesse intégrée selon la verticale, souvent surestimée à la ligne d'eau.

La troisième partie est enfin l'occasion de valider notre modèle numérique sur des cas plus complexes. Nous nous sommes intéressé d'une part à l'étude du phénomène de run-up d'ondes longues non déferlantes de type tsunami sur des topographies bi-dimensionnelles irrégulières. Nos résultats ont été qualitativement comparés avec ceux introduit dans la littérature et semblent prometteurs. La stabilité et la précision du schéma nous permettent d'obtenir des résultats très satisfaisants, pour des coûts de calcul modérés. De plus la convergence vers les états d'équilibre au repos après le passage de l'onde est une nouveauté dans ce type de problème.

Dans un second temps, nous nous sommes intéressé à l'étude de la propagation d'ondes déferlantes dans la zone de surf. L'utilisation du schéma équilibre semble particulièrement adaptée à la prise en compte des topographies complexes et permet de calculer la réfraction des vagues se propageant au dessus d'un système de barre/baine, induisant une focalisation d'énergie, des variations de set-up/set down le long de la côte et la génération d'un courant sagittal. Nos résultats sont qualitativement comparés

à ceux obtenus avec un code à modélisation statistique [39] et sont en bon accord. L'utilisation d'un code de type Saint-Venant nous permet d'avoir accès aux variables caractéristiques instantanées de l'écoulement, comme par exemple les oscillations de la vitesse ou le champ de vorticité. Cela permet aussi éventuellement d'obtenir des valeurs des courants moyens induits par les vagues comme dans le cas d'une approche statistique. Ce dernier travail constitue une nouveauté puisqu'à notre connaissance, aucune étude bi-dimensionnelles concernant la génération de courants moyens induits par les vagues dans la zone de surf n'a été réalisée à partir d'un modèle de Saint-Venant. Ce type d'étude nécessite en effet un schéma d'ordre élevé et une modélisation très précise des effets induits par la topographie, les fluctuations du set-up conduisant à la génération de tels courants étant de très faible amplitude.

## Perspectives

Les perspectives et pistes de recherches ouvertes sont nombreuses.

Sur le plan de la modélisation, un projet ambitieux consiste à intégrer à notre modèle des termes dispersifs "à la Boussinesq" afin d'étendre son domaine de validité à la zone de levée. En effet, de nombreux travaux sont consacrés depuis une bonne dizaine d'années à l'extension des modèles de type Boussinesq à la zone de surf interne et zone de swash, au prix de paramétrisations souvent complexes permettant de bien modéliser le déferlement et les mouvements de la ligne d'eau [47], [48]. Une autre approche consiste donc à étendre la validité du modèle de Saint-Venant à la zone de levée par l'adjonction d'effets dispersifs permettant de prévenir le "raidissement" anticipé des fronts d'onde. Ceci conduirait à un modèle ayant un vaste champ d'application.

Concernant le résultat d'existence pour le modèle bi-dimensionnel, il semble possible de lever assez facilement l'hypothèse faite sur la positivité au sens strict de la hauteur d'eau, par des arguments de compacité adéquats, au prix d'une perte de régularité sur la vitesse. Ce sujet est actuellement à l'étude. La prise en compte du terme complet de diffusion dans le cas bi-dimensionnel reste une difficulté et d'autres études semblent nécessaires.

Dans le domaine numérique, nous avons très récemment implémenté une extension simple de type ENO (Essentially Non Oscillatory) proposée dans [20], afin d'obtenir un schéma réellement d'ordre deux. La quantification du gain en précision reste à effectuer. Cette extension peut se révéler utile pour les futures études concernant le champ de vorticité instantané ou encore la génération des courants moyens.

Les schémas de type équilibre sont toujours un sujet d'étude pour de nombreuses équipes de recherche et l'intégration d'une méthode permettant la préservation et la convergence vers la totalité des états d'équilibre subsoniques est envisagée. Une amélioration de la modélisation des vitesses est également nécessaire.

Dans un autre domaine, la mise en place d'un algorithme de maillage adaptatif permettant de raffiner automatiquement le maillage cartésien dans certaines zones de fortes

variations topographiques ou en hauteur d'eau apporterait un gain certain en temps de calcul et en précision, nous permettant de déployer des grilles très fines dans les zones d'intérêts. Des collaborations sont actuellement envisagées pour parvenir à ce résultat.

Enfin, dans le domaine de la zone de surf, de nombreux champs d'investigation sont considérés. Tout d'abord l'étude de la macro-vorticité générée par le déferlement au dessus de topographies présentant des variations dans la direction longshore est un sujet complexe et encore ouvert. Nos premiers résultats sont encourageants et de futures études sont déjà initiées. La modélisation des courants moyens induits par la houle dans la zone de surf, typiquement les courants de dérive et courants sagittaux, a à peine été amorcée dans ce travail. La comparaison avec des données in-situ, la simulation de cas plus réalistes et pour d'autres géométries ainsi que la mise en valeur des apports dus au schéma équilibre sont à venir. Enfin l'extension numérique de notre modèle à la zone de levée par l'adjonction de termes dispersifs reste notre objectif le plus ambitieux. Un tel modèle intégrant des termes dispersifs permettrait en effet de décrire la quasi totalité de la zone littorale depuis la levée des vagues jusqu'au déferlement et phénomène de run-up sur la plage. Bien sûr, la zone de transition reste toujours difficilement modélisable par des approches de type BSV.

---

# Publications

At this day, two papers corresponding to Chapter 1 and Chapter 3 have been submitted :

- Marche F. **Derivation of a new two-dimensional viscous shallow water model with varying topography, bottom friction and capillary effects**, submitted to *European Journal of Mechanic /B: Fluid* [Recently recommended for publication with minor modifications]
- Marche F, bonneton P, Fabrie P, Seguin N. **Evaluation of well-balanced bore-capturing schemes for 2D wetting and drying processes**, submitted to *International Journal for Numerical Methods in Fluids*

Two other papers are still in progress...



---

# Bibliography

- [1] Agoshkov VI, Ambrosi D, Pennati V, Quarteroni A, Saleri F. Mathematical and numerical modelling of shallow water flow. *Comput. Mech.* 1993; **11**:280–299.
- [2] Alcrudo, F, García-Navarro P. A high resolution Godunov-type scheme in finite volume for the 2D shallow water equations. *Int. J. Numer. Meth. Fluids* 1993; **16**:489–505.
- [3] Audusse E, Bouchut F, Bristeau MO, Klein R, Perthame B. A fast and stable well-balanced scheme with hydrostatic reconstruction for shallow water flows. *SIAM J.Sci.Comp.* 2004; **25**(6):2050–2065.
- [4] Audusse E, Bristeau MO. A well-balanced positivity preserving “second order” scheme for shallow water flows on unstructured meshes. *J.Comp.Phys.* 2005; **206**:311–333.
- [5] Audusse E. A multilayer Saint-Venant model. to appear in *Discrete and Continuous Dynamical Systems-B*; 2004.
- [6] Backhaus JO. A semi-implicit scheme for the shallow water equations for application to shelf sea modelling. *Continental Shelf Res.*1983; **2**:243–254.
- [7] Battjes JA. Surf-zone dynamics. *Ann. Rev. Fluid Mech.*1988; **20**:257–293.
- [8] Battjes JA. Surf similarity. *Proc. Conf. Coastal Eng., 14th* 1974:466–479.
- [9] Benque JP, Cunge JA, Feuillet A, Hauguel A, Holly FM. New method for tidal current computations *J. Waterw. Port Coast. Ocean Division Proc ASCE.* 1982; **108**:396–417.
- [10] Bermudez A, Dervieux A, Desideri JA, Vasquez ME. Upwind schemes for two-dimensional shallow water equations with variable depth using unstructured meshes. *Comp. Meth. Appl. Mech. Engrg.* 1998; **155**:49–72.
- [11] Bermudez A, Vazquez-Cendon ME. Upwind methods for hyperbolic conservation laws with source terms. *Computers and Fluids* 1994; **23**:1049–1071.
- [12] Bermudez A, Rodriguez C, Vilar MA. Solving shallow water equations by a mixed implicit finite element method. *IMA J. Numer. Anal.* 1991; **11**:79–97.
- [13] Bernardi C, Pironneau O. On the shallow water equations at low Reynolds number. *Comm. Partial Diff. Eqs.* 1991; **16**:59–104.
- [14] Blumberg AF, Mellor GL. A coastal ocean numerical model. *Mathematical Modelling of Estuarine Physics, Proc. Int. Symp.* Springer Verlag, 1980; 102–132.
- [15] Bonneton P. A shock wave model for wave transformation and energy dissipation in the inner surf zone. preprint.
- [16] Bonneton P, Marieu V, Dupuis H, Sénéchal N, Castelle B. Wave transformation and energy disipation in the surf zone: comparison between a nonlinear model and field data. Submitted to *J. of Coastal Res.*, 2004.

- [17] Bonneton P. Dynamique non linéaire des vagues en zone de surf interne. *Génie côtiers* 2003; **7**:1061–1076.
- [18] Bonneton P. Analyse physique et modélisation des processus hydrodynamiques en zone de surf. *Oceanis* 2004, in press.
- [19] Bosseur F, Orenga P. Détermination de conditions aux limites en mer puerve par une méthode de contrôle optimal. *Studies in Mathematics. and Applications* 2002; **31**:104–132.
- [20] Bouchut F. *Non-linear stability of finite volume methods for hyperbolic conservation laws and well-balanced schemes for sources*, Frontiers in Mathematics, Birkhauser, 2004.
- [21] Boussinesq J. Théorie des ondes et de remous qui se propagent le long d'un canal rectangulaire horizontal en communiquant au liquide contenu dans ce canal des vitesses sensiblement pareilles de la surface au fond. *Journ. de Mathématiques pures et Appliquées - Deuxième série* 1872; **17**:55–108.
- [22] Boyer F, Fabrie P. *Elements d'analyse pour l'étude de quelques modèles d'écoulements de fluides visqueux incompressibles*, Cours de DEA, Université Bordeaux 1.
- [23] Brander R. Field observations on the morphodynamic evolution of low-energy rip current system. *Marine Geology* 1999; **157**:199–217.
- [24] Bresch D, Desjardins B, Lin CK. On some compressible fluid models : Korteweg, lubrication and shallow water systems, *Communications in partial differential equations* 2003; **28**(3,4):843-868.
- [25] Briggs MJ, Synolakis CE, Harkins GS. Tsunami runup on a conical island. *International symposium : waves - physical and numerical modelling*, University of British Columbia, Vancouver, Canada, 1994.
- [26] Brocchini M, Svendsen IA, Prasad RS, Belloti G. A comparison of two different types of shoreline boundary conditions. *Comput. Methods Appl. Mech. Engrg* 2002; **191**:4475–4496.
- [27] Brocchini M, Bernetti R, Mancinelli A, Albertini G. An efficient solver for nearshore flows based on the WAF method. *Coastal Engineering* 2001; **43**:105–129.
- [28] Brocchini M, Peregrine DH. Integral flow properties of the swash zone and averaging. *J. Fluid. Mech.* 1996; **317**:241–273.
- [29] Brocchini M, Mancinelli A, Soldini L, Bernetti R. Structure-generated macrovortices and their evolution in very shallow depths. *Proc. Coastal Eng.* 2002:772–783.
- [30] Brocchini M, Drago M, Lovenitti L. The modelling of short waves in shallow waters. Comparison of numerical models based on Boussinesq and Serre equations. *Proc. Coastal Eng.* 1992:76–88.
- [31] Buffard T, Gallouet T, Herard JM. A sequel to a rough Godunov scheme: application to real gases. *Computers and Fluids* 2000; **29**:813–847.
- [32] Buffard T, Gallouet T, Herard JM. A naive Godunov scheme to solve shallow water equations. *C R Acad Sci Paris* 1998; **326**:385–390.
- [33] Bühler O, Jacobson TE. Wave-driven currents and vortex dynamics on barred beaches. *J. Fluid. Mech.* 2001; **449**:313–339.
- [34] Bui AT. Existence and uniqueness of a classical solution of an initial boundary value problem of the theory of shallow waters. *SIAM J. Math. Anal.* 1981; **12**:229–241.
- [35] Carrier GF, Greenspan HP. Water waves of finite amplitude on a sloping beach. *J. Fluid Mech.* 1958; **4**:97–109.
- [36] Carrier GF. The dynamics of tsunamis. *Proc. 6th summer seminar on applied mathematics, Rensselaer Polytechnic Institute, Americal Mathematical Society* 1971;
- [37] Chatelon FJ, Orenga P. On a non-homogeneous shallow water problem. *Math. Model. Num. Anal.* 1997; **31**(1):27–55.
- [38] Castelle B, Bonneton P, Sénéchal N, Dupuis H, Butel R, Michel D. Dynamics of wave-induced currents over an alongshore non-uniform multiple-barred sandy beach on the Aquitanian coast, France. *Continental shelf research* under correction;

- [39] Castelle B. Modélisation de l'hydrodynamique sédimentaire au-dessus des barres sableuses soumises à l'action de la houle : application à la côte aquitaine. *Thèse de Doctorat, Université Bordeaux 1* 2204.
- [40] Casulli V. Semi-implicit finite difference methods for the two-dimensional shallow water equations. *J. Comput. Phys.* 1990; **4**:56–47.
- [41] Casulli V, Cheng RT. Semi-implicit finite difference methods for the three-dimensional shallow water flow. *Int. J. Numer. Meth. Fluids* 1992; **15**:629–648.
- [42] Chen Q, Kirby JT, Dalrymple RA, Kennedy AB, Haller MC. Boussinesq modelling of a rip current system. *J. Geophys. Res.* 1999; **104**(9):20617–20637.
- [43] Chinnayya A, Leroux AY.. A new general Riemann solver for the shallow water equations with friction and topography. Preprint.
- [44] Chippada S, Dawson CN, Martinez ML, Wheler MF. A Godunov-type finite volume method for the system of shallow water equations. *Comp. Meth. Applied. Mech. Eng* 1998; **157**(9):105–129.
- [45] Church J, Thornton E. Effects of breaking wave induced turbulence within a longshore current model. *Coastal Engineering* 1993; **20**(9):1–28.
- [46] Cienfuegos R, Barthélemy E, Bonneton P. A new breaking wave parametrization for Boussinesq type equations. *Proc. WAVES* 2005.
- [47] Cienfuegos R, Barthélemy E, Bonneton P. A fourth order compact finite volume scheme for fully nonlinear and weakly dispersive Boussinesq-type equations. Part I : Model development and analysis. Accepted in *Int. J. Num. Meth. Fluids.*; 2005.
- [48] Cienfuegos R, Barthélemy E, Bonneton P. A fourth order compact finite volume scheme for fully nonlinear and weakly dispersive Boussinesq-type equations. Part II : Boundary conditions and model validation. Preprint.
- [49] Courant R, Friedrichs K, Lewy H. Uber die partiellen Differenzengleichungen der mathematischen Physik. *Mathematische Annalen* 1928; **100**:32–74.
- [50] Cox DT. Experimental and numerical modelling of surf zone hydrodynamics. *PhD dissertation, Univ. of Delaware, Newark*, 1995.
- [51] Bresch D, Desjardins B. Existence of weak solutions for 2D viscous shallow water equations and convergence to the quasi-geostrophic model. *Commun. Math. Phys.* 2003; **238**(1,2):211–223.
- [52] Dal Maso G, Le Floch PG, Murat F. Definition and weak stability of nonconservative products. *J. Math. Pures Appl.* 1995; **74**:483–548.
- [53] Dingemans MA. *Water wave propagation over uneven bottoms-Part 1, 2*, World Scientific; 1997.
- [54] Erduran KS, Kutija V. Applications of finite volume methods with Osher scheme and split technique on different types of flow in channel. *Proc. Int. Conf. on Godunov Methods: Theory and Applications* 1999; Oxford UK.
- [55] Erduran KS, Kutija V, Hewett JM. Performance of finite volume solutions to the shallow water equations with shock-capturing schemes. *Int. J. Numer. Meth. Fluids* 2002; **40**:1237–1273.
- [56] Eymard R, Gallouet T, Herbin R. Finite volume methods. In *Handbook of numerical analysis, vol VII*, Ciarlet PG, Lions JL, editors. North Holland: Amsterdam, 2000; 729–1020.
- [57] Gallouet T, Herard JM, Seguin N. Some approximate Godunov schemes to compute shallow-water equations with topography. *Computers and Fluids* 2003; **32**:479–513.
- [58] Gallouet T, Herard JM, Seguin N. On the use of some symmetrizing variables to deal with vacuum. *Calcolo* 2003; **40**:163–194.
- [59] Gallouet T, Herard JM, Seguin N. Some recent finite volume schemes to compute Euler equations using real gas EOS. *Int. J. Numer. Methods Fluids* 2002; **39**:1073–1138.
- [60] Galvin CJ. Breaker type classification on three laboratory beaches. *J. Geophys. res.* 1968; **73**:3651–3659.
- [61] Garcia R, Kahawita RA. Numerical solutions of the St.Venant equations with the MacCormack finite-difference scheme. *Int. J. Numer. Methods Fluids* 1986; **6**:259–274.

- [62] Gerbeau JF, Perthame B. Derivation of viscous Saint-Venant system for laminar shallow water; Numerical validation. *Discrete and continuous dynamical systems-series B* 2001; **1**:89–102.
- [63] Gica E, Teng MH. Numerical modeling of earthquake-generated distant tsunamis in the pacific basin. *Proc. 16th ASCE Eng. Mech. Conf* 2003, Univ. Washington, Seattle.
- [64] Glaister P. Approximate Riemann solutions of the shallow water equations. *J. Hydr. Res.* 1988; **26**:293–305.
- [65] Glaister P. Prediction of supercritical flow in open channels. *Comput. and Math. Appl.* 1992; **24**(7):69–86.
- [66] Godlewski E, Raviart PA. Numerical approximations of hyperbolic systems of conservation laws. *Applied Mathematical Sciences 118* 1996, Springer Verlag, New York.
- [67] Godunov SK. A difference method for numerical calculation of discontinuous equations of hydrodynamics. *Mat Sb* 1959; 271–300.[in Russian]
- [68] Gosse L. A well balanced flux-vector splitting scheme designed for the hyperbolic systems of conservation laws with source terms. *Comput. Math Appl.* 2000; **39**(1):135–159.
- [69] Goto C. Nonlinear equations of long waves in the Lagrangian description. *Coastal Engineering in Japan* 1979; **22**(1):1–9.
- [70] Goto C, Shuto N Run-up of tsunamis by linear and nonlinear theories. *Proc 17th Coast. Eng. Conf. ASCE Sydney Australia* 1980;
- [71] Govender K, Mocke GP, Alport MJ. Video imaged surf zone wave and roller structures and flow fields. *J. Geophys. Res.* 2002; **107**:3072–3093.
- [72] Greenberg JM, Leroux AY. A well balanced scheme for the numerical processing of source terms in hyperbolic equations. *SIAM J.Numer.Anal.* 1996; **33**(1):1–16.
- [73] Greenberg JM, Leroux AY, Baraille R, Noussair A. Analysis and approximation of conservation laws with source terms. *SIAM J. Numer. Anal.* 1997; **34**(5):1980–2007.
- [74] Grenier E. On the derivation of homogeneous hydrostatic equations, *ESIAM : Math. Model. Numer. Anal.* 1999; **33**(5):965–970.
- [75] Gustafsson B, Sundstrom A. Incompletely parabolic problems in fluid dynamics. *SIAM J. Appl. Math.* 1978; **35**(5):343–357.
- [76] Hanouzet B. Applications bilinéaires compatibles avec un système a coefficients variables, continuité dans les espaces de Besov. *Comm. partial diff. equations.* 1985; **10**(4):433–465.
- [77] Harten A, Lax PD, van Leer B. On upstream differencing and Godunov-type schemes for hyperbolic conservation laws. *SIAM Rev.* 1983; **25**:35–61.
- [78] Heitner KL. A mathematical model for calculation of the run-up of tsunamis. *Phd. thesis. California Institute of Technology, Pasadena, California* 1969;
- [79] Hervouet JM. Hydrodynamique des écoulements à surface libre, modélisation numérique avec la méthode des éléments finis. *Presses des Ponts et Chaussées* 2003;
- [80] Hibberd S, Peregrine DH. Surf and run-up on a beach: a uniform bore. *J. Fluid. Mech.*, 1979; **95**(2):323–345.
- [81] Hirsch C. Numerical computation of internal and external flows, vol. 2. Wiley, England, U.K. 1990;
- [82] Hu K, Mingham CG, Causon DM. Numerical simulation of wave overtopping of coastal structures using the non-linear shallow water equations. *Coastal Engineering*, 2000; **41**:433–465.
- [83] Hu K, Mingham CG, Causon DM. A bore-capturing finite volume method for open-channel flows. *Int.J.Numer.Meth.Fluids*, 1998; **28**:1241–1261.
- [84] Hubbard ME, Dodd N. A 2D numerical model of wave run-up and overtopping. *Coastal Engineering* 2002; **47**:1–26.
- [85] Imamura F, Shuto N, Goto C. Numerical simulation of the transoceanic propagation of tsunamis. *Proc. 6th of the Congress of Asian and Pacific Regional Division, IAHR, Japan* 1988:265–272.

- [86] Janssen PSM. Laboratory observations of the kinematics in the aerated region of breaking waves. *Coast. Eng.* 1986; **9**(5):453–477.
- [87] Johns B. Numerical integration of the shallow water equations over a sloping shelf. *Int. J. Numer. Meth. Fluids.* 1982; **2**(5):253–261.
- [88] Jin S. A steady state capturing method for hyperbolic systems with geometrical source terms. *M2AN* 2001; **35**:631–645.
- [89] Kanayama H, Ushijima T. On the viscous shallow water equations II. A linearized system. *Bull. Univ. Electro-Comm* 1988; **1**:347–355.
- [90] Katsaounis T, Makridakis C. Relaxation models and finite element schemes for the shallow water equations. *Hyperbolic problems: Theory, Numerics, Applications.* 2003;621–631.
- [91] Kaviani O. Introduction à la théorie des points critiques. *Springer Verlag* 2003.
- [92] Keller JB, Keller HB. Water Wave Run-up on a Beach. *Research report for the Office of Naval Research, Department of the Navy. Service Bureau Corporation.* 1965, New York, N.Y.
- [93] Kennedy AB, Chen Q, Kirby JT, Dalrymple RA. Boussinesq modeling of wave transformation, breaking and run-up. *J. Waterw. Port Coast. Ocean Eng.* 2000; **126**(1):39–47.
- [94] Kloeden P. Global existence of classical solutions in the dissipative shallow water equations. *SIAM J. Math. Anal.* 1985; **16**(1):301–315.
- [95] Kobayashi N, Otta AK, Roy I. Wave reflection and run-up on rough slopes. *J. Waterw. Port Coast. Ocean Eng.* 1987; **113**(3):282–298.
- [96] Kobayashi N, Desilva GS, Watson KD. Wave transformation and swash oscillation on gentle and steep slopes. *J. Geophys. Res.* 1989; **94**:951–966.
- [97] Kobayashi N, Watson KD. Wave reflection and run-up on smooth slopes. *Proc. Coast. Hydrodynamics, ASCE* 1987:548–563.
- [98] Kobayashi N, Cox DT, Wurjanto A. Irregular wave reflection and run-up on rough impermeable slopes. *J. Waterw. Port Coast. Ocean Eng.* 1990; **116**(3):708–728.
- [99] Kobayashi N, Karjadi EA. Obliquely incident irregular waves in surf and swash zones. *J. Geophys. Res.* 1996; **101**(C3):6527–6542.
- [100] Kurganov A, Levy D. Central-upwind schemes for the Saint-Venant system. *M2AN* 2002; **36**:397–425.
- [101] Kuriyama Y, Nakatsukasa T. A one dimensional model for undertow and longshore current on a barred beach. *Coastal Engineering* 2000; **40**:39–59.
- [102] Lamb H. Hydrodynamics. *Cambridge Univ. Press. 6th ed.* 1932;
- [103] LeCoz O. Un schéma équilibre pour les écoulements a surface libre instationnaires avec bathymétrie. *Thèse de Doctorat - Université Bordeaux 1* 1996;
- [104] Leendertse RC. A new approach to three-dimensional free surface flow modelling. *Rep. R-3712-NETH/RC* 1989; Rand Corporation, Santa Monica.
- [105] Le Méhauté B. On the non-saturated breaker theory and the wave run-up. *Proc. 8th Coastal Engineering Conf.* 1962:77–92.
- [106] Leroux AY. Discrétisation des termes sources raides dans les problèmes hyperboliques. In: *Systèmes hyperboliques: nouveaux schémas et nouvelles applications. Ecoles CEA-EDF-INRIA 'Problèmes non-linéaires appliqués', INRIA (France)* 1998. Available from: <http://www-gm3.univ-mrs.fr/~leroux/publications/ay.leroux.html>.
- [107] Leveque RJ. Balancing source terms and flux gradients in high resolution Godunov methods: the quasi-steady wave-propagation algorithm. *J. Comp. Phys.* 1998; **146**:346–365.
- [108] Leveque RJ. *Finite volume methods for hyperbolic problems*, Cambridge Univ. Press, 2002.
- [109] Leveque RJ, Yee HC. A study of numerical methods for hyperbolic conservation laws with stiff source terms. *J. Comp. Phys.* 1990; **86**:187–201.
- [110] Levermore D, Sammartino M. A shallow water model with eddy viscosity for basins with varying bottom topography. *Nonlinearity* 2001; **14**(5):1493–1515.

- [111] Lin CK. Potential flow for the compressible viscous flow and its incompressible limit. *Indiana univ. Math. J.* 2000; **49**(4):1539–1561.
- [112] Lions PL, Mercier B. Splitting algorithms for the sum of two nonlinear operators. *SIAM J. Numer. Anal.* 1979; **16**(6):964–979.
- [113] Lions PL. Mathematical topics in fluid mechanics, Tome 1 : Incompressible models. *Oxford Lecture Series in Mathematics and Applications*, Oxford University Press, New York 1996.
- [114] Lions PL. Mathematical topics in fluid mechanics, Tome 2 : Compressible models. *Oxford Lecture Series in Mathematics and Applications, Vol 3*, Oxford University Press, New York 1996.
- [115] Liu PL-F, Cho YS, Briggs MJ, Kanoglu U, Synolakis CE. Runup of solitary waves on a circular island. *J.Fluid. Mech* 1995; **302**:259–285.
- [116] Liu PL-F. *Model equations for wave propagation from deep to shallow water*, Springer: Berlin, 1997. In *Advances in coastal engineering, vol. 1* Liu PL-F, 2000.
- [117] Liu PL-F, Woo SB, Cho YS. Computer programs for Tsunami Propagation and Inundation. *Technical Report, Cornell University, Ithaca, New York* 1998.
- [118] Liu PL-F, Synolakis CE, Yeh HH. Report on the international workshop on long-wave run-up. *J. Fluid Mech.* 1991; **229**:675–688.
- [119] Liu PL-F, Wu TR, Raichlen F, Synolakis CE, Borrero JC. Run-up and run-down generated by three dimensional sliding masses. *J. Fluid Mech.* 2005; **536**:107–144.
- [120] Lynch DR, Gray WG. Finite Element Simulation of Flow in Deforming Regions. *J. Comput. Phys.* 1980; **36**:135–153.
- [121] Lynett PJ, Wu TS, Liu PLF. Modeling wave runup with depth-integrated equations. *Coastal Engineering* 2002; **46**:89–107.
- [122] MacMahan J, Thornton E, Stanton T, Reniers A, Dean R. Ripex : Rip current pulsation measurements. *Coastal Engineering : Solving coastal conundrums* 2002; 736–746.
- [123] Madsen PA, Sorensen OR, Schäffer HA. Surf zone dynamics simulated by a Boussinesq model. Part 1. Model description and cross shore motion of regular waves. *Coastal Engineering* 1997; **32**:255–287.
- [124] Marche F. Derivation of a new two-dimensional viscous shallow water model with varying topography, bottom friction and capillary effects. Preprint, submitted to *European. J. Mech. B/Fluids*.
- [125] Masella JM, Faille I, Gallouet T. On an approximate Godunov scheme. *Int.J.Comp.Fluid.Dyn.* 1999; **12**:133–149.
- [126] Miglio E, Saleri F. An existence and uniqueness result for the 3D shallow water equation. *Di-partimento Di Matematica Politecnico di Milana. N 421/P* 2000;
- [127] Mingham CG, Causon DM. High resolution finite volume method for shallow water flows. *J. Hydr. Eng.* 1998; **124**:605–614.
- [128] Nadaoka K, Hino M, Koyano Y. Structure of the turbulent flow field under breaking waves in the surf zone. *J. Fluid Mech.* 1989; **204**:359–387.
- [129] Okayasu A. Characteristics of turbulence structure and undertow in the surf zone. *Ph.D. Dissertation, Department of Civil Engineering, University of Tokyo*, 1989.
- [130] Orona P. Un théorème d'existence de solutions d'un problème de shallow water. *Arch. Rat. Mech. Anal.* 1995; **130**(2):183–204.
- [131] Özkan-Haller HT, Kirby JT. A Fourier-Chebyshev collocation method for the shallow water equations including shoreline runup. *Appl. Ocean Res.* 1997; **19**:21–34.
- [132] Packwood A, Peregrine DH. The propagation of solitary waves and bores over a porous bed. *Coast. Eng.* 1980; **3**(3):221–242.
- [133] Pedloski J. *Geophysical Fluid Dynamics*, Springer Verlag, 1987.
- [134] Peraire J, Zienkiewicz OC, Morgan K. Shallow water problems: a general explicit formulation. *Int. J. Numer. Meth. Engrg* 1986; **22**:547–574.

- [135] Peregrine DH. Large-scale vorticity generation by breakers in shallow and deep water. *Eur. J. Mech. B/Fluids* 1999; **18**(2):403–408.
- [136] Peregrine DH. Breaking Waves On Beaches. *Ann. Rev. Fluid. Mech.* 1983; **15**:149–178.
- [137] Peregrine DH, Patterson MD, Bokhove O. Large eddies and vorticity in the surf and swash zone. *SASME Book of Abstracts* 2000.
- [138] Perthame B, Qiu Y. A variant of Van Leer method for multidimensional systems of conservation laws. *J. Comput. Phys.* 1994; **112**(2):370–381.
- [139] Ponce VM, Yabusaki SB. Modeling circulation in depth-averaged flow. *J. Hydr. Div. Proc. ASCE* 1981; **107**:1501–1517.
- [140] Prasad RS, Svendsen IA. Moving shoreline boundary condition for nearshore models. *Coastal Engineering* 2003; **49**:239–261.
- [141] Priestley A. Roe-type schemes for super-critical flows in rivers. *Numer. Anal. Report 13/89, Reading University* 1989;
- [142] Rajar R. Mathematical simulation of dam-break flow. *J. Hydr. Div. ASCE* 1978; **104**:1011–1026.
- [143] Raubenheimer B, Guza RT, Elgar S, Kobayashi N. Swash on a gently sloping beach. *J. Geophys. Res.* 1995; **100**:8751–8760.
- [144] Raubenheimer B, Guza RT, Elgar S. Wave transformation across the inner surf zone. *J. Geophys. Res.* 1996; **101**:25589–25597.
- [145] Roe PL. Approximate Riemann solvers, parameter vectors and difference schemes. *J. Comput. Phys.* 1981; **43**:357–372.
- [146] Roe PL. Upwind differenced schemes for hyperbolic conservation laws with source terms. *Proc. of the Conf. on Hyperbolic Problems* 1986; Springer-Verlag, New York.
- [147] Russo G. Central schemes for balance laws. *Hyperbolic problems: theory, numerics, applications. Vol I, II* 2000; Internat. Ser. Numer. Math., 140–141, Birkhauser, Basel:821–829.
- [148] de Saint Venant AJC. Théorie du mouvement non-permanent des eaux, avec application aux crues des rivières et à l'introduction des marées dans leur lit, *C.R. Acad. Sc. Paris* 1871; **73**:147–154.
- [149] Ferrari S, Saleri F. A new two dimensional shallow water model including pressure effects and slow varying bottom topography, *M2AN* 2004; **38**:211–234.
- [150] Schäffer HA, Madsen PA, Deigaard R. A Boussinesq model for waves breaking in shallow water. *Coastal Engineering* 1993; **20**:185–202.
- [151] Seguin N. Génération et validation de Rozavel, un code équilibre en hydraulique 2D. *Memoire de DEA. Université Bordeaux 1*, 1999.
- [152] Shapiro R. Smoothing, filtering and boundary effects. *Rev. Geophys.* 1970; **8**:359–387.
- [153] Shi F, Sun A. A variable boundary model for storm surge flooding in generalized curvilinear grids. *Int. J. Numer. Meth. Fluids* 1995; **21**:641–651.
- [154] Shuto N. Run-up of long waves on a sloping beach. *Coastal Engineering in Japan* 1967; **10**:23–38.
- [155] Shuto N, Goto T. Numerical simulation of tsunami run-up. *Coastal Engineering in Japan* 1967; **21**:13–20.
- [156] Short A. Rip current type, spacing and persistence, narrabeen beach, australia. *Marine Geology* 1985; **65**:103–137.
- [157] Simon J. Compact set in the space  $L^p(0, t; B)$ . *Ann. Mat. Pura appl.* 1987; **146**(4):65–96.
- [158] Simon J. Nonhomogeneous viscous incompressible fluids : existence of velocity, density and pressure. *SIAM J. Math. Anal.* 1990; **21**(5):1093–1117.
- [159] Sorensen OR, Schäffer HA, Madsen PA. Surf zone dynamics simulated by a Boussinesq type model. Part III. Wave-induced horizontal nearshore circulation. *Coast. Eng.* 1998; **33**:155–176.
- [160] de Saint Venant AJC. Théorie du mouvement non-permanent des eaux, avec application aux crues des rivières et à l'introduction des marées dans leur lit. *C.R. Acad. Sc. Paris* 1871; **73**:147–154.

- [161] Stocker JJ. *Water Waves*, Interscience: New York, 1957
- [162] Strang G. On the construction and comparison of difference schemes. *SIAM J. Numer. Anal.* 1968; **5**(3):506–517.
- [163] Sundbye L. Global existence for the Dirichlet problem for the viscous shallow water equations. *J. Math. Anal. Appl.* 1996; **202**(1):236–258.
- [164] Svendsen IA, Madsen PA, Hansen JB. Wave characteristics in the surf zone. *Proc. 16th Coastal Engineering Conf.*:520–539.
- [165] Svendsen IA, Petrevu U. Surf-zone hydrodynamics. *Advances in coastal and ocean engineering, Vol 2, World Scientific*, 1996.
- [166] Synolakis CE. The runup of solitary waves. *J. Fluid Mech.* 1987; **185**:523–545.
- [167] Tanaka T, Ono Y, Ishise T. The open boundary value problems in ocean dynamics by finite elements. *Finite Elements In Water Resources* 1980; **5**:47–63.
- [168] Thacker WC. Some exact solutions to the nonlinear shallow-water wave equations. *J. Fluid Mech.* 1981; **107**:499–508.
- [169] Titov VV, Synolakis CE. Numerical modelling of tidal wave run-up. *J. Wat. Port. Coast. Ocean Eng.* 1998; **124**(4):157–171.
- [170] Toro EF. *Riemann Solvers and Numerical Methods for Fluid Dynamics*, Springer: Berlin, 1997.
- [171] Toro EF. The weighted average flux method applied to the time-dependant Euler equation. *Phil. Trans. Roy. Soc. Lond. A* 1992; **341**:499–530.
- [172] Toro EF. Riemann problems and the WAF method for solving the two-dimensional shallow water equations. *Phil. Trans. Roy. Soc. Lond. A* 1992; **338**:43–68.
- [173] Toro EF, Brown RE. The WAF method and splitting procedure for viscous shocked flows. *Phil. Trans. Roy. Soc. Lond. A*[a retrouver] **338**:43–68.
- [174] Davis TA. UMFPACK Version 4.3. User Guide. Available on <http://www.cise.uft.edu/research/sparse/umfpack>
- [175] Van Dongeren AR, Svendsen IA. Absorbing-Generating Boundary Condition for shallow water models. *J. Waterw. Port Coast. Ocean Eng.* 1997; **123**(6):303–313.
- [176] Van Leer B. Toward the ultimate conservative difference scheme V. A second order sequel to Godunov's method. *J. Comp. Phys.* 1979; **32**:101–136.
- [177] Van Leer B. On the relation between the upwind the upwind-differencing schemes of Godunov, Engquist-Osher and Roe. *SIAM J.Sci.Stat.Comp.* 1984; **5**:1–20.
- [178] Vazquez-Cendon ME. Improved treatment of source terms in upwind schemes for the shallow water equations in channels with irregular geometry. *J. Comp. Phys.* 1999; **148**:497–526.
- [179] Vincent S, Bonneton P, Caltagirone JP. Numerical modelling of bore propagation and run-up on sloping beach using a MacCormack TVD scheme. *J. of Hydr. Research* 2001; **39**:41–49.
- [180] Watanabe A. Numerical models of nearshore currents and beach deformation. *Coast. Eng. Japan* 1982; **25**:147–161.
- [181] Wei G, Kirby JT. A time-dependant numerical code for extended Boussinesq equations. *J. Waterw. Port Coast. Ocean Eng.* 1995; **120**:251–261.
- [182] Whitham GB. *Linear and nonlinear waves*, John Wiley and Sons Inc., New York; 1999.
- [183] Wu CS, Liu PLF. Finite element modeling of nonlinear coastal currents. *J. Waterw. Port Coast. Ocean Eng.* 1985; **111**(2):417–432.
- [184] Yanenko NN. *Méthodes à pas fractionnaires. Résolution de problèmes polydimensionnels de physique mathématique*, Armand Colin, 1968.
- [185] Yang JY, Hsu CA. Computation of free surface flows part 2: two dimensional unsteady bore diffraction. *J.Hydr.Res.* 1993; **31**:403–414.
- [186] Yeh GT, Chou FK. Moving Boundary Numerical Surge Model. *J. Waterw. Port Coast. Ocean Div.* 1979; **105**:247–263.

- 
- [187] Zhao DH, Shen HW, Tabios III GQ, Lai JS, Tan WY. Finite volume two-dimensional unsteady-flow model for river basins. *J. Hydro. Eng.* 1994; **120**:863–882.
- [188] Zelt JA. Tsunamis: the response of harbors with sloping boundaries to long wave excitation. *Tech. Rep. KH-R-47* 1986; California Institute of Technology.
- [189] Zelt JA, Raichlen A. A Lagrangian model for wave-induced harbor oscillations. *J. Fluid Mech.* 1990; **213**:203–225.
- [190] Zhou JG, Causon DM, Mingham CG, Ingram DM. The surface gradient method for the treatment of source terms in the shallow-water equations. *J. Comp. Phys.* 2001; **168**:1–25.
- [191] Zoppou C, Roberts S. Catastrophic collapse of water supply reservoirs in urban areas. *J. Hydr. Eng.* 1999; **125**:686–695.
- [192] Zhouping X, Ping Z. On the uniqueness and large time behavior of the weak solutions to a shallow water equation. *Comm. Part. Diff. Equ.* 2002; **27**(9):1815–1844.